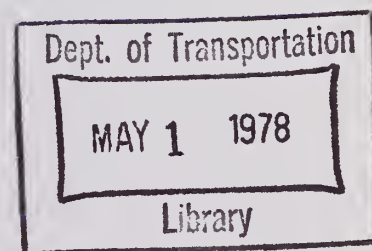


TE
662
.A3
no.
FHWA-
RD-
77-170

No. FHWA-RD-77-170

MINATION OF TOLERABLE FLAW SIZES IN FULL SIZE WELDED BRIDGE DETAILS



December 1977
Final Report

Document is available to the public through
the National Technical Information Service,
Springfield, Virginia 22161

Prepared for
FEDERAL HIGHWAY ADMINISTRATION
Offices of Research & Development
Washington, D. C. 20590

FOREWORD

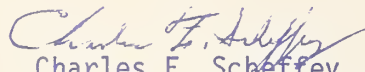
Recent fractures of steel bridges in the United States, along with the current trend of designing welded details with thick high-strength steel has prompted FHWA to sponsor this project. This contract is to determine the tolerable flaw size of typical weldments used in bridges. The smallest tolerable crack, which is stable in a particular weldment at the lowest service temperature, is needed to determine the degree of inspection sophistication and frequency necessary to insure the fracture safety of the structure.

Twenty-four full size beams with welded details were fabricated from A36, A588, and A514 steels which met the 1975 AASHTO toughness specifications. The types of details tested were cover-plated beams, lateral attachments, transverse stiffeners, and flange transitions. These beams were cyclically loaded at room temperature for at least 2 million cycles and then at temperatures -40°F (-40°C) and lower until rapid fracture occurred.

The second part of the study was a detailed material characterization. Materials from which these beams were fabricated were evaluated using several fracture toughness tests.

The third part was an analytical treatment of crack shapes, which were likely to be encountered during the beam tests.

This report contains the results and discussion of the beam tests and the material characterization. Also included, is a description of the tests and testing procedures.



Charles F. Scheffey
Director, Office of Research

1. Report No. FHWA-RD-77-170	2. Government Accession No.	3. Recipient's Catalog No.	
4. Title and Subtitle Determination of Tolerable Flaw Sizes in Full Size Welded Bridge Details		5. Report Date December 1977	6. Performing Organization Code
7. Author(s) R. Roberts, J. W. Fisher, G. R. Irwin, K. D. Boyer, H. Hausammann, G. V. Krishna, V. Morf, R. E. Slockbower		8. Performing Organization Report No.	
9. Performing Organization Name and Address Fritz Engineering Laboratory Lehigh University Bethlehem, PA 18015		10. Work Unit No. 35F2-132	11. Contract or Grant No. DOT-FH-11-8271
12. Sponsoring Agency Name and Address Federal Highway Administration Office of Research Washington, DC 20590		13. Type of Report and Period Covered Final Report December 1973-December 1977	
15. Supplementary Notes FHWA's Contract Manager for this study is J. Nishanian (HRS-11)		14. Sponsoring Agency Code	
16. Abstract Twenty-four full size beams with welded details and three welded gusset details were fabricated from A36, A588 and A514 steels which met the 1975 AASHTO toughness specifications. The types of beam details tested were cover-plated beams, lateral attachments, transverse stiffeners, and flange transitions. These beam and gusset details were cyclically loaded at room temperature for 2 million cycles and then at temperatures -40°F (-40°C) and lower until rapid fracture occurred. The fracture resistance of each beam and gusset was estimated using Linear Elastic Fracture Mechanics and compared to the material toughness test results. Current material toughness and fatigue specifications were also checked for applicability to full scale beams. Results of the beam and gusset fracture resistance estimations were in direct correlation with the slow bend (one second loading), 3 point bend, material tests. The residual stresses had a significant contribution to the fracture resistance estimation. Category E of the current AASHTO fatigue specifications was found to be applicable to the 12 in. (304.8 mm) flange attachment. However, this category was observed to overestimate the fatigue strength of the full size cover-plated beams. Categories B and C were found to be applicable to the flange transition and transverse stiffener details, respectively. At the time of fracture most of the fatigue life of the welded girders was exhausted. All beams except those with cover-plated details equaled or exceeded their design fatigue life before brittle fracture occurred. These tests confirm the necessity of an adequate fatigue design in any fracture control plan for bridges.			
17. Key Words Fracture, Fatigue, Bridge Steel, AASHTO CVN Requirements, AASHTO Fatigue Rules.		18. Distribution Statement No restrictions. This document is available to the public through the National Technical Information Service, Springfield, Virginia 22161.	
19. Security Classif. (of this report) Unclassified	20. Security Classif. (of this page) Unclassified	21. No. of Pages 427	22. Price

ACKNOWLEDGMENTS

This investigation is part of Fritz Laboratory research project No. 399, a study of the tolerable flaw sizes in full size welded bridge details, sponsored by the Federal Highway Administration. The testing was accomplished at Fritz Engineering Laboratory, Lehigh University. Dr. Lynn S. Beedle is the Director of Fritz Laboratory, and Dr. David A. VanHorn is the Chairman of the Civil Engineering Department.

Appreciation is expressed to the staff of Fritz Engineering Laboratory; namely R. R. Dales and K. R. Harpel and the technical staff who helped plan, set up and run the beam tests; to H. T. Sutherland and R. Longenbach, who helped with instrumentation, to R. Grimes, who typed the manuscript; to J. M. Gera, D. Wiltraut, and R. Troxell, draftsmen; and to R. N. Sopko, photographer.

TABLE OF CONTENTS

	<u>Page</u>
ABSTRACT	
1. INTRODUCTION	1
2. DESCRIPTION OF BEAM TESTS	5
2.1 Test Specimens	5
2.2 Test Setup	6
2.3 Instrumentation	7
2.4 Cooling Apparatus and Enclosure	8
2.5 Design Stresses	9
2.5.1 Lateral Attachment Details	9
2.5.2 Cover Plate Details	10
2.5.3 Flange Transition Details	10
2.5.4 Transverse Stiffener Details	11
2.6 Load and Deflection Control	11
2.7 General Testing Procedure	12
2.8 Fatigue Testing	13
2.9 Fracture Testing	15
3. MATERIALS CHARACTERIZATION	90
3.1 Test Plan	90
3.2 Charpy V-Notch Impact Tests and NDT	90
3.3 Fracture Toughness Measurements	91
3.3.1 Drop Weight Test Apparatus	91
3.3.2 Slow Bend Test Apparatus	92

	<u>Page</u>
3.3.3 K_c Specimen Preparation	93
3.3.4 Fracture Toughness Data Evaluation	93
3.4 Drop Tear Energy Measurements	95
3.5 Results of Fracture Tests	95
3.5.1 Charpy V-Notch Tests	95
3.5.2 K_c Test Results	96
3.5.3 Drop Tear Energy Test Results	98
3.6 Discussion of Test Results	99
4. LATERAL ATTACHMENT BEAM TEST RESULTS AND ANALYSIS	126
4.1 Fatigue Cracks	126
4.2 Remaining Fatigue Life	127
4.3 Beam Fracture Tests	128
4.4 Fracture Test Variables Affecting Fracture Toughness	133
4.5 Stress Intensity Estimates	134
4.5.1 Introduction	134
4.5.2 Contribution from the Applied Stress	135
4.5.3 Contributions from Stress Concentration	138
4.5.4 Contribution from the Nominal Residual Stresses	141
4.5.5 Contribution from the Local Weld Residual Stresses	142
4.5.6 Contribution from the Web Restraint	144
4.5.7 Summary and Discussion of the Various Contributions	144

	<u>Page</u>
5. COVER PLATE BEAM TEST RESULTS AND ANALYSES	182
5.1 Fatigue Cracks	182
5.2 Fatigue Life	182
5.3 Beam Fracture Tests	184
5.4 Stress Intensity Estimates for Cover Plate Details	187
5.4.1 Introduction	187
5.4.2 Contribution from the Applied Stress	189
5.4.3 Contribution from the Stress Concentration	190
5.4.4 Contribution from the Nominal Residual Stresses	191
5.4.5 Contribution from the Local Weld Residual Stresses	192
5.4.6 Summary and Discussion of the Various Contributions	192
6. FLANGE TRANSITION TEST RESULTS AND ANALYSIS	216
6.1 Fatigue Cracks	216
6.2 Fatigue Life	216
6.3 Beam Fracture Tests	217
6.4 Stress Intensity Estimates for Flange Transition Details	221
6.4.1 Introduction	221
6.4.2 Contribution from the Applied Stress	221
6.4.3 Contribution from Stress Concentration	222
6.4.4 Contribution from the Nominal Residual Stress	223
6.4.5 Contribution from the Local Weld Residual Stress	224
6.4.6 Summary and Discussion of the Various Contributions	224

	<u>Page</u>
7. TRANSVERSE STIFFENER TEST RESULTS AND ANALYSIS	239
7.1 Fatigue Cracks	239
7.2 Fatigue Life	239
7.3 Beam Fracture Tests	240
7.4 Stress Intensity Estimate for Transverse Stiffener Details	243
7.4.1 Introduction	243
7.4.2 Contribution from the Applied Stress	244
7.4.3 Contribution from the Stress Concentration	246
7.4.4 Contribution from the Nominal Residual Stresses	248
7.4.5 Contribution from the Local Weld Residual Stresses	249
7.4.6 Summary and Discussion of the Various Contributions	249
8. COMPARISON OF BEAM K ESTIMATES AND MATERIAL K_c TESTS	264
8.1 Lateral Attachment Details	264
8.2 Cover Plate Details	265
8.3 Flange Transition Details	267
8.4 Transverse Stiffener Details	268
9. GUSSET PLATE TESTS	282
9.1 Introduction	282
9.2 Description of Tests	282
9.2.1 Test Specimens	282
9.2.2 Preloading	283
9.2.3 Fatigue Testing	284

	<u>Page</u>
9.2.4 Fracture Testing	284
9.3 Test Results	285
9.3.1 Fatigue and Fracture Test	285
9.3.2 Stress Intensity Estimates	287
9.3.2.1 Contribution from Applied Stress	287
9.3.2.2 Contribution from Residual Stress	288
9.3.2.3 Summary and Discussion of Contributions	288
9.4 Comparison of Gusset Plate K Estimates with Material K_c Tests	289
9.5 Conclusions	289
10. CONCLUSIONS	302
11. REFERENCES	308
12. APPENDIXES	311
Appendix A - Web Restraint	312
Appendix B - Residual Stress Measurements	323
Appendix C - Material Tests	364
Appendix D - Stress Intensity Estimate	407
Appendix E - Nomenclature	416

ABSTRACT

Twenty-four full size beams with welded details were fabricated from A36, A588 and A514 steels which met the 1975 AASHTO toughness specifications. The types of details tested were cover-plated beams, lateral attachments, transverse stiffeners, and flange transitions. These beams were cyclically loaded at room temperature for at least 2 million cycles and then at temperatures -40° F (-40° C) and lower until rapid fracture occurred. The fracture resistance of each beam was estimated using Linear Elastic Fracture Mechanics and compared to the material toughness test results. Current material toughness and fatigue specifications were also checked for applicability to full scale beams.

Results of the beam fracture resistance estimations were in direct correlation with the slow bend (one second loading), 3 point bend, material tests. The residual stresses had a significant contribution to the fracture resistance estimation.

Category E of the current AASHTO fatigue specifications was found to be applicable to the 12 in. (304.8 mm) flange attachment. However, this category was observed to overestimate the fatigue strength of the full size cover-plated beams. Categories B and C were found to be applicable to the flange transition and transverse stiffener details, respectively. At the time of fracture most of the fatigue life of the welded girder was exhausted. All beams except those with cover-plated details equaled or exceeded their design

fatigue life before brittle fracture occurred. These tests confirm the necessity of an adequate fatigue design in any fracture control plan for bridge girders.

1. INTRODUCTION

Recent fractures of steel bridges in the United States, along with the current trend of designing welded details with thick high-strength steel has prompted FHWA to sponsor this project, entitled "Determination of Tolerable Flaw Sizes in Full Size Bridge Weldments." The scope and objectives as stated in the contract are: This contract is to determine the tolerable flaw size of typical weldments used in bridges. The smallest tolerable crack which is stable in a particular weldment at the lowest service temperature is needed to determine the degree of inspection sophistication and frequency necessary to insure the fracture safety of the structure. The complex state of stress and metalurgical gradients associated with most welded joints render accurate analytical evaluation of tolerable flaw sizes difficult. Therefore, the major thrust of this contract is to be an experimental fracture test program of full size bridge weldments. A parallel analytical study is also to be performed to provide estimates of tolerable flaw sizes for weld details similar to those tested.

A welded detail can be considered as a region of material with very small or microscopic flaws. These microscopic flaws can become macroscopic cracks after repeated application of load. The major factors affecting the development of the macroscopic cracks and the eventual fatigue life of a welded bridge member are the stress range, the stress concentration, and the initial flaw condition^{1,2}. In addition, the fabrication of a welded detail can result in significant

residual stresses. These residual stresses have large tensile components in or near the welds. This, in combination with the complex stress concentration and macroscopic fatigue flaws, can make welded details susceptible to rapid fracture. This is especially true of those details fabricated with thick high-strength steel.

This project consisted of three major parts. The first was the fatigue and fracture testing of 24 full-size welded beam specimens with details which are commonly used in bridge design. The details were chosen from the AASHTO categories for fatigue design³. Two Category E details were chosen along with a Category C and B detail. For the E details, the cover plate and the lateral attachment were used. The intermediate Category C detail was the transverse stiffener. The flange thickness transition, a Category B detail, provided the upper bound fatigue strength detail. Six beams were fabricated for each of the four detail categories. Each detail type was fabricated in three ASTM grades of steel, A36, A588 and A514. A list of the details is shown in Table 1.1. Also included in the portion of the research were fatigue and fracture tests of three gusset details.

The second part of the study was a detailed material characterization. Materials from which these beams were fabricated were evaluated using several fracture toughness tests.

The third part was an analytical treatment of crack shapes which were likely to be encountered during the beam tests. This work is described in a report by Irwin and Tada⁴. The results of this study were used in estimations of the critical stress intensity factor for

the fracture of each beam. Judgment decisions were unavoidable in order to cope with certain geometrical and stress distribution complexities as discussed in Section 4.

This report contains the results and discussion of the beam tests and the material characterization. Also included is a description of the tests and testing procedures.

Although the investigation was not planned for the purpose of measuring the influence of dimensional size on fatigue life, the information collected permits comments on that topic.

TABLE 1.1 LIST OF TEST BEAMS

Detail Type	Beam Numbers			
	Steel Type	A36	A588	A514
Lateral Attachment		B4	B6	B2
Category E		B4A	B6A	B2A
Cover Plate		B3*	B5*	B1
Category E		B3A*	B5A*	B1A
Transverse Stiffener		B9	B11	B7
Category C		B9A	B11A	B7A
Flange Transition		B10	B12	B8
Category B		B10A	B12A	B8A

* Rolled Beams, all others welded

24 Beams - Total

2. DESCRIPTION OF BEAM TESTS

2.1 Test Specimens

The 24 beam specimens outlined in Table 1.1 were fabricated by the Bethlehem Steel Corporation at their Bridge Division Fabrication Plant in Pottstown, Pennsylvania. All specimens were fabricated using current fabrication and inspection techniques.

Each thickness of material was furnished from the same heat for each of the three types of steel. As beam components and material testing samples were flame cut from the larger rolled plates, a cutting schedule was maintained (see Fig. 2.8).

After the beam components were cut to size, the edges of the web plate were blast cleaned. The web and flange components were then assembled in a beam welder and the web to flange longitudinal fillet welds were then made by an automatic submerged-arc process. These welds were kept continuous. Any visible flaw such as excessive porosity was gouged out and rewelded.

The lateral attachment plates, cover plates, and transverse stiffeners were connected after the cross-section was completed. The groove weld lateral attachment plates were welded by a semi-automatic submerged arc process. The run-out tabs were then ground to an approximate radius of 0.75 in. (19.1 mm). The transverse fillet welds at the overlapped lateral attachment plate were made manually.

For each type of steel, ASTM A36, A588 Gr50, and A514, two beams were fabricated for each type of detail. A detailed drawing of a beam specimen with lateral attachments (Beam B4) is shown in Fig. 2.1a. Note that Beams B2 and B2A have smaller flange dimensions which were necessary to satisfy the jack capacity.

The A36 and A588 cover-plated beams were rolled sections, W36X260 and W36X230 respectively, and the A514 was a built-up member. Each beam had two details, one with a transverse end weld and one without a transverse end weld. Detailed drawings of Beams B3 and B1 are shown in Figs. 2.1b and 2.1c. The measured beam dimensions are summarized in Table 2.1.

The flange transition and transverse stiffener beam specimens, Beam B10 (flange transition) and Beam B9A (transverse stiffener) are shown in Figs. 2.1d and 2.1e, respectively. Beams B7, B7A, B8, and B8A had smaller flange dimensions which were necessary to satisfy jack capacity. The flange transitions were welded prior to connecting the web and flange. The transverse stiffener details for Beams B9A, B11A, and B7A were welded to the bottom flange, while the stiffener details for Beams B9, B11, and B7 were terminated 0.5 in. (12.7 mm) short of the bottom flange.

2.2 Test Setup

All beam testing was done on the dynamic test bed in Fritz Engineering Laboratory, Lehigh University. The test span length was

21 ft. (6.40 m) for all the beams except Beams B7 and B7A. The test span for these beams was 23 ft. (7.01 m). Two 110 kip (489.5 kN) Amsler jacks driven by a single pulsator were used for the 260 cpm (4.3 Hz) cyclic load. A constant load jack was also used when needed to raise the level of maximum stress.

The constant load jack was a 200 kip (890 kN) Parker-Hannifin jack loaded with an Amsler accumulator and maintained by a column of nitrogen. A schematic of the loading setup and geometry is shown in Fig. 2.2. Photographs of the setup are shown in Figs. 2.3 and 2.5.

2.3 Instrumentation

SR-4 strain gages were used extensively to control the strain during the fatigue and fracture tests. Also, electrical resistance temperature gages were used to monitor the beam's temperature.

Four electrical resistance strain gages were mounted on the tension flange and used as strain control when determining the beam deflections and loads. Two gages on the compression flange were used as a lateral buckling indicator. Since the strain gages were mounted close to the section to be cooled, temperature compensation plates were used to counteract thermal effects. The position of these gages is shown in Fig. 2.4 for the lateral attachment beam specimens. The cover plate beam specimens used a similar strain gage layout.

Initially, temperature gages were mounted directly on the steel beam at the critical section. After two fracture tests, it was

found that the same surface temperature readings could be obtained by attaching the gages to steel plates, 0.06 in. x 1.5 in. x 1.5 in. (1.6 mm x 38.1 mm x 38.1 mm) and clamping these plates to the critical section of the beam. This procedure was very economical, since one gage could be reused for several tests. Usually three to five temperature gages were used on one beam section during a fracture test on the lateral attachment beam specimens. The position of these gages is also shown in Fig. 2.4. The cover plate beam fracture tests utilized only two temperature gages at the end of each cover plate on the outer flange surface.

To eliminate air temperature effects, the outer surface of the plates was covered with a 0.5 in. (12.7 mm) thick styrofoam insulation. The gages were positioned to avoid direct liquid nitrogen contact to assure accurate surface temperature.

2.4 Cooling Apparatus and Enclosure

Each beam was cooled from room temperature to a desired temperature with liquid nitrogen. The section or sections of the beam to be cooled were completely enclosed in a styrofoam box. The boxes were made relatively leak-proof by the use of sealing compound and duct tape. Inside each box was a copper tubing network which sprayed the top and both sides of the beam with liquid nitrogen.

Since cold gaseous nitrogen is heavy, the cold gas had a tendency to settle to the bottom of the cooling box. Without convective flow, this would cause a sharp temperature gradient across the beam

section. Therefore, the inlet for the nitrogen was placed at the top of the beam. Connected to this inlet was a pressurized dewar of liquid nitrogen. By regulating the pressure within this container, the temperature in the box could be controlled.

An attempt was made to achieve uniform temperature throughout the beam cross-section. Since most of the nitrogen still in its liquid state remained in a tray at the bottom of the box, trays were also placed in the upper section of the box. This device made temperatures noticeably more uniform across the section being cooled. A sketch and photographs are shown in Figs. 2.2 and 2.5.

2.5 Design Stresses

In accordance with the 1974 Interim Specifications, the lateral attachment details and the cover plate details are classified as Category E. The allowable stress range for these types of details for two million design cycles is 8 ksi (55.2 MPa). The flange transition details are classified as Category B with an allowable stress range of 18 ksi (124.2 MPa) and the transverse stiffener details are classified as Category C with an allowable stress range of 13 ksi (89.7 MPa) for two million cycles.

2.5.1 Lateral Attachment Details

Each beam had two different lateral attachment details as illustrated in Fig. 2.1a. One was an overlapped, 12 in. (304.8 mm) long attachment with transverse fillet welds on the inside of the

tension flange, and a longitudinal fillet weld along the beam flange-tip. The other was a 12 in. (304.8 mm) long, groove weld attachment welded to the flange-tip. The 1 in. (25.4 mm) thick plate was flush with the outer surface of the flanges. The groove welded attachment had a sharp radius of about 0.75 in. (19.1 mm) where the reinforcement was removed by grinding at the weld ends.

The maximum stress was governed by the outermost fiber of the tension flange. The stress range was set on the inside of the tension flange. This yielded a nominal applied maximum stress and stress range at the overlapped fillet weld detail of $(0.9) \times (0.55 \sigma_{ys})$ and 8 ksi (56.2 MPa) respectively. At the groove weld attachment the maximum stress and stress range were $0.55 \sigma_{ys}$ and 9 ksi (62.1 MPa). These values were slightly different for Beams B2 and B2A. Actual values are shown in a schematic for each steel type in Figs. 2.6a, b and c.

2.5.2 Cover Plate Details

The maximum stress, $0.55 \sigma_{ys}$, and the stress range, 8 ksi were set on the outermost fiber of the tension flange at the cover plate ends. Actual values of these stresses are shown in Figs. 2.6d, e, and f for each steel type.

2.5.3 Flange Transition Details

The maximum stress, $0.55 \sigma_{ys}$, and the stress range, 18 ksi (124.2 MPa), were set at the outermost fiber of the thinner flange

transition plate. Actual values of the maximum stresses during the final fracture test are summarized in Figs. 2.6g, h, i, and j.

2.5.4 Transverse Stiffener Details

The maximum stress $0.55 \sigma_{ys}$, was set at the outermost fiber of the tension flange directly under the transverse stiffener spaced 6 in. (152.4 mm) from the loading stiffener. Actual values of the maximum stress during the final fracture test are shown in Figs. 2.6k, l, m, n, and o.

A stress range of 13 ksi (89.7 MPa) or 15 ksi (103.4 MPa) was set at the interior tension flange face for Beams B9A, B11A, and B7A and at the end of the transverse stiffener for Beams B9, B11, and B7. The maximum stress and the stress range were controlled at the same cross-section.

2.6 Load and Deflection Control

Deflection control was used during the fatigue testing at room temperature. The desired stresses were obtained by averaging the four strain gages mounted on the tension flange. For each stress, deflections were obtained from a pair of deflection gages placed on either surface of the tension flange. When the maximum and minimum stresses were set, an appropriate set of deflections was obtained. The beam was then loaded cyclically between these deflections. Therefore, load adjustments for inertia forces were not required.

The fracture test loading could not be deflection controlled since any small temperature gradient across the beam section may have caused misleading deflections. Therefore, the dynamic loads were noted during the fatigue testing and these loads were then used to control loading during the fracture tests. Dynamic stress measurements confirmed the adequacy of the procedure.

2.7 General Testing Procedure

The first beam tested, B4A, served as a pilot study. Initially 1.5 million cycles of load were applied at a stress range of 8 ksi (55.3 MPa) at the fillet weld detail and 9 ksi (62.1 MPa) at the groove weld detail. At this point the beam section containing the largest fatigue cracks was tested at -40° F (-40° C) for one-half hour. No fracture occurred and the beam was fatigue cycled for an additional 250,000 cycles, at which time another -40° F (-40° C) test was run. This fatigue and fracture test sequence was repeated until a fracture occurred.

Failure did not occur when the fatigue cracks were small and still in the stress concentration area. The fatigue cracks destroyed about 70% of the tension flange area before fracture occurred. This extended fatigue and fracture sequence took considerable time to complete as altogether eight test sequences were carried out. For these reasons the test procedure was modified on subsequent tests as follows.

Each subsequent beam was cyclically loaded for two million cycles or until the fatigue cracks became a possible critical size,

whichever occurred first. At this point each section of the beam containing the details was cooled to -40° F (-40° C). The beam was then cycled for at least one-half hour between a maximum stress of $0.55\sigma_{ys}$ and a minimum stress of $0.55\sigma_{ys} - \sigma_r$. If no visible fatigue cracks existed after two million cycles the fracture test was discontinued and further fatigue cycles applied at room temperature.

If there was a possible critical fatigue crack at the beginning of the first fracture test and no fracture occurred in the first one-half hour, either an extended test at -40° F (-40° C) was run or the temperature was dropped below -40° F (-40° C). This temperature drop was done slowly to obtain accurate surface temperature readings. This extended test was continued until fracture or until the liquid nitrogen supply was depleted. If there was no fracture, the beam was again fatigue cycled at room temperature to increase the crack size.

The next low temperature test was run on the detail with the largest fatigue crack after the crack had grown a predetermined amount. This fatigue and fracture test sequence was continued until a fracture occurred.

2.8 Fatigue Testing

The stress range used in the fatigue test was in accordance with the 1974 AASHTO allowable range of stress for two million cycles at the fillet welded attachment for a Category E detail. An allowable stress range of 8 ksi (55.2 MPa) is permitted for a Category E detail.

It was initially intended to fatigue cycle between the same minimum and maximum stress limits as in the fracture tests. However, this was discontinued after three tests for several reasons. First, operating the constant load jack under cyclic deflection for such extended periods caused excessive wear and heating which caused damage to the hydraulic ram. In addition, it appeared that fatigue cracking at room temperature at the limit of allowable stress could cause effects known as "warm prestressing"^{5,6}. Such effects, if present, could result in a greater apparent fracture resistant condition. The earlier studies by Fisher, et al.^{1,2} have demonstrated that the level of maximum stress has no appreciable affect on fatigue. Hence, in subsequent tests, the cyclic stress range was applied at a lower level of maximum stress.

During the fatigue test period, frequent checks were made for visible fatigue cracks. Mainly, visual inspections were made with a 10X magnifying glass and a cleaner fluid. At times a magnetic particle probe was also used. Since the cycling was continued twenty-four hours a day, some of the cracks were 1 in. (25.4 mm) corner cracks before they were discovered. Crack detection records can be found in Tables 2.3 through 2.26.

An automatic deflection controlled shut-off switch was used to prevent extremely large cracks from occurring before the scheduled fracture tests.

2.9 Fracture Testing

During the pilot study, the beam was tested at low temperatures after an initial 1.5 million cycles of loading. In subsequent tests, the initial fracture test was generally run after accumulating two million cycles of cyclic load. It was apparent that no brittle fracture would occur prior to this stage of testing as the fatigue cracks were small.

In preparation for the fracture test, the moveable temperature gage plates were clamped to the beam at various points around both beam sections to be cooled as shown in Fig. 2.4. The gages used for test control were placed at the crack planes on the exterior surface of the tension flange. Actual temperature gage placement is noted in Table 2.2. The cooling apparatus was then put in place and the styrofoam boxes were sealed. Most leakage was stopped during the initial cooling period. The temperature was monitored constantly and recorded every five minutes. When the temperature at the test control gages reached -40° F (-40° C), the liquid nitrogen flow was regulated to maintain the test temperature.

During the first fracture test, both beam sections containing the welded details were cooled simultaneously. By regulating the liquid nitrogen flow, the temperature in each box was kept relatively close, $\pm 5^{\circ}\text{ F}$ ($\pm 2.8^{\circ}\text{ C}$).

When the temperatures at the critical details became stable, cyclic loads were applied. Prior to applying the maximum allowable

stress of $0.55 \sigma_{ys}$ and the full design stress range level, the crack tip was marked by applying cyclic stresses between the limits of $0.55 \sigma_{ys} - \sigma_r$ and $0.55 \sigma_{ys} - \sigma_r/2$. This cyclically applied stress was continued for approximately thirty minutes, after which the full stress range was applied to the maximum nominal stress of $0.55 \sigma_{ys}$. In most cases, the initial set of dynamic loads yielded a minimum stress of $0.55 \sigma_{ys} - \sigma_r$ and a maximum stress of $0.55 \sigma_{ys}$. A load history for each beam is shown in Tables 2.3 through 2.26.

During each low temperature test, one of the tension flange strain gages was monitored on a memory oscilloscope. This trace showed both the sinusoidal loading rate and the fracture point. the triggering at failure was manual, only one trace was obtained at fracture and is shown in Fig. 2.7.

A sinusoidal loading rate of 260 cpm (4.3 Hz) was provided by the Amsler pulsator. This resulted in a loading rate of about 0.12 sec. from the minimum stress to maximum stress level. The sinusoidal nature of the cyclic load yielded a maximum loading rate of 100 ksi/sec. (690 MPa/sec.). As can be seen in Fig. 2.7 the fracture occurred at a point approximately 95% of the maximum load. This was typical of subsequent tests as well. However, the nominal maximum load will be used for the fracture analysis.

TABLE 2.1a CROSS-SECTIONAL PROPERTIES OF TEST BEAMS

Beam Number	Steel	Flange Width (in.)	Flange Thickness (in.)	Web Thickness (in.)	Total Depth (in.)	Nominal Moment of Inertia (in. ⁴)	Nominal Section Modulus (in. ³)
B2	A514	5.97	1.567	0.385	36.08	6482	360.1
B2A	A514	6.15	1.561	0.386	36.19	6482	360.1
B4	A36	6.97	2.019	0.375	35.98	9125	506.9
B4A	A36	7.00	2.016	0.375	35.91	9125	506.9
B6	A588	7.03	2.035	0.387	36.00	9125	506.9
B6A	A588	6.98	2.032	0.393	35.98	9125	506.9
B3	A36 W36X260	16.50	1.478	0.883	36.25	17300	952
B3A	A36 W36X260	16.56	1.493	0.867	36.25	17300	952
B5	A588 W36X230	16.41	1.234	0.780	35.94	15000	837
B5A	A588 W36X230	16.50	1.246	0.777	35.94	15000	837
B1	A514	5.94	1.570	.376	36.06	6482	360.1
B1A	A514	6.00	1.573	.376	36.09	6482	360.1

TABLE 2.1b CROSS-SECTIONAL PROPERTIES OF TEST BEAMS

Beam Number	Steel	Flange Width (mm)	Flange Thickness (mm)	Web Thickness (mm)	Total Depth (mm)	Nominal Moment of Inertia (cm ⁴)	Nominal Section Modulus (cm ³)
B2	A514	152	39.67	9.78	916	269,801	5901
B2A	A514	156	39.65	9.80	919	269,801	5901
B4	A36	177	51.28	9.53	914	379,811	8307
B4A	A36	178	51.21	9.53	912	379,811	8307
B6	A588	179	51.69	9.83	914	379,811	8307
B6A	A588	177	51.61	9.98	914	379,811	8307
B3	A36 W36X260	419	37.54	22.43	921	720,080	15645
B3A	A36 W36X260	421	37.92	22.02	921	720,080	15645
B5	A588 W36X230	417	31.34	19.81	913	624,347	13702
B5A	A588 W36X230	419	31.65	19.74	913	624,347	13702
B1	A514	151	39.88	9.55	916	269,801	5901
B1A	A514	152	39.95	9.55	917	269,801	5901

TABLE 2.1c CROSS-SECTIONAL PROPERTIES OF TEST BEAMS

Beam Number	Steel	Flange		Web		Total Depth (in)	Nominal Moment of Inertia (in ⁴)	Nominal Section Modulus (in ³)
		Width (in)	Thickness (in)	Thickness (in)	Thickness (in)			
B8	A514	6.00	1.567	0.386		36.06	6482	360.1
B8A	A514	6.00	1.568	0.389		36.09	6482	360.1
B10	A36	6.99	2.021	0.375		35.88	9125	506.9
B10A	A36	6.94	2.022	0.391		36.00	9125	506.9
B12	A588	7.02	2.025	0.397		35.97	9125	506.9
B12A	A588	7.06	2.030	0.389		35.97	9125	506.9
B7	A514	6.06	1.563	0.406		36.09	6482	360.1
B7A	A514	6.00	1.563	0.391		36.00	6482	360.1
B9	A36	7.00	1.999	0.394		35.92	9125	506.9
B9A	A36	6.96	2.000	0.400		36.00	9125	506.9
B11	A588	7.03	2.026	0.382		35.98	9125	506.9
B11A	A588	7.00	2.029	0.384		35.92	9125	506.9

TABLE 2.1d CROSS-SECTIONAL PROPERTIES OF TEST BEAMS

Beam Number	Steel	Flange		Web		Total Depth (mm)	Nominal Moment of Inertia (cm ⁴)	Nominal Section Modulus (cm ³)
		Width (mm)	Thickness (mm)	Thickness (mm)	Thickness (mm)			
B8	A514	152	39.80	9.80		916	269,801	5901
B8A	A514	152	39.83	9.88		917	269,801	5901
B10	A36	178	51.33	9.53		911	379,811	8307
B10A	A36	176	51.36	9.93		914	379,811	8307
B12	A588	178	51.44	10.08		914	379,811	8307
B12A	A588	179	51.56	9.88		914	379,811	8307
B7	A514	154	39.70	10.31		917	269,801	5901
B7A	A514	152	39.70	9.93		914	269,801	5901
B9	A36	178	50.77	10.01		912	379,811	8307
B9A	A36	177	50.80	10.16		914	379,811	8307
B11	A588	179	51.46	9.70		914	379,811	8307
B11A	A588	178	51.54	9.75		912	379,811	8307

TABLE 2.2a CROSS-SECTION TEMPERATURES AT FRACTURE
(Lateral Attachment Beams)

Beam Number	Order of Test	Temperatures at Fracture**							
		Bottom Flange T1 (°F)	Web Stiff. T2 (°F)	Top Flange T3 (°F)	Bottom Flange T4 (°F)	Top Flange T5 (°F)	Bottom Flange T6 (°F)	Web Stiff. T7 (°F)	Top Flange T8 (°F)
B2	6	-155*	-106	-102	-171	---	---	---	---
B2A	4	-61	-71	---	-144*	-67	---	---	---
B4	2	-80*	-59	-45	---	---	---	---	---
B4A	1	---	-40	---	-105/-96*	-36	---	---	---
B6	3	---	---	---	---	---	-53*	-19	-08
B6A	5	-43	-77	---	-90/-94*	-68	---	---	---

* Denotes test control gage at critical detail

** See Fig. 2.4 for gage locations

TABLE 2.2b CROSS-SECTION TEMPERATURES AT FRACTURE
(Lateral Attachment Beams)

Beam Number	Order of Test	Temperatures at Fracture**							
		Bottom Flange T1 (°C)	Web Stiff. T2 (°C)	Top Flange T3 (°C)	Bottom Flange T4 (°C)	Top Flange T5 (°C)	Bottom Flange T6 (°C)	Web Stiff. T7 (°C)	Top Flange T8 (°C)
B2	6	-104*	-77	-74	-113	---	---	---	---
B2A	4	-52	-57	---	-98*	-55	---	---	---
B4	2	-62	-51	-43	---	---	---	---	---
B4A	1	---	-40	---	-76/-71*	-38	---	---	---
B6	3	---	---	---	---	---	-47*	-28	-22
B6A	5	-42	-61	---	-68/-70*	-56	---	---	---

* Denotes test control gage at critical detail

** See Fig. 2.4 for gage locations

TABLE 2.3a LOAD HISTORY FOR BEAM B2 (A514)

Testing Event	ID *	Subtotal N	Cumm. N	Fracture Test Data					Fatigue Data	
				Detail Tested	No.	** Temp. °F	Fract. Temp. °F	σ_r ksi	σ_{max} ksi	σ_r ksi σ_{max} ksi
Fatigue	a	2,009,100	2,009,100							G 8.7 F 8.0
Fracture	b	10,000	2,019,100	F, G	1	-40		8.7	55.0	
								8.0	55.0	
	b	5,000	2,024,100	G	1	-130 to -155	-155	8.7	55.0	

* See fracture surface sketches for banding identification

F - Fillet welded detail

G - Groove welded detail

Steel type A514

** Temperatures at controlling gages

TABLE 2.3b LOAD HISTORY FOR BEAM B2 (A514)

Testing Event	ID *	Subtotal N	Cumm. N	Fracture Test Data						Fatigue Data	
				Detail Tested	No.	** Temp. °C	Fract. Temp. °C	σ_r MPa	σ_{max} MPa	σ_r MPa	σ_{max} MPa
Fatigue	a	2,009,100	2,009,100							G 60 F 55	179
Fracture	b	10,000	2,019,100	F,G	1	-40		60	379		
								55			
	b	5,000	2,024,100	G	1	-90 to -104	-104	60	379		

* See fracture surface sketches for banding identification

F - Fillet welded detail

G - Groove welded detail

Steel type A514

** Temperatures at controlling gages

TABLE 2.4a LOAD HISTORY FOR BEAM B2A (A514)

Testing Event	ID *	Subtotal N	Cumm. N	Fracture Test Data				Fatigue Data	
				Detail Tested	No.	** Temp. °F	Fract. Temp. °F	σ_r ksi	σ_{max} ksi
Fatigue	a	1,982,800	1,982,800					G 8.7 F 8.0	26.0 23.8
Fracture	b	15,000 ⁺		G	1	-40		4.3	50.6
				F	1	-40		4.0	46.4
		35,000	2,017,800	G	1	-40		8.7	55.0
				F	1	-40		8.0	50.4
Fracture	c	13,800 ⁺		G	2	-40		4.3	50.6
		55,000	2,072,800	G	2	-40		8.7	55.0
Fatigue	d	407,500	2,480,300					G 8.7 F 8.0	26.0 23.8
Fracture	e	12,500 ⁺		G	3	-40		4.3	50.6
		48,750	2,529,050	G	3	-40		8.7	55.0
Fracture	f	87,500	2,616,550	G	4	-40		8.7	55.0
Fatigue	g	180,400	2,796,950					G 8.7 F 8.0	26.0 23.8
Fracture	h	68,750	2,865,700	G	5	-40 to -144	-144	8.7	55.0

* See fracture surface sketches for banding identification

** Temperature at controlling gages

Steel Type - A514

G - Groove welded detail

F - Fillet welded detail

+ - Cycles for marking crack front

TABLE 2.4b LOAD HISTORY FOR BEAM B2A (A514)

Testing Event	ID *	Subtotal N	Cumm. N	Fracture Test Data				Fatigue Data	
				Detail Tested	No.	** Temp. °C	Fract. Temp. °C	σ_r MPa	σ MPa
Fatigue	a	1,982,800	1,982,800						
Fracture	b	15,000 ⁺		G	1	-40		30	349
				F	1	-40		28	320
		35,000	2,017,800	G	1	-40		60	379
				F	1	-40		55	348
Fracture	c	13,800 ⁺		G	2	-40		30	349
		55,000	2,072,800	G	2	-40		60	379
Fatigue	d	407,500	2,480,300						
Fracture	e	12,500 ⁺		G	3	-40		30	349
		48,750	2,529,050	G	3	-40		60	379
Fracture	f	87,500	2,616,550	G	4	-40		60	379
Fatigue	g	180,400	2,796,950						
Fracture	h	68,750	2,865,700	G	5	-40 to -98	-98	60	379

* See fracture surface sketches for banding identification

** Temperature at controlling gages

Steel type - A514

G - Groove welded detail

F - Fillet welded detail

+ - Cycles for marking crack front

TABLE 2.5a LOAD HISTORY OF BEAM B4 (A36)

Testing Event	ID *	Subtotal N	Cumm. N	Fracture Test Data						Fatigue Data	
				Detail Tested	No.	Nominal Temp. °F	Fract. Temp. °F	σ _r ksi	σ _{max} ksi	σ _r ksi	σ _{max} ksi
Fatigue	a	2,001,800	2,001,800							G 9.0 F 8.0	19.8 17.6
Fracture	b	10,000 ⁺		G	1	-40		4.5	15.3		
				F	1	-40		4.0	13.6		
				G	1	-40		9.0	19.8		
				F	1	-40		8.0	17.6		
Fatigue	c	299,200	2,308,500							G/F 9.0/8.0	19.8/17.6
Fatigue	d	36,700	2,345,200							G/F 6.0/5.3	15.0/13.3
Fracture	e	5,000 ⁺	2,369,700	G	2	-55		4.5	15.3		
		10,000		G	2	-70		9.0	19.8		
		14,500		G	2	-70	-80	9.8	19.8		

* See fracture surface sketches for banding identification

** Temperature at controlling gages

G - Groove welded detail

F - Fillet welded detail

+ - Cycles for marking crack front

Steel type - A36

TABLE 2.5b LOAD HISTORY OF BEAM B4 (A36)

Testing Event	ID *	Subtotal N	Cumm. N	Fracture Test Data						Fatigue Data	
				Detail Tested	No.	** Nominal Temp. °C	Fract. Temp. °C	σ_r MPa	σ_{max} MPa	σ_r MPa	σ_{max} MPa
Fatigue	a	2,001,800	2,001,800							G 62 F 55	137 121
Fracture	b	10,000 ⁺ 7,500	2,009,300	G	1	-40		31	105		
				F	1	-40		28	94		
				G	1	-40		62	137		
				F	1	-40		55	121		
Fatigue	c	299,200	2,308,500							G/F 62/55	137/121
Fatigue	d	36,700	2,845,200							G/F 41/37	103/92
Fracture	e	5,000 ⁺	2,355,200 2,369,700	G	2	-48		31	105		
		10,000		G	2	-57		62	137		
		14,500		G	2	-57	-62	68	137		

* See fracture surface sketches for banding identification

** Temperature at controlling gages

G - Groove welded detail

F - Fillet welded detail

+ - Cycles for marking crack front

Steel type A36

TABLE 2.6a LOAD HISTORY OF BEAM B4A (A36)

Testing Event	ID *	Subtotal N	Cumm. N	Fracture Test Data				Fatigue Data	
				Detail Tested	No.	** Temp. °F	Fract. Temp. °F	S _r ksi	σ _{max} ksi
Fatigue	a	1,500,000	1,500,000	F	1	-40		G/F 9.0/8.0	1.98/17.6
Fracture	a	7,500 ⁺	7,500 ⁺	F	1	-40			
Fatigue	a	250,000	1,507,500					G/F 9.0/8.0	19.8/17.6
Fracture	a	7,500 ⁺	1,757,500	F	2	-40			
Fatigue	a	7,500	1,765,000	F	2	-40		G/F 9.0/8.0	19.8/17.6
Fracture	a	250,000	2,015,000						
Fatigue	b	7,500 ⁺	7,500 ⁺	G	3	-40		4.5 15.3	
Fracture	b	7,500	2,022,500	G	3	-40		9.0 19.8	
Fatigue	c	250,000	2,272,500						
Fracture	c	7,500 ⁺	7,500 ⁺	G	4	-40		4.5 15.3	
Fatigue	d	7,500	2,280,000	G	4	-40		9.0 19.8	
Fatigue	e	250,000	2,530,000						
Fracture	e	7,500 ⁺	7,500 ⁺	G	5	-60		4.5 15.3	
Fatigue	f	18,750	2,548,750	G	5	-60		9.0 19.8	
Fatigue	g	352,000	2,900,750						
Fracture	g	7,500 ⁺	7,500 ⁺	F	6	-40		G/F 9.0/8.0	19.8/17.6
Fatigue	g	7,500	2,908,250	F	6	-40		4.0 13.6	
Fatigue	g	67,900	2,976,150					8.0 17.6	
Fracture	h	7,500 ⁺	7,500 ⁺	G	7	-40		4.5 15.3	
Fatigue	h	7,500	2,983,650	G	7	-40		9.0 19.8	
Fatigue	h	5,000	2,988,650	G	7	-120 to -170		4.5 15.3	
Fatigue	h	27,500 ⁺	2,988,650	G	7	-170 to -100		9.0 19.8	
Fatigue	i	243,100	3,231,750						
Fracture	i	8,700 ⁺	3,231,750					G/F 9.0/8.0	19.8/17.6
Fatigue	j	5,000	3,236,750	G	8	-70		G/F 4.5/4.0	15.3/13.6
Fracture	j	40,000	3,276,750	G	8	-70 to -96	-96	4.5 15.3	
								9.0 19.8	

* See fracture surface sketches for banding identification

** Temperature at controlling gages

Steel type - A36

G - Groove welded detail

F - Fillet welded detail

+ - Cycles for marking crack front

TABLE 2.6b LOAD HISTORY OF BEAM B4A (A36)

Testing Event	ID *	Subtotal N	Cumulative N	Fracture Test Data				Fatigue Data	
				Detail Tested	No.	** Temp. °C	Fract. Temp. °C	σ_r MPa	σ_{max} MPa
Fatigue Fracture	a	1,500,000	1,500,000	F	1	-40		28	94
	a	7,500 ⁺	1,507,500	F	1	-40		55	121
Fatigue Fracture	a	250,000	1,757,500	F	2	-40		28	94
	a	7,500 ⁺	1,765,000	F	2	-40		55	121
Fatigue Fracture	a	250,000	2,015,000	G	3	-40		31	105
	b	7,500 ⁺	2,022,500	G	3	-40		62	137
Fatigue Fracture	c	250,000	2,272,500	G	4	-40		31	105
	d	7,500 ⁺	2,280,000	G	4	-40		62	137
Fatigue Fracture	e	250,000	2,530,000	G	5	-51		31	105
	f	7,500 ⁺	2,537,500	G	5	-51		62	137
Fatigue Fracture	g	18,750	2,556,250	F	6	-40		28	94
	g	352,000 ⁺	2,908,250	F	6	-40		55	121
Fatigue Fracture	g	7,500 ⁺	2,915,750	G	7	-40		31	105
	h	7,500 ⁺	2,923,250	G	7	-40		62	137
Fatigue Fracture	h	5,000	2,928,250	G	7	-84 to -112		31	105
		27,500 ⁺	2,955,750	G	7	-112 to -73		62	137
Fatigue Fracture	i	243,100	3,198,850	G	8	-57		31	105
	j	8,700 ⁺	3,207,550	G	8	-57 to -71	-71	62	137
Fatigue Fracture	j	5,000	3,212,550	G	8	-57 to -71	-71	31	105
		40,000	3,252,550	G	8	-57 to -71	-71	62	137

* See fracture surface sketches for banding identification

** Temperature at controlling gages

Steel type - A36

G - Groove welded detail

F - Fillet welded detail

+ - Cycles for marking crack front

TABLE 2.7a LOAD HISTORY OF BEAM B6 (A588)

Testing Event	ID *	Subtotal N	Cumm. N	Fracture Test Data						Fatigue Data	
				Detail Tested	No.	** Temp. °F	Fract. Temp. °F	σ_r ksi	σ_{max} ksi	σ_r ksi	σ_{max} ksi
Fatigue	a	1,999,800	1,999,800							G 9.0 F 8.0	27.5 24.4
Fracture	b	5,000 ⁺	2,007,300	G	1	-30		4.5	23.0		
				F	1	-30		4.0	20.4		
				G	1	-40		9.0	27.5		
				F	1	-40		8.0	24.4		
Fatigue	c	797,400	2,804,700							G 9.0 F 8.0	27.5 ^x 24.4
Fracture	d	18,750 ⁺ 75,000	2,879,700	F	2	-40		4.0	20.4		
				F	2	-40		8.0	24.4		
Fracture	e	7,500 75,000	2,954,700	F	3	-40		4.0	20.4		
				F	3	-40	-53	8.0	24.7 ^y		

* See fracture surface sketches for banding identification

** Temperature at controlling gages

G - Groove welded detail

F - Fillet welded detail

+ - Cycles for marking crack front

x - Static jack dropped load maximum stress changed from 27.5 to ≈ 23 for 400,000 cycles of load

y - Static jack increased load

Steel type - A588

TABLE 2.7b LOAD HISTORY OF BEAM B6 (A588)

Testing Event	ID *	Subtotal N	Cumm. N	Fracture Test Data					Fatigue Data		
				Detail Tested	No.	** Temp. °C	Fract. Temp. °C	σ _r MPa	σ _{max} MPa	σ _r MPa	σ _{max} MPa
Fatigue	a	1,999,800	1,999,800							G 62 F 55	190 168
Fracture	b	5,000 ⁺ 7,500	2,007,300	G	1	-34		31	159		
				F	1	-34		28	141		
				G	1	-40		62	190		
				F	1	-40		55	168		
Fatigue	c	797,400	2,804,700							G 62 F 55	190 ^x 168
Fracture	d	18,750 ⁺ 75,000	2,879,700	F	2	-40		28	141		
				F	2	-40		55	168		
Fracture	e	7,500 75,000	2,954,700	F	3	-40		28	141 ^y		
				F	3	-40	-47	55	170 ^y		

* See fracture surface sketches for banding identification

** Temperature at controlling gages

G - Groove welded detail

F - Fillet welded detail

+ - Cycles for marking crack front

x - Static jack dropped load maximum stress changed from 27.5 to ≈ 23 for 400,000 cycles of load

y - Static jack increased load

Steel type - A588

TABLE 2.8a LOAD HISTORY OF BEAM B6A (A588)

Testing Event	ID *	Subtotal N	Cumm. N	Fracture Test Data						Fatigue Data			
				Detail Tested	No.	** Temp. °F	Fract. Temp. °F	σ_r ksi	σ_{max} ksi	σ_r ksi	σ_{max} ksi		
Fatigue	a	2,042,600	2,042,600										
Fracture	b	22,500	2,065,100	G F	1 1	-40 -40			9.0 8.0	27.5 24.4		G 9.0 F 8.0	19.0 16.9
Fatigue	c	732,400	2,797,500									G 9.0 F 8.0	19.0 16.9
Fracture	d	25,000	2,822,500	G	2	-40/-90	-92		9.0	28.3 ^x			

* See fracture surface sketches for banding identification

** Temperature at controlling gages

G - Groove welded detail

F - Fillet welded detail

x - Static jack increased load

Steel type - A588

TABLE 2.8b LOAD HISTORY OF BEAM B6A (A588)

Testing Event	ID *	Subtotal N	Cumm. N	Fracture Test Data						Fatigue Data	
				Detail Tested	No.	** Temp. °C	Fract. Temp. °C	σ_r MPa	σ_{max} MPa	σ_r MPa	σ_{max} MPa
Fatigue	a	2,042,600	2,042,600							G 62 F 55	131 117
Fracture	b	22,500	2,065,100	G F	1 1	-40 -40		62 55	190 168		
Fatigue	c	732,400	2,797,500							G 62 F 55	131 117
Fracture	d	25,000	2,822,500	G	2	-40/-68	-69	62	195 ^x		

* See fracture surface sketches for banding identification

** Temperature at controlling gages

G - Groove welded detail

F - Fillet welded detail

x - Static jack increased load

Steel type - A588

TABLE 2.9a LOAD HISTORY/BEAM B1 (A514)

Testing Event	*ID	Subtotal N	Cumm. N	Fracture Test Data						Fatigue Data	
				Detail Tested	No.	** Temp. °F	Fract. Temp. °F	σ _r ksi	σ _{max} ksi	σ _r ksi	σ _{max} ksi
Fatigue	a	1,765,000	1,765,000								
Fracture	b	7,500	1,772,500	E,N	1	-40		8	55		
		33,800	1,806,300	E	1	-40/ -200	-200	8	55		
										8.0	26.0

TABLE 2.9b

Testing Event	*ID	Subtotal N	Cumm, N	Fracture Test Data						Fatigue Data	
				Detail Tested	No.	** Temp. °C	Fract. Temp. °C	σ_r MPa	σ_{max} MPa	σ_r MPa	σ_{max} MPa
Fatigue	a	1,765,000	1,765,000								
Fracture	b	7,500	1,772,500	E,N	1	-40		55	379		
		33,800	1,806,300	E	1	-40/ -129	-129	55	379		
										55	179

* See Fracture Surface Sketches for banding identification

E - End Weld Coverplate

N - No End Weld Coverplate

** Temperatures at controlling gage

TABLE 2.10a LOAD HISTORY/BEAM B1A (A514)

Testing Event	*ID	Subtotal	Cumm.	Fracture Test Data					Fatigue Data		
				Detail Tested	No.	** Temp. °F	Fract. Temp. °F	σ _r ksi	σ _{max} ksi	σ _r ksi	σ _{max} ksi
Fatigue	a	1,134,200	1,134,200								
Fracture	b		1,134,200	E†,N	1	-48	-48	8	55	8.0	26.0

TABLE 2.10b

Testing Event	*ID	Subtotal	Cumm.	Fracture Test Data						Fatigue Data	
				Detail Tested	No.	** Temp. °C	Fract. Temp. °C	σ_r MPa	σ_{max} MPa	σ_r MPa	σ_{max} MPa
Fatigue	a	1,134,200	1,134,200								
Fracture	b		1,134,200	E†,N	1	-44	-44	55	379	55	179

* See Fracture Surface Sketches for banding identification

E - End Weld Coverplate

N - No End Weld Coverplate

** Temperature at controlling gage

† Critical Detail

TABLE 2.11a LOAD HISTORY/BEAM B3 (A36X260)

Testing Event	*ID	Subtotal	Cumm.	Fracture Test Data				Fatigue Data	
				Detail Tested	No.	** Temp. °F	Fract. Temp. °F	σ_r ksi	σ_{max} ksi
Fatigue	a	N	2,001,200	E,N	1	-40		8.0	9.8
Fracture	b		7,500						
Fatigue	c		162,000						
Fracture	d		2,170,700	E†,N	2	-40	-45	5.4	17.2

TABLE 2.11b

Testing Event	*ID	Subtotal	Cumm.	Fracture Test Data				Fatigue Data	
				Detail Tested	No.	** Temp. °C	Fract. Temp. °C	σ_r MPa	σ_{max} MPa
Fatigue	a	N	2,001,200	E,N	1	-40		55	68
Fracture	b		7,500						
Fatigue	c		162,000						
Fracture	d		2,170,700	E†,N	2	-40	-43	37	119

* See Fracture Surface Sketches for banding identification

E - End Weld Coverplate

N - No End Weld Coverplate

** Temperature at controlling gage

† Critical Detail

TABLE 2.12a LOAD HISTORY/BEAM B3A (A36, W36X260)

Testing Event	*ID	Subtotal	Cumm.	Fracture Test Data					Fatigue Data		
				Detail Tested	No.	** Temp. °F	Fract. Temp. °F	σ _r ksi	σ _{max} ksi	σ _r ksi	σ _{max} ksi
Fatigue	a	1,790,900	1,790,900								
Fracture	b	15,000	1,805,900	E,N	1	-40					
		11,300	1,817,200		1	-43/-96	-96	8.0	19.8	8.0	19.8

TABLE 2.12b

Testing Event	*ID	Subtotal	Cumm.	Fracture Test Data						Fatigue Data	
				Detail Tested	No.	** Temp. °C	Fract. Temp. °C	σ_r MPa	σ_{max} MPa	σ_r MPa	σ_{max} MPa
Fatigue	a	1,790,900	1,790,900								
Fracture	b	15,000	1,805,900	E,N	1	-40		55	137		
		11,300	1,817,200		1	-42/-71	-71	55	137		

* See Fracture Surface Sketches for banding identification

E - End Weld Coverplate

N - No End Weld Coverplate

** Temperature at controlling gage

TABLE 2.13a LOAD HISTORY/BEAM B5 (A588, W36X260)

Testing Event	*ID	Subtotal N	Cumm. N	Fracture Test Data						Fatigue Data	
				Detail Tested	No.	** Temp. °F	Fract. Temp. °F	σ_r ksi	σ_{max} ksi	σ_r ksi	σ_{max} ksi
Fatigue	a	2,000,000	2,000,000								
Fracture	b	7,500	2,007,500	E	1	-40			8.0	27.5	
		5,000	2,012,500	E	1	-150	-150		8.0	27.5	

TABLE 2.13b

Testing Event	*ID	Subtotal	Cumm.	Fracture Test Data						Fatigue Data	
				Detail Tested	No.	** Temp. °C	Fract. Temp. °C	σ_r MPa	σ_{max} MPa	σ_r MPa	σ_{max} MPa
Fatigue	a	2,000,000	2,000,000							55	72
Fracture	b	7,500	2,007,500	E	1	-40			55	190	
		5,000	2,012,500	E	1	-101	-101		55	190	

* See Fracture Surface Sketches for banding identification

E - End Weld Coverplate

N - No End Weld Coverplate

** Temperature at controlling gage

TABLE 2.14a LOAD HISTORY/BEAM B5A (A588, W36X260)

Testing Event	*ID	Subtotal N	Cumm. N	Fracture Test Data						Fatigue Data	
				Detail Tested	No.	** Temp. °F	Fract. Temp. °F	σ_r ksi	σ_{max} ksi	σ_r ksi	σ_{max} ksi
Fatigue	a	1,862,500	1,862,500								
Fracture	b	15,000	1,877,000	E,N	1	-129/ -190		8.0	27.5	8.0	12.9
Fatigue	c	123,000	2,000,000								
Fracture	c	7,500 10,000	2,007,500 2,017,500	E,N	2	-40 -40/ -99		8.0	27.5	8.0	12.9

TABLE 2.14b

Testing Event	*ID	Subtotal	Cumm.	Fracture Test Data						Fatigue Data	
				Detail Tested	No.	** Temp. °C	Fract. Temp. °C	σ_r MPa	σ_{max} MPa	σ_r MPa	σ_{max} MPa
Fatigue	a	1,862,500	1,862,500								
Fracture	b	15,000	1,877,000	E,N	1	-40		55	190	55	89
Fatigue	c	1,230,000	2,000,000								
Fracture	c	7,500 10,000	2,007,500 2,017,500	E,N	2	-40 -40/ -73		55	190		

* See Fracture Surface Sketches for banding identification

E - End Weld Coverplate

N - No End Weld Coverplate

** Temperature at controlling gage

TABLE 2.15a LOAD HISTORY FOR BEAM B8 (A514)

Testing Event	ID **	Subtotal N	Cumm. N	Fracture Test Data				Fatigue Data	
				Detail Tested	No.	*** Temp. °F	Fract. Temp. °F	σ_r ksi	σ_{max} ksi
Fatigue	*	2,000,000	2,000,000						
Fracture	*	11,250	2,011,250	E, W	1	-40		18.0	55.0
Fatigue	a	934,600	2,945,850						
Fracture	b	6,250	2,952,100	E	2	-40 to -69	-69	11.8	48.8
								18.0	26.7

* No fatigue crack observed at detail
 ** See fracture surface sketches for banded identification
 E East welded detail
 W West welded detail
 *** Temperature at controlling gages
 Steel type A514

TABLE 2.15b LOAD HISTORY FOR BEAM B8 (A514)

Testing Event	ID **	Subtotal N	Cumm. N	Fracture Test Data					Fatigue Data		
				Detail Tested	No.	*** Temp. °C	Fract. Temp. °C	σ_r MPa	σ_{max} MPa	σ_r MPa	σ_{max} MPa
Fatigue	*	2,000,000	2,000,000							124.1	184.1
Fracture	*	11,250	2,011,250	E,W	1	-40		124.1	379.2		
Fatigue	a	934,600	2,945,850							124.1	184.1
Fracture	b	6,250	2,952,100	E	2	-40 to -56	-56	81.4	336.5		

* No fatigue crack observed at detail

** See fracture surface sketches for banded identification

E East welded detail

W West welded detail

*** Temperature at controlling gages

Steel type A514

TABLE 2.16a LOAD HISTORY FOR BEAM B8A (A514)

Testing Event	ID	Subtotal	Cumm.	Fracture Test Data					Fatigue Data		
				Detail Tested	No.	Temp. °F	*** Fract. Temp. °F	σ _r ksi	σ _{max} ksi	σ _r ksi	σ _{max} ksi
Fatigue	*	2,000,000	2,000,000	N							
Fracture	*	11,250	2,011,250	E,W	1	-40			18.0	55.0	
Fatigue	**	2,155,400	4,166,650								
Fracture	**	15,000	4,181,650	W	2	-150 to -250			18.0	55.0	

* No fatigue crack observed at detail

** See Fig. 6.5 for crack dimensions

E East welded detail

W West welded detail

*** No fracture occurred

Steel type A514

TABLE 2.16b LOAD HISTORY FOR BEAM B8A (A514)

Testing Event	ID	Subtotal N	Cumm. N	Fracture Test Data						Fatigue Data			
				Detail Tested	No.	Temp. °C	*** Fract. Temp. °C	σ_r MPa	σ_{max} MPa	σ_r MPa	σ_{max} MPa		
Fatigue	*	2,000,000	2,000,000										
Fracture	*	11,250	2,011,250	E,W	1	-40			124.1	379.2		124.1	
Fatigue	**	2,155,400	4,166,650									124.1	184.1
Fracture	**	15,000	4,181,650	W	2	-101 to -157			124.1	379.2			

* No fatigue crack observed at detail

** See Fig. 6.5 for crack dimensions

E East welded detail

W West welded detail

*** No fracture occurred

Steel type A514

TABLE 2.17a LOAD HISTORY FOR BEAM B10 (A36)

Testing Event	ID **	Subtotal		Cumm.	Fracture Test Data				Fatigue Data	
		N	N		Detail Tested	No.	*** Temp. °F	Fract. Temp. °F	σ_r ksi	σ_{max} ksi
Fatigue	*	2,171,200	2,171,200						18.0	19.8
Fracture	*	10,000 ⁺ 7,500		2,178,700	E E	1 1	-40 -40		9.0 18.0	10.8 19.8
Fatigue	a	1,022,400		3,201,100					18.0	19.8
Fracture	b	82,500		3,283,600	E	2	-40 to -140		18.0	19.8
Fatigue	c	26,300		3,309,900						
Fracture	d	2,500		3,312,400	E	3	-40	-40	18.0	19.8

* No fatigue crack observed at detail

** See fracture surface sketches for banded identification

E East welded detail

W West welded detail

*** Temperature at controlling gages

+ Cycles for marking crack front

Steel type A36

TABLE 2.17b LOAD HISTORY FOR BEAM B10 (A36)

Testing Event	ID **	Subtotal N	Cumm. N	Fracture Test Data						Fatigue Data	
				Detail Tested	No.	*** Temp. °C	Fract. Temp. °C	σ_r MPa	σ_{max} MPa	σ_r MPa	σ_{max} MPa
Fatigue	*	2,171,200	2,171,200							124.1	136.5
Fracture	*	10,000 ⁺		E	1	-40		62.1	74.5		
		7,500	2,178,700	E	1	-40		124.1	136.5		
Fatigue	a	1,022,400	3,201,100							124.1	136.5
Fracture	b	82,500	3,283,600	E	2	-40 to -96		124.1	136.5		
Fatigue	c	26,300	3,309,900							124.1	136.5
Fracture	d	2,500	3,312,400	E	3	-40	-40	124.1	136.5		

* No fatigue crack observed at detail

** See fracture surface sketches for banded identification

E East welded detail

W West welded detail

*** Temperature at controlling gages

+ Cycles for marking crack front

Steel type A36

TABLE 2.18a LOAD HISTORY FOR BEAM B10A (A36)

Testing Event	ID **	Subtotal	Cumm.	Fracture Test Data						Fatigue Data	
				Detail Tested	No.	*** Temp. °F	Fract. Temp. °F	σ _r ksi	σ _{max} ksi	σ _r ksi	σ _{max} ksi
Fatigue	*	N 2,000,000	N 2,000,000								
Fracture	*	15,000 ⁺ 15,000	2,015,000	E, W E, W	1 1	-40 -40		9.0 18.0	10.8 19.8		
Fatigue	a	1,049,000	3,064,000							18.0	19.8
Fracture	b	5,000	3,069,000	E	2	-39	-39	18.0	19.8		

* No fatigue crack observed at detail

** See fracture surface sketches for banded identification

E East welded detail

W West welded detail

*** Temperature at controlling gages

+ Cycles for marking crack front

Steel type A36

TABLE 2.18b LOAD HISTORY FOR BEAM B10A (A36)

Testing Event	ID **	Subtotal	Cumm.	Fracture Test Data						Fatigue Data	
				Detail Tested	No.	*** Temp. °C	Fract. Temp. °C	σ_r MPa	σ_{max} MPa	σ_r MPa	σ_{max} MPa
Fatigue	*	N 2,000,000	N 2,000,000								
Fracture	*	15,000 ⁺ 15,000	2,015,000	E,W E,W	1 1	-40 -40		62.1 124.1	74.5 136.5		
Fatigue	a	1,049,000	3,064,000							124.1	136.5
Fracture	b	5,000	3,069,000	E	2	-39.4	124.1	136.5			

- * No fatigue crack observed at detail
- ** See fracture surface sketches for banded identification
- E East welded detail
- W West welded detail
- *** Temperature at controlling gages
- + Cycles for marking crack front
- Steel type A36

TABLE 2.19a LOAD HISTORY FOR BEAM B12 (A588)

Testing Event	ID *	Subtotal	Cum.	Fracture Test Data				Fatigue Data	
				Detail Tested	No.	Temp. °F	Fract. Temp. °F	σ_r ksi	σ_{max} ksi
Fatigue		N 2,000,000	N 2,000,000						
Fracture		5,000 ⁺ 15,000		E,W E,W	1 1	-40 -40		9.0 18.0	18.5 27.5
Fatigue		2,153,200	4,168,200					18.0	19.8

TABLE 2.19b LOAD HISTORY FOR BEAM B12 (A588)

Testing Event	ID *	Subtotal	Cum.	Fracture Test Data				Fatigue Data	
				Detail Tested	No.	Temp. °C	Fract. Temp. °C	σ_r MPa	σ_{max} MPa
Fatigue		N 2,000,000	N 2,000,000						
Fracture		5,000 ⁺ 15,000		E,W E,W	1 1	-40 -40		62.1 124.1	127.6 189.6
Fatigue		2,153,200	4,168,200					124.1	136.5

* No fatigue crack observed at detail

E East welded detail

W West welded detail

** No fracture occurred

+ Cycles for marking crack front

Steel type A588

TABLE 2.20a LOAD HISTORY FOR BEAM B12A (A588)

Testing Event	ID *	Subtotal N	Cumm. N	Fracture Test Data						Fatigue Data	
				Detail Tested	No.	** Temp. °F	Fract. Temp. °F	σ_r ksi	σ_{max} ksi	σ_r ksi	σ_{max} ksi
Fatigue	a	2,000,000	2,000,000							18.0	19.8
Fracture	b	17,500 ⁺ 17,500	2,017,500	E, W E, W	1 1	-40 -40		9.0 18.0	18.5 27.5		
Fatigue	c	662,300	2,679,800							18.0	19.8
Fracture	d	5,000 ⁺ 25,000	2,704,800	E E	2 2	-40 -40 to -90		9.0 18.0	18.5 27.5		
Fatigue	e	361,700	3,066,500							18.0	19.8
Fracture	f	2,500	3,069,000	E	3	-80 to -89	-89	18.0	27.5		

* See fracture surface sketches for banded identification

E East welded detail

W West welded detail

** Temperature at controlling gages

Steel type A588

TABLE 2.20b LOAD HISTORY FOR BEAM B12A (A588)

Testing Event	ID *	Subtotal N	Cumm. N	Fracture Test Data					Fatigue Data		
				Detail Tested	No.	** Temp. °C	Fract. Temp. °C	σ_r MPa	σ_{max} MPa	σ_r MPa	σ_{max} MPa
Fatigue	a	2,000,000	2,000,000							124.1	136.5
Fracture	b	17,500 ⁺		E,W	1	-40		62.1	127.6		
	b	17,500	2,017,500	E,W	1	-40		124.1	189.6		
Fatigue	c	662,300	2,679,800							124.1	136.5
Fracture	d	5,000 ⁺		E	2	-40		62.1	127.6		
	d	25,000	2,704,800	E	2	-40 to -68		124.1	189.6		
Fatigue	e	361,700	3,066,500							124.1	136.5
Fracture	f	2,500	3,069,000	E	3	-62 to -67	-67	124.1	189.6		

* See fracture surface sketches for banded identification

E East welded detail

W West welded detail

** Temperature at controlling gages

Steel type A588

TABLE 2.21a LOAD HISTORY FOR BEAM B7 (A514)

Testing Event	ID	Subtotal	Cumm.	Fracture Test Data					Fatigue Data		
				Detail Tested	No.	Temp. °F	*** Fract. Temp. °F	σ_r ksi	σ_{max} ksi	σ_r ksi	σ_{max} ksi
Fatigue	*	N 2,188,100	N 2,188,100							E 13.6 W 13.6	28.0 29.1
Fracture	*	7,500	2,195,600	E W	1 1	-40 -40		13.0 13.5	55.0 58.8		
Fatigue	**	6,165,200	8,360,800							E 13.0 W 13.6	28.0 29.1

* No fatigue crack observed in flange

** At 6.60×10^6 cycles fatigue crack observed at toe of east stiffener

E East welded detail

W West welded detail

*** No fracture occurred

Steel type A514

TABLE 2.21b LOAD HISTORY FOR BEAM B7 (A514)

Testing Event	ID	Subtotal N	Cumulative N	Fracture Test Data					Fatigue Data		
				Detail Tested	No.	Temp. °C	*** Fract. Temp. °C	σ_r MPa	σ_{max} MPa	σ_r MPa	σ_{max} MPa
Fatigue	*	2,188,100	2,188,100							E 89.6 W 93.0	193.0 200.6
Fracture	*	7,500	2,195,600	E W	1 1	-40 -40		89.6 93.0	379.2 405.4		
Fatigue	**	6,165,200	8,360,800							E 89.6 W 93.0	193.0 200.6

* No fatigue crack observed in flange
 ** At 6.60×10^6 cycles fatigue crack observed at toe of east stiffener
 E East welded detail
 W West welded detail
 *** No fracture occurred

Steel type A514

TABLE 2.22a LOAD HISTORY FOR BEAM B7A (A514)

Testing Event	ID **	Subtotal N	Cummm.	Fracture Test Data					Fatigue Data		
				Detail Tested	No.	*** Temp. °F	Fract. Temp. °F	σ_r ksi	σ_{max}^* ksi	σ_r ksi	σ_{max} ksi
Fatigue	a	1,451,700	1,451,700							E 15.0 W 15.6	28.9 30.0
Fracture	b	0	1,451,700	W	1	-36	-36		11.5	50.2	

TABLE 2.22b LOAD HISTORY FOR BEAM B7A (A514)

Testing Event	ID **	Subtotal	Cumm.	Fracture Test Data					Fatigue Data		
				Detail Tested	No.	*** Temp. °C	Fract. Temp. °C	σ_r MPa	σ_{max} MPa	σ_r MPa	σ_{max} MPa
Fatigue	a	1,451,700	1,451,700							E 103.4 W 107.6	199.3 206.8
Fracture	b	0	1,451,700	W	1	-38	-38	79.3	346.1		

* No fatigue crack observed at detail
 ** See fracture surface sketches for banded identification
 E East welded detail
 W West welded detail
 *** Temperature at controlling gages
 Steel type A514

TABLE 2.23a LOAD HISTORY FOR BEAM B9 (A36)

Testing Event	ID	Subtotal	Cumm.	Fracture Test Data					Fatigue Data		
				Detail Tested	No.	Temp. °F	** Fract. Temp. °F	σ _r ksi	σ _{max} ksi	σ _r ksi	σ _{max} ksi
Fatigue		N 2,000,000	N 2,000,000							E 13.0 W 13.6	19.8 20.7
Fracture		7,500 ⁺ 15,000	2,015,000	E W E	1 1 1	-40 -40 -40		6.5 6.8 13.0 13.6	16.0 16.7 19.8 20.7		
Fatigue		7,548,400	9,563,400							E 13.0 W 13.6	19.8 20.7
Fracture		7,500 ⁺ 15,000	9,578,400	E W E W	2 2 2 2	-40 -40 -40 -40		6.5 6.8 13.0 13.6	16.0 16.7 19.8 20.7		

* No fatigue crack observed at detail
 E East welded detail
 W West welded detail
 ** No fracture occurred
 + Cycles for marking crack front
 Steel type A36

TABLE 2.23b LOAD HISTORY FOR BEAM B9 (A36)

Testing Event	ID *	Subtotal N	Cumm. N	Fracture Test Data				Fatigue Data	
				Detail Tested	No.	Temp. °C	Fract. Temp. °C **	σ_r MPa	σ_{max} MPa
Fatigue		2,000,000	2,000,000					E 89.6 W 93.8	136.5 142.7
Fracture		7,500 ⁺ 15,000	2,015,000	E W E W	1 1 1 1	-40 -40 -40 -40		44.8 46.9 89.6 93.8	110.3 115.1 136.5 142.7
Fatigue		7,548,400	9,563,400					E 89.6 W 93.8	136.5 142.7
Fracture		7,500 ⁺		E W E W	2 2 2 2	-40 -40 -40 -40		44.8 46.9 89.6 93.8	110.3 115.1 136.5 142.7

* No fatigue crack observed at detail

E East welded detail

W West welded detail

** No fracture occurred

+ Cycles for marking crack front

Steel type A36

TABLE 2.24a LOAD HISTORY FOR BEAM B9A (A36)

Testing Event	ID **	Subtotal N	Cumulative N	Fracture Test Data					Fatigue Data		
				Detail Tested	No.	*** Temp. °F	Fract. Temp. °F	σ_r ksi	σ_{max} ksi	σ_r ksi	σ_{max} ksi
Fatigue	*	2,000,000	2,000,000							E 13.0 W 13.6	19.8 20.7
Fracture	*	7,500 ⁺ 15,000		E W E W	1 1 1 1	-40 -40 -40 -40		6.5 6.8 13.0 13.6	16.1 16.8 19.8 20.7		
Fatigue	a	3,379,600	5,394,600							E 13.0 W 13.6	19.8 20.7
Fracture	b	5,000 ⁺ 45,000	5,439,600	W W	2 2	-40 -40 to -195	-195	13.6	20.7		

* No fatigue crack observed at detail

** See fracture surface sketches for banded identification

E East welded detail

W West welded detail

*** Temperature at controlling gages

+ Cycles for marking crack front

Steel type A36

TABLE 2.24b LOAD HISTORY FOR BEAM B9A (A36)

Testing Event	ID **	Subtotal N	Cumm. N	Fracture Test Data				Fatigue Data	
				Detail Tested	No.	*** Temp. °C	Fract. Temp. °C	σ_r MPa	σ_{max} MPa
Fatigue	*	2,000,000	2,000,000						
Fracture	*	7,500 ⁺		E	1	-40			
				W	1	-40			
		15,000	2,015,000	E	1	-40			
				W	1	-40			
Fatigue	a	3,379,600	5,439,600						
Fracture	b	5,000 ⁺							
		45,000	5,439,600	W	2	-40	-126	93.8	142.7
				W	2	-40 to -126			

- * No fatigue crack observed at detail
 ** See fracture surface sketches for banded identification
 E East welded detail
 W West welded detail
 *** Temperature at controlling gages
 + Cycles for marking crack front
 Steel type A36

TABLE 2.25a LOAD HISTORY FOR BEAM B11 (A588)

Testing Event	ID **	Subtotal N	Cumm. N	Fracture Test Data						Fatigue Data			
				Detail Tested	No.	*** Temp. °F	Fract. Temp. °F	σ _r ksi	σ _{max} ksi	σ _r ksi	σ _{max} ksi		
Fatigue	*	2,000,000	2,000,000										
Fracture	*	15,000	2,015,000	E W	1 1	-40 -40			15.0 15.6	27.5 29.3			
Fatigue	a	1,029,200	3,044,200									E 15.0 W 15.7	19.8 20.7
Fracture	b	20,000	3,064,200	E	2	-40 to -110	-110	15.0	27.5				

* No fatigue crack observed at detail

** See fracture surface sketches for banded identification

E East welded detail

W West welded detail

*** Temperature at controlling gages

Steel type A588

TABLE 2.25b LOAD HISTORY FOR BEAM B11 (A588)

Testing Event	ID **	Subtotal N	Cumm. N	Fracture Test Data				Fatigue Data			
				Detail Tested	No.	*** Temp. °C	Fract. Temp. °C	σ_r MPa	σ_{max} MPa	σ_r MPa	σ_{max} MPa
Fatigue	*	2,000,000	2,000,000							E 103.4 W 108.2	136.5 142.7
Fracture	*	15,000	2,015,000	E W	1 1	-40 -40		103.4 108.2	189.6 202.0		
Fatigue	a	1,029,200	3,044,200							E 103.4 W 108.2	136.5 142.7
Fracture	b	20,000	3,064,200	E	2	-40 to -79	-79	103.4	189.6		

* No fatigue crack observed at detail

** See fracture surface sketches for banded identification

E East welded detail

W West welded detail

*** Temperature at controlling gages

Steel type A588

TABLE 2.26a LOAD HISTORY FOR BEAM B11A (A588)

Testing Event	ID *	Subtotal	Cumm.	Fracture Test Data				Fatigue Data	
				Detail Tested	No.	** Temp. °F	Fract. Temp. °F	σ_r MPa	σ_{max} MPa
Fatigue	a	N 1,824,600	N 1,824,600						E 15.0 W 15.7
Fracture	b	0	1,824,600	W	1	-40 to -45	-45	6.9	22.2

TABLE 2.26b LOAD HISTORY FOR BEAM B11A (A588)

Testing Event	ID	Subtotal	Cumm.	Fracture Test Data				Fatigue Data	
				Detail Tested	No.	** Temp. °C	Fract. Temp. °C	σ_r	σ_{max}
Fatigue	a	N 1,824,600	N 1,824,600						E 103.4 W 108.2
Fracture	b	0	1,824,600	W	1	-40 to -43	-43	47.6	153.1

* See fracture surface sketches for banded identification

E East welded detail

W West welded detail

** Temperature at controlling gages

Steel type A588

"West" Region | "East" Region

22'-0"

(6705.6 mm)

Top View

6" (152.4 mm)

8'-0" (2438.4 mm)

2'-6" (762 mm)

2'-6" (762 mm)

8'-0" (2438.4 mm)

6" (152.4 mm)

3'-0" (914.4 mm)

$\frac{3}{8}$ (9.5 mm)

$\frac{3}{8}$ (9.5 mm)

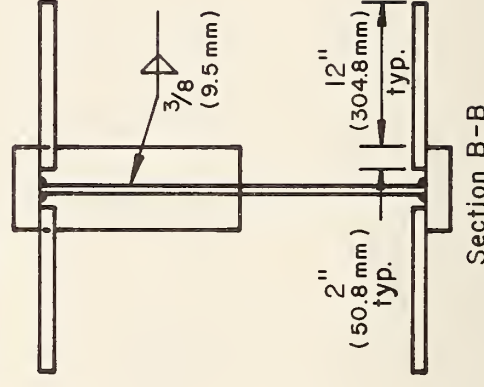
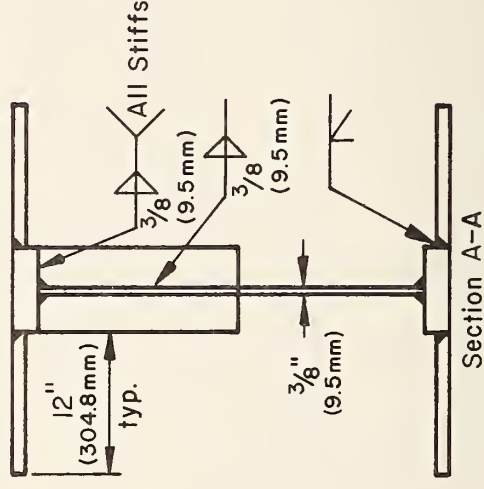
$\frac{1}{2}$ (12.7 mm)

typ. $\frac{3}{8}$ (9.5 mm)

typ. $\frac{3}{8}$ (9.5 mm)

B

A



Flange Size	Steel
2 x 7	A36
2 x 7	A588
1 1/2 x 6	A514

Fig. 2.1a Beam B4

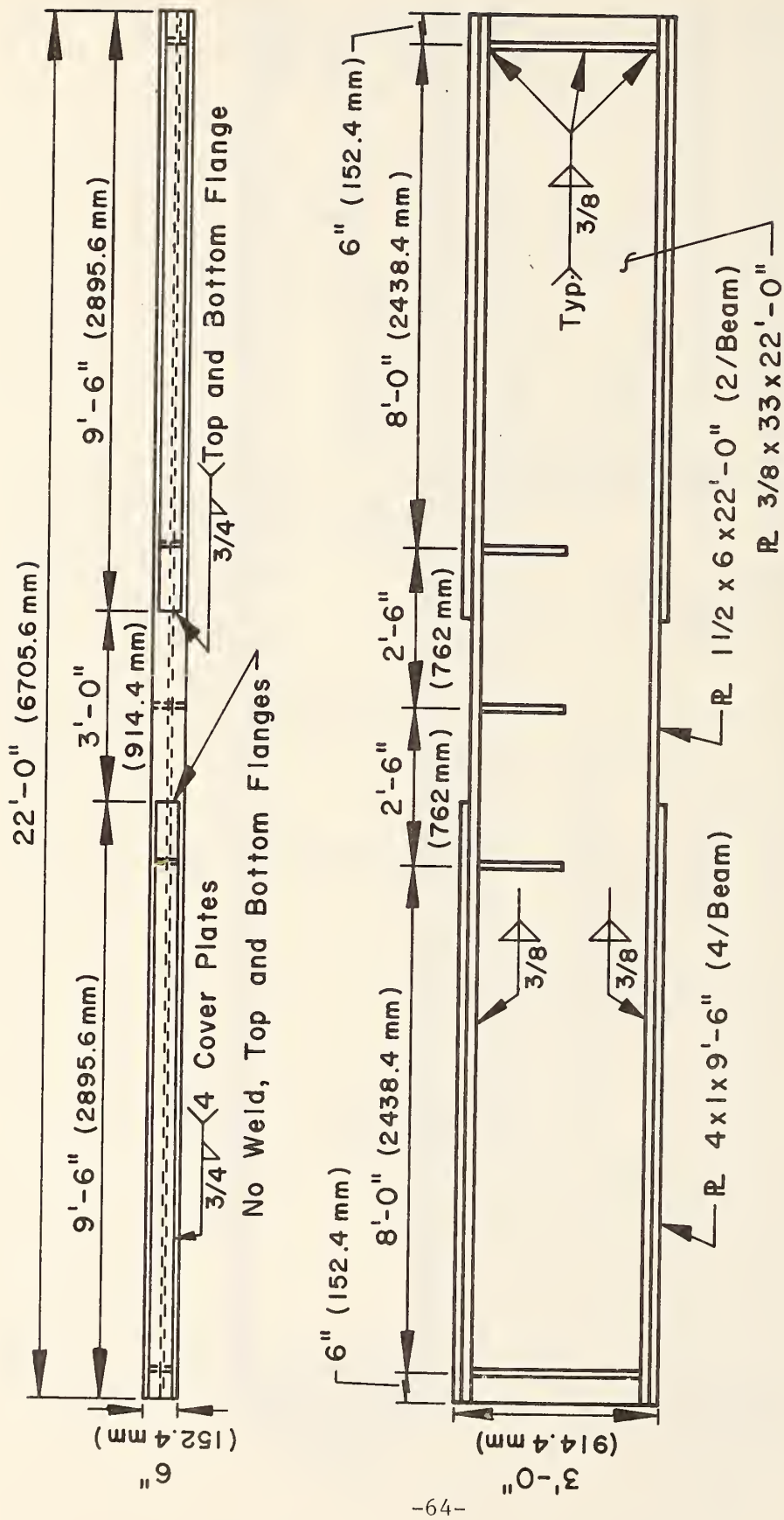


Fig. 2.1c Beam B1

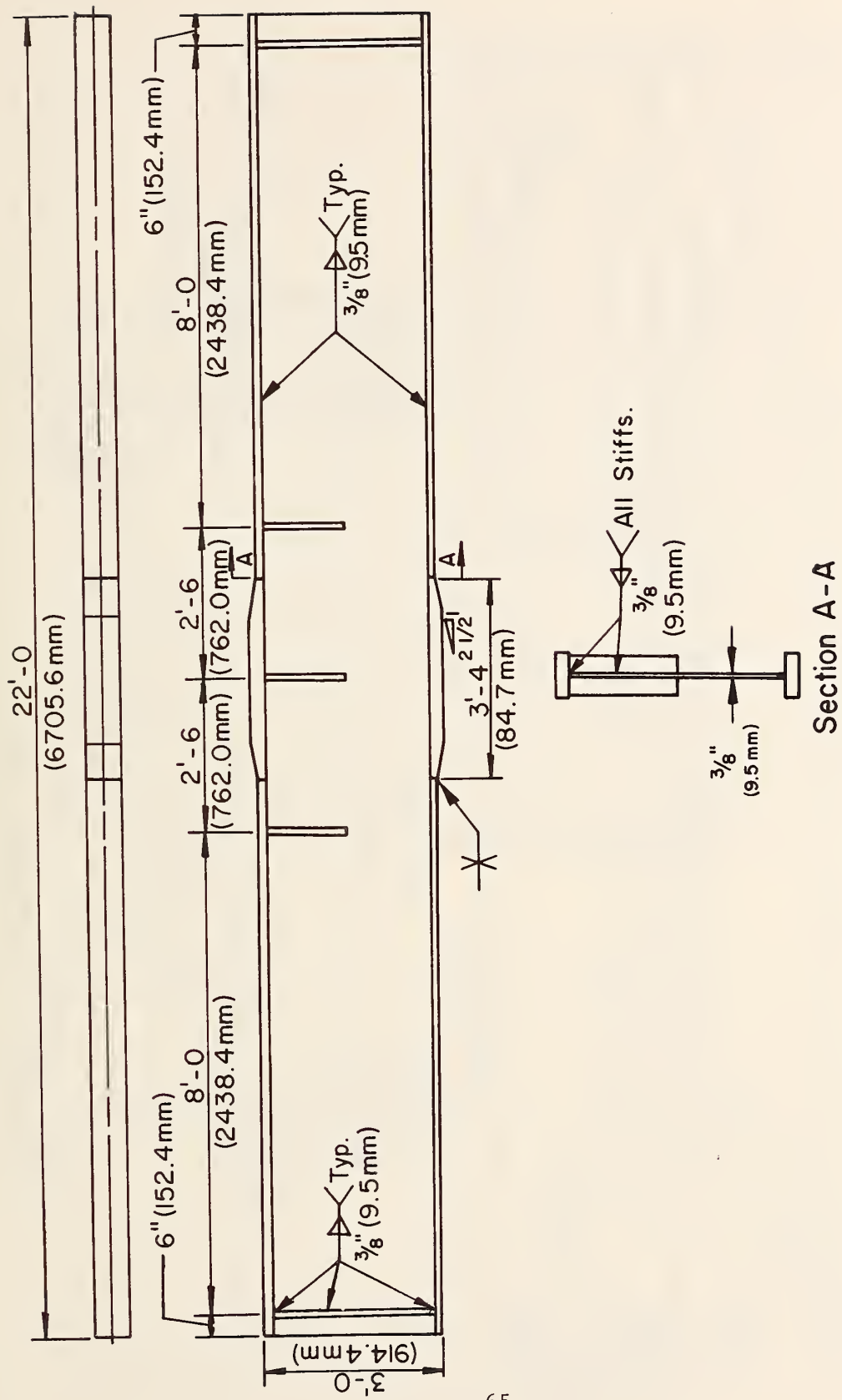


Fig. 2.1d Beam B10

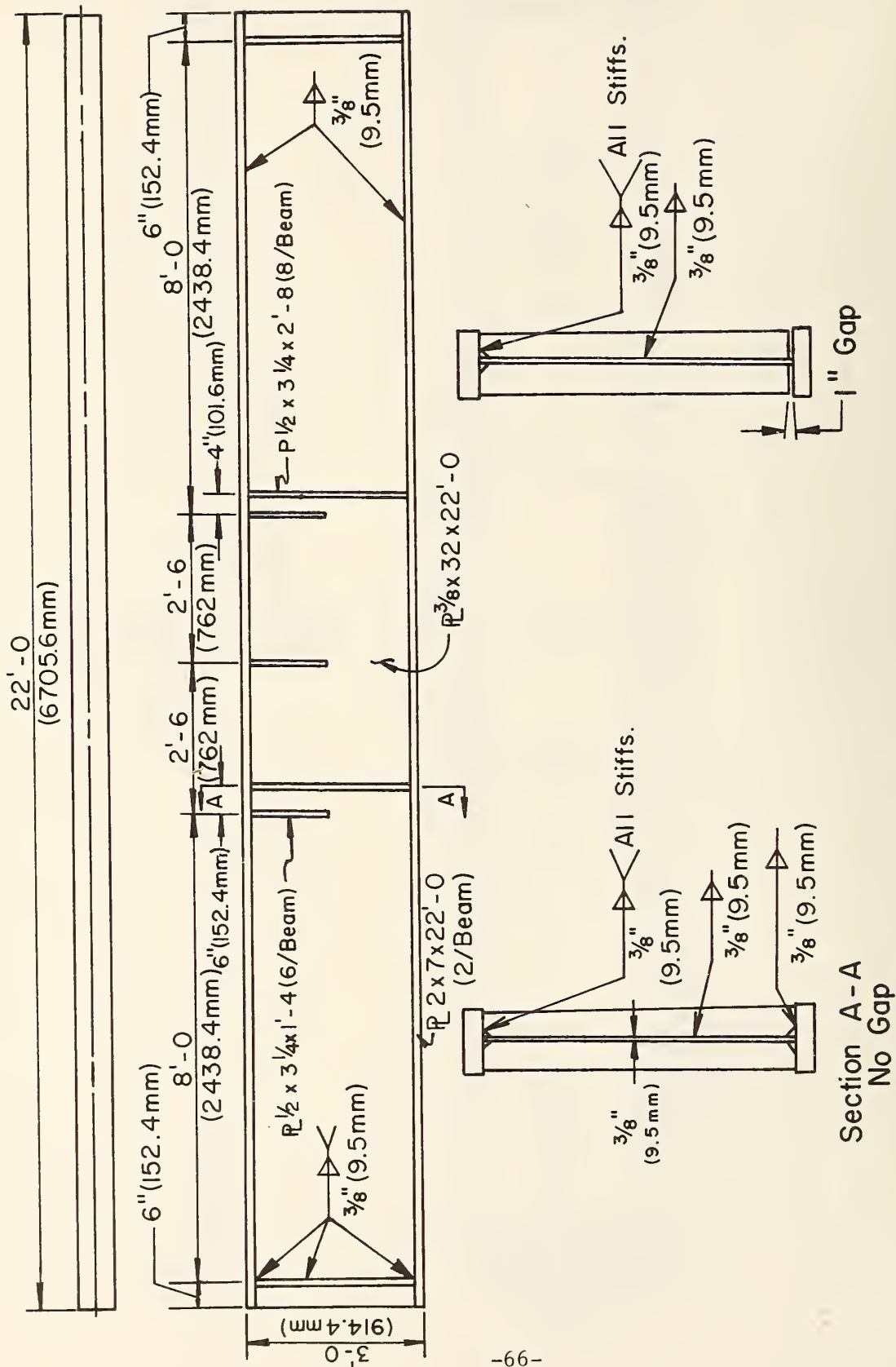


Fig. 2.1e Beam B9A

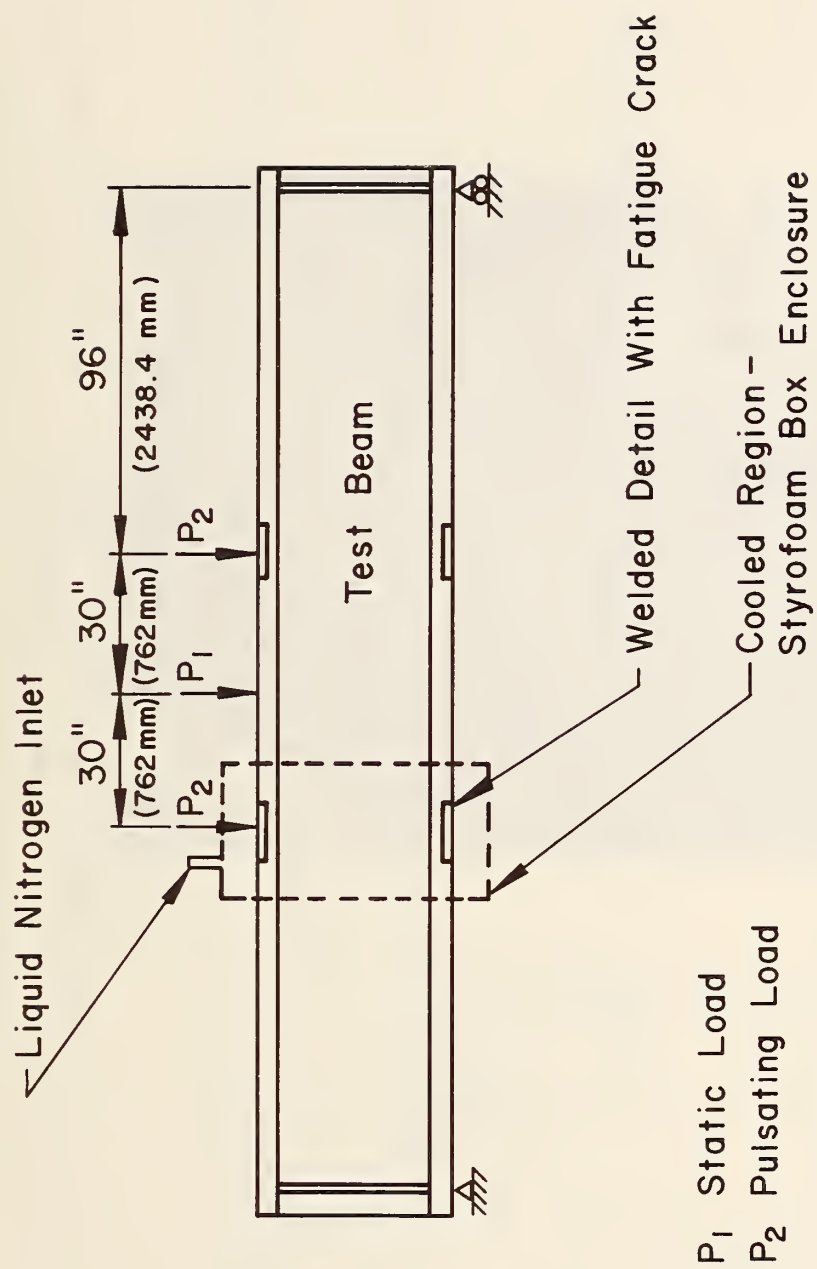


Fig. 2.2 Schematic of Fracture Test Setup

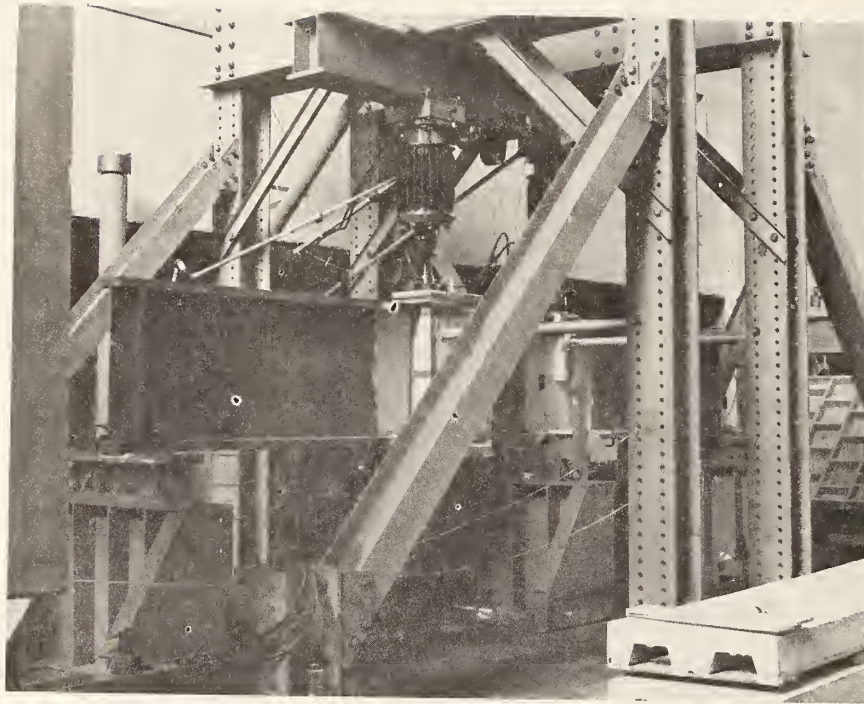


Fig. 2.3 Photograph of Test Setup

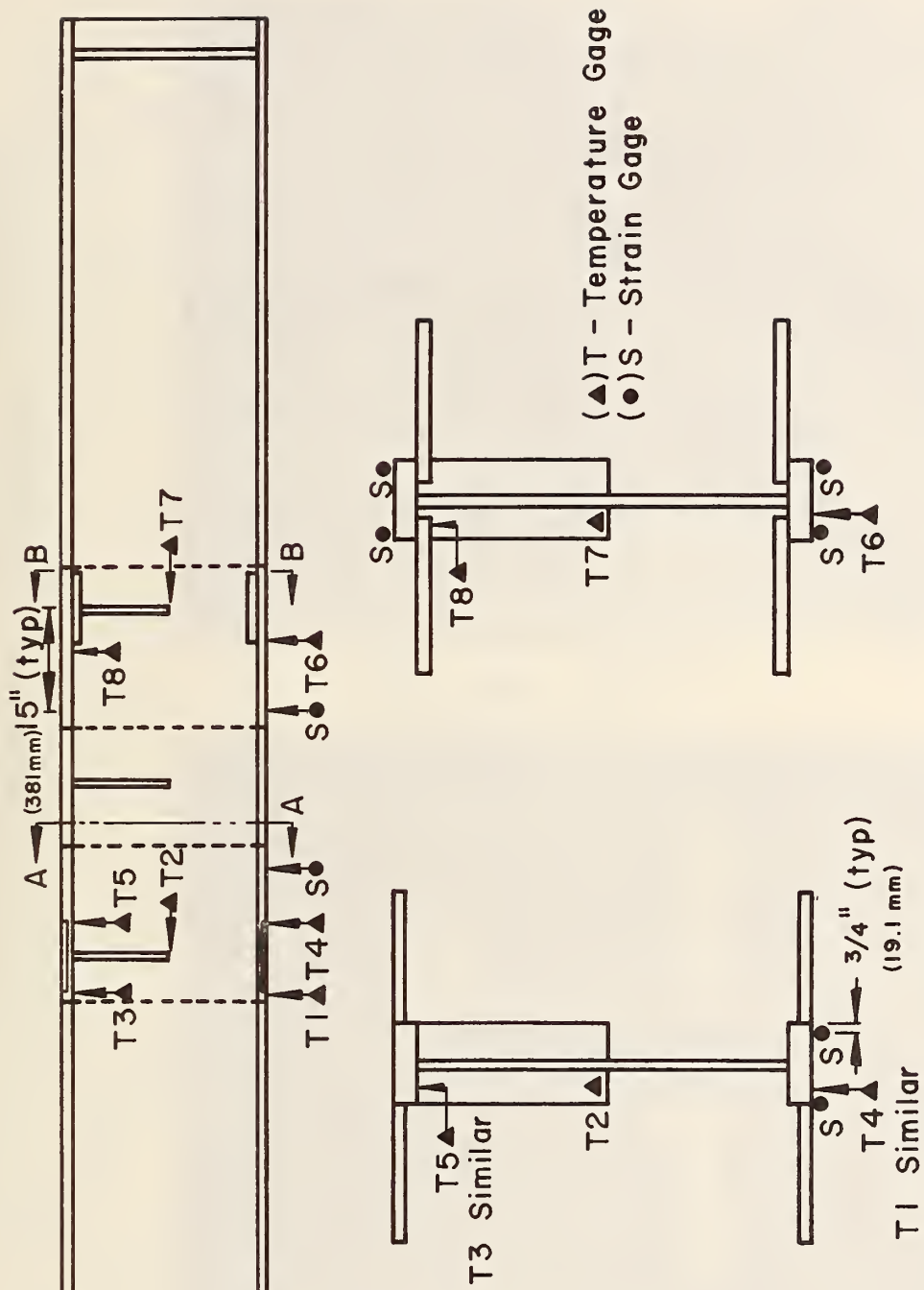


Fig. 2.4 Positions of Temperature and Strain Gages

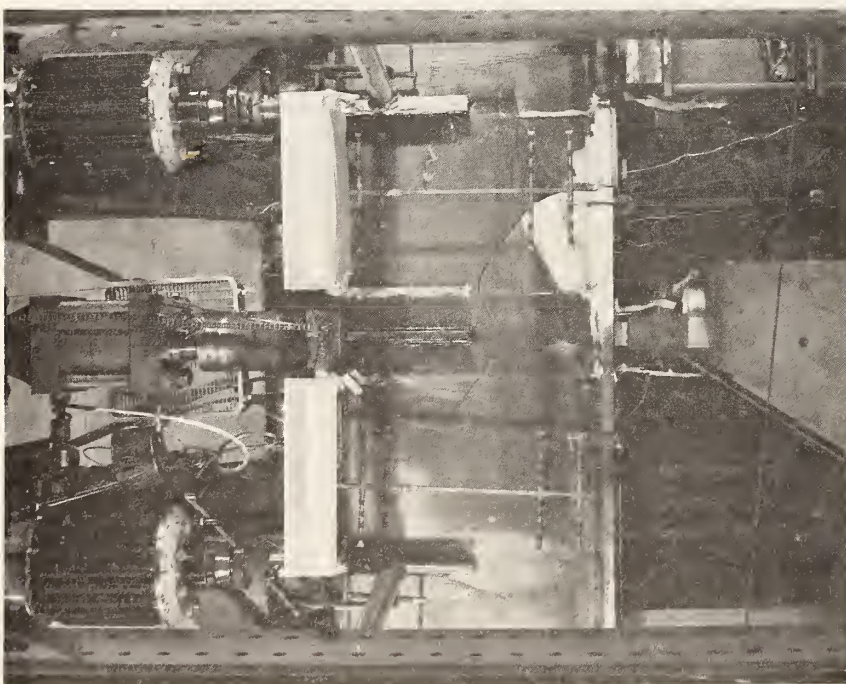
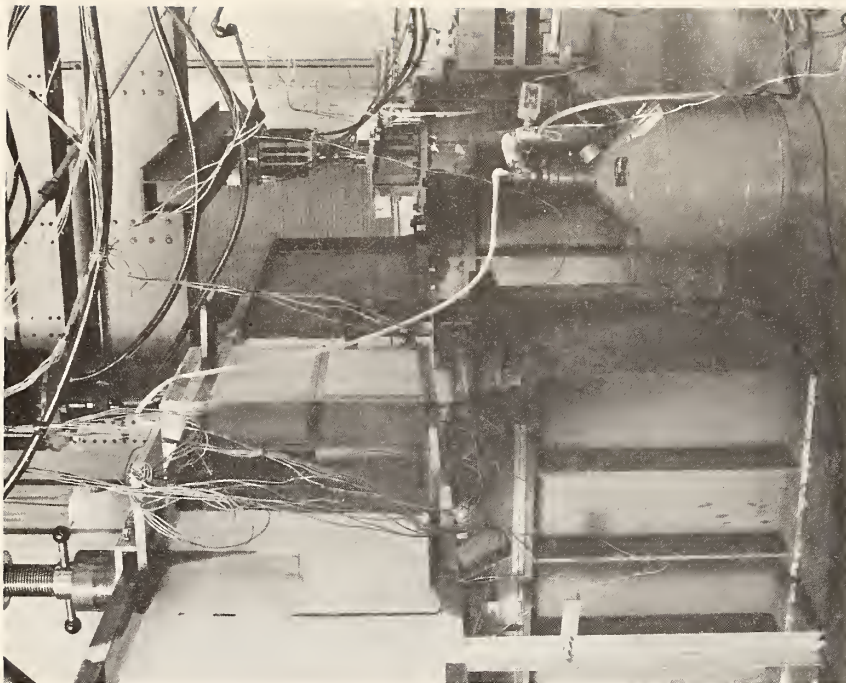


Fig. 2.5 Photograph of Cooling Network

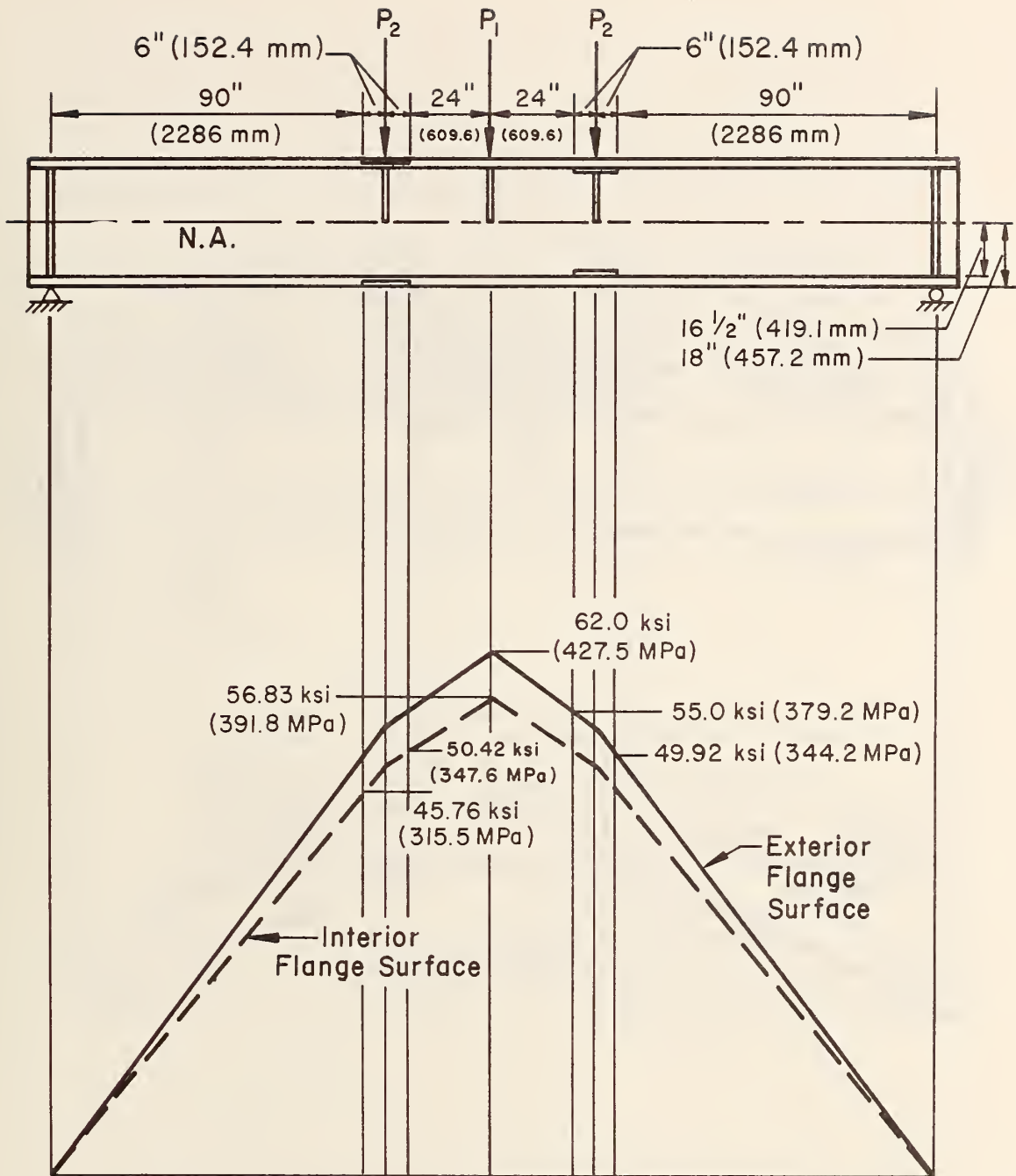


Fig. 2.6a Maximum Stress on Interior and Exterior Flange Surfaces of Beams B2 and B2A (A514)

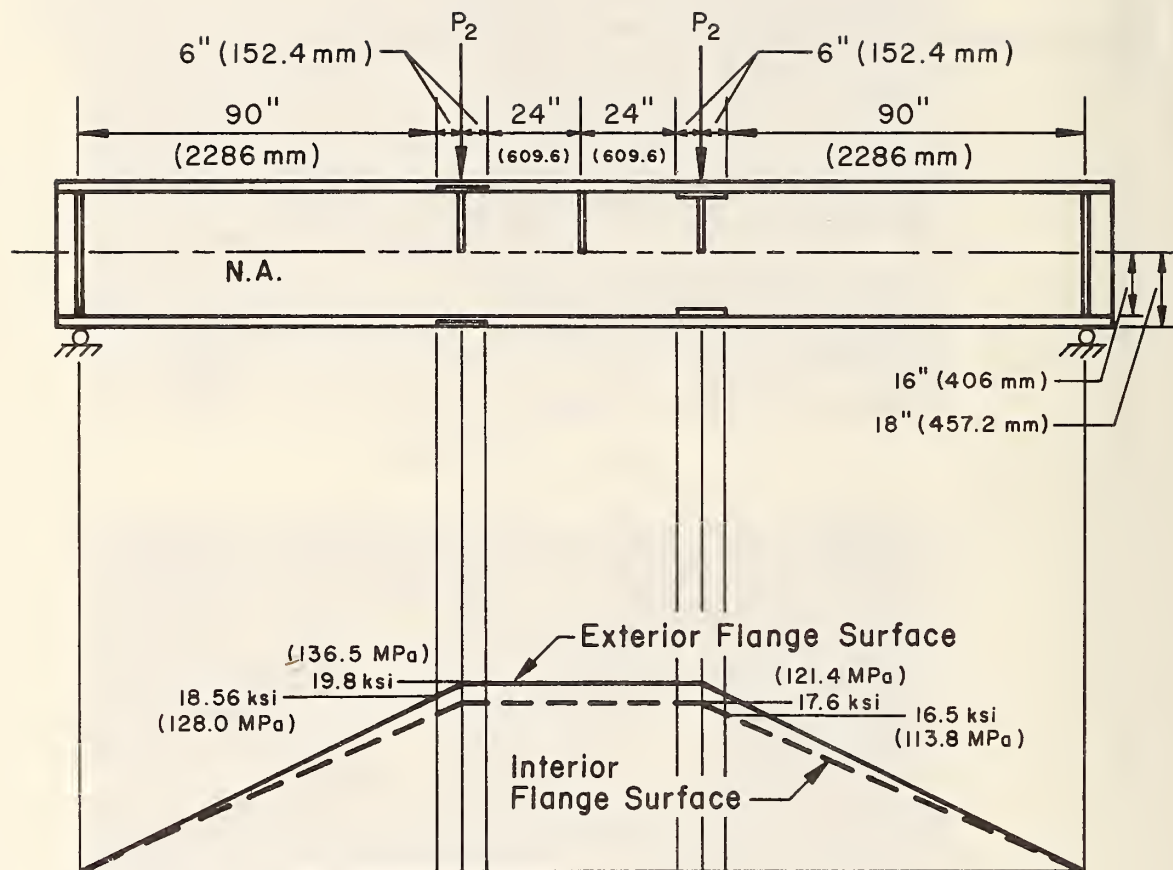


Fig. 2.6b Maximum Stress on Interior and Exterior Flange Surfaces of Beams B4 and B4A (A36)

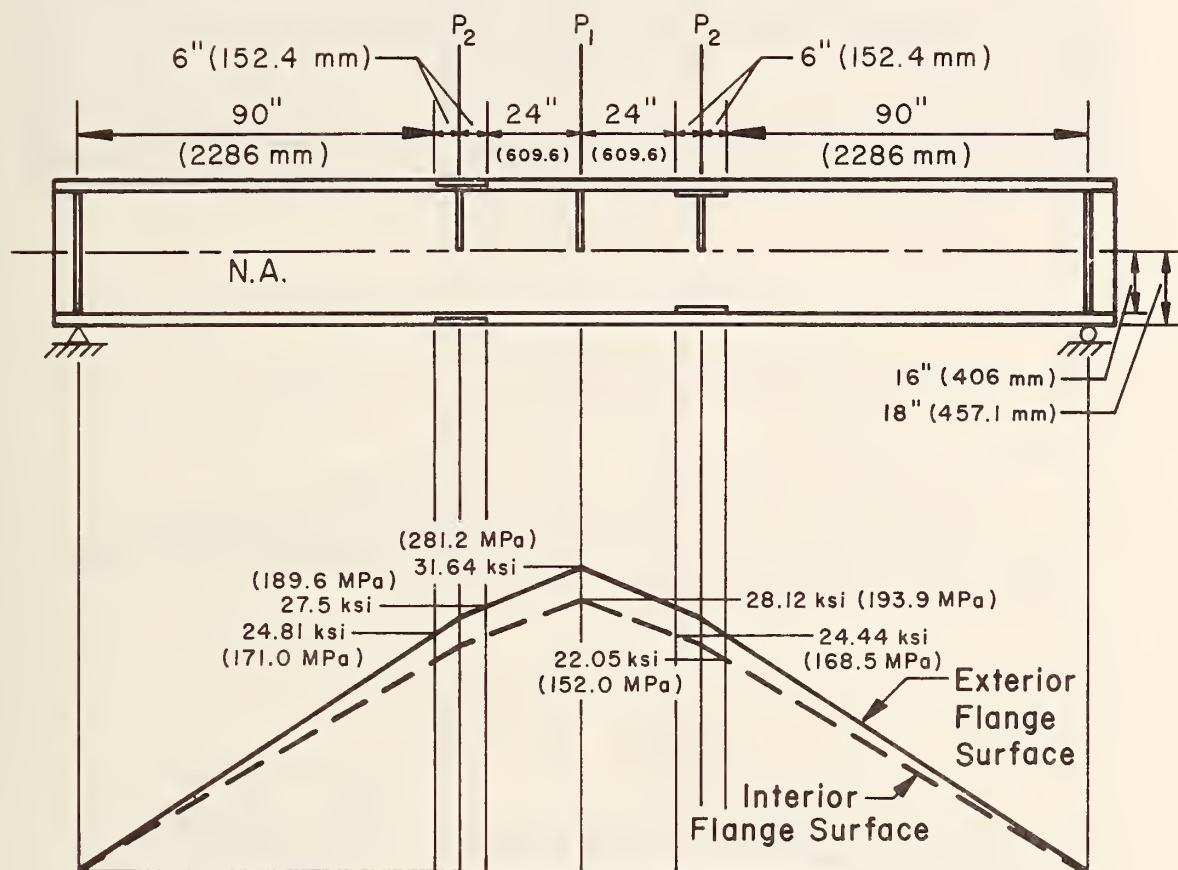


Fig. 2.6c Maximum Stress on Interior and Exterior Flange Surfaces of Beams B6 and B6A (A588)

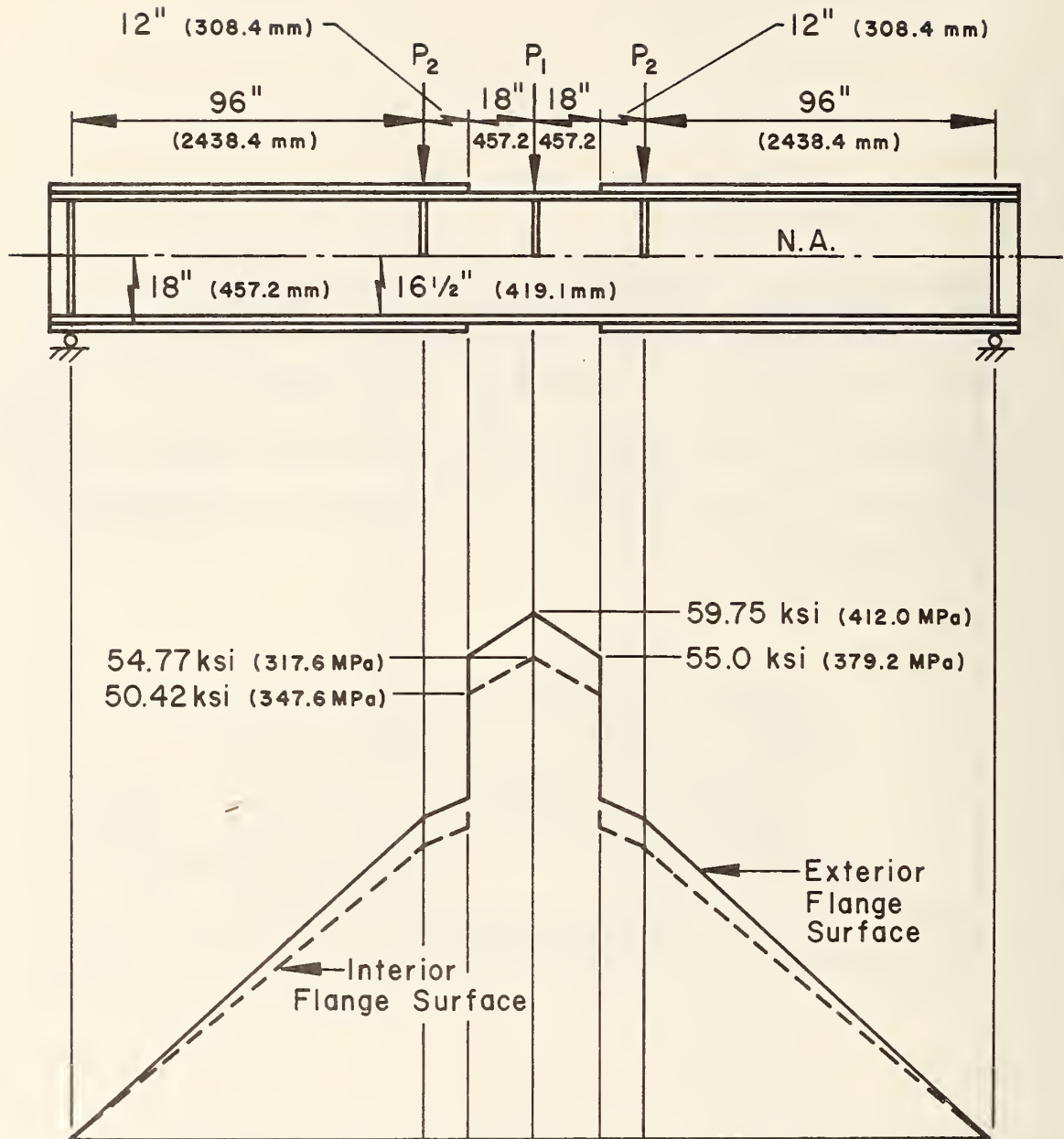


Fig. 2.6d Maximum Stress on Interior and Exterior Flange Surfaces of Beams B1 and B1A (A514)

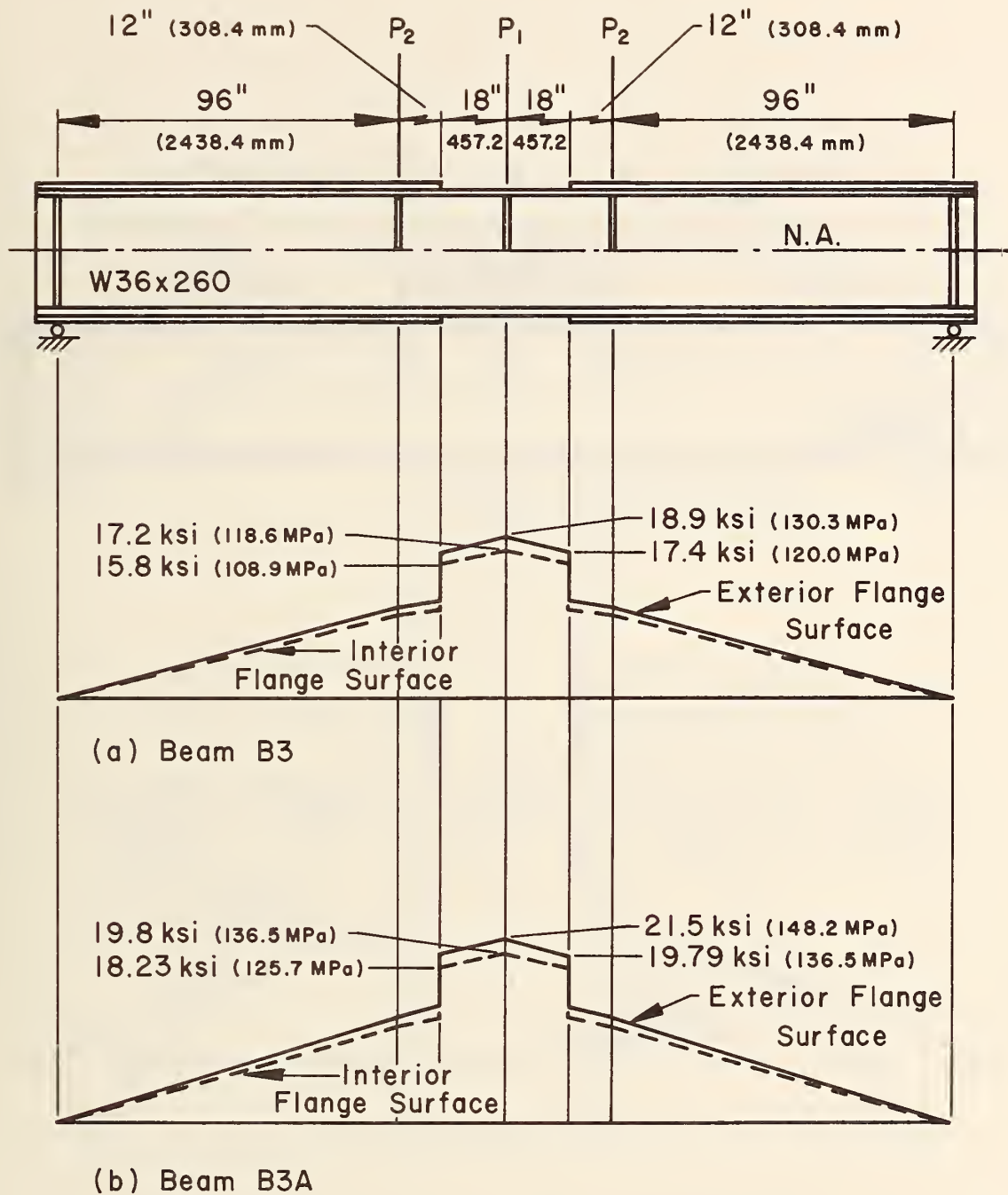


Fig. 2.6e Maximum Stress on Interior and Exterior Flange Surfaces of Beams B3 and B3A (A36, W36X260)

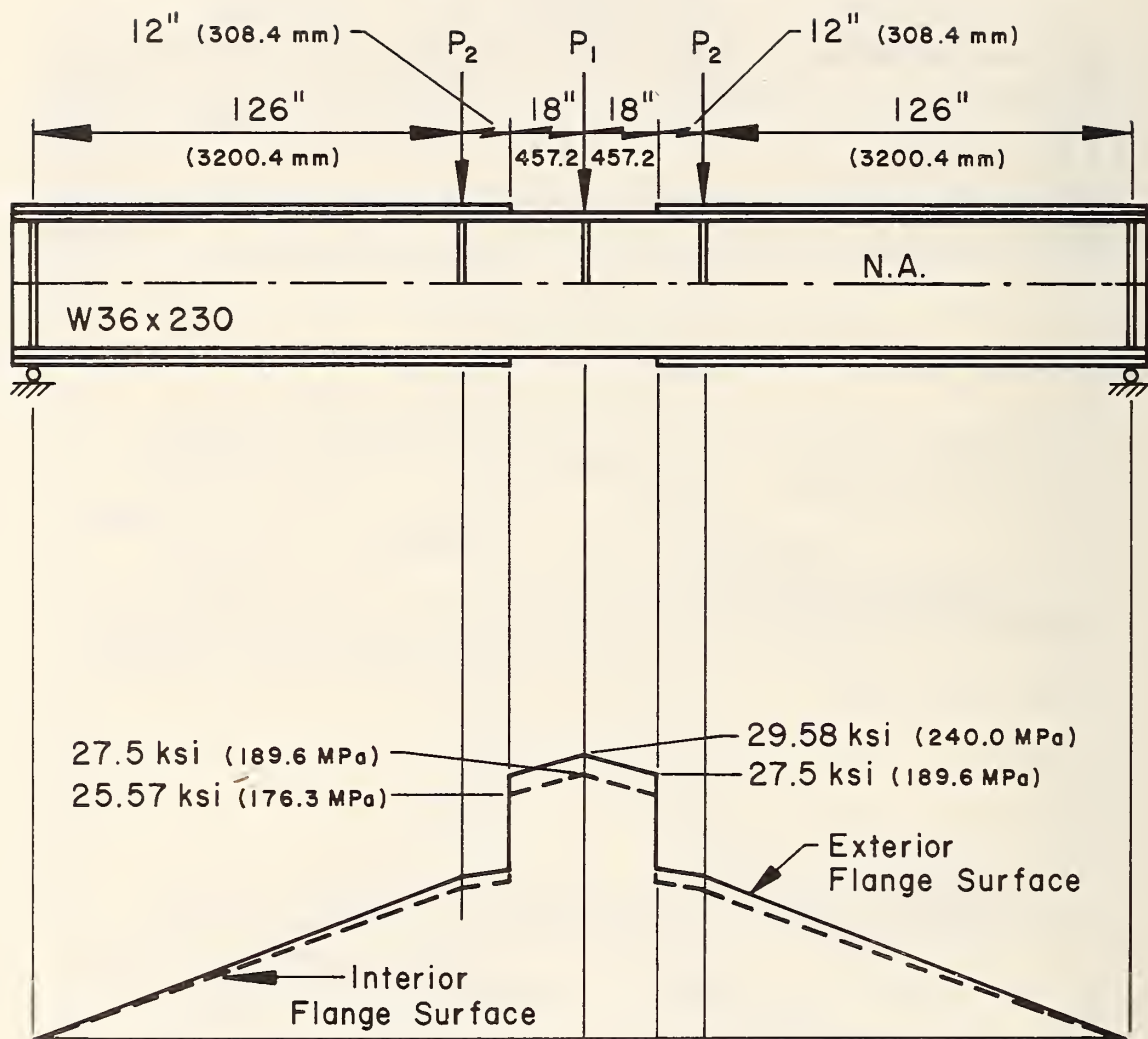


Fig. 2.6f Maximum Stress on Interior and Exterior Flange Surfaces of Beams B5 and B5A (A588, W36X230)

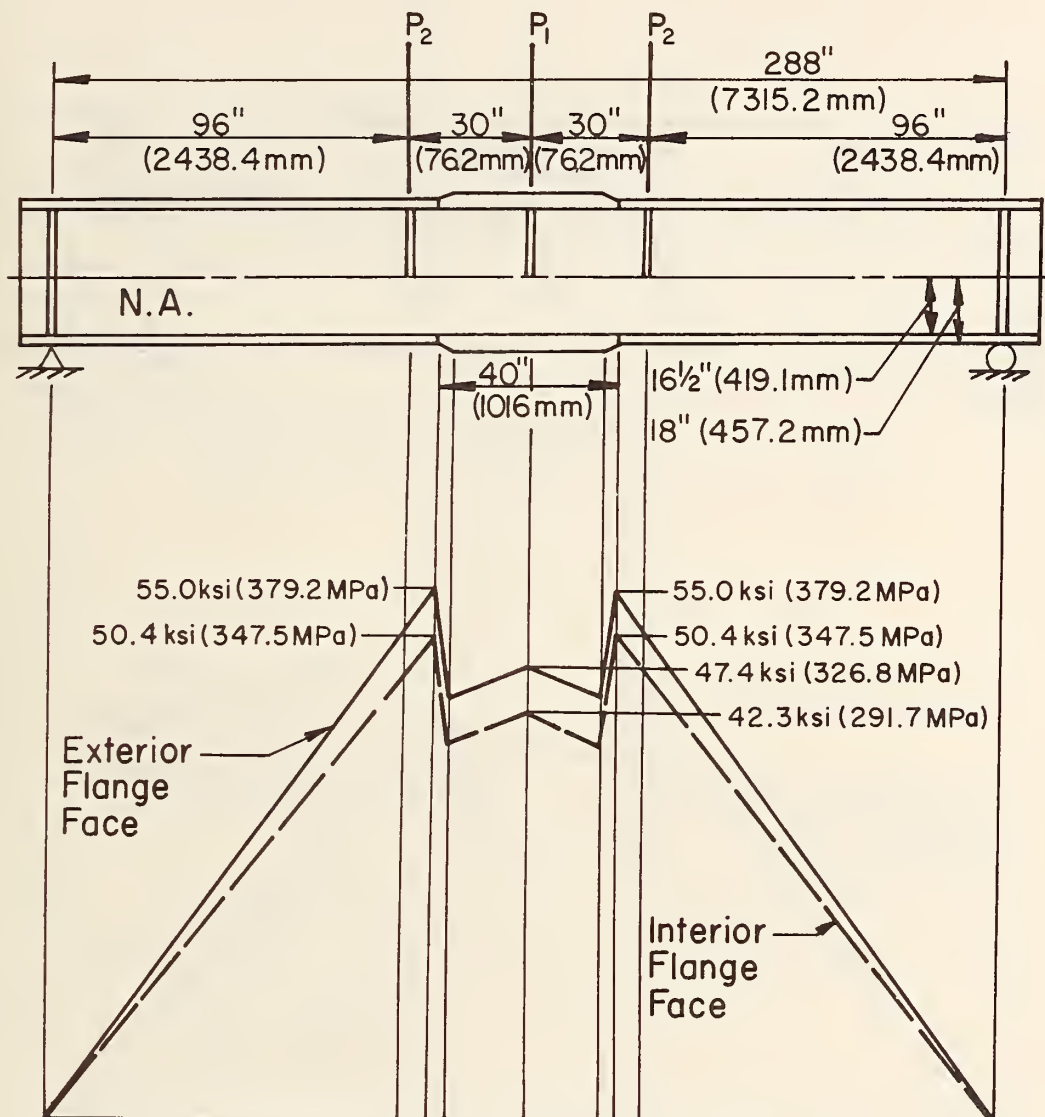


Fig. 2.6g Maximum Stress on Interior and Exterior Flange Surface of Beam B8A (A514)

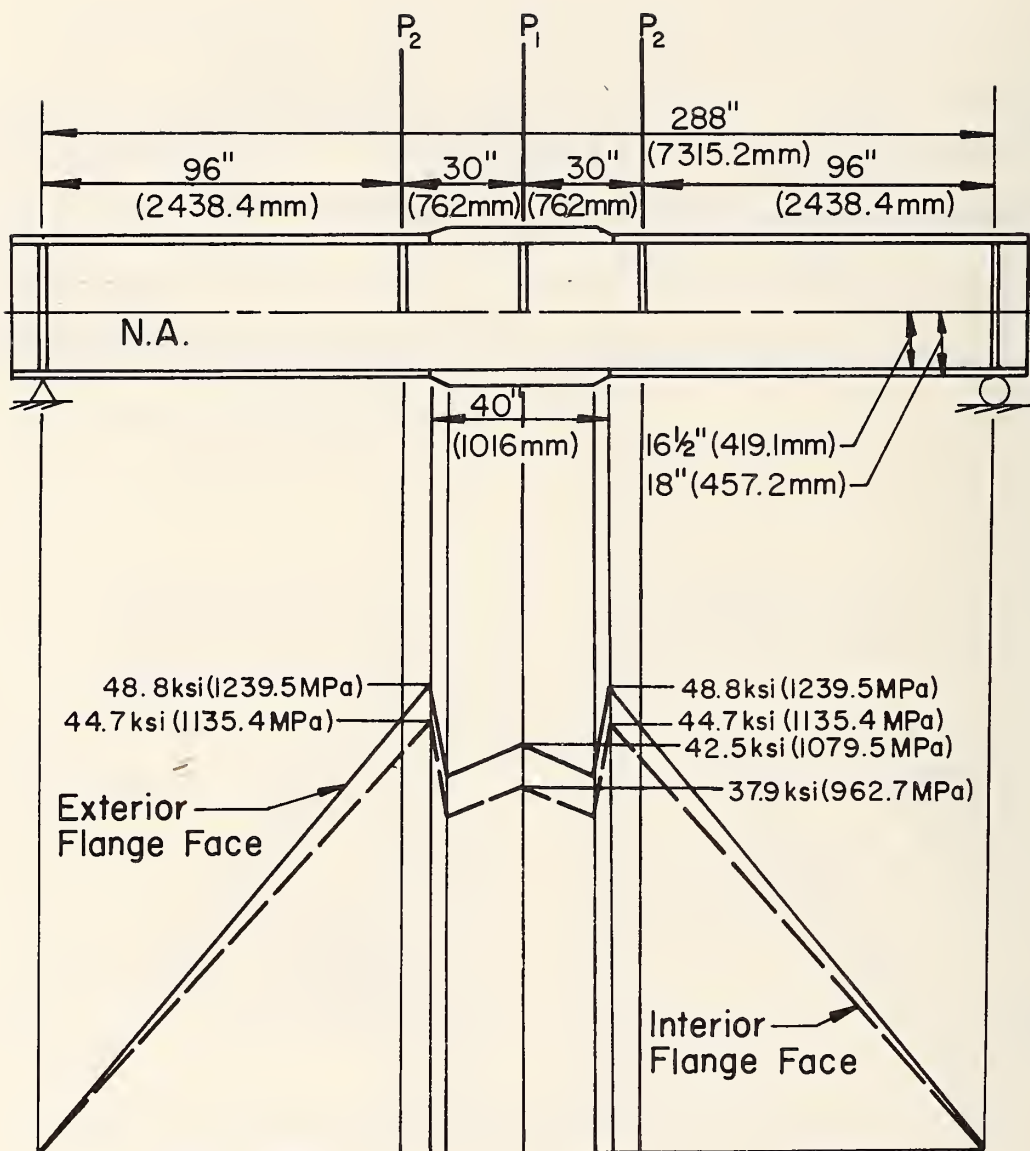


Fig. 2.6h Maximum Stress of Interior and Exterior Flange Surface of Beam B8 (A514)

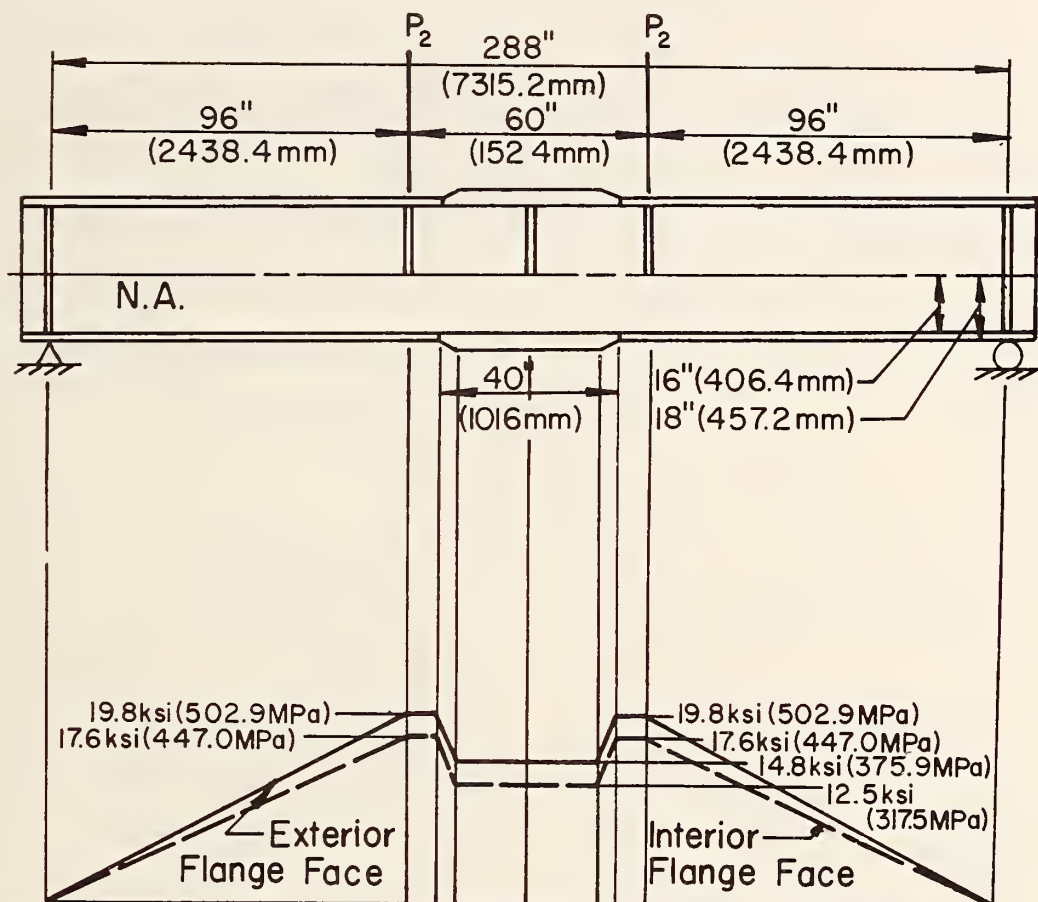


Fig. 2.6i Maximum Stress of Interior and Exterior Flange Surfaces of Beams B10 and B10A (A36)

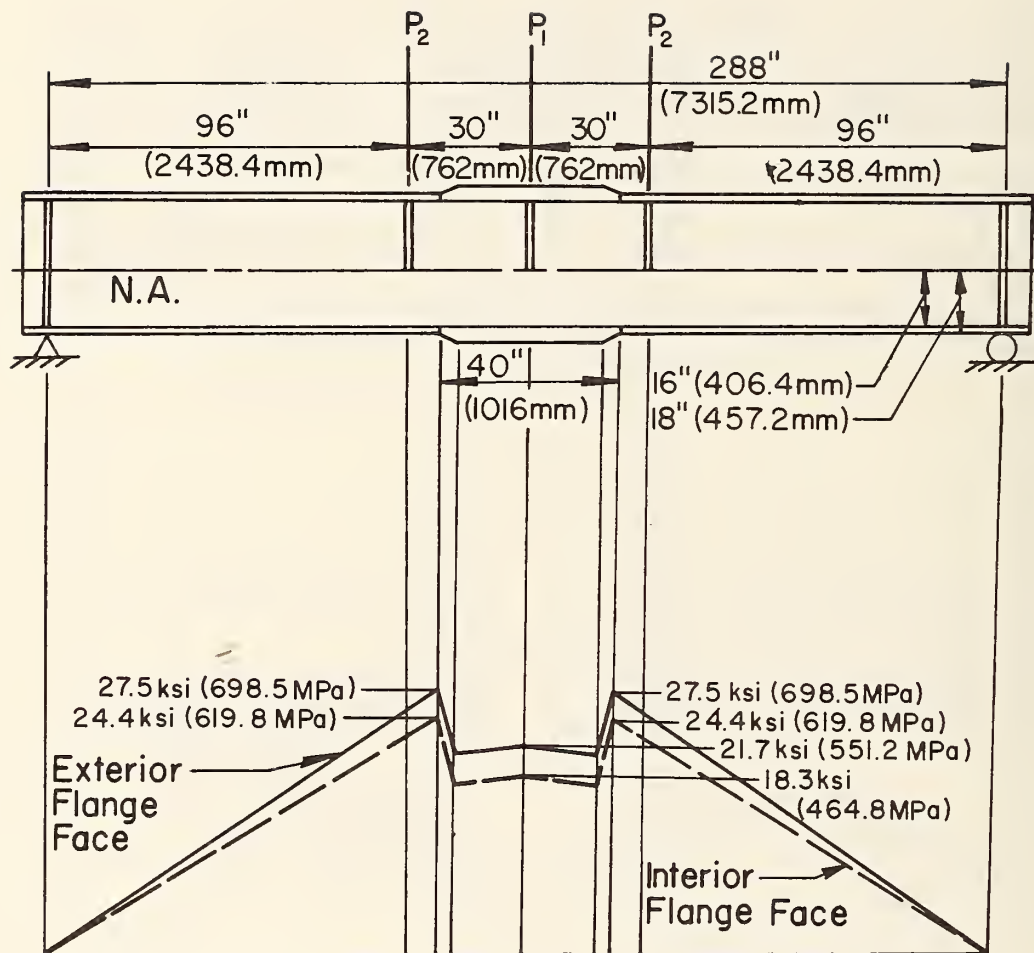


Fig. 2.6j Maximum Stress of Interior and Exterior Flange Surfaces of Beams B12 and B12A (A588)

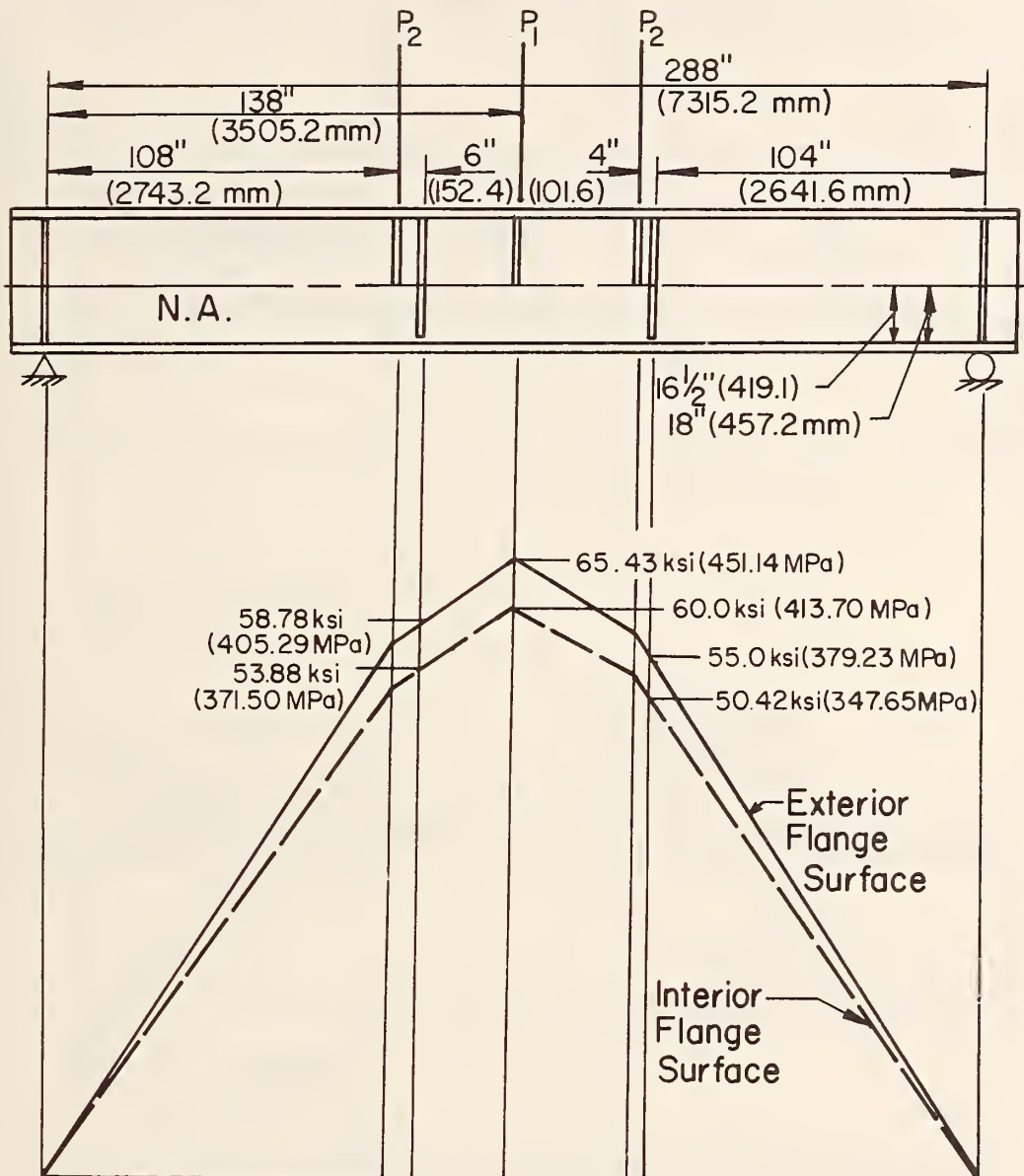


Fig. 2.6k Maximum Stress of Interior and Exterior Flange Surface of Beam B7 (A514)

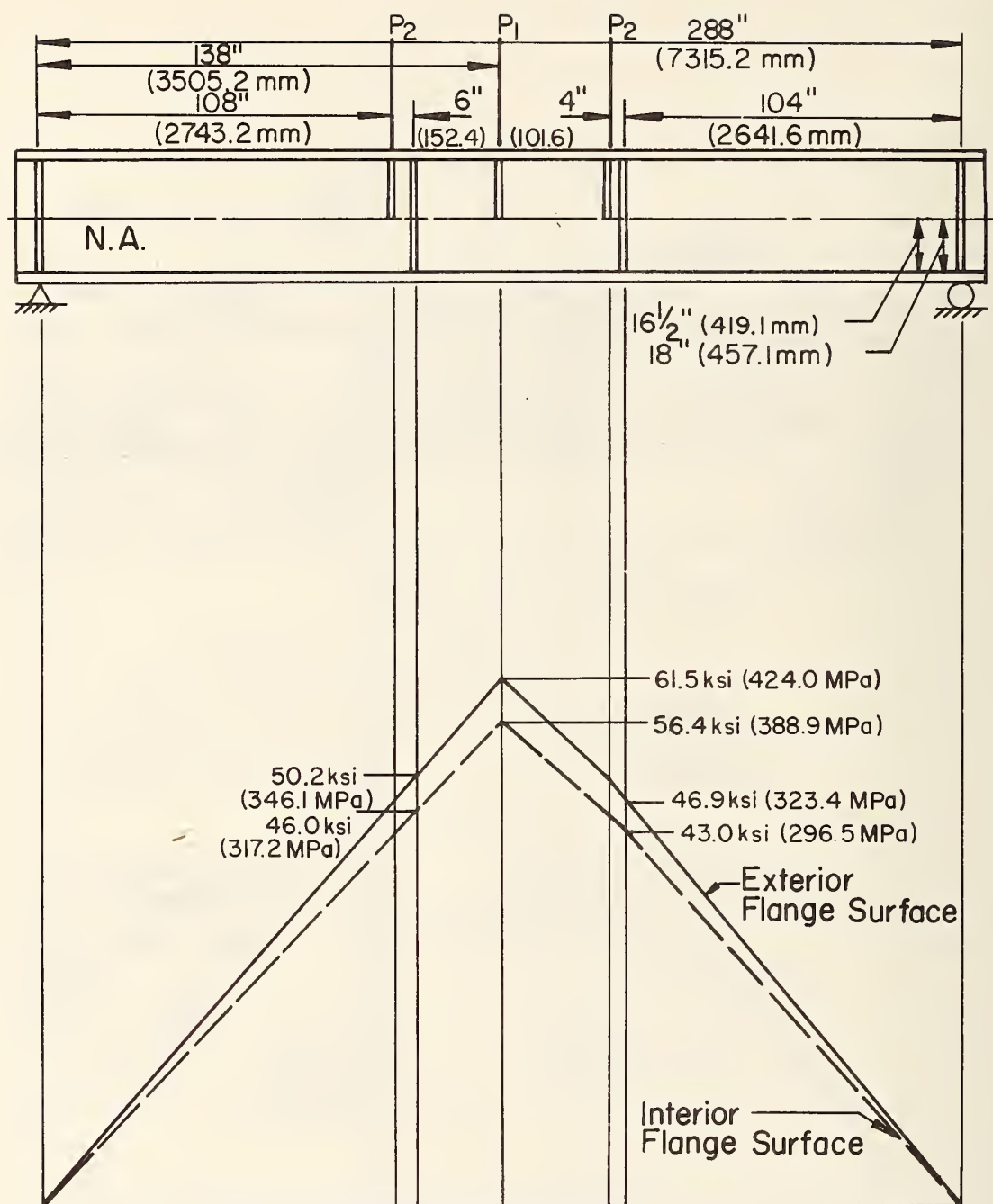


Fig. 2.6ℓ Maximum Stress of Interior and Exterior Flange Surface of Beam B7A (A514)

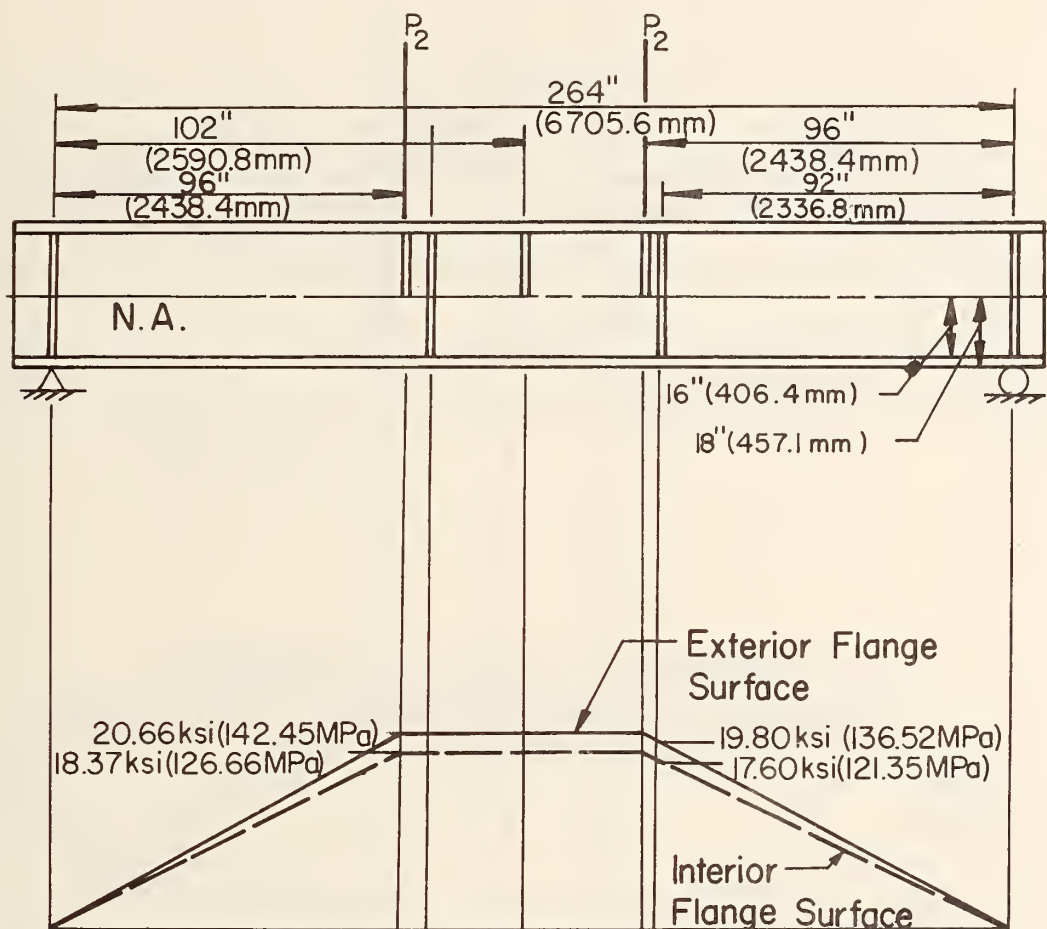


Fig. 2.6m Maximum Stress of Interior and Exterior Flange Surfaces of Beams B9 and B9A (A36)

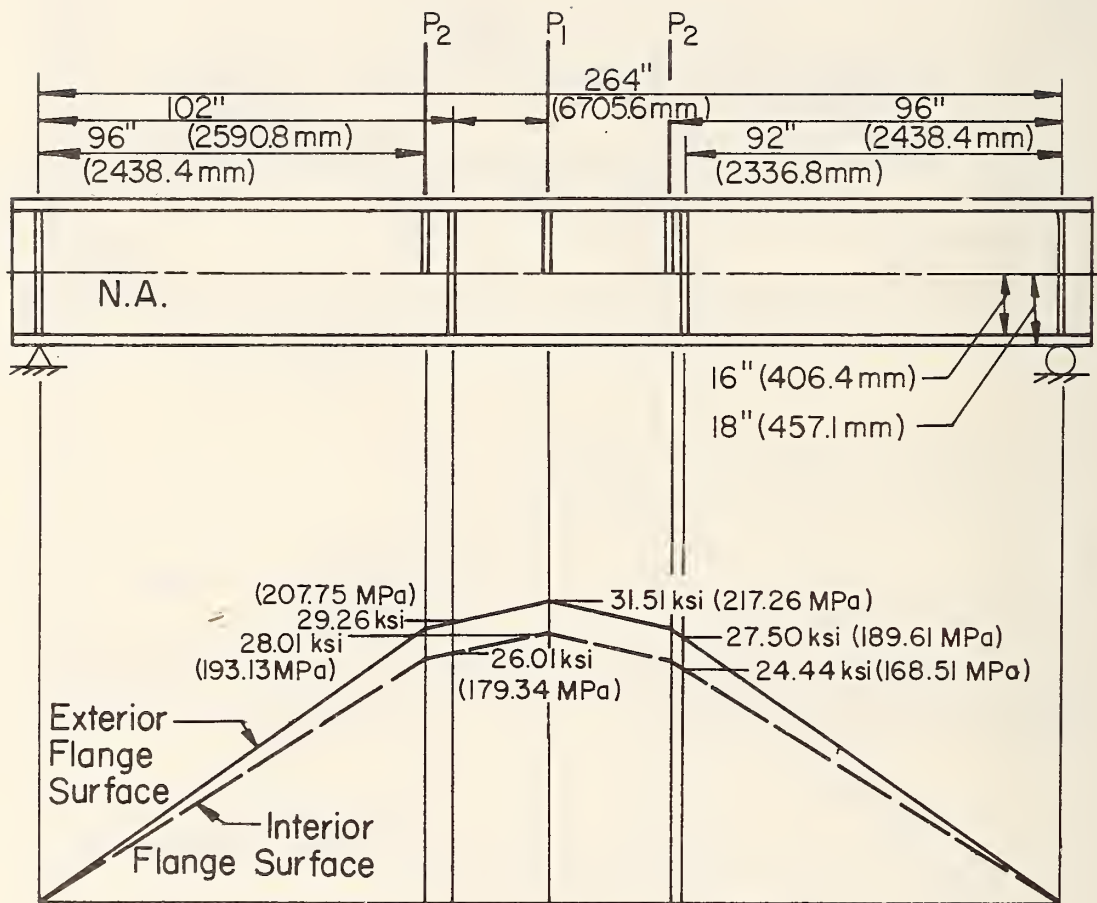


Fig. 2.6n Maximum Stress on Interior and Exterior Flange Surface of Beam B11 (A588)

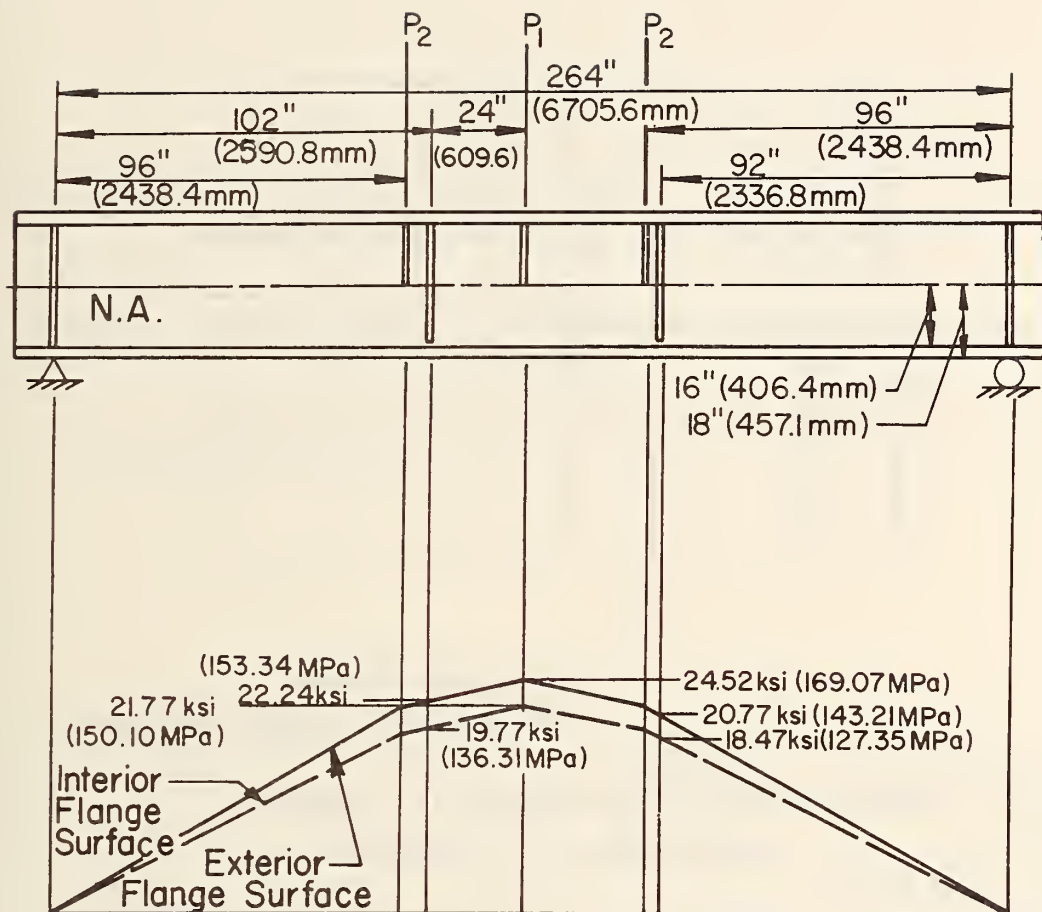
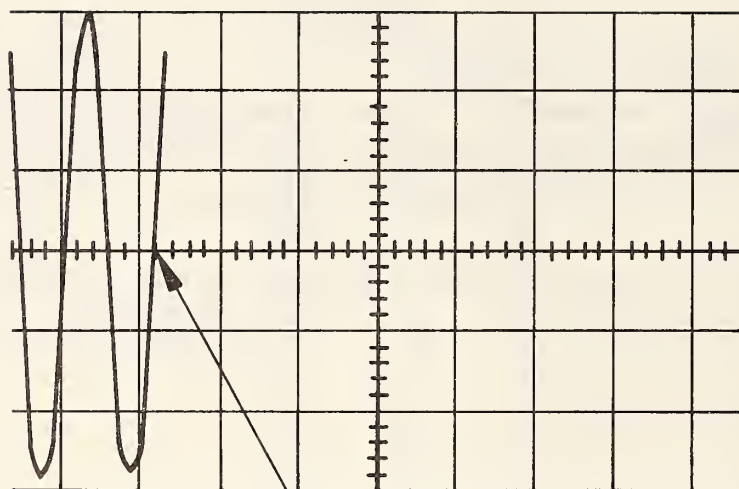


Fig. 2.6o Maximum Stress on Interior and Exterior Flange Surface of Beam B11A (A588)



Maximum Slope
100 ksi/sec (689.5 MPa/Sec)

Note: Horizontal Scale: 0.2 sec/cm
Vertical Scale: 1.5 ksi/cm

Fig. 2.7 Strain Rate Trace at Fracture (Beam B2)

B5 W36 x 230 x 24'-0"	Classification Mat'l. W36 x 230 x 10'-0"	B5A W36 x 230 x 24'-0"
--------------------------	--	---------------------------

1 - W36 x 230 x 58'-1"

30"	Ten. Flg. \mathbb{R} 7 x 3'-4" B12 \mathbb{E} 12A	Classification Mat'l. 18 x 12'-0"
	" " "	
	Comp. Flg. \mathbb{R} " "	Excess
	" " "	

1 - \mathbb{R} 30" x 3" x 15'-6"

62"	Ten. Flg.	7 x 22'-0"	B6 \mathbb{E} 6A	4' x 4'
	"	"	"	
	"	"	B11 \mathbb{E} 11A	
	"	"	"	
	Ten. Flg.	7 x 9'-4"	Ten. Flg. 7 x 9'-4"	Scrap
	" B12 \mathbb{E} 12A "	" B12 \mathbb{E} 12A	"	
	Classification Mat'l. 18 x 12'-0"		Excess	Scrap

1 - \mathbb{R} 62" x 2" x 26'-2"

Fig. 2.8a Layout for A588 Steel Girders

B3 W36 x 260 x 22'-0"	Classification Mat'l. W36 x 260 x 10'-0"	B3A W36 x 260 x 22'-0"
--------------------------	---	---------------------------

1 - W36 x 260 x 54'-1"

30"	Ten. Flg. \mathbb{R} 7"x3'-4" B10 & 10A	Classification Mat'l. 18" x 12'-0"
	" " "	
	Comp. Flg. " "	
	" " "	Excess

1 - \mathbb{R} 30" x 3" x 15'-6"

62"	Ten. Flg. R		7 x 22'-0"		B4 & 4A		4' x 4'		
	"		"		B4 & B4A				
	"		"		B9 & B9A				
	"		"		B9 & B9A				
	Ten. Flg. R		7 x 9'-4"		Ten. Flg. R		7 x 9'-4"		Scrap
	"		B10 & 10A		"		B10 & 10A		
	Classification Mat'l. 18 x 12'-0"				Excess				Scrap

1 - \mathbb{R} 62" x 2" x 26'-2"

Fig. 2.8b Layout for A36 Steel Girders

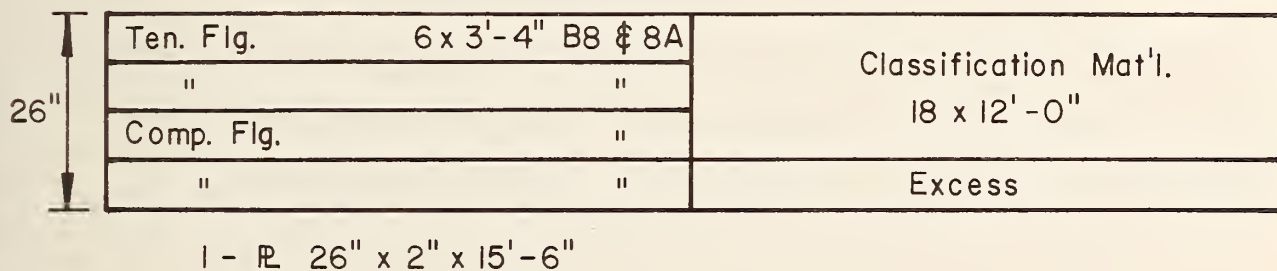
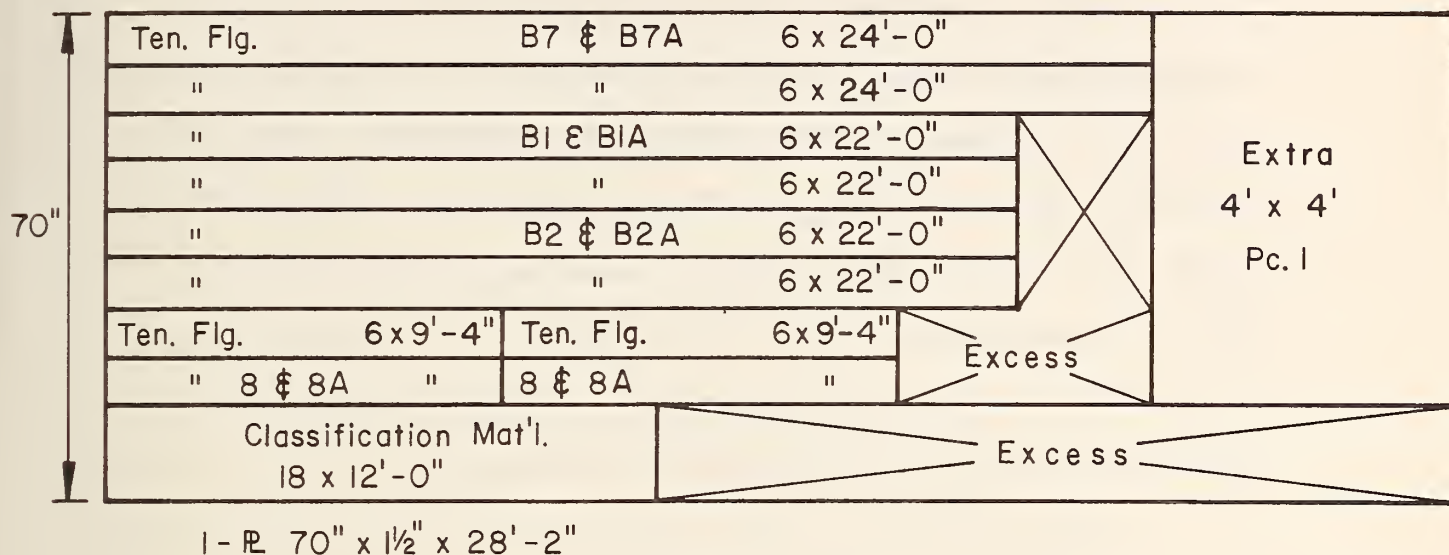


Fig. 2.8c Layout for A514 Steel Girders

3. MATERIALS CHARACTERIZATION

3.1 Test Plan

For the purposes of material characterization Standard Charpy V-Notch (CVN), precracked CVN, Dynamic Fracture Toughness, Static Fracture Toughness, and NDT tests were carried out on each plate thickness. Mill test data for each plate was also available. The chemical composition and mill test data as well as tensile data obtained at Lehigh University for all plates are summarized in Tables 3.1a, b, c and d. These plates were used to fabricate the test beams described in this report. In this section, a brief description of the experimental procedure and the test results are presented.

3.2 Charpy V-Notch Impact Tests and NDT

In order to determine the macroscopic brittle-ductile transition behavior of the plate materials, conventional ASTM standard A370-68 Type A Charpy V-Notch specimens and precracked CVN specimens were prepared from each of these plates. The specimens were all transverse (LT) with notch direction perpendicular to the rolling direction. The impact test data was analyzed using a least squares best fit sigmoidal computer program developed at Lehigh University.

Standard NDT specimens were prepared and tested from all plate materials. The results are listed in Table 3.2.

3.3 Fracture Toughness Measurements

The standard Charpy V-Notch data was used to select a test temperature range so that valid fracture toughness data could be acquired for the plates. Temperatures of 0° F (18° C), -40° F (-40° C) and -80° F (-62° C) were chosen for dynamic testing. A lower temperature range based on the transition temperature shift was selected for the slow bend (intermediate loading rate) tests. Equation 1 was used to estimate where additional tests were conducted at other temperatures

$$T_{\text{shift}} = 215 - 1.5 \sigma_{\text{ys}} \quad (1)$$

T_{shift} = transition temperature shift (° F)

σ_{ys} = room temperature static yield stress (ksi)

3.3.1 Drop Weight Test Apparatus

The dynamic K_{Ic} testing was carried out using the Lehigh drop weight test machine (see Fig. 3.1). The details of this apparatus are described in Ref. 8. The impact loading of the three-point bend specimen (Fig. 3.2) was achieved by means of a falling mass (400 lbs.) guided vertically along two parallel rails. An instrumented loading tup⁸ at the bottom of the mass was calibrated to act as a load-dynamometer. As the specimen was loaded the strain output from the tup was recorded. A typical load-time relationship is shown in Fig. 3.3.

The drop weight mass in a given set of tests was chosen to minimize the test specimen inertia. In order to minimize the influence of the specimen inertia, 0.75 in. x 0.50 in. (19.1 mm x 12.7 mm) half-rounds were positioned on the test specimen. This cushioned the application of the load and increased the loading time to about one millisecond. The half round cushions were machined from unhardened drill rods. The test specimen temperatures were controlled by a variety of means. All were held at the required test temperature for at least ten minutes prior to testing. A test was completed within ten seconds of the specimen's removal from the temperature bath.

3.3.2 Slow Bend Test Apparatus

Slow bend tests* were carried out on a standard 120 kip Tinius-Olsen screw-type tensile testing machine. The cross head of the machine could be moved at various speeds. The specimen was loaded with the same tup used for the dynamic testing. A loading rate of 20 kips per second (approximately 55 ksi/sec.) was selected for all slow bend tests. This resulted in a loading time of about 1 second. Load-time data was recorded on x-y recorders. Fracture tests of the customary "static" type, with a loading time to fracture of several minutes, were not conducted.

* Tests in which the fracture load occurs about one second after the start of loading are not "slow" in the customary usage of the term. Such tests are sometimes termed "intermediate speed" tests. However, for simplicity of language in this report, the one second loading time tests will be termed "slow bend."

3.3.3 K_c Specimen Preparation

The test specimen geometry for all K_c tests in this program is shown in Fig. 3.2. All specimens were saw cut from the original plate with their long dimension in the rolling direction. This resulted in the crack being perpendicular to the rolling direction. After the individual specimens were saw cut from the plates the cut surfaces were shaped so as to be normal to the plate surfaces. The thickness of the A36 and A588 steel specimens was reduced to 1.50 in. (38.1 mm). A notch with a 30° chevron front was machined at the center of the specimens to help initiate crack growth during the precracking process. The cyclic-loading for precracking was done on a 10 ton Amsler Vibrafore using three-point bending. The fatigue crack was formed in two stages. During the first stage, the crack was grown as quickly as possible. The final 0.125 in. (3.2 mm) of the crack was grown slowly so that the average crack growth rate was equal or less than 1 microinch per cycle (25.4 nm per cycle). The maximum K during fatigue precracking was about 40 ksi $\sqrt{\text{in.}}$ (44 MPa $\sqrt{\text{m}}$).

3.3.4 Fracture Toughness Data Evaluation

The fracture toughness, K_c, values were determined from the maximum load at the fracture of the three-point bend specimens⁹. K was determined from the relationship²⁵

$$K = \frac{Y P L}{4 (W - a)^{1.5} \frac{B}{B}} \quad (2)$$

where Y = dimensionless ratio of (a/w) approximately 4
 \bar{B} = specimen width
 W = specimen depth (3.0 in.)
 P = applied load
 L = span length (10.0 in.)
 a = effective crack length, a_e
 r_y = plastic-zone size
 $a_e = a_p + r_y$
 a_p = visual indication of physical crack size at fracture

The plastic-zone size, r_y , was defined as

$$r_y = \frac{1}{2\pi} \left(\frac{K}{\sigma_y} \right)^2 \quad (3)$$

where σ_y is the yield strength

Equations 2 and 3 were solved by a simple iteration method⁹. The value of σ_y corresponded to the temperature and loading speed of the test conditions. This was determined by the following equation¹⁰.

$$\sigma_y = \sigma_{ys} \left| + 75^\circ \text{ F}, t_o \right. + \frac{174,000}{(T + 459) \log (2 \times 10^{10} t)} - 27.4 \quad (4)$$

where t = loading time to maximum load
 t_o = time of load application for a static test (50 sec.)
 T = testing temperature ($^\circ\text{F}$)
 σ_{ys} = yield stress (ksi) at room temperature static test
 σ_y = values of σ_{ys} adjusted for temperature and strain rate

3.4 Drop Tear Energy Measurements

A method of direct measurement of fracture energy was described in Ref. 8. After the specimen is fractured the drop weight is arrested by two cushions made from Type 1100-0 or 6061-0 electrical grade aluminum 1 in. (25.4 mm) diameter rods. Figure 3.1 shows the test setup. When the drop weight impacts the aluminum blocks, they are compressed inelastically and their difference in height is a measure of the energy absorbed. In addition, the drill rod cushions are subjected to permanent diamond shaped indentation during loading of the specimen. The length of the indentation is also a function of the energy absorbed.

The initial potential energy in the system less the sum of the energies absorbed by the aluminum and drill rod cushions represents the net energy absorbed by the fractured specimen. This value divided by the severed area yields the drop tear energy (DTE). Material behavior in terms of DTE as a function of temperature is obtained simultaneously with the K tests.

3.5 Results of Fracture Tests

3.5.1 Charpy V-Notch Tests

Figures 3.4 through 3.8 summarize the CVN test results for the flange materials in the form of standard and precracked Charpy V-Notch curves. For the three materials the energy absorption and the lateral expansion data, plotted against temperature, show a conventional

form with relatively sharp transition behavior. The 15 ft.-lb. (20 joule) energy level and the 15 mil. (0.38 mm) lateral expansion transition temperatures for the standard CVN test are listed in Table 3.3 for each flange plate. Corresponding figures for the remaining beam materials are given in Appendix C.

3.5.2 K_c Test Results

The dynamic and static fracture toughness for the flange plates are summarized in Figs. 3.9 through 3.13. Also shown is the limiting test validity requirement¹⁰.

$$\bar{B} > 2.5 \left(\frac{K_c}{\sigma_y} \right)^2 \quad (5)$$

where \bar{B} = specimen thickness

K_c = fracture toughness value

σ_y = yield stress of the material at test conditions

Figures of K vs. T for the remaining beam materials and tabulated values are given in Appendix C. Significant scatter was noted in the one second fracture toughness tests for A588 steel.

In some cases, computed K_c values were obtained which did not satisfy the above ASTM thickness requirement. The trend curves for the limited test data were based on earlier results. Although from these curves it was possible to indicate the brittle-ductile transition temperatures, it appears that another independent method to

evaluate fracture toughness values at these temperatures will be needed. The J-integral¹¹ type tests with three-point bend specimens might provide the required data points to confirm the fracture behavior in the transition temperature range.

Seventy-five percent of Barsom's temperature shift relationship⁷ (see Eq. 1) was used to determine the expected temperature shift caused by the change in loading rates between dynamic and one second tests. These values are listed below for each steel.

	<u>Temperature Shift</u>		<u>75% Temperature Shift</u>	
	°F	°C	°F	°C
A36	149	83	112	62
A588	124	69	93	52
A514	34	19	26	14
A36 Rolled	128	71	96	53
A588 Rolled	116	64	87	48

The actual temperature shifts are shown in the K_{Ic} vs. temperature plots (Figs. 3.9 through 3.13 and Appendix C) for the dynamic and intermediate loading rate tests used in this project. These actual values are larger than or equal to the shifts predicted by Barsom.

The standard CVN and dynamic K_{Ic} results were compared by using the relationship proposed by Barsom⁷ for the transition temperature region of the CVN plots.

$$K_{Id} = [5E (CVN)]^{\frac{1}{2}} \quad (6)$$

E = modulus of elasticity (psi)

K_{Id} = fracture toughness (psi $\sqrt{\text{in.}}$)

CVN = Charpy energy (ft.-lbs.)

These values are also plotted on the K_c vs. temperature plots in Figs. 3.9 through 3.13 and Appendix C. There is a generally conservative correlation between the measured K_{Id} values and the plot given by Eq. 6 for all materials tested except the A36 rolled beam flange.

The temperature shift between the beam fracture temperature and the 15 ft.-lb. (20 joule) standard CVN test temperature is compared in Fig. 3.17 to the temperature shift from the 1974 AASHTO Material Specification. Beam B5A (A588 rolled) fractured at a relatively small crack size (see Fig. 5.6). However, the temperature shift applicable to the specification was 55° F because its mill report yield point exceeded 65 ksi (448 MPa). This can be seen in Fig. 8.5.

3.5.3 Drop Tear Energy Test Results

The DTE data points were obtained simultaneously with the K_{Id} test data. A full DTE vs. Temperature plot was not obtained. Most of the points were on the lower shelf or in the transition region. The DTE vs. Temperature plots for the flange plate material are presented in Figs. 3.14 through 3.16. Generally, the transition temperatures from these diagrams are higher and more conservative than the

respective CVN transition temperature for the same plate. Tabulated data for all materials is included in Appendix C.

3.6 Discussion of Test Results

The test methods described in the preceding sections of Chapter 3 are generally standard techniques for evaluating the toughness behavior of steel products. The standard CVN test, the DT test, the NDT test and the K_{Ic} test are all currently listed as ASTM Standard Test Methods which in one form or another are used to measure a material's toughness.

Since the primary interest in this report is to examine the ability of a cracked welded bridge detail to resist fracture it could be deemed sensible to only evaluate the materials K_{Ic} behavior. This is because fracture mechanics as embodied in K_{Ic} type measurements is the only accepted way of evaluating the interaction of flaw size, stress level and material toughness. However, the AASHTO bridge specifications use correlations between CVN and K measurements to provide the desired toughness level in the steel. For this reason it was desirable to run K_{Ic} and CVN tests for this project. These data, K_{Ic} and CVN, form the basis for the analysis of the beam and gusset details described in Chapters 4 through 10.

The additional tests, precracked CVN, NDT, and DT were included in the program to provide reference points with other existing structural steel standards which utilize NDT and DT type measurements for specification purposes. Furthermore, at the initial stages

of the current project it was not known whether the standard K_{Ic} and CVN measurements would provide an adequate basis for the evaluation of the welded detail fracture tests. As will be seen in the remaining chapters, only the CVN and K_{Ic} results were used in the fracture analysis as these provided an adequate basis for evaluating the large beam and gusset test results. With regard to the actual performance of the steel materials used in the current project, it was found that all of the test methods, the precracked CVN, the standard CVN, the K_{Ic} test, the NDT test, and the DT test provided a basis for evaluating the toughness of the steel. None of the various tests produced results which could be viewed as unusual. The results were typical of those previously reported for similar steels in Ref. 8.

TABLE 3.1a RESULTS OF MILL TESTS

Plate t	Steel	Heat Number	Yield Pt. (ksi)	Tensile Strength (ksi)	Elong. Gage/%	C	M _n	P	S	S _i	C _u	N _i	C _r	V	M _o	B
1/2"	A36	401P1041	44.10	66.20	8/31	.14	1.06	.013	.017	.19						
1"	A36	411P4511	40.70	61.40	8/32	.14	1.06	.014	.032	.19						
2"	A36	402P7031	44.00	70.00	2/34	.17	1.06	.013	.022	.21						
3"	A36	432N4711	45.00	72.00	2/32	.17	1.09	.015	.024	.21						
1/2"	A588	401N6061	57.20	74.70	8/26	.13	1.09	.019	.028	.28	.28	.37	.57	.038		
1/2"	A588	432N2461	53.50	74.60	8/27	.12	1.17	.011	.023	.25	.29	.34	.50	.031		
2"	A588	401P8161	56.50	78.50	2/33	.12	1.09	.013	.019	.24	.26	.32	.54	.033		
2"	A588	402P7731	61.00	80.00	8/33	.10	1.12	.011	.025	.28	.29	.28	.55	.030		
3"	A588	494N5681	57.50	79.50	2/30	.12	1.08	.010	.027	.29	.29	.31	.51	.028		
3/8"	A514/J	801P03810	113.63	118.50	2/24	.17	.61	.008	.023	.27					.57	.0025
1/2"	A514/J	801P03810	113.00	120.25	2/30	.17	.61	.008	.023	.27					.57	.0025
1"	A514/J	801P03810	114.55	121.80	2/32	.17	.61	.008	.023	.27						
1-1/2"	A514/M	802P50780	125.10	134.15	2/31	.18	.61	.008	.023	.31		1.40			.52	.0028
1-1/2"	*A514/M	802N80660	117.00	129.50	2/21	.17	.59	.008	.021	.29		1.37			.49	.0022
2"	A514/M	801N18640	110.00	122.25	2/19	.18	.66	.007	.023	.26		1.33			.50	.0036

* Compression Flange

TABLE 3.1b RESULTS OF MILL TESTS

Plate t	Steel	Heat Number	Yield Pt. (MPa)	Tensile Strength (MPa)	Elong. Gage/%	C	M _n	P	S	S _i	C _u	N _i	C _r	V	M _o	B
1/2"	A36	401P1041	304	456	8/31	.14	1.06	.013	.017	.19						
1"	A36	411P4571	281	423	8/32	.14	1.06	.014	.032	.19						
2"	A36	402P7031	303	483	2/34	.17	1.06	.013	.022	.21						
3"	A36	432N4711	310	496	2/32	.17	1.09	.015	.024	.21						
1/2"	A588	401N6061	394	515	8/26	.13	1.09	.019	.028	.28	.28	.37	.57	.038		
1/2"	A588	432N2461	369	514	8/27	.12	1.17	.011	.023	.25	.29	.34	.50	.031		
2"	A588	401P8161	390	541	2/33	.12	1.09	.013	.019	.24	.26	.32	.54	.033		
2"	A588	402P771	421	552	8/33	.10	1.12	.011	.025	.28	.29	.28	.55	.030		
3"	A588	494N5681	396	548	2/30	.12	1.08	.010	.027	.29	.29	.31	.51	.028		
3/8"	A514/J	801P03810	783	817	2/24	.17	.61	.008	.023	.27					.57	.0025
1-1/2"	A514/J	801P03810	779	829	2/30	.17	.61	.008	.023	.27					.57	.0025
1"	A514/J	801P03810	790	840	2/32	.17	.61	.008	.023	.27					.57	.0025
1-1/2"	A514/M	802P50780	863	925	2/31	.18	.61	.008	.023	.31		1.40			.52	.0028
1-1/2"	*A514/M	802N80660	807	893	2/21	.17	.59	.008	.021	.29		1.37			.49	.0022
2"	A514/M	801N18640	758	843	2/19	.18	.66	.007	.023	.26		1.33			.50	.0036

* Compression Flange

TABLE 3.1a,b (CONT'D.) RESULTS OF MILL TESTS

Steel	Heat Number	Yield Pt (ksi)	Tensile Strength (ksi)	Elong. Gage/%	C	M _n	P	S	S _i	C _u	N _i	C _r	V
A36													
W36X260	122N478	57.9	75.4	8/28.5	.16	1.23	.015	.012					
A588													
W36X230	185N056	66.4	85.2	8/25.2	.16	.94	.012	.024	.24	.31	.34	.55	.02

TABLE 3.1a,b (CONT'D.) RESULTS OF MILL TESTS

Steel	Heat Number	Yield Pt (MPa)	Tensile Strength (MPa)	Elong. Gage/%	C	M _n	P	S	S _i	C _u	N _i	C _r	V
A36													
A36X260	122N478	399	520	8/28.5	.16	1.23	.050	.012					
A588													
W36X230	185N056	458	587	8/25.5	.16	.94	.012	.024	.24	.31	.34	.55	.02

TABLE 3.1c MILL TEST CVN RESULTS

Plate t	Steel	Heat Number	Charpy Results (Ft-lbs.)			Test Temp. (°F)	Spec. Ft-lbs. @ °F	Charpy Results (Joules)			Test Temp. (°C)	Spec. Joules @ °C
			1	2	3			1	2	3		
1/2"	A36	401P1041	157	170	163	40	15 @ 40	213	231	221	4.5	20 @ 4.5
1"	A36	411P4571	68	53	34	40	15 @ 40	92	72	46	4.5	20 @ 4.5
2"	A36	402P7031	39	54	53	40	15 @ 40	53	73	72	4.5	20 @ 4.5
3"	A36	432N4711	74	75	60	40	15 @ 40	100	102	81	4.5	20 @ 4.5
1/2"	A588	401N6061	52	46	49	40	15 @ 40	71	62	67	4.5	20 @ 4.5
1/2"	A588	432N2461	48	44	22	40	15 @ 40	65	60	30	4.5	20 @ 4.5
2"	A588	401P8161	82	65	83	40	15 @ 40	111	88	113	4.5	20 @ 4.5
2"	A588	402P7731	65	77	40	40	15 @ 40	88	105	54	4.5	20 @ 4.5
3"	A588	494N5681	37	41	57	40	15 @ 40	50	56	77	4.5	20 @ 4.5
3/8"	A514/J	801P03810	28/39	20/34	19/28	0	25 @ 0	38/53	27/46	26/38	-18	34 @ -18
1/2"	A514/J	801P03810	32	32	34	0	25 @ 0	43	43	46	-18	34 @ -18
1"	A514/J	801P03810	62/26	56/26	47/26	0	25 @ 0	84/35	76/35	64/35	-18	34 @ -18
1-1/2"	A514/M	802P50780	55	56	49	0	25 @ 0	75	76	67	-18	34 @ -18
1-1/2"	*A514/M	802N80660	28	27	27	0	25 @ 0	38	37	37	-18	34 @ -18
2"	A514/M	801N18610	64	62	60	0	25 @ 0	87	84	81	-18	34 @ -18

* Compression Flange

TABLE 3.1c (CONT'D) MILL TEST CVN RESULTS

Steel	Heat Number	Charpy Results (Ft-lbs)			Test Temp (°F)	Spec Ft-lbs @ °F	Charpy Results (Joules)			Test Temp. °C	Spec. Joules @ °C
		1	2	3			1	2	3		
A36 W36X260	122N478	239	239	239	40	15@40	324	324	324	4.5	20@4.5
A588 W36X230	185N056	87	75	60	40	15@40	118	102	81	4.5	20@4.5

TABLE 3.1d LEHIGH TENSILE TESTS

Component	Thickness in. (mm)	Steel Type	No. of Tension Spec.	Static Yield Stress		Tensile Strength		Mean Elong. %	Mean Reduc. in Area %
				ksi (MPa)	St.Dev.	ksi (MPa)	St.Dev.		
Web PL	0.125 (3.2)	A36	3	44.36 (305.9)	1.37	64.07 (441.8)	0.20	29.5 ^b	62.3
Flange PL	2.000 (50.8)	A36	3	35.66 (245.9)	1.24	65.50 (451.6)	0.16	42.4 ^a	58.7
Flange PL	3.000* (76.2)	A36	10	35.89 (247.5)	0.56	67.11 (462.7)	0.80	40.6 ^a	60.3
Web PL	0.125 (3.2)	A588	5	59.40 (409.6)	3.62	80.72 (556.6)	1.15	23.2 ^a	65.0
Flange PL	2.000 (50.8)	A588	5	47.70 (328.9)	0.84	69.79 (481.2)	0.50	45.7 ^a	72.3
Flange PL	3.000* (76.2)	A588	10	45.86 (316.2)	1.44	72.07 (496.9)	1.59	38.9 ^a	67.6
Web PL	0.125 (3.2)	A514	3	111.39 (768.0)	0.81	116.05 (800.2)	0.72	11.4 ^b	50.8
Flange PL	1.500 (38.1)	A514	5	116.02 (800.0)	3.66	122.85 (847.1)	4.11	28.0 ^a	64.0
Flange PL	2.000 (50.8)	A514	5	122.92 (847.5)	1.36	131.86 (909.2)	1.13	27.1 ^a	62.4
Web Rolled	0.813 (20.6)	A36	4	51.18 (352.9)	1.03	71.79 (495.0)	1.10	30.2 ^b	67.5
Flange Rolled	1.438 (36.5)	A36	4	47.51 (327.6)	0.67	70.55 (486.4)	0.52	45.8 ^a	70.3
Web Rolled	0.750 (19.1)	A588	4	59.65 (411.3)	2.77	81.26 (560.3)	1.06	25.3 ^b	64.8
Flange Rolled	1.250 (31.8)	A588	4	57.96 (399.6)	0.68	81.01 (558.6)	0.68	37.6 ^a	68.0

* Tensile specimens half thickness

a 4 in. (101.6 mm) gage length

b 8 in. (203.2 mm) gage length

** Variation between mill results and Lehigh data are within 22% for A36 PL, 23% for A588 PL, 11% for A514 PL, 12% for A36 rolled, and 11% for A588 rolled. This difference can be attributed to differences in strain rates.

TABLE 3.2 NIL DUCTILITY TEMPERATURE

Steel Type	Plate Thickness		NDT	
	(in)	(cm)	(°F)	(°C)
A36	2	51	-5	-21
A36	3	76	15	-9
A588	2	51	5	-15
A588	3	76	15	-9
A514	1-1/2	38	-85	-65
A514	3	76	-115	-82
A36 W36X260 web	13/16	21	5	-15
A36 W36X260 flange	1-7/16	37	5	-15
A588 W36X230 web	3/4	19	-35	-37
A588 W36X230 flange	1-1/4	32	*	*

* Greater than 10° F (-12° C)

TABLE 3.3a TRANSITION TEMPERATURE DATA FOR FLANGE PLATES

Material	Transition Temperature (°F)	
	(15 ft.-lb.)	(15 mil)
A36 (2" P1)	-15	-24
A588 (2" P1)	-14	-19
A514 (1-1/2" P1)	-122*	-106
A36 (1-7/16" P1)	-38	-56
A588 (1-1/4" P1)	-59*	-76

(a)

TABLE 3.3b

Material	Transition Temperature (°C)	
	(20 Joule)	(0.38 mm)
A36 (51 mm P1)	-26	-31
A588 (51 mm P1)	-25.5	-28
A514 (38 mm P1)	-85.5*	-77
A36 (37 mm P1) W36X260	-39	-49
A588 (32 mm P1) W36X260	-50.5*	-60

(b)

*Transition Temperature of 17 ft-lbs (23 Joules)

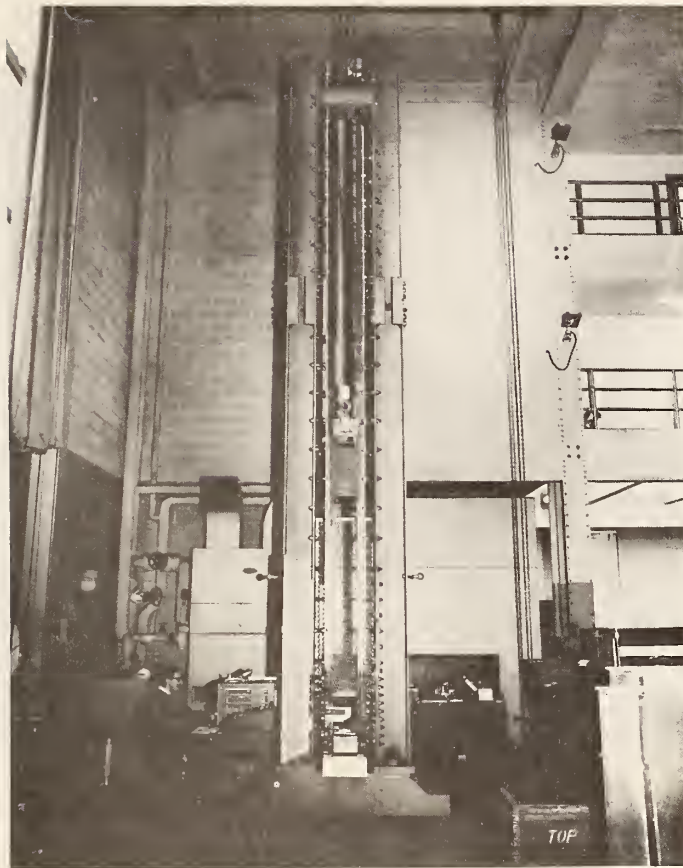
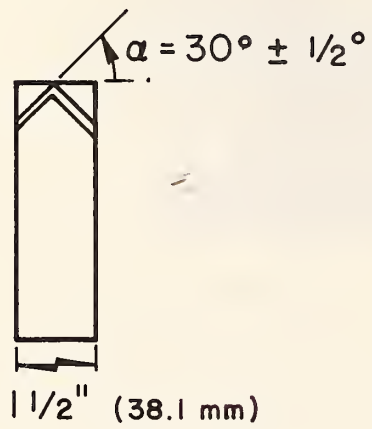
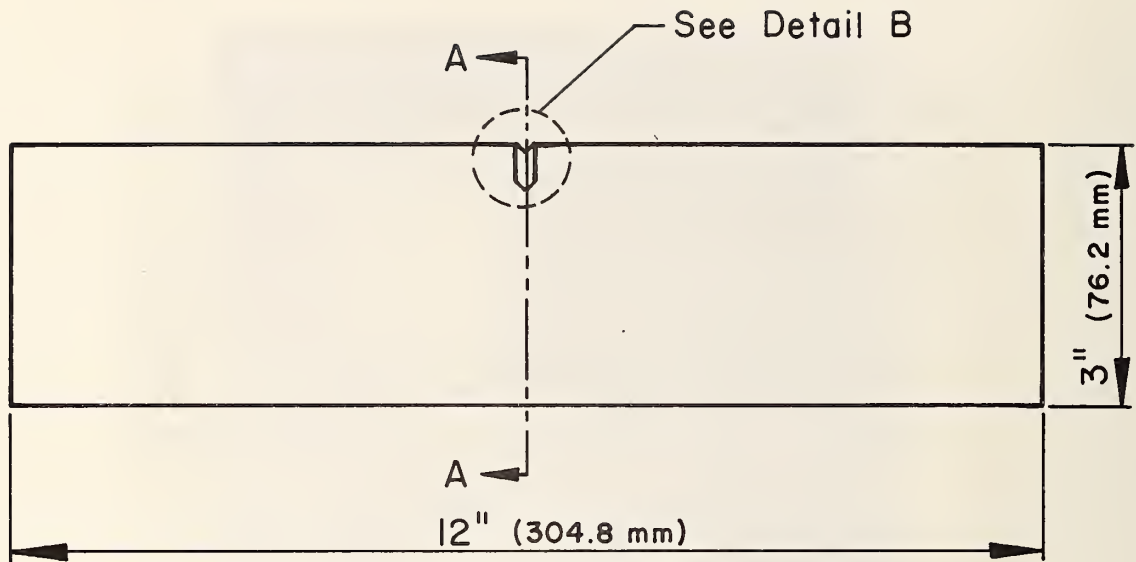
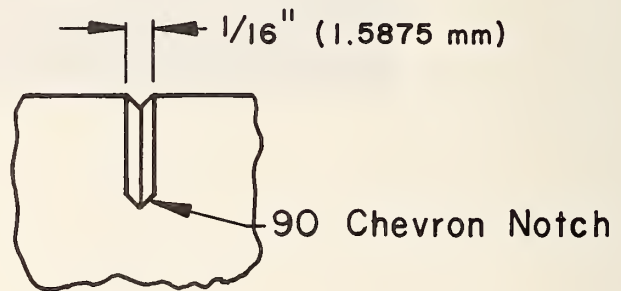


Fig. 3.1 Lehigh Drop Weight Machine

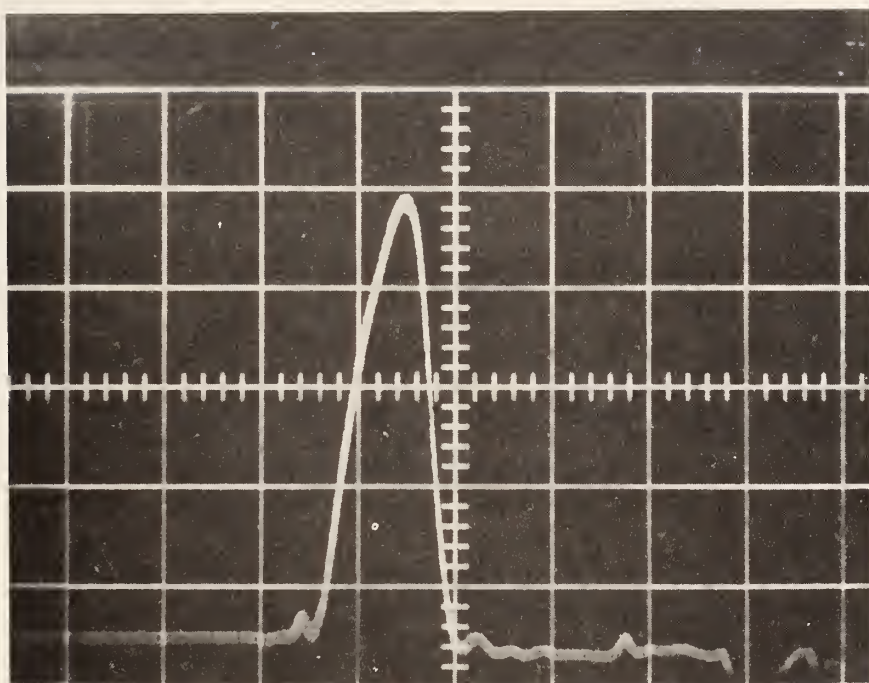


Section A-A



Detail B

Fig. 3.2 Three-Point Bend Specimen



Note: Horizontal Scale: 1.0 millisecond/cm
Vertical Scale: 4.0 kips/cm

Fig. 3.3 Load-Time Relationship

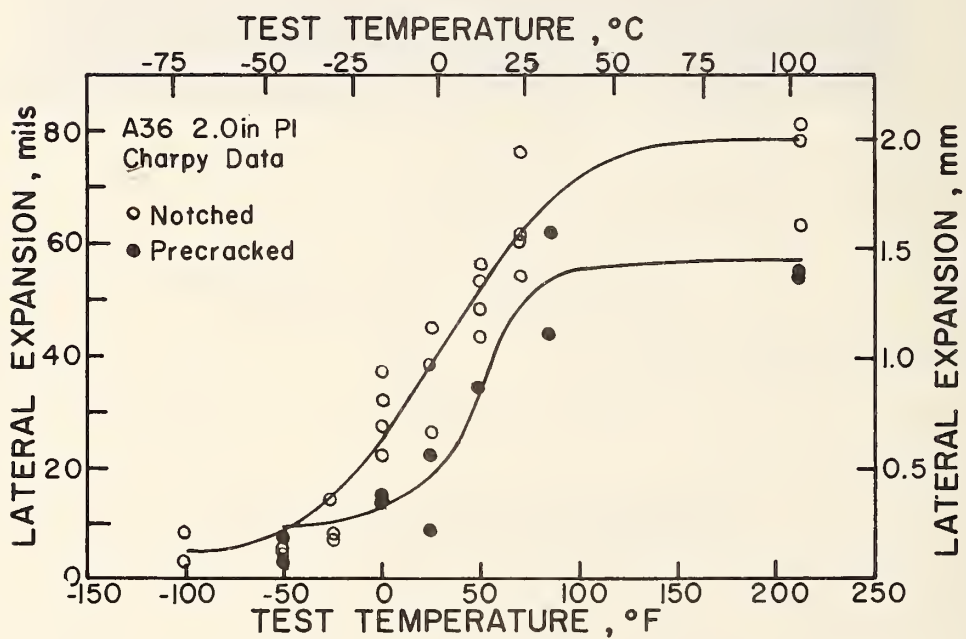
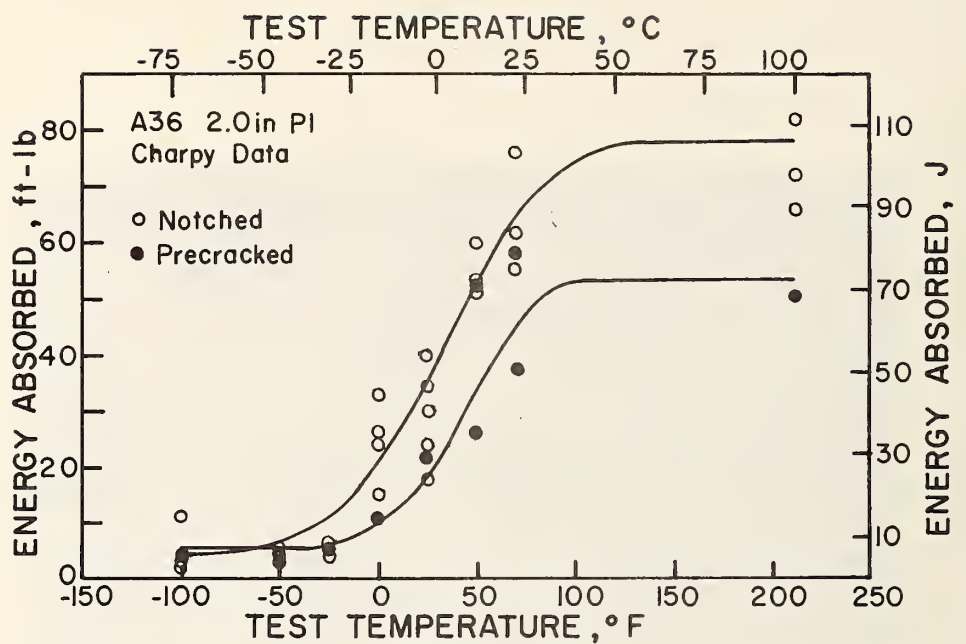


Fig. 3.4 A36, 2 inch PL CVN

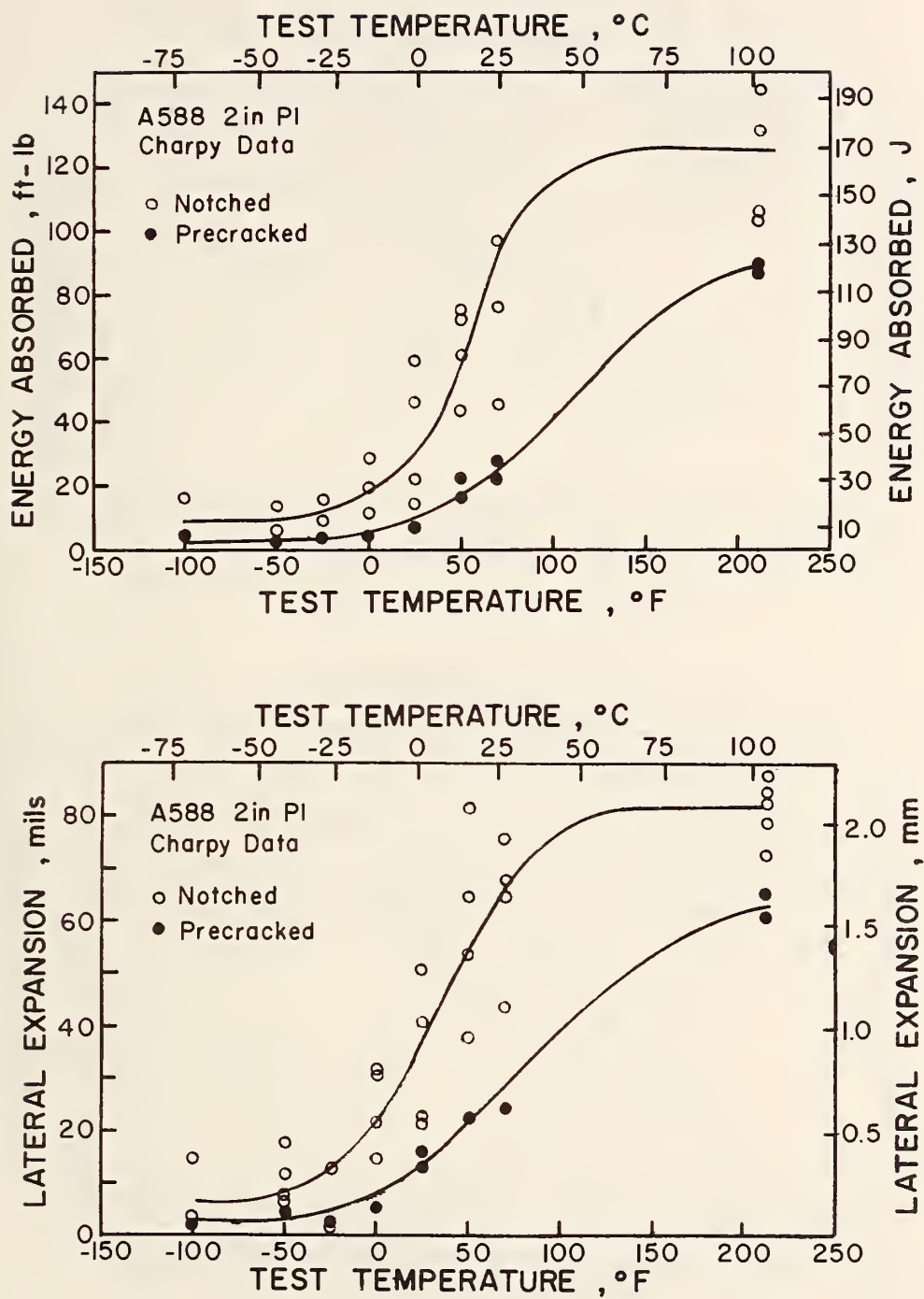


Fig. 3.5 A588, 2 inch PL CVN

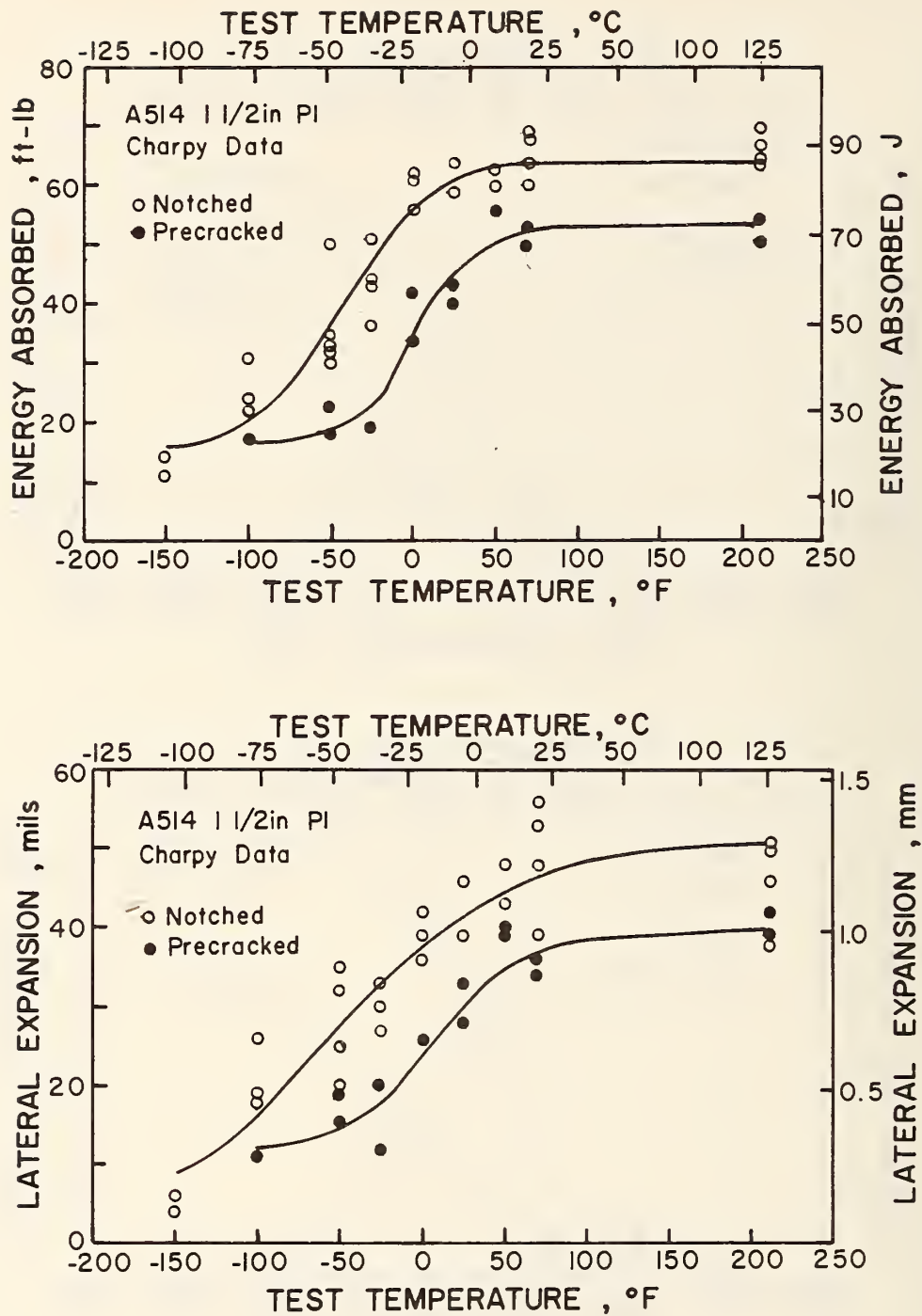


Fig. 3.6 A514, 1-1/2 inch PL CVN

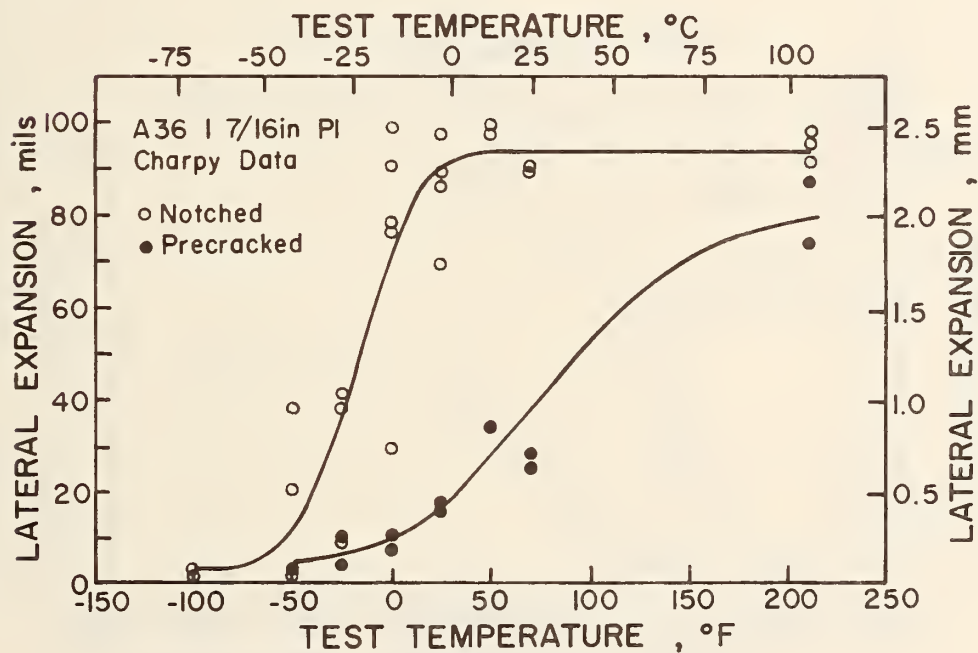
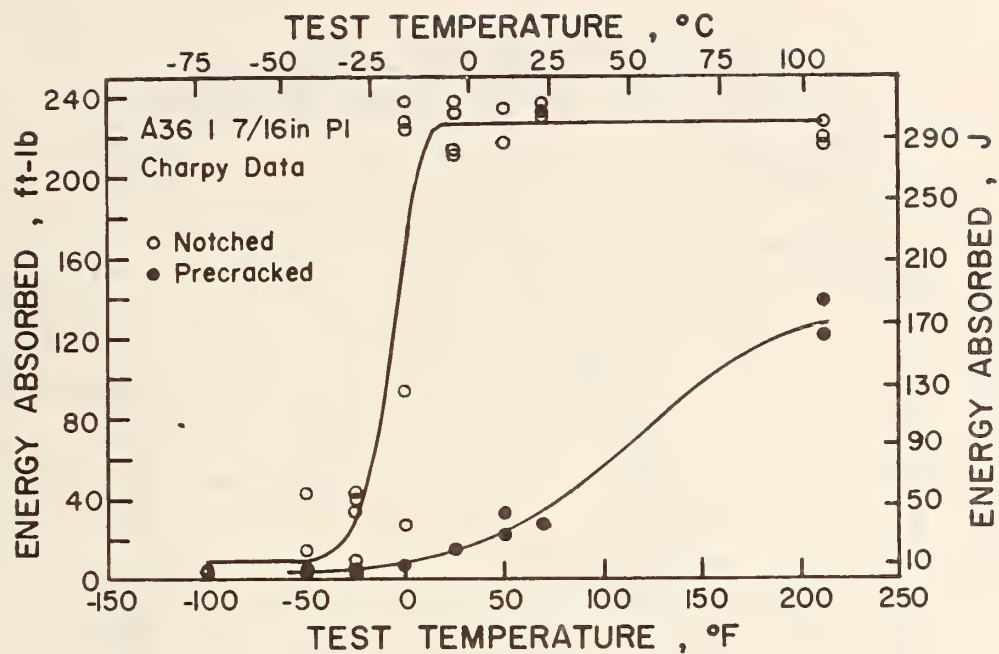


Fig. 3.7 A36, W36X260, Flange CVN

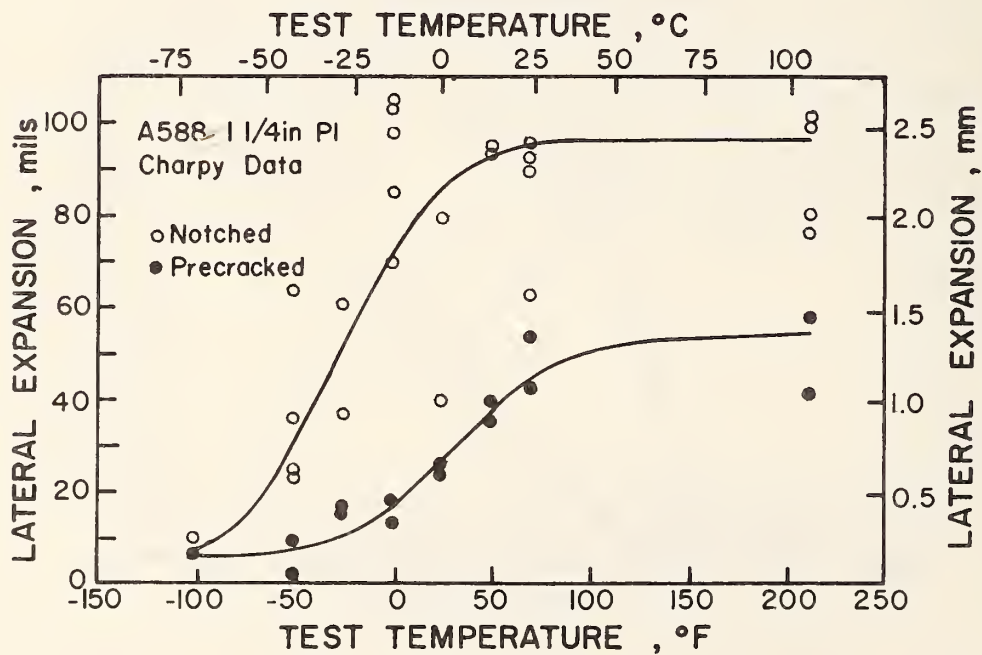
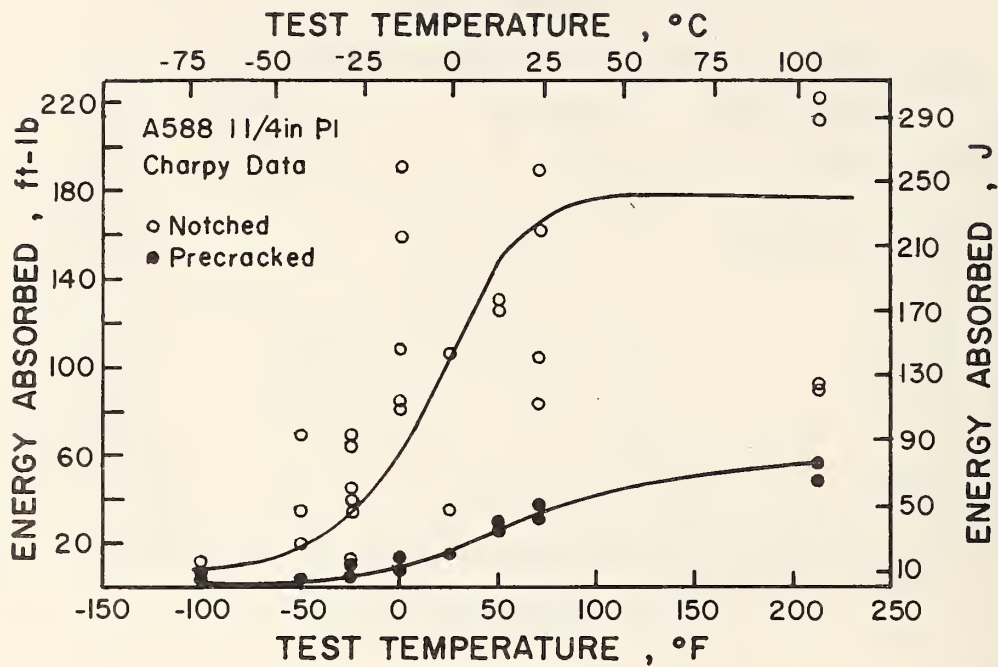


Fig. 3.8 A588, W36X230, Flange CVN

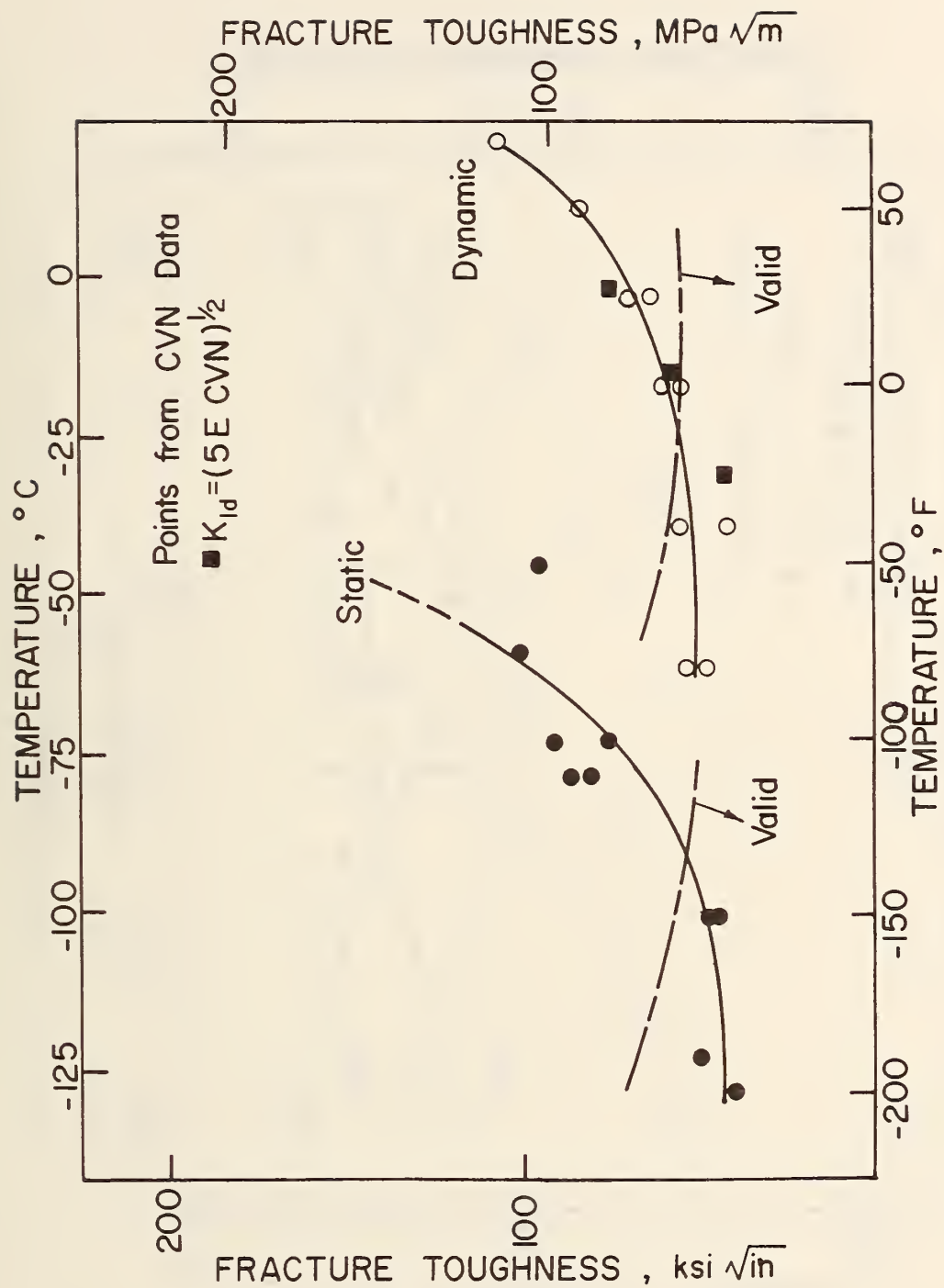


Fig. 3.9 Fracture Toughness vs. Temperature (A36, 2 Inch PL)

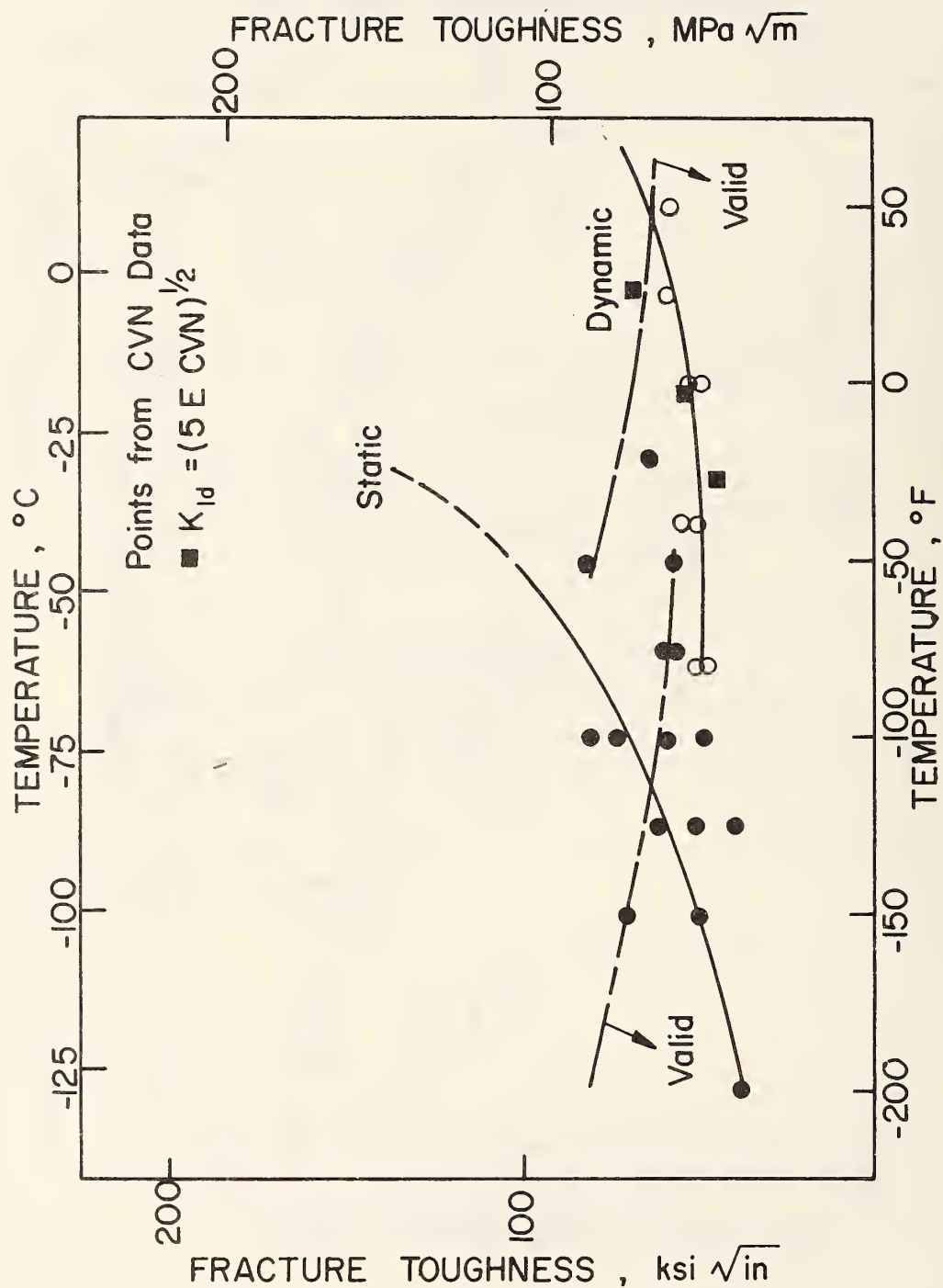


Fig. 3.10 Fracture Toughness vs. Temperature (A588, 2 inch PL)

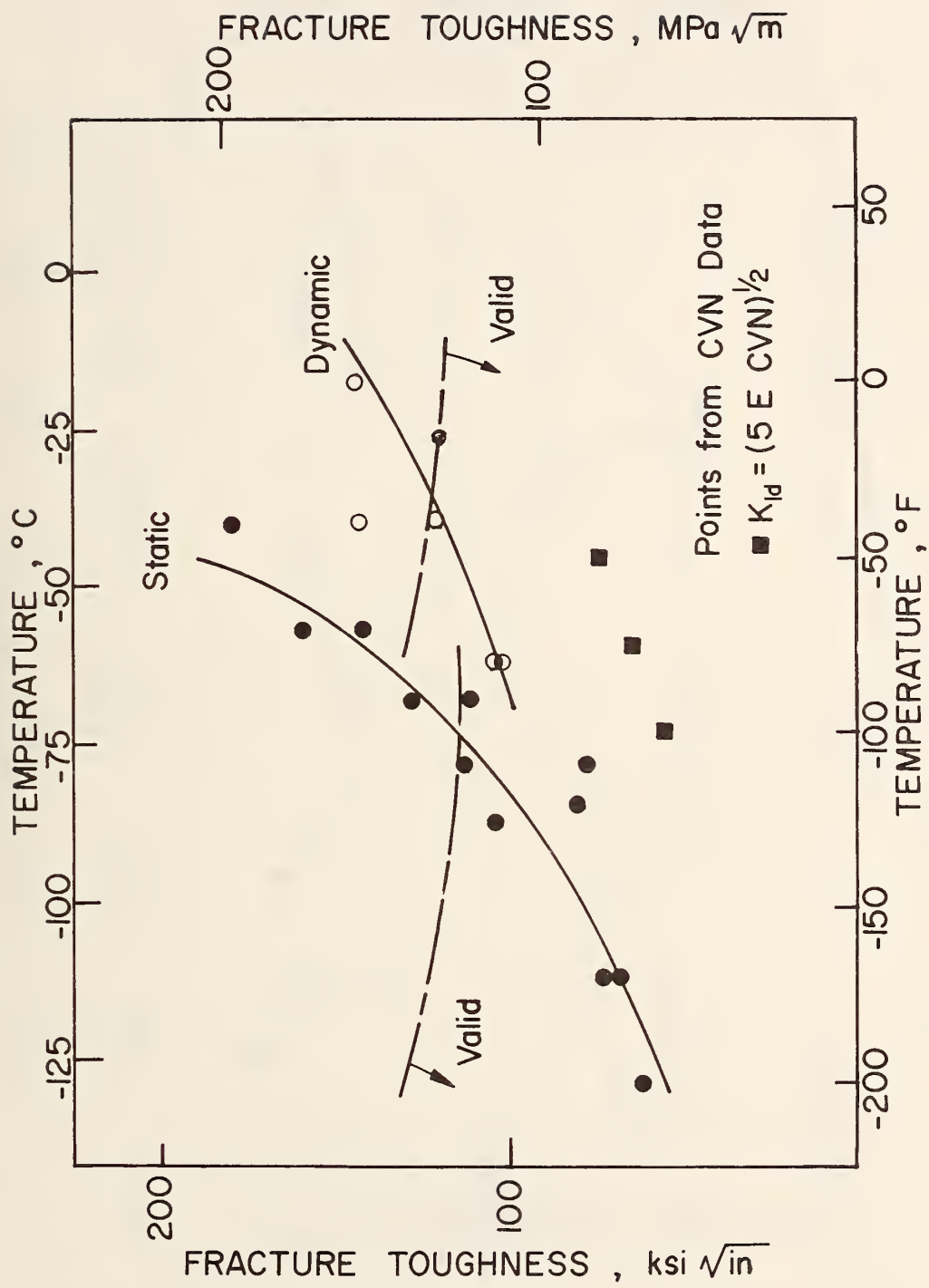


Fig. 3.11 Fracture Toughness vs. Temperature (A514, 1-1/2 inch PL)

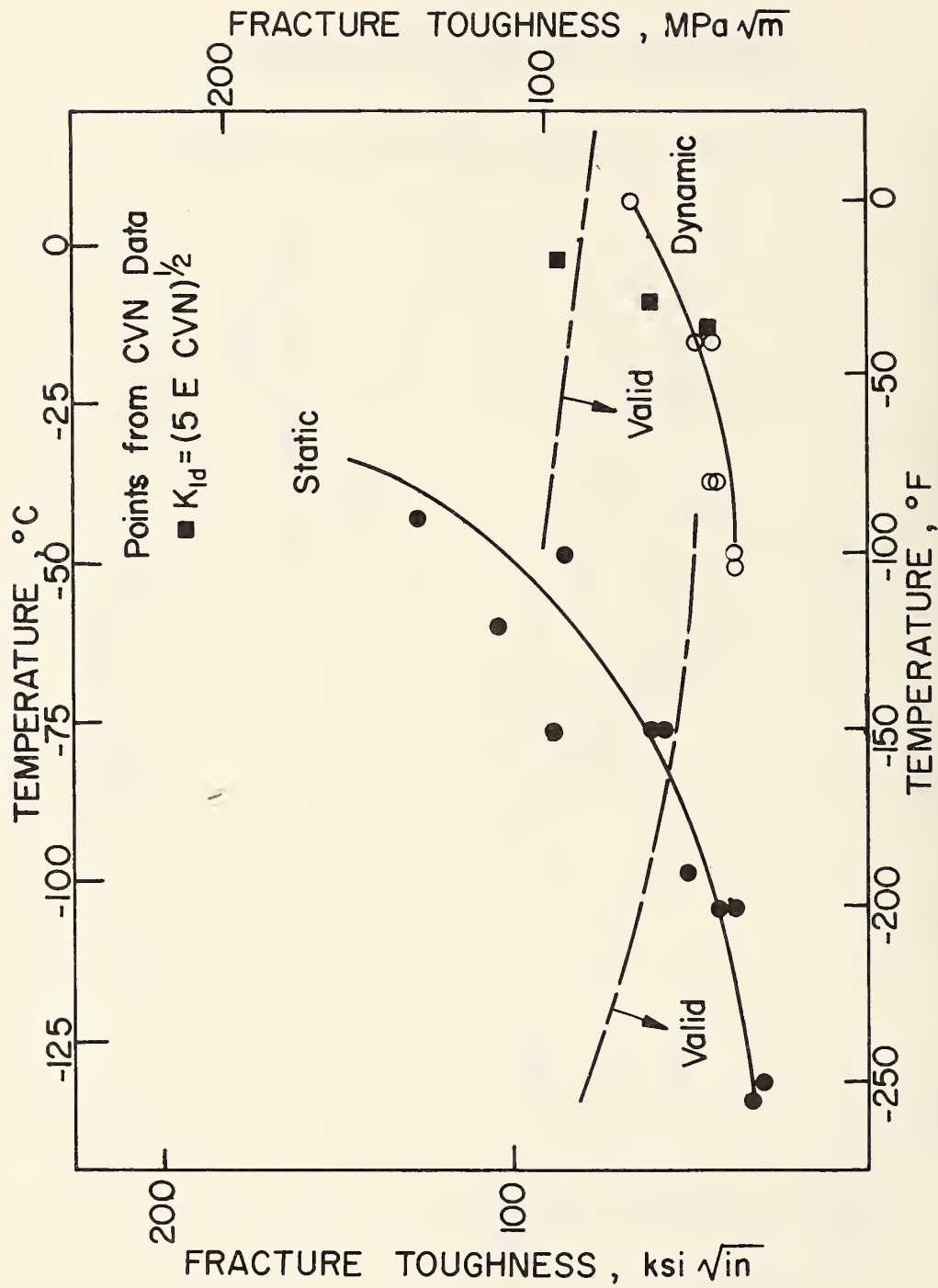


Fig. 3.12 Fracture Toughness vs. Temperature (A36, W36X260, Flange)

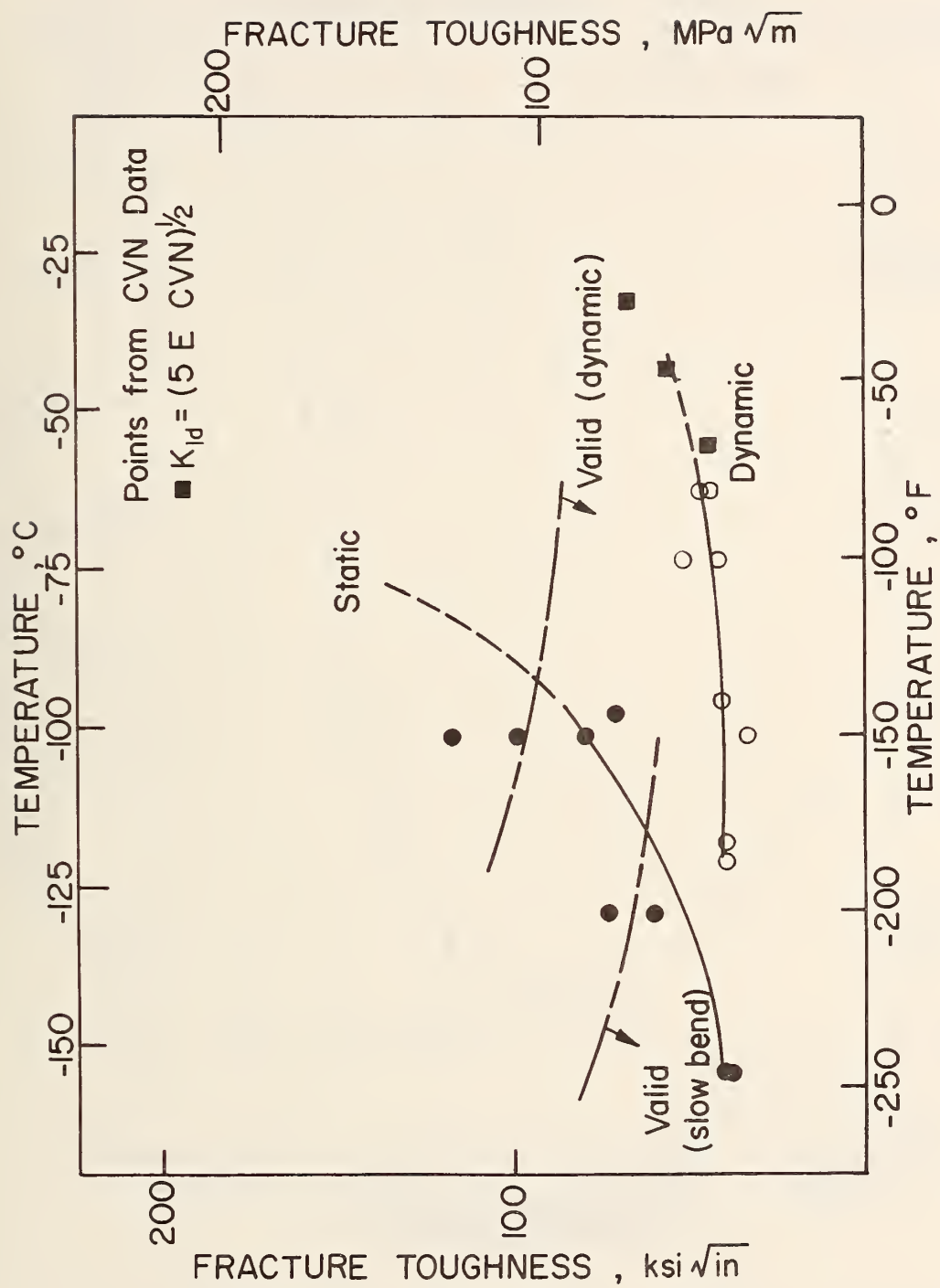


Fig. 3.13 Fracture Toughness vs. Temperature (A588, W36X230, Flange)

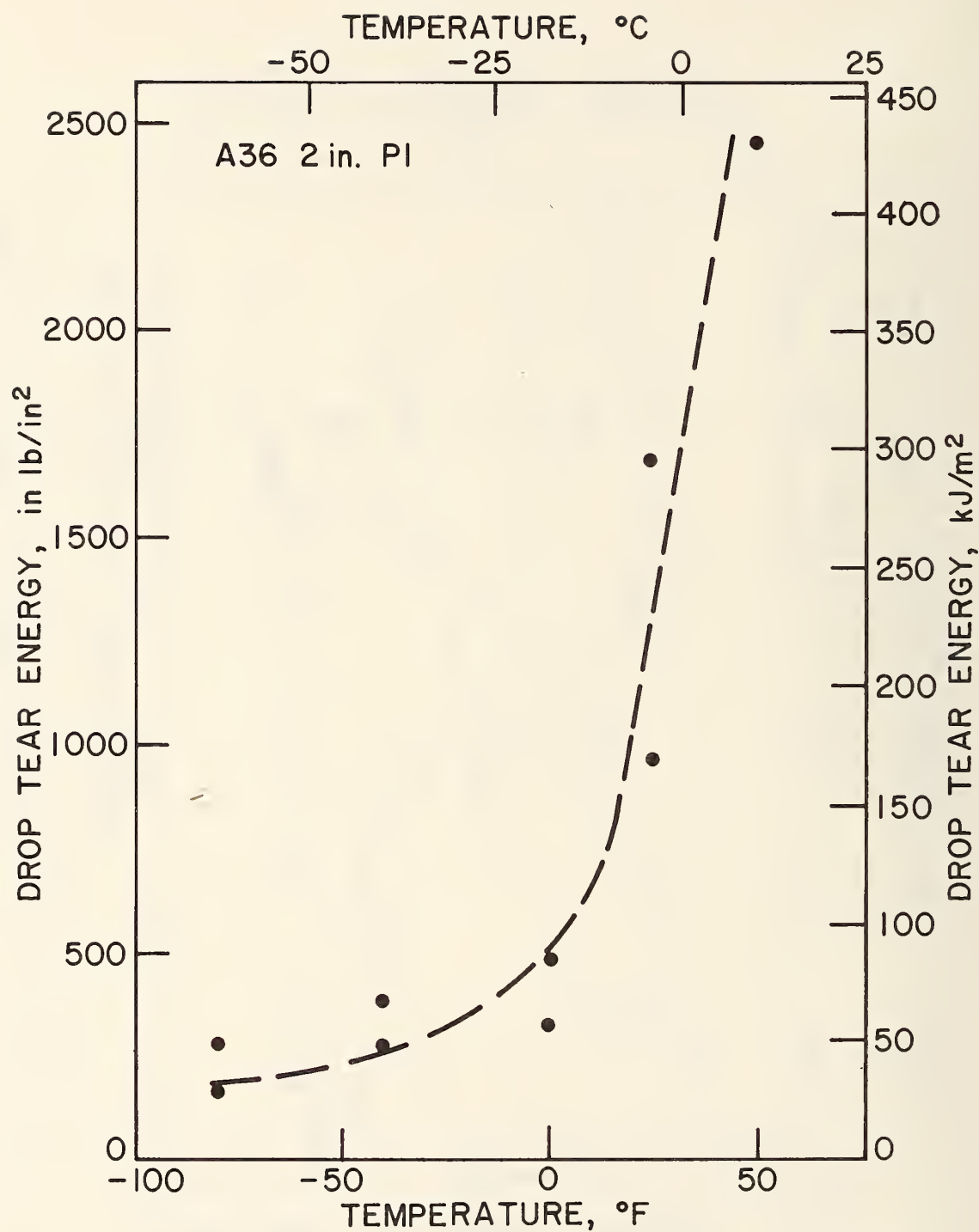


Fig. 3.14 Drop Tear Energy vs. Temperature (A36, 2 inch PL)

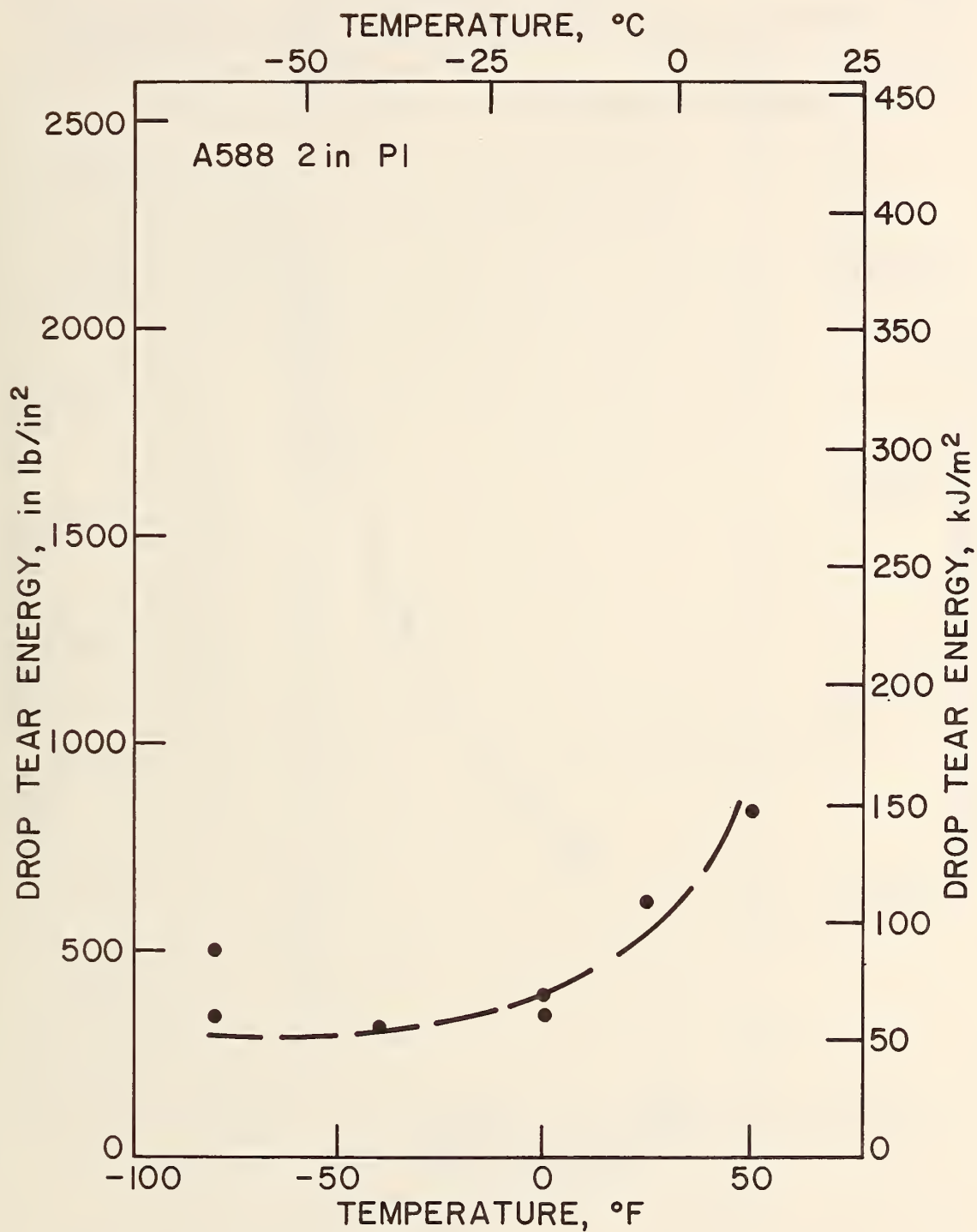


Fig. 3.15 Drop Tear Energy vs. Temperature (A588, 2 inch PL)

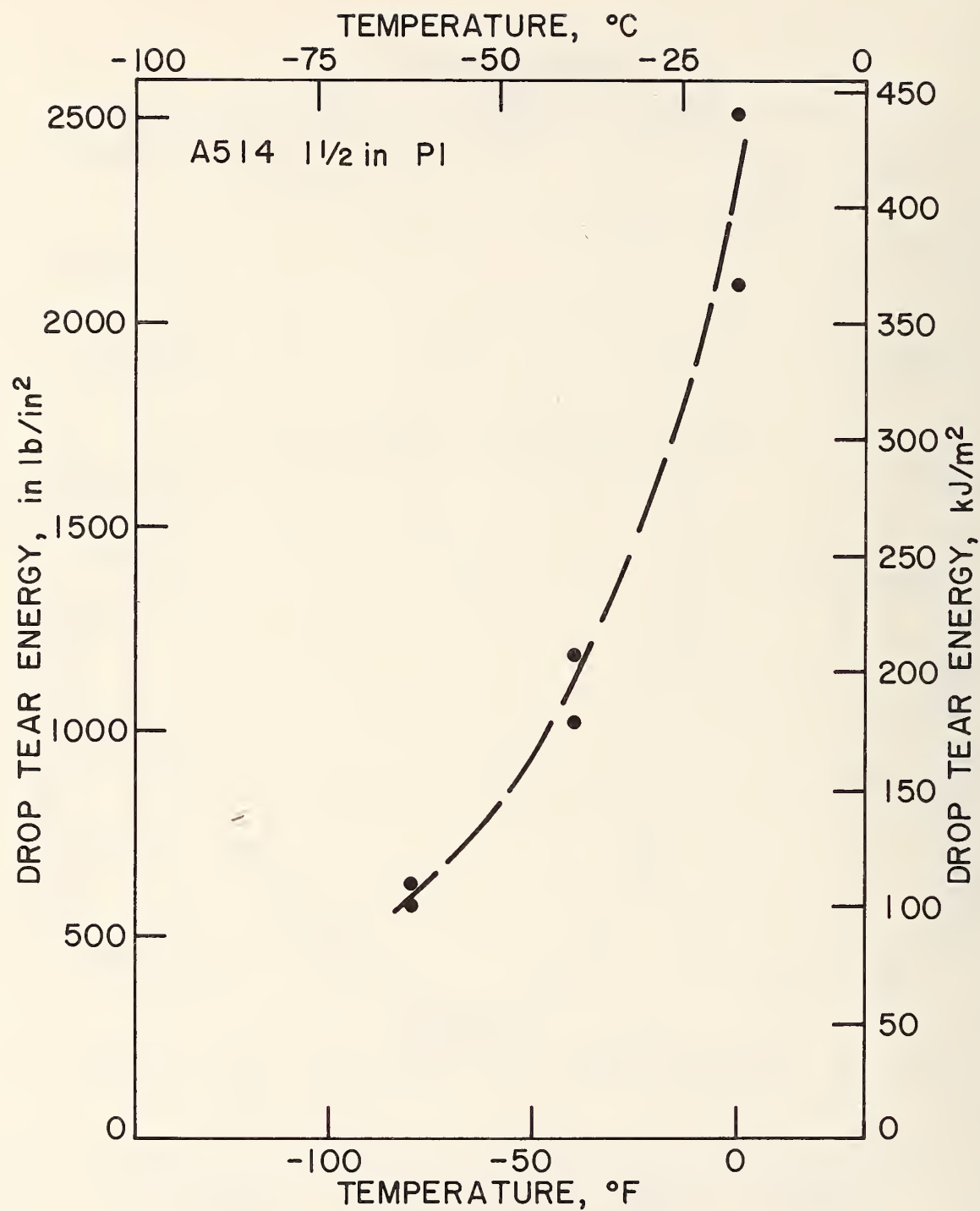
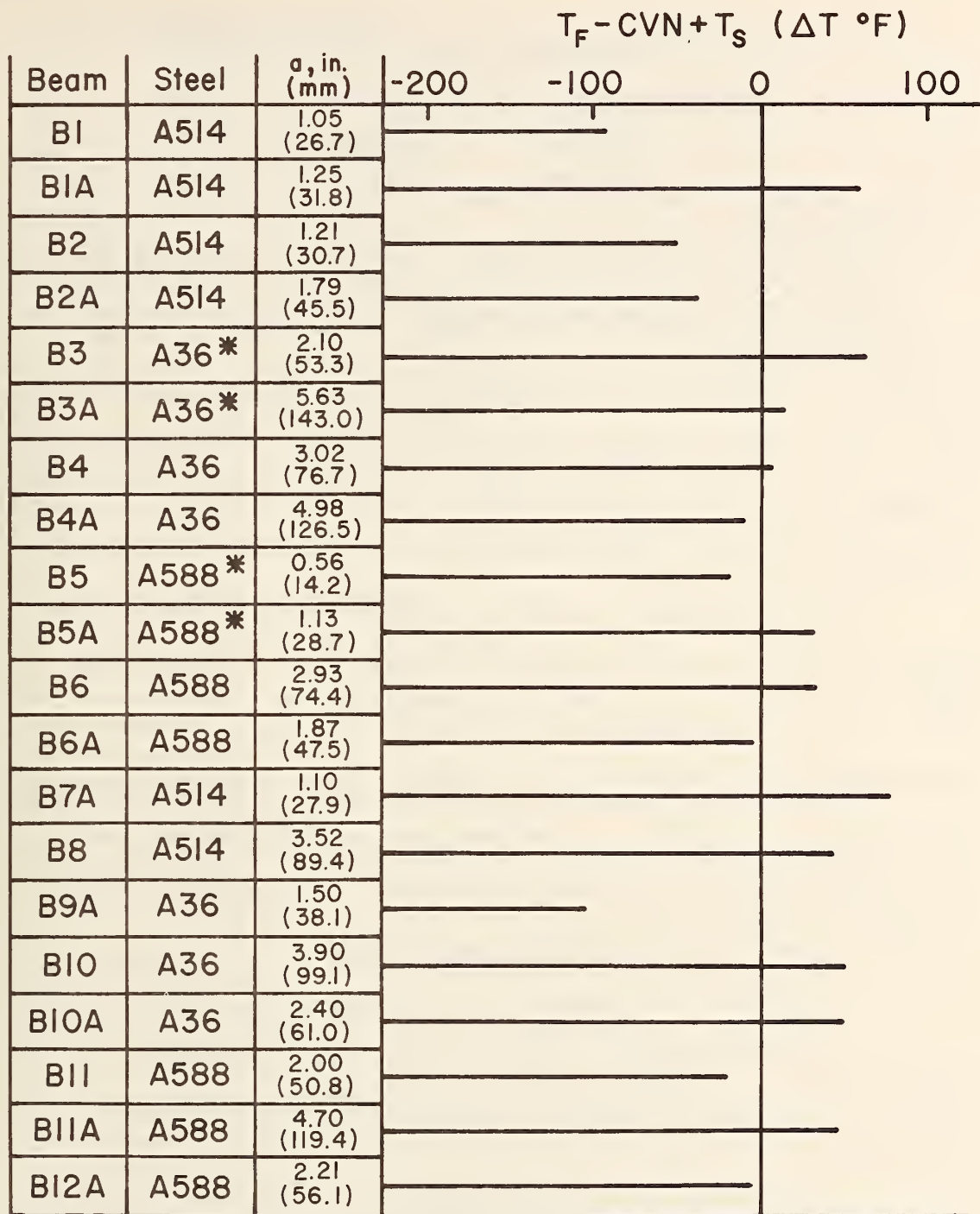


Fig. 3.16 Drop Tear Energy vs. Temperature (A514, 1-1/2 inch PL)



T_S = Temperature shift

70°F for A36 and A588, 30°F for A514

T_F = Failure temperature, °F

CVN = 15 ft-lb temperature, A36 and A588

CVN = 25 ft-lb temperature, A514

* Rolled beam

Fig. 3.17 Beam Failure Temperature Shift

4. LATERAL ATTACHMENT BEAM TEST RESULTS AND ANALYSIS

(Specimen No.	Material)
B4, B4A	A36
B6, B6A	A588
B2, B2A	A514

4.1 Fatigue Cracks

The fatigue cracks at the groove weld lateral attachments were initially detected on the flange edge, at the sharp 0.75 in. (19.1 mm) or less radius, as about 0.25 in. (6.3 mm) elliptical surface cracks. These surface cracks soon became elliptical corner cracks and then edge cracks. All final fractures at this detail were precipitated from an edge crack.

On the overlapped fillet weld detail, fatigue cracks were initiated at the toe of the transverse fillet weld. Most of these cracks were initially detected as several 0.5 in. (12.7 mm) elliptical surface cracks which eventually connected to form one large elliptical surface crack. As with the groove weld detail, these cracks then became corner cracks and finally edge cracks. Beam B6 was the only specimen to fracture from this overlapped detail.

The size of the fatigue cracks at each critical detail can be found by referencing the small letters on the fracture surface drawings in Figs. 4.1 to 4.6 with the load history tables given in Tables 2.3 to 2.8.

Many additional fatigue cracks existed at other details on the beams. Figures 4.7 and 4.8 show these fatigue cracks at all details at two million cycles and prior to the last fracture test. The surface measurements of these cracks are shown adjacent to the crack. The crack shapes are merely estimates from these surface measurements.

4.2 Remaining Fatigue Life

The number of cyclic loads needed to propagate an edge crack from its fracture initiation point to an edge crack size of 75% of the flange width, b , was defined as the remaining useful fatigue life had brittle fracture not occurred. The following crack growth relationship determined from earlier studies on welded details was used^{1,2}.

$$\frac{da}{dN} = 2 \times 10^{-10} \Delta K^3 \quad (7)$$

where ΔK = stress intensity range, ksi $\sqrt{\text{in.}}$

As defined in Section 4.5.2 the stress intensity range can be found from the following relationship

$$\Delta K = \sqrt{\frac{2b}{\pi a} \tan \frac{\pi a}{2b}} \Delta \sigma \sqrt{\pi a} \quad (8)$$

Secondary stress intensity effects from residual stresses were neglected for this analysis. Also by this stage of growth the crack had grown out of the stress concentration zone. Through numerical integration of Eq. 8 the remaining fatigue life was estimated. The results for each beam are listed in Table 4.1.

Figure 4.9 shows the mean S-N curve and its confidence limits for Category E details. The data base used to develop this curve utilized tests on 12 to 14 in. (304.8 to 355.6 mm) deep beams with a maximum flange thickness of 0.5 in. (12.7 mm)^{1,2}. The fatigue results for the lateral attachment beams, which had a maximum flange thickness of 2 in. (50.8 mm) are plotted on the same curve. The open figures

represent the point at which the fatigue cracks were first observed and the closed figures represent the point of fracture. The number of cycles accumulated at low temperatures were small in comparison to the number of cycles at room temperature. There is a good correlation between the fracture points and the Category E fatigue-life relationship.

As can also be seen from Fig. 4.9 and the additional life estimates tabulated in Table 4.1, the incremental addition to fatigue life was small and would not have significantly altered the strength as all the points were well within the 95% confidence limits. Hence even if rapid fracture had not occurred very little residual life would have remained.

4.3 Beam Fracture Tests

Beam B4A (A36 Steel)

Eight fracture tests were carried out on Beam B4A as the test procedure was developed. Three of these tests were on the overlapped fillet weld detail while five were on the groove weld detail.

The first five fracture tests were run with fatigue cracks still in the stress concentration zone. After 1.5 million cycles the largest fatigue crack found was a 1 in. x 0.06 in. (25.4 mm x 1.6 mm) elliptical corner crack (see Fig. 4.7) at a transverse fillet weld. The first two fracture tests were on this detail. At two million cycles, a 0.38 in. x 1 in. (9.5 mm x 25.4 mm) elliptical corner crack was observed at a groove weld detail. The fracture tests were carried out at test temperatures between -40° F (-40° C) and -60° F (-51° C)

as can be seen in Table 2.6. No crack instability developed during any of these three tests.

A test was run on the fillet weld detail where a 1.88 in. x 0.56 in. (47.8 mm x 14.2 mm) elliptical corner crack existed. No fracture occurred there as well. With a 1.50 in. x 1.75 in. (38.1 mm x 44.6 mm) corner crack at the groove weld detail (test h) the next test reached a temperature of -170° F (112° C), however, no fracture occurred.

The cracks were extended by applying 250,000 cycles of fatigue loading at room temperature. The critical fatigue crack at the groove weld detail had grown to a ~ 2.75 in. (69.9 mm) edge crack during this cyclic loading. At this point a -70° F (-57° C) fracture test was run. The test lasted 2.67 hours. During this test, the fatigue crack grew very rapidly through the high tensile residual stress region of the web to flange fillet welds. Finally, the beam fractured with an average edge crack size of 4.8 in. (122 mm) and temperature of -96° F (-71° C). Fatigue crack extension of approximately 2 in. (50.8 mm) was experienced during this test prior to crack instability.

Beam B4 (A36 Steel)

It was apparent from experience with Beam B4A that rapid fracture was not likely to occur at -40° F (-40° C) with small cracks in the stress concentration zone. Therefore, the beam was cycled at room temperature for two million cycles. At this point several large elliptical corner cracks existed as shown in Figs. 4.3 and 4.7. The

first fracture test lasted for one-half hour and both details were tested simultaneously. No fracture occurred.

The beam was then cycled at room temperature to extend the fatigue cracks. When the crack at the critical detail became a ~ 2.38 in. (60.3 mm) edge crack, a second fracture test was run. A temperature of -70° F (-57° C) was obtained before the cyclic load was applied. A stress range of 9 ksi (62.1 MPa) was applied for forty minutes. To speed the incipient fracture, the load range was increased to 9.8 ksi (67.6 MPa) while maintaining the same maximum stress. After one hour at this stress range and a nominal temperature of -70° F throughout most of the test (-57° C) fracture occurred. At fracture, the temperature was -80° F (-62° C). A ~ 0.75 in. (19.1 mm) fatigue crack extension was experienced during this test. The fracture occurred when the crack tip was in the high tensile residual stress zone of the web to flange weld.

Beam B6 (A588 Steel)

The first fracture test was run on both details simultaneously after two million fatigue cycles. Since very small fatigue cracks existed (see Fig. 4.7) no fracture occurred. After 800,000 cycles of additional fatigue load the elliptical surface crack at the critical fillet weld detail grew to a large 2.38 in. x 1.50 in. (60.3 mm x 38.1 mm) elliptical corner crack. At this point two consecutive five hour fracture tests were run (test d and e, see Fig. 4.5) on this detail. Fracture occurred after the elliptical fatigue crack

became an edge crack. The fracture temperature was -53° F (-47° C). This was the only fracture to occur at a fillet weld detail.

During the fatigue cycling of this beam, the ram in the constant load jack overheated. This caused the maximum load to decrease during the fatigue cycling overnight. Although the maximum load decreased, the stress range remained the same. The actual drop in maximum stress was 4.5 ksi (31.0 MPa) for 400,000 cycles.

Beam B6A (A588 Steel)

The first fracture test was run on both details (see Fig. 4.7) at -40° F (-40° C). No fracture occurred. After an additional 730,000 cycles of fatigue load at room temperature, a corner crack at the groove weld detail became a $\sim 1.25\text{ in.}$ (31.8 mm) edge crack. The subsequent fracture test lasted 1.67 hours during which the temperature was slowly dropped from -40° F (-40° C) to -92° F (-69° C) at which point rapid fracture occurred. An average fatigue crack extension of 0.25 in. (6.4 mm) (see test d, Fig. 4.6) was experienced prior to fracture.

Beam B2A (A514 Steel)

Five fracture tests were run on this beam (see Fig. 4.2). The first test at two million cycles was on both details. Both details contained large corner cracks at this point (see Fig. 4.7), however no fracture occurred at -40° F (-40° C). Since the elliptical corner crack at the groove weld detail grew quickly to a critical edge crack, the remainder of the fracture tests were conducted on this

detail alone. During the last test, the temperature was maintained at -40° (-40° C) for 1.5 hours. While the beam was still being cyclically loaded, the temperature was slowly dropped to -140° F (-96° C) in over 1.5 hours. The -140° F (-96° C) temperature was maintained for another 1.5 hours before fracture occurred at -144° F (-98° C). About 0.25 in. (6.4 mm) fatigue crack extension was experienced during the test prior to crack instability.

Note that the beam was fatigue cycled at a lower maximum stress than that during the fracture test. The same stress range was maintained during both fatigue and fracture testing. See Table 2.4 for the actual stresses and stress ranges used.

Beam B2 (A514 steel)

At two million cycles, a 1 in. (25.4 mm) edge crack existed at the groove weld detail while smaller elliptical corner cracks existed at the fillet weld detail (see Fig. 4.7). Both details were tested for forty minutes at -40° F (-40° C). At this time the cyclic load was stopped and the groove weld detail was cooled to -140° F (-96° C). After this temperature was obtained, the cyclic load was reapplied. After twenty minutes of cycling, fracture occurred at a temperature of -155° F (-104° C). A 0.25 in. (6.4 mm) fatigue crack extension was experienced during the last test (see test b, Fig. 4.1).

The beam was fatigue cycled at a lower maximum stress than that during the fracture test. The same stress range was maintained during both fatigue and fracture testing. See Table 2.3 for the actual stresses and stress ranges used.

4.4 Fracture Test Variables Affecting Fracture Toughness

Each fracture test had two major variables affecting the fracture resistance of the steel beam. These were the fatigue crack size and test temperature.

Since no beam fractured on the first cycle of load an effort was made to induce rapid fracture at -40° F (-40° C) by growing the fatigue crack to a critical size. As noted in Section 4.3, Beams B4, B4A, and B6 experienced average fatigue crack extensions of 0.65 in. (16.5 mm), 2.0 in. (50.8 mm), and 1.3 in. (33.0 mm), respectively, prior to brittle fracture. These large crack extensions took several hours to achieve.

Since time was a limiting factor, the test temperature was as another variable. The slow cooling rate of approximately 1° F (0.6° C) per minute was used. Temperature at the critical details are shown graphically in Figs. 4.10 to 4.12 for the final sixty minutes of the last fracture test. In every case the temperature was slowly decreasing when fracture occurred.

Although large temperature gradients existed around the critical beam section, as shown in Table 2.2, an effort was made to keep accurate account of the surface temperature at the critical welded detail. The temperature gages were positioned at the critical detail on the exterior of the tension flange, thus being out of direct contact with the liquid nitrogen.

The cyclic loading, during the fracture testing, of 4.3 Hz resulted in a maximum rate of loading of 100 ksi/sec. (689.5 MPa/sec.). This was about twice as fast as the loading rate of 55 ksi/sec. (379.2 MPa/sec.) that was used for the slow bend tests.

4.5 Stress Intensity Estimates

4.5.1 Introduction

All the flange cracks in the lateral attachment details were large edge cracks at fracture. This tended to simplify the calculations of the stress intensity factor. However, since the plates were flame cut and the beams and details were welded, a rather complex residual stress pattern was present at the detail cross-section. Therefore several steps were used to estimate the value of the stress intensity factor, K .

By the method of superposition the following contributions were used to determine the magnitude of K . The primary contribution was from the applied stresses at failure. A secondary contribution was from the residual stresses at the detail cross-section. The residual stresses at the cracked section resulted from two contributions. One contribution to K was from the residual stresses at a typical cross-section of the welded beam. These stresses were caused by the web-to-flange welds and the flame cut plate edges. The other contribution was due to the residual stresses caused by the local detail welds.

In one case, Beam B4A, the flange edge crack grew through the web-to-flange welds. The fatigue crack growth continued in two directions, upward into the web and across the flange. Therefore, when estimating the stress intensity, the web interaction had to be considered as well. The web restrained the large flange crack from opening. Thus the

contribution of this web restraint to the stress intensity estimate was negative.

The actual value of K was found to be the sum of three or four terms as shown in Eq. 9

$$K = K_{AS} + K_{RS} + K_{LW} + K_{WR} \quad (9)$$

The subscripts K_{ij} in Eq. 9 are the various contributions to the critical stress intensity. These include contributions from the applied stress, K_{AS} ; the residual stress caused by flame cut edges and web-to-flange welds, K_{RS} ; the residual stress caused by local detail welds, K_{LW} ; and the web restraint of the flange for Beam B4A, K_{WR} .

Plastic-zone corrections were made by using the following plane stress relationship.

$$r_y = \frac{1}{2\pi} \left(\frac{K_c}{\sigma_y} \right)^2 \quad (10)$$

Using an iterative process between Eqs. 9 and 10 values of K were obtained.

4.5.2 Contribution from the Applied Stress

To estimate the stress intensity from the applied stress for a flange edge crack, the following format was used. Generally,

$$K_{AS} = F(a) \sigma_{AS} \sqrt{\pi a} \quad (11)$$

where $F(a)$ consists of four parts as discussed by Albrecht and Yamada¹³.

$$F(a) = F_E F_S F_W F_G$$

F_E = elliptical crack front correction

F_S = free surface correction

F_G = stress concentration correction

F_W = finite width correction

For the final-fracture calculations used in this study, it was concluded that the product $F_E F_S F_G$ could be assumed to be united without appreciable error. The factor F_E is below unity by an amount dependent upon crack front curvature. However, the cracks of interest were large, through-the-flange cracks and the crack front shape had a large radius of curvature. Thus the estimated deviation from unity of F_E was quite small. The F_S factor is larger than unity. In this case the difference from unity was judged to be small because the lateral attachment prevented in-plane displacements parallel to the crack along a considerable portion of the flange adjacent to the crack. F_G represents the influence of loading-stress redistribution (geometry) due to the notch formed when the lateral member is attached to the flange. The effect of this stress redistribution upon K becomes negligible when the crack front is well removed from the lateral attachment as was true for the final-fracture cracks encountered in this study. With regard to the early growth of the fatigue cracks, which involve small surface and corner cracks, F_G has a significant influence as discussed in the next section.

Initially the finite width correction, F_W , was defined by

Eq. 12.

$$F_W = \sqrt{\frac{2b}{\pi a} \tan \frac{\pi a}{2b}} \quad (12)$$

b = flange width

$a = a_p + r_y$

a_p = physical crack size

r_y = plastic-zone correction

This finite width correction is exact for the model shown in Fig. 4.13a. This is not exactly the situation with the flange edge cracks adjacent to the lateral attachment details, however it is a good approximation. The web was assumed to prevent in-plane bending of the flange and the lateral attachment plates were assumed to partially prevent Poisson contractions on the flange tip as shown in Fig. 4.13b. For these reasons the dimensions used are those shown in Fig. 4.13b.

In the final analysis the finite width correction, F_W , was de-

$$F_W = \sqrt{\frac{2b}{\pi a} \tan \frac{\pi a}{2b}} \left(1 - \left(1 - \sqrt{0.5} \right) \left(1 - \frac{a}{b} \right) \right) \quad (13)$$

b = flange width

$a = a_p + r_y$

a_p = physical crack size

r_y = plastic zone correction

The finite width correction defined by Eq. 12 was modified to conform to the model shown in Fig. 4.13c. The lateral attachment provides fixity to one side of the crack. When the crack is small the finite width correction is factored by $\sqrt{0.5}$ to conform to a crack opening of

approximately half that provided by the model shown in Fig. 4.13b. As the crack grows this compliance correction to the finite width correction increases linearly to a value of 1.0 for the case where the crack length is equal to the flange width.

In the actual beam fractures, the stresses were not uniform through the plate thicknesses nor were the edge crack fronts. For these reasons the critical stress intensity was estimated for third levels through the flange thickness. The average crack size and stress were used for the respective one-third thickness of the flange (see Fig. 4.25). The measured values of the critical crack size, a_p , for each beam are listed in Table 4.2.

4.5.3 Contributions from Stress Concentration

The stress concentrations for the groove weld details were determined from a current study at Fritz Engineering Laboratory¹⁴. In this study, similar details were modeled using a three-dimensional finite element analysis. For the groove weld detail, stress concentration was defined by Eq. 14.

$$K_T = \log_e \left[\left(\frac{R}{b} \right)^{-0.4842} \left(\frac{L_g}{b} \right)^{0.2332} \left(\frac{W_g}{b} \right)^{0.06} \right] + 0.2848 \left(\frac{T_g}{T_f} \right) \quad (14)$$

R = transition radius

L_g = length of attachment

W_g = gusset width

b = flange width

T_f = flange thickness

T_g = gusset thickness

The stress concentration for the uncracked detail was determined to be 2.22 for the groove weld detail with a 0.75 in. (19.1 mm) radius transition at the 1.5 in. x 6 in. (38.1 mm x 152.4 mm) flange. Similarly, the stress concentration for the groove weld detail attached to the 2 in. x 7 in. (50.8 mm x 177.8 mm) flange was estimated as 2.19. These stress concentration factors are lower bound estimates. Examination of the fabricated details showed that for the critical details that cracked, the transition was irregular and not a smooth radius (see Fig. 4.14a). These irregularities were modeled for the most severe case, a 45° angle reentrant corner with 0.75 in. (19.1 mm) legs (see Fig. 4.14b). A stress concentration factor of about 7.9 was estimated for this case.

The overlapped fillet weld detail had a comparable stress concentration of approximately 7.1 for the 1.5 in. x 6 in. (38.1 mm x 156.2 mm) flange and 7.3 for the 2 in. x 7 in. (50.8 mm x 177.8 mm) flange. However, only one beam failed from this detail. There are at least two reasons for this. First, surface fabrication discontinuities at the radius elevated the apparent stress concentration. Second, the stress range at the groove weld detail was 12.5% higher than that at the fillet weld detail. The combination of these two differences made the groove weld detail more critical in all but one case.

The stress concentration, K_T , decays as a crack initiates and grows at the detail. This decay is also described in Ref. 14. The study matches the decay described by Albrecht and Yamada¹³, to an uncracked elliptical hole model. By varying the size of the ellipse

in an infinite plate the effect of stress concentration decay can be matched. The purpose of this approximation is to develop a quick and inexpensive method to determine this decay for any detail and stress concentration situation. This analysis was used to model a groove weld detail for stress intensity variation with crack size.

The A514 steel groove weld detail on Beam B2A was examined for stress concentration effects on the stress intensity factor, K . Results were obtained for two attachment-to-flange reentrant corner models: Case A was the smooth 0.75 in. (19.1 mm) radius transition (see Fig. 4.14a), Case B was the 0.75 in. (19.1 mm), 45° straight line transition shown in Fig. 4.14b. The stress concentration decay with crack size, F_G , is shown in Fig. 4.15 for both cases. Since the stress concentration value, K_T , in Case B was much higher than that used in Case A, the decay of K_T with crack growth for Case B was more rapid than Case A. Because of this the maximum stress intensity obtained for Case B was lower than the value obtained for Case A (see Fig. 4.16). Hence, this elevated stress concentration (Case B) at these details did not appreciably alter the residual fatigue strength nor the fracture resistance as the K value was not appreciably different when the crack size exceeded 0.1 in. (2.5 mm).

Based upon the preliminary analysis assumptions including residual stresses, the variation of stress intensity and crack size is summarized in Fig. 4.16 for both cases. It was conservatively assumed that the small cracks began as small elliptical corner cracks. The variation of the semi-major and semi-minor axes was defined by Eq. 15.

$$c = 1.465a^{0.202} \quad (15)$$

where c = semi-major axis, in.

a = semi-minor axis, in.

This relationship was determined from crack size measurement data. As can be seen in Fig. 4.16, the maximum stress intensity obtained for elliptical corner cracks was 126 ksi $\sqrt{\text{in.}}$ (139 MPa $\sqrt{\text{m}}$) for a crack size of 0.35 in. (8.9 mm). This value is less than any slow bend material test result at -40° F (-40° C) (see Fig. 8.3).

4.5.4 Contribution from the Nominal Residual Stresses

K_{RS} is either positive or negative depending upon the magnitude and distribution of the cross-section residual stresses and the crack size. When a crack grows through a tensile residual stress field there is an additional crack opening caused by the residual stresses which yields a positive K_{RS} . Similarly, when a crack grows through a compressive residual stress field there is crack closure and thus K_{RS} is negative. When a crack grows through both positive and negative residual stress fields, the residual stress condition near the crack tip, along the path of the crack, has an overriding effect.

The residual stress field through which the crack has grown can be approximated by superposition of small block stresses (see Fig. 4.17). In the preliminary analysis K_{RS} was obtained by using the following equation along with the method of superposition¹⁵.

$$K_{\text{RS}} = \frac{2}{\pi} \sigma_{\text{rs}} \sqrt{\pi a} \sqrt{\frac{2b}{\pi a} \tan \frac{\pi a}{2b}} \sin^{-1} \left(\frac{\sin \frac{\pi c}{2b}}{\sin \frac{\pi a}{2b}} \right) \quad (16)$$

a = edge crack size + plastic zone correction (see Table 4.2)

c = dimension from the plate edge to the end or beginning of the approximated block of residual stress

b = plate width

σ_{rs} = magnitude of the residual stress block

To obtain a good approximation of K_{RS} , stress block widths of 0.02 in. (0.5 mm) were used over the entire crack length. Results of K_{RS} for the preliminary analysis of each beam fracture are listed in Table 4.3a,b and plotted as a function of crack size in Figs. 4.18 to 4.23.

In the final analysis the measured nominal section residual stress distributions were used. These are shown in Figs. B.3 to B.5. Also, Eq. 16 was modified by the compliance correction that was applied to the finite width correction for the stress intensity contribution due to applied stress. K_{RS} was obtained by multiplying Eq. 16 by the factor used in Section 4.5.2 to modify F_w . Results of K_{RS} for each beam are listed for the critical level of each beam fracture in Table 4.4a,b.

4.5.5 Contribution from the Local Weld Residual Stresses

The local detail welds change the nominal section residual stress pattern over the entire cross-section at the detail. Ideally, there should be only one residual stress contribution from the actual

residual stresses at this critical section. A two step procedure was used to estimate the effect of residual stresses along with the principle of superposition. After the nominal beam section residual stresses were estimated, an additional local residual stress was assumed to account for the detail welds.

In the final analysis of the groove weld and fillet weld details the measured local weld residual stress distributions were used. There are shown in Figs. B.21 and B.22.

The local residual stress distribution along the flange tip at the groove weld detail was assumed as is shown in Fig. B.21 from the surface measurements. The decay of the stress along the flange tip was assumed to be rapid beyond the attachment edge. The stress at the location where most of the cracks initiated was estimated to be about $\sigma_{ys}/2$. This stress was assumed to be distributed over 0.25 in. (6.4 mm) of the flange tip and decayed to zero at 1.5 in. (38.1 mm). The procedure in Section 4.5.4 was used to determine the contribution from local welding. These values are also listed in Table 4.4a,b.

The fillet weld detail, top one-third analysis produced a different local residual stress distribution because the detail had a fillet weld along the inside surface of the flange. It was estimated that the magnitude of the local residual stress, $\sigma_{ys}/2$, at the flange tip decayed to $\sigma_{ys}/4$ at the end of the transverse weld (see Fig. B.22).

4.5.6 Contribution from the Web Restraint

Only Beam B4A was observed to develop web restraint since the fatigue crack at fracture had grown as an edge crack through the web-to-flange welds and then became a two ended crack. This is shown in Fig. 4.4. The analysis of the web restraint and the apparent reduction of the stress intensity is an iterative solution which is very involved. The actual analysis is discussed in detail in Appendix A. The web restraint was predicted to decrease K by $-12 \text{ ksi } \sqrt{\text{in.}}$ ($-13.2 \text{ MPa } \sqrt{\text{m}}$).

4.5.7 Summary and Discussion of the Various Contributions

The final values of K_{AS} , K_{RS} , K_{LW} , and K_{WR} are listed in Table 4.4a,b for the one-third level of the flange thickness with the maximum stress intensity for each critical fatigue crack. These final values are based on the measured nominal residual stresses (Figs. B.3 to B.5) and the local weld residual stresses (Figs. B.21 and B.22).

The preliminary analysis values are listed in Table 4.3a,b for each one-third level of the flange thickness. The critical value for each beam was taken as the maximum value. Plots showing the variation of each K_{ij} parameter with crack size are presented in Figs. 4.18 to 4.23 for the critical one-third level of flange thickness.

For crack growth less than approximately 1.1 in. (27.9 mm), the crack shape was an elliptical corner crack as described in Section 4.5.3 for the groove weld details. The local weld tensile

residual stresses and the nominal section tensile residual stresses on the flange tip both influenced the total stress intensity value in addition to the applied stress magnification by the stress concentration parameter, F_G . These variations with crack size, a , are shown in Fig. 4.16 for Beam B2A. When the crack size for the elliptical corner cracks was approximately 1.1 in. (27.9 mm) the semi-major axis became equal to the flange thickness. At this point the crack rapidly became a 1.1 in. (27.9 mm) edge crack and the stress intensity suddenly increased. This discontinuity is shown in Fig. 4.16.

The residual stress effects on stress intensity for edge cracks can readily be seen in the K_{RS} vs. edge crack size plots (see Figs. 4.18 to 4.23). As the edge crack grew from a size of 1.1 in. (27.9 mm) into the negative residual stress zone there was a decrease in K_{RS} which extended over the next 1 in. (25.4 mm) of crack growth. In most cases this decrease in K_{RS} held the total stress intensity value, K , constant over this region.

Continued crack growth resulted in a rapid increase in K_{RS} as the fatigue crack grew into the high tensile residual stress region caused by the web-to-flange fillet welds. This also caused K to increase rapidly. This residual stress influence on K greatly affected the fracture of Beam B4 (top one-third analysis, Fig. 4.20) and B6 (top one-third analysis, Fig. 4.22). Each beam fractured with a crack size at or near the peak K value caused by K_{RS} . The point of fracture is marked on each "K vs. a " plot.

K_{AS} increased at a near constant rate for edge crack growth. Since the applied stresses were very high in the A514 beams this parameter had an overriding effect on K_{RS} and K_{LW} . This is shown in the bottom one-third analysis for Beams B2 and B2A, Figs. 4.18 and 4.19, respectively.

K_{LW} had its greatest influence on small elliptical corner cracks (see Fig. 4.16). For edge cracks at the groove weld details this contribution became constant and comparatively small. This contribution was slightly higher for the overlapped fillet weld detail.

The fracture of B4 was precipitated by the presence of the high tensile residual stress area at the web-to-flange welds. Beam B4A had a fatigue crack which grew through the same area during a fracture test and at a 6% higher applied stress but did not fail. This can only be explained by a difference in test temperatures when the fatigue cracks grew into this critical area. As can be seen from the material tests K vs. Temperature plot for A36 steel (Fig. 8.1) a slight difference in the test temperatures would cause a large change in the critical stress intensity factor, K_C . This was the case as the Beam B4A test temperature $\{-70^\circ \text{ F } (-57^\circ \text{ C})\}$ was warmer than the temperature of Beam B4 $\{-80^\circ \text{ F } (-62^\circ \text{ C})\}$ when the fatigue crack grew into this region. As the fatigue crack in Beam B4A grew through the web-to-flange welds K_{RS} was continually increasing. However, this was counter balanced by the flange crack opening restraint of the web. Only when the crack grew ~ 1.25 in. (~ 31.8 mm) past the web did fracture occur. K_{RS} had only a small effect on the estimated stress intensity since, at the time of fracture, the critical K was determined at the bottom one-third level of flange thickness.

TABLE 4.1 ESTIMATED REMAINING FATIGUE LIFE:
LATERAL ATTACHMENT DETAILS

Steel	Beam Number	Remaining Fatigue Life* (Cycles)	Life to Fracture (Cycles)
A514	B2	1,168,100	2,024,100
	B2A	576,500	2,865,700
A36	B4	175,200	2,369,700
	B4A	9,800	3,276,750
A588	B6	408,000	2,954,700
	B6A	669,600	2,822,500

* Fatigue failure defined at an edge
crack size = $\frac{3}{4}$ flange width

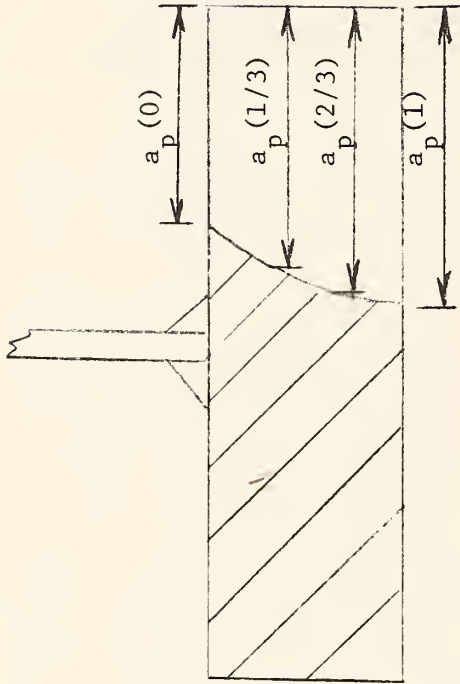


TABLE 4.2a CRACK SIZE MEASUREMENTS: LATERAL ATTACHMENT DETAILS

Beam Number	Measured Crack Sizes				Averaged Crack Sizes (in.)				r_y^* Correction Pl. Stress (in.)
	(1) $a_p(0)$ (in.)	(2) $a_p(1/3)$ (in.)	(3) $a_p(2/3)$ (in.)	(4) $a_p(1)$ (in.)	(1)+(2) a_{ave}	(1)+(2)	(2)+(3)	(3)+(4)	
B2	0.60	0.90	1.17	1.26	0.98	0.75	1.04	1.21	0.08
B2A	1.37	1.64	1.78	1.80	1.68	1.51	1.71	1.79	0.11
B4	2.92	3.12	3.32	3.38	3.19	3.02	3.22	3.35	0.25
B4A	4.62	4.90	5.03	4.93	4.87	4.76	4.96	4.98	0.27
B6	2.97	2.85	2.58	2.19	2.65	2.93	2.72	2.39	0.85
B6A	0.93	1.41	1.82	1.96	1.53	1.17	1.61	1.87	0.06

* Correction used at critical flange 1/3 thickness (see Table 4.4)

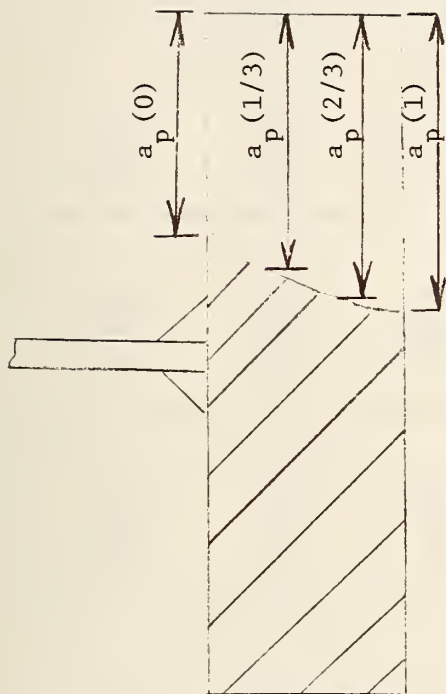


TABLE 4.2b CRACK SIZE MEASUREMENTS: LATERAL ATTACHMENT DETAILS

Beam Number	Measured Crack Sizes				Averaged Crack Sizes (mm)				r_y^* Correction Pl. Stress (mm)
	(1) $a_p(0)$ (mm)	(2) $a_p(1/3)$ (mm)	(3) $a_p(2/3)$ (mm)	(4) $a_p(1)$ (mm)	(1)+(2)+(3)+(4) a_{ave}	(1)+(2) a_T	(2)+(3) a_M	(3)+(4) a_B	
B2	15	23	30	32	25	19	26	31	2
B2A	35	42	45	46	42	38	43	45	3
B4	74	79	84	86	81	77	82	85	6
B4A	117	124	128	125	124	120	126	126	7
B6	75	72	66	56	67	74	69	61	22
B6A	24	36	46	50	39	40	41	48	2

* Correction used at critical flange 1/3 thickness (see Table 4.4)

TABLE 4.3a STRESS INTENSITY ESTIMATES: LATERAL ATTACHMENT DETAILS
(Preliminary Analysis)

Beam No./ Flange Thickness Level	Applied Stress (ksi)	Crack Size $a + r_p + r_y$ (in)	(1) K_{AS} (ksi√in)	(2) K_{RS} (ksi√in)	(3) K_{LW} (ksi√in)	(4) K_{WR} (ksi√in)	(1)+(2)+ (3)+(4) K (ksi√in)
B2 ($\sigma_{yd} = 154.6$ ksi)							
TOD	46.5	0.78	74	-28	21	NA	67
MID	47.8	1.10	92	-16	17	NA	93
*BOT	49.2	1.30	101	-3	16	NA	114
B2A($\sigma_{yd} = 152.5$ ksi)							
TOP	51.2	1.56	118	50	15	NA	83
MID	52.7	1.80	130	-29	14	NA	115
*BOT	54.2	1.93	139	-9	14	NA	144
B4 ($\sigma_{yd} = 65.5$ ksi)							
*TOP	16.8	3.43	62	39	4	NA	105
MID	17.5	3.54	66	23	4	NA	93
BOT	18.2	3.57	69	4	4	NA	77
B4A($\sigma_{yd} = 67.7$ ksi)							
TOP	18.0	5.20	103	15	5	-12	112
MID	18.7	5.43	116	0	5	-6	115
*BOT	19.4	5.45	102	9	5	0	116
B6 ($\sigma_{yd} = 79.3$ ksi)							
*TOP	25.0	4.20	110	83	30	NA	223
MID	26.0	2.92	85	-3	6	NA	88
BOT	27.0	2.54	81	-8	6	NA	79
B6A($\sigma_{yd} = 84.1$ ksi)							
TOP	25.0	1.18	49	-38	8	NA	19
MID	26.0	1.64	61	-30	7	NA	38
*BOT	27.0	1.99	70	-11	7	NA	66

* Denotes critical flange thickness level

σ_{yd} = Yield stress at test temperature and loading rate (Eq. 4)

σ_{ys} = The mill report yield stress

t = .12 sec.

TABLE 4.3b STRESS INTENSITY ESTIMATES: LATERAL ATTACHMENT DETAILS
(Preliminary Analysis)

Beam No./ Flange Thickness Level	Applied Stress (MPa)	Crack Size $a + r_y$ (mm)	(1) K_{AS} (MPa \sqrt{m})	(2) K_{RS} (MPa \sqrt{m})	(3) K_{LW} (MPa \sqrt{m})	(4) K_{WR} (MPa \sqrt{m})	(1)+(2)+ (3)+(4) K (MPa \sqrt{m})
B2 (σ_{yd} = 1066 MPa)							
TOP	321	20	81	-31	23	NA	73
MID	330	30	101	-18	19	NA	102
*BOT	339	33	111	-3	18	NA	126
B2A (σ_{yd} = 1052 MPa)							
TOP	353	40	130	-55	17	NA	92
MID	363	46	143	-32	15	NA	126
*BOT	374	49	153	-10	15	NA	158
B4 (σ_{yd} = 452 MPa)							
*TOP	116	87	68	43	4	NA	115
MID	121	90	73	25	4	NA	102
BOT	125	91	76	4	4	NA	84
B4A (σ_{yd} = 467 MPa)							
TOP	124	132	113	17	6	-13	123
MID	129	138	128	0	6	-7	127
*BOT	134	138	112	10	6	0	128
B6 (σ_{yd} = 547 MPa)							
*TOP	172	91	121	91	33	NA	245
MID	179	74	94	-3	7	NA	98
BOT	186	65	89	-9	7	NA	87
B6A (σ_{yd} = 580 MPa)							
TOP	172	30	54	-42	9	NA	21
MID	179	42	67	-33	8	NA	42
*BOT	186	51	77	-12	8	NA	73

* Denotes Critical Flange Thickness Level

σ_{yd} = Yield stress at test temperature and loading rate (Eq. 4)

σ_{ys} = The mill report yield stress

t = .12 sec.

TABLE 4.4a STRESS INTENSITY ESTIMATES: LATERAL ATTACHMENT DETAILS

Beam No./ Critical Flange Thickness Level	Applied Stress (ksi)	Crack Size $a_p + r_y$ (in)	(Final Analysis)				
			(1) K_{AS} (ksi√in)	(2) K_{RS} (ksi√in)	(3) K_{LW} (ksi√in)	(4) K_{WR} (ksi√in)	(1)+(2)+ (3)+(4) K (ksi√in) K^* (ksi√in)
B2 ($\sigma_{yd} = 148.6$ ksi)							
BOT	49.2	1.29	78	-12	37	NA	103 103
B2A ($\sigma_{yd} = 146.5$ ksi)							
BOT	54.2	1.90	110	-21	30	NA	119 117
B4 ($\sigma_{yd} = 63.5$ ksi)							
TOP	16.8	3.27	50	28	1	NA	79 66
B4A ($\sigma_{yd} = 65.7$ ksi)							
BOT	19.4	5.25	104	-32	12	0	85 79
B6 ($\sigma_{yd} = 76.3$ ksi)							
TOP	25.0	3.78	86	59	32	NA	176 122
B6A ($\sigma_{yd} = 81.1$)							
BOT	27.0	1.93	54	-18	14	NA	50 50

* No plastic zone correction

 σ_{yd} = Yield stress at test temperature and loading rate (Eq. 4) σ_{ys} = 95% of the mill report yield stress $t_{ys} = .12$ sec.

TABLE 4.4b STRESS INTENSITY ESTIMATES: LATERAL ATTACHMENT DETAILS

Beam No./ Critical Flange Thickness Level	Applied Stress (MPa)	Crack Size $a_p + r_y$ (mm)	(Final Analysis)				
			(1) K_{AS} (MPa \sqrt{m})	(2) K_{RS} (MPa \sqrt{m})	(3) K_{LW} (MPa \sqrt{m})	(4) K_{WR} (MPa \sqrt{m})	(1)+(2)+ (3)+(4) K (MPa \sqrt{m}) K^* (MPa \sqrt{m})
B2 ($\sigma_{yd} = 1025$ MPa)							
BOT	339	32.8	86	-13	41	NA	113 113
B2A ($\sigma_{yd} = 1010$ MPa)							
BOT	374	48.3	121	-23	33	NA	131
B4 ($\sigma_{yd} = 438$ MPa)							
TOP	116	83.1	55	31	1	NA	87 73
B4A ($\sigma_{yd} = 453$ MPa)							
BOT	135	133.4	114	-35	13	0	94 87
B6 ($\sigma_{yd} = 526$ MPa)							
TOP	172	96.0	95	65	35	NA	194 134
B6A ($\sigma_{yd} = 559$ MPa)							
BOT	186	49.0	59	-20	15	NA	55 55

* No plastic zone correction

 σ_y = Yield stress at test temperature and loading rate (Eq. 4) σ_{yd}^y = 95% of the mill report yield stress $t_y^y = 0.12$ sec.

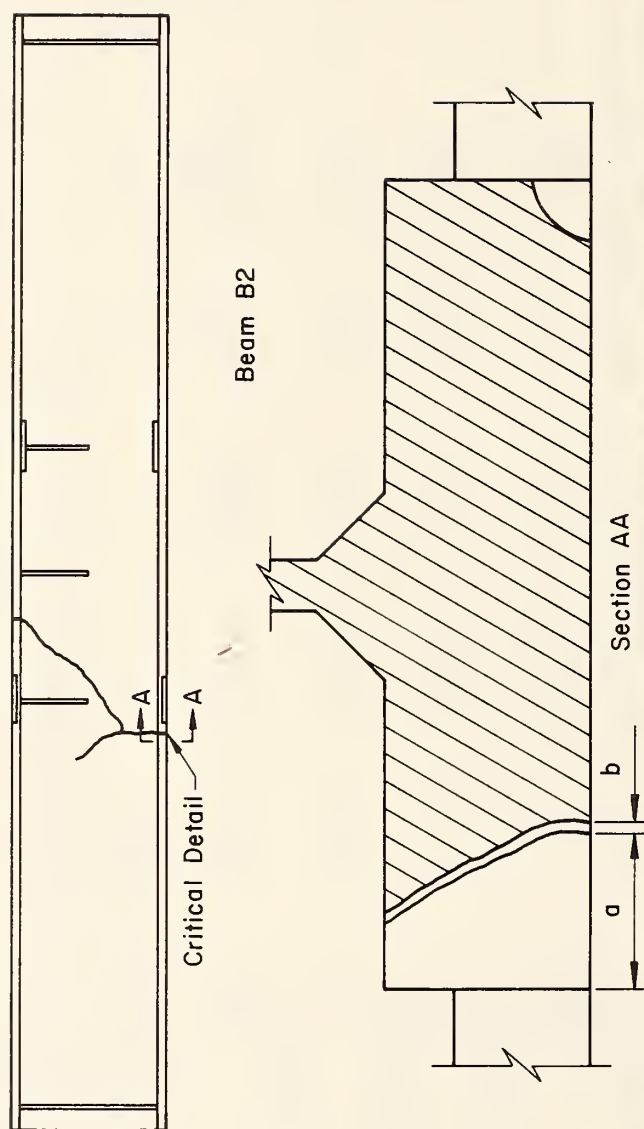


Fig. 4.1 Fatigue and Fracture Surface, B2 (A514)

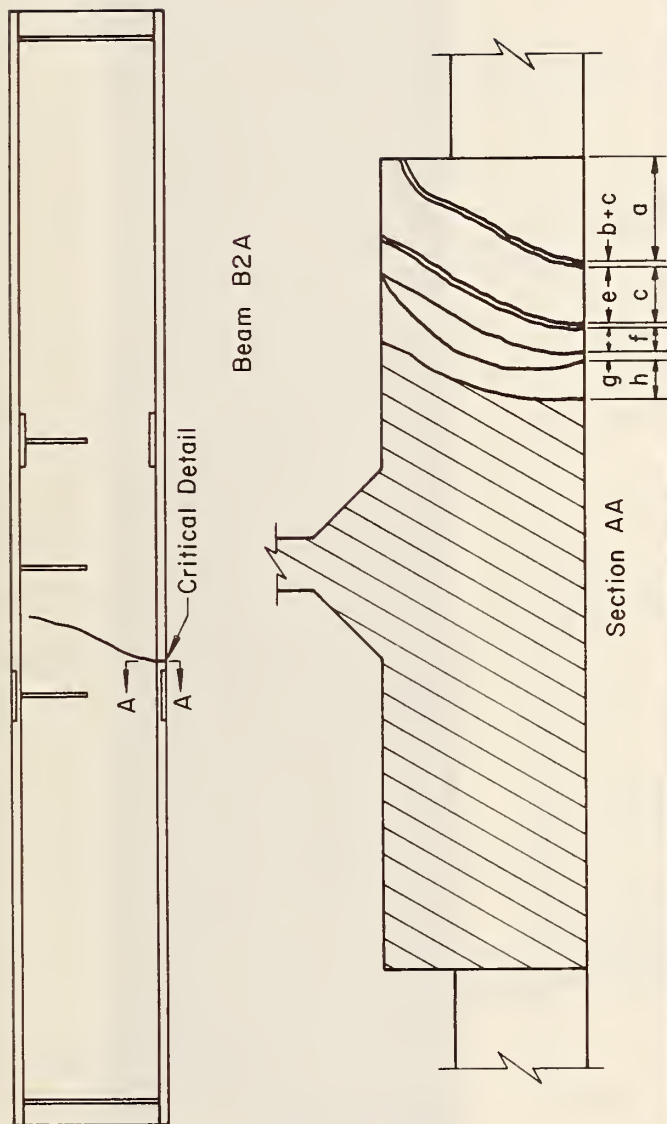


Fig. 4.2 Fatigue and Fracture Surface, B2A (A514)

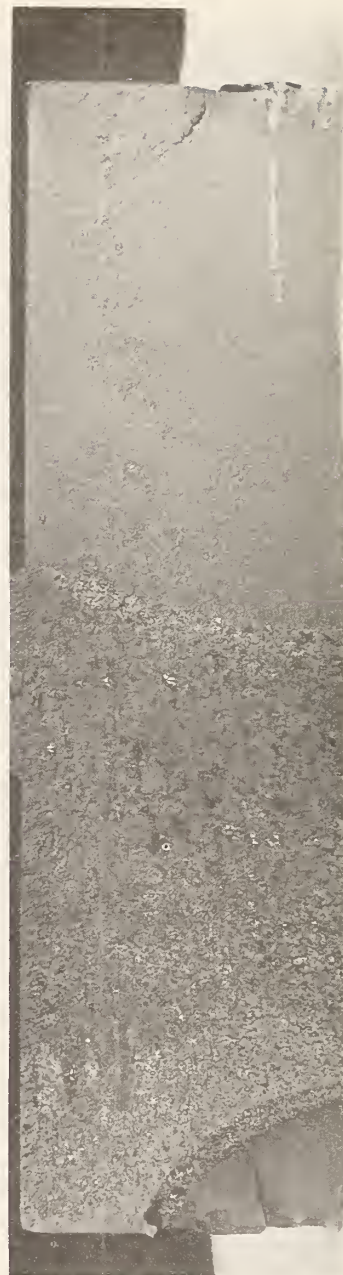
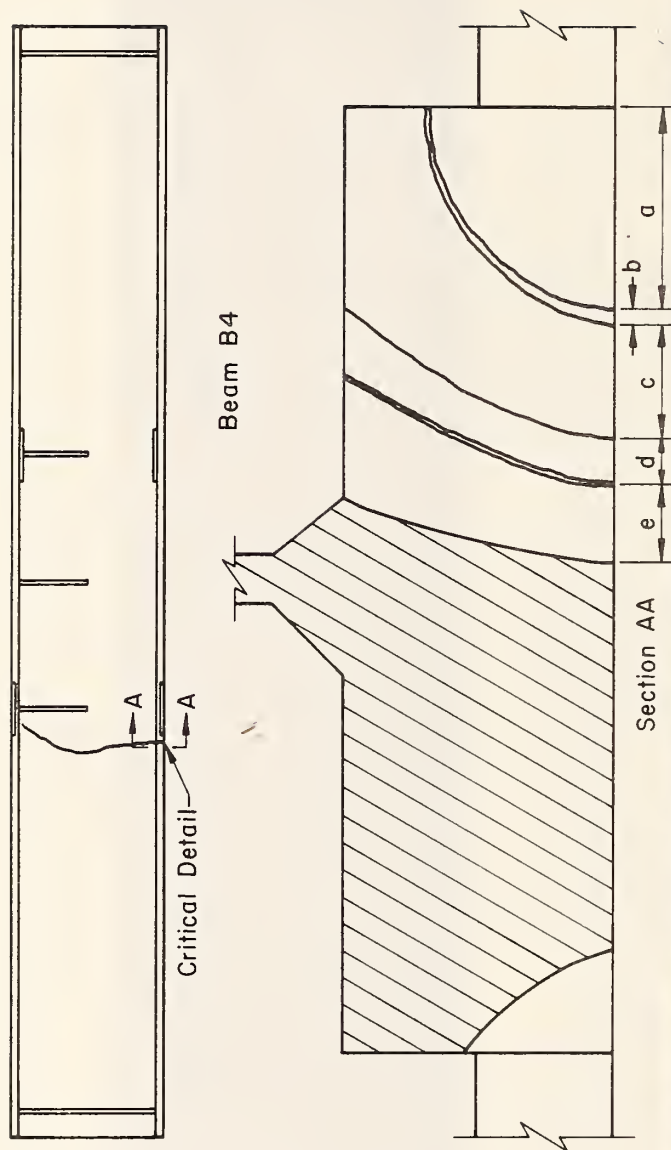


Fig. 4.3 Fatigue and Fracture Surface, B4 (A36)

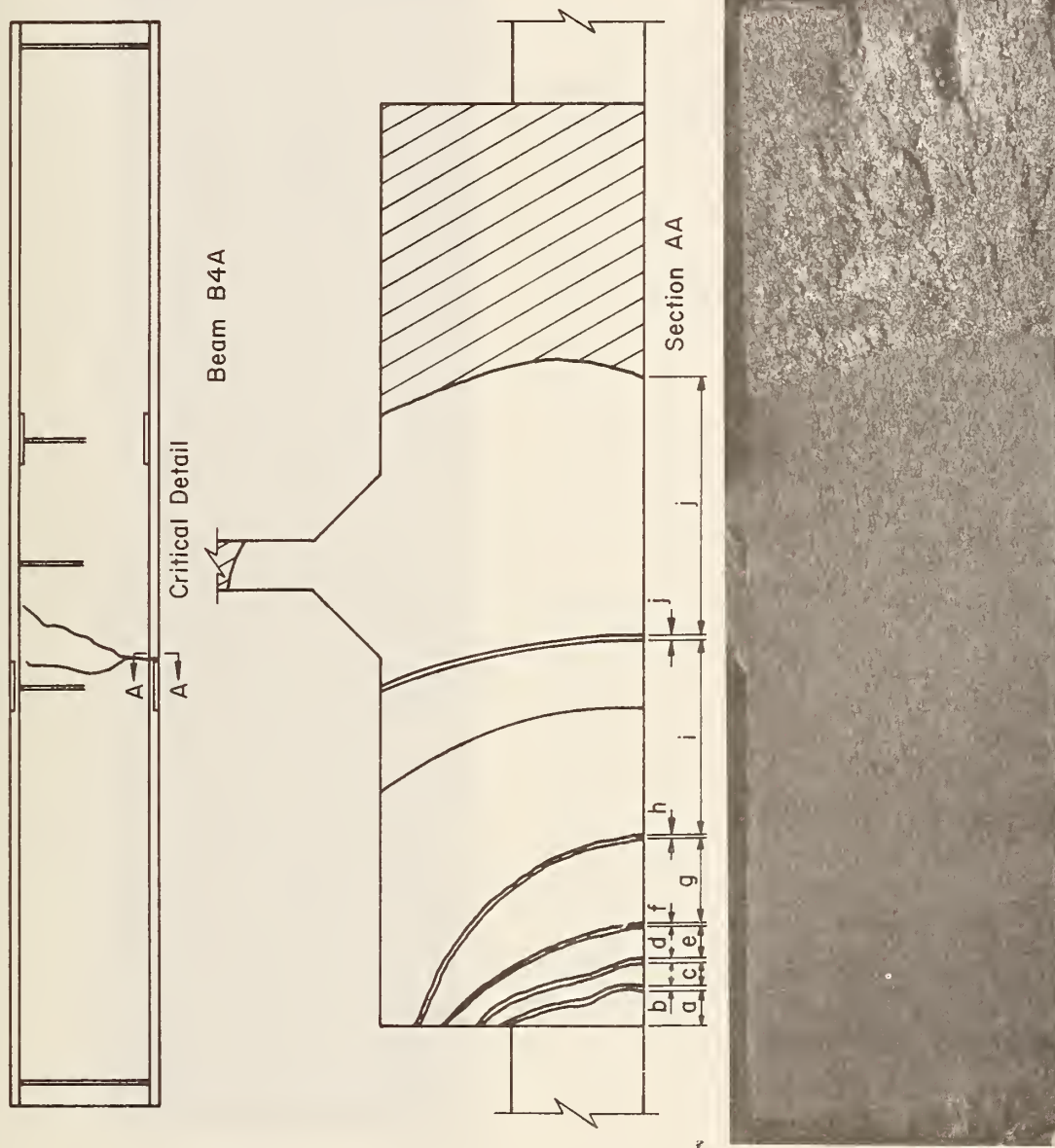


Fig. 4.4 Fatigue and Fracture Surface, B4A (A36)

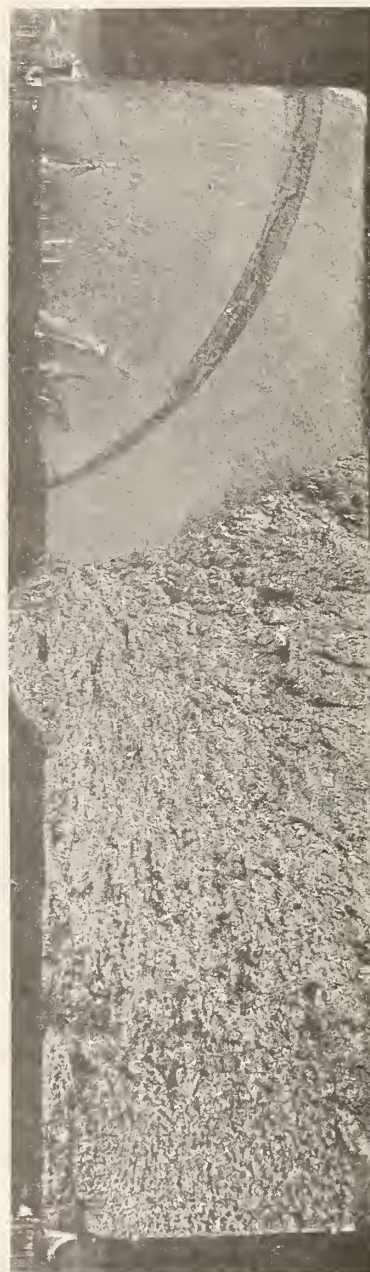
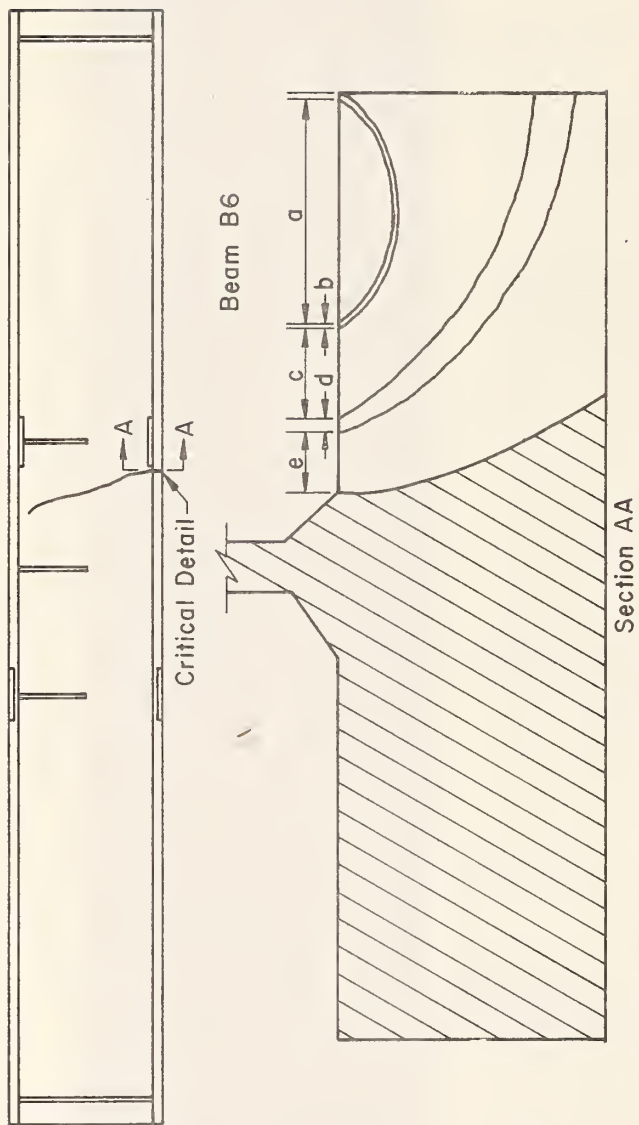


Fig. 4.5 Fatigue and Fracture Surface, B6 (A588)

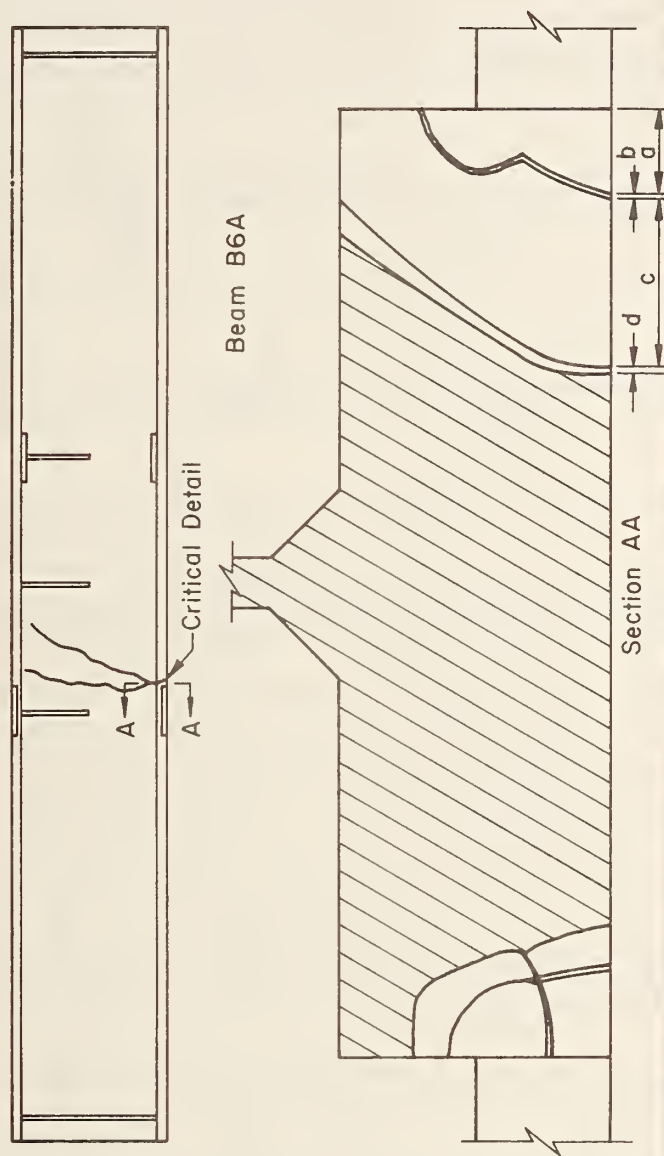


Fig. 4.6 Fatigue and Fracture Surface, B6A (A588)

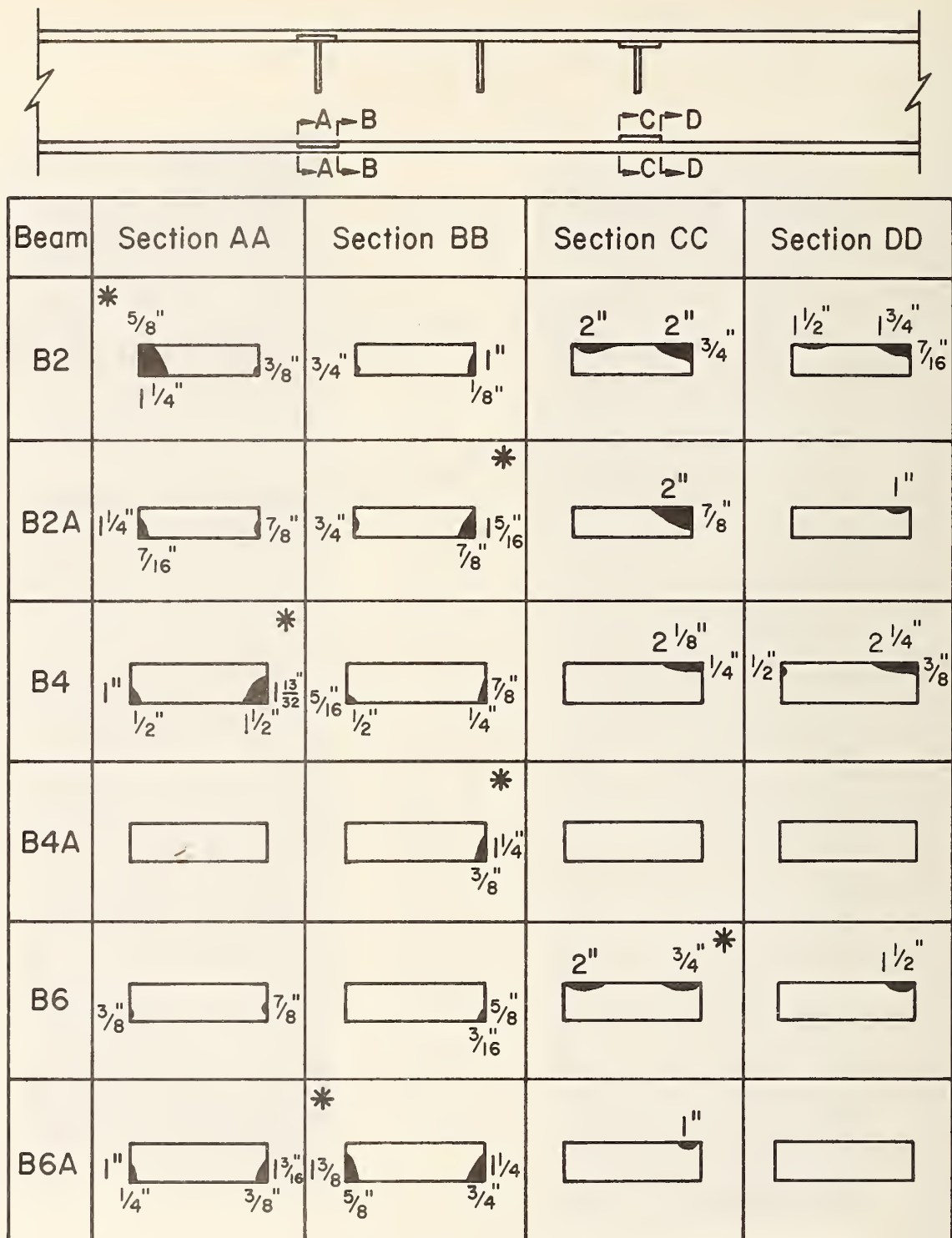
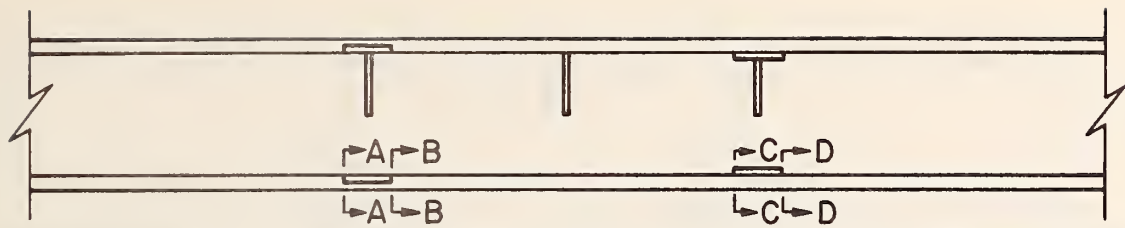


Table Scale 1 1/2" = 1'-0"
* Beam Fractured At This Section

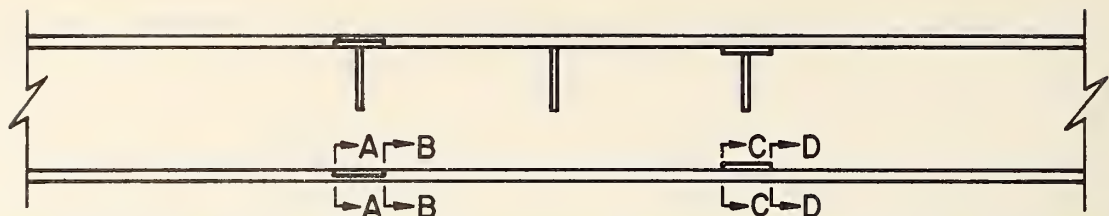
Fig. 4.7a Fatigue Cracks at Two Million Cycles



Beam	Section AA	Section BB	Section CC	Section DD
B2	* 15.9 31.8 9.5	6.4 25.4	50.8 50.8 19.1	38.1 44.5 11.1
B2A	31.8 22.2	19.1 33.3 22.2	50.8 22.2	25.4
B4	25.4 35.7 12.7 38.1	* 7.9 22.2 12.7 6.4	54.0 6.4	57.2 12.7 9.5
B4A		31.8 9.5		
B6	9.5 22.2	15.9 4.8	50.8 44.5	38.1
B6A	25.4 30.2 6.4 9.5	* 34.9 31.8 15.9 19.1	25.4	

* Beam Fractured At This Section
Crack Measurements In mm

Fig. 4.7b Fatigue Cracks at Two Million Cycles



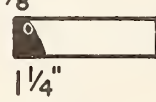

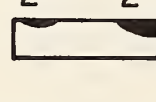
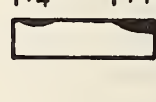
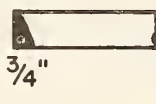
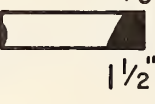
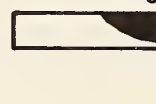

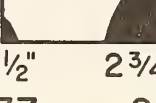
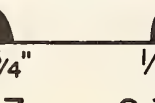
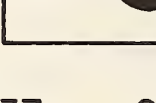

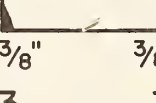
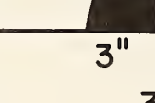
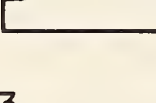
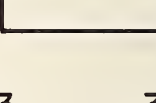
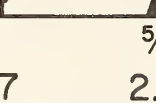
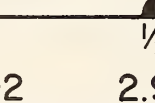
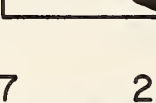
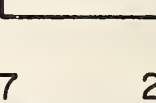
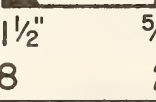
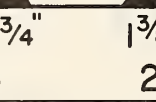
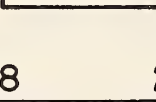
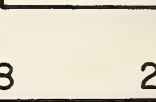
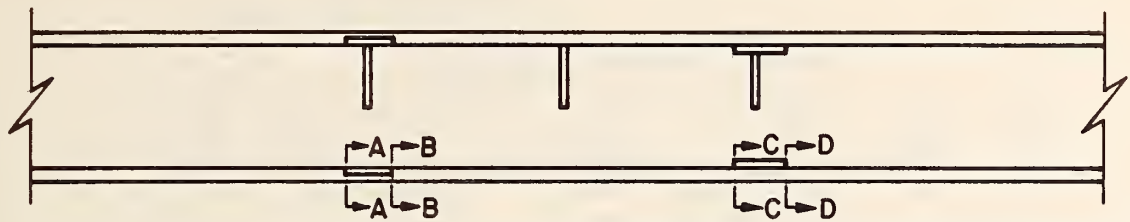
Beam	Section AA	Section BB	Section CC	Section DD
B2	$\ast \frac{5}{8}$ "  $\frac{1}{4}$ " 2.0 2.0	$\frac{1}{4}$ "  $\frac{1}{4}$ " 2.0 2.0	2 " 2 " $\frac{3}{4}$ "  2.0 2.0	$\frac{1}{4}$ " $\frac{3}{4}$ " $\frac{7}{16}$ "  2.0 2.0
B2A	$\frac{5}{16}$ " $\frac{5}{8}$ "  $\frac{3}{4}$ " 2.7 2.48	$\frac{13}{16}$ " $\frac{7}{8}$ " \ast  $\frac{1}{2}$ " 2.48 2.8	$2\frac{3}{8}$ " $\frac{13}{16}$ "  2.8 2.8	$\frac{1}{4}$ "  2.8 2.8
B4	2 " \ast  $\frac{1}{8}$ " $\frac{1}{2}$ " $2\frac{3}{4}$ " 2.37 2.37	$\frac{1}{2}$ " $\frac{3}{4}$ " $\frac{1}{8}$ "  2.37 2.37	$2\frac{5}{16}$ " $\frac{3}{8}$ "  2.37 2.37	$1\frac{7}{8}$ " $2\frac{1}{4}$ " $\frac{3}{8}$ "  2.37 2.37
B4A	$\frac{1}{4}$ " $\frac{3}{8}$ " $\frac{3}{8}$ "  3.3 3.3	$\frac{1}{2}$ " \ast  $\frac{3}{8}$ " 3 " 3.3 3.3	2 " $\frac{1}{4}$ " $\frac{3}{4}$ "  3.3 3.3	$\frac{1}{4}$ " $\frac{5}{8}$ " $\frac{3}{8}$ "  3.3 3.3
B6	$\frac{3}{8}$ " $\frac{1}{2}$ " $\frac{5}{8}$ "  2.7 2.92	$\frac{1}{8}$ " $\frac{1}{2}$ "  2.92 2.92	2 " $2\frac{1}{2}$ " \ast $\frac{1}{4}$ "  2.7 2.92	$\frac{1}{8}$ " $\frac{1}{4}$ "  2.7 2.7
B6A	$\frac{1}{8}$ " $\frac{1}{2}$ " $\frac{5}{8}$ " $\frac{3}{8}$ "  2.8 2.8	$\ast \frac{5}{8}$ " $\frac{1}{4}$ " $\frac{3}{8}$ "  2.8 2.8	1 " $2\frac{1}{8}$ " $\frac{1}{4}$ "  2.8 2.8	 2.8 2.8

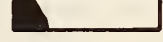

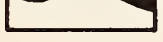
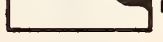
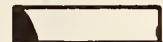
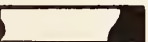

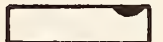
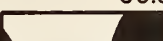
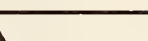
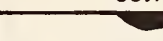
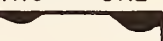
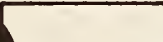

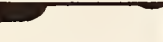
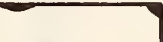
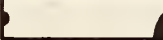

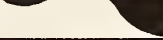
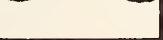
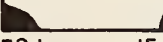
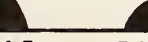


Table Scale $1\frac{1}{2} = 1'-0"$

Measurements Taken At Cycles Listed At Bottom
Of Cross Section (in millions of cycles)

\ast Beam Fractured At This Section

Fig. 4.8a Fatigue Cracks Prior to Last Fracture Test



Beam	Section AA	Section BB	Section CC	Section DD
B2	* 15.9  31.8 2.0 2.0	6.4  25.4 2.0 2.0	50.8 50.8  19.1 2.0 2.0	31.8 44.5  11.1 2.0 2.0
B2A	7.9  15.9 19.1 2.7 2.48	22.2 *  38.1 20.6 2.48 2.8	60.3  30.2 2.8 2.8	31.8  2.8 2.8
B4	50.8 *  69.9 28.6 12.7 2.37 2.37	38.1  19.1 2.37 2.37	58.7  9.5 2.37 2.37	47.6 57.2  9.5 2.37 2.37
B4A	31.8  34.9 9.5 9.5 3.3 3.3	53.5 *  76.2 9.5 3.3 3.3	50.8 31.8  3.3 3.3	31.8 15.9  9.5 3.3 3.3
B6	9.5  38.1 12.7 2.7 2.92	28.6  12.7 2.92 2.92	50.8 63.5 *  44.5 2.7 2.92	28.6 44.5  2.7 2.7
B6A	28.6  38.1 15.9 34.9 2.8 2.8	* 15.9  34.9 44.5 34.9 2.8 2.8	25.4 54.0  6.4 2.8 2.8	 2.8 2.8

Measurements Taken At Cycles Listed At Bottom
 Of Cross Section (In millions of cycles)
 * Beam Fractured At This Section
 Crack Measurements In mm

Fig. 4.8b Fatigue Cracks Prior to Last Fracture Test

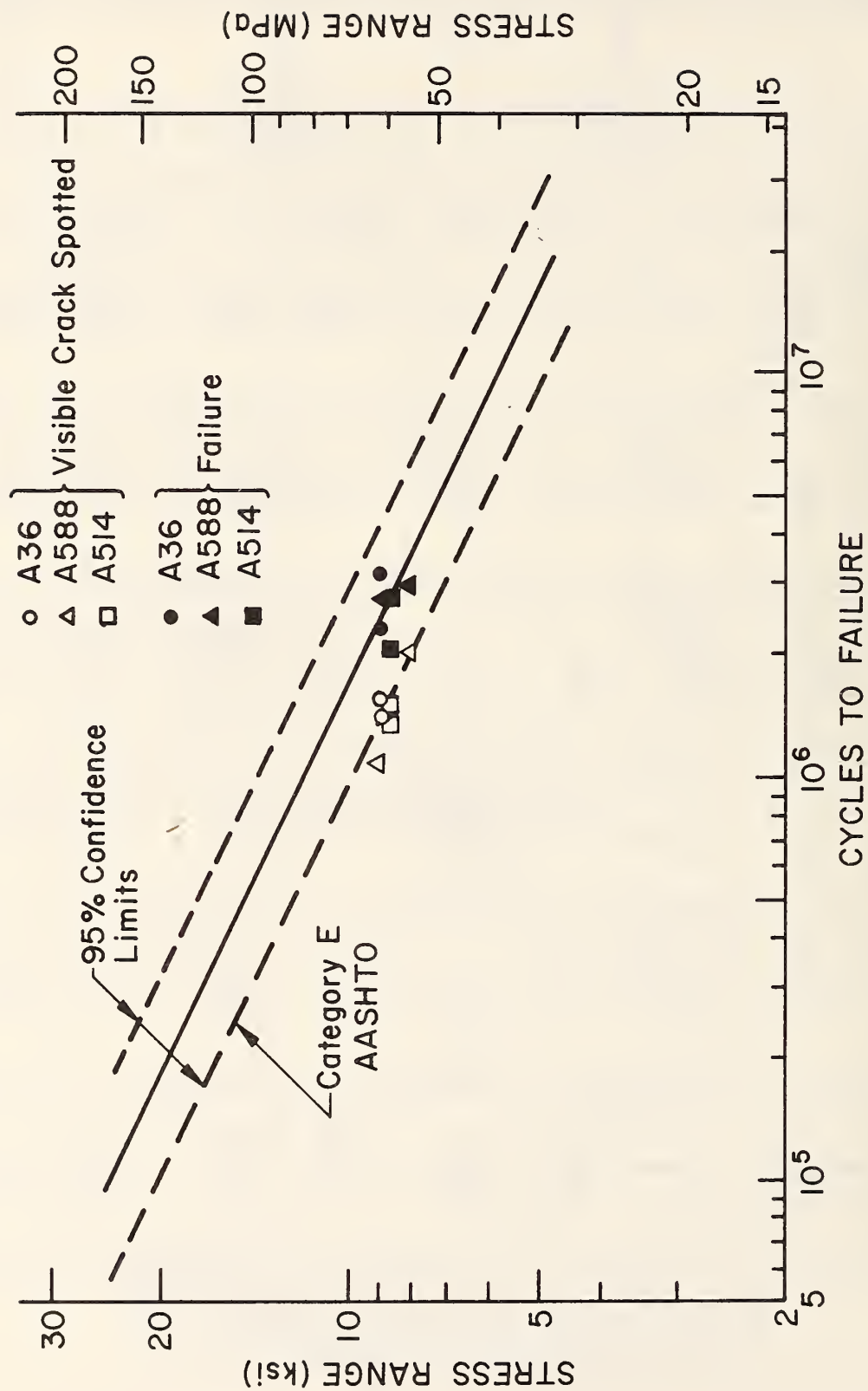


Fig. 4.9 Category E S-N Plot, Lateral Attachment Beams

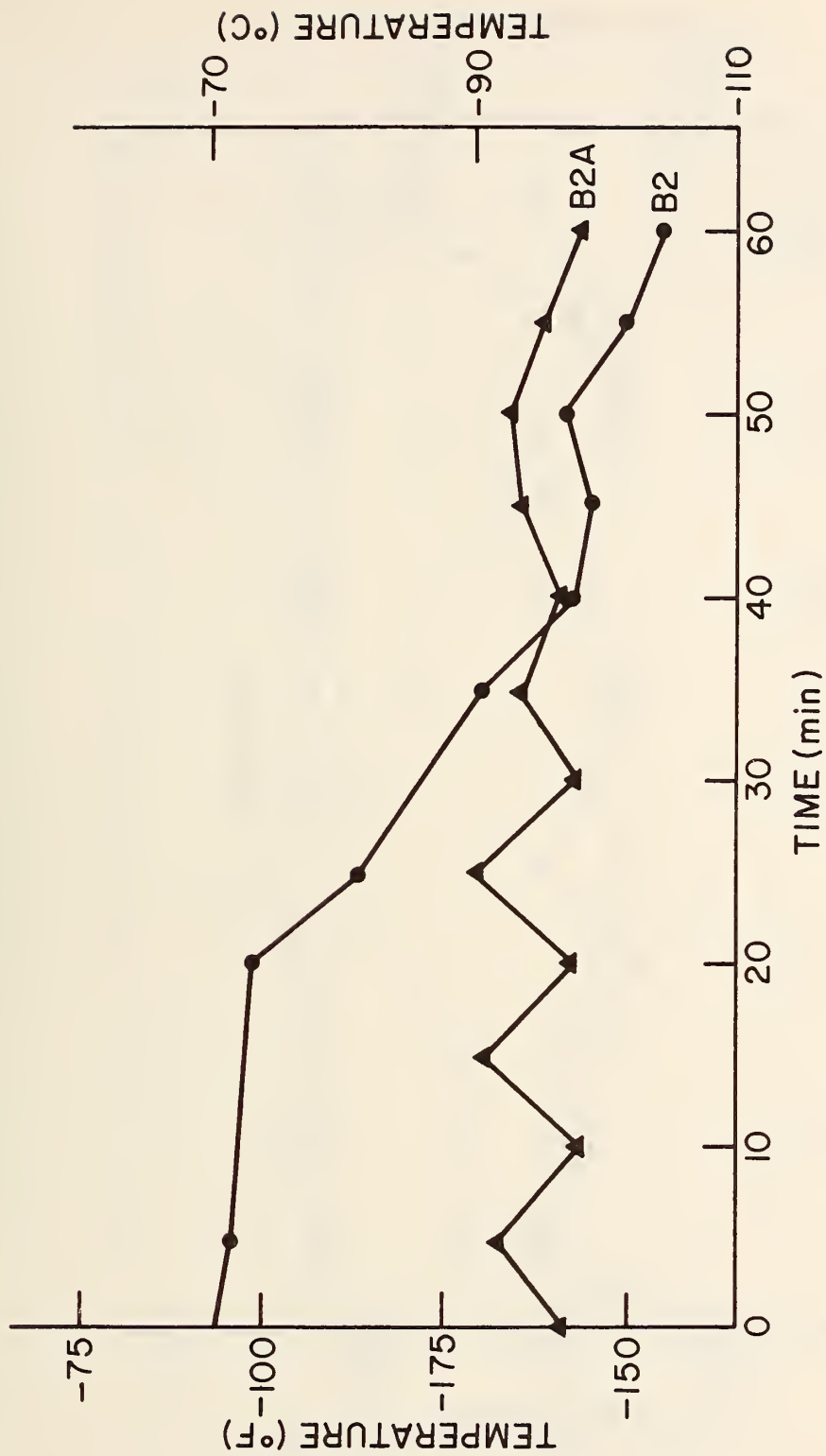


Fig. 4.10 Critical Detail Temperature/Sixty Minutes Prior to Fracture (A514)

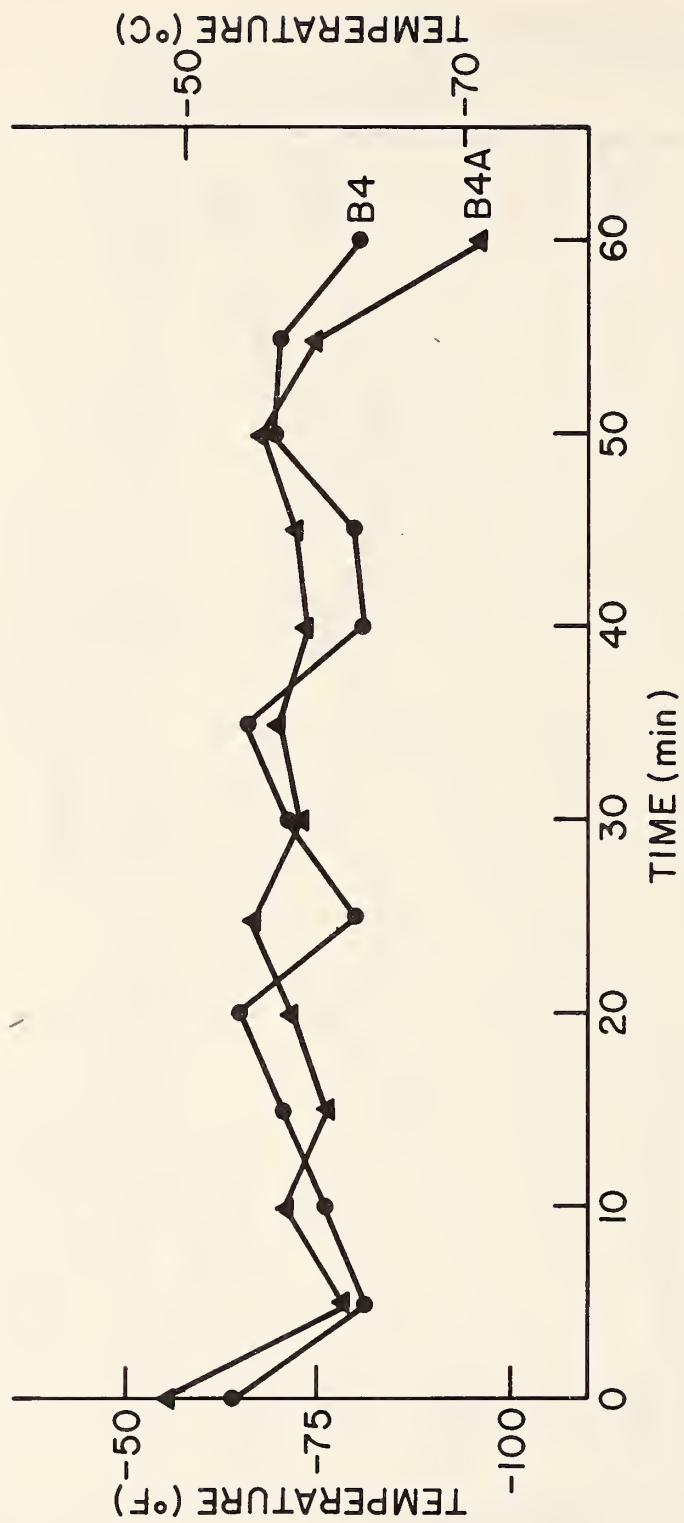


Fig. 4.11 Critical Detail Temperature/Sixty Minutes Prior to Fracture (A36)

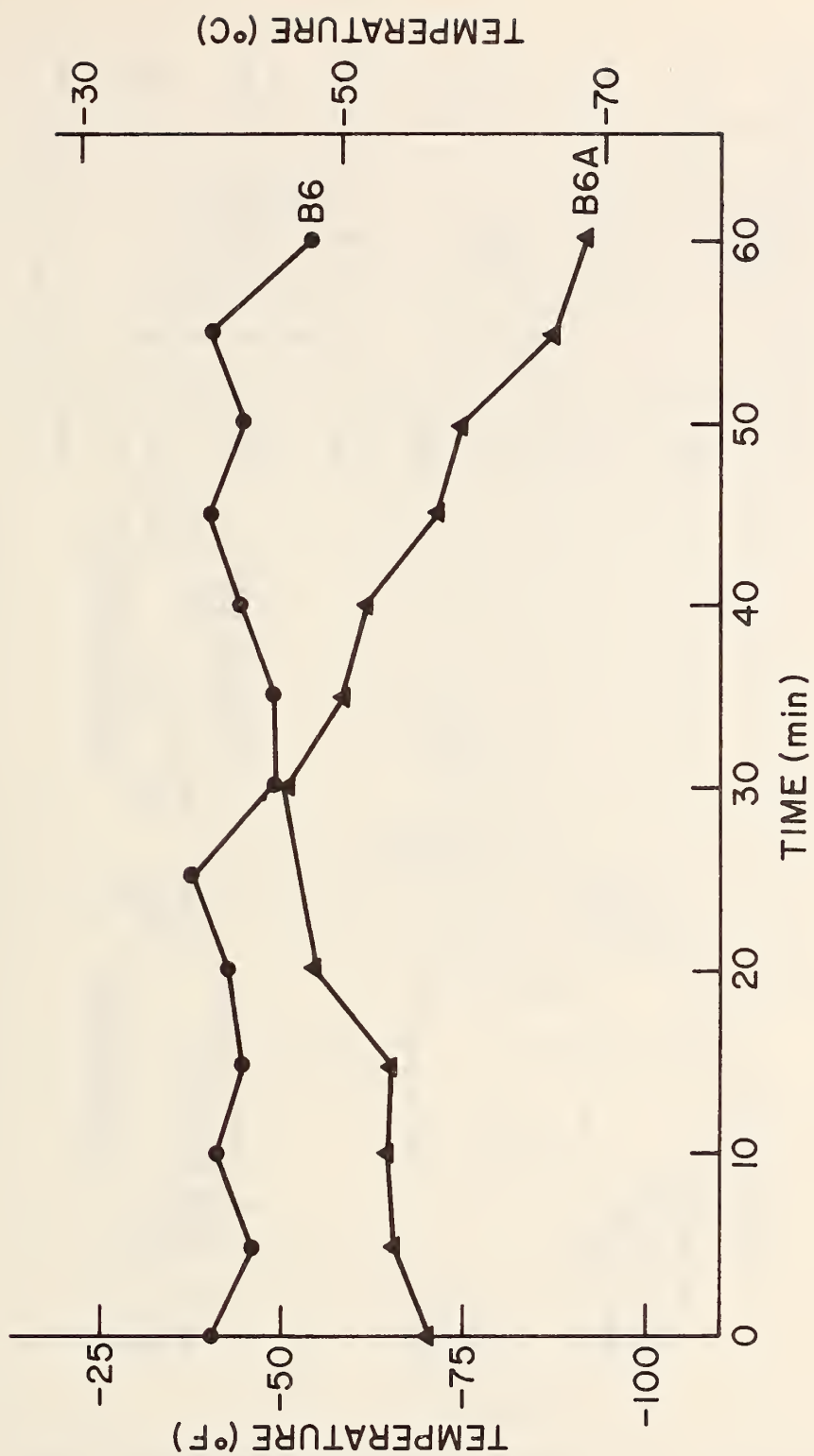


Fig. 4.12 Critical Detail Temperature/Sixty Minutes Prior to Fracture (AA588)

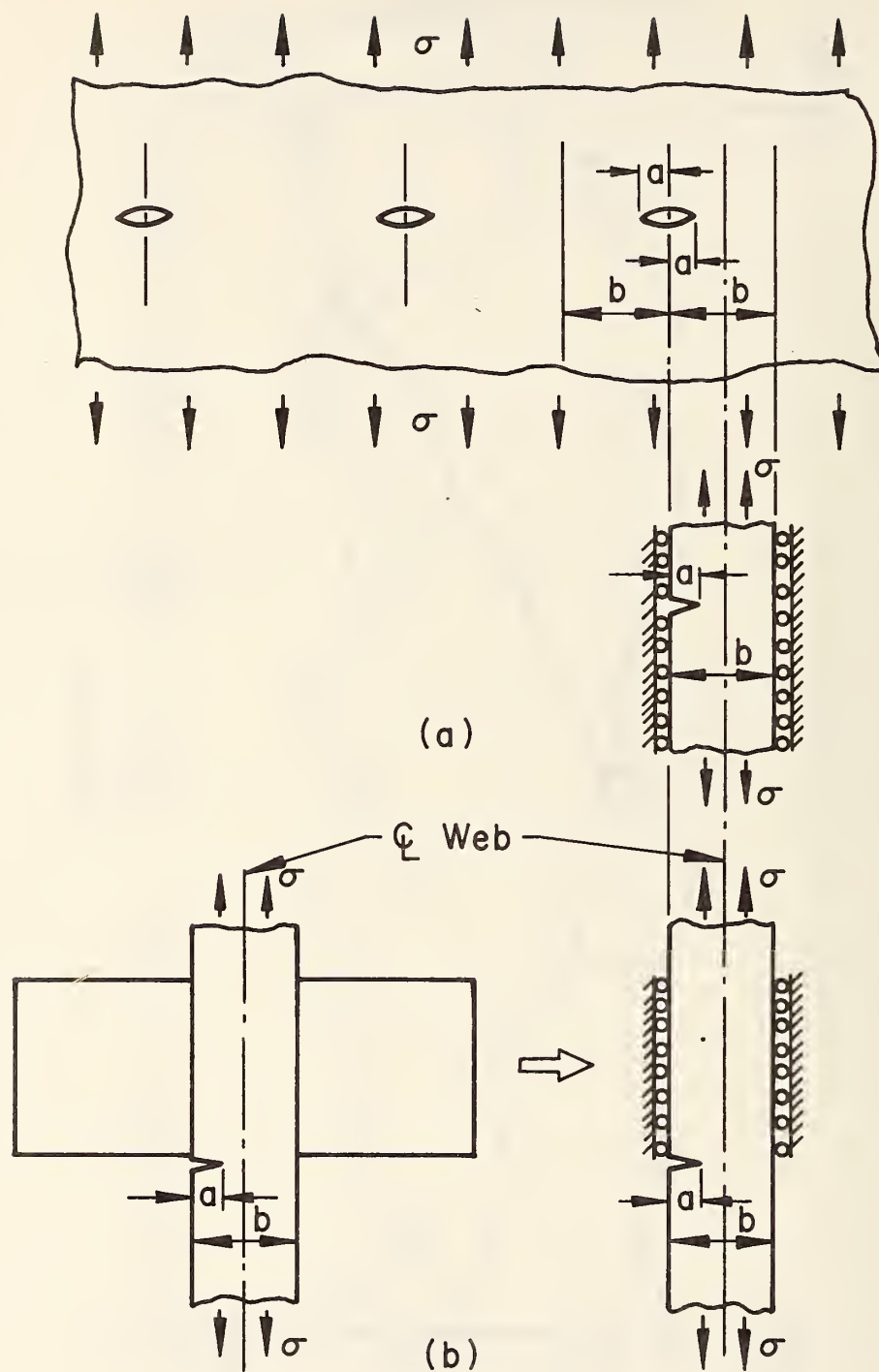


Fig. 4.13a,b Stress Intensity Model for Flange Edge Crack for Applied Stress

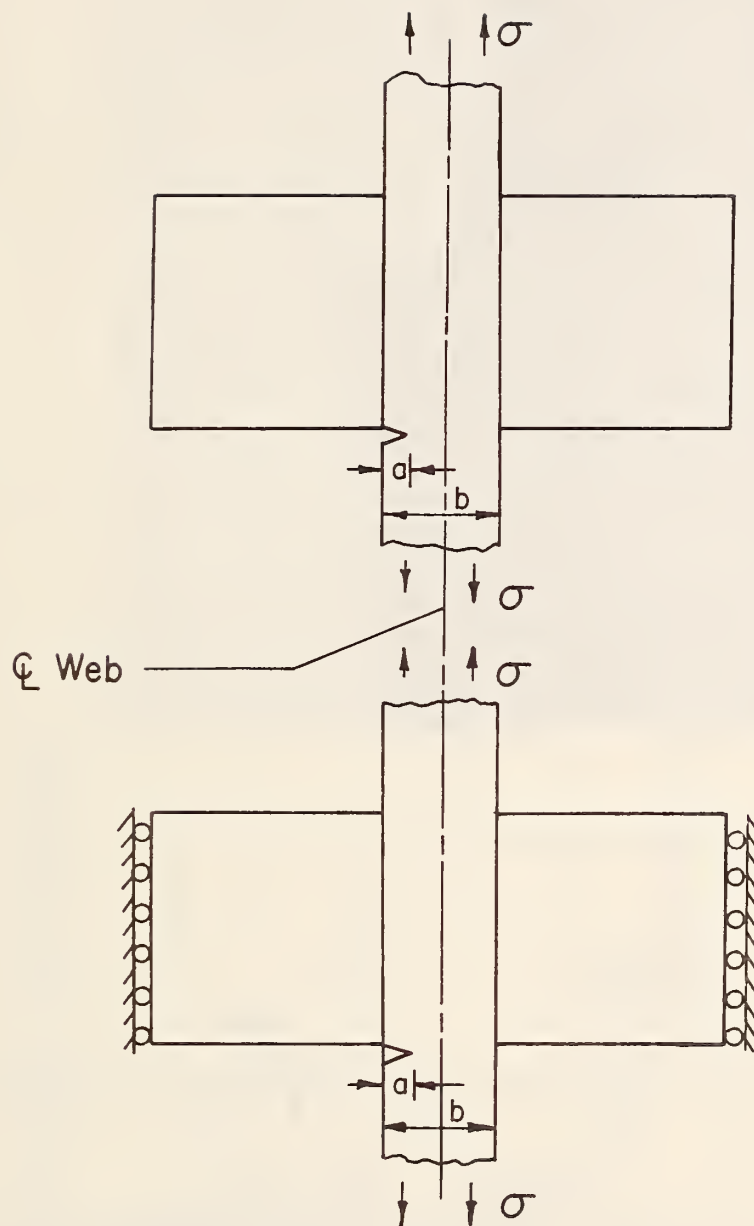
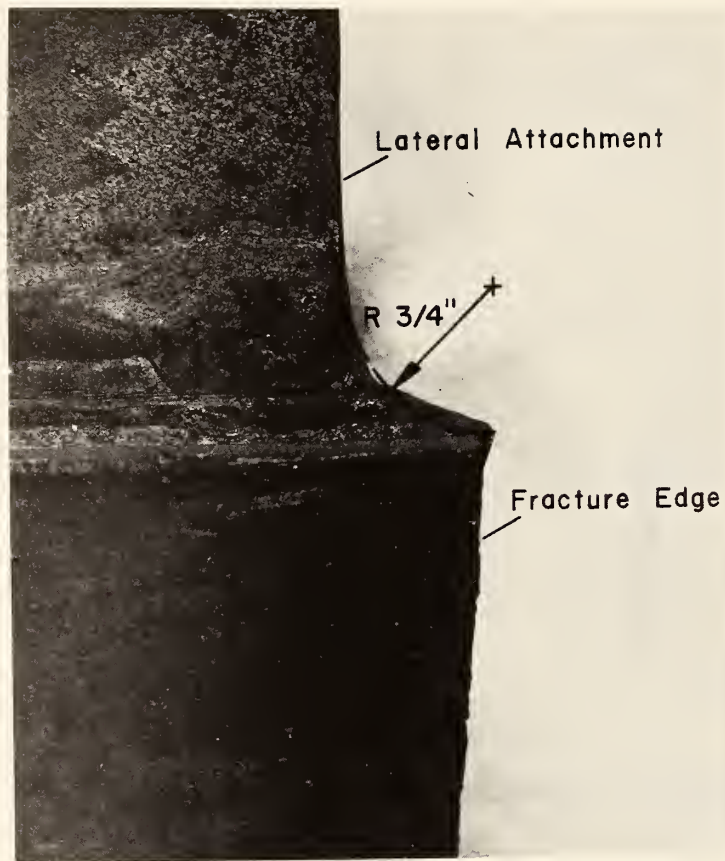
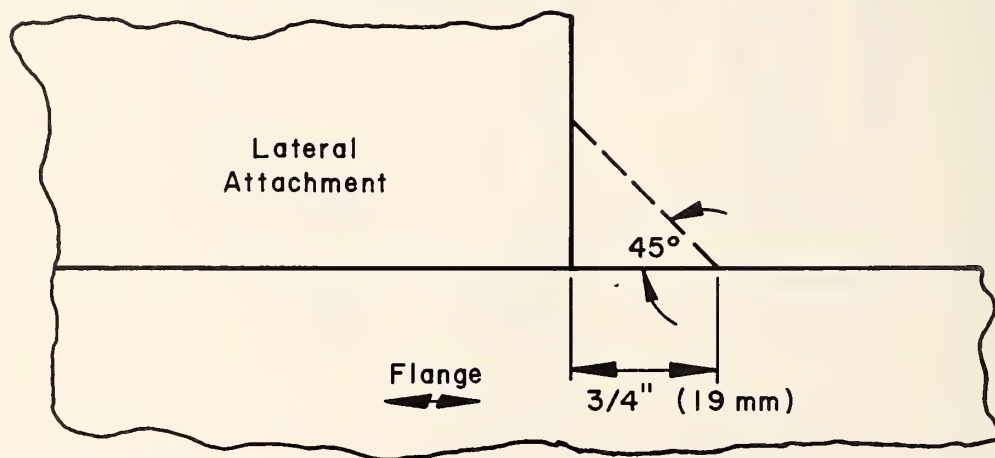


Fig. 4.13c Stress Intensity Model for Flange Edge Crack
for Applied Stress



(a)



(b)

Fig. 4.14 Groove Weld Detail Reentrant Corner

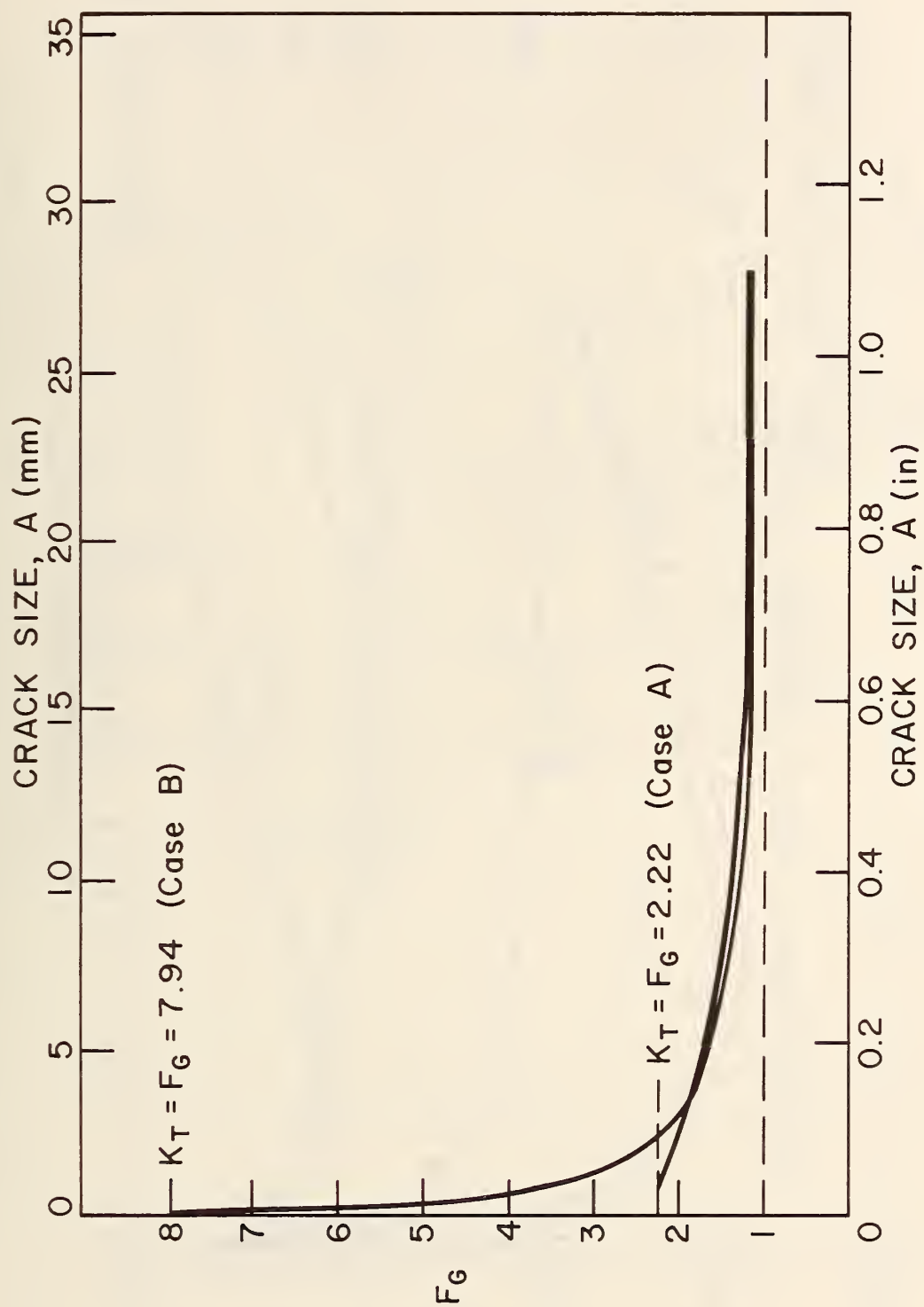


Fig. 4.15 Stress Concentration Decay with Crack Size (B2A)

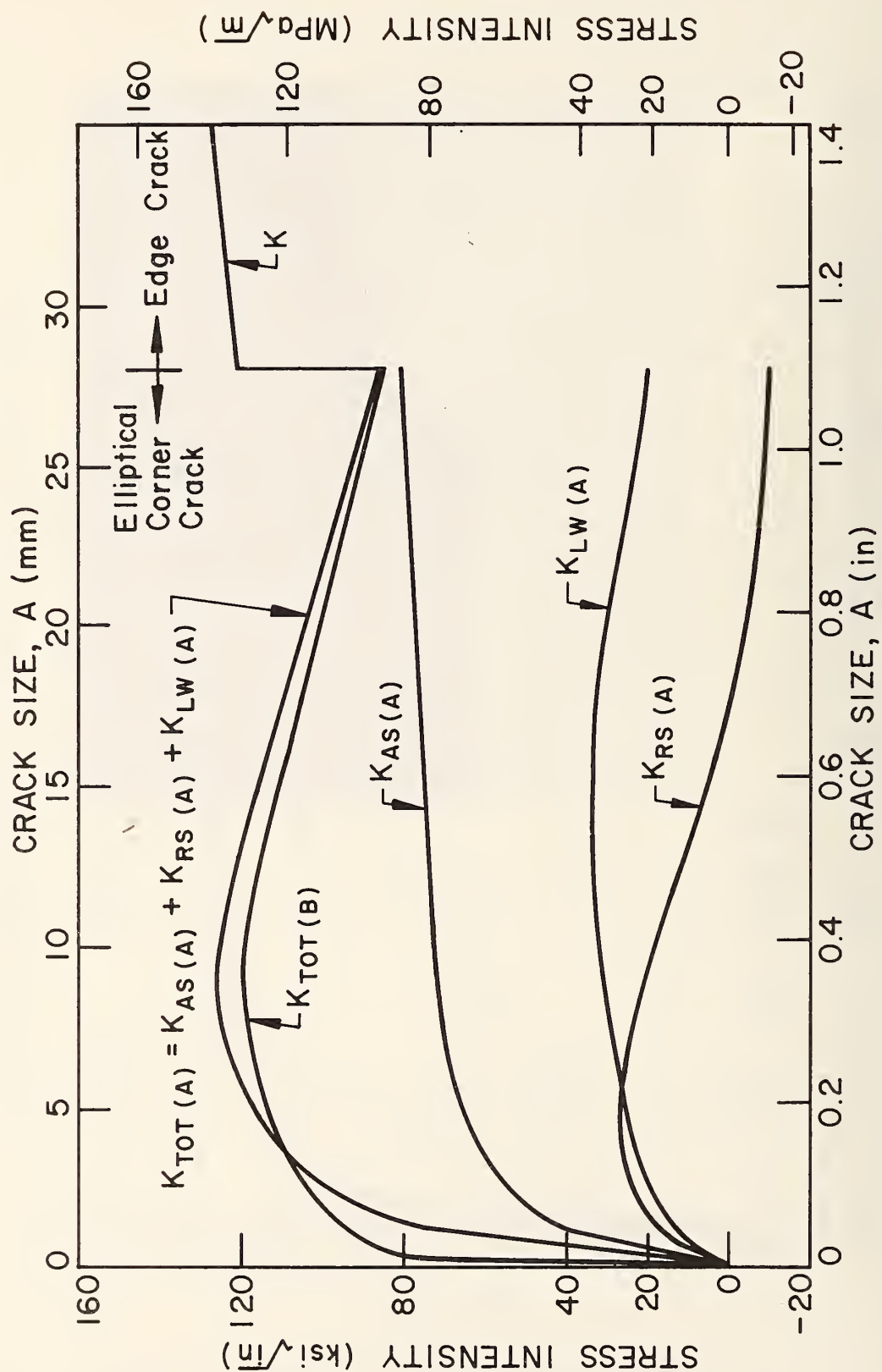
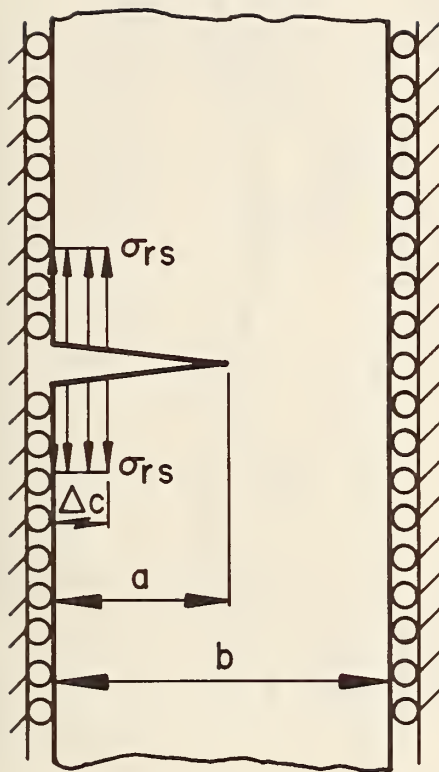


Fig. 4.16 Stress Intensity vs. Crack Size for Elliptical Corner Cracks (B2A)



$$K_{RS} = \frac{2}{\pi} \sigma_{rs} \sqrt{\pi a} F(a/b) F(c/a)$$

$$F(a/b) = \sqrt{\frac{2b}{\pi a}} \tan \frac{\pi a}{2b}$$

$$F(c/a) = \sin^{-1} \left(\frac{\sin \frac{\pi c}{2b}}{\sin \frac{\pi a}{2b}} \right)$$

$$\Delta c = 0.02''$$

Fig. 4.17 Superposition Model for Residual Stress

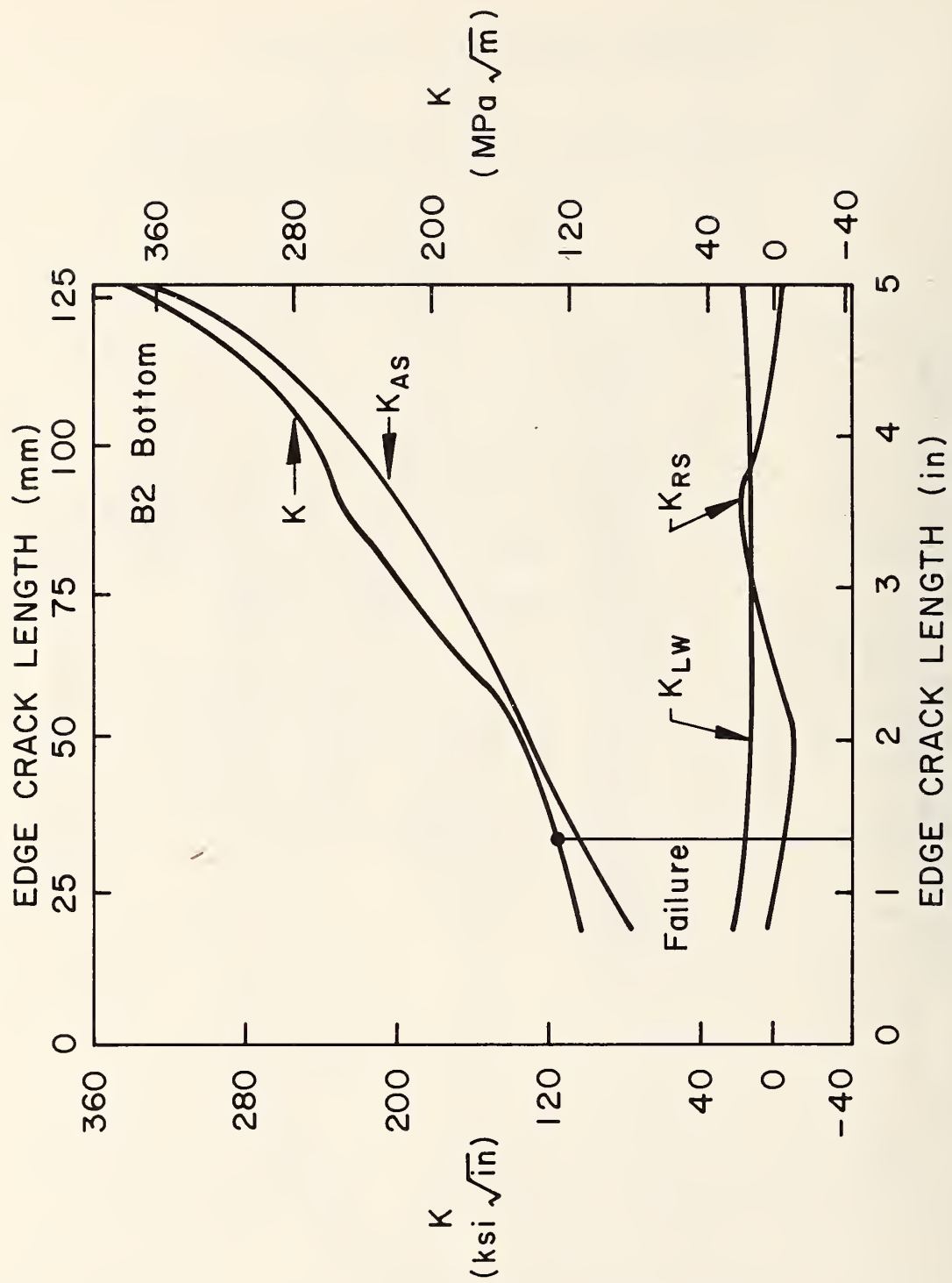


Fig. 4.18 K vs. Edge Crack Size, B2 (A514)

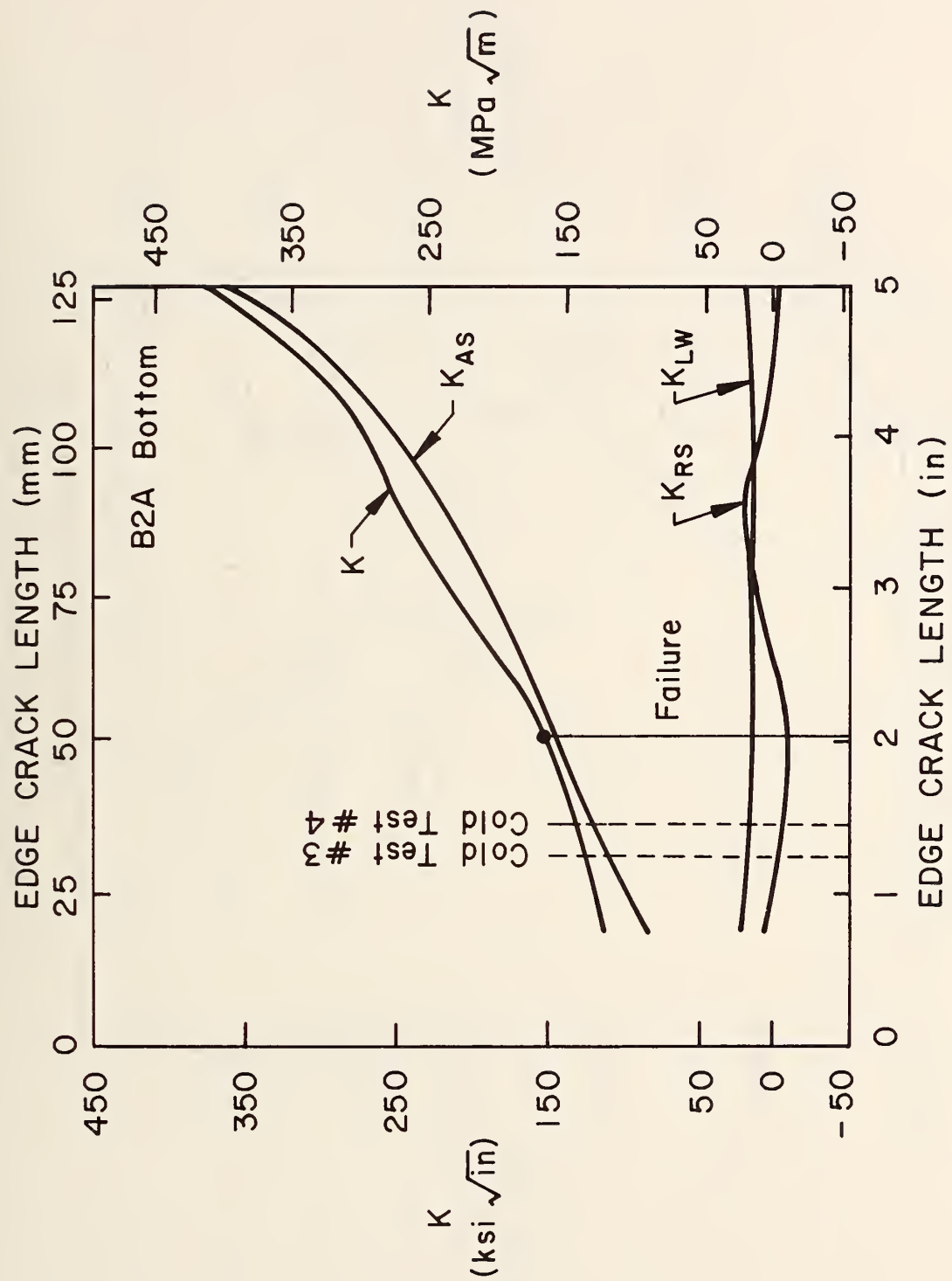


Fig. 4.19 K vs. Edge Crack Size, B2A (A514)

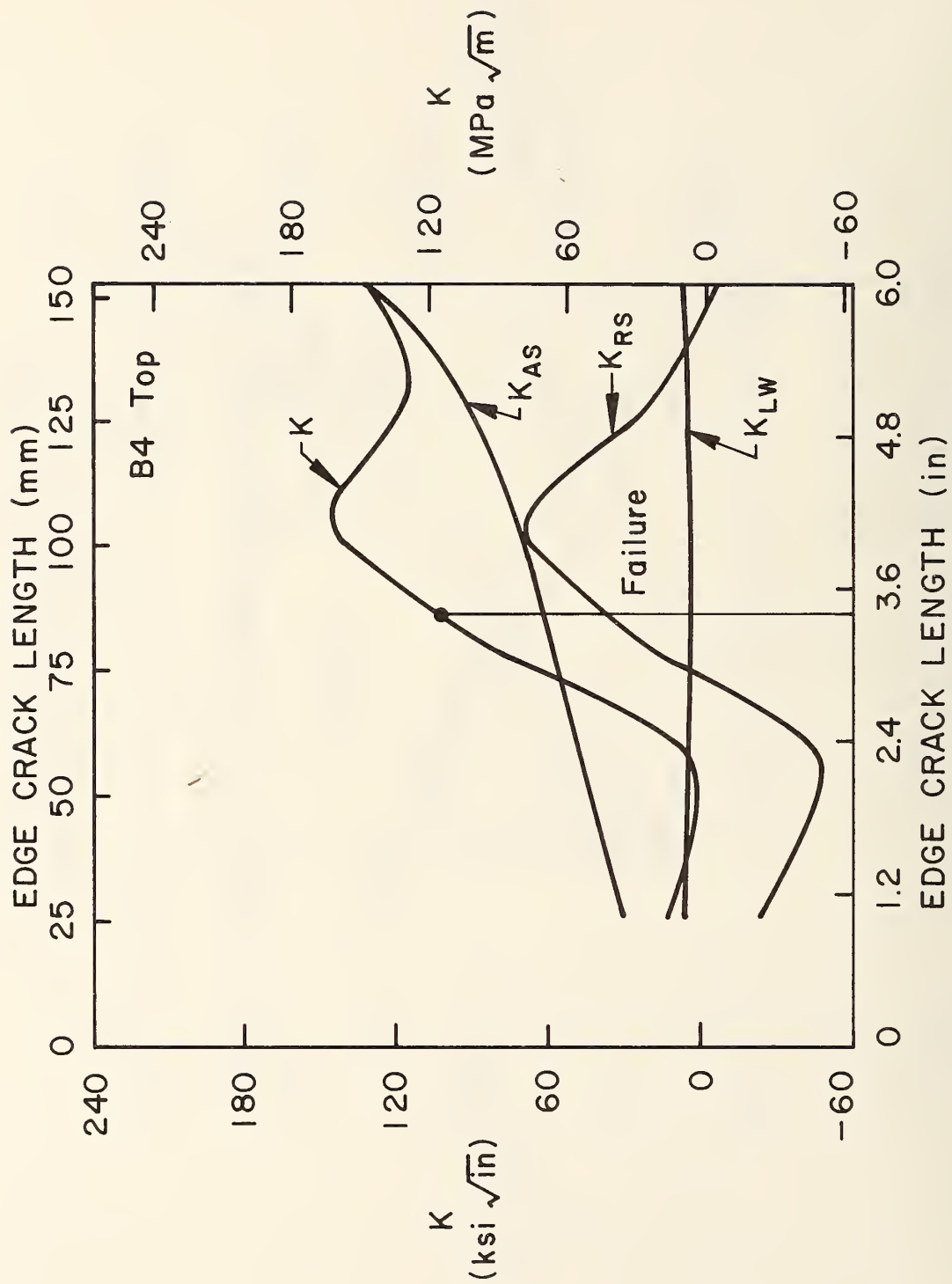


Fig. 4.20 K vs. Edge Crack Size, B4 (A36)

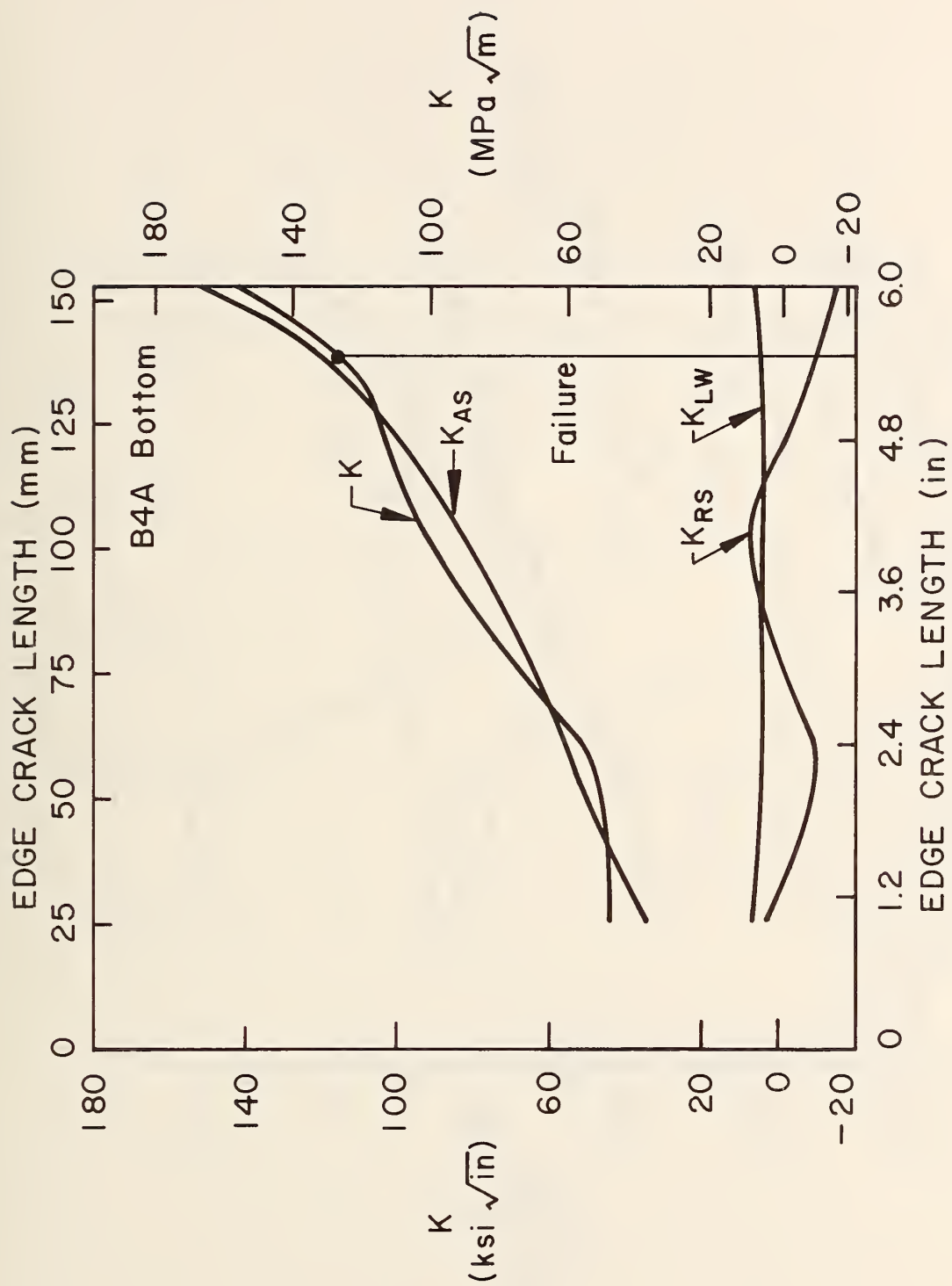


Fig. 4.21 K vs. Edge Crack Size, B4A (A36)

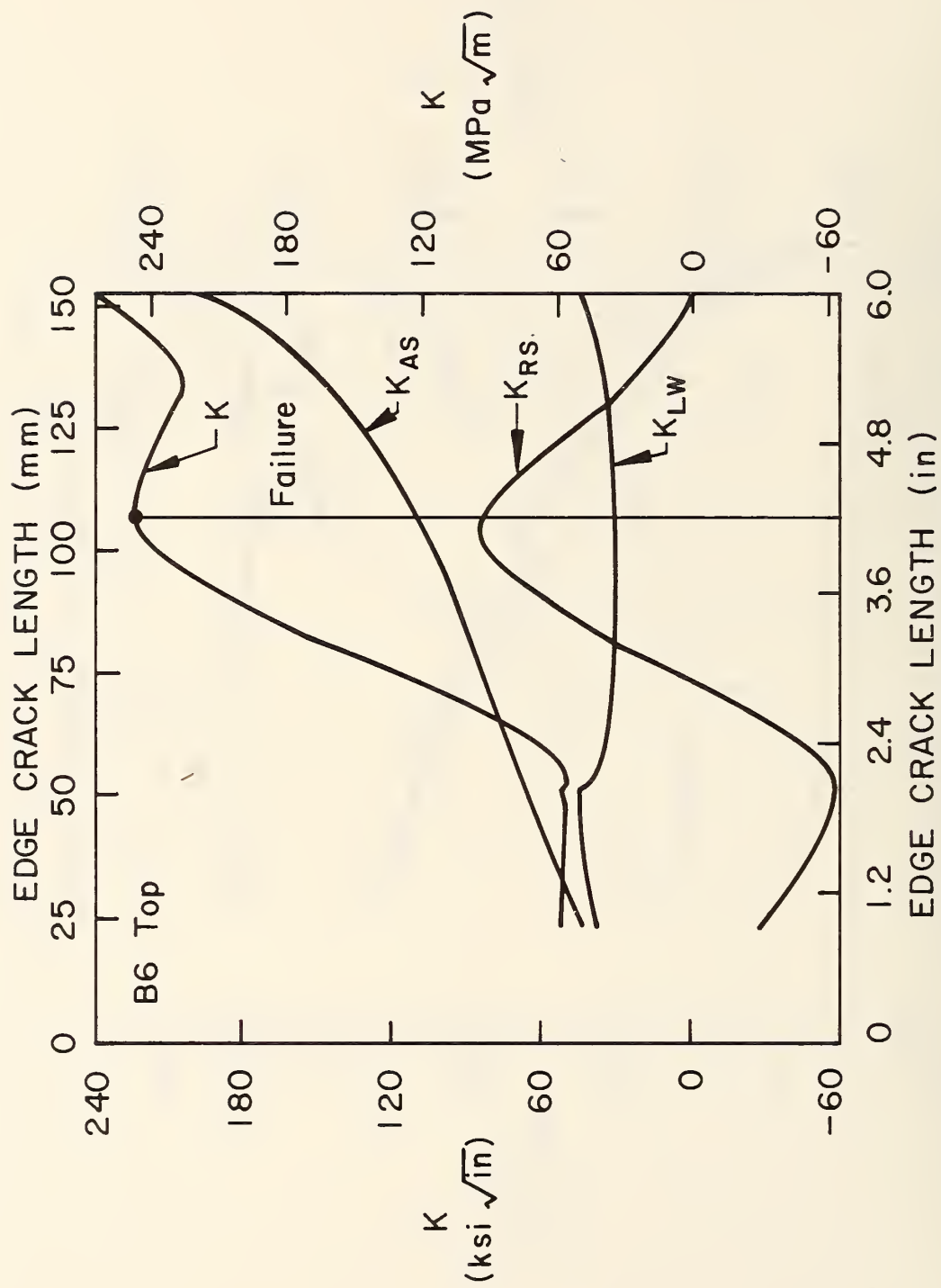


Fig. 4.22 K vs. Edge Crack Size, B6 (A588)

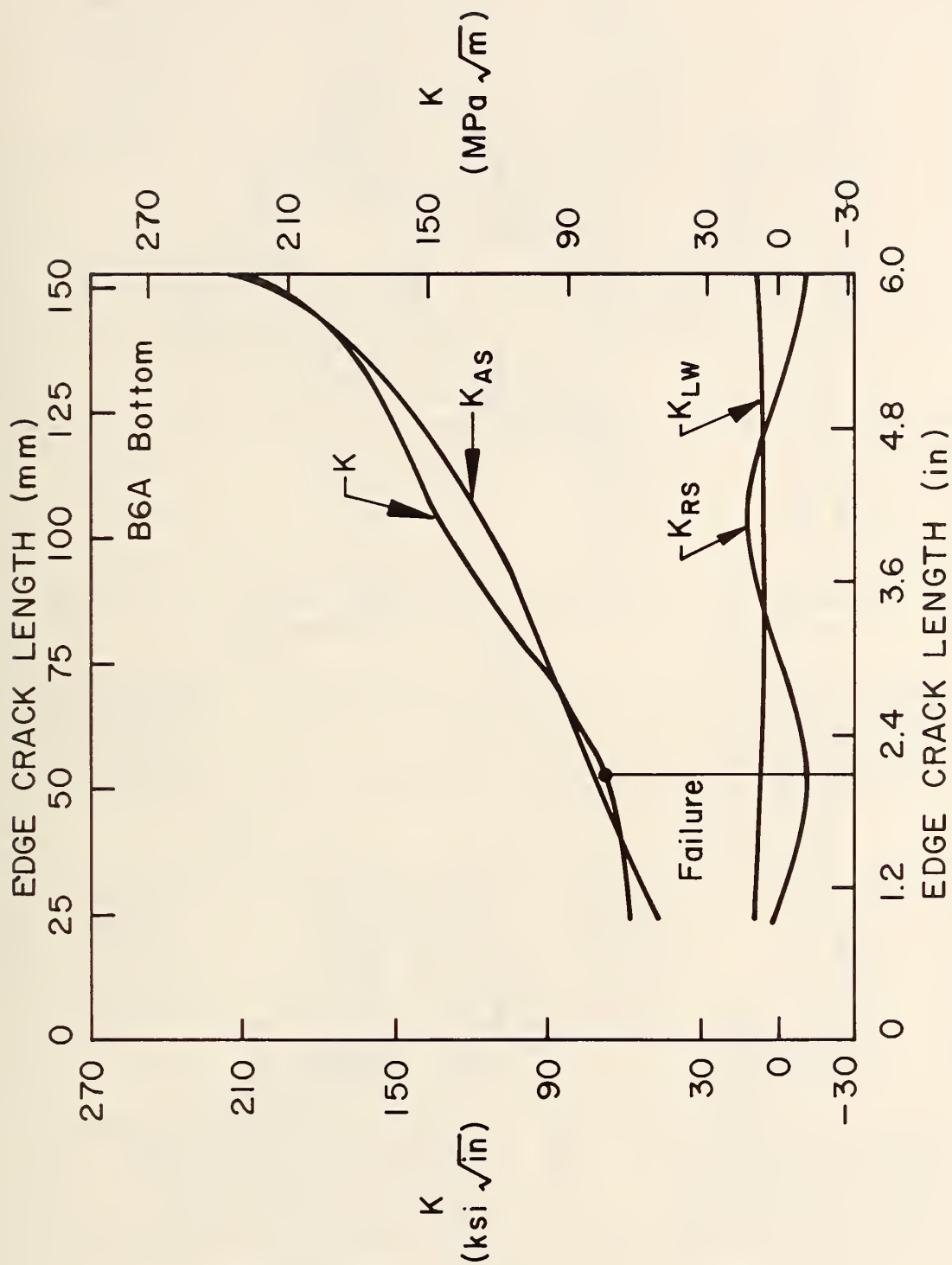


Fig. 4.23 K vs. Edge Crack Size, B6A (A588)

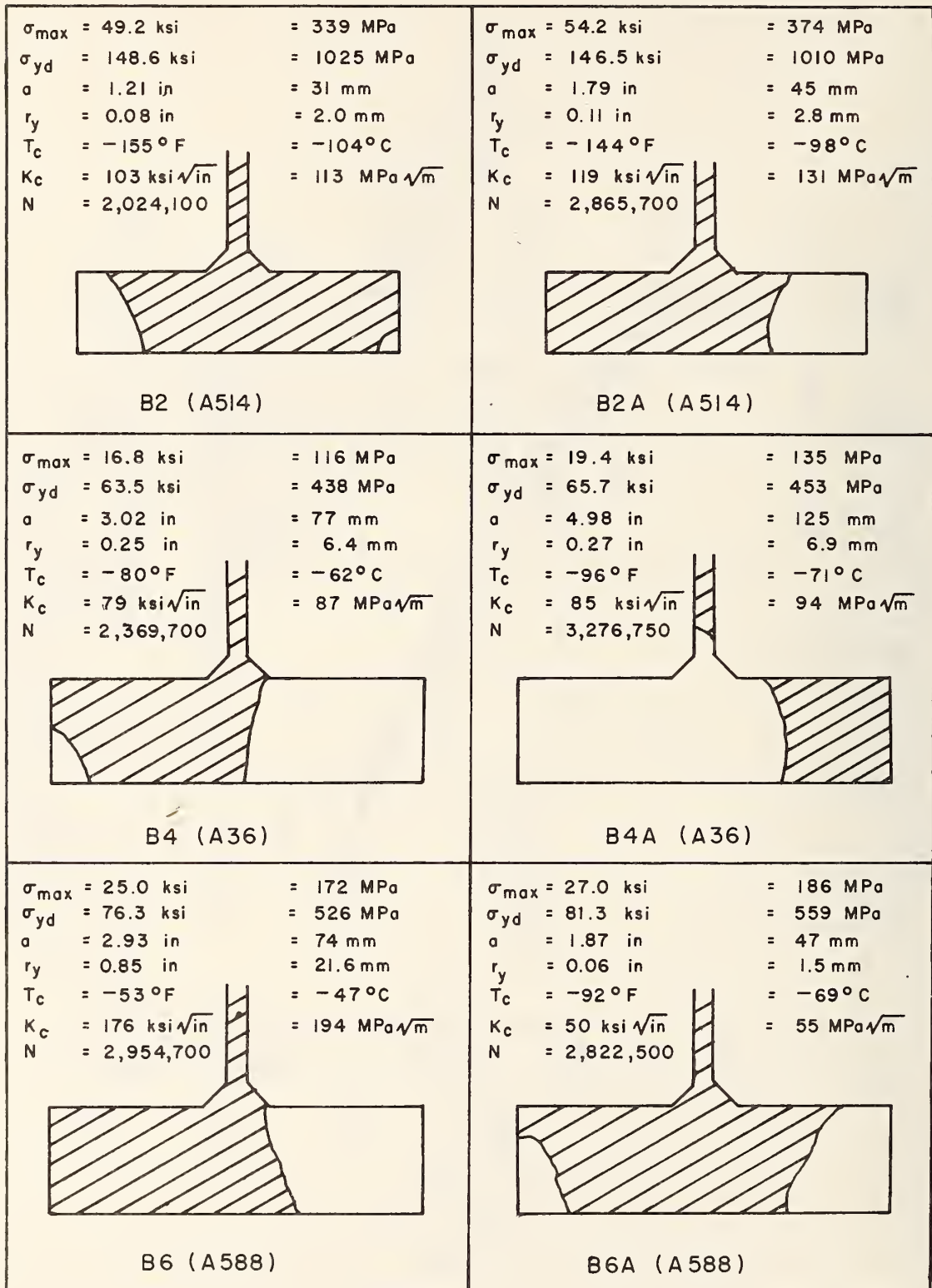


Fig. 4.24 Fracture Surface Sketches and Data Summary

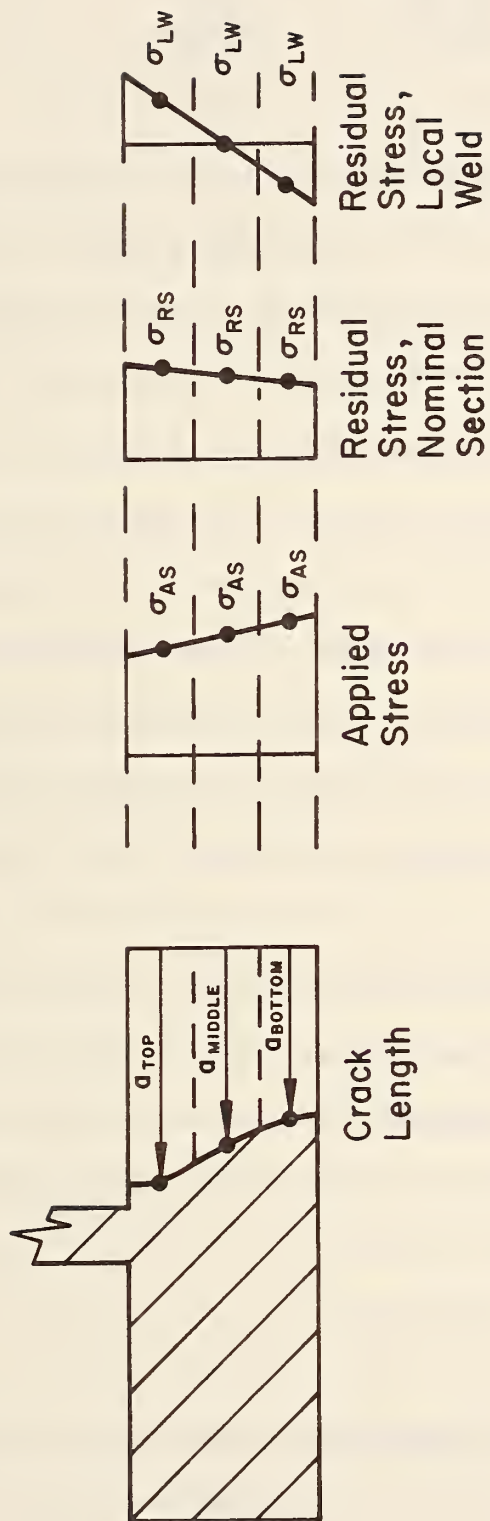


Fig. 4.25 One-third Levels for Edge Crack Analysis

5. COVER PLATE BEAM TEST RESULTS AND ANALYSES

(Specimen No.	Material)
B3, B3A	A36
B5, B5A	A588
B1, B1A	A514

5.1 Fatigue Cracks

The fatigue cracks on the end-welded cover-plated beams were initially detected as 0.5 in. (12.7 mm) surface cracks. As these surface cracks grew larger they became either elliptical corner cracks (see Beam B1A, Fig. 5.2) or through cracks (see B3, Fig. 5.3).

On the cover plate detail without end weld the fatigue cracks were detected as 0.5 in. (12.7 mm) surface cracks at the end of the longitudinal fillet weld. After extended crack growth the fatigue cracks became elliptical corner cracks and then quickly edge cracks.

The size of the fatigue cracks at each critical detail can be found by referencing the small letters on the crack surface drawings in Figs. 5.1 to 5.6 with the load history tables given in Tables 2.9 to 2.14.

Additional fatigue cracks existed at the other detail on each beam. Fig. 5.7 shows the fatigue cracks at all details prior to the last fracture test. The surface measurements of these cracks are shown adjacent to the crack. The crack shapes were estimated from these surface measurements.

5.2 Fatigue Life

The number of cycles needed to propagate an elliptical surface crack from its fracture initiation point to a through thickness

flange crack was defined as the remaining useful fatigue life had brittle fracture not occurred. The remaining fatigue life was estimated by a numerical integration routine using Eqs. 7 and 11 as presented in Section 4.2. Secondary stress intensity effects from the residual stresses were neglected. Appropriate correction factors, F_S , F_W , F_G and F_E were used for the cover plate details.

Beams B1A, B3 and B3A had no appreciable remaining fatigue life at the time of fracture. Beams B1, B5 and B5A had 106,000, 607,000 and 70,000 cycles of remaining fatigue life, respectively.

Figure 5.8 shows the mean S-N curve and its confidence limits for the Category E details. The data base used to develop this curve utilized tests on 12 to 14 in. (304.8 to 355.6 mm) deep beams with a maximum flange thickness of 0.5 in. (12.7 mm)¹. The fatigue results for the cover-plated beams, which had flange thicknesses between 1.25 in. (31.8 mm) and 1.5 in. (38.1 mm), are plotted on the same curve. The open figures represent the point at which the cracks were first observed and the closed figures represent the point of fracture.

The fatigue life of each cover plate detail at fracture was near or below the lower 95% confidence limit which corresponds to the design strength for Category E details. The rapid fatigue crack initiation and growth was apparently caused by the higher stress concentration which existed at these full size details. These fatigue results were similar to those obtained in Ref. 1 on thirty smaller scale cover-plated beams with cover plates wider than the flange and without end

welds. The lower confidence limit for these details is also shown in Fig. 5.8. All cover plate details presented in this section had fatigue lives between the mean and the upper 95% confidence limit for this lower fatigue life detail type. This study has indicated that additional tests are needed on the fatigue behavior of full size welded cover plate details, particularly at low stress range levels.

5.3 Beam Fracture Tests*

Beam B1 (A514 Steel)

Since the fatigue crack at the end-welded detail initiated and grew very rapidly (see Fig. 5.1), the first fracture test was conducted before the beam reached its two million cycle fatigue design life. At this point only a small 0.63 in. (16.0 mm) long elliptical surface crack existed at the unwelded end (see Fig. 5.7).

Only one fracture test was run on this beam. Both the end-welded detail and the unwelded end details were tested at -40° F (-40° C) for 0.5 hour. Since no fracture occurred at this point, the critical detail was cooled further while being cyclically loaded for 2.25 hours until fracture occurred at -200° F (-129° C). The fatigue crack extension during this fracture test was approximately 0.13 in. (3.3 mm) as can be seen in Fig. 5.1.

* Temperature at the critical details are shown graphically in Figs. 5.9 to 5.11 for the final sixty minutes of the last fracture test.

Beam B1A (A514 Steel)

A very large 5.88 in. x 1.25 in. (149.4 mm x 31.8 mm) elliptical corner crack existed at the end-welded detail after 1.134 million cycles (see Fig. 5.2). No cracks were found at the unwelded end.

Only one fracture test was run on Beam B1A. Both details were cooled to -40°F (-40°C) and then cyclically loaded. Just as the maximum stress and stress range was obtained, fracture occurred at the end-welded detail. The temperature at fracture was -48° F (-44° C).

Beam B3 (A36 Steel)

After 2 million cycles a large 12 in. (304.8 mm) elliptical surface crack existed along the weld toe of the end-welded detail. Two 1.25 in. (31.8 mm) long elliptical shaped cracks also existed at the detail without a transverse end weld.

Both details were cooled to -40°F (-40°C) and cyclically tested for 0.5 hour. No fracture occurred. An additional 162,000 fatigue cycles were applied at room temperature. At this stage of crack growth the large elliptical surface crack at the end welded detail became a through-thickness crack (see Figs. 5.3 and 5.7). Both details were again cooled to -40°F (-40°C) and cyclically loaded. Fracture occurred while loading. A maximum stress of 17.2 ksi (118.6 MPa) and stress range of 5.4 ksi (37.2 MPa) was applied at the time of fracture.

Beam B3A (A36 Steel)

After 1.79 million cycles of fatigue loading at room temperature, a 5 in. (127.0 mm) edge crack existed at the unwelded detail (see Figs. 5.4 and 5.7). A series of small elliptical shaped surface cracks also existed along the weld toe of the end-welded detail (see Fig. 5.7).

Both details were cooled to -40°F (-40°C) and cyclically loaded for 1 hour. No fracture occurred at either detail during this phase of testing. Testing was continued at the unwelded end with the large edge crack. The detail was slowly cooled to -96°F (-71°C) at which point fracture occurred.

Beam B5 (A588 Steel)

A series of small elliptical surface flaws existed at the end-welded detail while only a small 1.25 in. (31.8 mm) surface flaw existed at the unwelded detail (see Figs. 5.5 and 5.7) after application of 2,000,000 load cycles.

Only the end-welded detail was cooled to -40°F (-40°C). The beam was then cyclically loaded for 30 min. without any sign of distress. After loading was removed, the detail was then cooled further to -140°F (-96°C). Then the cyclic load was reapplied and in 20 minutes fracture occurred at approximately -150°F (-101°C).

Beam B5A (A588 Steel)

After 1.863 million cycles of fatigue loading there was a 2.5 in. (63.5 mm) elliptical surface crack at the unwelded end. At the end-welded detail there also existed a 2 in. (50.8 mm) long elliptical surface crack (see Figs. 5.6 and 5.7). Both details were cooled to -123°F (-86°C) and cyclic load was applied for 1 hour during which time the temperature was slowly lowered to -190°F (-123°C). No fracture occurred.

Additional cyclic loading 123,000 was applied at room temperature until the 2 million cycle fatigue design life was reached. Little fatigue crack growth was experienced (see Figs. 5.6 and 5.7). At this time both details were cooled to -40°F (-40°C) and cyclically loaded for 0.5 hour. Since no fracture occurred, the unwelded end was cooled further to -99°F (-73°C) while being cyclically loaded. Fracture occurred at -99°F (-73°C).

5.4 Stress Intensity Estimates for Cover Plate Details

5.4.1 Introduction

All the cover-plated beam specimens, except Beam B3A, fractured from an elliptical surface crack or an elliptical corner crack. The method of superposition was used to estimate the effects of applied load and residual stresses. This method was presented in section 4.5 for the lateral attachment detail edge cracks. Beam B3A and the elliptical cracks in Beams B1 and B1A were also analyzed using

the edge crack relationships presented in Section 4.5. This section summarizes the relationships used to evaluate the elliptical cracks encountered at the cover plate details.

Several contributions to the stress intensity were estimated separately as presented in Eq. 9. The contribution from the applied stress, K_{AS} , was estimated from known solutions under uniform applied stress (see Fig. 5.12). Both the nominal section residual stress contribution, K_{RS} , and the local weld residual stress contribution, K_{LW} , had nonuniform stresses over an elliptical crack surface. To estimate these effects a stress-free state was created on the crack surface as was done with the flange attachments. A numerical integration method was used which is presented in Section 5.4.4.

The variation of stress intensity with crack size was not obtained since many of the elliptical cracks had different crack geometry relationships. Therefore, the semimajor axis, C , and the semiminor axis, a , values were used as shown in the fatigue and fracture surface sketches (Figs. 5.1 to 5.6) for the crack size at fracture. C was held constant while the semiminor axis, a , was varied ± 0.3 in. (± 7.6 mm) to calculate several values of K to incorporate the plastic zone correction.

The plastic zone correction, r_y , (see Eq. 10) was used when possible when evaluating the stress intensity, K . Several stress intensity estimates for the critical crack sizes would not converge when this correction was used (see Tables 5.2 a,b).

5.4.2 Contribution from the Applied Stress

The stress intensity for elliptical crack shapes is defined by Eq. 11 (see Section 4.5.2). The factor,

$$F(a) = F_E F_G F_S F_W \quad (11)$$

can be determined for the elliptical cracks encountered at the cover plate details as:

F_E = crack shape correction

$$F_E = \frac{1}{E_k} [1 - k^2 \cos^2 \Phi]^{\frac{1}{4}}$$

E_k , k , and Φ are defined in Fig. 5.12

F_G = Stress concentration correction

F_S = Free surface correction

F_W = Finite width or thickness correction

For this study F_E varied between 1.0 and $\frac{2}{\pi}$ for an elliptical crack growing from a shallow semi-elliptical crack to a semi-circular crack. F_G varied with crack size as shown in Fig. 5.13. For crack sizes greater than 0.9 in. (22.9 mm), $F_G \approx 1.0$. F_S was taken as 1.0 because of the lateral restraint offered by the cover plate in the through thickness direction of the flange. For the details without an end weld F_W was defined as a function of plate thickness, T_f , and crack sizes as equal to:

$$F_W = \sqrt{\frac{2T_f}{\pi a} \tan \frac{\pi a}{2T_f}} \quad (17)$$

where $a = a_p + r_y$

F_w approaches infinity when a approaches T_f . For the end-welded details the finite width correction was modified to account for the fixity provided to one side of the crack by the cover plate end weld. In this case, F_w was defined by Eq. 18.

$$F_w = \sqrt{\frac{2T_f}{\pi a} \tan \frac{\pi a}{2T_f}} \left(1 - \left(1 - \sqrt{0.5} \right) \left(1 - \frac{a}{T_f} \right) \right) \quad (18)$$

5.4.3 Contribution from the Stress Concentration

In a recent study Zettlemoyer¹⁴ developed a relationship for stress concentration factors, K_T at uncracked cover plate details. Values equal to about 6.5 were determined from Eq. 19 for the various cover-plated beam specimens discussed herein.

$$K_T = \log_e \left[\left(\frac{Z}{T_f} \right)^{-1.54} \left(\frac{T_{cp}}{T_f} \right)^{0.86} \right] + 5.80 \quad (19)$$

T_f = thickness of flange

T_{cp} = thickness of cover plate

Z = fillet weld leg size

The stress concentration effect decays rapidly as the crack size increases. This is discussed in more detail in Section 4.5.2. A plot of the decay with crack size, a , is shown in Fig. 5.13 for a typical end-welded cover-plated beam specimen (W36X260). The decay is quite rapid. For points below the plate surface at the weld toe of 0.01 in. (0.3 mm) and 0.10 in. (2.5 mm), the stress concentration is 4.56 and 1.73 respectively.

The effect of stress concentration on stress intensity is shown in Fig. 5.14 for an elliptical crack growing at the toe of an end-welded cover plate. Because of the rapid decay of the stress concentration, K_T , crack instability did not develop at small elliptical cracks. However, the stress concentration significantly affected initiation of fatigue cracking and crack growth and reduced the fatigue strength of the beams.

5.4.4 Contribution from the Nominal Residual Stresses

The nominal beam cross-section residual stresses were obtained from measurements on a beam section cut from a length of a typical beam. The results shown in Figs. B.5 to B.7 (Appendix B) were determined by using the sectioning method¹⁸. The stresses were adjusted for equilibrium and variation through the flange thickness was assumed to be linear.

The contribution to stress intensity from the cross-section residual stresses, K_{RS} , will be positive or negative depending on the orientation of the crack and the residual stress distribution. An edge crack growing through the residual stress field can be analyzed in the same manner presented in Section 4.5.6. However, the estimate of K_{RS} , becomes more involved when an elliptical crack grows in the non-uniform residual stress field.

To estimate K_{RS} for an elliptical crack, a numerical integration procedure was developed. An approximate solution for the stress intensity, at a point on the crack front from applied splitting forces at a point on the crack surface was presented in Ref. 4 and is

shown in Fig. 5.15. A computer program was developed using this point by point approximation of K , to numerically integrate over the area of an elliptical crack. The crack surface was approximated by a 0.03 in. (0.8 mm) mesh. The stress at each mesh point was estimated by assuming a linear variation between the flange surfaces. This permitted the average force acting on each mesh point to be determined.

5.4.5 Contribution from the Local Weld Residual Stresses

The local stresses at the ends of the cover plate were obtained by using the hole drilling method¹⁹. By drilling several holes near each detail a good estimate of the local residual stresses at the crack plane could be made. Results of these studies are presented in Figs. B.23 to B.25 for cover-plated beams with and without end welds.

Using the same numerical integration procedure as presented in Section 5.4, the local weld contribution, K_{LW} , to stress intensity was estimated.

5.4.6 Summary and Discussion of the Various Contributions

The values of K , K_{AS} , K_{RS} , and K_{LW} are summarized in Tables 5.2a,b for each cover-plated beam specimen. The stress intensity values listed for Beams B1, B1A, B3 and B5A are for the actual crack size at fracture. The plastic zone correction to the semiminor crack size, a , would not converge for these beams.

Each estimate of K_{RS} and K_{LW} was checked by numerically integrating a uniform stress over the same crack size mesh. The

stress intensity values obtained were compared with the stress intensity results for uniform stress from the known solutions presented in Section 5.4. Table 5.1 shows the sensitivity of this numerical integration technique to the a/c ratio and Φ . Generally, the errors encountered were less than 10%. However, when a/c was less than 0.25 and Φ other than 90° , large errors were encountered. When comparing the solutions of the stress intensity estimated by numerical integration and a direct solution for Beam B1A, there was an 80.3% overestimate in the numerical integration solutions. To account for this gross overestimate the values obtained for K_{RS} and K_{LW} were scaled by a factor of 1.0/1.803.

Because of this overestimate and the small a/c ratio, the large elliptical cracks in Beams B1 and B1A were also analyzed as edge cracks for the center third of the flange width (see Figs. 5.1 and 5.2). The nominal section and local weld residual stresses were averaged over the central third width and assumed to vary linearly through the flange thickness. An analysis similar to that presented in Section 4.5 was used. The results shown in Table 5.2 are very similar to the results obtained by the elliptical crack numerical integration method presented in Section 5.4.4.

A major contribution was from the applied stress, K_{AS} . Values of K_{AS} were at least 50% of the total stress intensity values obtained for each beam fracture analysis, except for Beam B3 where K_{AS} was 37% of K .

The contribution from the nominal residual stress, K_{RS} , was much less than K_{AS} . Values of K_{RS} were less than 26% of the total stress intensity estimate, K . The elliptical cracks present in these welded cover plate details grew in both positive and negative nominal residual stress areas which tended to compensate and minimize their effect.

The contribution from the local weld residual stress, K_{LW} , ranged from 6% to 44% of the total stress intensity estimate, K . The local weld residual stress contribution to stress intensity for Beams B1, B1A, and B3 were approximately 40% of the total stress intensity. In the remaining beams, the local residual stresses had little effect (10% or less).

There are two areas of uncertainty related to the local weld residual stress estimates. First, the stress measurements made by the hole drilling method were made 0.25 in. (6.4 mm) away from the weld toe. Hence, the actual stresses at the crack growth planes were not known. Second, the stresses measured were only surface residual stresses. Therefore, the distribution through the thickness was unknown and had to be approximated.

The stress concentration effects had a negligible effect on the stress intensity factor. The stress concentration was predicted to decay rapidly with crack growth. At the fracture point the stress concentration correction, F_G , was approximately 1.0 for each cover plate fracture.

All of the analyses in this study utilized linear elastic fracture mechanics. Whenever the net ligament at an elliptical crack, or flange thickness at an edge crack, becomes less than the plastic zone size using one-half the value of Eq. 10, the validity of this method is diminished. Beam B1A had obvious plasticity on the fracture surfaces at the 0.25 in. (6.4 mm) net ligament (see Fig. 5.2). An elastic plastic method might have been more applicable for this case even though the estimated fracture resistance was in agreement with the material resistance. Table 5.3 shows the net ligament sizes for all the cover-plated beam specimens.

TABLE 5.1 NUMERICAL INTEGRATION ERRORS, COVER PLATE DETAILS

Beam No.	Crack Size $a_p + r_y$ (in/mm)	Semi-Major Axis C (in/mm)	$(a_p + r_y)/C$	ϕ Degree	Percent Error in K_{LW}, K_{RS}
B1	1.05/27	2.95/75	.36	90°	+5.8
B1A	1.25/52	5.9/150	.21	120°	+80.3*
B3	2.1/53	7.15/182	.29	90°	+9.6
B3A	N.A.	N.A.	N.A.	N.A.	N.A.†
B5	0.60/15	1.175/30	.51	90°	-1.3
B5A	1/13/29	1.95/50	.58	46.2°	-7.9

* K_{RS} and K_{LW} were scaled down in proportion to this overestimate

† Flange Edge Crack Analysis

TABLE 5.2a STRESS INTENSITY ESTIMATES, COVER PLATE DETAILS

Beam No.	Steel Type	Crack Size, a_p in.	Plastic zone size r_y in.	Applied Stress (ksi)	σ_{yd}^{**} (ksi)	Fracture Temp. °F	(1) K_{AS} (ksi√in)	(2) K_{RS} (ksi√in)	(3) K_{LW} (ksi√in)	(1)+(2) +(3) K (ksi√in)
⁺ B1	A514	1.00	----*	52.71	159	-200	102	5	84	190
B1	A514	1.05	----*	52.71	159	-200	108	25	86	218
⁺ B1A	A514	1.10	----*	52.71	133	-48	115	12	90	218
B1A	A514	1.25	----*	52.71	133	-48	152	40	110	302
B3	A36 Rolled	2.10	----*	17.20	71	-45	70	49	70	189
B3A	A36 Rolled	.63	0.470	19.80	78	-96	80	21	7	109
B5	A588 Rolled	0.56	0.004	26.54	96	-150	30	10	6	47
B5A	A588 Rolled	1.13	----*	26.54	87	-99	82	29	13	124

* No convergence was obtained when the plastic zone correction was used. Results are shown for the actual crack size at fracture.

** From Eq. 4 with $t = .12$ sec. $\sigma_{ys} = 95\%$ of mill report yield stress

+ Edge crack analysis on center third of flange width

TABLE 5.2b STRESS INTENSITY ESTIMATES, COVER PLATE DETAILS

Beam No.	Steel Type	Crack Size, a_p (mm)	Plastic zone size r_y (mm)	Applied Stress (MPa)	σ_{yd}^{**} (MPa)	Fracture Temp. ($^{\circ}\text{C}$)	(1) K_{AS} (MPa $\sqrt{\text{m}}$)	(2) K_{RS} (MPa $\sqrt{\text{m}}$)	(3) K_{LW} (MPa $\sqrt{\text{m}}$)	(1)+(2)+(3) K (MPa $\sqrt{\text{m}}$)
⁺ B1	A514	25.4	----*	363	1096	-129	112	6	92	209
B1	A514	26.7	----*	363	1096	-129	119	28	95	240
⁺ B1A	A514	27.9	----*	363	917	-44	127	13	99	240
B1A	A514	31.8	----*	363	917	-44	167	44	121	332
B3	A36 Rolled	53.0	----*	119	490	-43	77	54	77	208
B3A	A36 Rolled	143.0	11.9	137	538	-71	88	23	8	120
B5	A588 Rolled	14.2	1.0	183	662	-101	33	11	7	52
B5A	A588 Rolled	28.7	----*	183	600	-73	90	32	14	136

* No convergence was obtained when the plastic zone correction was used.

Results are shown for the actual crack size at fracture.

** From Eq. 4 with $t = 0.12$ sec. $\sigma_{ys} = 95\%$ of mill report yield stress

+ Edge crack analysis on center third of flange width

TABLE 5.3 NET LIGAMENT SIZES

Beam No.	Steel Type	$\frac{1}{4\pi} \left(\frac{K}{\sigma_y} \right)^2$ (in.) / (mm)	Net Ligament B-a (in.) / (mm)
B1	A514	.15/4	.45/11
B1A	A514	.41/10	.25/6
B3	A36 (W36X260)	.56/14	.84/21**
B3A	A36 (W36X260)	.16/4	1.44/37*
B5	A588 (W36X230)	.02/.5	.69/18
B5A	A588 (W36X230)	.16/4	.12/3

* Flange Thickness - Edge Crack (see Fig. 5.4)

** Web Thickness - (see Fig. 5.3)

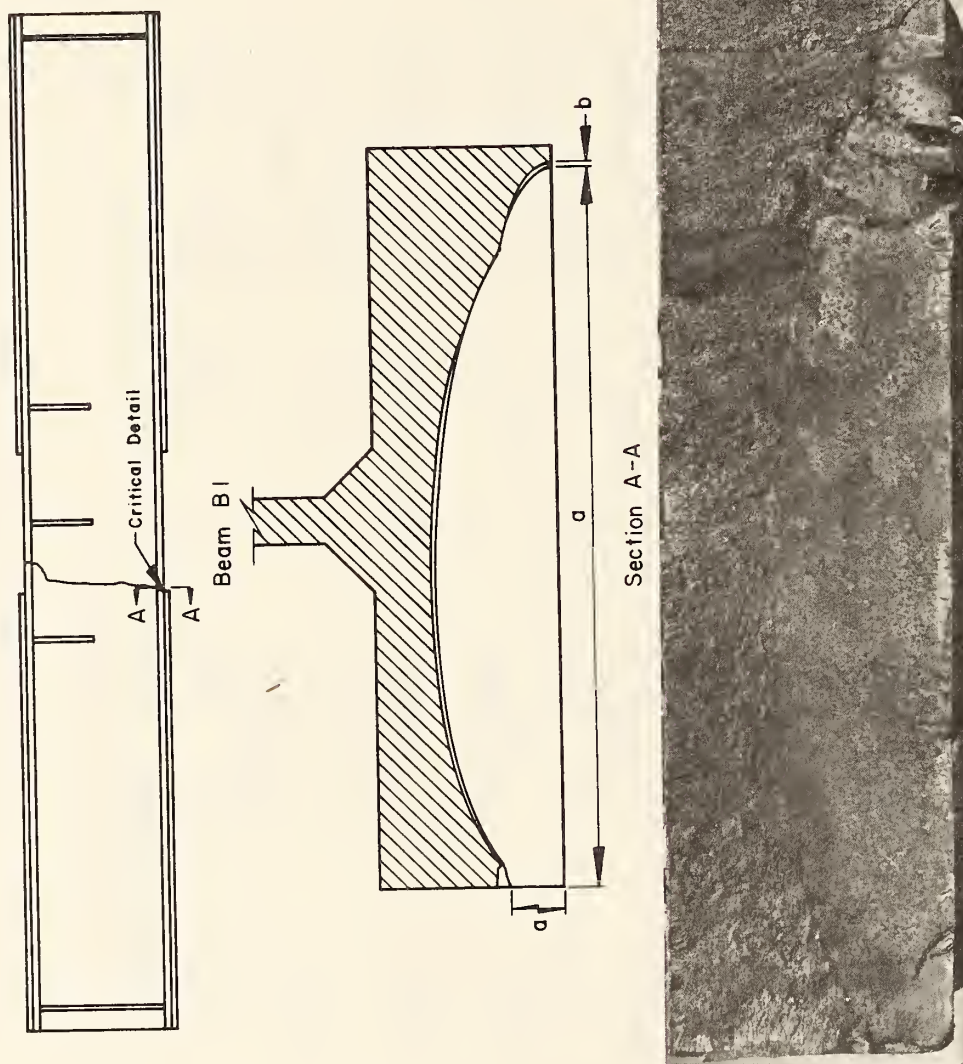


Fig. 5.1 Fatigue and Fracture Surface, B1 (A514)

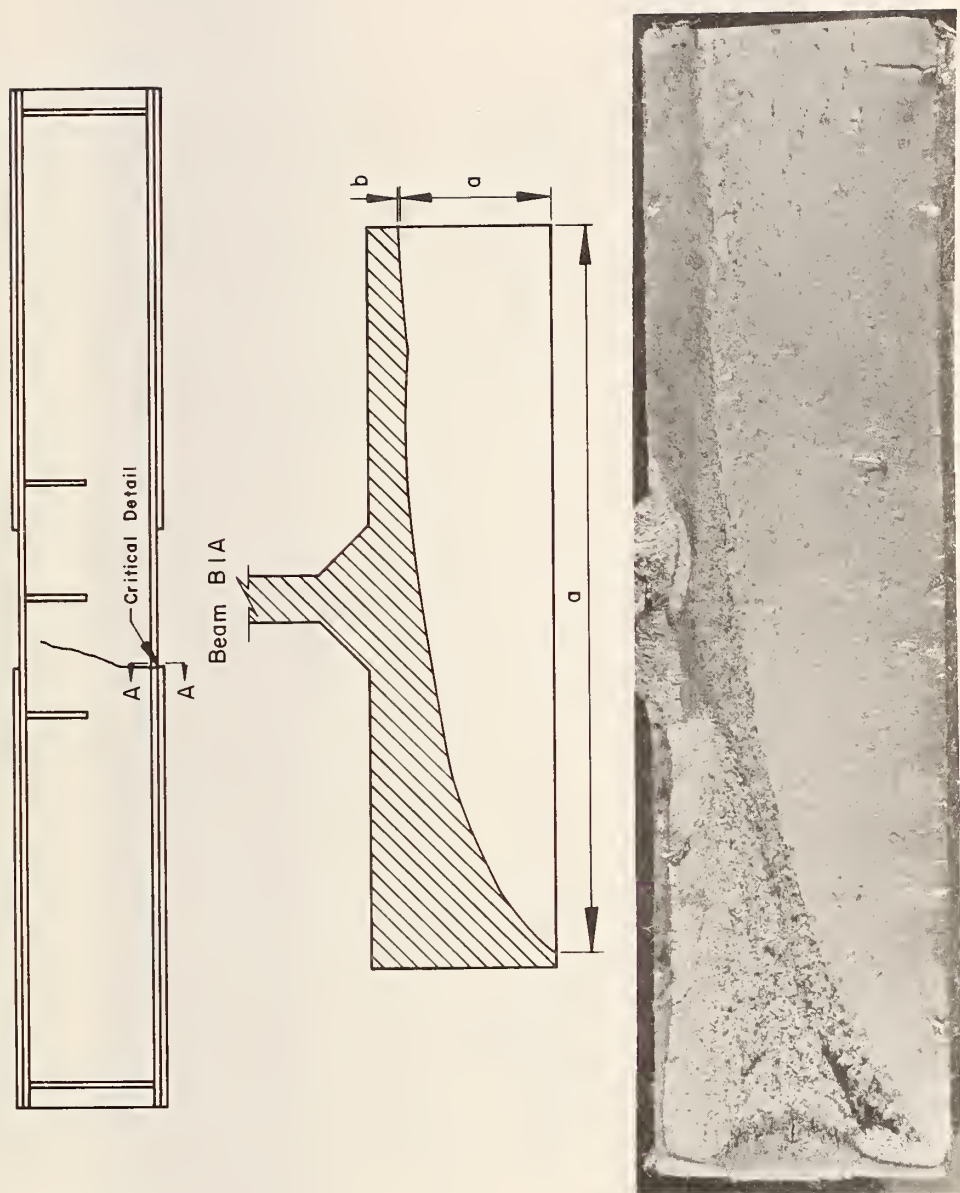


Fig. 5.2 Fatigue and Fracture Surface, B1A (A514)

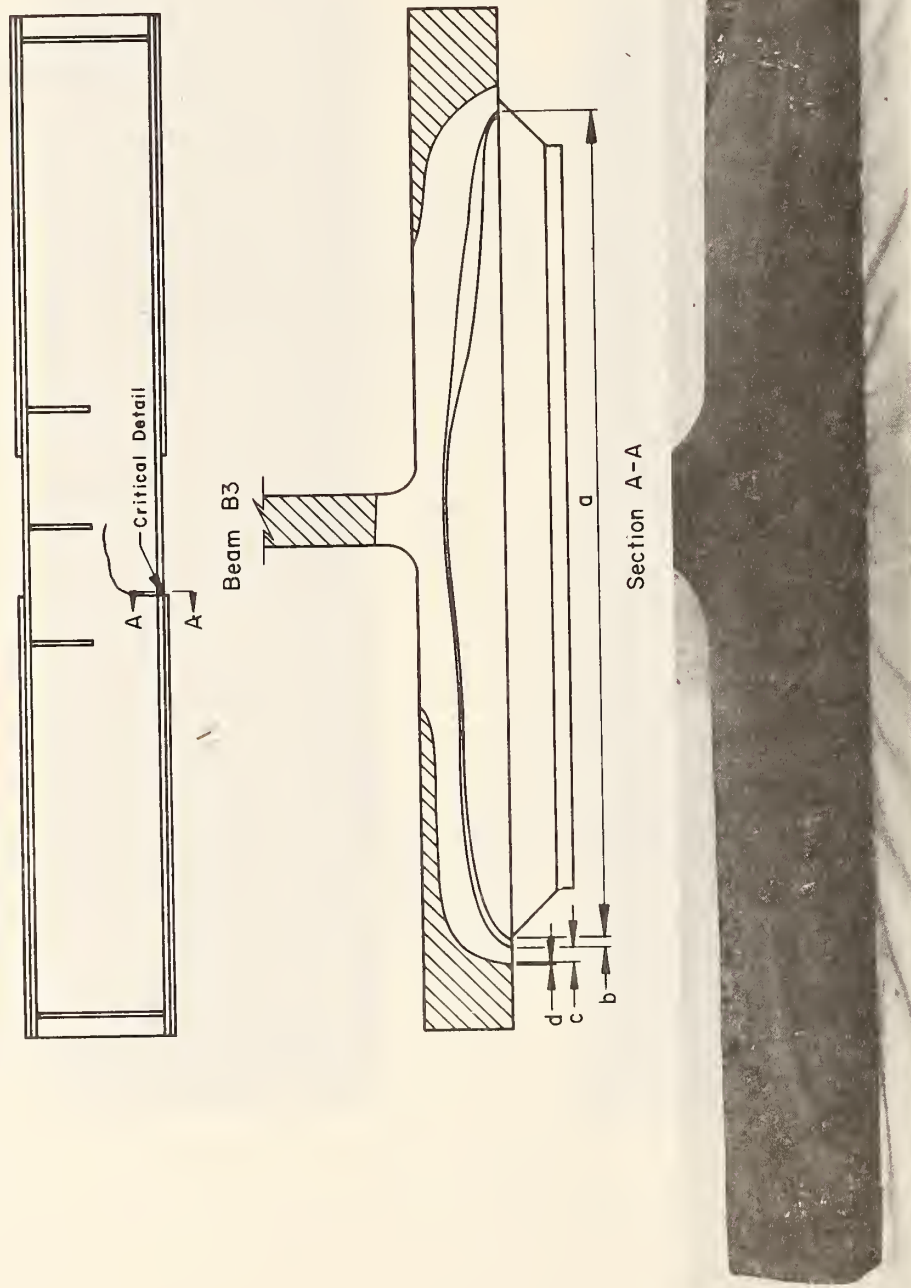


Fig. 5.3 Fatigue and Fracture Surface, B3 (A36, W36X260)

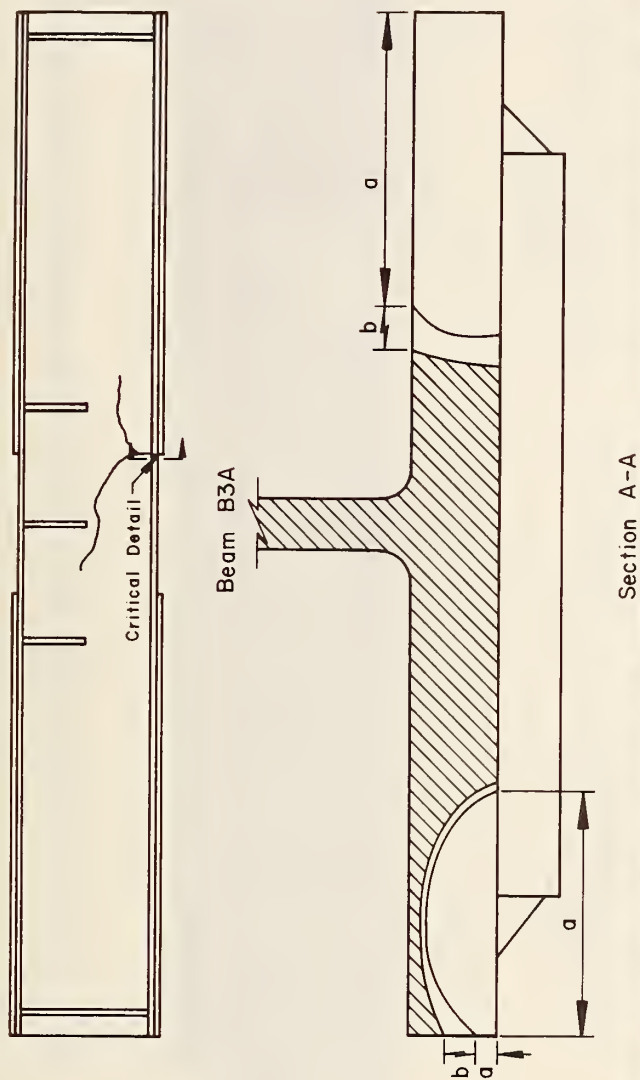


Fig. 5.4 Fatigue and Fracture Surface, B3A (A36, W36X260)

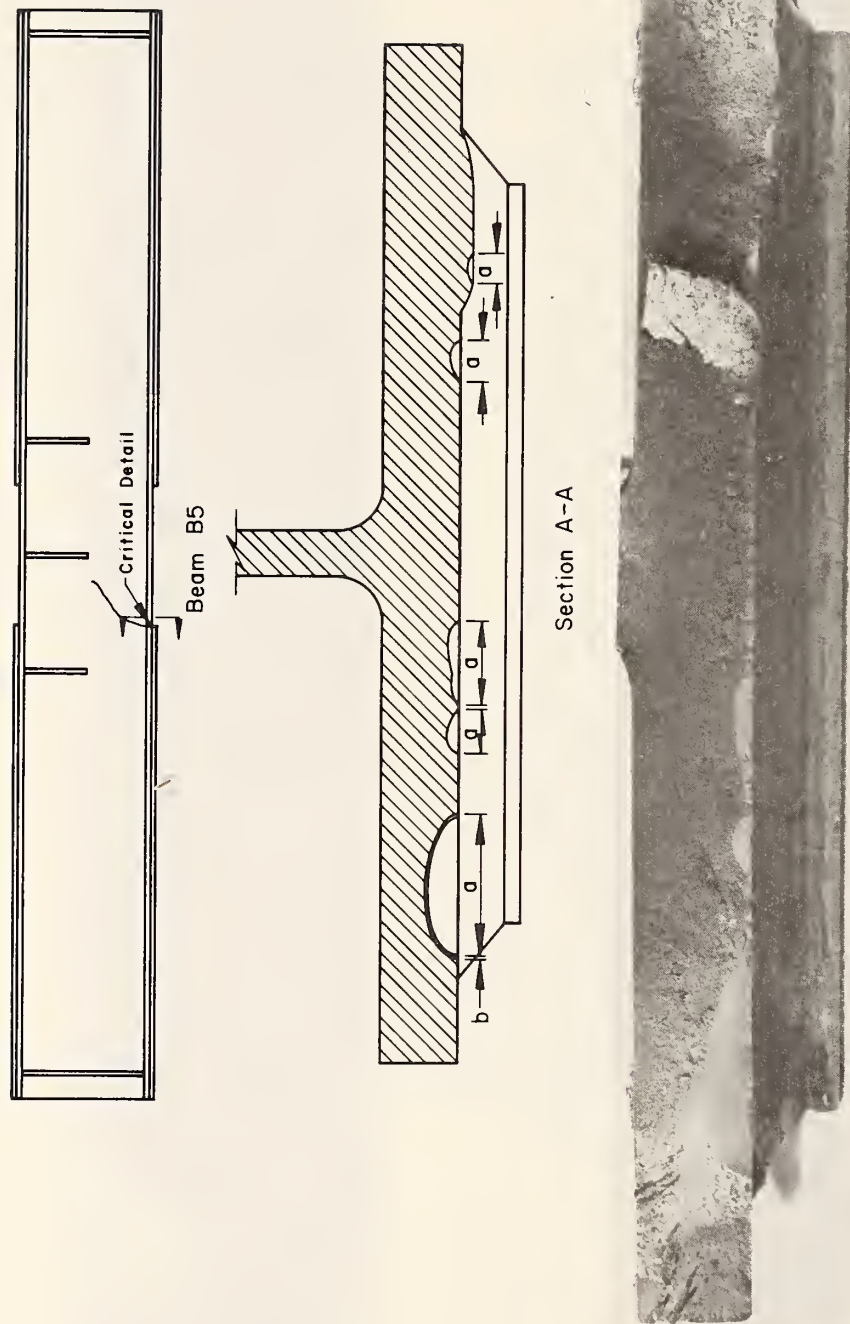


Fig. 5.5 Fatigue and Fracture Surface, B5 (A588, W36X230)

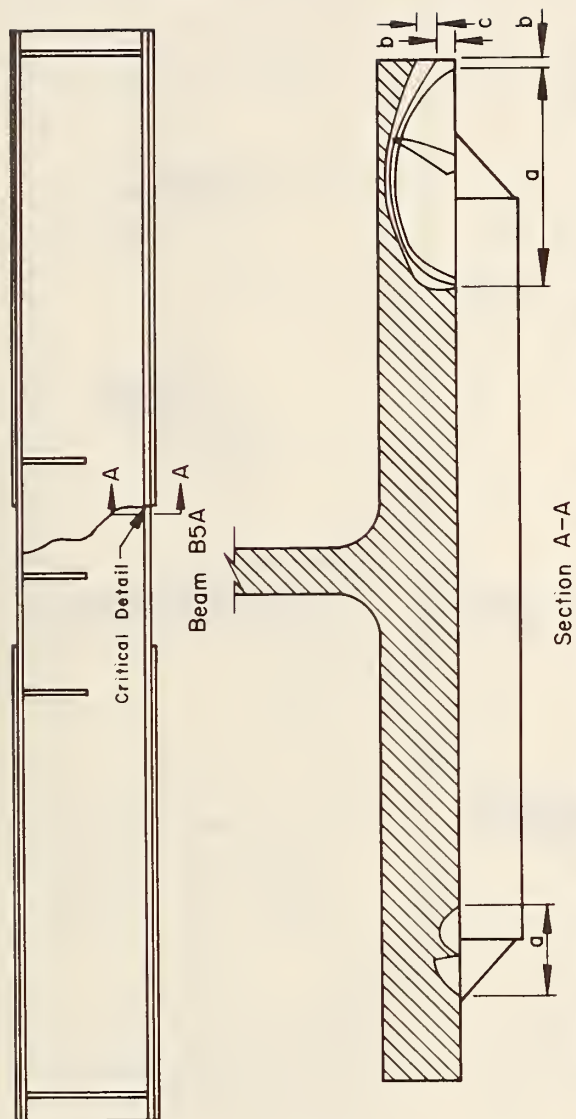
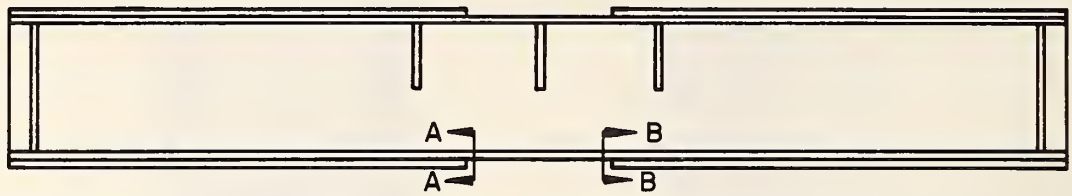


Fig. 5.6 Fatigue and Fracture Surface, B5A (A588, W36X230)



BEAM	SECTION A-A	SECTION B-B
B1	 5/8" (16)	* (11) 7/16" 3/16" (5)
B1A	 	* (3) 1/8" 1 1/4" (32)
B3	 2 1/4" (57) 1" (25) 2 3/4" (70)	* 5 1/4" (133) 3 3/4" (95) 1" (25) 1 1/4" (32)
B3A	* 3/8" (10) 4" (102) 4 3/4" (121) 5 1/4" (133)	 1 3/8" (35) 4" (102) 5" (127)
B5	 1 1/4" (32)	* 2 5/8" (67) 2 5/8" (67) 1/2" (13)
B5A	* 1 1/4" (32) 3 1/2" (89) 1/4" (6)	 2 3/8" (60)

X Denotes Critical Detail
Measurements In Brackets, In mm

Fig. 5.7 Fatigue Crack Prior to Last Fracture Test

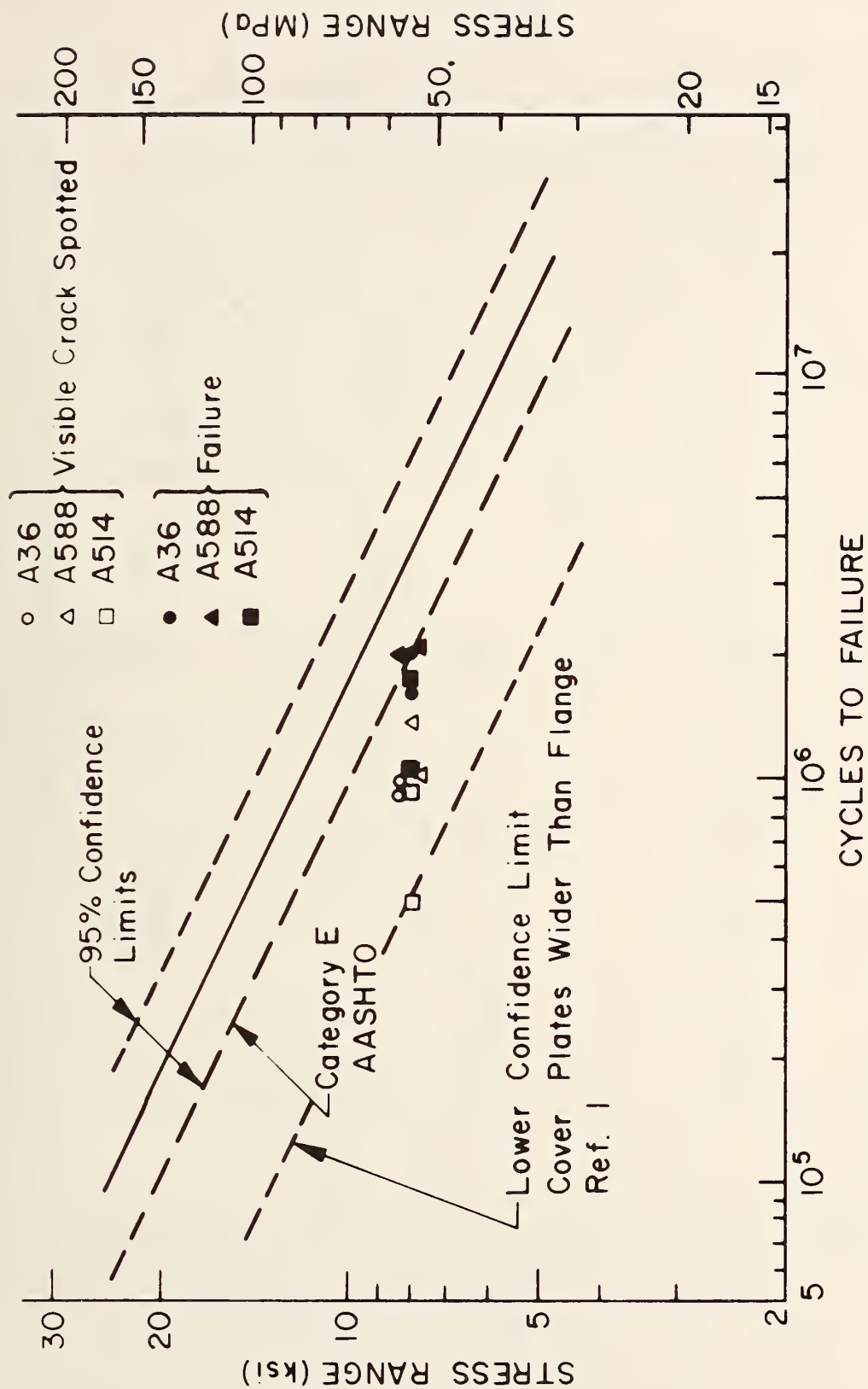


Fig. 5.8 Category E S-N Plot, Cover Plate Beams

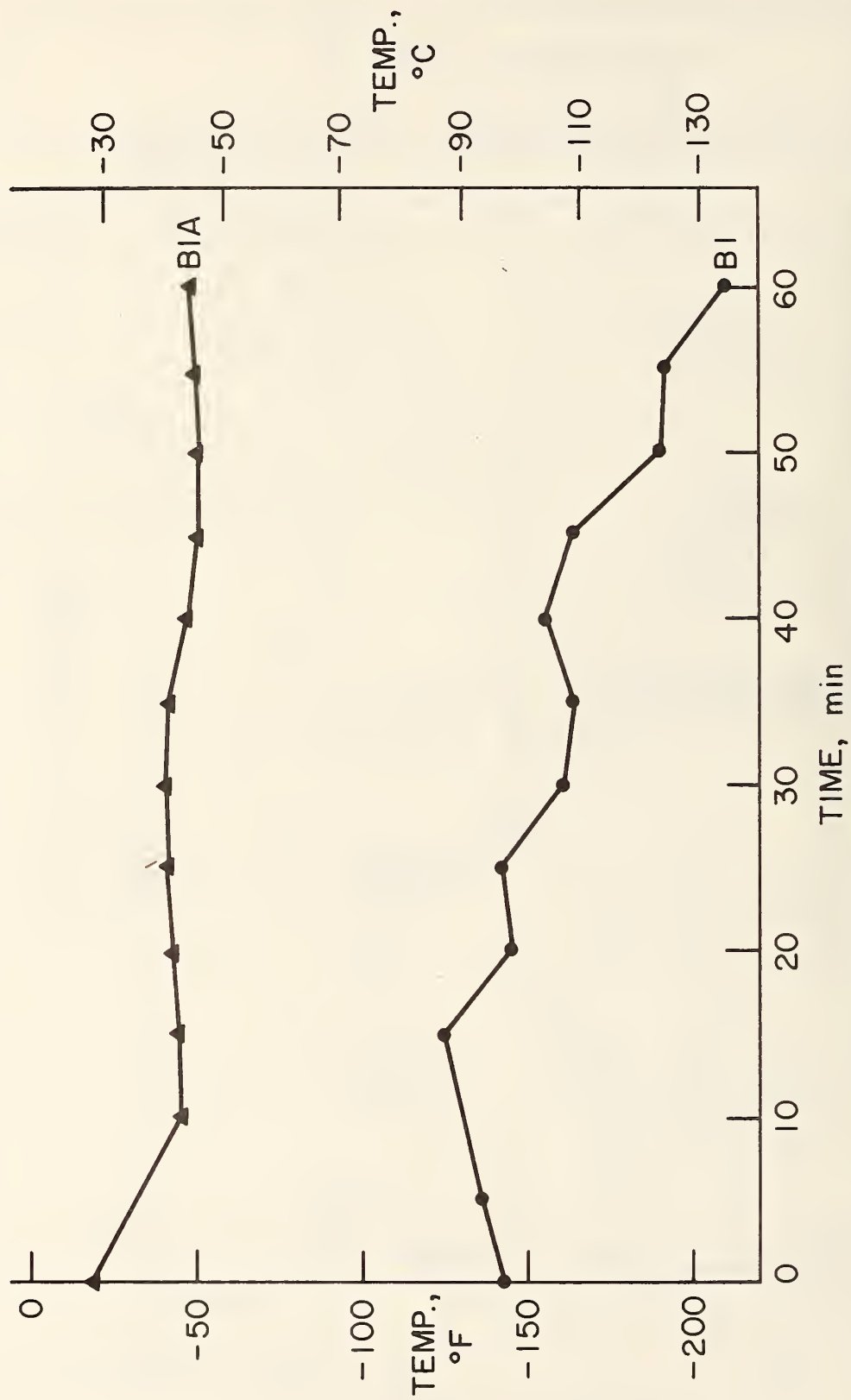


Fig. 5.9 Critical Detail Temperature/Sixty Minutes Prior to Fracture (A514)

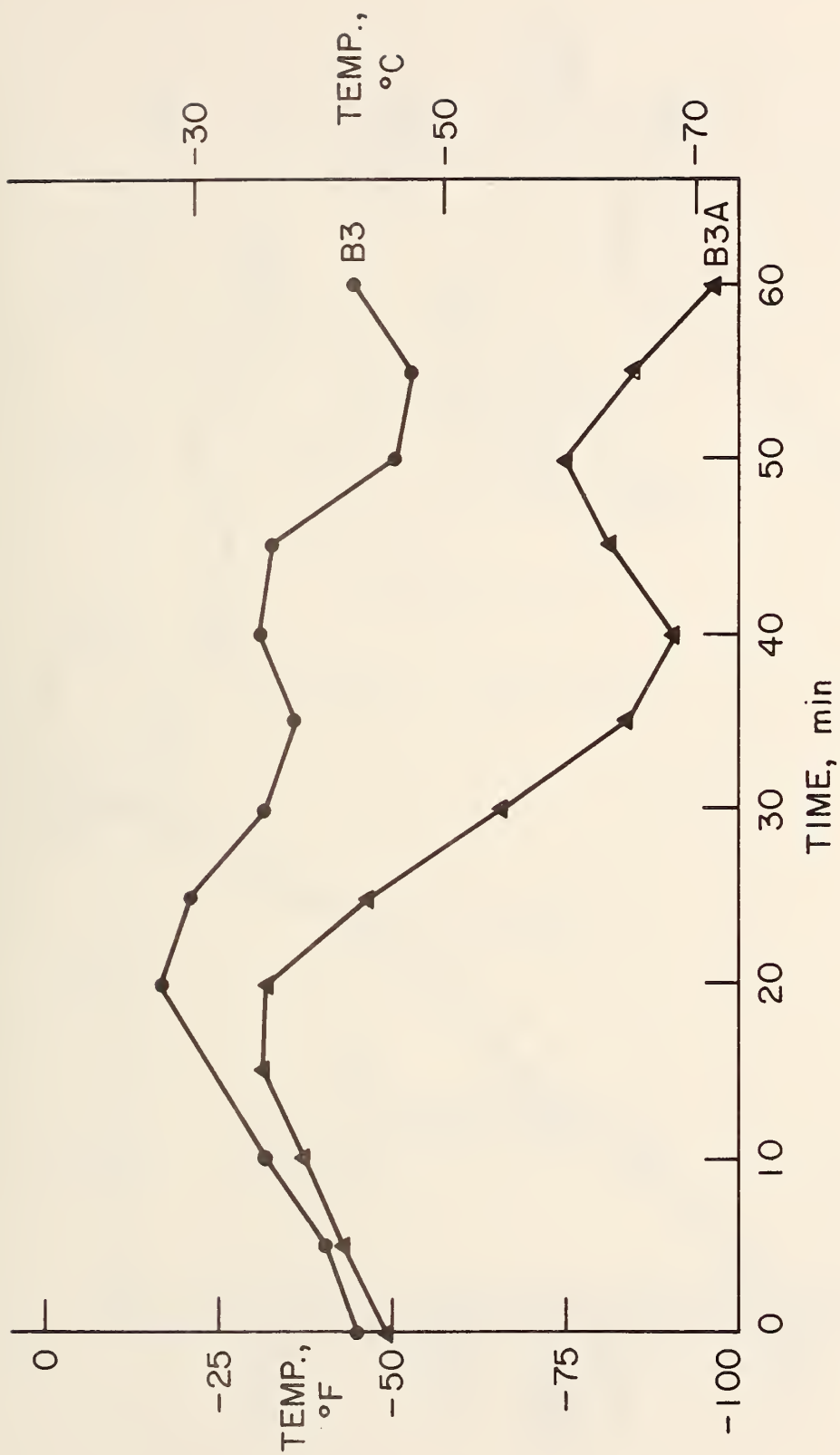


Fig. 5.10 Critical Detail Temperature/Sixty Minutes Prior to Fracture (A36, W36X260)

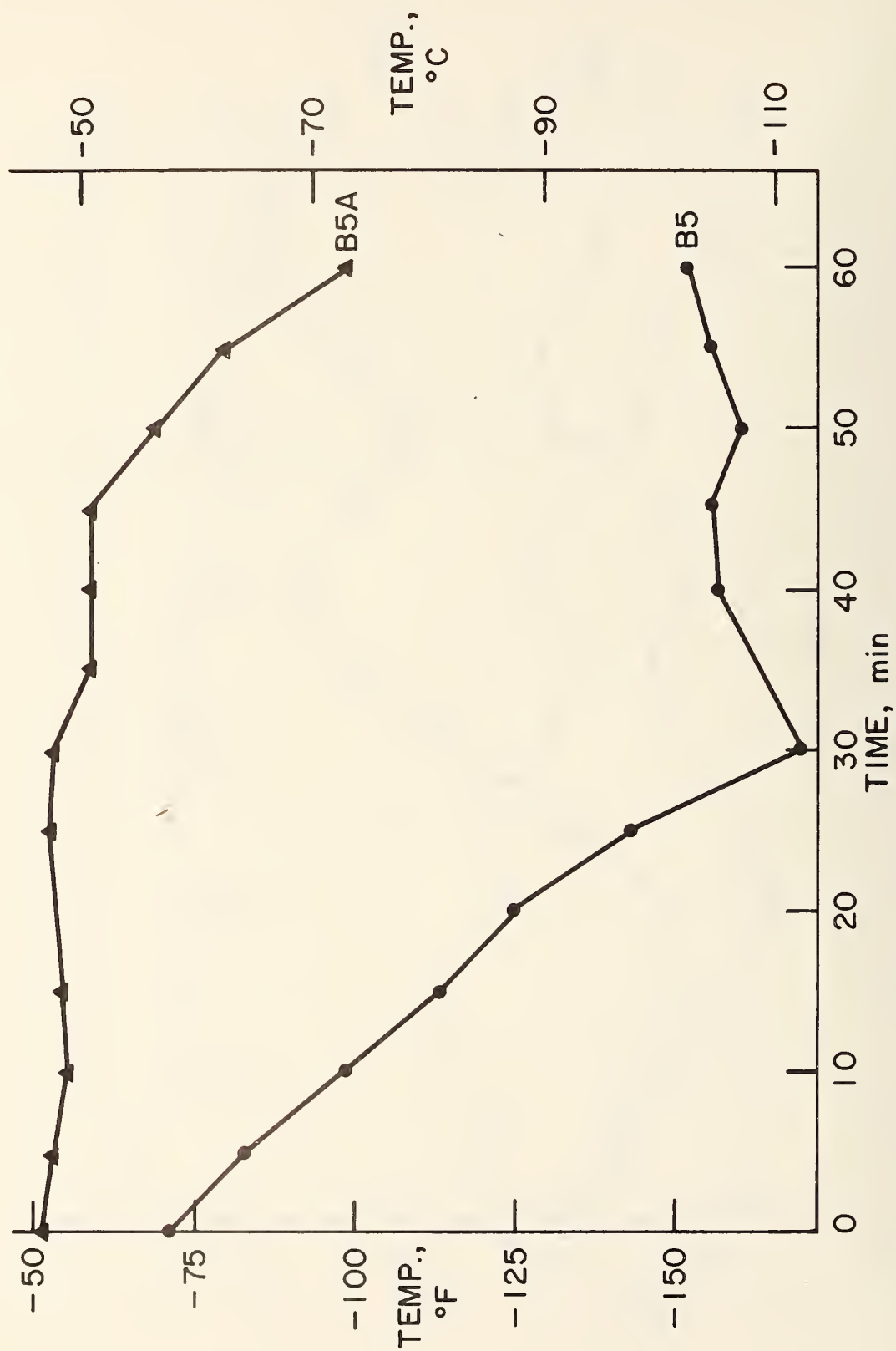
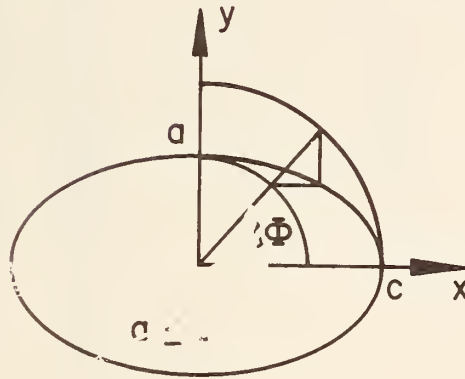


Fig. 5.11 Critical Detail Temperature/Sixty Minutes Prior to Fracture (A588, W36X230)

$$K^2 = \frac{\sigma^2 \pi a}{E_k^2} \sqrt{1 - k^2 \cos^2 \Phi}$$



$$x = c \cos \Phi \quad y = a \sin \Phi$$

$$k^2 = 1 - (a/c)^2$$

$$E_k = \int_0^{\pi/2} \sqrt{1 - k^2 \sin^2 u} \, du$$

Fig. 5.12 Stress Intensity Model for Elliptical Crack Under Uniform Applied Stress

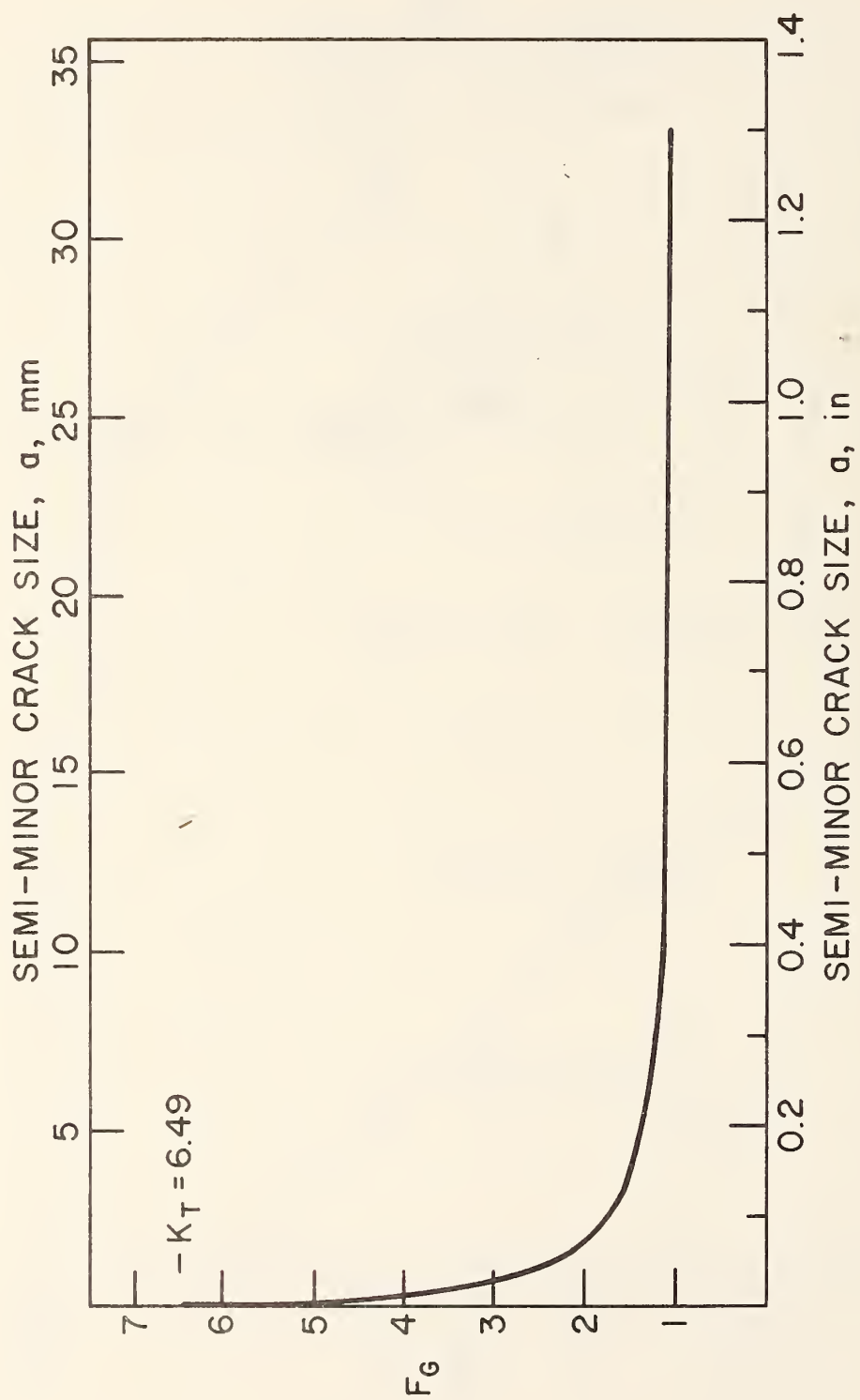


Fig. 5.13 Stress Concentration Decay with Crack Size (B3)

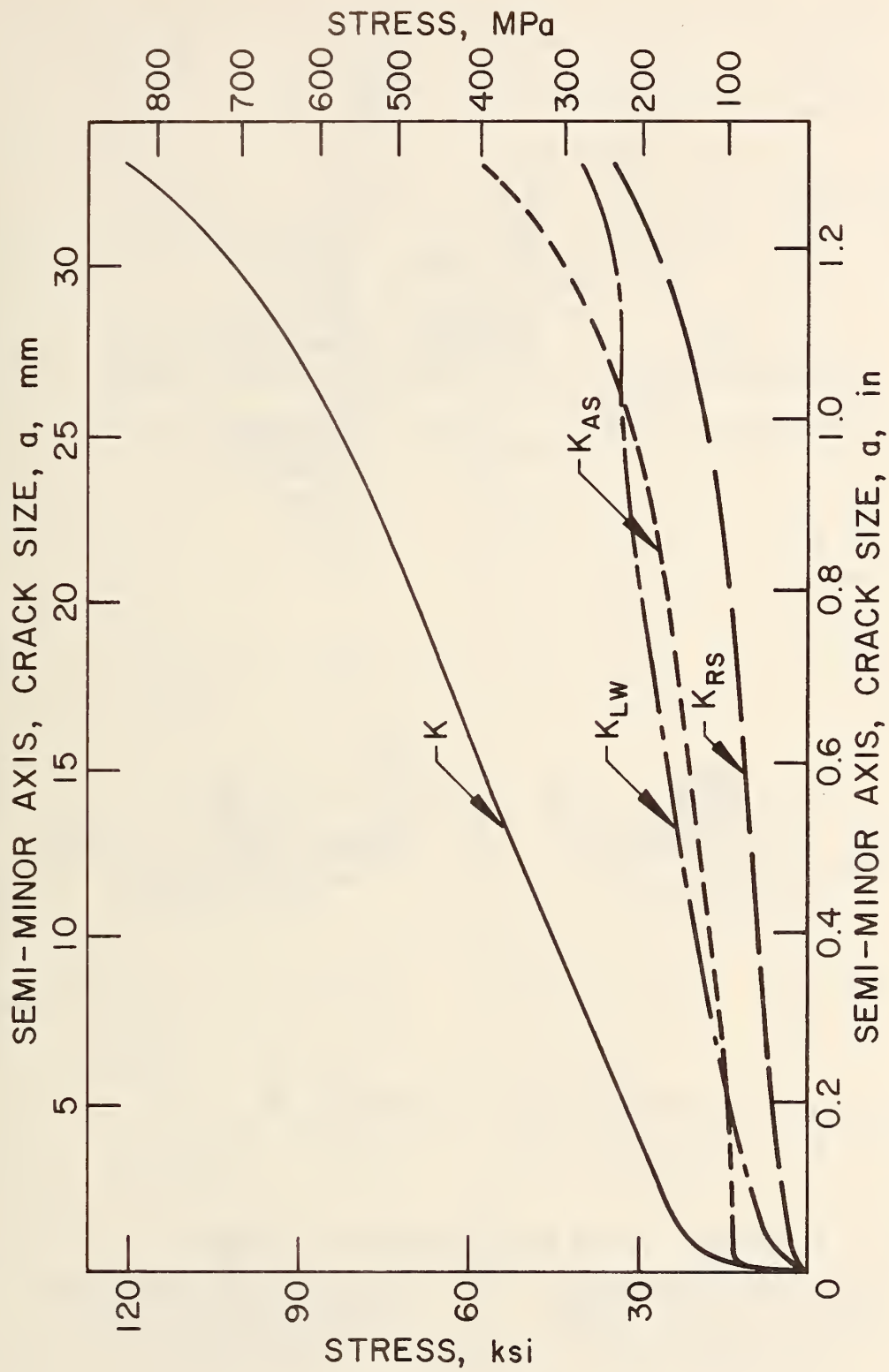
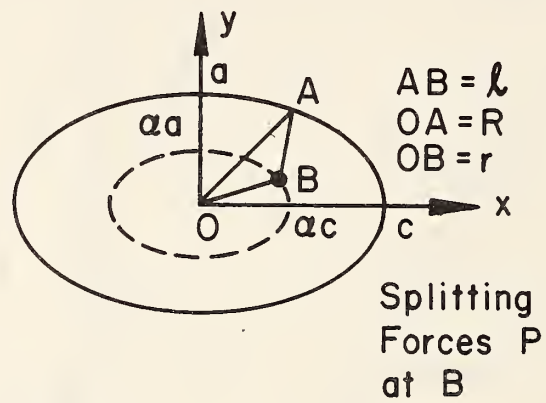


Fig. 5.14 Stress Intensity vs. Crack Size for Elliptical Surface Cracks (B3)



$$K = \frac{P\sqrt{a}}{\pi^{3/2}\ell^2} \sqrt{\frac{r}{R}} \frac{\sqrt{\frac{1}{\alpha^2} - 1}}{\{1 - k^2 \cos^2 \Phi\}^{1/4}}$$

$$x = \alpha c \cos \Phi, \quad y = \alpha a \sin \Phi$$

Fig. 5.15 Residual Stress Point Load Model for Elliptical Cracks




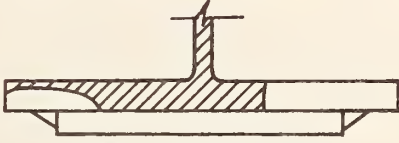


$\sigma_{\max} = 55.0 \text{ ksi} = 379 \text{ MPa}$ $\sigma_{YD} = 159 \text{ ksi} = 1096 \text{ MPa}$ $a = 1.05 \text{ in} = 27 \text{ mm}$ $r_y = \text{N.A.}$ $T_c = -200^\circ\text{F} = -129^\circ\text{C}$ $K_c = 218 \text{ ksi} \sqrt{\text{in}} = 240 \text{ MPa} \sqrt{\text{m}}$ $N = 1,806,300$	$\sigma_{\max} = \sim 55 \text{ ksi} = 379 \text{ MPa}$ $\sigma_{YD} = 133 \text{ ksi} = 917 \text{ MPa}$ $a = 1.25 \text{ in} = 32 \text{ mm}$ $r_y = \text{N.A.}$ $T_c = -48^\circ\text{F} = -44^\circ\text{C}$ $K_c = 302 \text{ ksi} \sqrt{\text{in}} = 332 \text{ MPa} \sqrt{\text{m}}$ $N = 1,134,200$
 <p>B1 (A514)</p>	 <p>B1A (A514)</p>
$\sigma_{\max} = 17.2 \text{ ksi} = 119 \text{ MPa}$ $\sigma_{YD} = 71 \text{ ksi} = 490 \text{ MPa}$ $a = 2.1 \text{ in} = 53 \text{ mm}$ $r_y = \text{N.A.}$ $T_c = -45^\circ\text{F} = -43^\circ\text{C}$ $K_c = 189 \text{ ksi} \sqrt{\text{in}} = 208 \text{ MPa} \sqrt{\text{m}}$ $N = 2,170,700$	$\sigma_{\max} = 19.8 \text{ ksi} = 136 \text{ MPa}$ $\sigma_{YD} = 78 \text{ ksi} = 538 \text{ MPa}$ $a = 5.63 \text{ in} = 143 \text{ mm}$ $r_y = 0.47 \text{ in} = 11.9 \text{ mm}$ $T_c = -96^\circ\text{F} = -71^\circ\text{C}$ $K_c = 109 \text{ ksi} \sqrt{\text{in}} = 120 \text{ MPa} \sqrt{\text{m}}$ $N = 1,817,200$
 <p>B3 (A36 Rolled)</p>	 <p>B3A (A36 Rolled)</p>
$\sigma_{\max} = 27.5 \text{ ksi} = 190 \text{ MPa}$ $\sigma_{YD} = 96 \text{ ksi} = 662 \text{ MPa}$ $a = 0.56 \text{ in} = 14 \text{ mm}$ $r_y = 0.04 \text{ in} = 1.0 \text{ mm}$ $T_c = -150^\circ\text{F} = -101^\circ\text{C}$ $K_c = 47 \text{ ksi} \sqrt{\text{in}} = 52 \text{ MPa} \sqrt{\text{m}}$ $N = 2,012,500$	$\sigma_{\max} = 27.5 \text{ ksi} = 190 \text{ MPa}$ $\sigma_{YD} = 87 \text{ ksi} = 600 \text{ MPa}$ $a = 1.13 \text{ in} = 29 \text{ mm}$ $r_y = \text{N.A.}$ $T_c = -99^\circ\text{F} = -73^\circ\text{C}$ $K_c = 124 \text{ ksi} \sqrt{\text{in}} = 136 \text{ MPa} \sqrt{\text{m}}$ $N = 2,017,500$
 <p>B5 (A588 Rolled)</p>	 <p>B5A (A588 Rolled)</p>

Fig. 5.16 Fracture Surface Sketches and Data Summary

6. FLANGE TRANSITION TEST RESULTS AND ANALYSIS

(Specimen No.	Material)
B10, B10A	A36
B12, B12A	A588
B8, B8A	A514

6.1 Fatigue Cracks

The fatigue cracks at the flange transition details were initially observed to grow as elliptical corner cracks. The smallest corner crack observed was approximately 0.5 in. (12.7 mm). The fracture surfaces of Beams B10 (Fig. 6.2) and B10A (Fig. 6.3) indicated that these corner cracks resulted from growth at the surface where a small stress concentration occurred. After additional crack growth the corner cracks became edge cracks.

The size of the fatigue cracks at each critical detail can be found by referencing the smaller letters on the crack surface drawings in Figs. 6.1 to 6.4 with the load history tables given in Tables 2.15 to 2.20.

Additional fatigue cracks existed at the other details on the beams. Figure 6.5 shows the fatigue cracks at all details prior to the last fracture test. The surface measurements of these cracks are shown adjacent to the crack. The crack shapes were estimated from these surface measurements.

6.2 Fatigue Life

Figure 6.6 shows the mean S-N curve and its confidence limits for the Category B details. The open figures represent the point at which the fatigue cracks were first observed and the closed figures represent the point of fracture. Beams B8A and B12 did not fracture due

to the proximity of the design stress range to the fatigue threshold. There is a good correlation between the fracture points and the Category B fatigue-life relationship.

The number of cycles needed to propagate an edge or corner crack from its final fracture test to an edge crack of 75% the flange width, b , was defined as the remaining useful fatigue life. The remaining fatigue life was estimated by a numerical integration routine using Eqs. 7 and 11 as presented in Section 4.2. Secondary stress intensity effects from the residual stresses were neglected.

Beams B10 and B10A were predicted to have no appreciable remaining fatigue life at the time of fracture. Beams B8, B8A, B12, and B12A were predicted to have 5000, 86,000, 106,000, and 47,000 cycles of remaining fatigue life, respectively. The estimated additional fatigue life was small and would not significantly alter the total life within the 95% confidence limits.

6.3 Beam Fracture Tests*

Beam B8 (A514 Steel)

No visible fatigue cracks were observed at 2 million cycles. The first low temperature test was conducted at 2 million cycles. Both details were cooled to -40° F (-40° C) and then cyclically loaded for 45 minutes. No fracture occurred.

* Temperature at the critical details are shown graphically in Figs. 6.7 and 6.8 for the final 60 minutes of the last fracture test.

The beam was then cycled at room temperature until visible fatigue cracks developed. There was generally 3/8 in. to 1/2 in. surface cracks detected with a 10X magnifier. When the crack at the critical detail was approximately a 3.25 in. (82.6 mm) edge crack (Fig. 6.1), a second fracture test was run. The critical detail was initially cooled to -40° F (-40° C) and then cyclically loaded. After cycling for 25 minutes the temperature at the critical detail was further cooled until fracture occurred at -69° F (-56° C). During the final fracture test the beam deflections increased causing the test to be stopped. When the beam was reloaded fracture occurred at 48.8 ksi (336.7 MPa), prior to reaching maximum load.

Beam B8A (A514 Steel)

No fatigue cracks were observed at 2 million cycles. The first low temperature test was conducted at 2 million cycles. Both details were cooled to -40° F (-40° C) and then cyclically loaded for 45 minutes without any evidence of cracking.

The beam was then further cycled at room temperature to develop visible fatigue cracks. At 4.17 million cycles there existed a corner crack in one detail (Fig. 6.5). This detail was cooled to -150° F (-101° C) and then cyclically loaded. While cycling for one hour the temperature at the critical detail was reduced to -250° (-157° C). No fracture occurred and the test was discontinued.

Beam B10 (A36 Steel)

No fatigue cracks were observed at 2 million cycles. The first low temperature test was conducted at 2.17 million cycles. The

test detail was cooled to -40° F (-40° C) and then cyclically loaded for 30 minutes. No fracture occurred.

The beam was then cycled at room temperature to develop visible fatigue cracks. After 3.20 million cycles a small corner crack existed in one detail (Fig. 6.2). The detail was cooled to -40° F (-40° C) and then cyclically loaded for one hour. The detail was then cooled from -40° F (-40° C) to -140° F (-96° C) while cycling for the next 4.5 hours. No fracture occurred.

The beam was then cycled at room temperature for an additional 26,300 cycles. By 3.31 million cycles the corner crack had grown to an edge crack (Fig. 6.2). The detail was cooled to -40° F (-40° C) and then cyclically loaded. Failure occurred after ten minutes of loading.

Beam B10A (A36 Steel)

No fatigue cracks were observed at 2 million cycles. The first low temperature test was conducted at 2 million cycles. Both details were cooled to -40° F (-40° C) and then cyclically loaded for one hour. No fracture occurred.

The beam was then cycled at room temperature to develop visible fatigue cracks. After 3.06 million cycles a large edge crack and a corner crack had developed in one detail (Fig. 6.3). The two cracks were offset by approximately 0.5 in. (12.7 mm). The detail was cooled to -40° F (-40° C) and then cyclically loaded for twenty minutes. Fracture occurred at -39° F (-39° C).

Beam B12 (A588 Steel)

No fatigue cracks were observed at 2 million cycles. The only low temperature test was conducted at 2 million cycles. Both details were cooled to -40° F (-40° C) and then cyclically loaded for 20 minutes. No fracture occurred.

The beam was then cycled at room temperature to develop visible fatigue cracks. After 4.17 million cycles a 0.88 in. (22.4 mm) elliptical corner crack was observed in one detail (Fig. 6.5). No further fracture tests were conducted and the test was discontinued.

Beam B12A (A588 Steel)

A corner crack (Fig. 6.4) existed in one detail at 2 million cycles. The first low temperature test was conducted at 2 million cycles. Both details were cooled to -40° F (-40° C) and then cyclically loaded for 80 minutes. No fracture occurred.

The beam was cycled at room temperature to grow the fatigue crack. At 2.68 million cycles, a 1 in. (25.4 mm) edge crack had developed in the east detail (Fig. 6.4). This detail was cooled to -40° (-40° C) and then cyclically loaded. While cycling for 100 minutes the temperature at the critical detail was reduced to -90° F (-68° C). No fracture occurred.

The beam was again cycled at room temperature to permit further growth of the fatigue crack. At 3.07 million cycles a 2 in. (50.8 mm) edge crack had developed in the east detail (Fig. 6.4). The

detail was cooled to -40° F (-40° C) and then cyclically loaded. While cycling for ten minutes the critical detail was cooled to -89° F (-67° C) where fracture occurred.

6.4 Stress Intensity Estimates for Flange Transition Details

6.4.1 Introduction

Fracture occurred for Beams B8, B10, B10A, and B12A. Beams B8 and B12A fractured from well defined edge cracks. Beams B8A and B12 had developed approximately 0.88 in. (22.4 mm) circular corner cracks at 4.2 million cycles, at which time the tests were stopped. Beams B10 and B10A fractured from large cracks that cannot be clearly defined as edge cracks. All of the flange transition beam fractures were analyzed using the edge crack relationships presented in Section 4.5 except for the free surface correction.

The method of superposition was used to estimate the effects of applied load and residual stress. This method was presented in Section 4.5 for the analysis of the lateral attachment details. A plastic zone correction, r_y , (Eq. 10) was used when evaluating the stress intensity, K . Several stress intensity estimates for the critical crack sizes would not converge when this correction was used (Tables 6.1a,b).

6.4.2 Contribution from the Applied Stress

Equation 11 was used to estimate the stress intensity due to applied stress for the flange transition edge cracks. F_E was taken

as 1.0 since the cracks were modeled as edge cracks. F_S was assumed to be equal to 1.122 for an edge crack with a uniform stress distribution⁴. F_G was taken as 1.0 for the large edge cracks present in these details. This correction only affects small corner and edge cracks that will be discussed in the next section. The finite width correction, F_W , was defined by Eq. 12.

When determining the residual fatigue life the secant finite width correction (Eq. 20) was used.

$$F_W = \sqrt{\sec \frac{\pi a}{2b}} \quad (20)$$

b = flange width or thickness

a_p = physical crack size

$a = a_p + r_y$

The difference between the tangent and secant corrections varied from 3% to 12% for $(a_p + r_y)/b$ ratios of 0.377 and 0.720.

6.4.3 Contribution from Stress Concentration

The stress concentrations for the flange transition details were estimated by modifying the stress concentration equation (Eq. 13) used in the groove weld lateral attachment detail. For the flange transition detail, stress concentration was defined by Eq. 21.

$$K_T = \log_e \left[\left(\frac{R}{2T_f} \right)^{-0.4842} \left(\frac{L_g}{2T_f} \right)^{0.2332} \left(\frac{\Delta T}{2T_f} \right)^{0.0601} \right] + 0.9649 \quad (21)$$

T_f = initial transition flange thickness

$T_f + \Delta T$ = final transition flange thickness

L_g = effective length of attachment

R = effective transition radius

The stress concentration for the uncracked detail was estimated to be 2.15 with $T_f = 2.0$ in. (50.8 mm), $\Delta T = 1.0$ in. (25.4 mm), $L = 12$ in. (304.8 mm) and $R = 0.5$ in. (12.7 mm). The stress concentration effect decays as the crack size increases. A plot of the decay with crack size, a , is shown in Fig. 6.9 for a typical flange transition detail.

The variation of stress intensity with crack size for Beam B12A is summarized in Fig. 6.10. It was assumed on the basis of visual observations that the cracks began as small circular corner cracks. The maximum stress intensity obtained for the circular corner crack in Beam B12A was 59 ksi $\sqrt{\text{in.}}$ (65 MPa $\sqrt{\text{m}}$) for a crack size of 0.55 in. (14.0 mm). This value was less than the critical stress intensity of 133 ksi $\sqrt{\text{in.}}$ (146 MPa $\sqrt{\text{m}}$). This value is also less than any slow bend material test result at -40° F (-40° C).

6.4.4 Contribution from the Nominal Residual Stress

The nominal beam cross-section residual stresses were estimated from measurement on a beam section cut from a length of a typical beam. The results shown in Figs. B.3 to B.5 were determined by using the sectioning method¹⁸. The stresses were adjusted for equilibrium and the variation through the flange thickness was assumed to be linear.

All flange transition beams were analyzed in the same manner as presented in Section 4.5 except a free surface correction of 1.15 was applied to Eq. 16 due to the lack of restraint along the edge of the flange.

6.4.5 Contribution from the Local Weld Residual Stress

The local residual stresses at the flange transitions were estimated by using the hole drilling method¹⁹. By drilling holes in the vicinity of the flange transition a good estimate of the local residual stresses at the crack plane could be made. The result of this study is summarized in Fig. B.26.

Using the same procedure presented in Section 6.4.4, the local weld contribution, K_{LW} , to stress intensity was estimated.

6.4.6 Summary and Discussion of the Various Contributions

The values of K , K_{AS} , K_{RS} , and K_{LW} are summarized in Table 6.1 for four flange transition details. The stress intensity values listed for Beam B10 are for the actual crack size at fracture. The plastic zone correction to the crack size, would not converge for this beam.

Beams B8 and B12A were analyzed as edge cracks at each third level. For Beam B8 the bottom third was critical and for Beam B10A the top third was critical. The middle third was never critical due to the local compressive residual stress field near the center of the flange.

The entire bottom half of the flange of Beam B10A was destroyed by the fatigue crack. The local weld residual stress was compressive in the middle third level, therefore the stress intensity estimate was based on the average crack length, applied stress, and residual stresses for the top third level.

For Beam B10 only a 0.5 in. (12.7 mm) ligament of the bottom third of the flange remained at the time of fracture. By inspection of the fracture surface it was observed that the fracture initiated at the 0.5 in. (12.7 mm) ligament connecting the web to the flange. Therefore, the stress intensity estimate was calculated for an edge crack at the top third level.

The major contribution to the total stress intensity was from the applied stress, K_{AS} . All estimates of K_{AS} were at least 46% of the total stress intensity values obtained for each fractured beam.

The contribution from the nominal residual stress, K_{RS} , was less than K_{AS} . The values of K_{RS} ranged from 10% to 35% of the total stress intensity estimates.

The contribution from the local residual stress, K_{LW} , was less than K_{AS} . The values of K_{LW} ranged from 18% to 37% of the total stress intensity estimated.

The stress concentration at the flange transition details had a negligible effect on the stress intensity factor. At the point of fracture the stress concentration correction, F_G , was approximately 1.0 for all the flange transition details.

TABLE 6.1a STRESS INTENSITY ESTIMATES, FLANGE TRANSITION DETAILS

Beam No./ Level	Steel Type	Crack Size, a _p (in)	Plastic size zone r _y (in)	Applied Stress (ksi)	σ _{yd} ^{**} (ksi)	Fracture Temp. (°F)	(1) K _{AS} (ksi√in)	(2) K _{RS} (ksi√in)	(3) K _{LW} (ksi√in)	(1)+(2) + (3) K (ksi√in)
B8/BOT	A514	3.52	0.80	48.12	135	-69	272	-79	111	303
B10/TOP	A36	3.90	---*	17.97	59	-40	83	63	33	179
B10A/TOP	A36	2.40	0.78	17.97	59	-39	70	33	28	131
B12A/TOP	A588	2.21	0.43	24.95	81	-89	86	13	34	133

* No convergence was obtained when the plastic zone correction was used. Results are shown for the actual crack size at fracture.

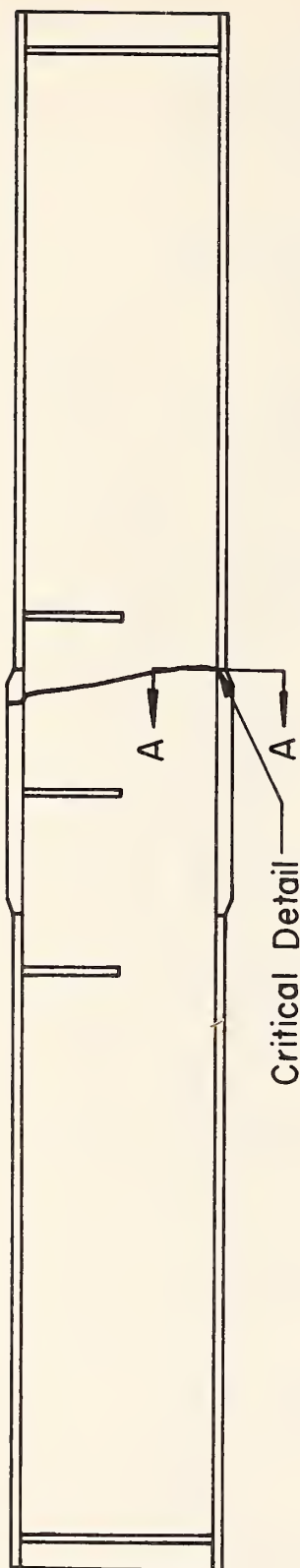
** From Eq. 4 with t = 0.12 sec. σ_{ys} = 95% of mill report yield stress.

TABLE 6.1b STRESS INTENSITY ESTIMATES, FLANGE TRANSITION DETAILS

Beam No./ Level	Steel Type	Crack Size, a_p (mm)	Plastic Size Zone r_y (mm)	Applied Stress (MPa)	σ_{yd}^{**} (MPa)	Fracture Temp. (°C)	(1) K_{AS} (MPa√m)	(2) K_{RS} (MPa√m)	(3) K_{LW} (MPa√m)	(1)+(2) + (3) K (MPa√m)
B8/BOT	A514	89.4	20.3	332	931	-56	299	-87	122	333
B10/TOP	A36	99.1	---*	124	407	-40	91	69	36	197
B10A/TOP	A36	61.0	19.8	124	407	-39	77	36	31	144
B12A/TOP	A588	56.1	10.9	172	558	-67	95	14	37	146

* No convergence was obtained when the plastic zone correction was used. Results are shown for the actual crack size at fracture.

** From Eq. 4 with $t = 0.12$ sec. $\sigma_{ys} = 95\%$ of mill report yield stress.



Beam B8

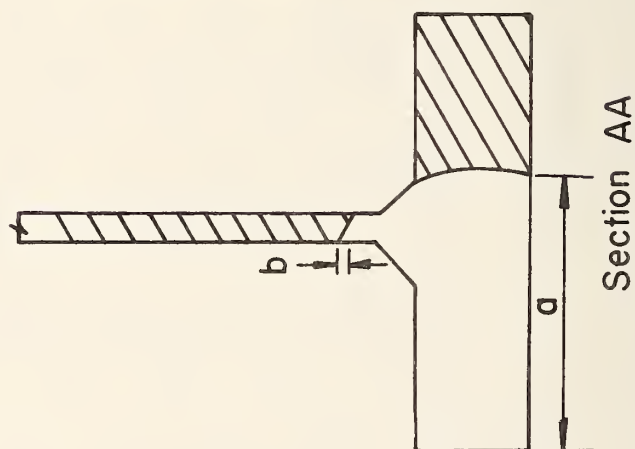


Fig. 6.1 Fatigue and Fracture Surface, B8 (A514)

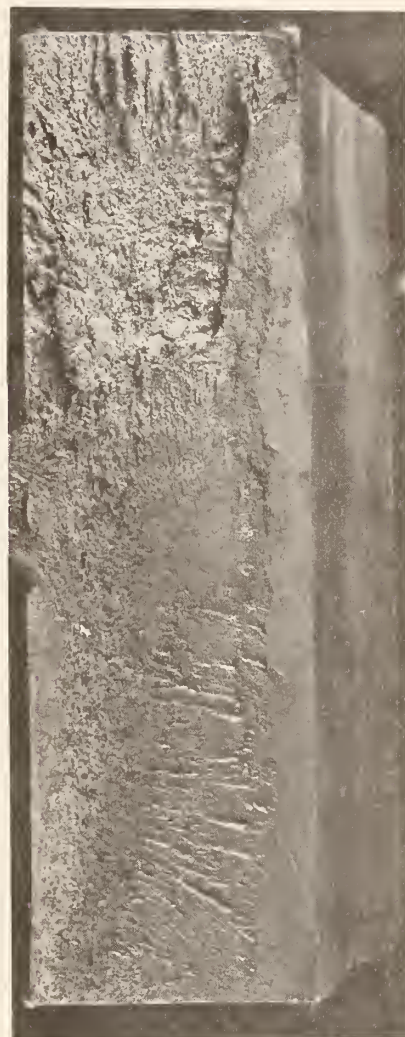
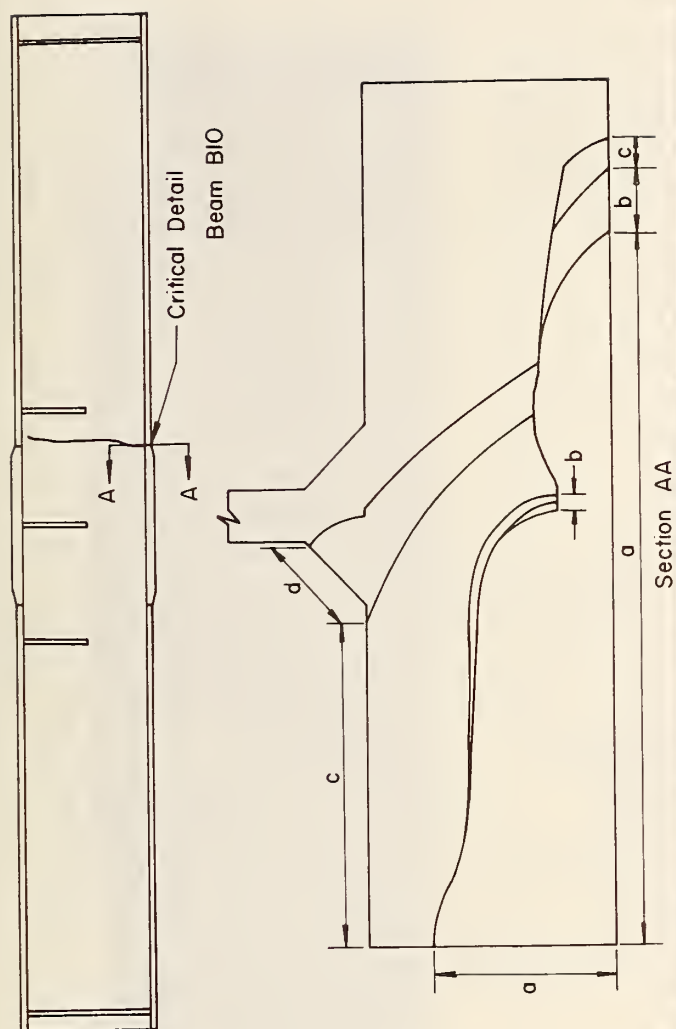


Fig. 6.2 Fatigue and Fracture Surface, B10 (A36)

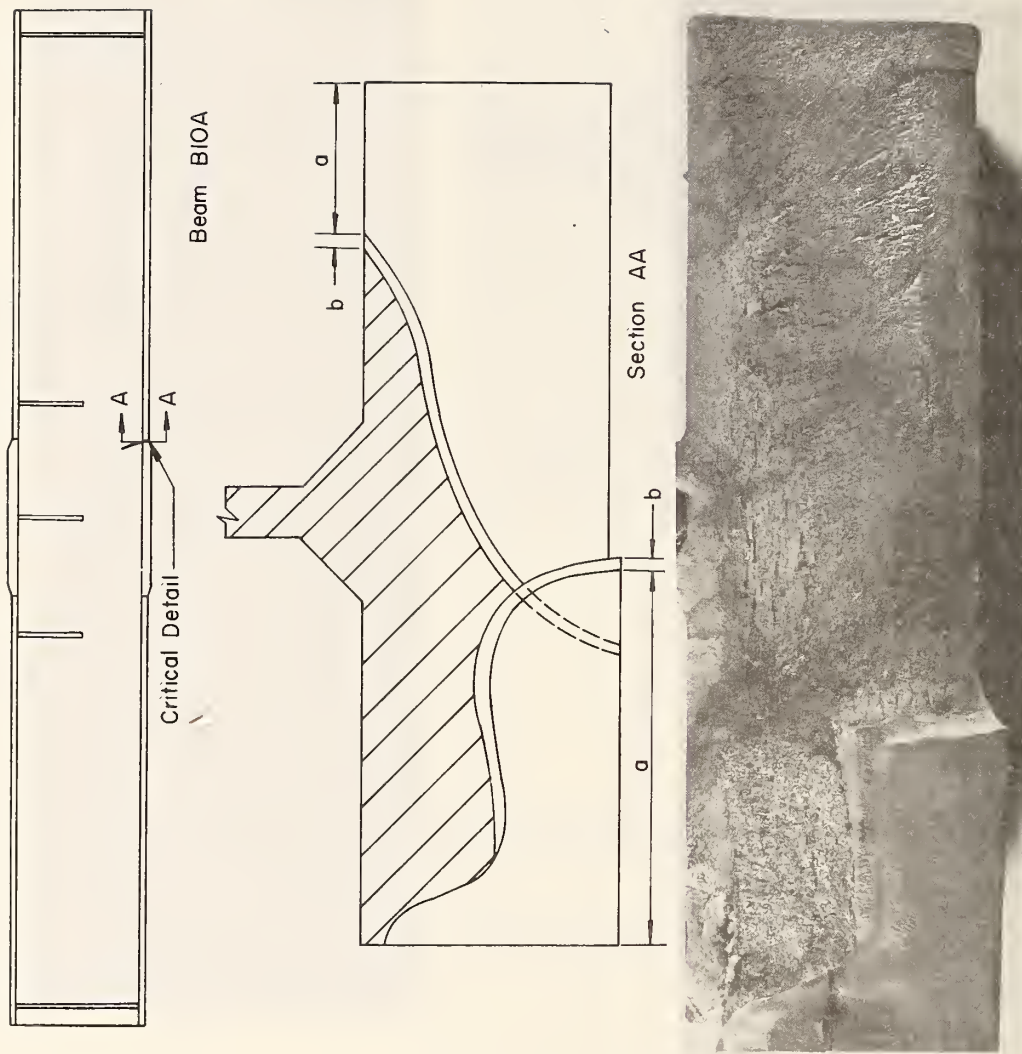


Fig. 6.3 Fatigue and Fracture Surface, B10A (A36)

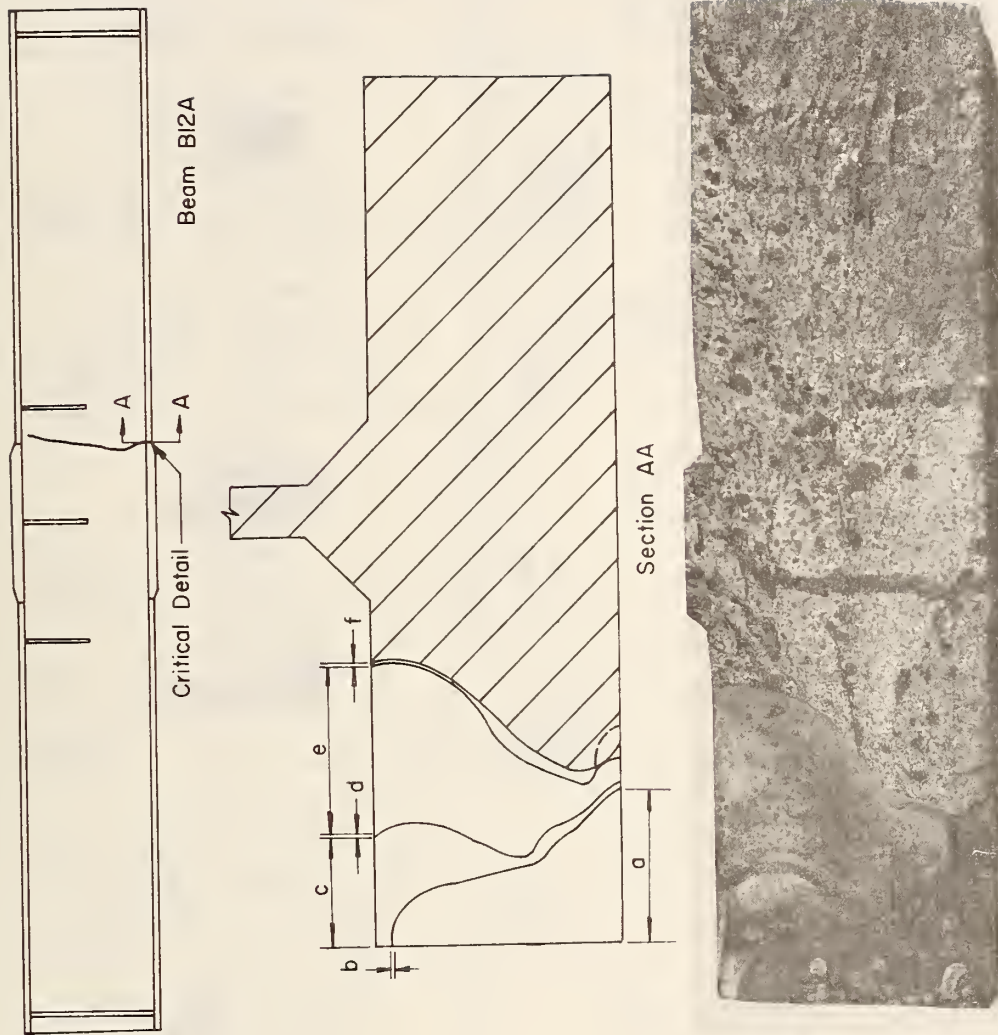
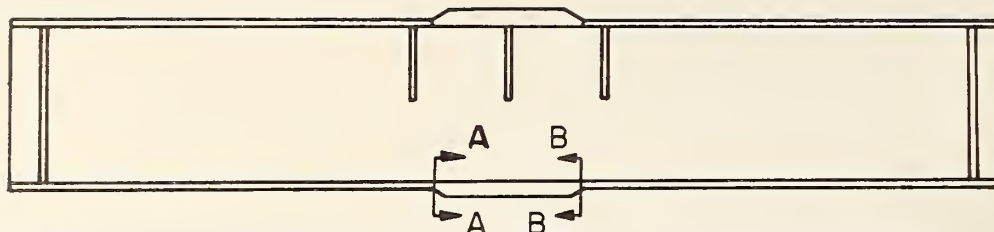


Fig. 6.4 Fatigue and Fracture Surface, B12A (A588)



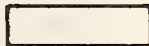
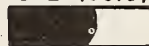
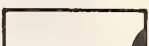
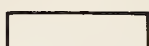
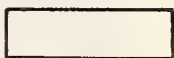
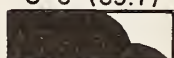
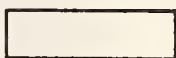
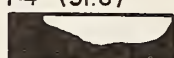
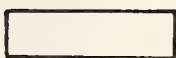

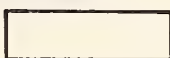
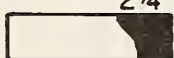
Beam	Section AA	Section BB
B8	 2.95	*  3 1/2" (85.8) 3 1/8" (79.4) 2.95
B8A	 15/16" (23.8) 3/4" (19.1) 4.17	 4.17
B10	 3.31	*  3 3/8" (85.7) 6 1/2" (165.1) 3.31
B10A	 3.06	*  1 1/4" (31.8) 1 7/8" (47.6) 3.06
B12	 4.17	 7/8" (22.2) 7/8" (22.2) 4.17
B12A	 3.07	*  2 1/4" (57.1) 1 1/2" (38.1) 3.07

Table Scale 1 1/2" = 1' - 0
 Measurements Taken At Cycles Listed At Bottom
 Of Cross Section (in millions of cycles)
 * Beam Fractured At This Section
 Fatigue Crack Prior To Last Fracture Test
 Measurements In Brackets, mm

Fig. 6.5 Fatigue Cracks Prior to Last Fracture Test

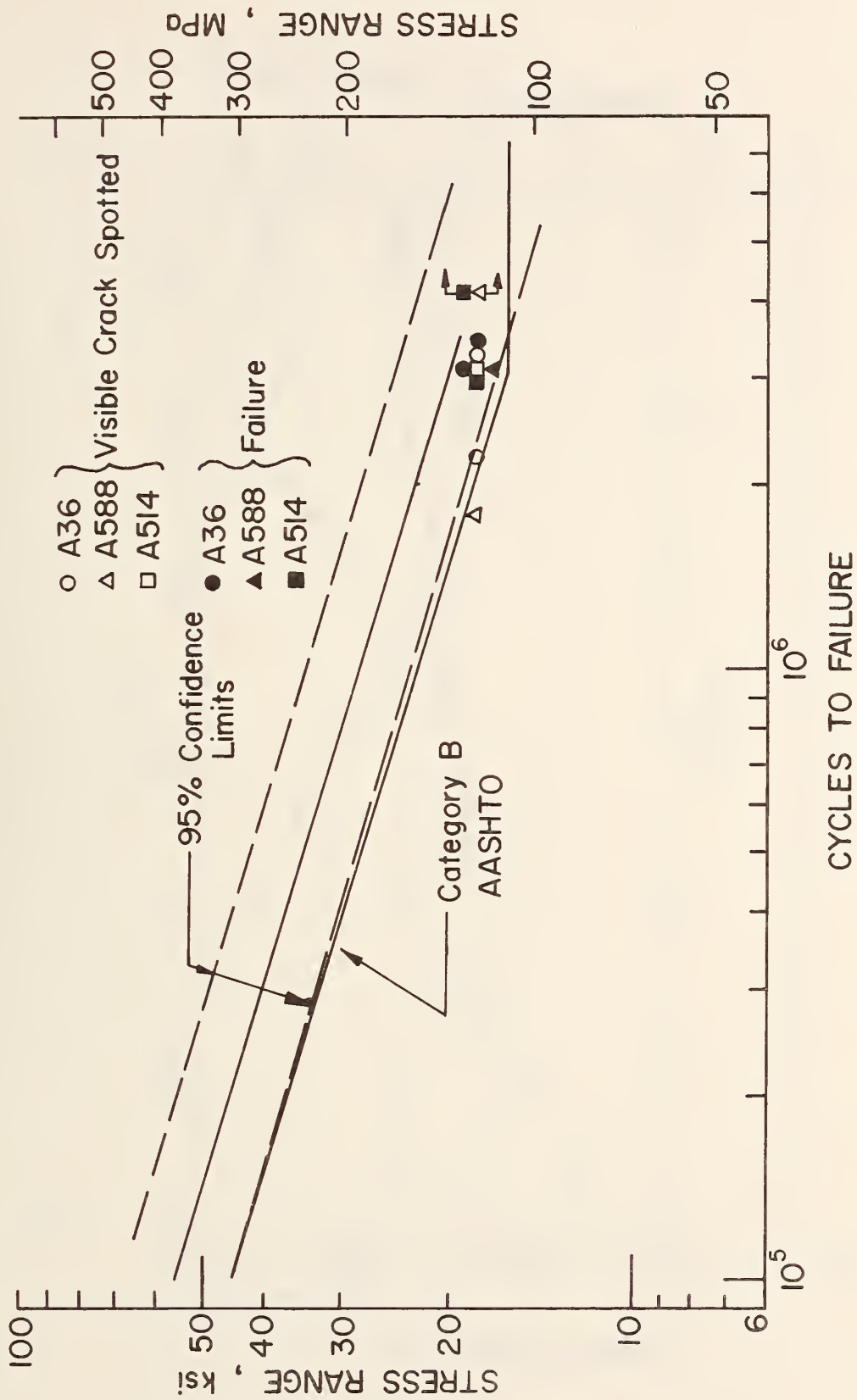


Fig. 6.6 Category B S-N Plot, Flange Transition

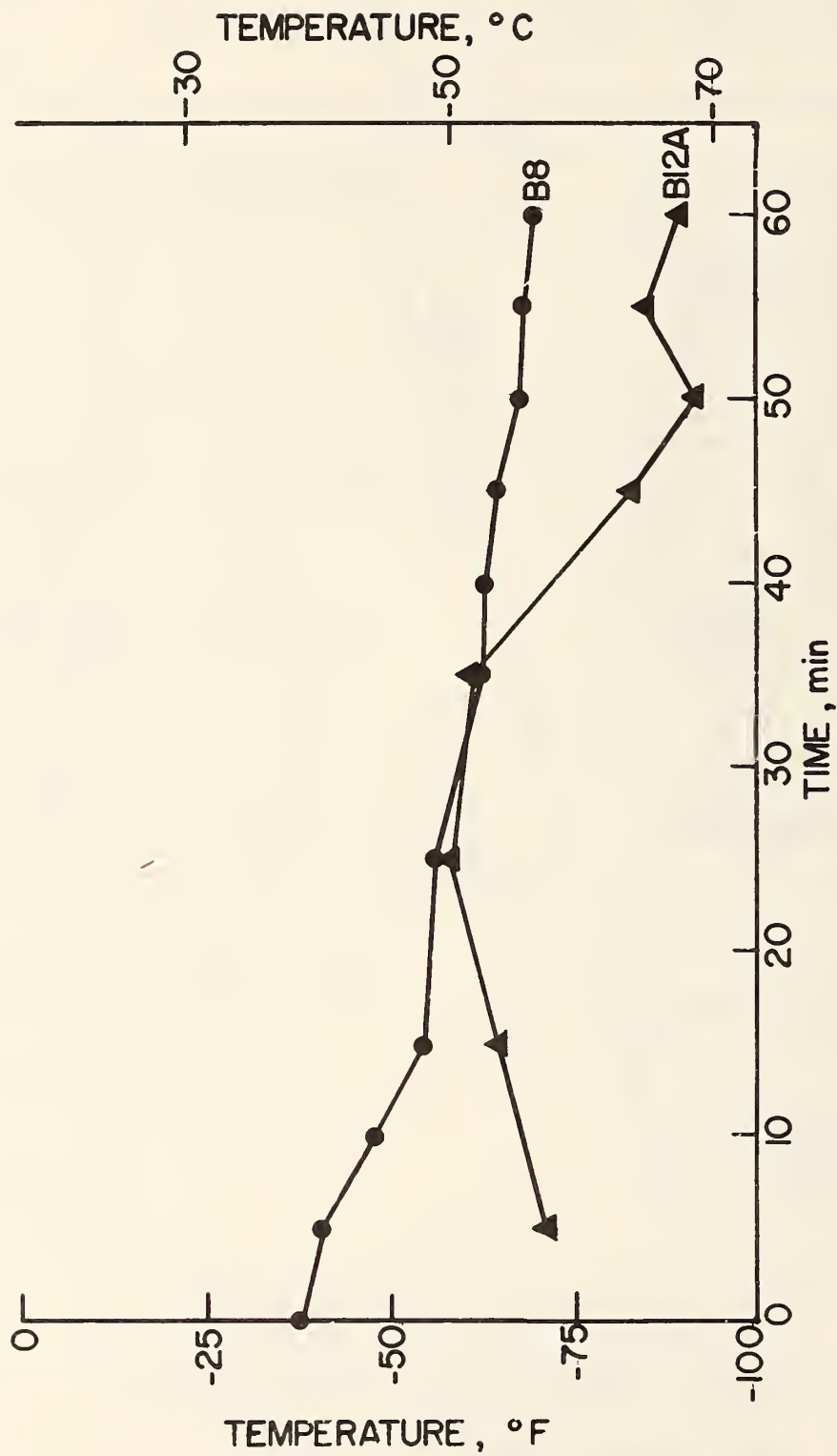


Fig. 6.7 Critical Detail Temperature/Sixty Minutes Prior to Fracture (B8, B12A)

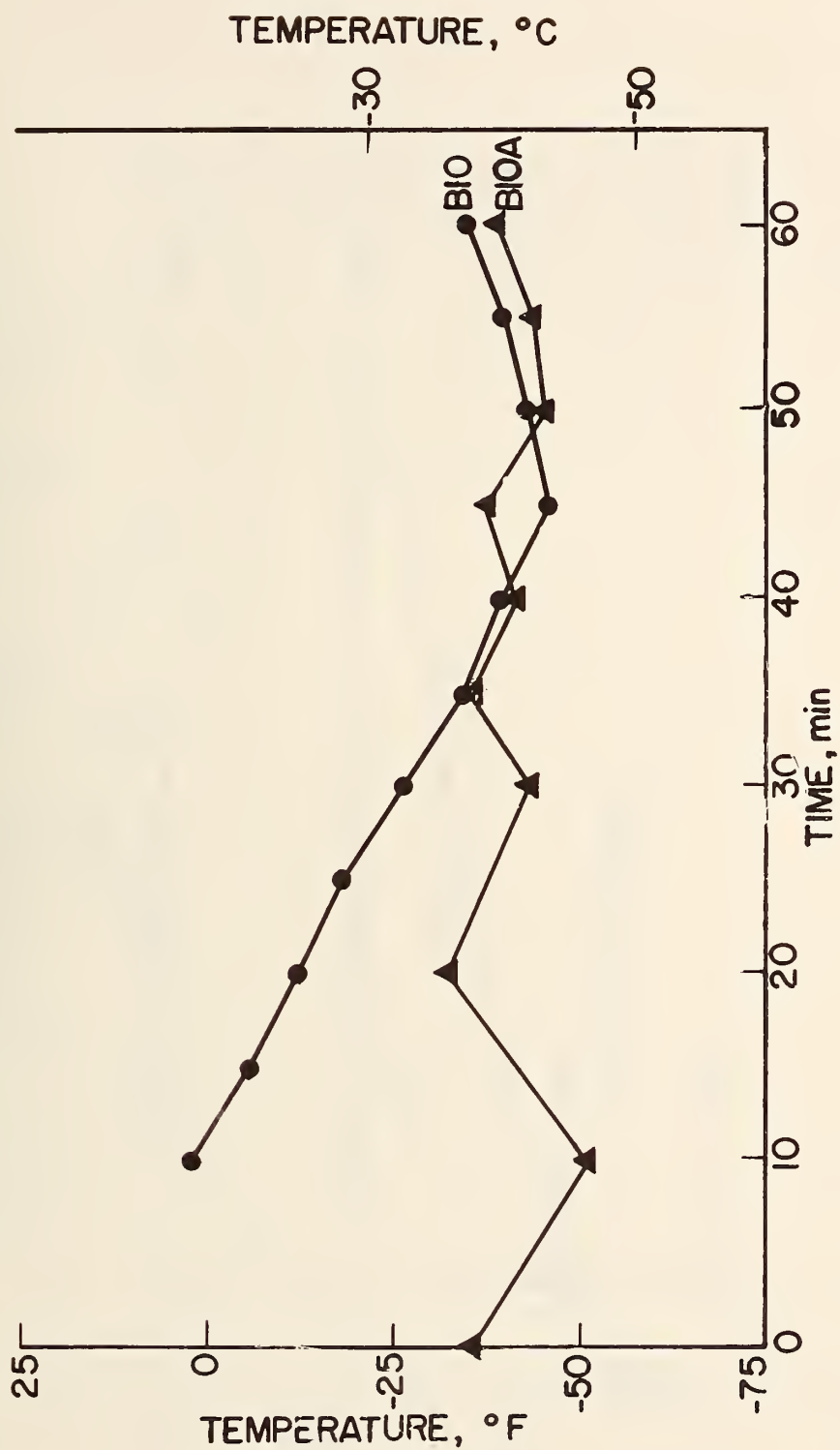


Fig. 6.8 Critical Detail Temperature/Sixty Minutes Prior to Fracture (B10, B10A)

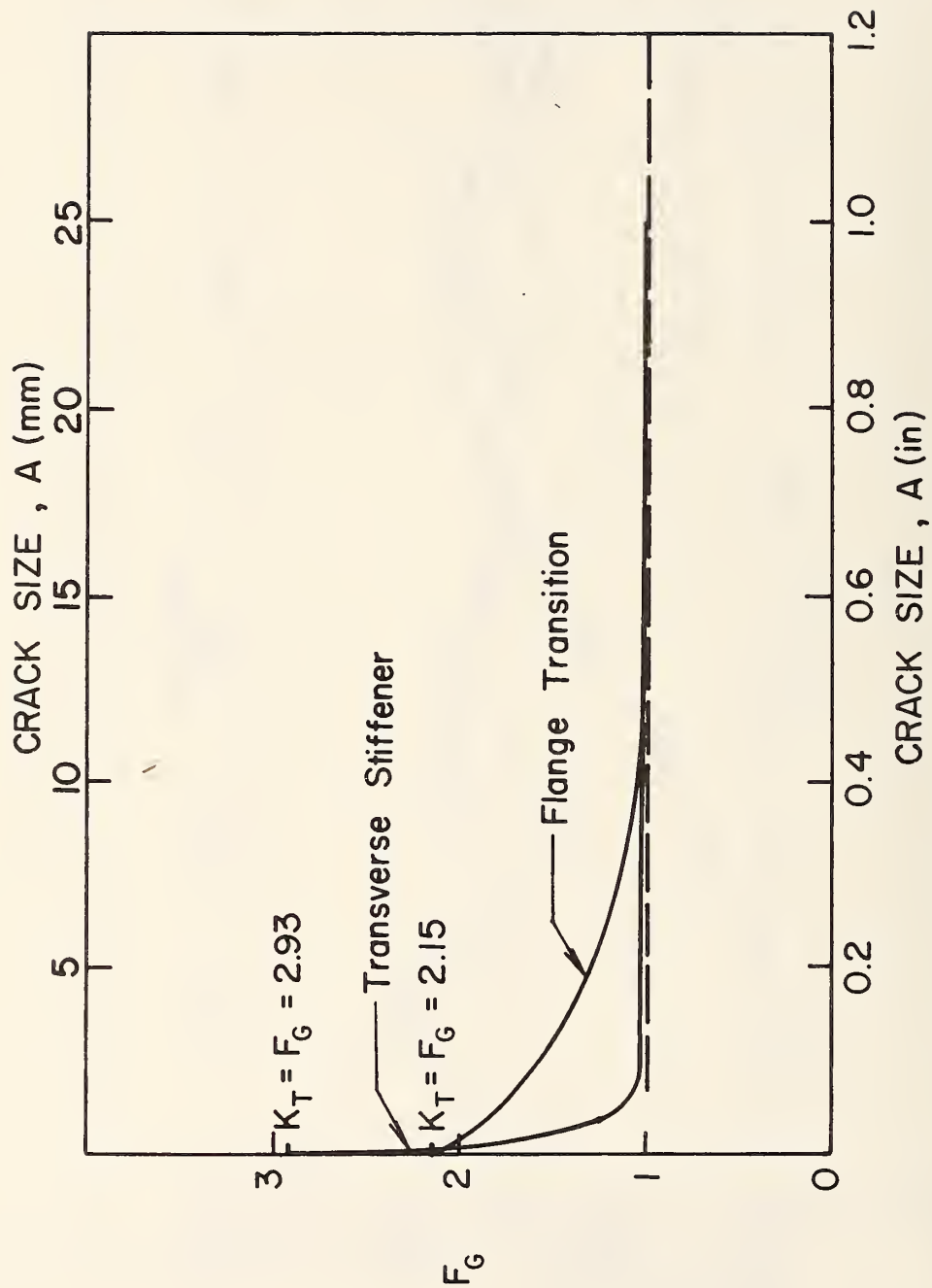


Fig. 6.9 Stress Concentration Decay with Crack Size (B12A, B9)

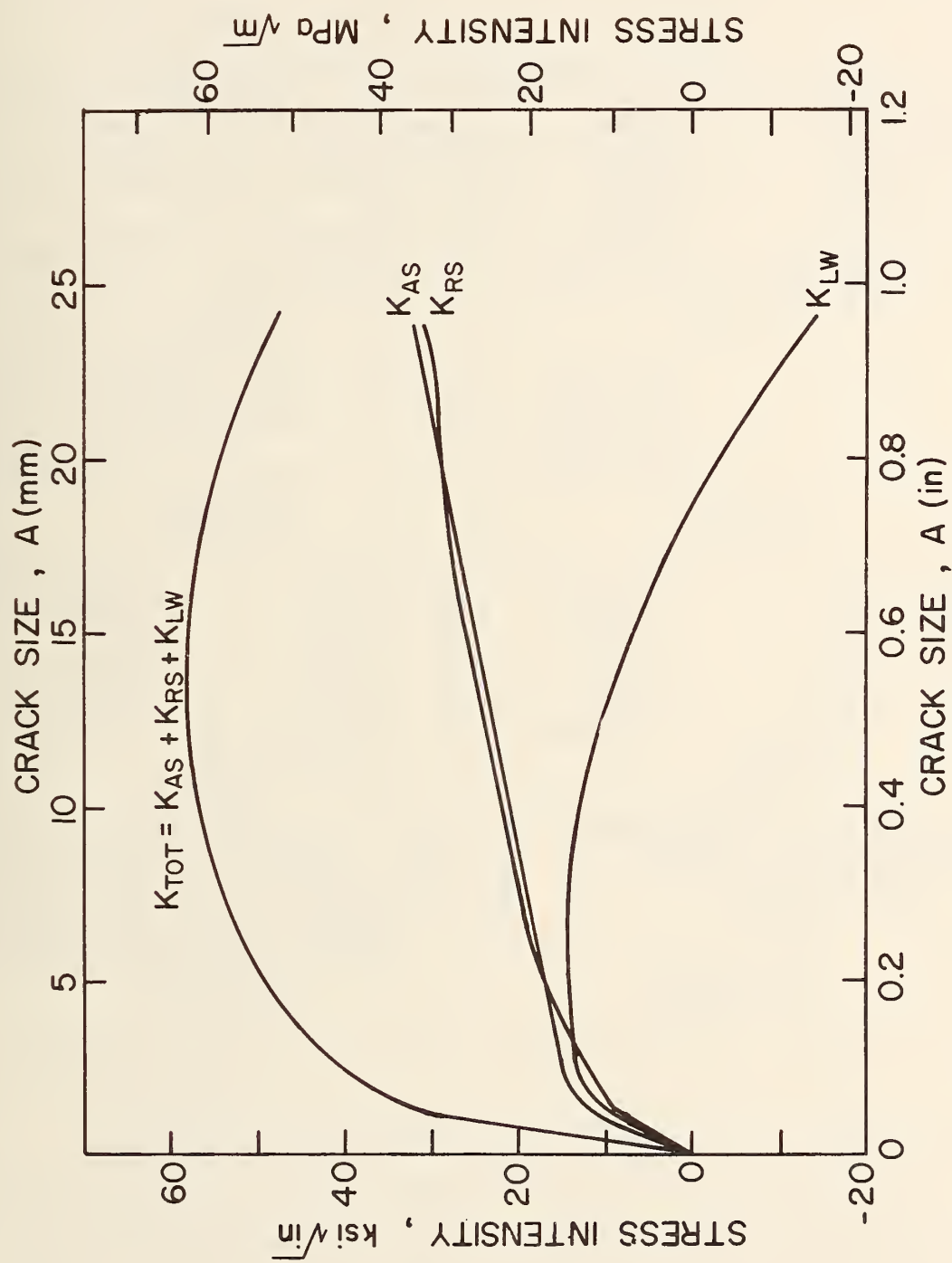


Fig. 6.10 Stress Intensity vs. Crack Size (B12A)

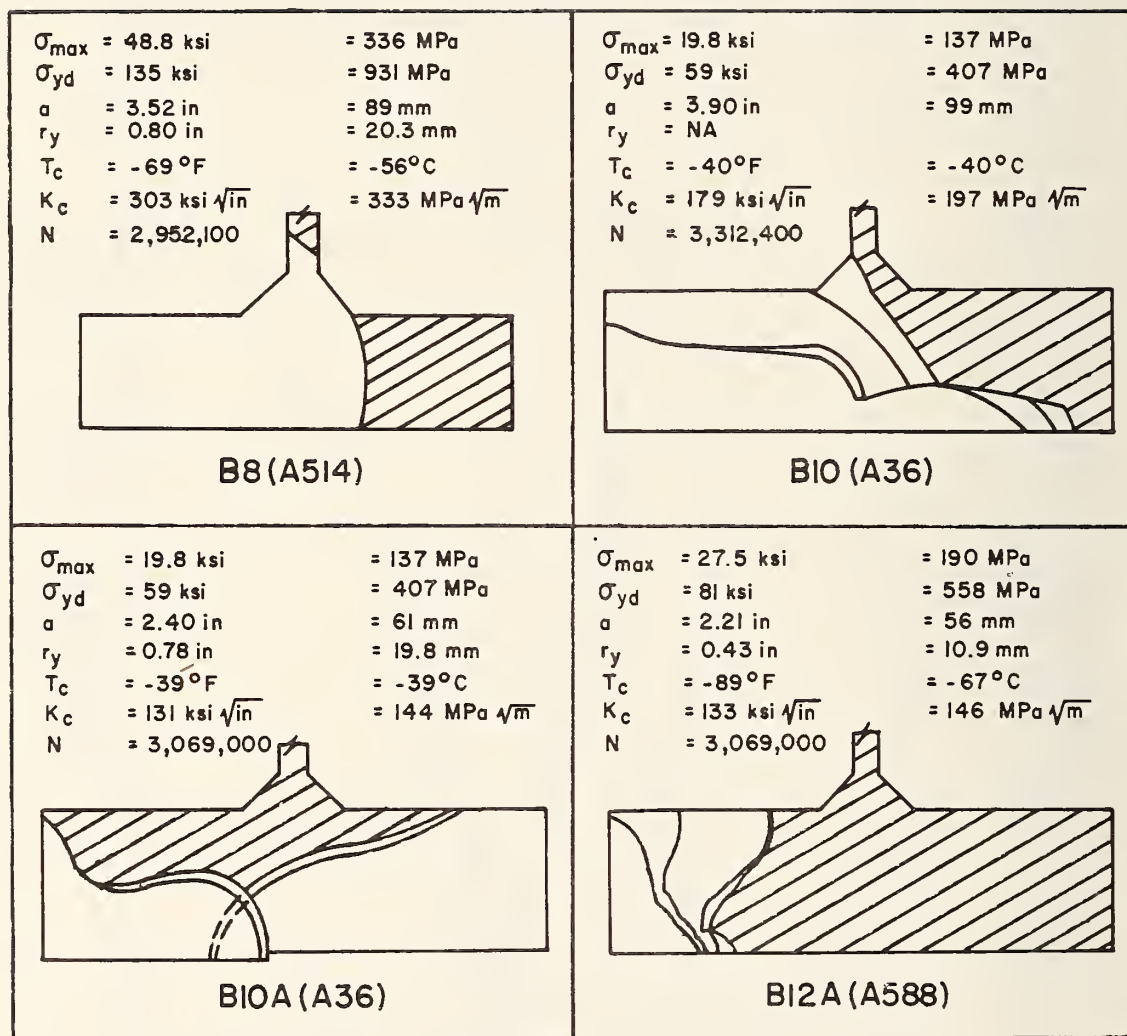


Fig. 6.11 Fracture Surface Sketches and Data Summary

7. TRANSVERSE STIFFENER TEST RESULTS AND ANALYSIS

(Specimen No.	Material)
B9, B9A	A36
B11, B11A	A588
B7, B7A	A514

7.1 Fatigue Cracks

The fatigue cracks at the transverse stiffener details welded to the bottom flange were initially detected as 1 in. (25.4 mm) surface cracks at the toe of the stiffener weld on the interior flange face. As these surface cracks grew larger they became elliptical corner cracks (Beams B7A, B9A, and B11A) and in the case of Beam B11A the crack grew to become an edge crack.

The fatigue cracks on the transverse stiffener details not welded to the bottom flange were initially detected at the toe of weld near the end of the stiffener. No fatigue cracks were detected on Beam B9 after 9.56 million cycles at 13 ksi (89.7 MPa) stress range and the test was discontinued. For Beam B7 a 0.25 in. (6.4 mm) elliptical surface crack was detected at the toe of the stiffener weld after 6.66 million cycles. At 8.36 million cycles the crack had grown to 0.5 in. (12.7 mm) and the test was discontinued. Only Beam B11 developed a fatigue crack at the cut short stiffener which grew into the bottom flange (Fig. 7.3).

7.2 Fatigue Life

Figure 7.6 shows the mean S-N Curve and its confidence limits for the Category C details tested at 13 ksi (89.7 MPa) and 15 ksi (103.4 MPa) stress range. The open figures represent the point at which the cracks were first observed and the closed figures represent

the point of fracture. Beams B7 and B9 did not fracture due to the proximity of the design stress range to the fatigue threshold. There is a good correlation between the fracture point and the Category C fatigue-life relationships.

The number of cycles needed to propagate an edge or corner crack from its fracture initiation point to an edge crack of 75% of the flange width, b , was defined as the remaining useful fatigue life had brittle fracture not occurred. This remaining fatigue life was estimated by a numerical integration routine using Eqs. 7 and 11 as presented in Section 4.2.

Beams B11 and B11A had no appreciable residual fatigue life at the time of fracture. Beams B7A and B9A had 37,000 and 56,000 cycles of remaining fatigue life, respectively. Even if rapid fracture had not occurred very little life would have remained.

7.3 Beam Fracture Tests*

Beam B7 (A514 Steel)

The transverse stiffener details for Beams B7 were cut 0.5 in. (12.7 mm) short of the bottom flange. No fatigue cracks were observed at 2 million cycles. The first low temperature test was conducted at 2.19 million cycles. Both details were cooled to -40° F (-40° C) and then cyclically loaded for thirty minutes. No fracture occurred.

*Temperature at the critical details are shown graphically in Figs. 7.7 and 7.8 for the final sixty minutes of the last fracture test.

The beam was then cycled at room temperature to develop visible fatigue cracks. A 0.25 in. (6.4 mm) surface crack was detected at the toe of the east stiffener weld at 6.66 million cycles. By 8.36 million cycles the surface crack had grown to a 0.5 (12.7 mm) length. The test was discontinued at that time.

Beam B7A (A514 Steel)

The transverse stiffener details for Beam B7A were welded to the bottom flange. Since the fatigue crack at the stiffener to flange weld initiated and grew very rapidly (Fig. 7.1) as it was tested at a stress range of 15 ksi (103.4 MPa), the first fracture test was conducted before reaching 2 million cycles.

Only one low temperature test was run on this beam. The west detail was cooled to -40° F (-40° C). Just as maximum load was reached fracture occurred at -37° F (-38° C).

Beam B9 (A36 Steel)

The transverse stiffener details for Beam B9 were cut 0.5 in. (12.7 mm) short of the bottom flange. No fatigue cracks were observed at 2 million cycles at 13 ksi (89.7 MPa) stress range. The first low temperature test was conducted at 2 million cycles. Both details were cooled to -40° F (-40° C) and then cyclically loaded for one hour. No fracture occurred.

The beam was then cycled at room temperature to develop visible fatigue cracks. At 9.56 million cycles no fatigue cracks were observed. Both details were cooled to -40° F (-40° C) and then

cyclically loaded for one hour. No fracture occurred and the test was discontinued.

Beam B9A (A36 Steel)

The transverse stiffener details for Beam B9A were welded to the bottom flange. No fatigue cracks were observed at 2 million cycles at a stress range of 13 ksi (89.7 MPa). The first low temperature test was conducted at 2 million cycles. Both details were cooled to -40° F (-40° C) and then cyclically loaded for one hour. No fracture occurred.

The beam was then cycled at room temperature to develop visible fatigue cracks. At 5.39 million cycles an elliptical corner crack existed at the west detail (Fig. 7.2). The detail was cooled to -40° F (-40° C) and then cyclically loaded. While cycling for three hours the temperature at the critical detail was decreased to -195° F (-126° C) at which time fracture occurred.

Beam B11 (A588 Steel)

The transverse stiffener details for Beam B11 were cut 0.5 in. (12.7 mm) short of the bottom flange. No visible fatigue cracks were observed at 2 million cycles at a stress range of 15 ksi (103.4 MPa). Later examination of the fracture surface indicated that an approximately 2.5 in. (63.5 mm) long and 0.13 in. (3.3 mm) deep surface crack existed along the web to stiffener weld of the east detail when the first low temperature test was conducted at 2 million cycles. Both details were cooled to -40° F (-40° C) and cyclically loaded for one hour. No fracture occurred.

The beam was then cycled at room temperature to develop visible fatigue cracks. At 3.04 million cycles an elliptical crack existed in the flange of the east detail (Fig. 7.3). This detail was cooled to -40° F (-40° C) and then cyclically loaded. While cycling for 80 minutes the temperature at the critical detail was decreased to -110° F (-79° C), at which time fracture occurred.

Beam B11A (A588 Steel)

The transverse stiffener details for Beam B11A were welded to the bottom flange. A fatigue crack developed at the west detail and grew very rapidly. The low temperature test was conducted after the beam had experienced 1.8 million cycles of 15 ksi (103.4 MPa) stress range. The fatigue crack had extended over approximately 75% of the flange (Fig. 7.4). The critical detail was cooled to -45° F (-43° C). When the beam was loaded fracture occurred at 22.2 ksi (153.1 MPa), prior to reaching maximum load.

7.4 Stress Intensity Estimate for Transverse Stiffener Details

7.4.1 Introduction

Only Beams B11, B7A, B9A, and B11A experienced brittle fracture. Beams B7A and B9A fractured from elliptical corner cracks. Beam B11 fractured from a semi-elliptical crack which was very near to full thickness. Beam B11A fractured from an extremely large, but poorly defined edge crack. Beams B7A, B9A, and B11A were analyzed assuming they were both elliptical corner and edge cracks. Beam B11 was analyzed as both a semi-elliptical crack and as a center cracked plate.

The plastic zone correction, r_y , was not used when evaluating the stress intensity, K . The approximations necessary for defining the crack shape for the various analyses of these details did not justify including the plastic zone correction.

7.4.2 Contribution from the Applied Stress

The stress intensity for elliptical crack shapes is defined by Eq. 11. For the elliptical corner crack analyses (Beams B9A, B7A, and B11A) the crack shape correction, F_e , varied between 1.0 and $2/\pi$ for an elliptical crack growing from a shallow quarter-elliptical crack to a semi-circular crack. The stress concentration correction, F_G , varied with crack size as shown in Fig. 6.9. For crack sizes greater than 0.20 in. (5.1 mm) $F_G \approx 1.0$. F_S was taken as 1.0 because of the restraint provided by the stiffener. F_W was defined as a function of the plate thickness and the crack size as equal to:

$$F_W = \sqrt{\frac{2T_{f'}}{\pi a'} \tan \frac{\pi a'}{2T_{f'}}} \quad (22)$$

$T_{f'}$ = equivalent flange thickness

a' = equivalent crack size

where F_W approaches infinity when a' approaches $T_{f'}$. For Beams B9A and B7A $T_{f'}$ and a' were equal to T_f and a , respectively. For Beam B11A, $T_{f'}$ was equal to T_f , but a' was defined as the crack size at the point on the leading edge of the crack where the stress intensity, K , was calculated.

For the semi-elliptical surface crack analysis of Beam B11, the stress concentration correction, F_G , was taken as 1.0. The free surface correction, F_S , for a half-circular surface crack was used⁴:

$$F_S = 1.211 - 0.186 \sqrt{\sin \phi} \quad (23)$$

where ϕ is defined in Fig. 5.12. The finite width correction, F_W , was defined by Eq. 22 where T_f , and a' were defined along a line drawn from the center of the ellipse through the point on the leading edge of the crack, where the stress intensity was being calculated, and to the exterior flange face.

For the edge crack analysis of Beam B11A the crack shape correction factor, F_e , and the stress concentration factor, F_G , were taken as 1.0. The free surface correction for the uniformly applied stress was taken as 1.122. Due to the irregular crack shape, the average crack length for the edge crack was assumed to be the crack size, a' . F_W was defined as a function of plate width, b , and the equivalent crack size, a' , as equal to:

$$F_W = \sqrt{\frac{2b}{\pi a'} \tan \frac{\pi a'}{2b}} \quad (24)$$

The average applied and residual stresses (i.e., the mid-flange stresses) in the flange were used for the edge crack analysis of Beam B11A.

The total stress intensity for the detail was calculated as a summation of the contributions of the applied and residual stresses. For the center crack analysis of Beam B11 only the applied stress was

considered. For the edge crack analysis of Beams B9A and B7A the stress was assumed at the tensile yield point.

The semi-elliptical crack in Beam B11 was transformed into an equivalent center crack of equal area. Half of the total crack length of this center crack was defined as the equivalent crack length, a' . The stress intensity, K , was calculated by Eq. 25.

$$K = \sigma_{AS} \sqrt{\pi a'} \sqrt{\frac{b}{\pi a'} \tan \frac{\pi a'}{b}} \quad (25)$$

where b equals the flange width.

For Beams B7A and B9A, the vertical edge crack was taken at the point where the fracture surface provided a visual indication of fracture initiation. This occurred in a region where tensile residual stresses at yield would be expected. Due to the restraint provided by the transverse stiffener, the free surface correction, F_G , was taken as 1.0. F_G and F_E were also taken as 1.0. The finite width correction, F_W , was defined by Eq. 22.

When determining the residual fatigue life, the secant finite width correction (Eq. 20) was used. The difference between the tangent and secant correction varied from 10% to 3% for a/C ratios of respectively 0.671 and 0.375.

7.4.3 Contribution from the Stress Concentration

In a recent study, Zettlemoyer¹⁴ has developed a relationship for stress concentration factors, K_T , at uncracked transverse

stiffener details as a function of flange thickness, and weld size. Values equal to about 2.93 were estimated for the transverse stiffener welded to the bottom flange from Eq. 26.

$$K_T = \log_e \left(\frac{Z}{T_f} \right)^{0.70} + 4.10 \quad (26)$$

T_f = thickness of flange

Z = fillet weld leg size

The stress concentration effect decays as the crack size increases. A plot of the decay with crack size, a , is shown in Fig. 6.9 for a typical transverse stiffener detail welded to a 2 in. (50.8 mm) thick flange.

The effect of stress concentration on stress intensity is shown in Fig. 7.9 for an elliptical crack growing at the toe of the stiffener-flange weld for Beam B9. It was assumed that the small cracks began as elliptical surface cracks with the center of the ellipse 1.65 in. (41.9 mm) from the flange tip. The variation of the semi-minor, a , and semi-major, c , axes was defined by Eq. 27².

$$c = 1.088a^{0.946} \quad (27)$$

For a 1.0 in. (25.4 mm) elliptical surface crack a stress intensity of 30 ksi $\sqrt{\text{in.}}$ (33 MPa $\sqrt{\text{m}}$) was obtained under the applied load. This value was less than the critical stress intensity of Beam B9A.

Because of the rapid decay of the stress concentration, K_T , crack instability did not develop at small elliptical cracks.

However, the stress concentration affects the fatigue strength of the beams.

7.4.4 Contribution from the Nominal Residual Stresses

The nominal beam cross-section residual stresses were assumed to be the same as other welded built-up beams. The results shown in Figs. B.3 to B.5 were also used for the gusset attachments. The stresses were adjusted for equilibrium and variation through the flange thickness was assumed to be linear.

The nominal residual stress contribution to stress intensity for the edge crack analysis of Beam B11A was calculated in the same manner as was presented in Section 4.5 except that a free surface correction of 1.15 was applied to Eq. 16 due to the lack of restraint along the edge of the flange.

The estimate of K_{RS} for the elliptical crack was accomplished by the numerical integration procedure presented in Section 5.4.4. The free surface and stress concentration corrections were taken as approximately 1.0 for Beams B7A, B9A, and B11A. The finite width and crack shape corrections were the same as used for the applied stress contribution. In the elliptical crack analysis of Beam B11, a free surface correction of 1.15 was used due to the non-uniform stress distribution. The finite width, stress concentration, and crack shape correction factors were assumed to be the same as the applied stress contributions.

7.4.5 Contribution from the Local Weld Residual Stresses

The local stresses at the toe of the stiffener-to-flange weld were estimated by using the hole drilling method¹⁹. The result of this study is summarized in Fig. B.27. No local residual stress contribution to the stress intensity was attributed to the stiffener details which were cut short of the bottom flange.

Weld contribution, K_{LW} , was estimated using the same numerical integration procedure presented in Section 7.4.4.

7.4.6 Summary and Discussion of the Various Contributions

The values of K , K_{AS} , K_{RS} , and K_{LW} are summarized in Table 7.2 for each transverse stiffener beam detail. The stress intensity values listed are for the actual crack sizes at failure. No plastic zone correction was applied to these beams.

The estimates of K_{RS} and K_{LW} for each of the elliptical crack analyses were checked by numerically integrating a uniform stress field using the same crack size mesh. The stress intensity values obtained were compared with the stress intensity results for a uniform stress from known solutions. The errors between the known solution and the numerical integration solution are summarized in Table 7.1. To correct this error, the estimate of K_{RS} and K_{LW} were scaled by a factor of the known applied stress solution divided by the numerical integration solution.

The major contribution to the total stress intensity estimates was from the applied stress, K_{AS} . The applied load accounted for at least 50% of the total stress intensity estimates for each beam detail.

The contribution from the nominal residual stress, K_{RS} , was less than 30% of the total stress intensity estimate.

There was no local weld residual stress contribution to stress intensity, K_{LW} , for the stiffener details cut short of the bottom flange. For the stiffener details welded to the bottom flange the local residual stresses were estimated to contribute 20 to 38% of the total stress intensity.

Due to the size of the failure crack, the stress concentration for the stiffener details welded to the bottom flange had a negligible effect on the stress intensity factor. At the point of fracture the stress concentration correction, F_G , was approximately 1.0 for all stiffener details.

TABLE 7.1 NUMERICAL INTEGRATION ERRORS, TRANSVERSE STIFFENER DETAILS

Beam No.	Crack Size a (in/mm)	Semi-Major Axis C (in/mm)	a/C	ϕ Degree	Percent Error in K_{LW}, K_{RS} *
B7A	1.1/28	3.25/83	.388	143°	+55.5
B9A	1.5/38	3.56/90	.421	147°	+59.4
B11	2.0/51	2.57/65	.781	132°	-6.7
B11A	2.0/51	6.50/165	.307	140°	+69.3

* K_{RS} and K_{LW} were scaled in proportion to this error

TABLE 7.2a STRESS INTENSITY ESTIMATES, TRANSVERSE STIFFENER DETAILS

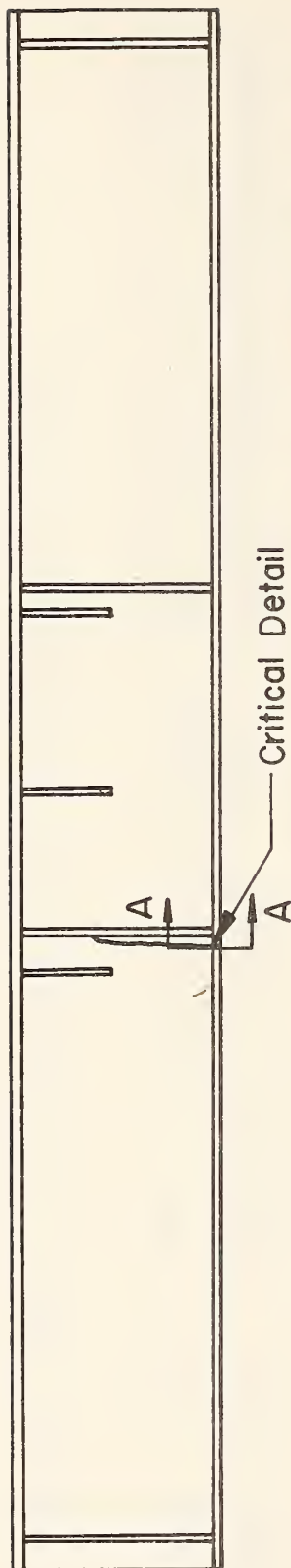
Beam No.	Steel Type	Analysis Type	Crack Size, a_p (in)	Applied Stress (ksi)	Fracture Temp. (°F)	(1) K_{AS} (ksi√in)	(2) K_{RS} (ksi√in)	(3) K_{LW} (ksi√in)	(1)+(2) + (3) K (ksi√in)
B7A	A514	Elliptical	1.10	48.10	-36	90	55	72	217
B7A	A514	Edge	0.70	115.00*	-36	189	NA	NA	189
B9A	A36	Elliptical	1.50	19.52	-195	41	25	30	97
B9A	A36	Edge	0.75	42.00*	-195	69	NA	NA	69
B11	A588	Elliptical	2.00	25.97	-110	70	-12	0	58
B11	A588	Center	2.00	25.97	-110	77	NA	NA	77
B11A	A588	Elliptical	2.00	21.00	-45	44	-5	31	70
B11A	A588	Edge	4.70	21.00	-45	117	5	73	195

* Applied + Residual + Local weld stress = 95% of mill report yield stress

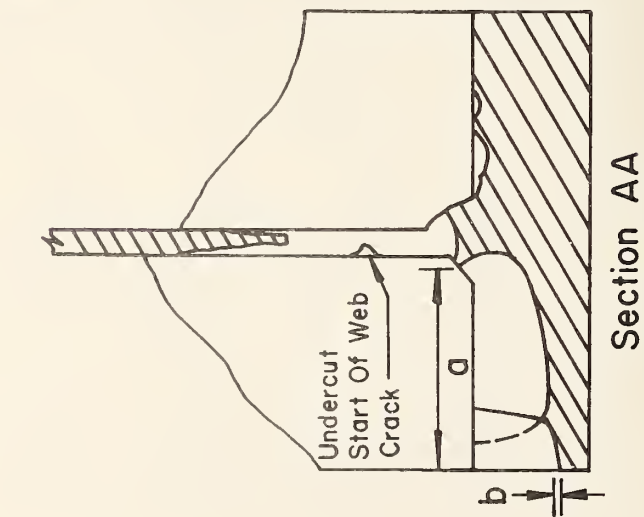
TABLE 7.2b STRESS INTENSITY ESTIMATES, TRANSVERSE STIFFENER DETAILS

Beam No.	Steel Type	Analysis Type	Crack Size, a_p (mm)	Applied Stress (MPa)	Fracture Temp. ($^{\circ}$ C)	(1) K_{AS} (MPa \sqrt{m})	(2) K_{RS} (MPa \sqrt{m})	(3) K_{LW} (MPa \sqrt{m})	(1)+(2) +(3) K (MPa \sqrt{m})
B7A	A514	Elliptical	27.90	323	-38	99	61	79	239
B7A	A514	Edge	17.80*	793	-38	208	NA	NA	208
B9A	A36	Elliptical	38.10	135	-126	45	28	33	107
B9A	A36	Edge	19.10*	290	-126	76	NA	NA	76
B11	A588	Elliptical	50.80	179	-79	77	-13	0	64
B11	A588	Center	50.80	179	-79	85	NA	NA	85
B11A	A588	Elliptical	50.80	145	-43	48	-6	34	77
B11A	A588	Edge	119.40	145	-43	129	6	80	215

* Applied + Residual + Local weld stress = 95% of mill report yield stress



Beam B7A



Section AA

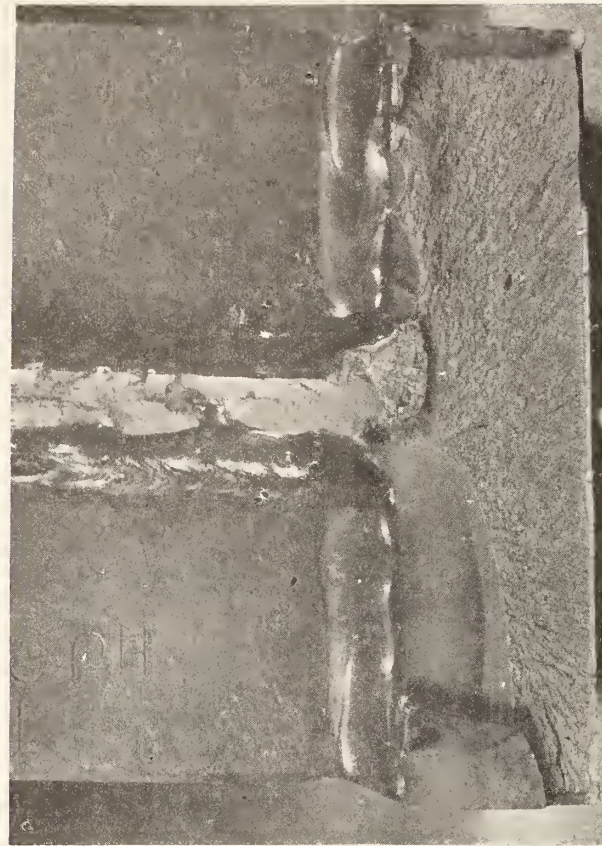
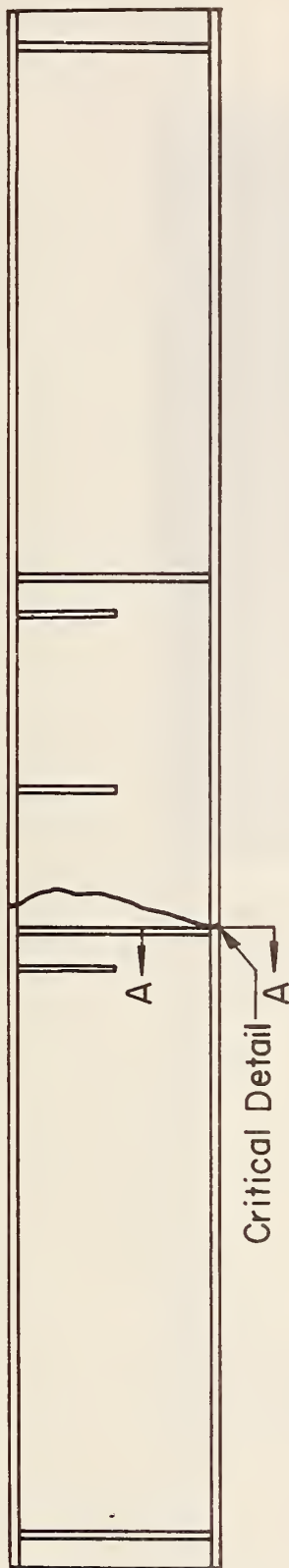
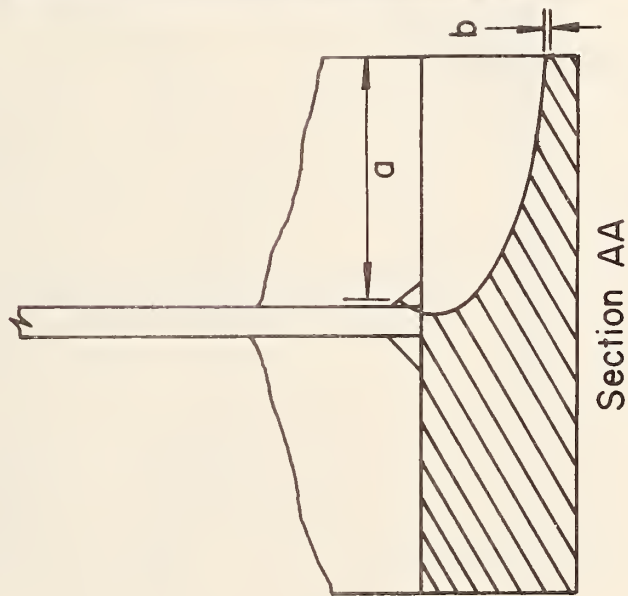


Fig. 7.1 Fatigue and Fracture Surface, B7A (A514)



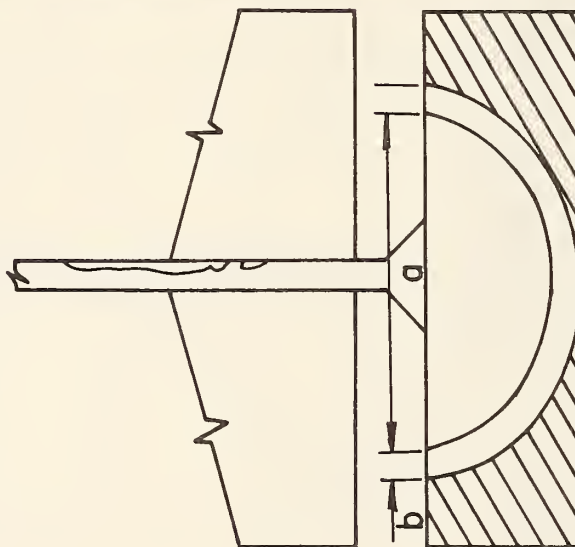
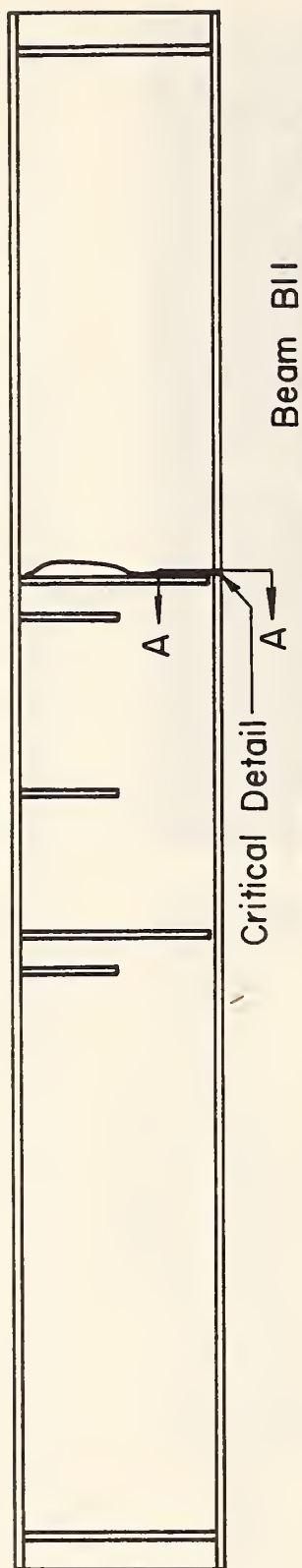
Beam B9A



Section AA



Fig. 7.2 Fatigue and Fracture Surface, B9A (A36)



Section AA

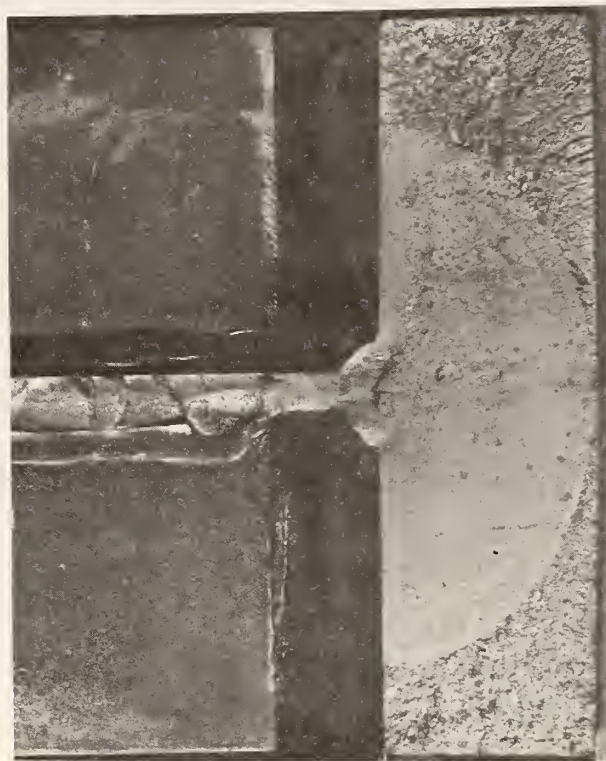
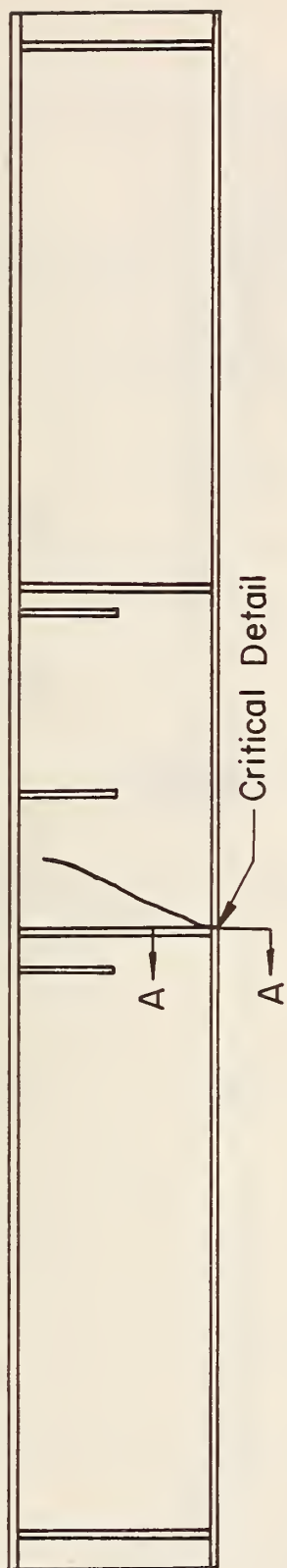
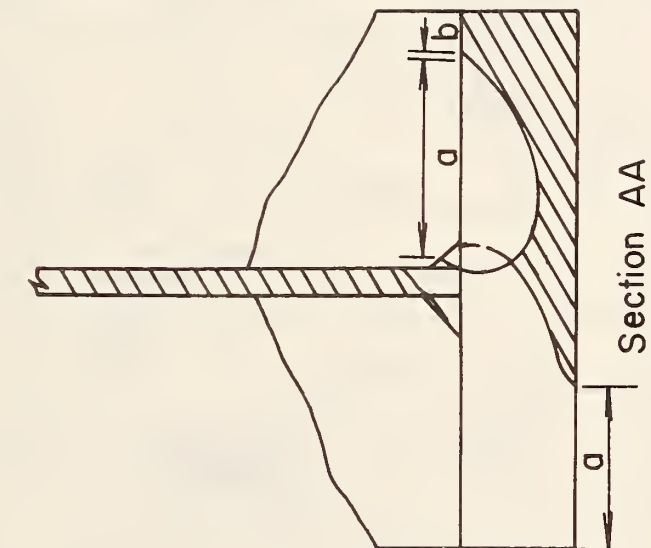


Fig. 7.3 Fatigue and Fracture Surface, B11 (A588)



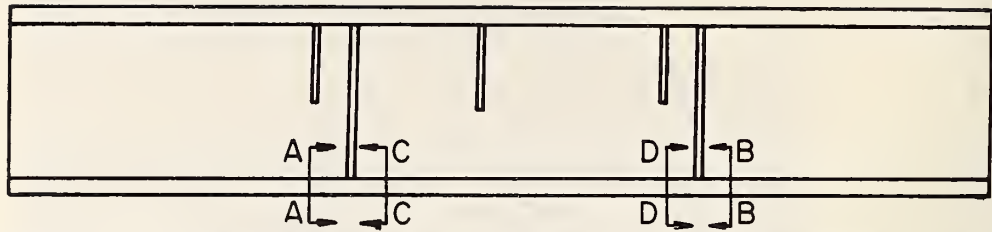
Beam B11A



Section AA



Fig. 7.4 Fatigue and Fracture Surface, B11A (A588)




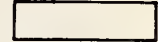
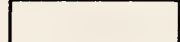
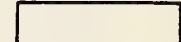
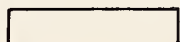
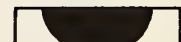
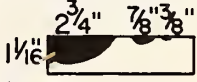

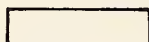
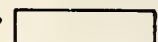

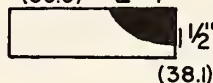
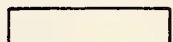

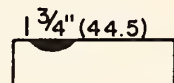
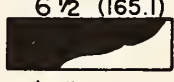
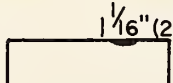
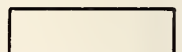
Beam	Section AA		Section BB	
B7	 8.36		 8.36	
B9	 9.56		 9.56	
B11	 3.04		*  3.04	
	Section AA	Section CC	Section DD	Section BB
B7A	* (69.9) (22.2) (9.5)  1 1/16" (27.0) 1.45	 1.45	 1.45	 1.45
B9A	 5.39	* (69.9) 2 3/4"  1 1/2" (38.1) 5.39	 5.39	 5.39
B11A	 1 3/4" (44.5) 1.82	* 6 1/2" (165.1)  2 1/16" (52.4) 1.82	 1 1/16" (27.0) 1.82	 1.82

Table Scale 1 1/2" = 1'-0"

Measurements Taken At Cycles Listed At Bottom
Of Cross Section (in millions of cycles)

* Beam Fractured At This Section

Fatigue Crack Prior To Last Fracture Test

Measurements In Brackets, mm

Fig. 7.5 Fatigue Cracks Prior to Last Fracture Test

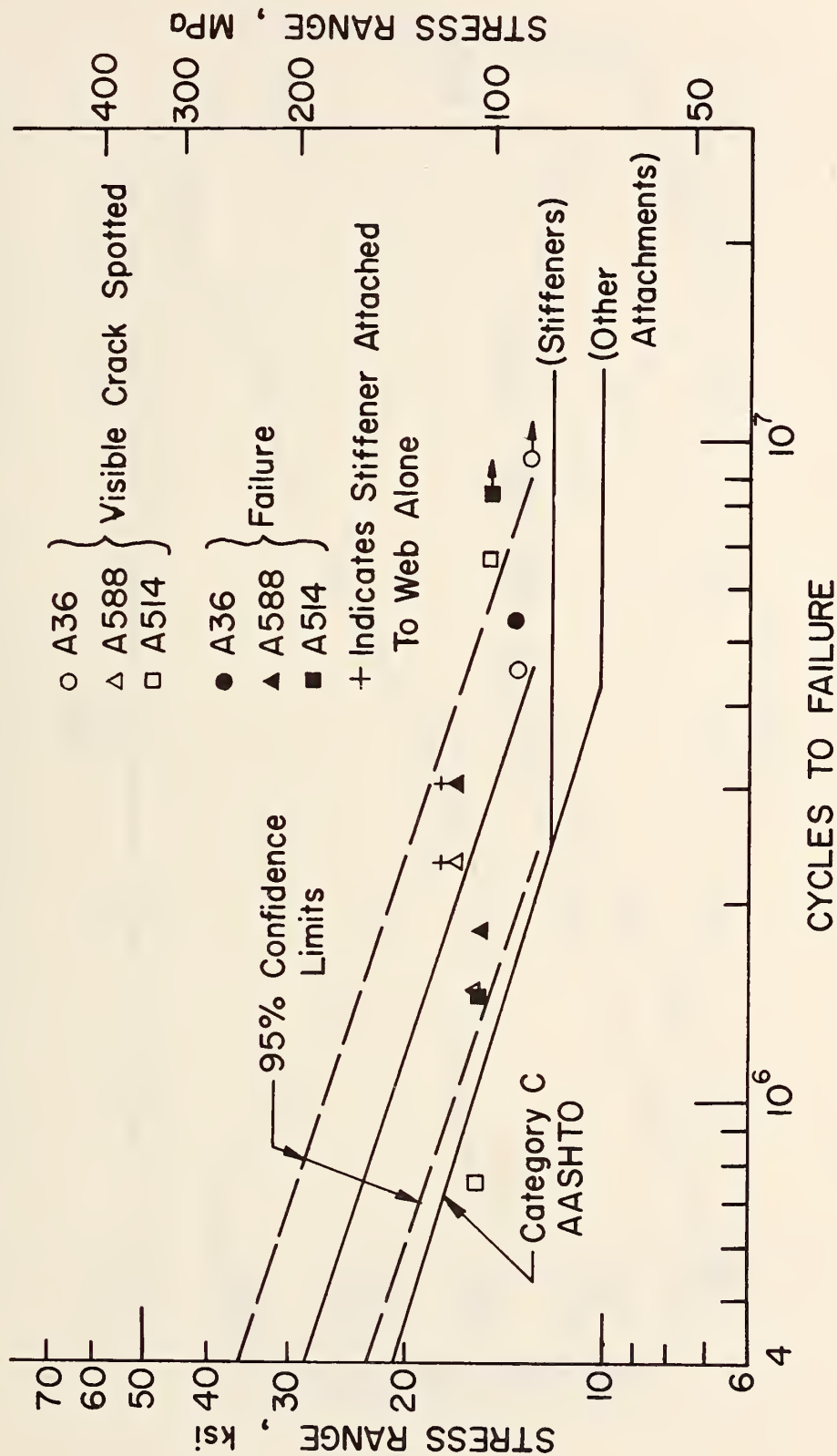


Fig. 7.6 Category C S-N Plot, Transverse Stiffener

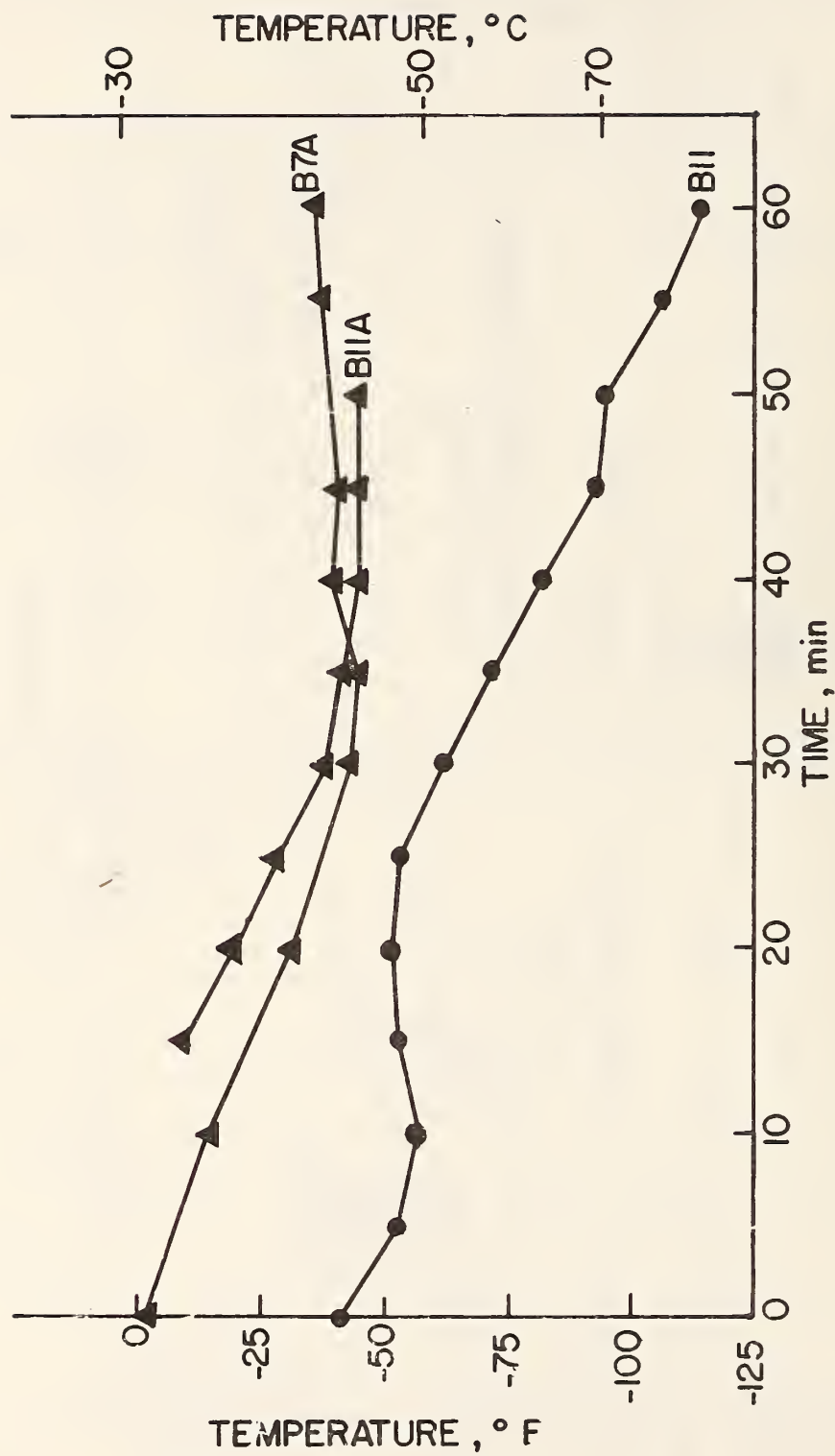


Fig. 7.7 Critical Detail Temperature/Sixty Minutes Prior to Fracture (B7A, B11, B11A)

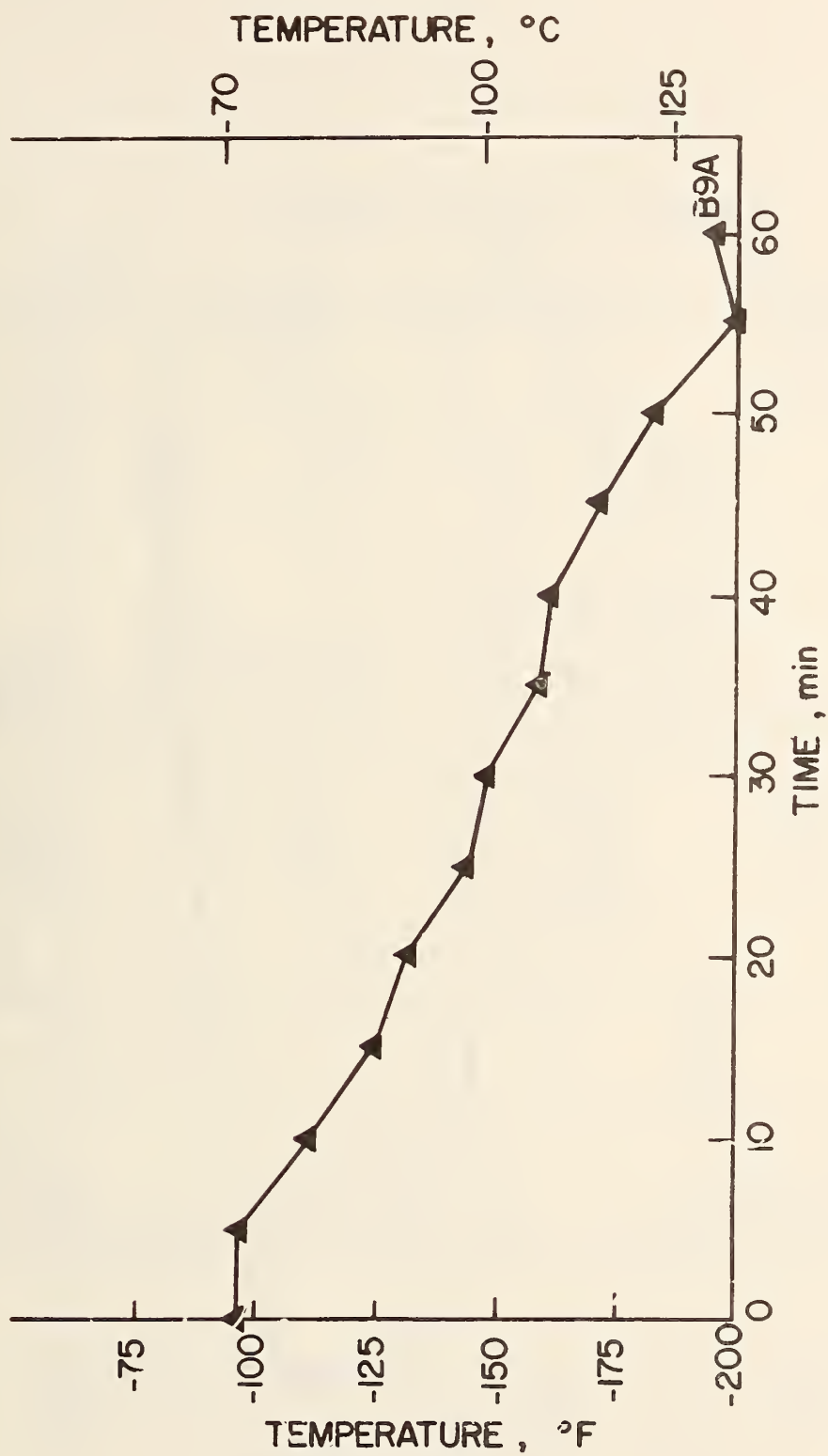


Fig. 7.8 Critical Detail Temperature/Sixty Minutes Prior to Fracture (B9A)



Fig. 7.9 Stress Intensity vs. Crack Size (B9)

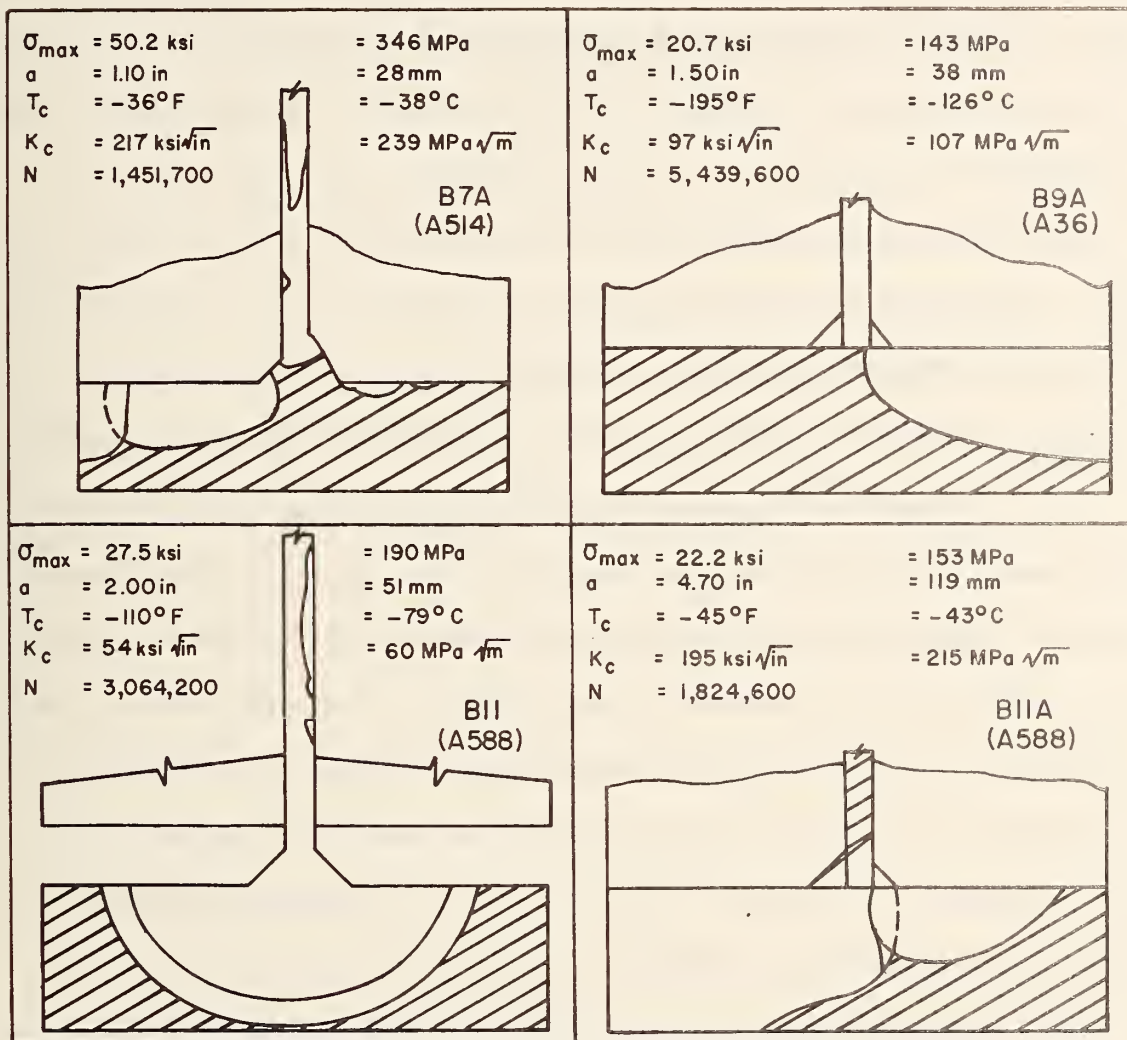


Fig. 7.10 Fracture Surface Sketches and Data Summary

8. COMPARISON OF BEAM K ESTIMATES AND MATERIAL K_{IC} TESTS

8.1 Lateral Attachment Details

The beam fracture stress intensity estimates were correlated with the static and dynamic material toughness characterizations. Both the A36 and A588 beam fractures occurred at temperatures in the transition temperature region of the slow bend K_{IC} material tests. As can be seen in Figs. 8.1 to 8.3 there is a very good correlation between the beam K estimates and the slow bend material tests. Both A514 beam fractures occurred at temperatures below the slow bend curve transition temperature region. The beam stress intensity estimates, however, were conservative since these points were above the K_{IC} value.

The good correlation between the beam stress intensity estimates and the slow bend K_{IC} material tests can be attributed to their similar loading rates. As discussed in Section 2.9, the beam fracture test loading rate was between 70 and 100 ksi/sec. and occurred as the crack front was being advanced under cyclic loading. The slow bend, three-point bend specimens were loaded at a rate of 20 kips/sec. which is 55 ksi/sec. at the crack tip. The dynamic K_{ID} specimens were fractured in approximately 1×10^{-3} .

Also plotted in Figs. 8.1 to 8.3 are the beam stress intensity estimates from the applied stress alone (K_{AS}). There is good correlation between K_{AS} for Beams B2, B2A, B4A, and B6A and their respective slow bend material test results. This demonstrates that in

these tests, the residual stresses from welding and flame cutting did not significantly alter the fracture resistance. However, the contribution to the stress intensity estimate from the residual stress field, K_{RS} should be considered when the crack tip is in the high tensile residual stress region of the web-to-flange welds. This can readily be seen in Figs. 4.3 and 4.5 for Beams B4 and B6, respectively. Both of these beams had a contribution from K_{RS} which was greater than 50% of K_{AS} .

The K_{Id} value estimated from Eq. 6 for the AASHTO minimum Charpy V-Notch value is also plotted in each figure at the applicable test temperature. Also plotted in each figure is the temperature shift corresponding to the minimum service temperature condition. It is visually apparent from each comparison that large cracks comparable to those observed in this study would be necessary for brittle fracture to occur. All beams would fail in a region where rapid increases in fracture toughness is taking place. The crack sizes provided by beams B4, B4A, B6A and B2 and B2A would be indicative of the minimum critical crack size at these details.

8.2 Cover Plate Details

The cover-plated beam stress intensity estimates at fracture were correlated with the static and dynamic fracture toughness characterizations. Beams B1A (A514), B3, B3A (A36, rolled) and B5A (A588, rolled) fractured at temperatures in the transition region of the slow bend K_{IC} material tests. As can be seen in Figs. 8.4 to 8.6 there is

good correlation between the predicted stress intensity estimates, K , and the static material test curve.

Both B1 (A514) and B5 (A588, rolled) fractured at temperatures lower than the transition temperatures for the slow bend material tests. The stress intensity estimate, K , for Beam B5 was slightly below with the K_{IC} material tests results (see Fig. 8.5). However, the stress intensity estimate, K , for Beam B1 was quite conservative (see Fig. 8.6).

With the exception of Beam B3, the stress intensity estimates of beam fractures which precipitated from the large fatigue cracks in Beams B1, B1A, and B3A, were adequately predicted by K_{AS} alone (see Figs. 8.4 and 8.6). The stress intensity estimates of beams which fractured from small elliptical cracks (Beams B5 and B5A) were best estimated by including all of the residual stress contributions, K_{RS} and K_{LW} (see Fig. 8.5).

The K_{Id} value estimated from Eq. 6 for the minimum AASHTO CVN value and the vertical line representing the temperature shift used in the AASHTO Specification again show that rapid increases in fracture toughness can be expected at the minimum AASHTO Charpy V-Notch values. The crack sizes provided by beams B3, B5A and B1 would be most indicative of the minimum critical crack size at these details.

8.3 Flange Transition Details

The flange transition stress intensity estimates were also correlated with the static and dynamic material toughness. Both the A36 and A514 beam fractures occurred at temperatures in the transition temperature region of the slow bend K_{IC} material tests. As can be seen in Figs. 8.7 and 8.9, there is good correlation between the predicted stress intensity estimates, K , and the slow bend material tests. The A588 beam fracture (B12A) occurred at a temperature below the slow bend curve transition region. However, the stress intensity estimate is conservative.

All fractures initiated from large fatigue cracks. With the exception of Beams B10 and B10A, the stress intensity estimates at fracture were adequately predicted from the applied load, K_{AS} , alone (see Figs. 8.8 and 8.9). The stress intensity estimates for Beams B10 and B10A were improved by including all the residual stress contributions (see Fig. 8.7).

The beam fracture toughness was in good agreement with the slow bend K_{IC} material test results. Again, this can be attributed to the similarities in the loading rates and the reasonableness of the critical K estimates.

The K_{Id} value estimated from Eq. 6 for the minimum AASHTO CVN value and the vertical lines which show the temperature shift used in the AASHTO specifications indicate that fracture would be expected to occur as the fracture toughness started to increase rapidly. The

crack size provided by beam B12A would be indicative of the minimum critical crack size at these details.

8.4 Transverse Stiffener Details

The transverse stiffener stress intensity estimates were correlated with the static and dynamic material toughness. Beams B7A (A514) and B11A (A588) fractured at temperatures in the transition region of the slow bend K_{IC} material tests. As can be seen in Figs. 8.11 and 8.12, there is good correlation between the predicted stress intensity estimates, K and the material tests.

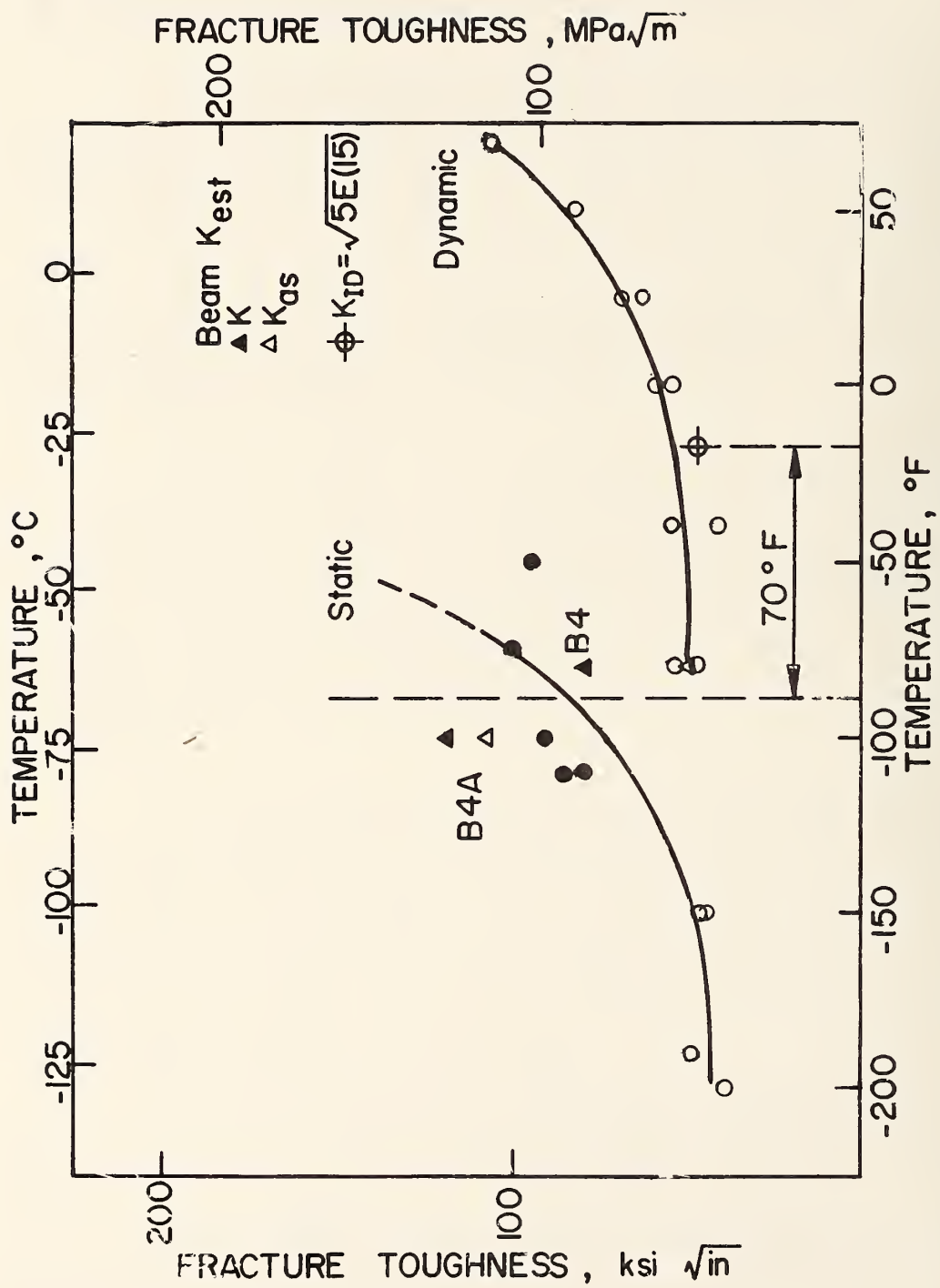
Beams B11 (A588) and B9A (A36) fractured at temperatures below the transition region of the slow bend K_{IC} material tests. The stress intensity estimate, K , for Beam B11 was in good agreement with the K_{IC} material test results (see Fig. 8.11). However, the stress intensity estimate, K , for beam B9A was very conservative (see Fig. 8.10).

The stress intensity estimate due to applied stress, K_{AS} , was in good agreement with the material resistance for beams B9A and B11 (see Figs. 8.10 and 8.11). The stress intensity estimates for Beams B7A and B11A were improved by including all the residual stress contributions (see Figs. 8.11 and 8.12).

Again the beam fracture toughness was in good agreement with the slow bend K_{IC} material test results.

The K_{Id} value estimated from Eq. 6 for the minimum AASHTO CVN value and the vertical lines which show the temperature shift

used in the AASHTO specifications indicate that the crack sizes provided by beam B11 would be indicative of the minimum critical crack size at these details. Edge cracks between B9A and B11A would also be typical.



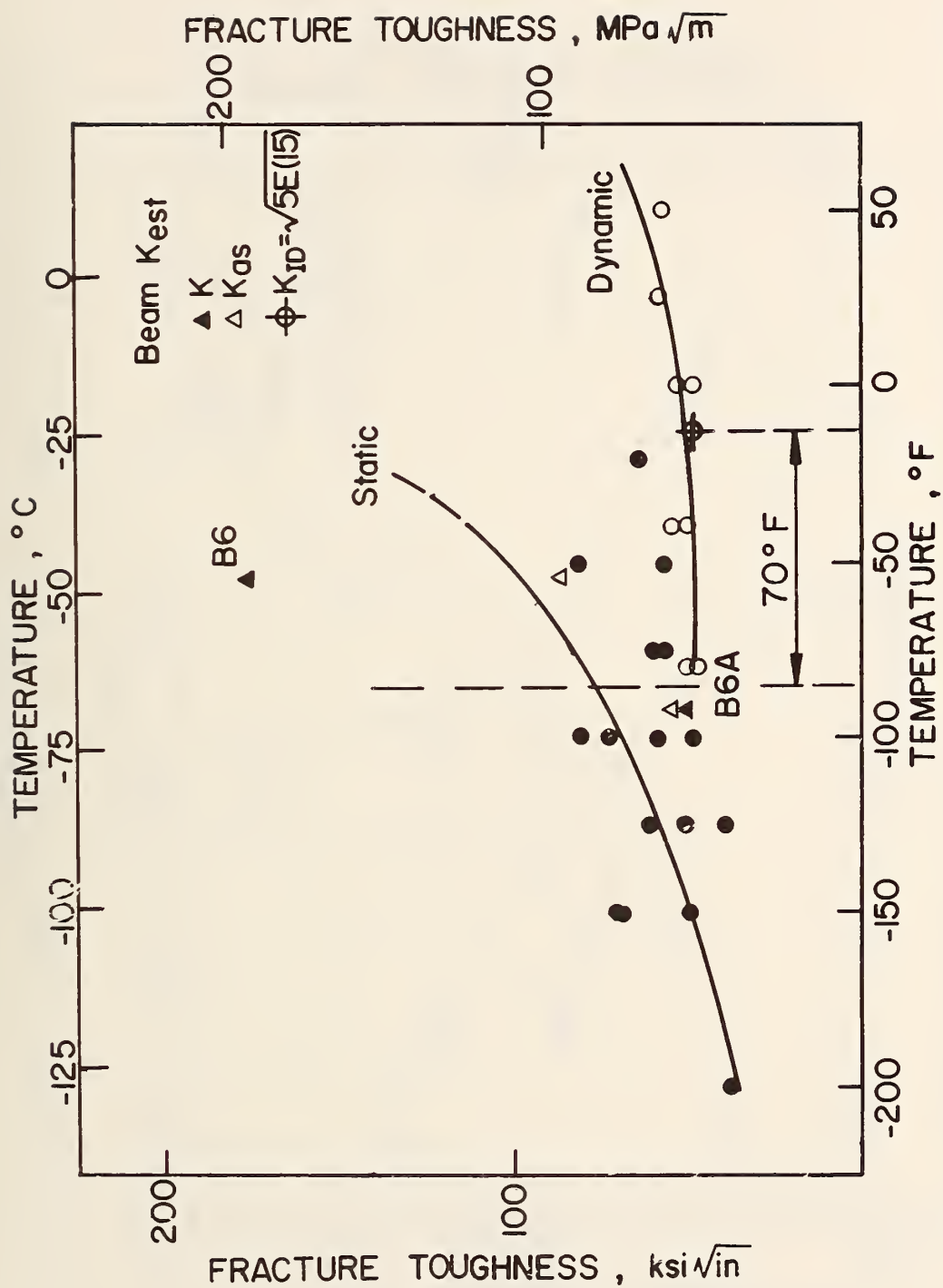


Fig. 8.2 Correlation of Beam K_{est} and Material Toughness Characterization, B6, B6A (A588)

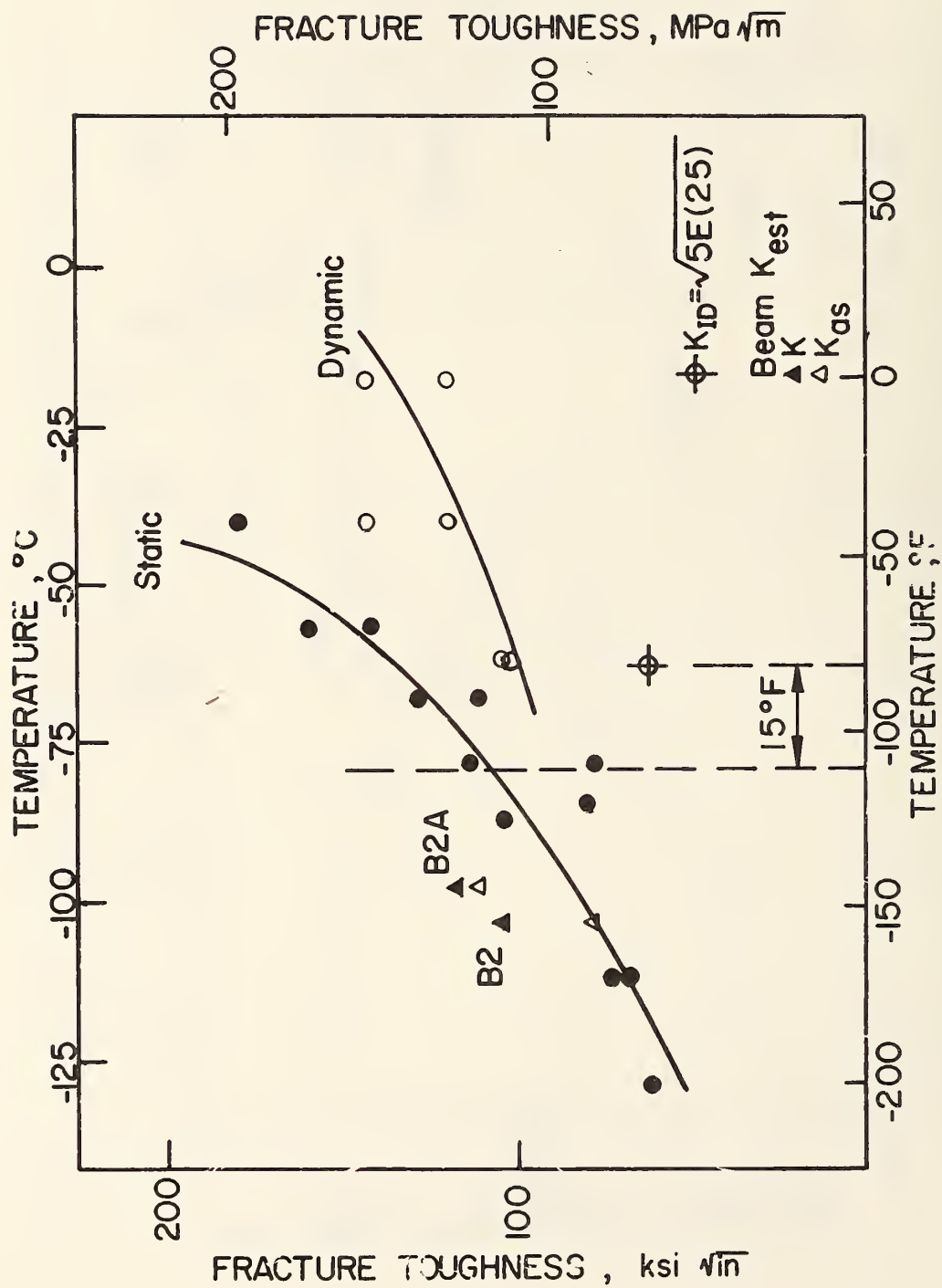


Fig. 8.3 Correlation of Beam K_{est} and Material Toughness Characterization, B2, B2A (A514)

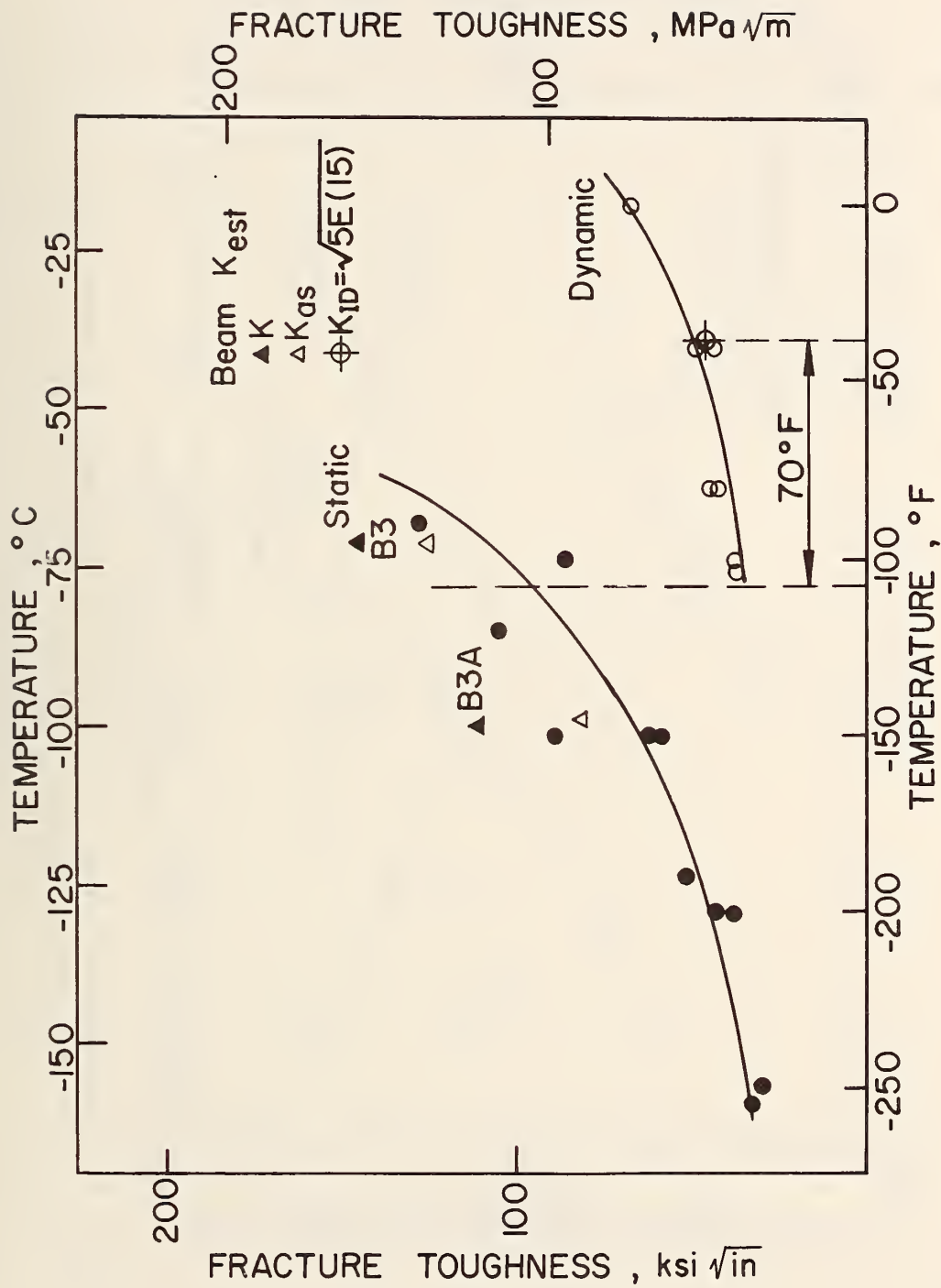


Fig. 8.4 Correlation of Beam K_{est} and Material Toughness Characterization, B3, B3A (A36, Rolled)

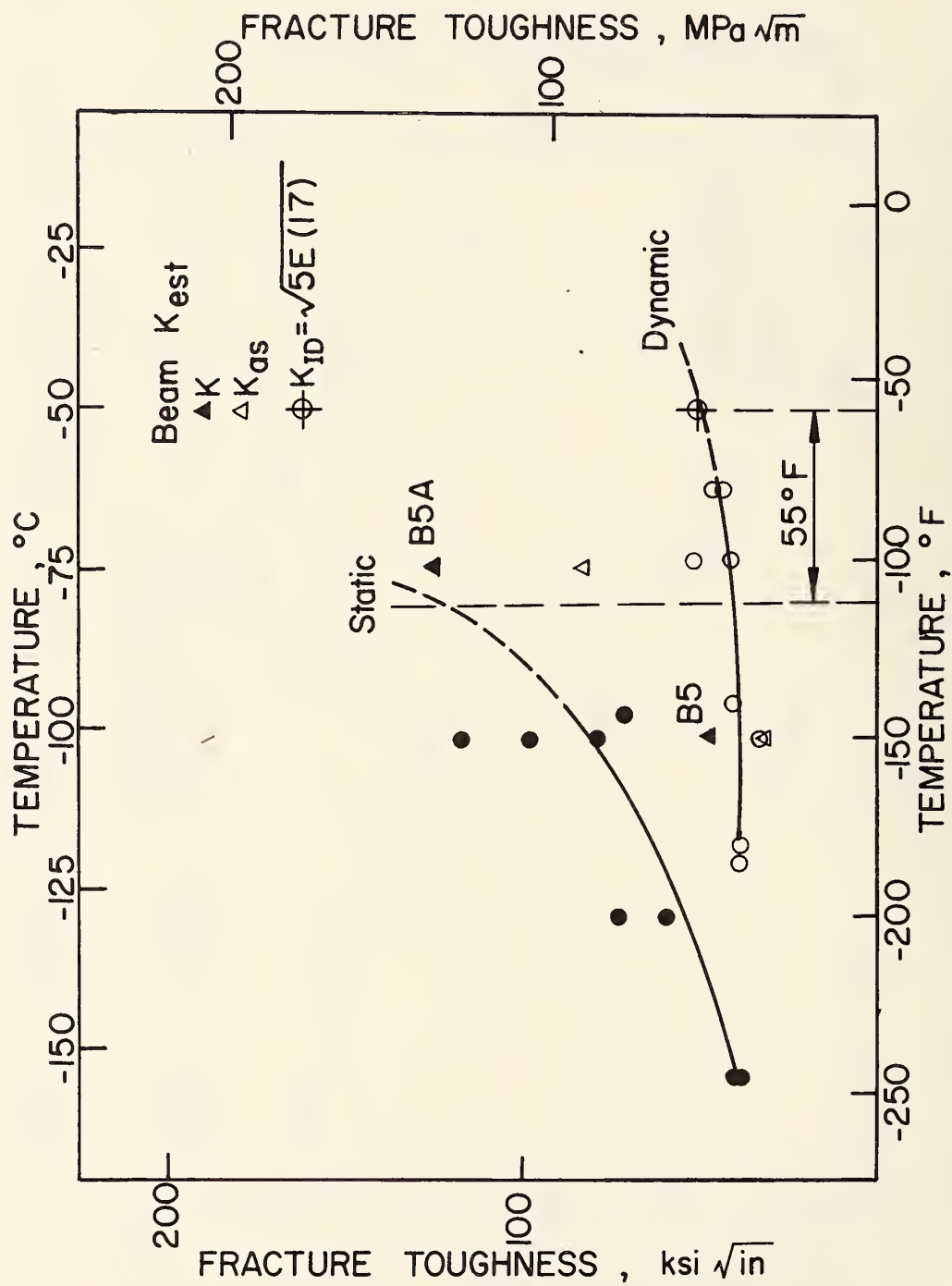


Fig. 8.5 Correlation of Beam K_{est} and Material Toughness Characterization, B5, B5A (A588, Rolled)

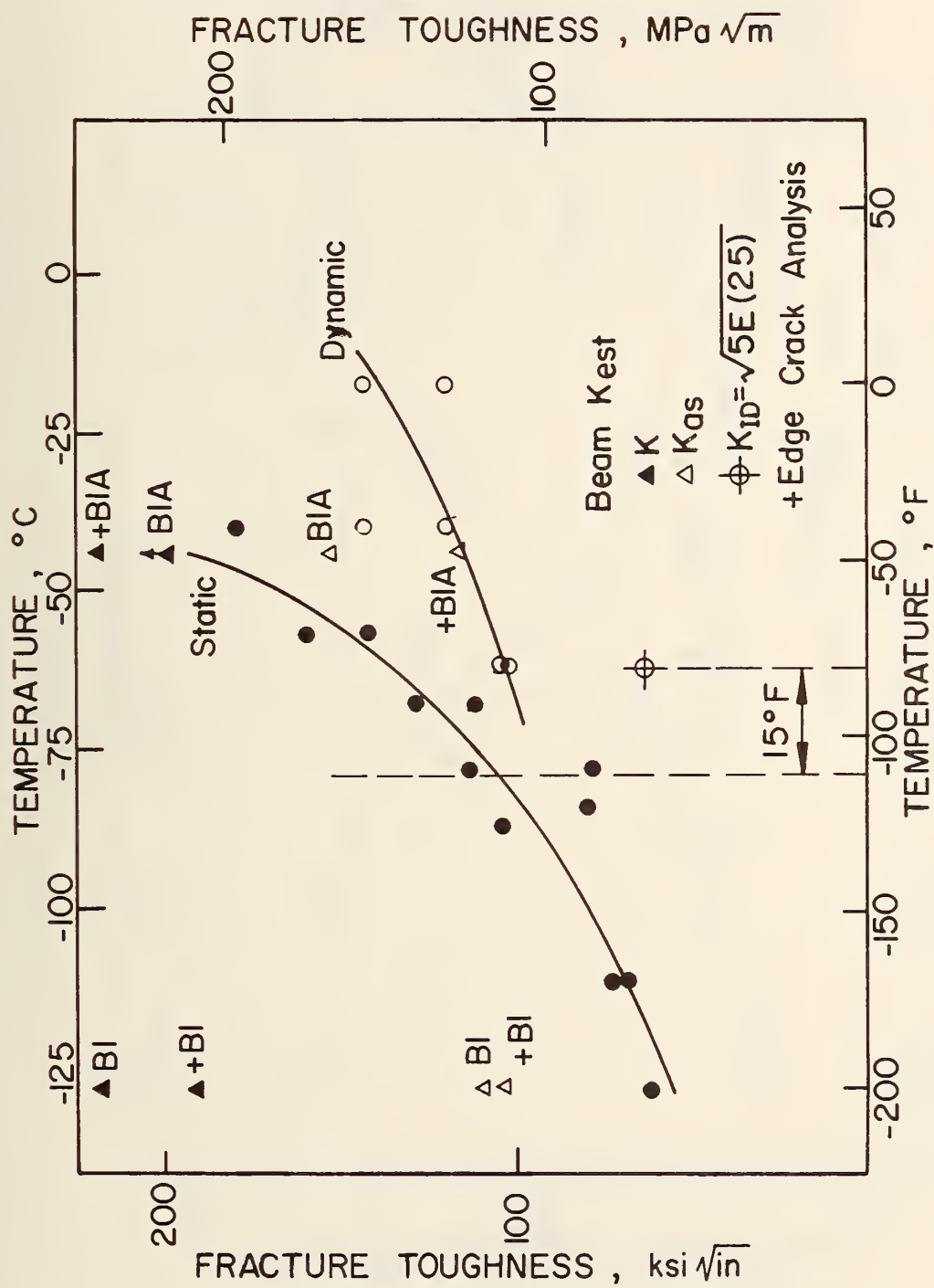


Fig. 8.6 Correlation of Beam K_{est} and Material Toughness Characterization, B1, B1A (A514)

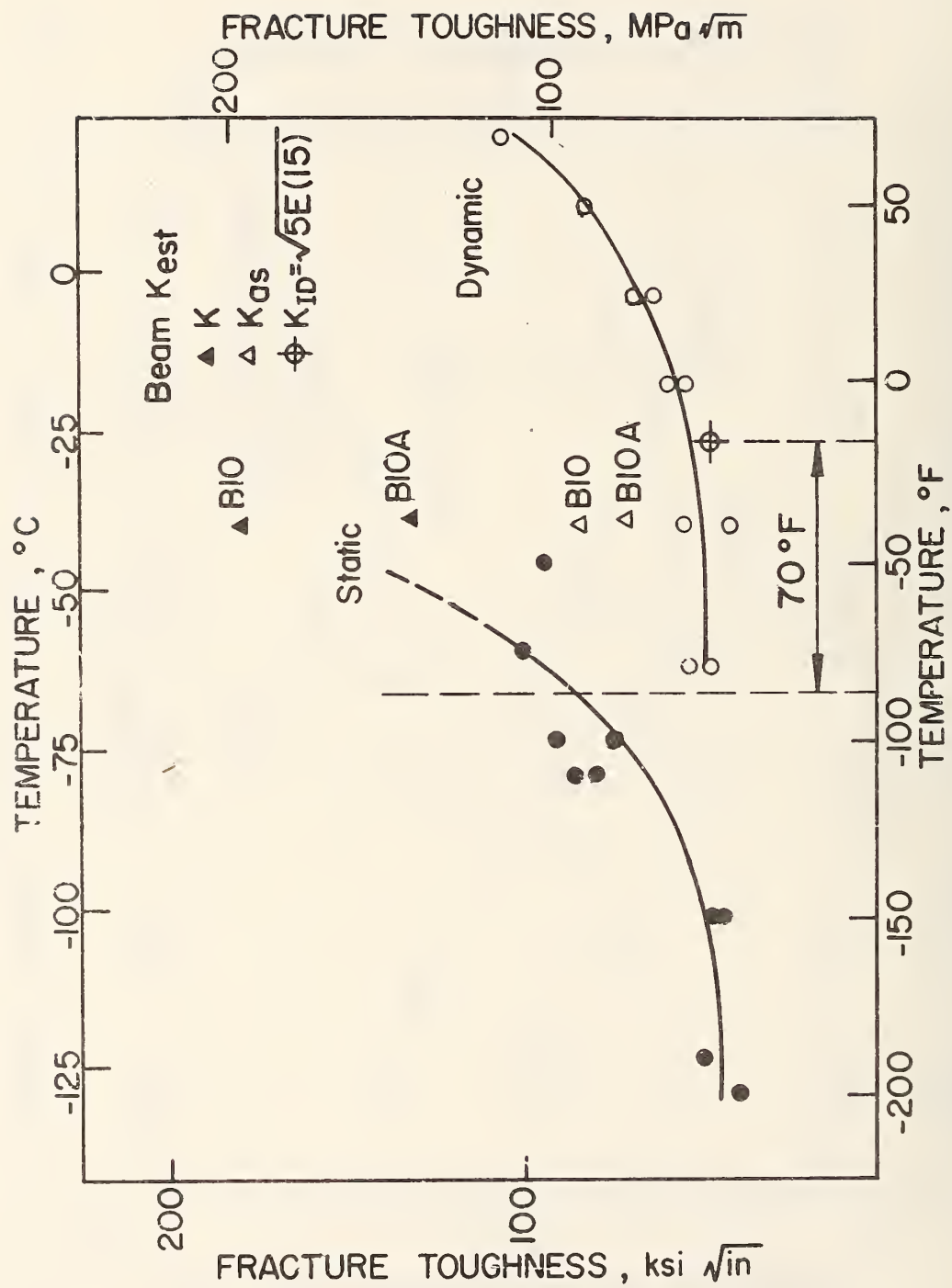


Fig. 8.7 Correlation of Beam K_{est} and Material Toughness Characterization, B10, B10A (A36)

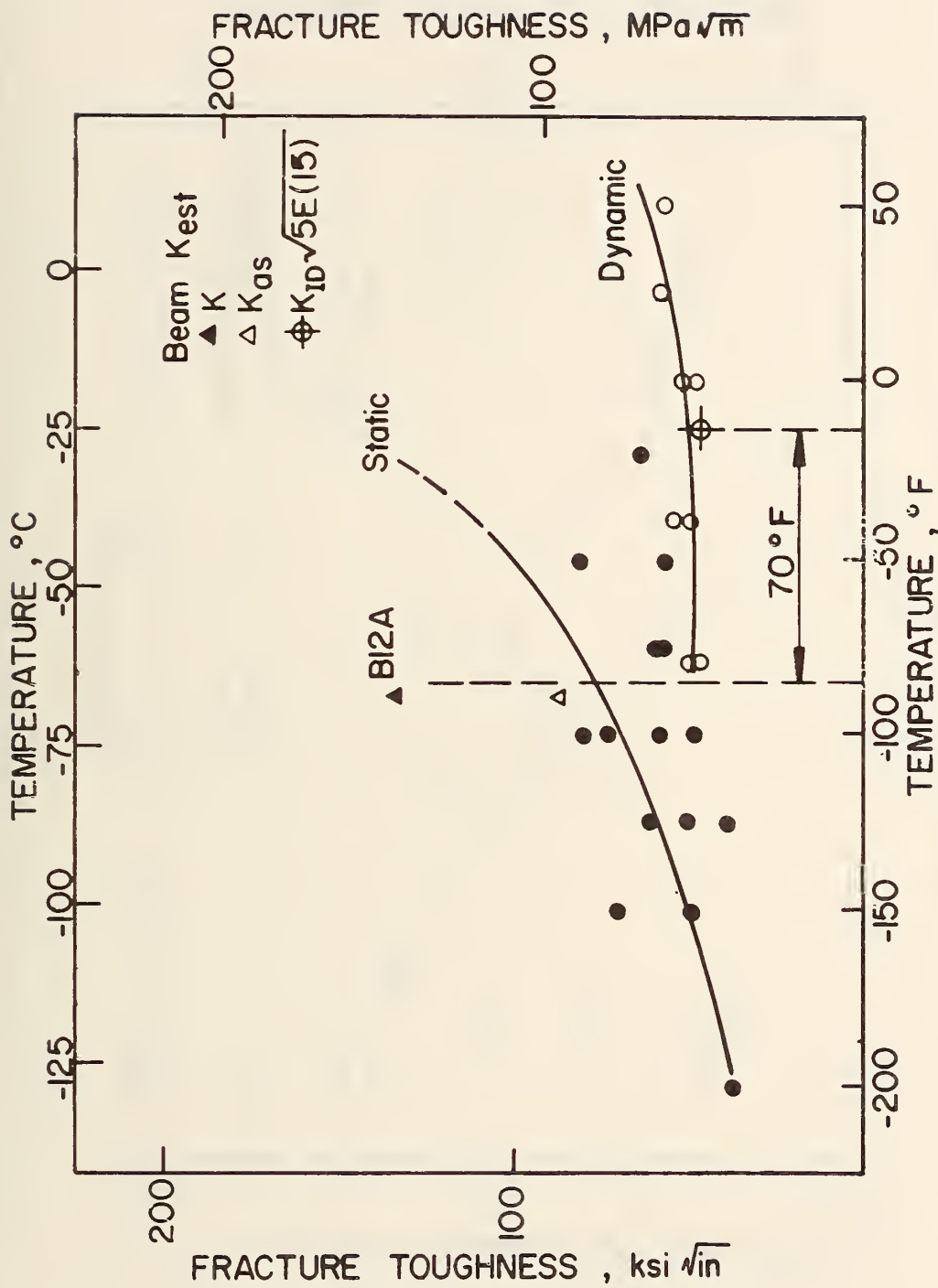


Fig. 8.8 Correlation of Beam K_{est} and Material Toughness Characterization, B12A (A588)

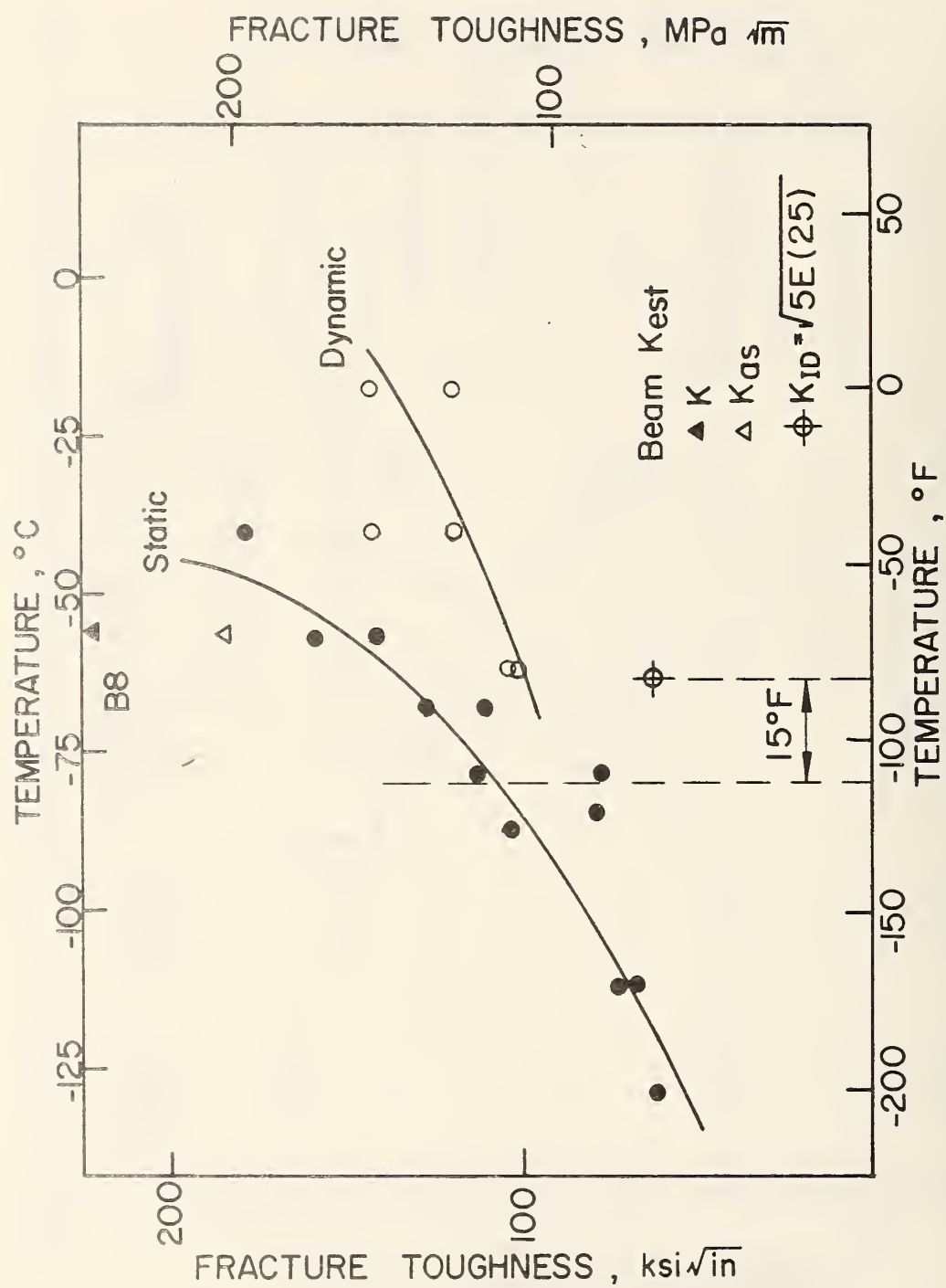


Fig. 8.9 Correlation of Beam K_{est} and Material Toughness Characterization, B8 (A514)

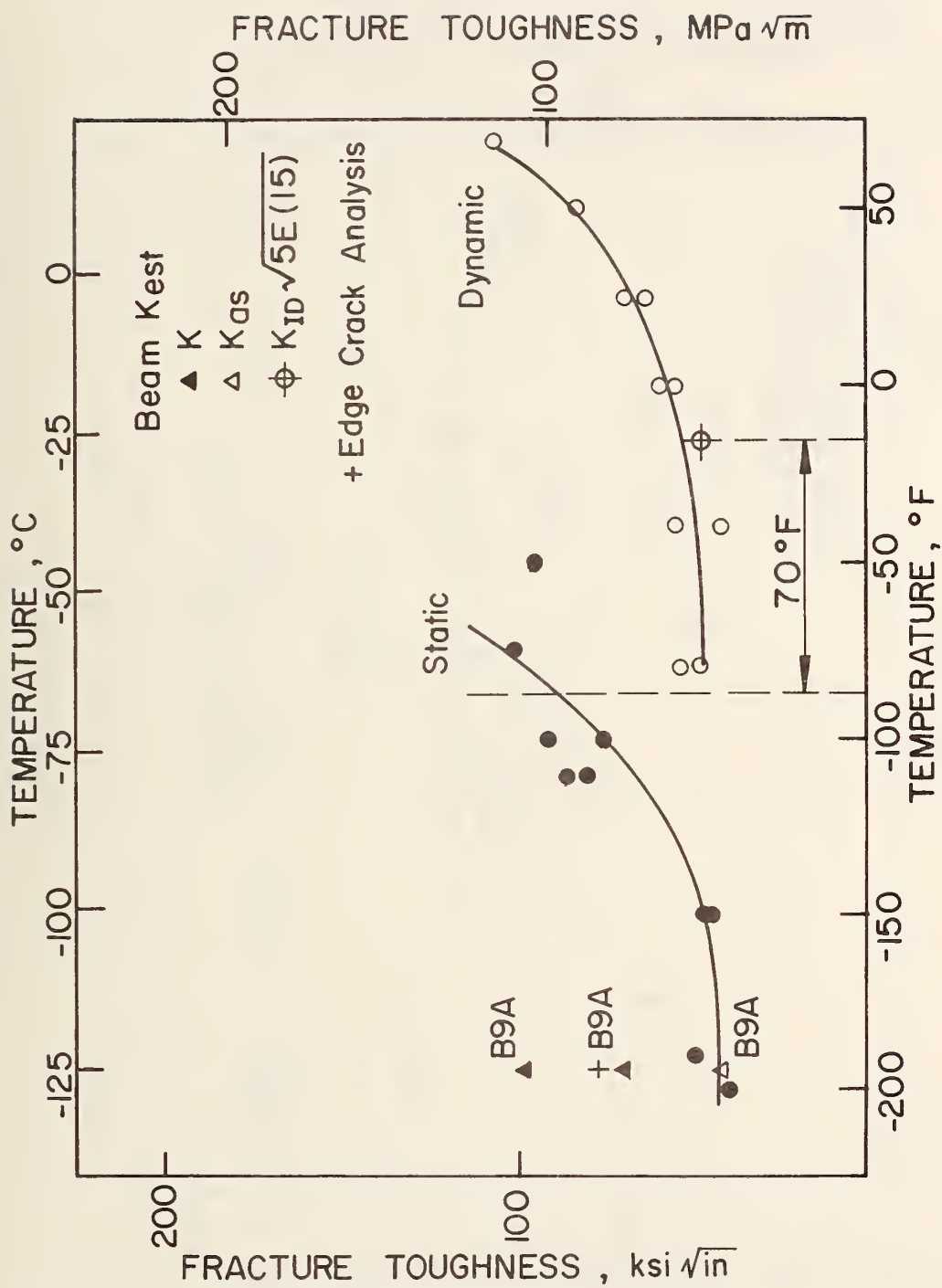


Fig. 8.10 Correlation of Beam K_{est} and Material Toughness Characterization, B9A (A36)

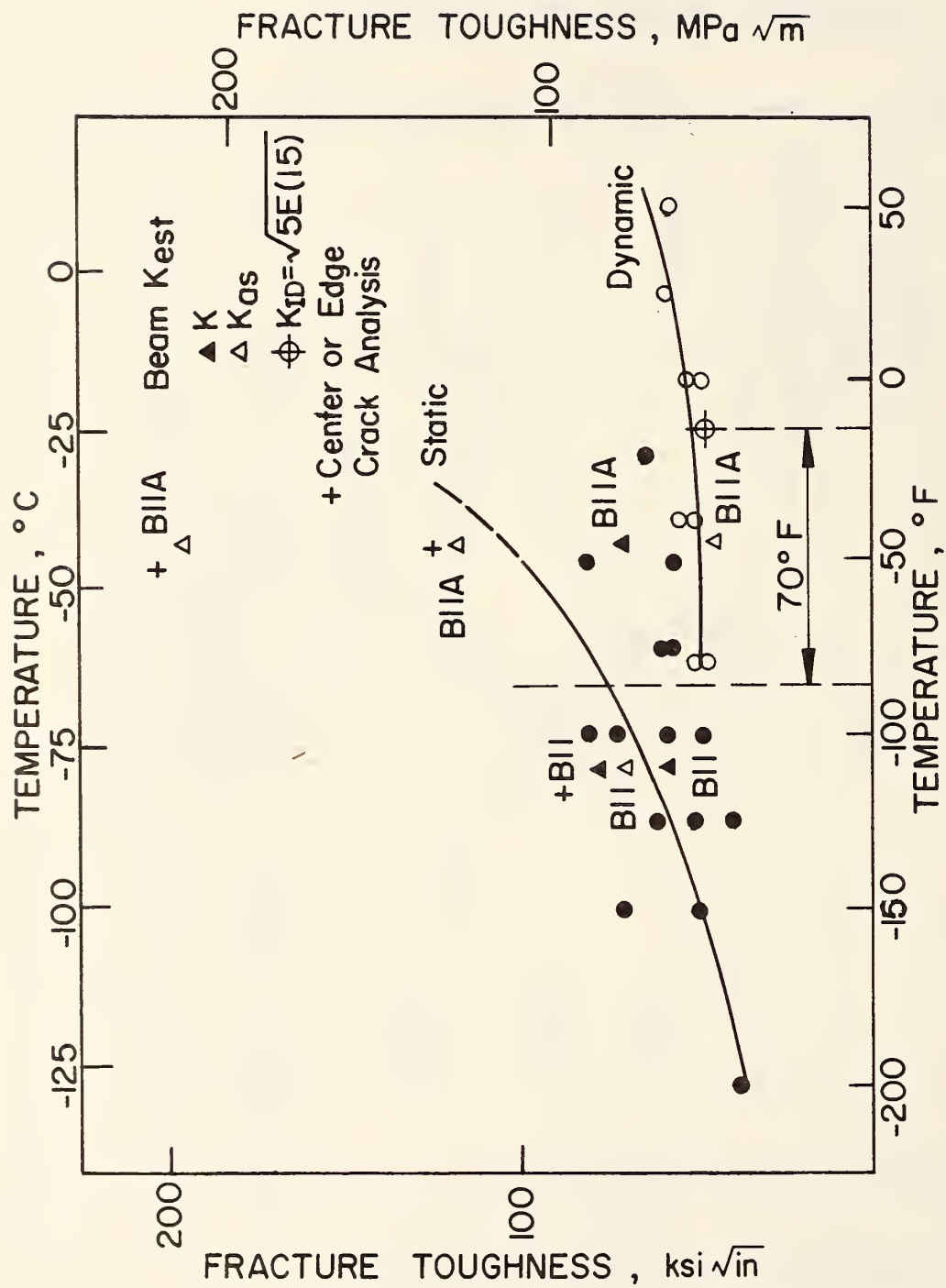


Fig. 8.11 Correlation of Beam K_{est} and Material Toughness Characterization, BII, BIIA (A588)

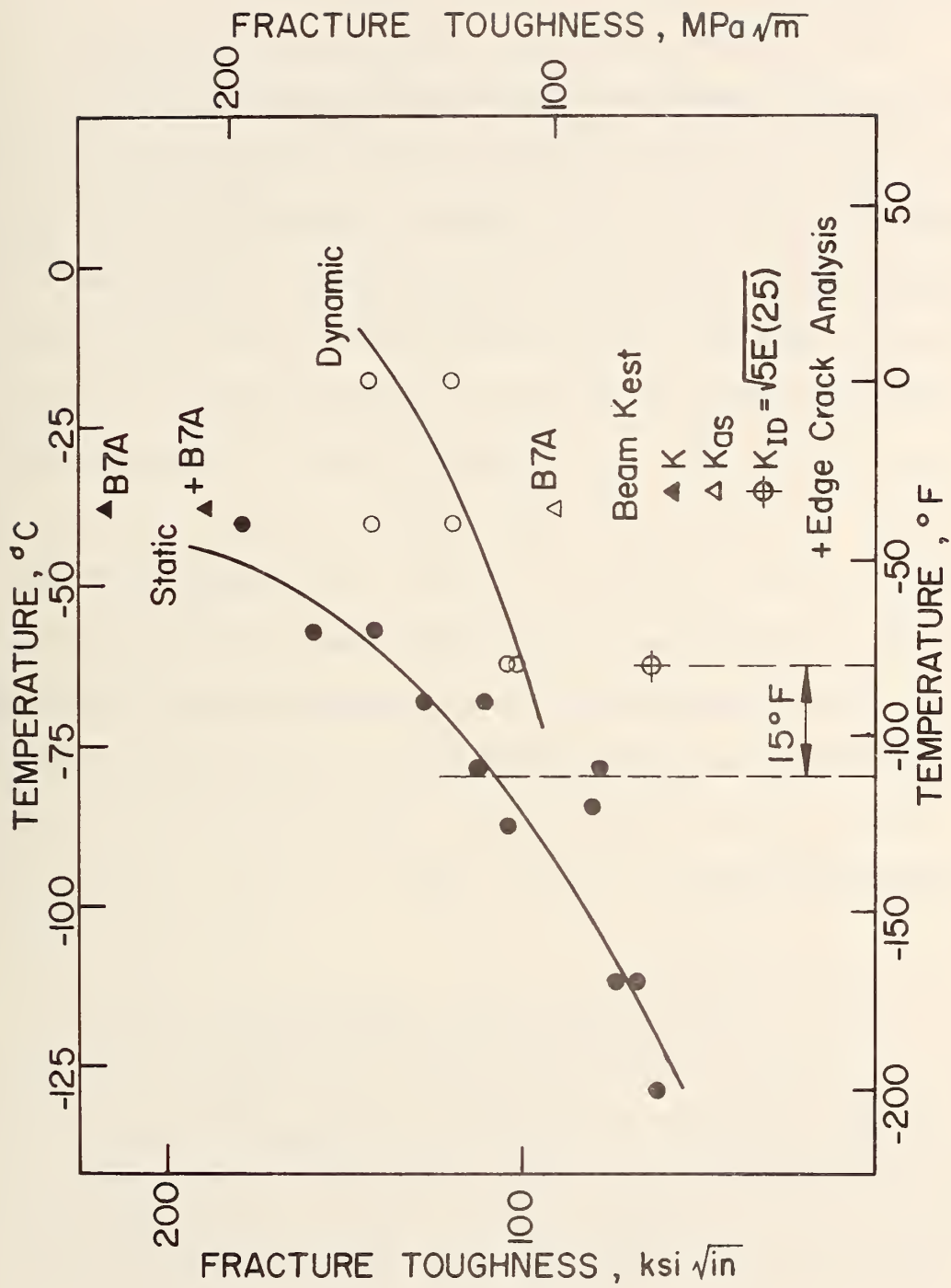


Fig. 8.12 Correlation of Beam K_{est} and Material Toughness Characterization, B7A (A514)

9. GUSSET PLATE TESTS

9.1 Introduction

The objective of the gusset plate tests is to correlate fracture of a full size gusset detail with current material characterization tests. One specimen was fabricated from each grade of steel (A36, A588, and A514) from material from the same heats of steel used in the beam tests. The gussets were preloaded with a longitudinal axial stress to simulate the dead load stresses in a truss type structure. After preloading, the gussets were cyclically loaded at room temperature until visibly fatigue cracked and then at a temperature of -40° F (-40° C) and lower until rapid fracture occurred. The cyclic loading was intended to simulate the primary and secondary live load stresses that are generated at truss connections. The fracture resistance of each precracked gusset section was estimated using linear Elastic Fracture Mechanics and compared to the material toughness results.

9.2 Description of Tests

9.2.1 Test Specimens

The three gusset specimens were fabricated by Air Products and Chemicals in Wilkes-Barre, Pennsylvania. All specimens were fabricated using AWS fabrication and inspection techniques. A detailed drawing of the test specimens is shown in Fig. 9.1. The longitudinal tabs welded to the gusset were intended to simulate the flanges of a

box and introduce the residual stress distribution that would normally be found in the corners of a box section. The gusset transition was ground to a short radius (0.25 in., 6.4 mm) so that pre-cracking could be achieved quickly.

After the gusset components were cut to size, they were assembled and the longitudinal and transverse groove welds were made by an automatic submerged-arc process. Any visible flaw in the longitudinal welds such as excessive porosity was gouged out and rewelded. The transverse welds were X-ray inspected and any defects that violated the AWS Specification were repaired. The gusset assemblies were also straightened prior to testing.

9.2.2 Preloading

Each gusset assembly was preloaded in the 5000 kip (22.3 MN) Baldwin universal testing machine at Lehigh University (see Fig. 9.2). The end 2.5 ft. (0.8 m) of each end of the gusset was used to grip the specimen in the testing machine. The A36, A588, and A514 gussets were preloaded to 410 kip (1.8 MN), 700 kip (3.1 MN), and 950 kip (4.2 MN), respectively.

After preloading, 3 in. (76.2 mm) spacer plates were placed on both sides of the gusset in the bolted connection region. A WT18X130 beam was then bolted to each side of the gusset assembly. High strength A490 bolts and blast cleaned faying surfaces were used to insure a slip resistant joint. The load applied by the testing machine was released after bolt installation. A residual tensile

preload stress of 8.8 ksi (60.7 MPa), 21.8 ksi (150.3 MPa), and 34.0 ksi (234.4 MPa) was measured for the A36, A588, and A514 gussets, respectively.

9.2.3 Fatigue Testing

The fatigue testing was conducted on the dynamic test bed in Fritz Laboratory, Lehigh University. Two 55 kip (244.8 kN) Amsler jacks driven by a single pulsator were used to apply 260 cpm (4.3 Hz) cyclic load.

A plate was bolted perpendicular to the longitudinal axis of the gusset assembly. The other end of the plate was pin connected to the floor. The amsler jacks were positioned to react against the floor as shown schematically in Fig. 9.3.

9.2.4 Fracture Testing

A copper tubing network was placed adjacent to the fatigue cracked detail and the entire cross-section was enclosed in a styro-foam box. The gusset temperature was reduced by controlled pumping of liquid nitrogen into the tubing network. Electrical resistance temperature gages were used to monitor the gusset plate temperature.

When the gusset temperature reached approximately -40° F (-40° C), cyclic load was reapplied. The temperature was then lowered until rapid fracture occurred.

9.3 Test Results

9.3.1 Fatigue and Fracture Test

A36 Steel Gusset Plate

The stress range recorded at the gusset transition was 7.1 ksi (49.0 MPa) and 6.5 ksi (44.8 MPa) for the east and west details, respectively. The first fatigue crack was detected at 0.82 million cycles as a 0.3 in. (8.0 mm) long elliptical surface crack at the west detail. No cracking was observed at the east detail.

The fracture test was conducted at the west detail after 1.22 million cycles. The detail was cooled to -40° F (-40° C) and cyclic load was continued. The temperature was incrementally lowered until fracture occurred at -82° F (-63° C). At the time of fracture, the quarter-elliptical crack was 1.08 in. (27.4 mm) deep and 1.60 in. (40.6 mm) long. A photo of the fractured gusset and the fracture surface is shown in Fig. 9.4. Fracture occurred at 1.23 million cycles. The maximum applied stress at the transition was 15.4 ksi (106.2 MPa).

A588 Steel Gusset Plate

The stress range recorded at the gusset transition was 7.7 ksi (53.1 MPa) and 7.9 ksi (54.5 MPa) for the east and west detail, respectively. The first fatigue crack was observed at 1.04 million cycles as a 0.20 in. (5.1 mm) long elliptical surface crack at the

east detail. A 0.47 in. (11.9 mm) long elliptical crack was also observed at 1.65 million cycles at the west detail.

The fracture test was conducted at the west detail after 1.65 million cycles. The detail was initially cooled to -30° F (-34° C) and cyclic loading was continued. The temperature was incrementally lowered until fracture occurred at -110° F (-79° C). At the time of fracture the quarter-elliptical crack was 0.92 in. (23.4 mm) deep and 1.66 in. (42.2 mm) long. A photo of the fractured gusset and the fracture surface is shown in Fig. 9.5. Fracture occurred at 1.68 million cycles. The maximum applied stress at the transition was 30.0 ksi (206.9 MPa).

A514 Steel Gusset Plate

The stress range recorded at the gusset transition was 7.3 ksi (50.3 MPa) and 6.2 ksi (42.7 MPa) for the east and west detail, respectively. The first fatigue crack was observed at 0.32 million cycles as a 0.12 in., (3.0 mm) deep elliptical corner crack at the east detail. A 0.31 in. (7.9 mm) long elliptical surface crack was observed after 0.77 million cycles at the west detail.

The fracture test was conducted at the east detail after 0.88 million cycles. The detail was first cooled to -66° F (-54° C) and cyclic loading was continued. Fracture occurred after a few additional minutes of cyclic loading. At the time of fracture the quarter-circular crack was 1.88 in. (47.8 mm) deep. A photo of the

fractured gusset and the fractured surface is shown in Fig. 9.6. The maximum applied stress at the transition was 41.3 ksi (284.8 MPa).

9.3.2 Stress Intensity Estimates

9.3.2.1 Contribution from Applied Stress

The stress intensity factor for the elliptical crack shapes is defined by Eq. 11 (see Section 4.5.2). The applied stress was taken as the average applied stress over the crack. The fatigue cracking did not significantly decrease the preload stress. The factor,

$$F(a) = F_E F_G F_S F_W$$

can be determined for the elliptical cracks encountered at the gusset detail using the relationships:

F_E = crack shape correction

$$\text{where } F_E = \frac{1}{E_k} [1 - k^2 \cos^2 \phi]^{1/4}$$

E_k , k , and ϕ are defined in Fig. 5.12

F_G = stress concentration correction

F_S = free surface correction

F_W = finite width correction

For this study F_G was set equal to 1.0 since the stress concentration effect was expected to decay rapidly from the gusset transition for the large crack sizes. F_W was also set equal to 1.0.

The stress intensity estimate for each fracture was made at $\phi = 45^\circ$. The F_s correction was defined by the following equation for a quarter-circular crack in a uniform stress field⁴:

$$F_s = 1.38 - 0.29 \sin 2\phi \quad (28)$$

Therefore, at 45° F_s equals 1.09.

9.3.2.2 Contribution from Residual Stress

The computer program described in Section 5.4.4 was used to calculate the stress intensity contribution due to residual stress. The assumed residual stress distribution for the gusset assembly at the critical cross-section is shown in Fig. 9.7. E70 electrode was used in the gusset welds. Due to configurational constraint, the size of the groove welds, and the elevated yield strength of the E70 electrode deposits, the A36 yield stress was assumed to be 95% of the A588 mill report yield strength. The yield stress for the A588 and A514 residual stress distribution was taken as 95% of the mill report yield values listed in Table 3.1.

9.3.2.3 Summary and Discussion of Contributions

The values of K , K_{AS} , and K_{RS} are summarized in Fig. 9.8 for each gusset specimen. No plastic zone corrections were used. The estimate of K_{RS} was checked by numerically integrating a uniform stress over the same crack mesh. The stress intensity values obtained were compared with the stress intensity results from the solution

presented in Section 5.4. The values of K_{RS} were factored by the error found in the integrated uniform stress solution. This correction required the reduction of K_{RS} by approximately 65%.

The residual stress contribution to stress intensity factor was larger than the applied stress contribution for the A36 and A514 gusset plates. The applied stress contribution was only slightly larger than the residual stress contribution for the A588 fracture.

9.4 Comparison of Gusset Plate K Estimates with Material K_C Tests

The gusset fracture stress intensity estimates were correlated with the static and dynamic material toughness characterizations. As can be seen in Figs. 9.9 to 9.11, there is good correlation between the gusset plate K estimates and the slow bend material tests. The residual stress contribution to stress intensity was necessary to obtain good correlation with the test data for the A36 and A514 specimens.

The correlation between the gusset plate stress intensity estimates and the slow bend material tests can be attributed to their similar loading rates, as was the case with all beam tests.

9.5 Conclusions

1. The stress intensity estimates for the gusset plate fractures were best modeled by the slow bend K_{IC} fracture toughness. The gusset plate fracture tests and the slow bend K_{IC} tests had similar loading rates.

2. The residual stress contribution to the stress intensity was approximately equal to the applied stress contribution for these gusset plate specimens.
3. Relatively short fatigue lives were observed for all three gusset specimens. The gusset transitions were ground to a short radius (0.25 in., 6.4 mm). Category E of the current AASHTO fatigue specification overestimates the fatigue strength of this detail.

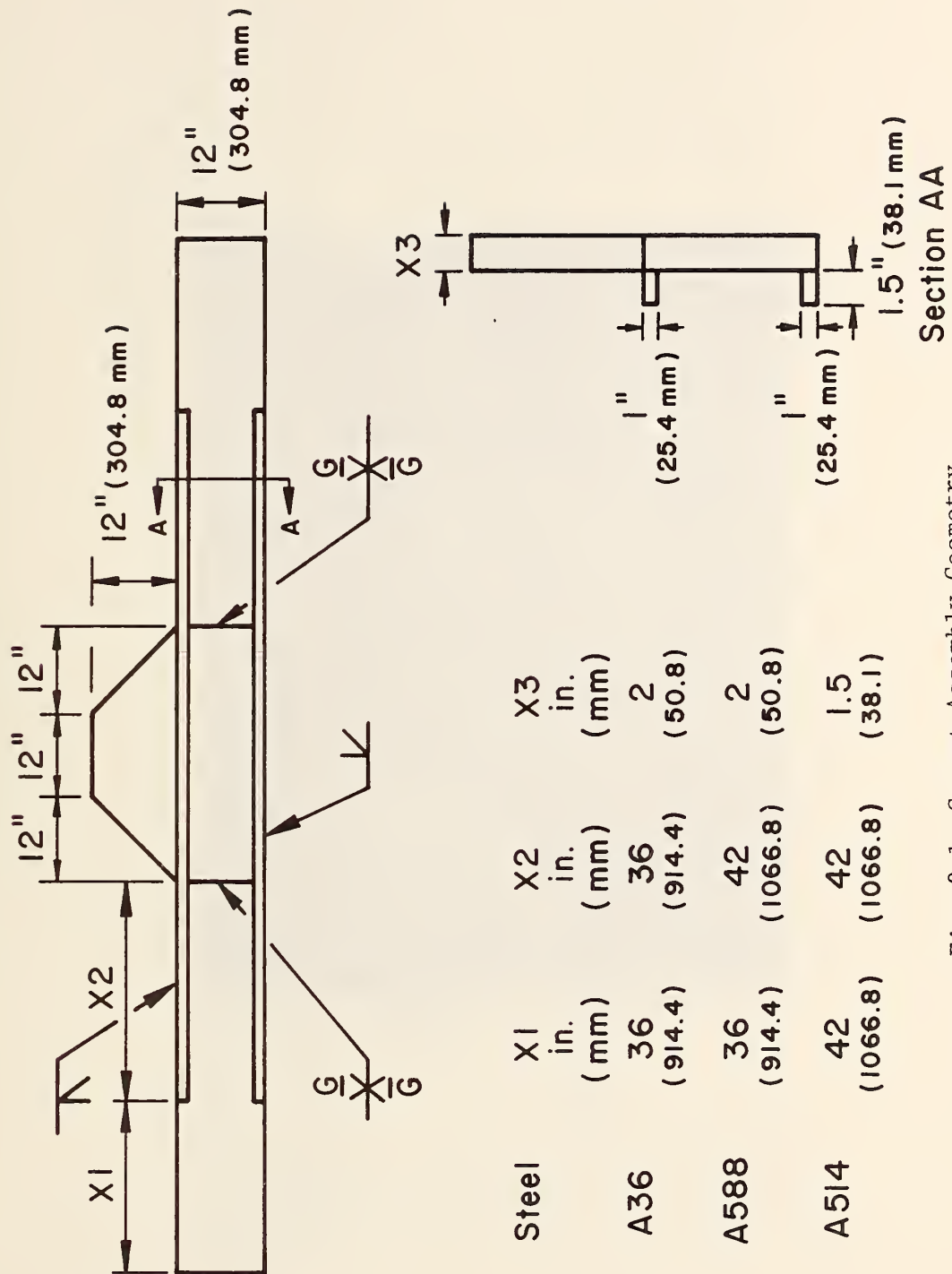


Fig. 9.1 Gusset Assembly Geometry

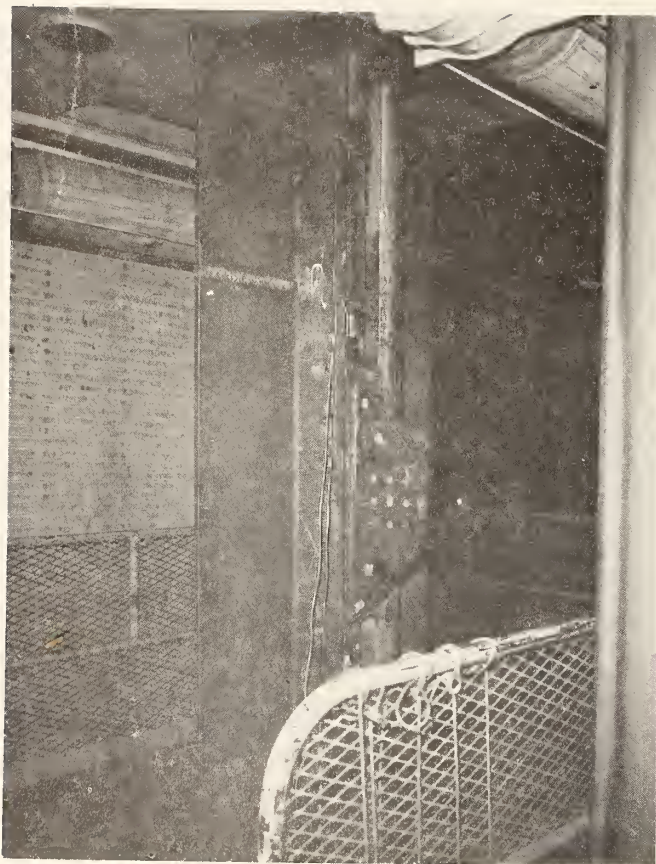


Fig. 9.2 Preloading Gusset Assembly

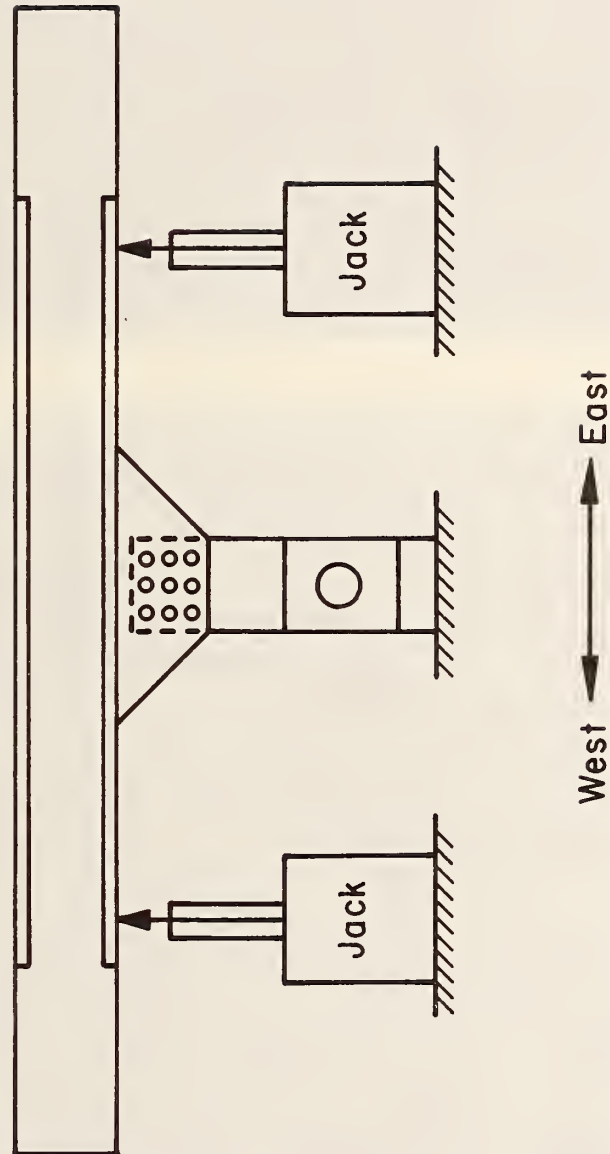


Fig. 9.3 Schematic of Gusset Assembly



Fig. 9.4 A36 Fracture and Fatigue Crack



Fig. 9.5 A588 Fracture and Fatigue Crack



Fig. 9.6 A514 Fracture and Fatigue Crack

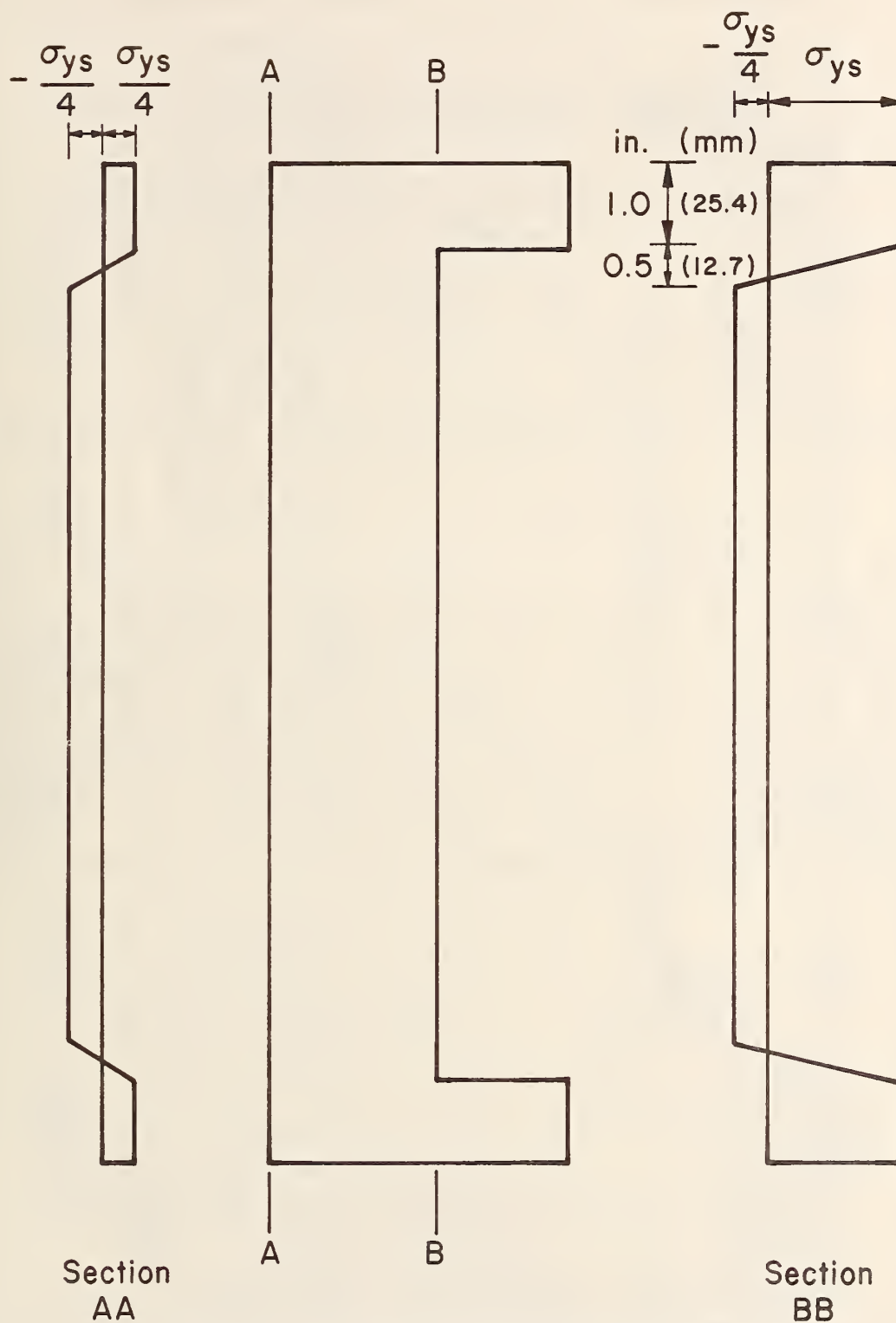


Fig. 9.7 Gusset Residual Stress Distribution

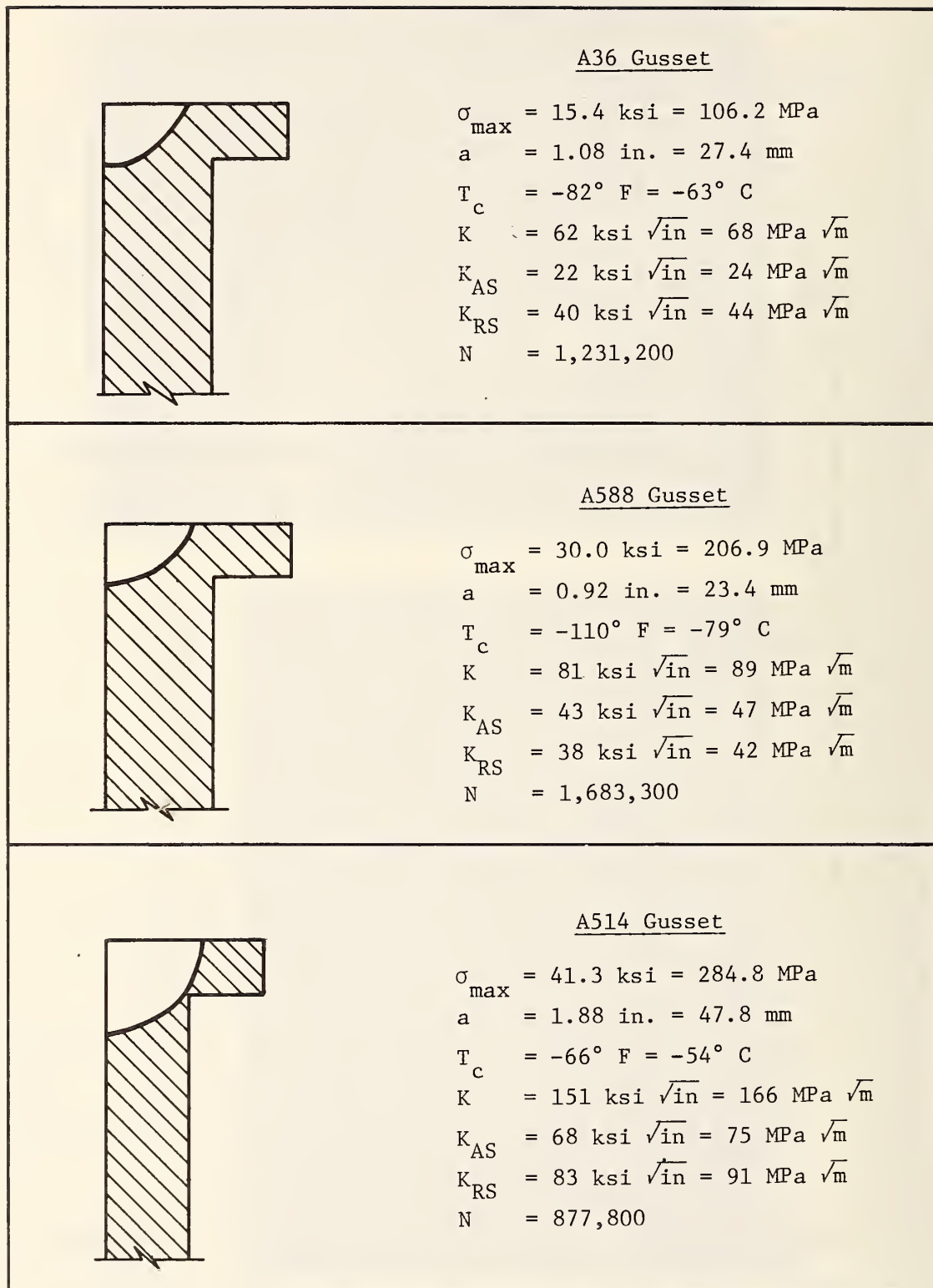


Fig. 9.8 Fracture Surface Sketches and Data Summary

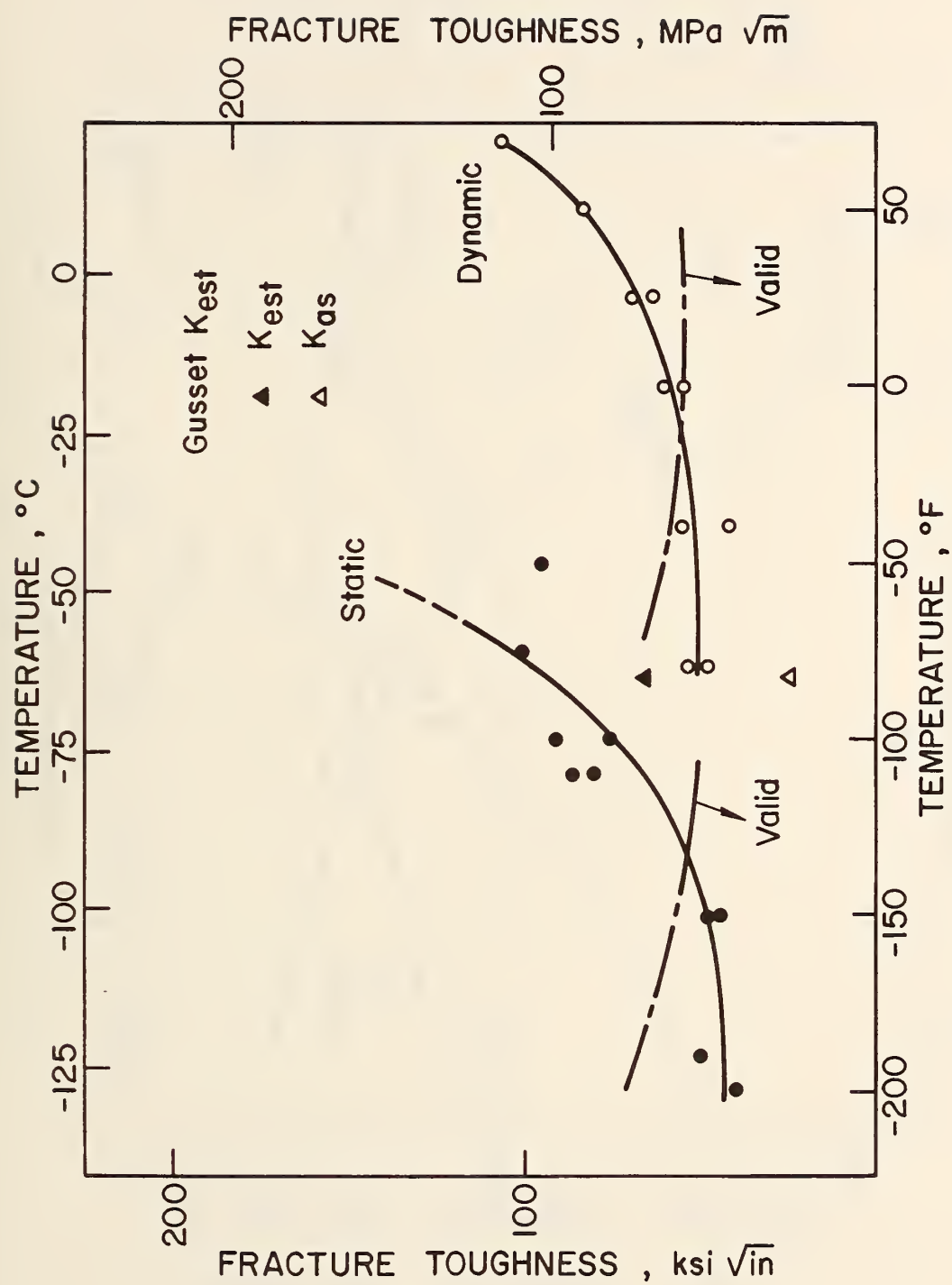


Fig. 9.9 Correlation of Gusset K_{est} and Material Toughness
Characterization (A36, 2 in. PL)

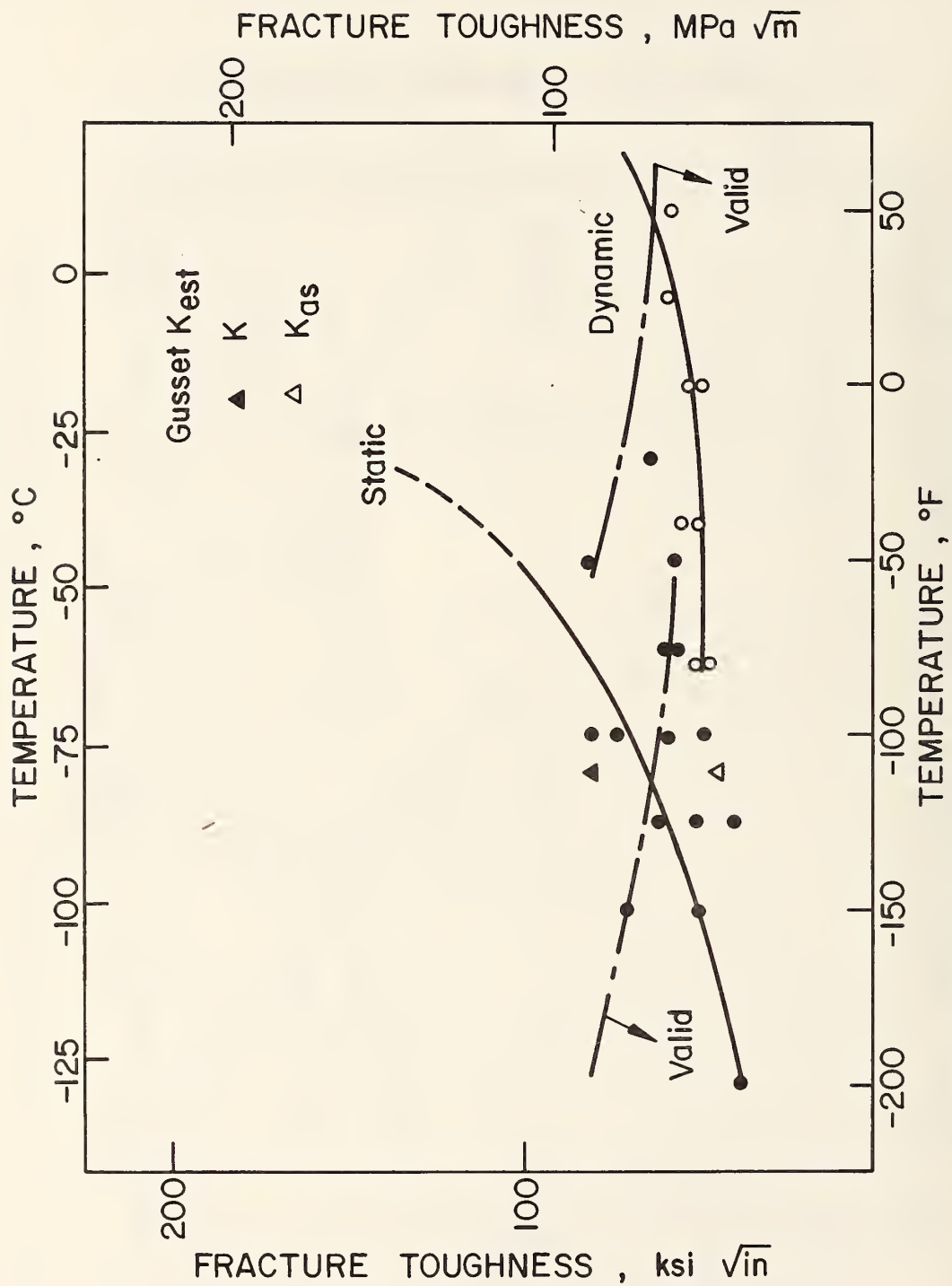


Fig. 9.10 Correlation of Gusset K_{est} and Material Toughness
Characterization (588, 2 in. PL)

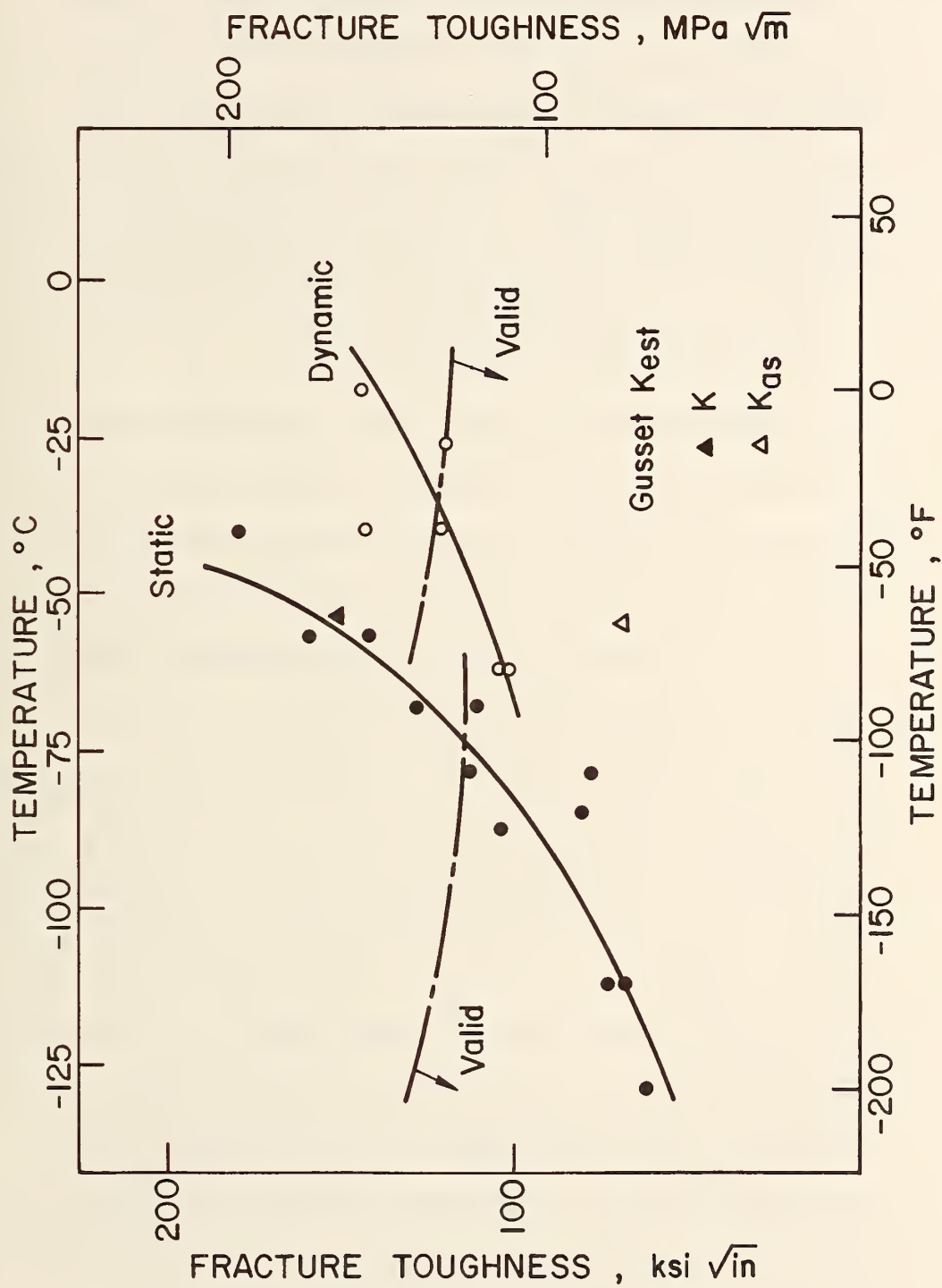


Fig. 9.11 Correlation of Gusset K_{est} and Material Toughness
Characterization (A514, 1-1/2 in. PL)

10. CONCLUSIONS

This report summarizes the fatigue and fracture resistance of full scale welded beams with lateral attachments, cover plates, flange transitions, transverse stiffeners and gusset tests. The fatigue test results for the beams were correlated with available test data obtained from smaller beams. The beam and gusset fracture resistance was correlated with fracture control tests made on the same material. The following observations can be made:

1. The stress intensity estimates from the beam fractures were best modeled by the one-second K_{IC} fracture toughness. The beam fracture tests and the slow bend K_{IC} tests had similar loading rates. Strain measurements on actual bridges have shown that a one-second loading time is about the maximum loading rate experienced by steel bridges²⁷.
2. For relatively large edge cracks, at the lateral attachment details, a good approximation of the critical stress intensity factor, K , for beam fractures can be made by considering the applied stress alone. However, if the edge crack tip moved into the high tensile residual stress field near the web-to-flange welds, the residual stress contribution, K_{RS} , should be included. Fracture usually occurred when the crack tip was in this region. In one instance there was rapid fatigue crack growth through this region due to a rise in K , however, fracture did not occur until the fatigue crack was larger.

3. For the cover-plated beams, groove welded flange transitions, and transverse stiffener details, a good approximation of the critical stress intensity factor, K , at fracture was obtained by considering the applied stress contribution alone when the crack tip was not in a high tensile residual stress region.
4. Category E of the current AASHTO fatigue specifications was found to be applicable to the 12 in. (305 mm) long flange attachment. However, the fatigue strength of the full size cover-plated beam details was less than predicted by Category E. The fatigue life for each cover plate detail was at or below the design fatigue strength which is based on the lower confidence limit of tests of smaller scale cover-plated beams. The current fatigue specification is based on the results obtained from the smaller scale cover-plated beams. Categories B and C of the AASHTO fatigue specification were found to be applicable to the flange transition and transverse stiffener, respectively. Only the cover-plated beams appeared to exhibit a dimensional effect when compared to earlier fatigue tests.
5. The stress concentration effects for small elliptical corner cracks at a groove weld detail was analyzed. The maximum stress intensity was at an elliptical corner crack with a semi-minor axis of 0.4 in. (10 mm). The predicted stress intensity factor was less than the estimated resistance at

fracture. This value was also less than the predicted fracture toughness value from the slow bend material tests at a service temperature of -40° F (-40° C). Similar results and comparisons were obtained for the cover plate, flange transition, and transverse stiffener details. Hence small fatigue cracks in materials satisfying the AASHTO toughness specification should not become unstable.

6. The Charpy V-notch data in the transition zone was converted to stress intensity values using Barsom's empirical equation. Barsom's equation generally predicted conservative results for all steels except the A36 rolled flange.
7. The measured loading rate temperature shift was always equal to or greater than the empirical approximation suggested by Barsom. Hence this approximation is adequate for the materials tested.
8. Solutions which are both exact and simple were not applicable to the cracks which caused beam fractures in this study due to crack shape and residual stress complexities.
9. Large variability in fracture toughness of A588 steel was observed in this study and earlier work⁸. Also, the temperature shift exhibited by the A588 steel beams was marginal. A reexamination of the fracture toughness requirements and further work on A588 steel appears desirable.

With respect to the questions of tolerable flaw size in typical bridge weldments and the smallest tolerable crack in a weldment at its lowest service temperature, the test results of the current program indicate that the crack sizes expected at the minimum service temperature in steel just meeting the specification requirements was provided by beams B1, B2, B2A, B3, B4, B4A, B5A, B6A, B9A, B11 and B12A. Other beams were fractured at larger cracks at somewhat higher temperature or at smaller cracks at temperatures well below the equivalent minimum service temperature.

In all beam tests where fracture did occur the flaw size at fracture, except for one A588 rolled beam, was as great or greater than the thickness of the flange material in the particular test. In the one A588 test in which the crack size was not as large as the flange thickness, it was found that the surface dimensions of the flaw at the time of fracture was approximately 0.6 in. (14 mm) and the specimen was tested well below the minimum service temperature. Thus one can conclude from these results that the current AASHTO fatigue and fracture specifications provide welded details that will nearly exhaust all fatigue life before a fatigue crack will become unstable at the lowest anticipated service temperature. These cracks will generally be through the plate thickness (1.5 in. or greater in this study). The crack sizes in beams B1, B2, B2A, B3, B4, B4A, B5A, B6A, B9A, B11 and B12A are indicative of the critical crack sizes that can be expected in material just meeting the specification provisions. Hence, they provide some indication as to the level of sophistication

needed in inspection. This study and the work in references in 1 and 2 show the critical locations at which inspection must be carried out in welded bridge members. In inspecting a welded bridge one does not have to concern himself with the majority of the bridge structure but only the specific areas of the weldments which is where cracks develop. Also when considering these areas it is clear that the size of the flaw which is being looked for is of the order of $1/2$ in. (12 mm) or larger. The frequency of inspection needed to insure the fracture safety of a structure cannot be determined from the results of this study alone. However, the results of the current study incorporated with the predicted or actual operating service the structure sustains can be used to establish this needed frequency. When a surface fatigue crack is detected with surface dimensions of approximately $1/2$ in. or greater, about 80% of the fatigue life of the detail has already been exhausted. This implies that by inspecting for all cracks $1/2$ in. or greater the remaining useful fatigue life would be 20% of the original life. This estimate should allow an inspection program to be established with some level of confidence depending upon the actual expected frequency of loading for the structure during its future life.

Based on these observations and comments it is quite reasonable to conclude that:

1. In terms of the fracture response of a welded bridge member, the smallest tolerable crack at the lowest service temperature as provided for by the present toughness requirements will generally be of the order of the flange plate thickness or greater.

2. The current fatigue and fracture requirements of the AASHTO specifications appear satisfactory except for the cover plate detail.

11. REFERENCES

1. Fisher, J. W., Frank, K. H., Hirt, M. A. and McNamee, B. M.
EFFECT OF WELDMENTS ON THE FATIGUE STRENGTH OF STEEL BEAMS,
NCHRP Report No. 102, Highway Research Board, National
Academy of Science - National Research Council,
Washington, D.C., 1970.
2. Fisher, J. W., Albrecht, P. A., Yen, B. T., Klingerman, D. J.
and McNamee, B. M.
FATIGUE STRENGTH OF STEEL BEAMS WITH TRANSVERSE STIFFENERS
AND ATTACHMENTS, NCHRP Report No. 147, Highway Research
Board, National Academy of Science - National Research
Council, Washington, D.C., 1974.
3. American Association of State Highway Officials
STANDARD SPECIFICATIONS FOR HIGHWAY BRIDGES, AASHTO,
Washington, D.C., 1973.
4. Tada, H. and Irwin, G. R.
K-VALUE ANALYSIS FOR CRACKS IN BRIDGE STRUCTURES, Fritz
Engineering Laboratory Report No. 399.1, Lehigh University,
June 1975.
5. Brothers, A. J. and Yukawa, S.
THE EFFECT OF WARM PRESTRESSING ON NOTCH FRACTURE STRENGTH,
Paper No. 62-Met-1, ASME Headquarters, January 1962.
6. Succop, L. N., Pense, A. W. and Stout, R. D.
THE EFFECTS OF WARM OVERSTRESSING ON PRESSURE VESSEL STEEL
PROPERTIES, Welding Journal Research Supplement, August 1970.
7. Barsom, J. M.
INVESTIGATION OF TOUGHNESS CRITERIA FOR BRIDGE STEELS,
U.S.S. Research Laboratory Report No. 97.018-001(5),
February 1973.
8. Roberts, R., Irwin, G. R., Krishna, G. V. and Yen, B. T.
FRACTURE TOUGHNESS OF BRIDGE STEELS, Federal Highway
Administration Report No. FHWA RD-74-57, September 1974.

9. Luft, D. E., Madison, R. B. and Irwin, G. R.
MEASUREMENT OF DYNAMIC K_c FROM DROP-WEIGHT TEAR TEST, Fritz
Engineering Laboratory Report No. 335.1, Lehigh University,
1969.
10. Irwin, G. R.
LINEAR FRACTURE MECHANICS, FRACTURE TRANSITION AND FRACTURE
CONTROL, Engineering Fracture Mechanics, Vol. 1, pp. 241-257,
1968.
11. Begley, J. A. and Landes, J. D.
THE J-INTEGRAL AS A FAILURE CRITERION, paper presented at
the National Symposium on Fracture Mechanics, University of
Illinois, August 1971.
12. Paris, P. D., Gomez, M. P. and Anderson, W. E.
A RATIONAL ANALYTICAL THEORY OF FATIGUE, The Trend in
Engineering, University of Washington, Vol. 13, No. 1,
January 1961.
13. Albrecht, P. and Yamada, K.
RAPID CALCULATION OF STRESS INTENSITY FACTORS, paper sub-
mitted for publication in the Journal of the Structural
Division, ASCE.
14. Zettlemoyer, N.
STRESS CONCENTRATION AND FATIGUE OF WELDED DETAILS, Ph.D.
Dissertation, 1976.
15. Tada, H., Paris, P. and Irwin, G.
THE STRESS ANALYSIS OF CRACKS HANDBOOK, Del Research Corpor-
ation, Hellertown, Pennsylvania, 1973.
16. Alpsten, G. A. and Tall, L.
RESIDUAL STRESSES IN HEAVY WELDED SHAPES, Welding Journal,
Vol. 49, March 1970.
17. McFalls, R. K. and Tall, L.
A STUDY OF WELDED COLUMNS MANUFACTURED FROM FLAME-CUT PLATES,
Welding Journal, Vol. 43, April 1969.

18. Tebedge, N., Alpsten, G. and Tall, L.
RESIDUAL-STRESS MEASUREMENT BY THE SECTIONING METHOD, Experimental Mechanics, Vol. 13, No. 2, pp. 88-96, February 1973.
19. Tebedge, N., Alpsten, G. and Tall, L.
MEASUREMENT OF RESIDUAL STRESSES, A STUDY OF METHODS, Fritz Engineering Laboratory Report No. 337.8, Lehigh University, February 1971.
20. Madison, R. B.
APPLICATIONS OF FRACTURE MECHANICS TO BRIDGES, Fritz Engineering Laboratory Report No. 335.2, Lehigh University, June 1969.
21. Brozzetti, J. and Foucraut, J.
PLANNING AND DESIGN OF TALL BUILDINGS, "Stability," State-of-Art Report 1, ASCE-IABSE International Conference, II (16), pp. 14, August 1972.
22. Redner, S.
MEASUREMENT OF RESIDUAL STRESSES BY THE BLIND HOLE DRILLING METHOD, Photolastic, Inc., Bulletin TDG-5, 1974.
23. Doi, D. and Guell, D.
PERMANENT DEFLECTIONS AND LOSS OF CAMBER IN STEEL BRIDGE BEAMS, Vol. II, NCHRP 12-1 and 12-6, Appendix IV, Flame Cambering of Wide Flange Steel Beams.
24. Tall, L.
RESIDUAL STRESSES IN WELDED PLATES - A THEORETICAL STUDY, Fritz Engineering Laboratory Report No. 249.11, Lehigh University, July 1961.
25. Wilson, W. K.
STRESS INTENSITY FACTORS FOR DEEP CRACKS IN BENDING AND COMPACT TENSION SPECIMENS, Engineering Fracture Mechanics, Vol. II, pp. 169, 1970.
26. Schilling, C. G., Klippstein, K. H., Barsom, J. M. and Blake, G. T.
FATIGUE OF WELDED STEEL BRIDGE MEMBERS UNDER VARIABLE-AMPLITUDE LOADINGS, NCHRP 12-12, U. S. Steel Research, August 1975.
27. Viest, I. M. and Fisher, J. W.
BRIDGE RESEARCH, AASHTO Road Test Report No. 4, Highway Research Board Special Report No. 61D, 1962.

12. APPENDIXES

A.1 Introduction

The two-ended crack (e.g. Beam B4A) and the three-ended crack (e.g. Beam B3) were analyzed by using a method similar to that proposed by Madison²⁰. The openings of the flange crack and the web crack at a compatibility point are known to be equal (see Fig. A.1). Therefore, to satisfy this condition, an opening or closing interaction force must be applied in an opposite sense to the flange crack and a closing or opening interaction force must be applied to the web crack. These forces also affect the stress intensity.

A.2 Calculations

A.2.1 Crack Displacement

Neglecting the interaction force, the crack opening at the compatibility point is a function of the stress and the geometry of the crack. The stress is the sum of the applied stress, residual stress in the beam and the residual stress due to local welding

$$v = f(a, \sigma_{AS} + \sigma_{RS} + \sigma_{LW}) \quad (A1)$$

The stress itself is a function of x and z .

The displacement of a through crack loaded with a line load in the z -direction can be obtained from the formulation presented in Ref. 20 (see Fig. A.2). This yields

$$v(x) = \frac{4}{E\pi} P f(a, b, x)$$

$$\text{where } f(a, b, x) = \tanh^{-1} \left(\frac{a^2 - x^2}{a^2 - b^2} \right)^{1/2} \quad \text{for } b < x < a \quad (A2)$$

$$\text{and } f(a, b, x) = \coth^{-1} \left(\frac{a^2 - x^2}{a^2 - b^2} \right)^{1/2} \quad \text{for } 0 \leq x < b$$

and is not defined for $x = b$.

The displacement for a crack loaded with a smoothly varying load $\sigma(x)$ can be calculated by taking the stress constant over each interval da and numerically integrating over the crack length (see Fig. A.2.b)

To take into account the variation of the load in the z -direction, the following model was used:

The solution for a semi-infinite straight-fronted three-dimensional crack as shown in Fig. A.3 is given in Ref. 15. This solution can be used to make a reasonable estimate of the influence of a three-dimensional stress distribution on crack openings near the leading edge of a large flange crack. The model for a finite plate with a large crack is shown in Fig. A.2.c. To use this model, a method is needed to average the stress values on the crack plane in the z -direction of the flange, so that a two-dimensional analysis can be used. The idea of this method is to assume that the influence of the three-dimensional stress distribution upon crack opening, v , is the same as their influence upon the stress intensity K . For a straight-line crack-front in a three-dimensional solid, the average can be estimated as follows:

$$K \sim \frac{P}{c} \cos^2 \theta \quad (A3)$$

If $P = \sigma(z) dz da$ along a line with a fixed x value, Eq. (A3) becomes:

$$K \sim \int_{-\infty}^{\infty} \frac{\sigma(z)}{c} \cos^2 \theta dz \quad (A4)$$

From Fig. A.3 it follows that

$$z = c \tan \theta$$

and

$$dz = c \frac{d\theta}{\cos^2 \theta}$$

Integrating Eq. (A4) gives

$$K \sim \frac{1}{\pi} \int_{-\pi/2}^{\pi/2} \sigma(z) d\theta da \quad (A5)$$

In order to employ this result with two-dimensional analysis equations, insertion of the normalizing constant $1/\pi$ as shown and integration from $-\pi/2$ to $\pi/2$ is needed.

Due to the finite depth of the flange, the stress distribution in the flange is assumed to be repeated (above and below) as shown in Fig. A.4. Thus shear stresses on the upper and lower edges of the flange are removed.

At this point it is assumed that crack openings in the flange can be calculated using two-dimensional equations in which the stresses to be removed along the crack line are average stresses.

Thus Eq. (A2)

$$v(x) = \frac{4}{E\pi} P f(a, b, x)$$

becomes

$$v(x, y) = \frac{4}{E\pi^2} f(a, b, x) \int_{-\pi/2}^{\pi/2} \int_0^a \sigma(a, \theta) da d\theta \quad (A6)$$

The integration of Eq. (A6) was done numerically; the crack length was divided into n-intervals with $da = a/n$. This yielded:

$$v(x, y) = \frac{4}{E\pi^2} \sum_{j=1}^n \sum_{i=-5}^{i=5} \sigma_j da (\theta_{i2} - \theta_{i1}) f(a, b, x) \quad (A7)$$

To take into account the part for $i > 5$ and $i < -5$ an average stress

$$\bar{\sigma} = \frac{\sum_{j=1}^a \sigma_j}{n} \quad \text{was calculated and the additional displacement}$$

$$v(x, y) = \frac{4}{E\pi^2} \bar{\sigma} da \left(\frac{\pi}{2} - \theta_o \right) f(a, b, x) \quad (A7a)$$

was added to Eq. (A7).

A2.2 Compatibility Condition

If the opening of the flange crack is smaller than the opening of the web crack, the opening force was to be an opening force for the flange and a closing force for the web. The difference, Δv , between v_f and v_w has to be negligible to satisfy the compatibility condition.

$$\Delta v = v_f - v_w \approx 0 \quad (A8)$$

After defining an interaction area (see Fig. A5) the restraint forces were applied to the flange and to the web. These forces are line loads in the z-direction along the lines AB and CD for the flange and along AC and BC for the web. Since the length of both lines (AB + CD) and (AC + BC) is the same, the magnitude of the forces is the same.

$$|P_f| = |P_w| \quad (A9)$$

Equations (A7) and (A9) were solved iteratively and simultaneously. To calculate the crack opening due to a line force, σda was replaced by P_f respectively P_w in Eq. (A7).

A2.3 Stress Intensity Calculations

For the stress intensity calculations a model that prevented bending along both edges (see Fig. A.2.c) was used. This yields:

$$K = \frac{P}{b} \frac{\cos \frac{\pi c}{2b}}{\sqrt{\sin^2 \frac{\pi a}{2b} - \sin^2 \frac{\pi c}{2b}}} \sqrt{2b \tan \frac{\pi a}{2b}} \quad (A10)$$

This equation was modified to take into account variations in the x- and z-directions of the load.

A2.4 Plastic Zone Correction

The procedure used to calculate the stress intensity is an iterative one using the plane stress plastic zone correction

$$r_y = \frac{1}{2\pi} \frac{K_c}{\sigma_y}^2$$

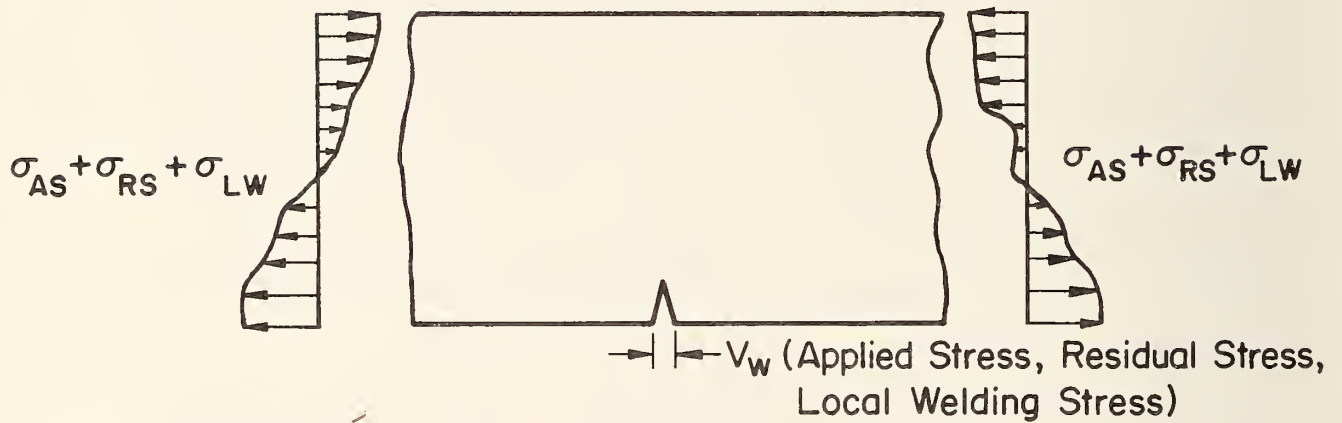
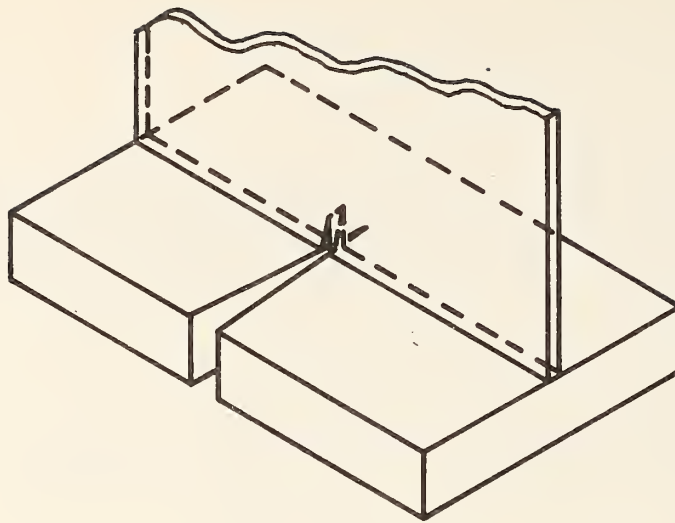
Initially K_c was estimated ignoring the plastic zone correction. The calculated K_c value was used to estimate r_y and a new calculation was made with

$$a' = a + r_y$$

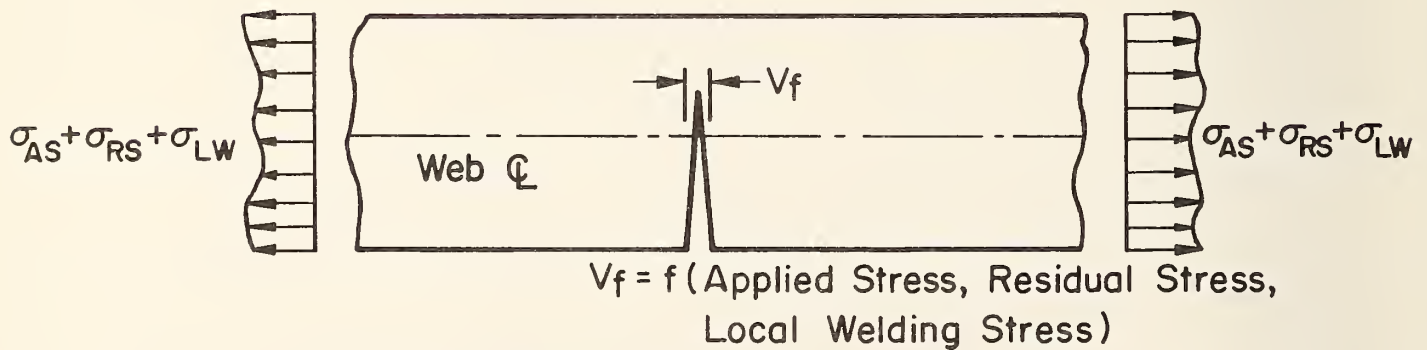
This procedure was repeated until the estimates converged.

A.3 Results

Because the compatibility point is in the upper part of the flange and the crack front close to the applied restraint force, decreasing K_{WR} values were obtained. For the flange K_{WR} in the order of 15 ksi $\sqrt{\text{in.}}$ for the top level and 2 ksi $\sqrt{\text{in.}}$ for the lower level were obtained (see Fig. 8.1, Fig. 8.4, and Fig. 8.9).



Web Crack Opening



Flange Crack Opening

Fig. A.1 Flange and Web Crack Interaction

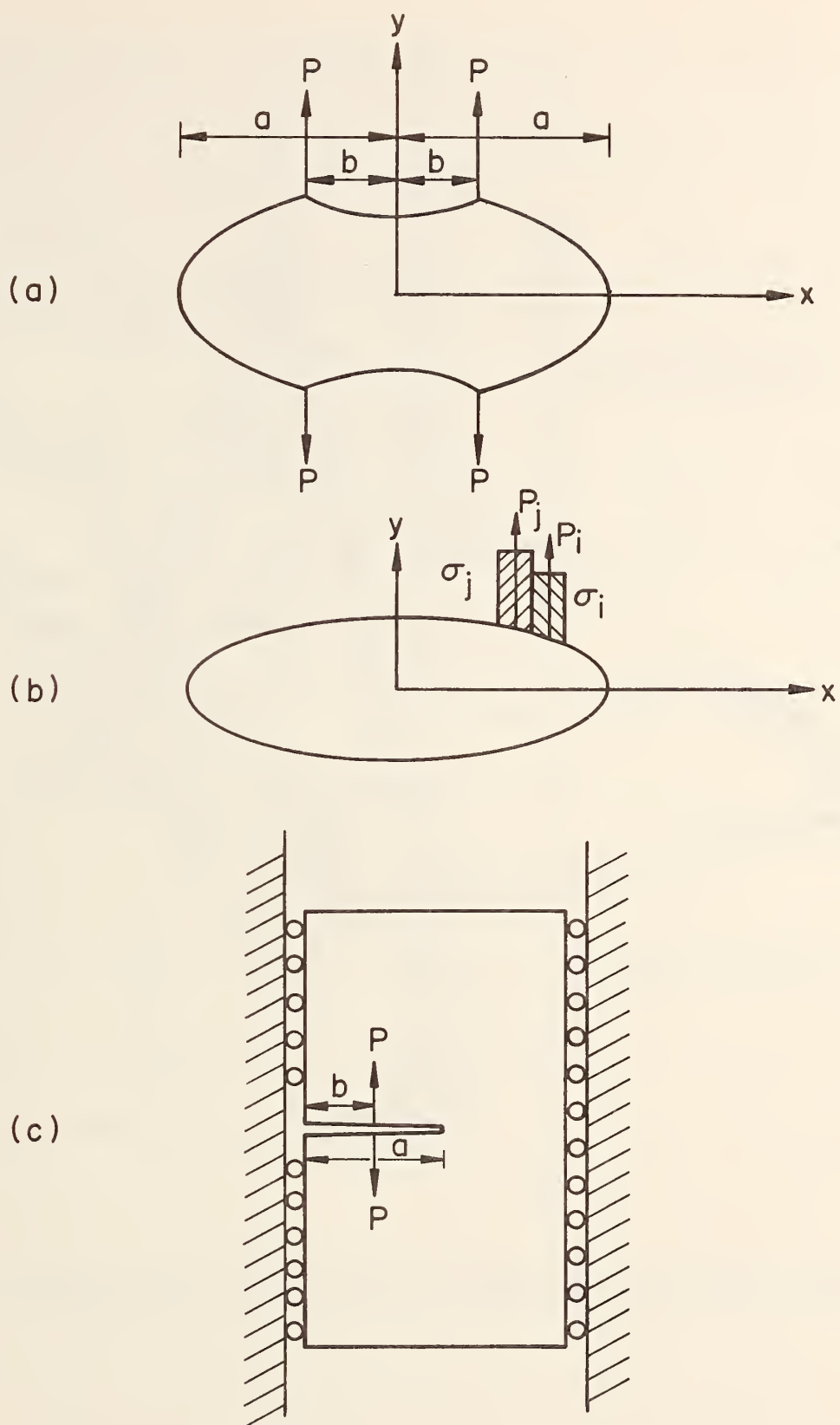
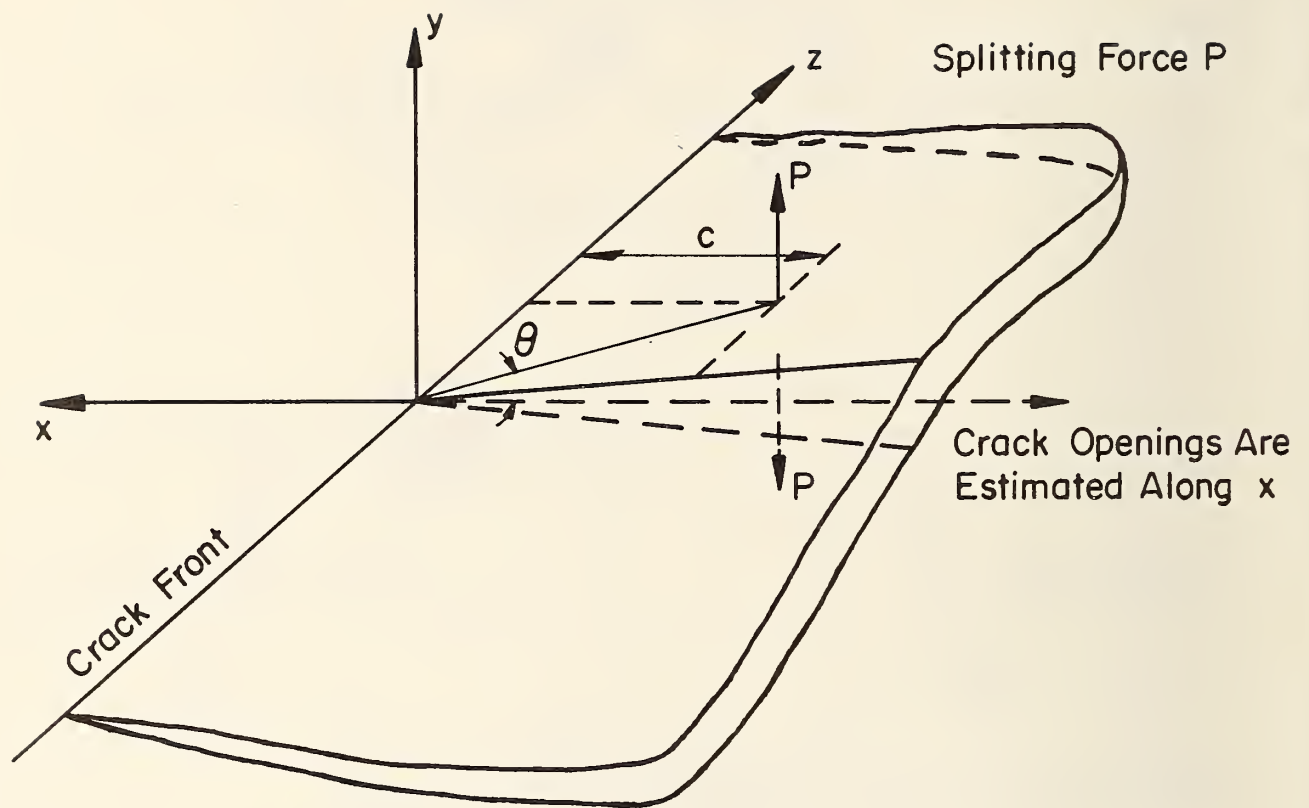


Fig. A.2 Fixed Edge Model for Crack Opening and Stress Intensity Calculation



$$z = c \tan \theta$$

$$dz = c \frac{d\theta}{\cos^2 \theta}$$

Fig. A.3 Model for a Straight Line Crack-Front in a three-dimensional solid

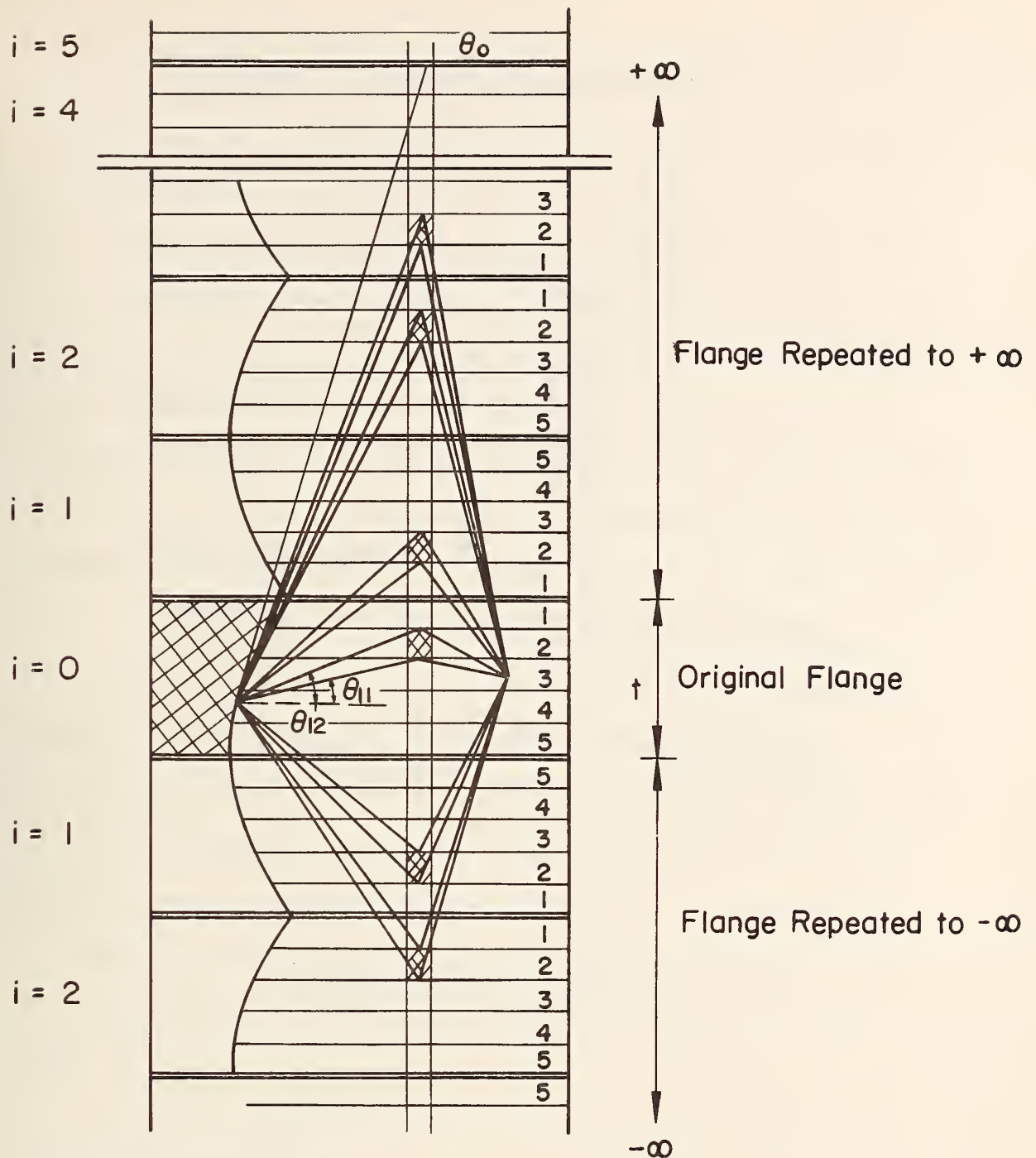


Fig. A.4 Stress Intensity Representing Crack Opening due to a Load

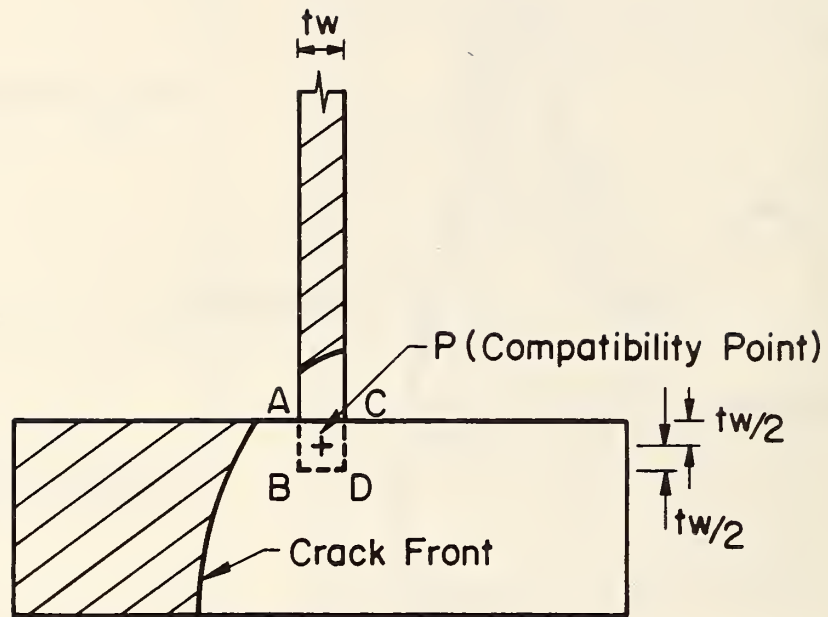


Fig. A.5 Assumed Interaction Area for
Web Restraint Analysis

APPENDIX B - RESIDUAL STRESS MEASUREMENTS

B.1 Introduction

The residual stress distribution in a welded built-up beam can be attributed to two components. The first component consists of the residual stresses in the nominal section prior to the attachment of any welded details. A considerable amount of research has been undertaken to assess this phenomenon with particular emphasis on column behavior^{16,17,21}. The second contribution consists of the residual stresses due to the attachment of details to the welded beam or girder.

The method of sectioning was employed to determine the nominal section residual stress pattern in typical welded beams B2(A36), B4(A588), and B6(A514) and in rolled beams B3(A36) and B5(A588). The hole drilling method¹⁹ was used to evaluate the residual stresses local to the welded details. The details investigated by the hole drilling method included the lap weld lateral attachment, groove weld lateral attachment, end-welded cover plate, cover plate with unwelded end, flange transition, and transverse stiffener welded to the bottom flange.

B.2 Nominal Section Residual Stresses

The method of sectioning was employed to determine the longitudinal distribution of stress in the nominal section of typical test beams fabricated from each steel grade. This technique is based

upon the principle that the internal stresses in the beam are relieved by sectioning the beam into small strips. Measurements with a mechanical strain gage of the length of each strip before and after slicing provides a method of assessing the residual stress in each strip. Using Hooke's Law the residual stress (σ_{rs}) at the measured surface can be calculated by Eq. B1.

$$\sigma_{rs} = \frac{-E}{L} (\Delta \bar{L}) \quad (B1)$$

\bar{L} = gage length

E = modulus of elasticity

Where ΔL is positive for an increase in length and σ_{rs} is positive for a tensile residual stress. It is assumed in this analysis that the slicing operation does not introduce significant strains and that the transverse stresses are negligible¹⁹.

B.2.1 Preparation of Test Specimens

The lateral attachment beams were selected for determining the nominal residual stress pattern for all the welded sections. Half the beam was sectioned since symmetry about the center of the web was expected. The measurements were conducted on the welded sections between the loading point and the reaction. The sections to be sliced were selected as close as possible to the lateral attachment without overlapping the region where the local residuals would have effect. The local weld effect was expected to rapidly decay in the longitudinal direction, therefore the region to be sliced was laid out

4 in. (101.6 mm) from the attachment as illustrated in Fig. B.1. The section sliced from the rolled shapes was taken from a 10 ft. (3.05 m) length of the rolled beam that was not used during the fabrication of the cover plate beam specimens.

The spacing of the saw cuts for a typical welded beam section is shown in Fig. B.2. The spacing of the cuts was dependent upon the expected stress gradient. In regions where the stress gradient is large such as the flange tips of the rolled and welded shapes, and the web to flange weld of the welded shapes, smaller slices were used (Fig. B.2). The strain measurements were made using a Whittemore mechanical strain gage (0.0001 in. accuracy of dial gage) with reference bar. A 10 in. (0.25 m) gage length was used for these measurements. This gage length was laid out by drilling pairs of small gage holes on both faces of each slice prior to cutting. To avoid transverse sawing effects the gage holes were maintained 2 in. (50.8 mm) from the transverse cut.

B.2.2 Procedure for Measurement

Measurements of the distance between gage holes must be made both before and after slicing to determine the change in length of each slice due to cutting. Special precautions must be made to ensure the accuracy of these mechanical strain measurements. The gage holes were cleaned with solvent and air blasted. A set of readings was taken on a reference bar before any readings on the specimen were made. The readings on the specimen were taken in groups of approximately ten

and then the reference bar was read again. This procedure was repeated until all the sets of holes had been measured three times. If any of the readings differed by more than 0.00008 in. (2 μ m) additional readings were taken.

B.2.3 Evaluation of Data

Equilibrium requires that the residual stresses must be balanced such that the net stress on the cross-section is equal to zero. The residual stress patterns for the welded and rolled sections in Figs. B.3 to B.7 were adjusted to satisfy this equilibrium condition.

B.3 Local Residual Stresses From Welded Attachments

The hole drilling method was employed to determine the local residual stress distributions adjacent to the welded details under investigation. This technique is based upon the principle that drilling a hole in a stress field disturbs the stress equilibrium. The process of returning the disturbed stress field to equilibrium results in deformations of the surface adjacent to the hole. Measurement of these surface deformations is accomplished by use of bonded electrical strain gages. The strain gages are mounted in a 45° strain rosette (Fig. B.8). The direction (β) and magnitude (σ_1, σ_2) of the principal residual stresses can be calculated by the relationships presented in Ref. 22. The gage and stress field orientation is shown in Fig. B.9.

The principal advantage of the hole drilling method is that it permits evaluation of residual stresses at a point. The major

drawback is that the method is limited to the plate surface. When drilling, the strains recorded on the surface increase until the drilled depth is approximately equal to the diameter of the hole. The fully relieved surface stresses are those stresses that correspond to the strains that are asymptotically approached at a drilled depth approximately equal to the hole diameter. In order to evaluate residual stresses near the fillet weld toes, it was necessary to select the smallest gage available. A rosette designed for a 0.0675 in. (1.59 mm) diameter hole was selected. Since the required gage diameter was small, only a surface residual stress measurement was obtained.

B.3.1 Preparation of Test Specimens

Micro-measurements EA-06-062RE 45° rosette electrical strain gages were selected for the hole drilling residual stress measurements. These gages were positioned on the interior and exterior flange faces in the vicinity of the welded details as shown schematically in Fig. B.13 through Fig. B.18. Each of the gages of the rosette were wired to either a Vishay Instruments P-350 strain indicator or to a channel of a B & F Data Acquisition System.

The feet of the drill stand were cemented to the plate so that the tool guide was positioned roughly over the center of the strain-rosette. A microscope was inserted in the tool guide and the positioning screws were adjusted so that the microscope was centered over the gage to within ± 0.001 in. (± 0.0254 mm) (Fig. B.10).

B.3.2 Procedure for Measurement

After the tool guide was aligned with the telescope, a milling bar with drill bit and depth micrometer was inserted into the tool guide (Fig. B.11). A specially dressed end mill was used to ensure that the bottom of the hole would remain flat. The holes were drilled in 0.0065 in. (0.165 mm) increments. Special precautions were taken to ensure that the specimens were not heated by the drilling operation. The end mill bit was set to cut at a speed of 1-2 rps. After drilling each increment of depth the drill bit was removed from the hole and the strain gages were allowed to stabilize before readings were taken. The drilling procedure was repeated until the strain readings approached a limiting value. Usually ten incremental readings were made. After the drilling was completed the milling bar was removed and the telescope was used to measure the hole diameter.

B.3.3 Evaluation of Surface Data

Values of σ_1, σ_2 , and β were calculated for each increment of depth. Plots of principal stresses (σ_1, σ_2) vs. depth showed that a stable value was asymptotically approached. An example of such a plot is shown in Fig. B.12. Since the β angle and the orientation of the gages was known with respect to the transverse and longitudinal axes of the beam, the principal stresses could be resolved into transverse and longitudinal normal components. The results of these surface residual stress measurements are summarized in Figs. B.13 to B.18.

B.4 Local Residual Stress Decay at Welded Attachments

The local residual stress measurements acquired by the hole drilling method provide only surface residual stresses. The residual stress decay with depth must be approximated by a distribution which is compatible with the surface residual stresses adjacent to the welded attachment and on the opposite flange face. Since the stress measurements adjacent to weldments were made 0.25 in. (6 mm) from the weld toe, the residual stress decay from the crack growth plane to the gage must also be taken into account. A computer analysis²³ as explained in the next section was used to estimate the shape and magnitude of the residual stress decay with depth for a simple case. Estimating the general form of the residual stress decay from the theoretical analysis, the exterior flange face, mid-flange, and interior flange face local residual stresses were approximated from the surface residual stress measurements in the vicinity of the welded details.

B.4.1 Theoretical Analysis

A computer program²³ was used to estimate the residual stresses in the cross-section of a beam subjected to a temperature variation. The program adjusts the stress state, which is a function of temperature, in the beam until both force and moment equilibrium are satisfied to within a specified allowable error. The A36 cover-plated beam (W36X260) with end weld was selected for the computer analysis. The end weld is almost across the entire width of the flange for this detail, therefore the temperature in the flange was assumed constant

for a constant depth. The beam cross-section was divided into elements and an assumed temperature distribution with depth was estimated to simulate the element temperatures in the beam due to welding. The nominal section residual stress distribution for the A36 rolled shape (Fig. B.6) was assigned as the stress state for the beam cross-section prior to welding.

The nominal section and local weld components of the residual stress distribution with depth at three sections of the flange are shown in Fig. B.19. In the analytical study, tensile stresses at yield occurred near the welded surface and compressive stresses occurred at the flange face opposite the weld. The magnitude of the local weld residual stress component is dependent on the nominal section residual stresses prior to welding.

B.4.2 Correlation with Surface Residual Stress Measurements

The centers of all the holes drilled adjacent to a weld were approximately 0.25 in. (6.4 mm) from the toe of the weld. The longitudinal residual stress measurements adjacent to the welds resulted in tensile stresses on the order of half the yield strength. For the lap weld lateral attachment, end-welded cover plate, and unwelded and cover plate details the residual stress measurements were also obtained at distances from 2 in. (50.8 mm) to 3 in. (76.2 mm) from the weldment. The longitudinal residual stress decays from the weldments are summarized in Figs. B.20a, b, and c. In all but one case (holes 1 and 2 in Fig. B.20a) a rapid residual stress decay was observed.

Extrapolation suggested that the residual stress at the weld toe should be at yield. This rapid longitudinal decay confirmed that the residual stress at the end of weldments is very localized. Similar results were obtained in Ref. 24.

The stresses measured at the gages placed on the flange face directly opposite the gages adjacent to the weld generally indicate longitudinal compressive stresses significantly smaller in magnitude than the tensile stresses adjacent to the weld. Tensile residual stresses near yield on the flange face adjacent to the weld and compressive residual stresses of moderate magnitude on the flange face opposite the weld are in agreement with the results of the analytical study.

Based upon the longitudinal surface residual stresses reported in Figs. B.13 through B.18 and the residual stress distribution from the analytical study, the local weld residual stress distributions for the groove weld lateral attachment (Fig. B.21), lap weld lateral attachment (Fig. B.22), end-welded cover plate (Fig. B.23 and B.25) unwelded end cover plate (Fig. B.24 and B.25), flange transition (Fig. B.26), and transverse stiffener welded to the flange (Fig. B.27) were determined. Any discrepancy in equilibrium for the local weld residual stresses were assumed to be balanced by residual stresses in the uncracked portions of the flange and web.

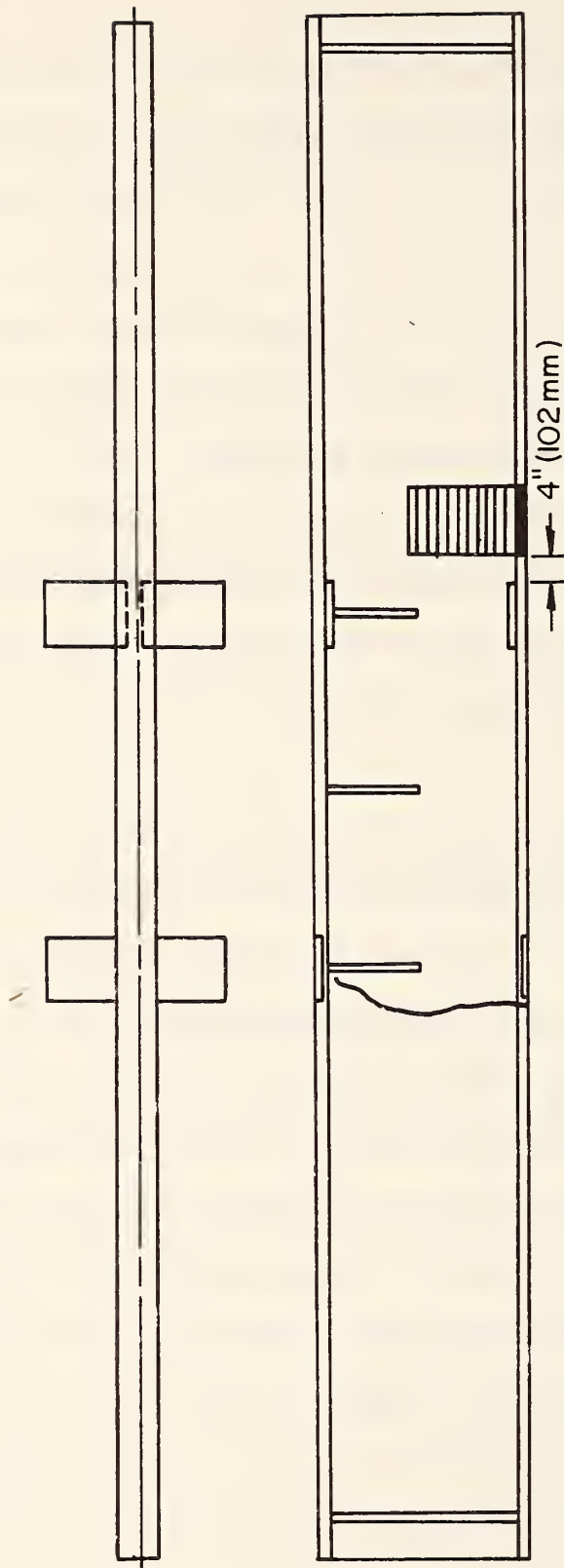


Fig. B.1 Sliced Region of Welded Beam (B4, A36)

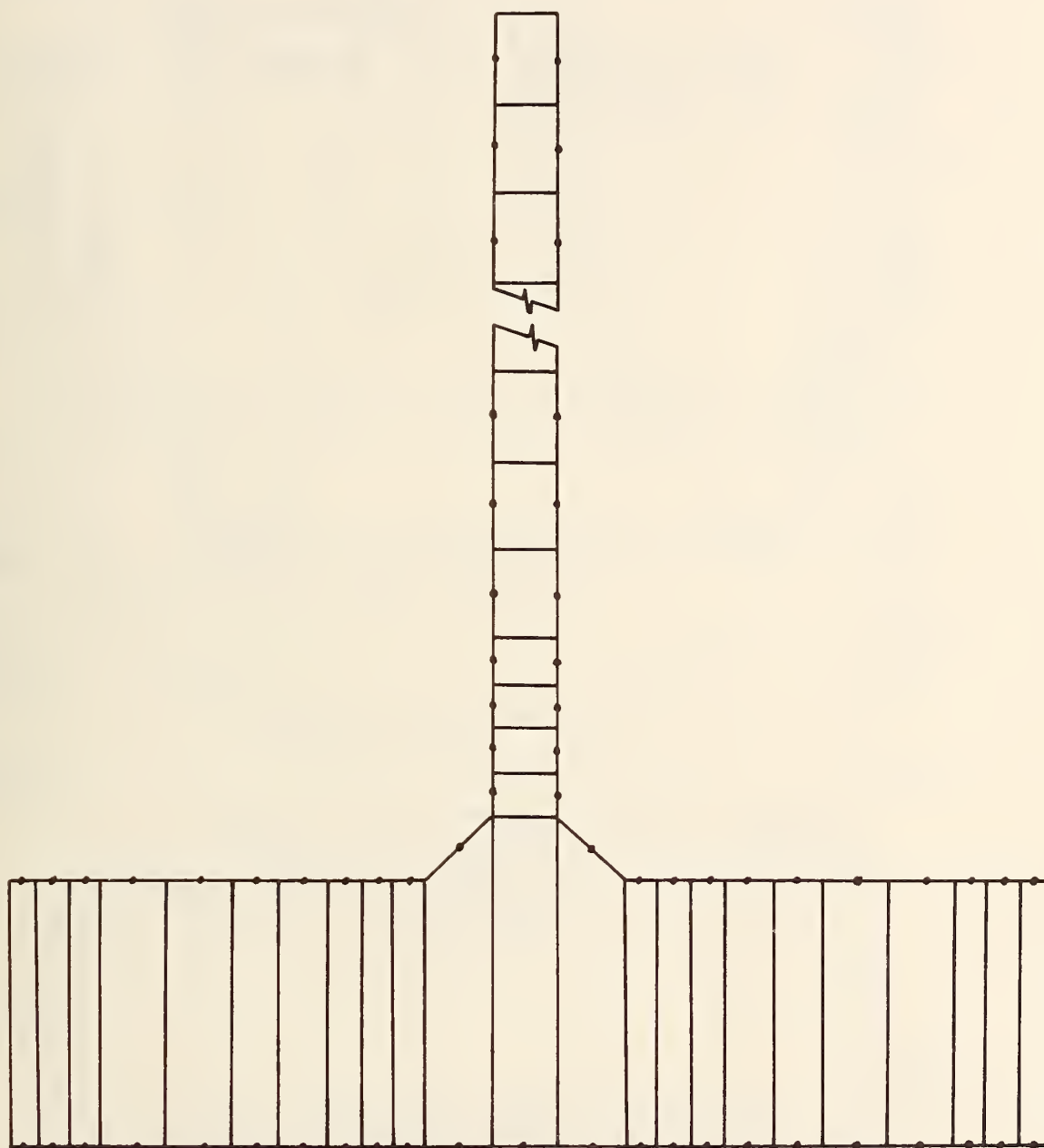


Fig. B.2 Cross-Section of Sliced Welded Beam

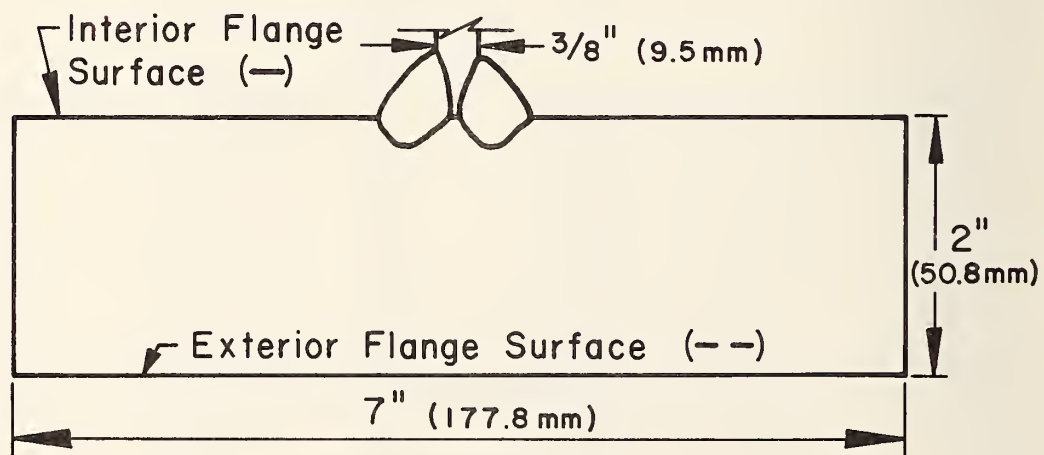
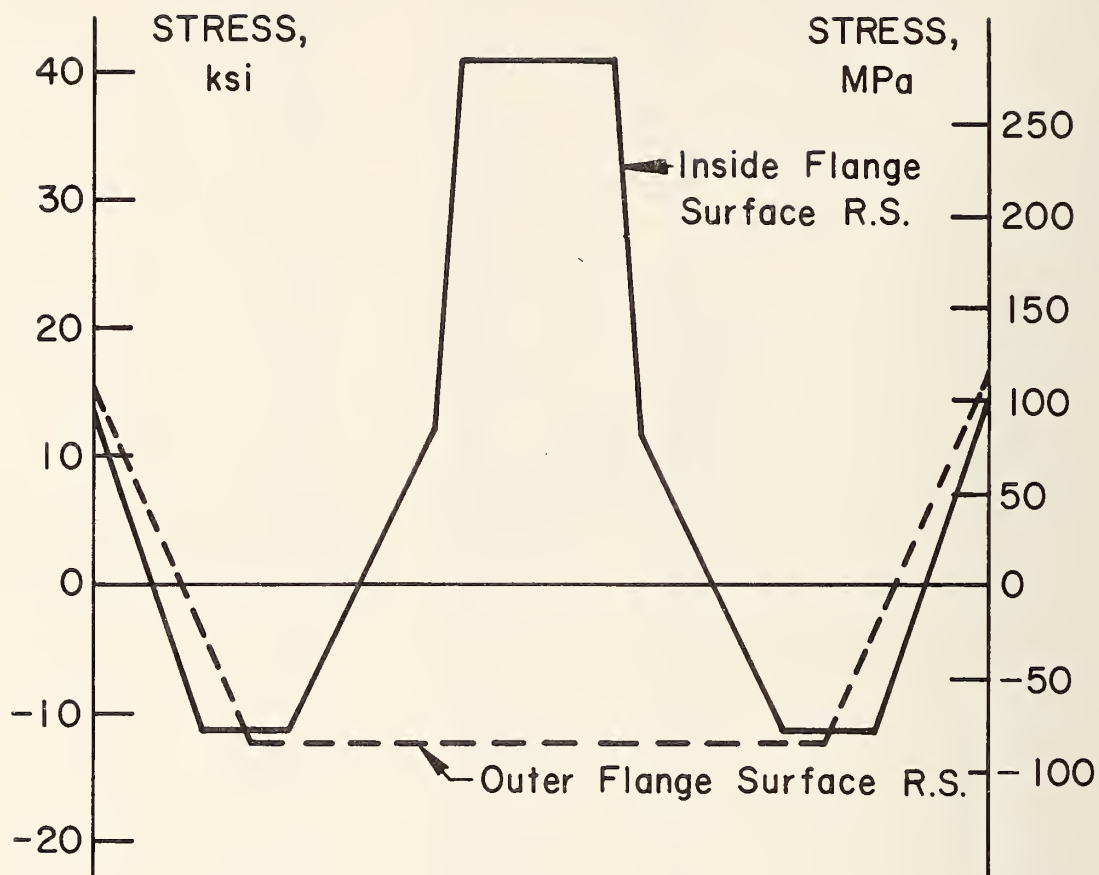


Fig. B.3 Measured Residual Stress Distribution for A36 Flange

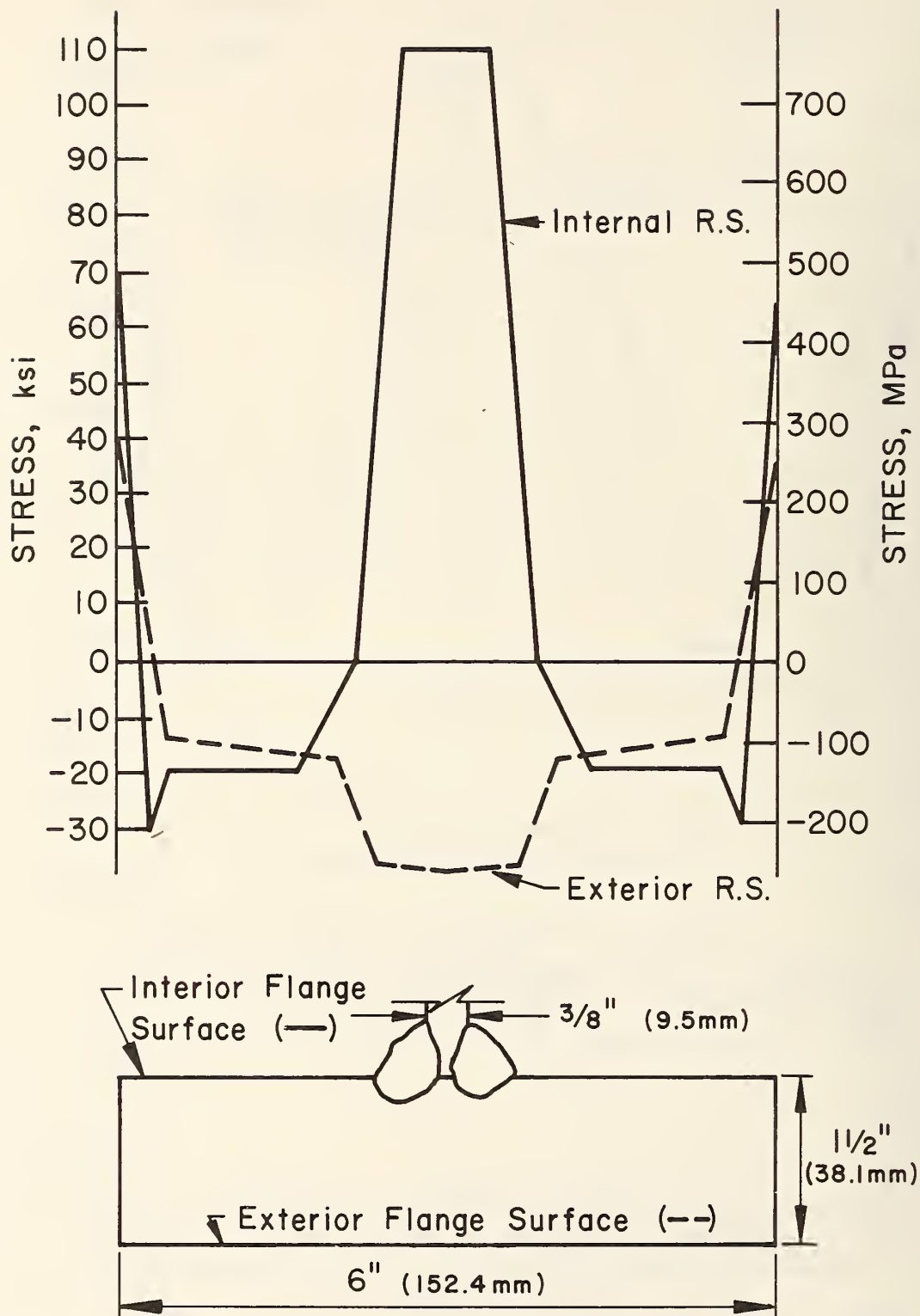


Fig. B.5 Measured Residual Stress Distribution for A514 Flange

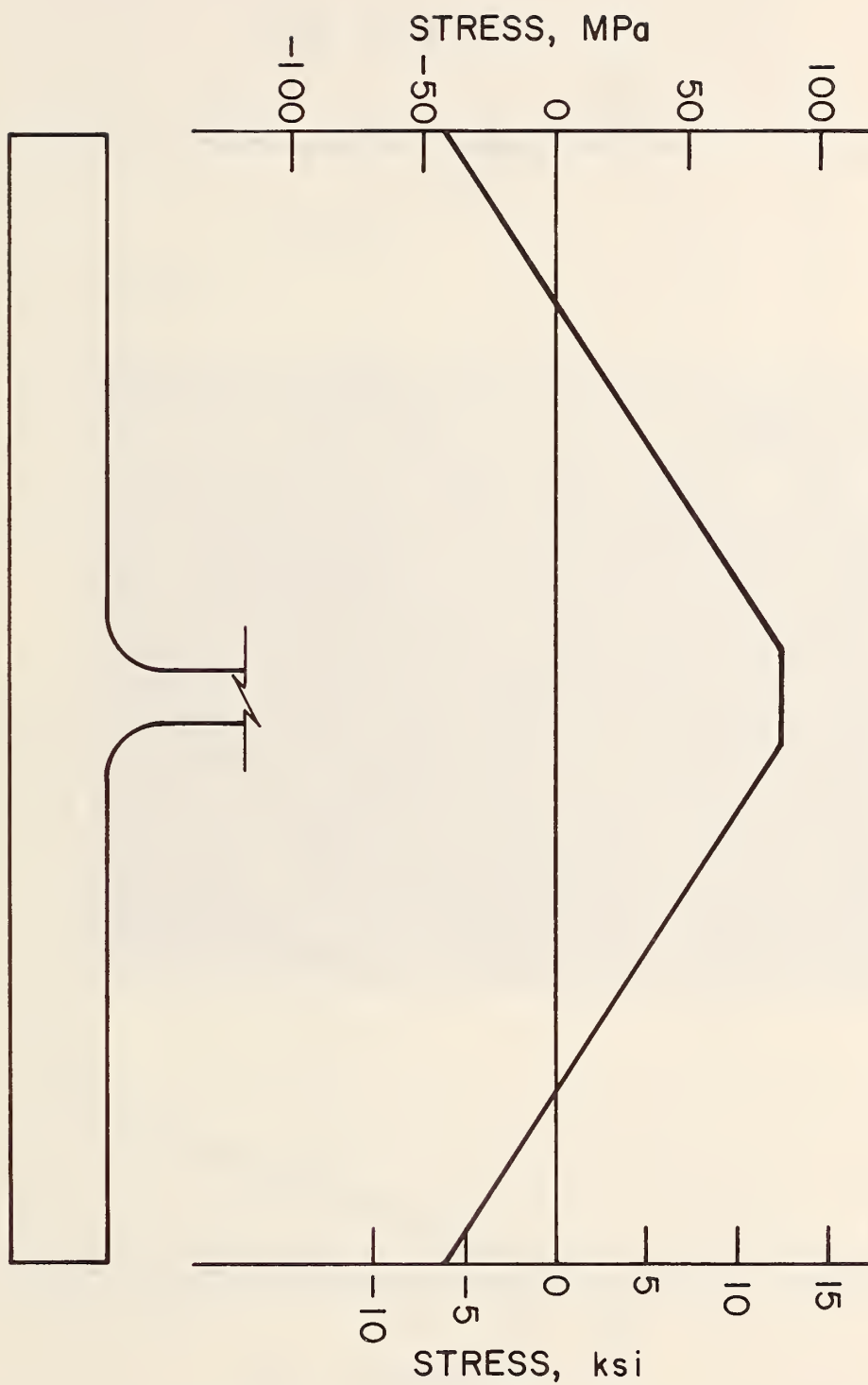


Fig. B.6 Measured Residual Stress Distribution for A36, W36X2360, Flange

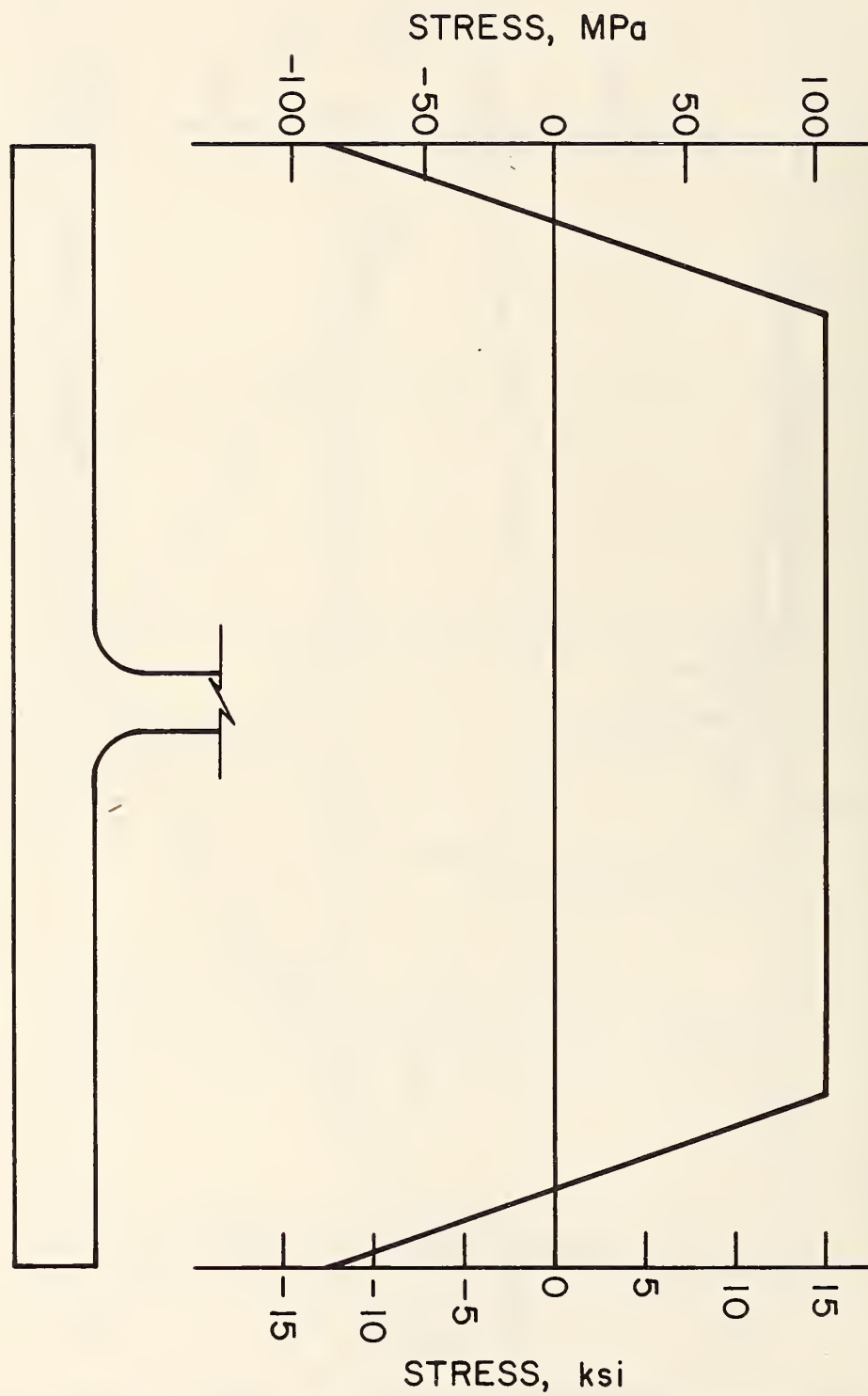


Fig. B.7 Measured Residual Stress Distribution for A588, W36X230, Flange

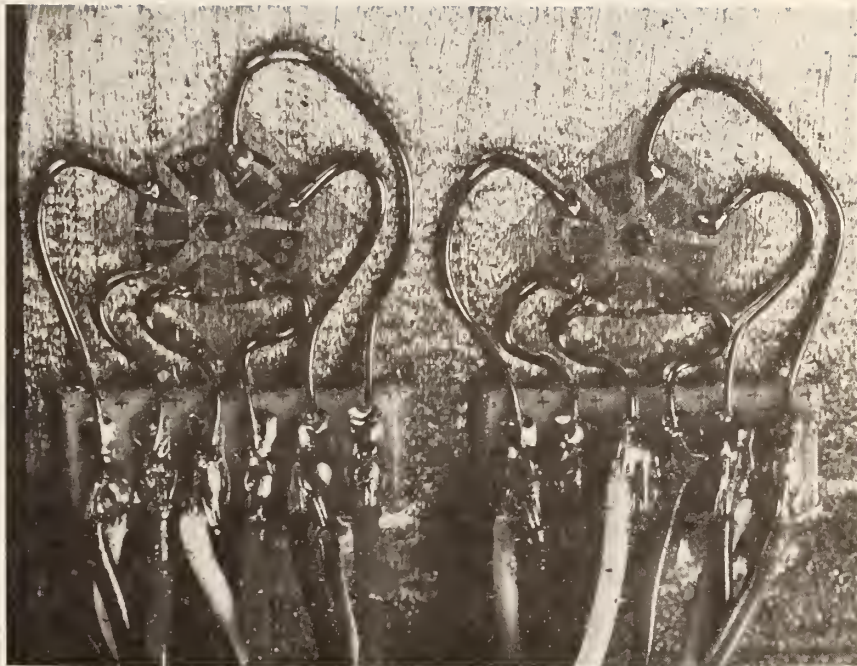


Fig. B.8 Two Mounted Strain Rosettes

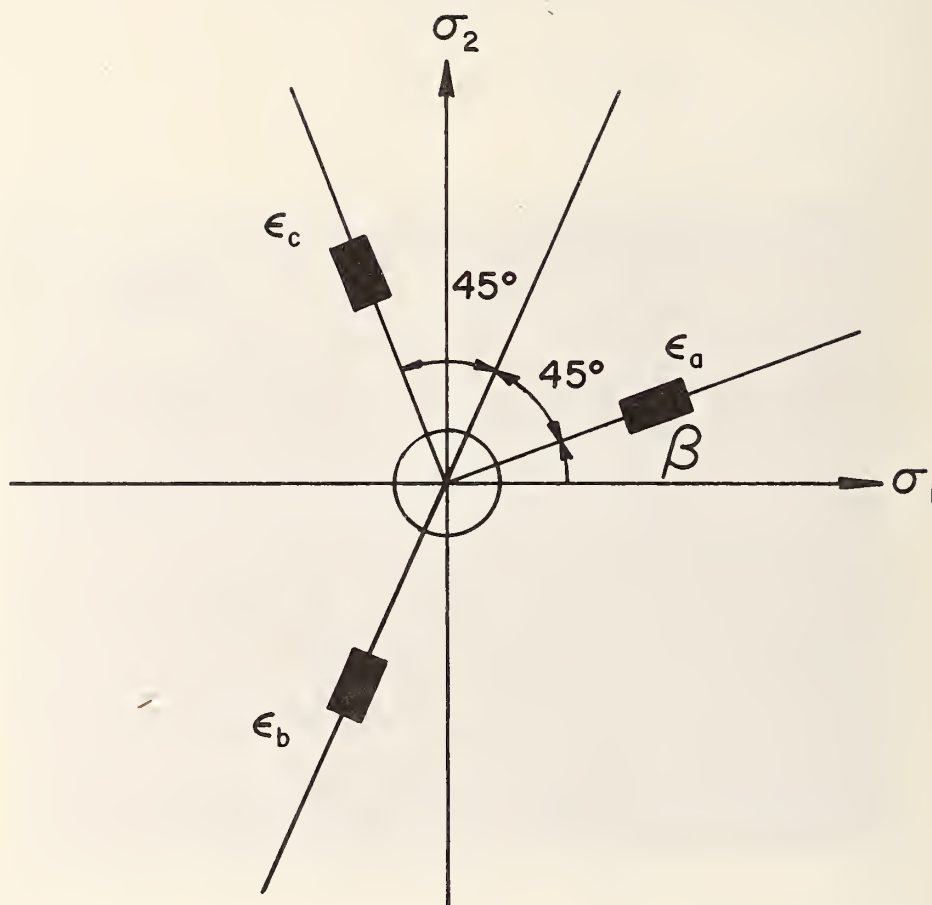


Fig. B.9 Strain Rosette Stress Field Orientation

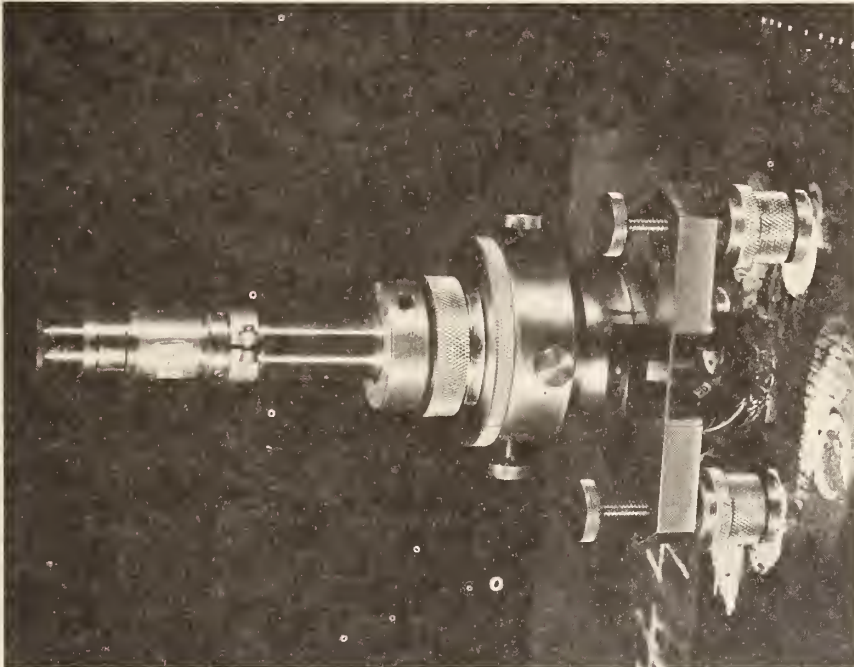


Fig. B.10 Drill Stand with Telescope

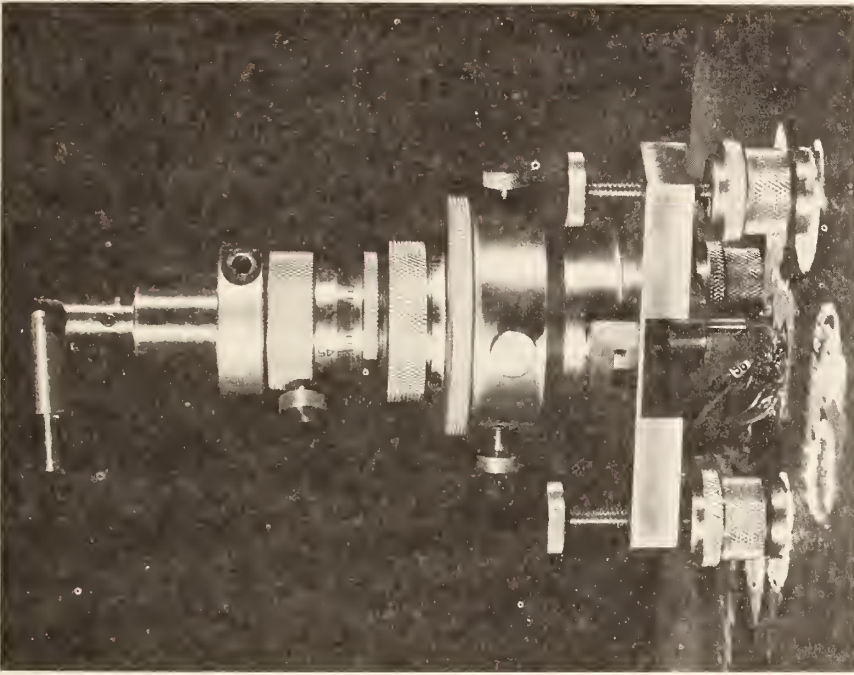


Fig. B.11 Drill Stand with Milling Bar

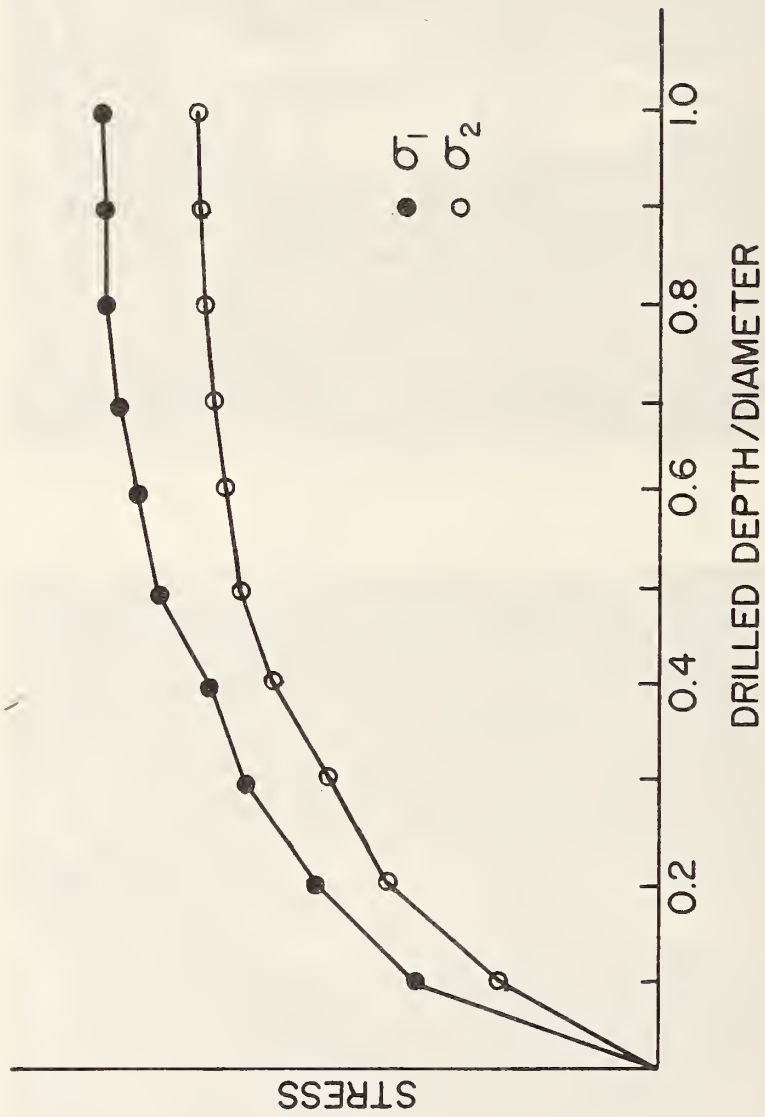


Fig. B.12 Stress Relaxation as a Function of Depth

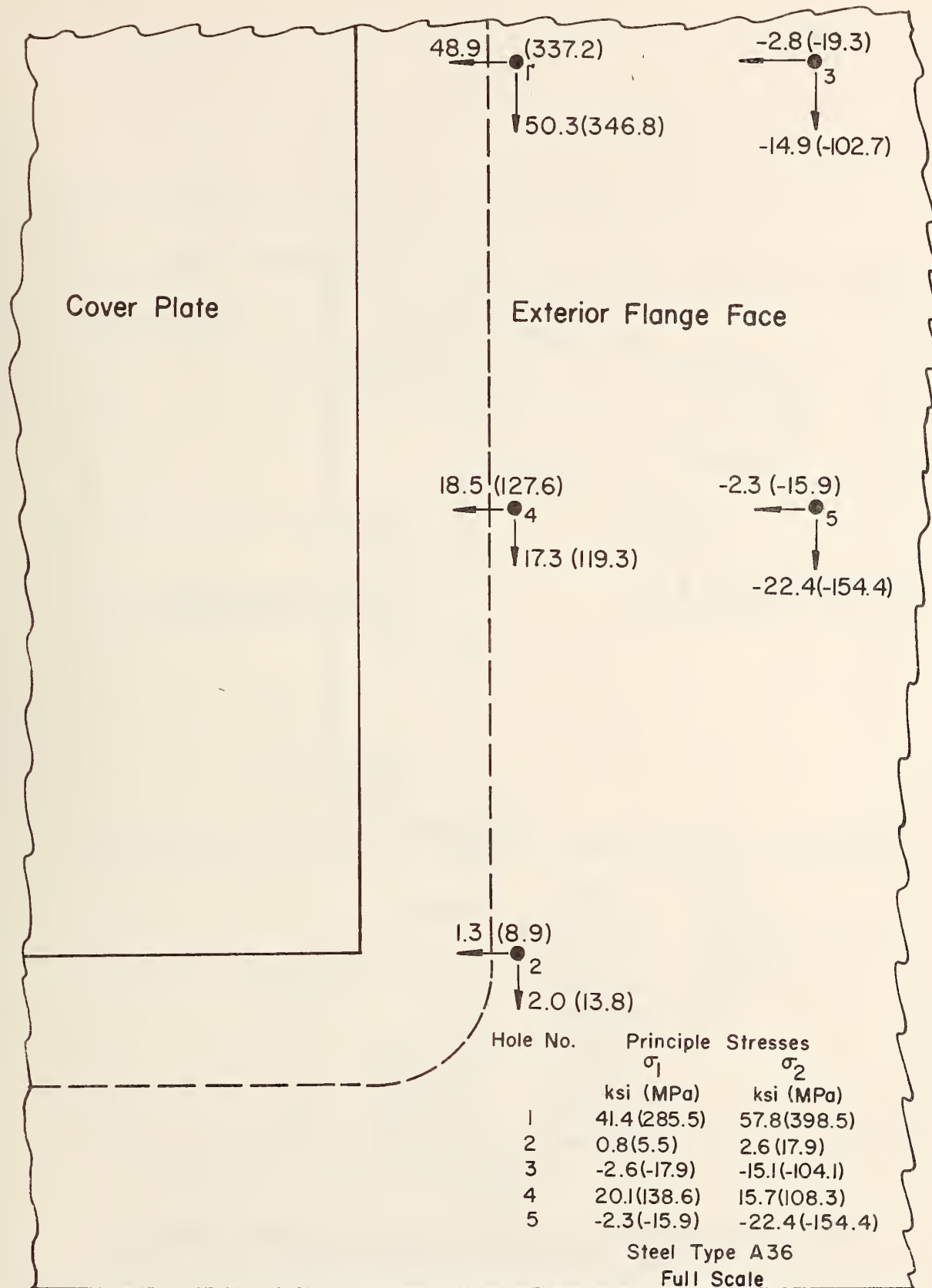


Fig. B.13a End-Welded Cover Plate Surface Residual Stress (Exterior Flange Face)

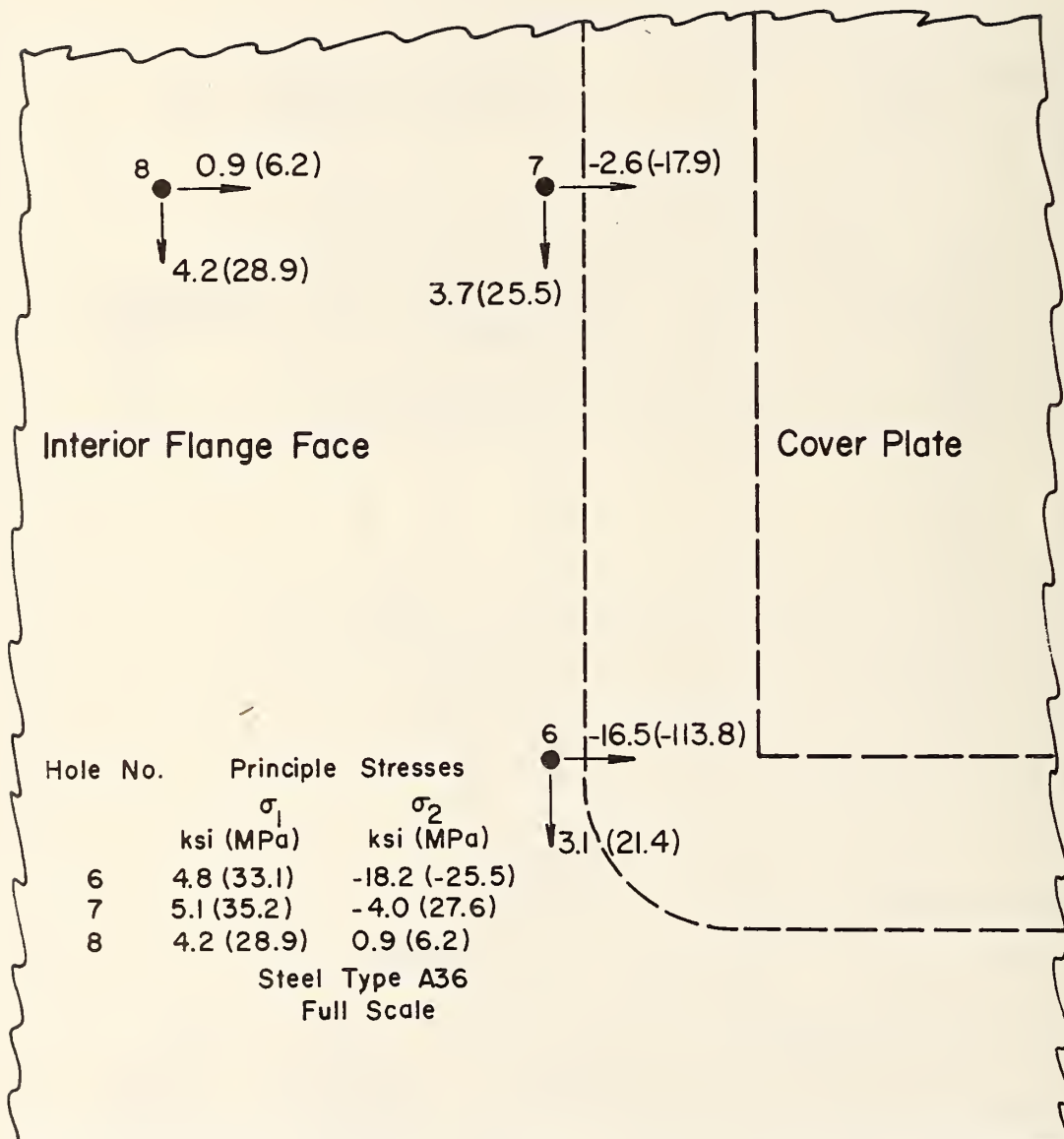
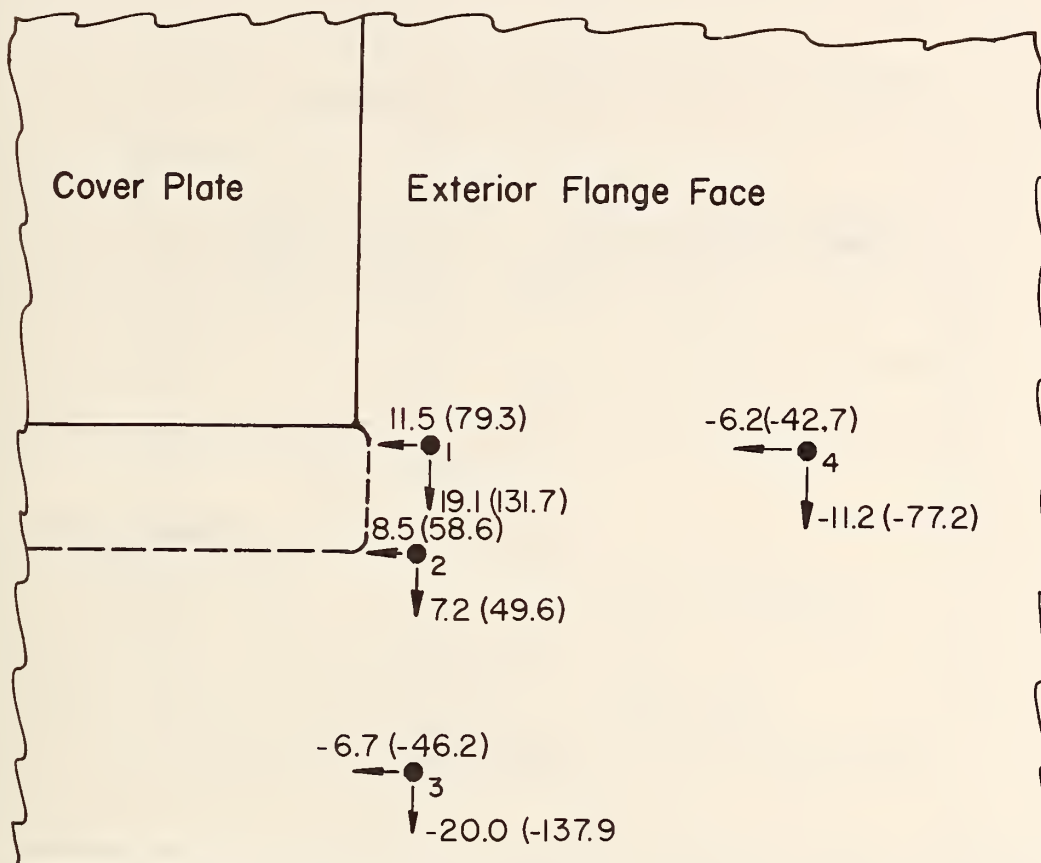
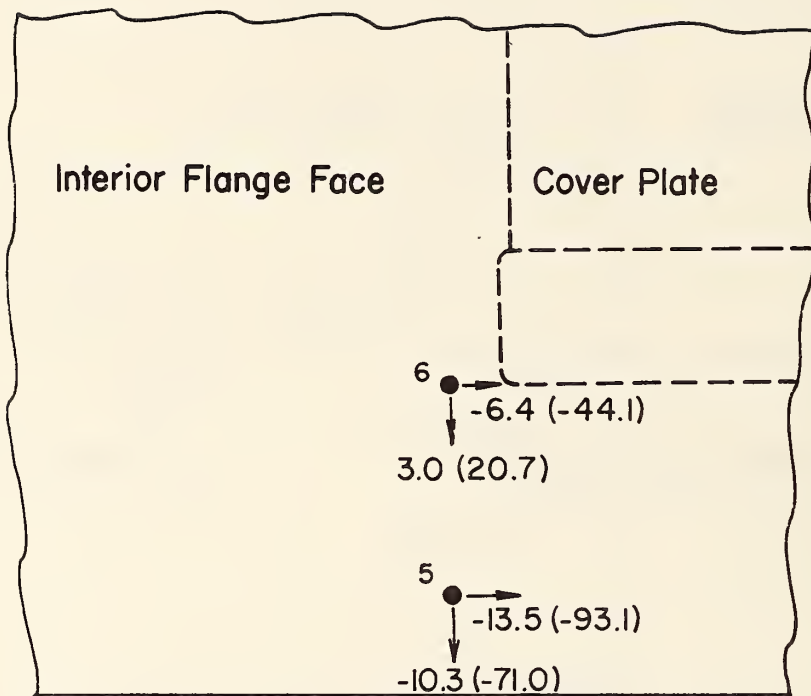


Fig. B.13b End-Welded Cover Plate Surface Residual Stress
(Interior Flange Face)



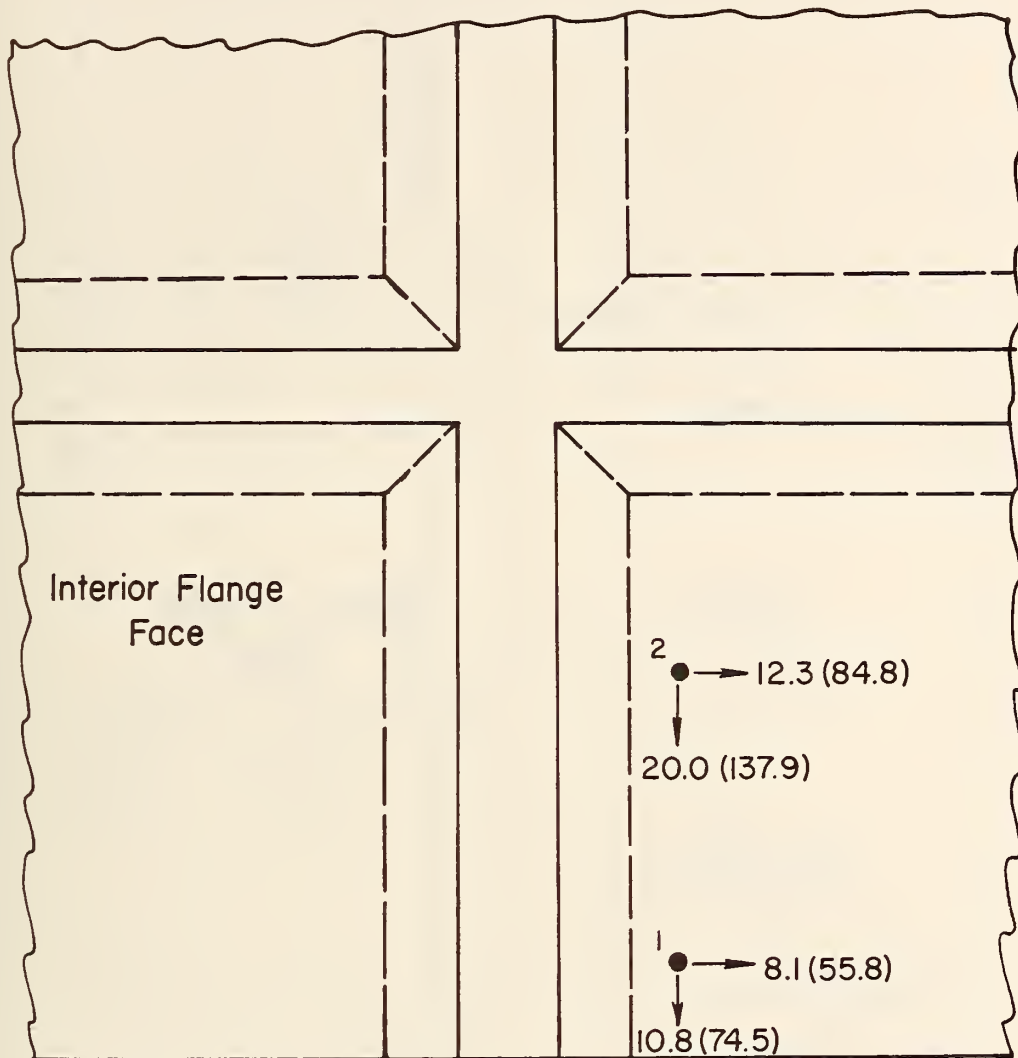
Hole No.	Principle Stresses	
	σ_1	σ_2
	ksi (MPa)	ksi (MPa)
1	19.3 (133.1)	11.3 (77.9)
2	17.0 (117.2)	-1.3 (-8.9)
3	-5.0 (34.5)	-21.7 (-149.6)
4	-2.4 (-16.5)	-15.0 (-103.4)
Steel Type A36		
Full Scale		

Fig. B.14a Unwelded End Cover Plate Surface Residual Stress
(Exterior Flange Face)



Hole No.	Principle Stresses	
	σ_1	σ_2
	ksi (MPa)	ksi (MPa)
5	-3.3 (-22.8)	-20.5 (-141.3)
6	5.2 (35.9)	-8.6 (-59.3)
Steel Type A36		
Full Scale		

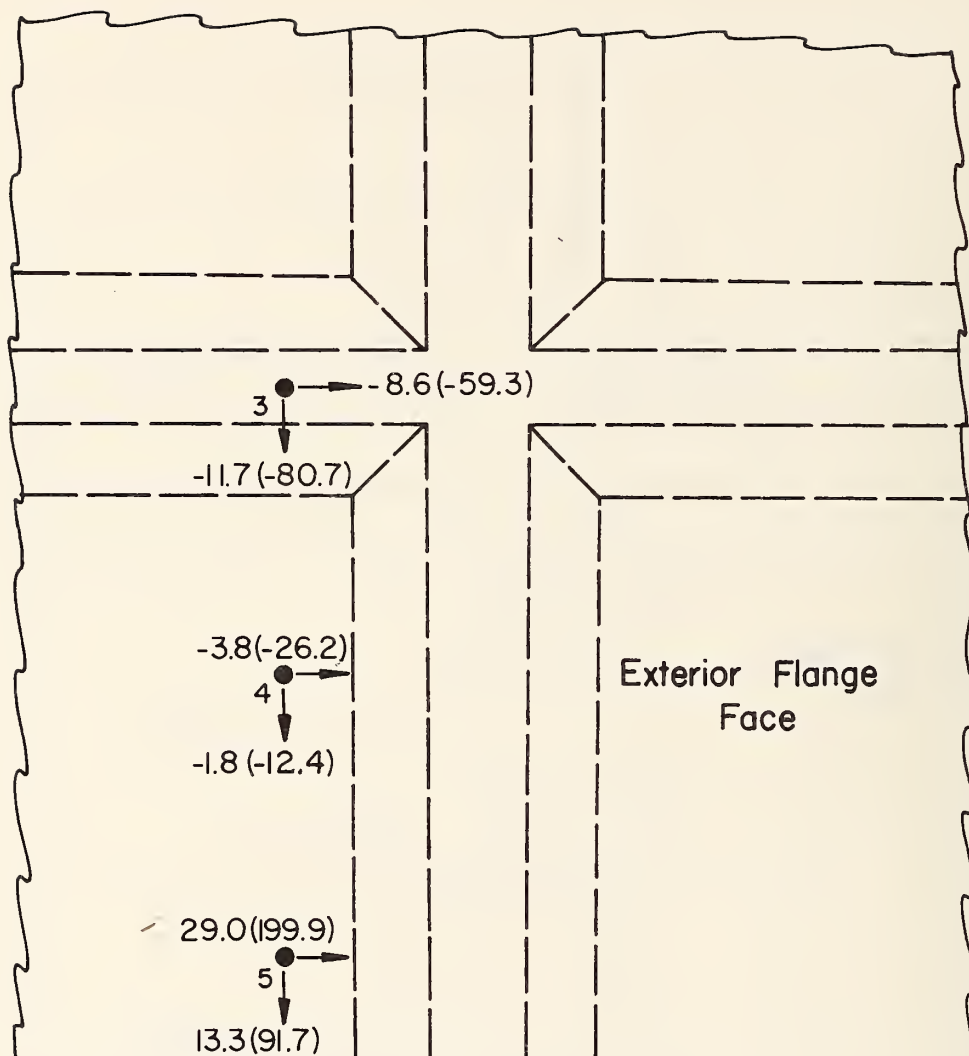
Fig. B.14b Unwelded End Cover Plate Surface Residual Stress
(Interior Flange Face)



Hole No.	Principle Stresses	
	σ_1	σ_2
	ksi (MPa)	ksi (MPa)
1	17.3 (119.3)	1.6 (11.0)
2	21.0 (144.8)	11.3 (77.9)

Steel Type A588
Full Scale

Fig. B.15a Stiffener Surface Residual Stresses
(Interior Flange Face)



Hole No.	Principle Stresses	
	σ_1	σ_2
	ksi (MPa)	ksi (MPa)
3	-13.3(-91.7)	-7.0(-48.3)
4	-6.3(-43.4)	0.7(4.8)
5	29.0(199.9)	13.3(91.7)

Steel Type A588
Full Scale

Fig. B.15b Stiffener Surface Residual Stresses
(Exterior Flange Face)

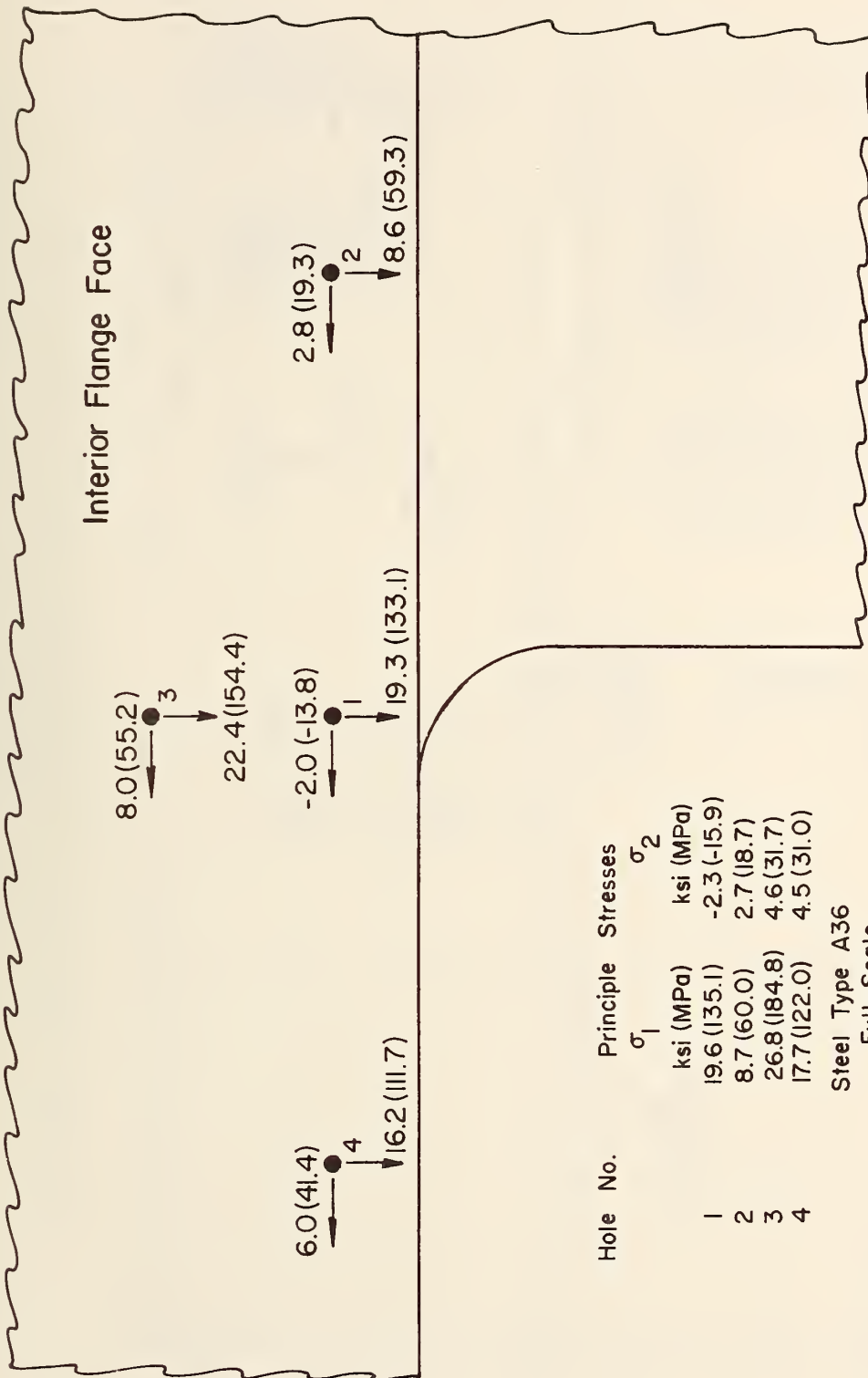


Fig. B.16a Groove Weld Lateral Attachment Surface Residual Stresses
(Interior Flange Face)

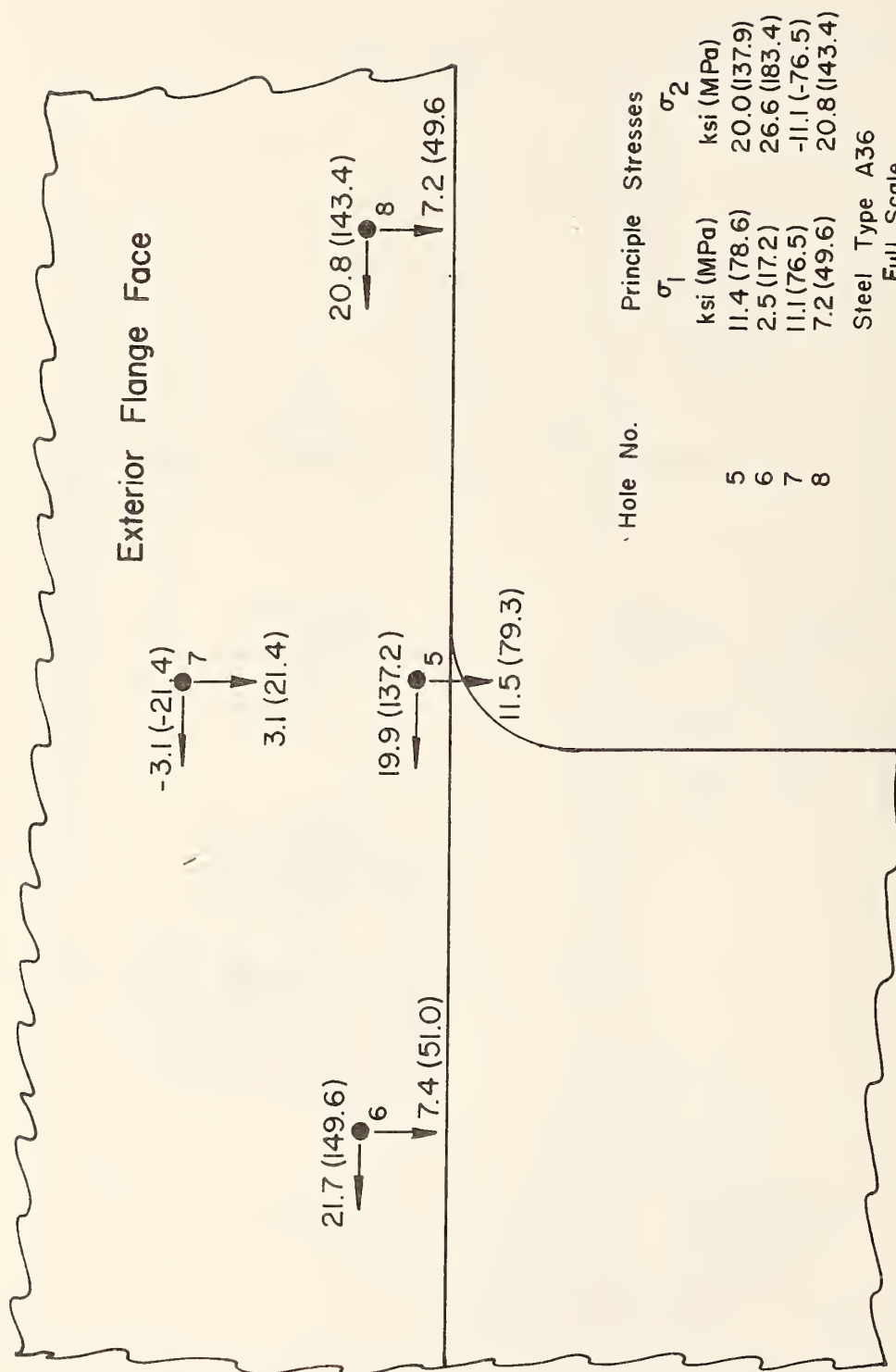


Fig. B.16b Groove Weld Lateral Attachment Surface Residual Stresses
(Exterior Flange Face)

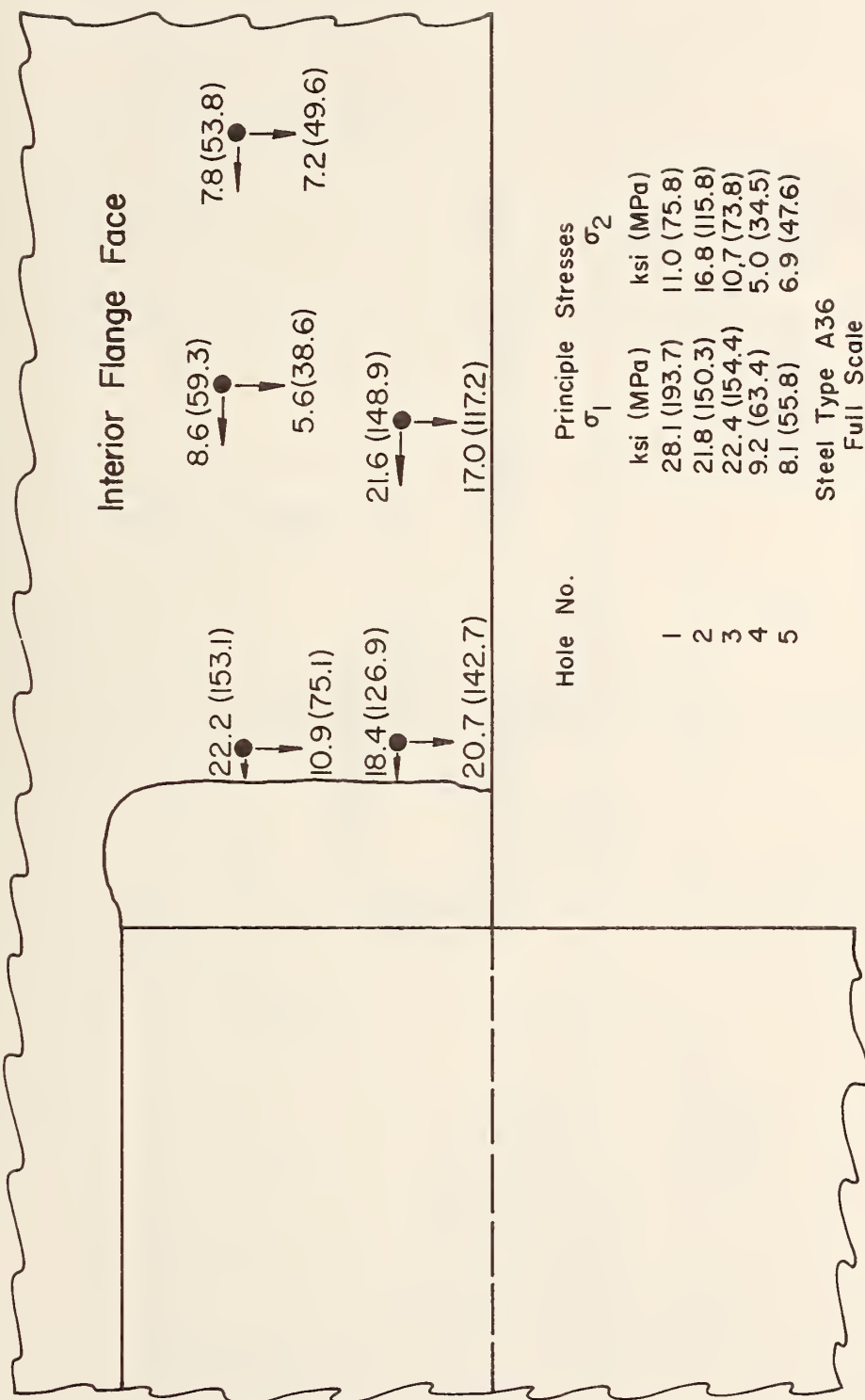


Fig. B.17a Lap Weld Lateral Attachment Surface Residual Stresses
(Interior Flange Face)

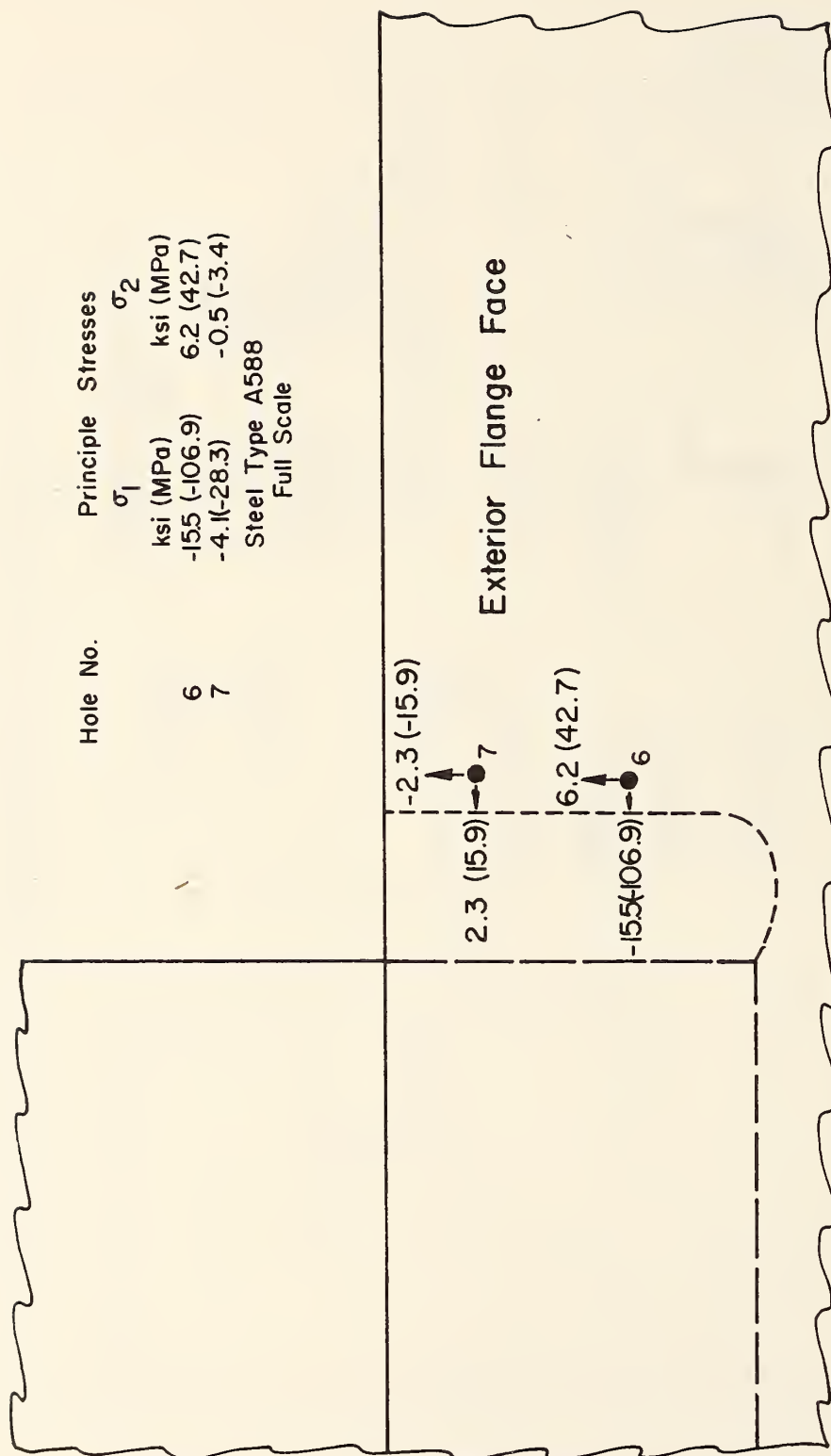
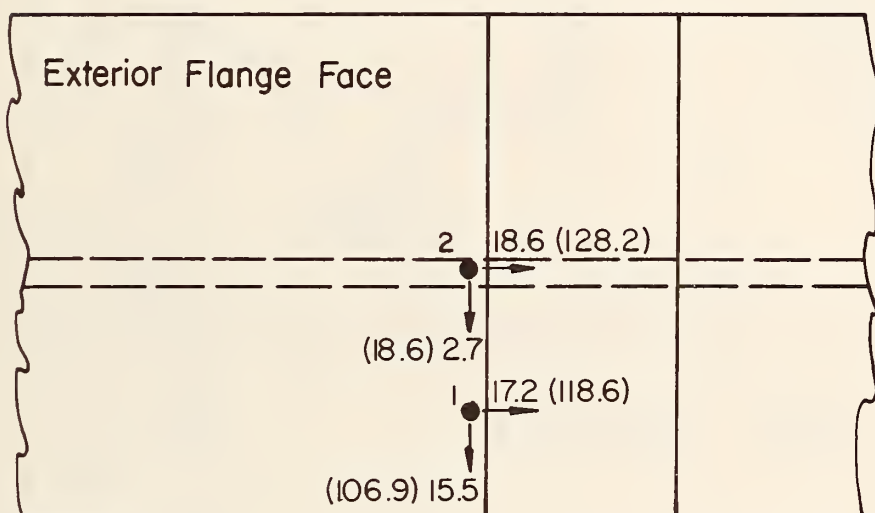
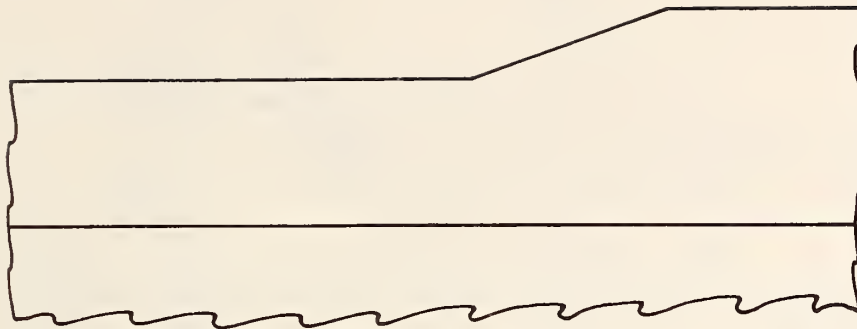


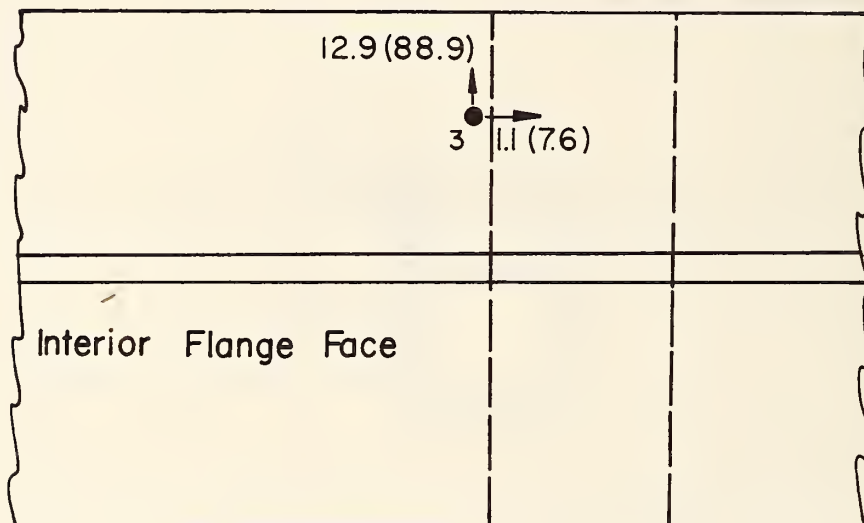
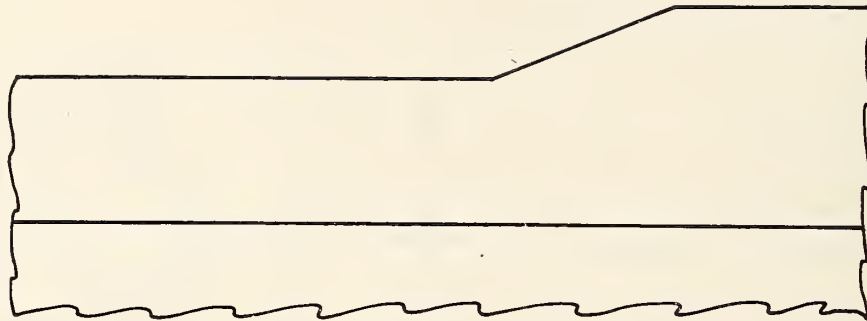
Fig. B.17b Lap Weld Lateral Attachment Surface Residual Stresses
(Exterior Flange Face)



Hole No.	Principle Stresses	
	σ_1	σ_2
	ksi (MPa)	ksi (MPa)
1	29.3 (202.0)	3.4 (23.4)
2	18.7 (128.9)	2.6 (17.9)

Steel Type A36
Scale 3/8" = 1"

Fig. B.18a Flange Transition Surface Residual Stresses
(Exterior Flange Face)



Hole No.	Principle Stresses	
	σ_1	σ_2
	ksi (MPa)	ksi (MPa)
3	13.0 (89.6)	1.0 (6.9)

Hole 3 Is 5/8" From The Weld Toe On The
Interior Flange Face
Steel Type A 36
Scale 3/8"=1"

Fig. B.18b Flange Transition Surface Residual Stresses
(Interior Flange Face)

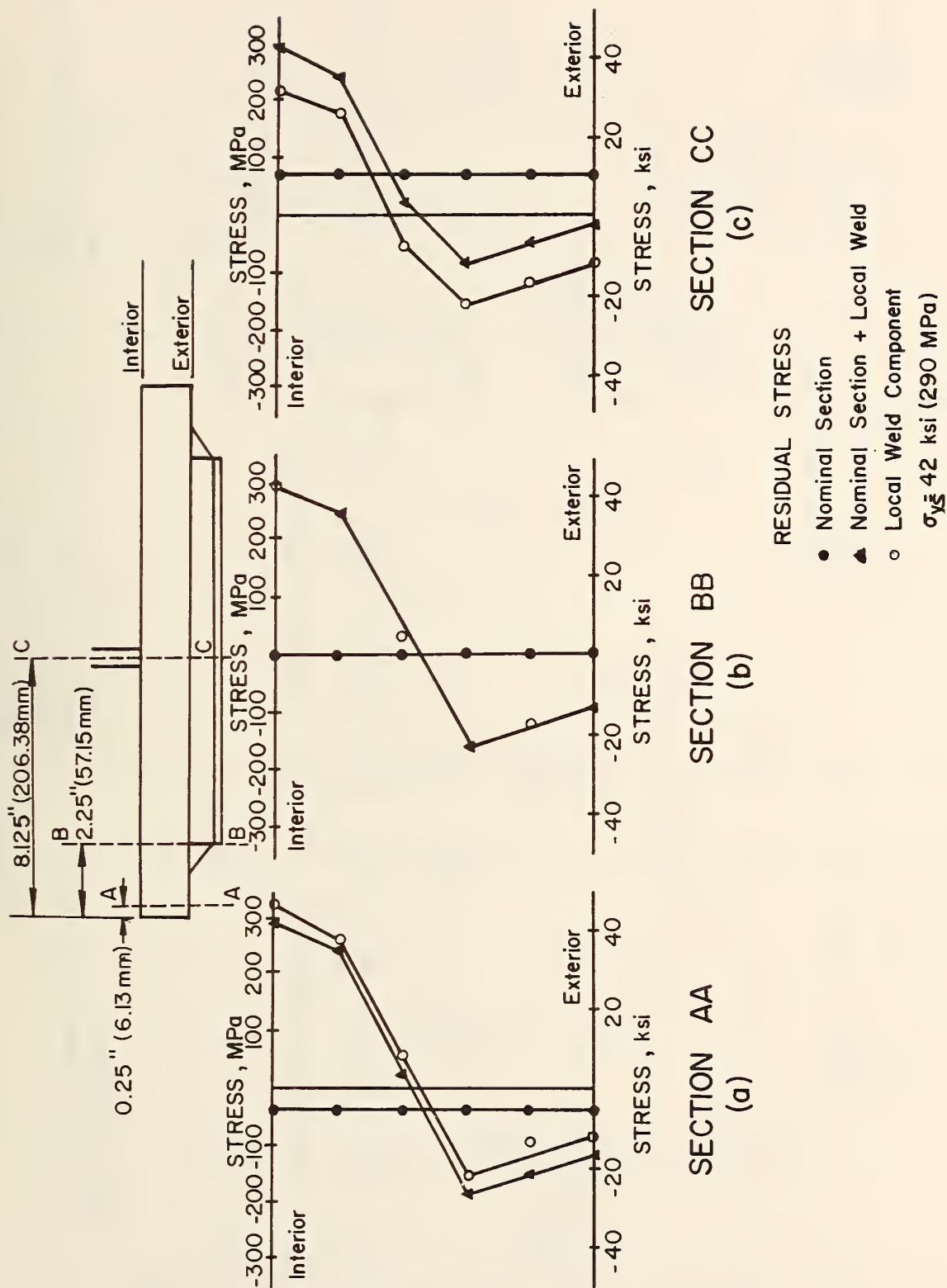


Fig. B.19 Analytical Study Stress Distribution

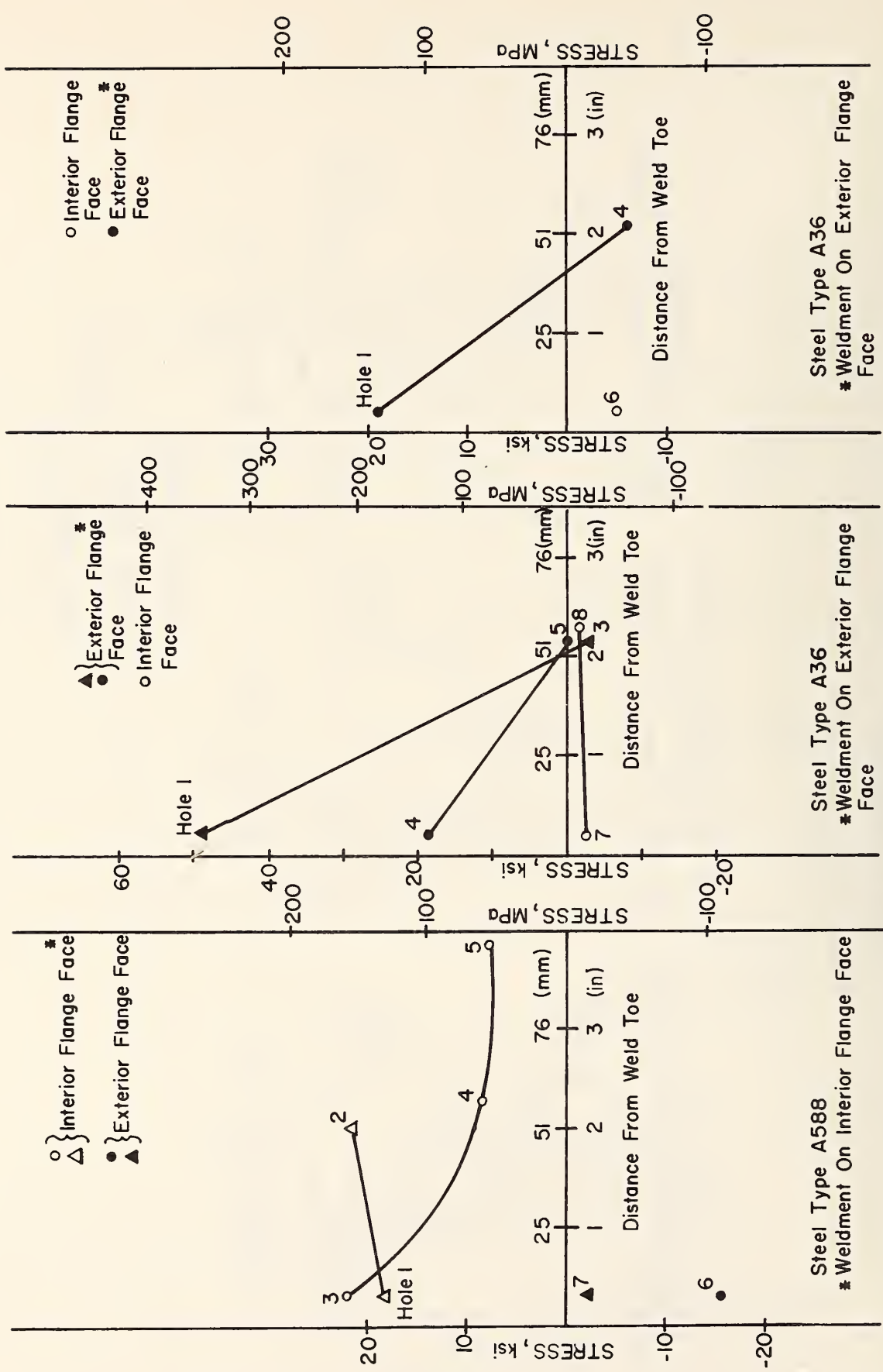


Fig. B.20 Longitudinal Residual Stress Decay

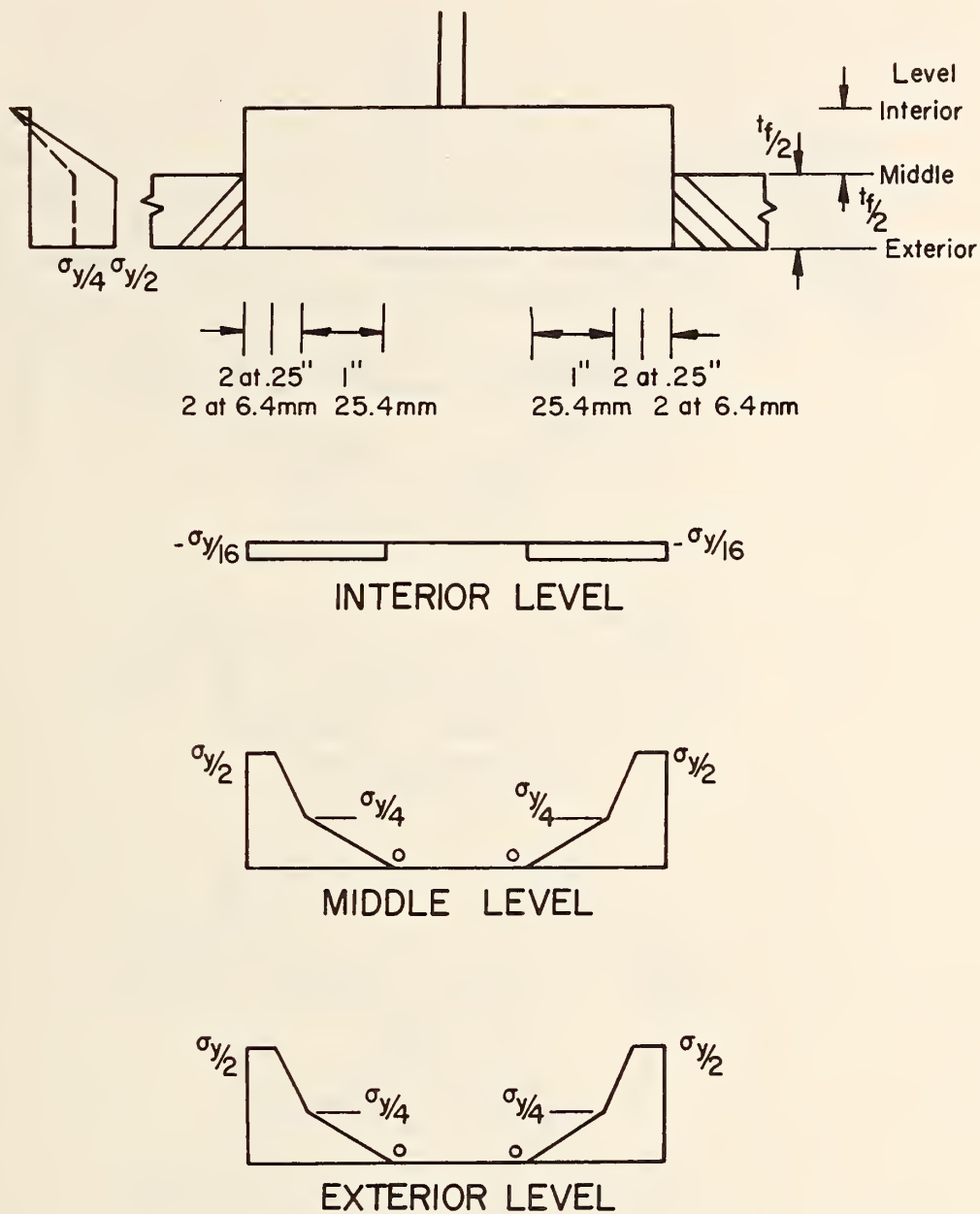
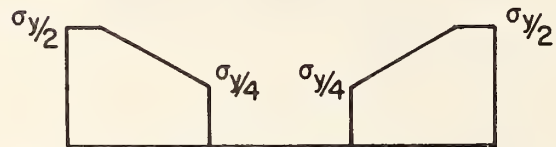
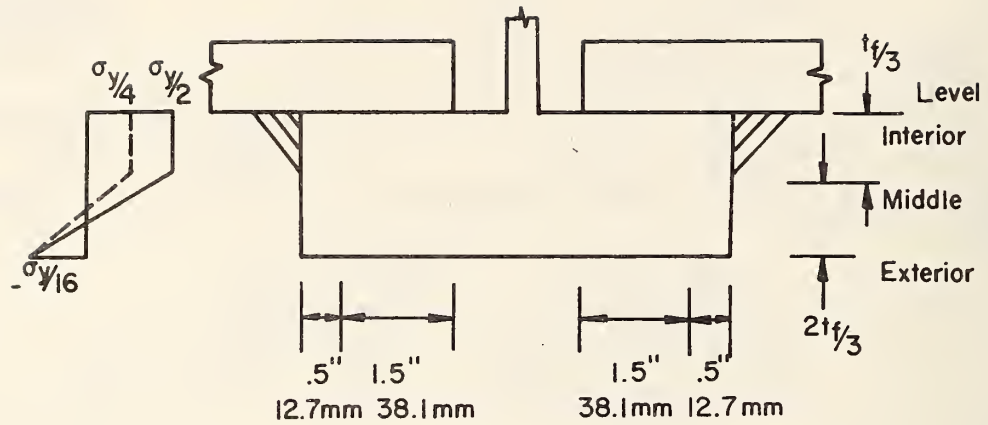
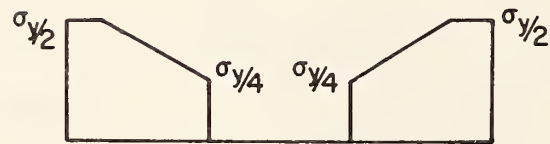


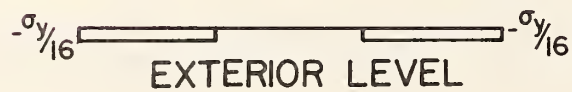
Fig. B.21 Local Weld Residual Stress Distribution
for Groove Weld Lateral Attachment



INTERIOR LEVEL



MIDDLE LEVEL



EXTERIOR LEVEL

Fig. B.22 Local Weld Residual Stress Distribution for Lap Weld Lateral Attachment

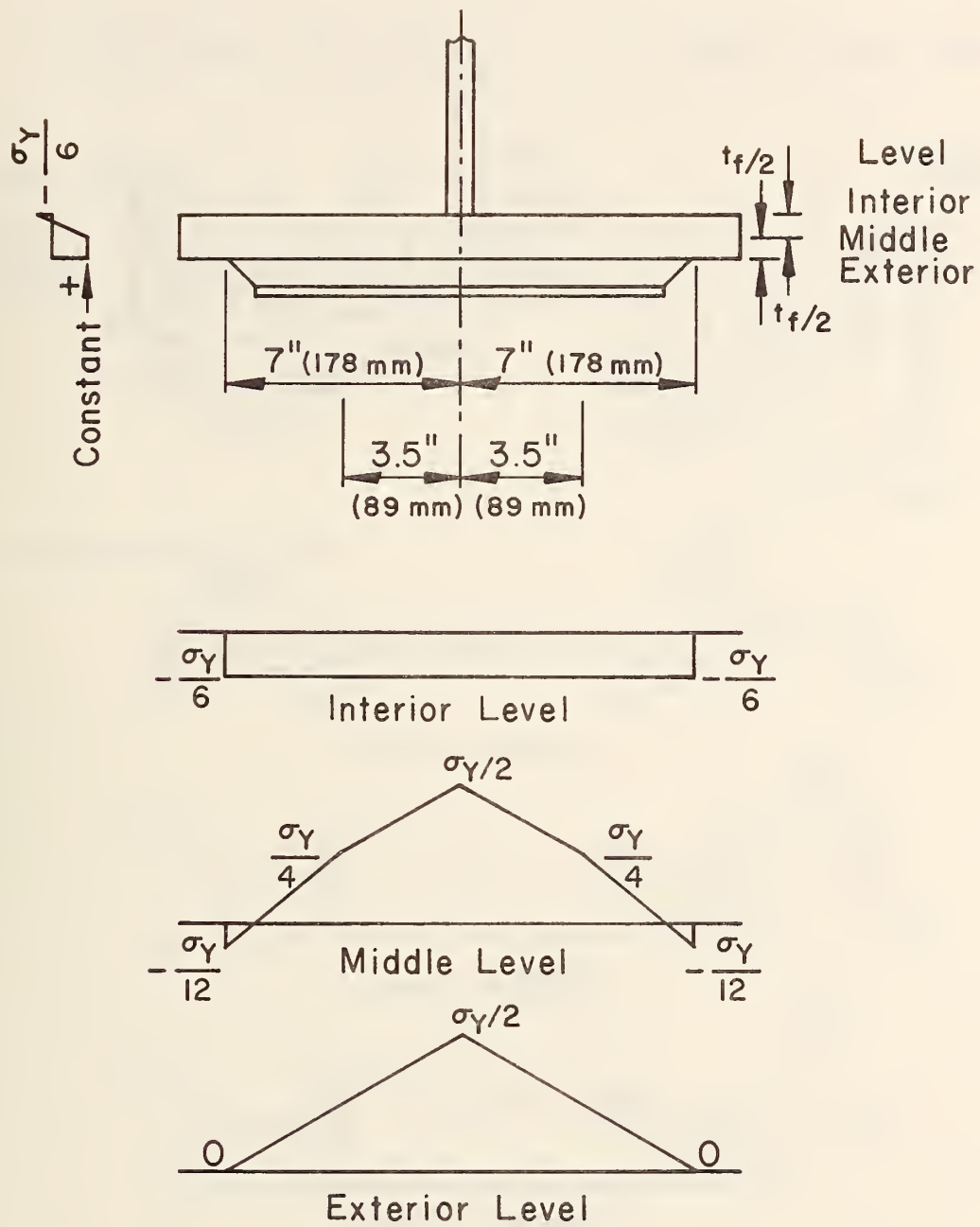


Fig. B.23 Local Weld Residual Stress Distribution for Cover Plate with End-Weld (Rolled)

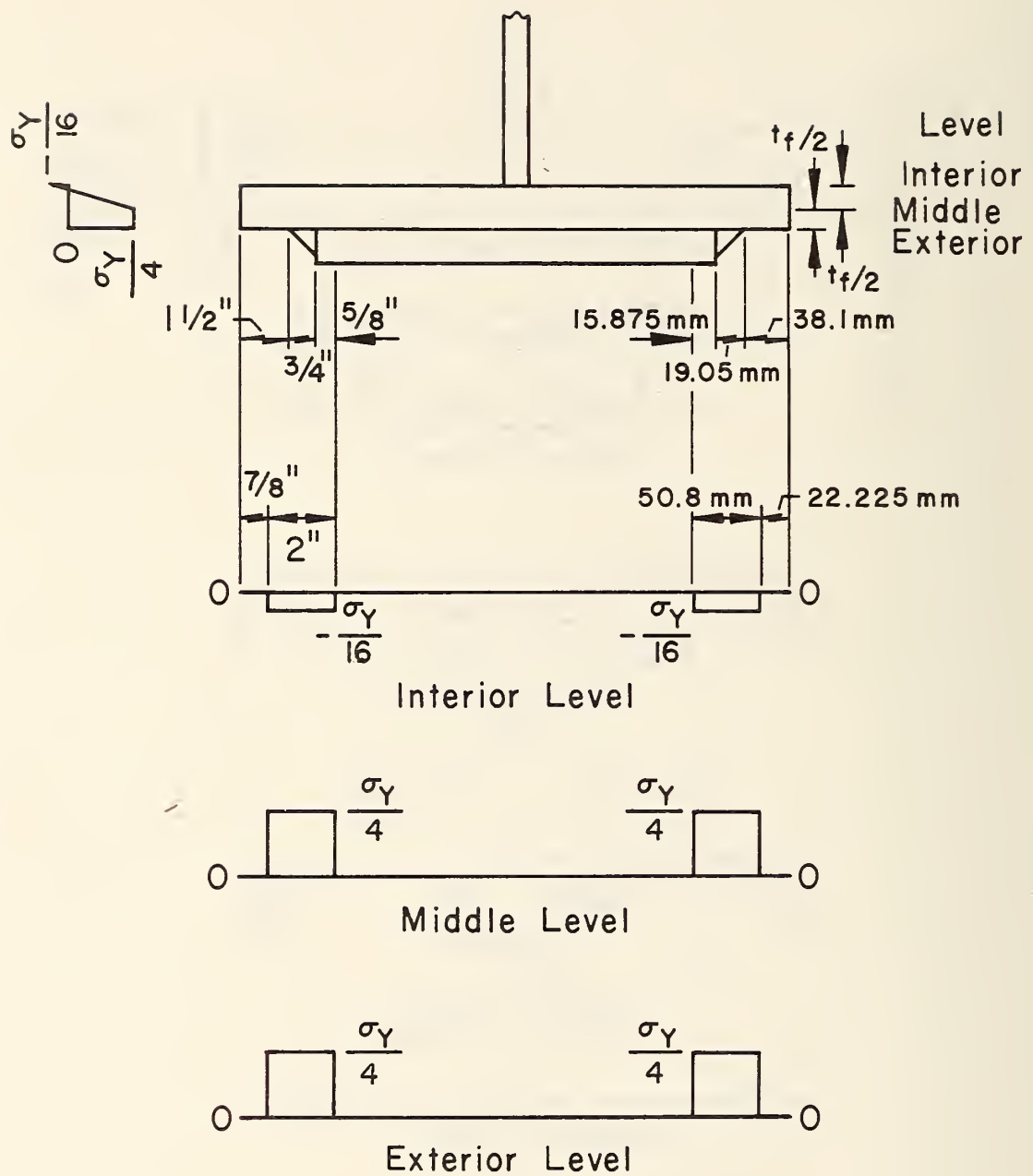


Fig. B.24 Local Weld Residual Stress Distribution for Cover Plate with No-End-Weld (Rolled)

No-End-Weld Cover Plate

End-Weld Cover Plate

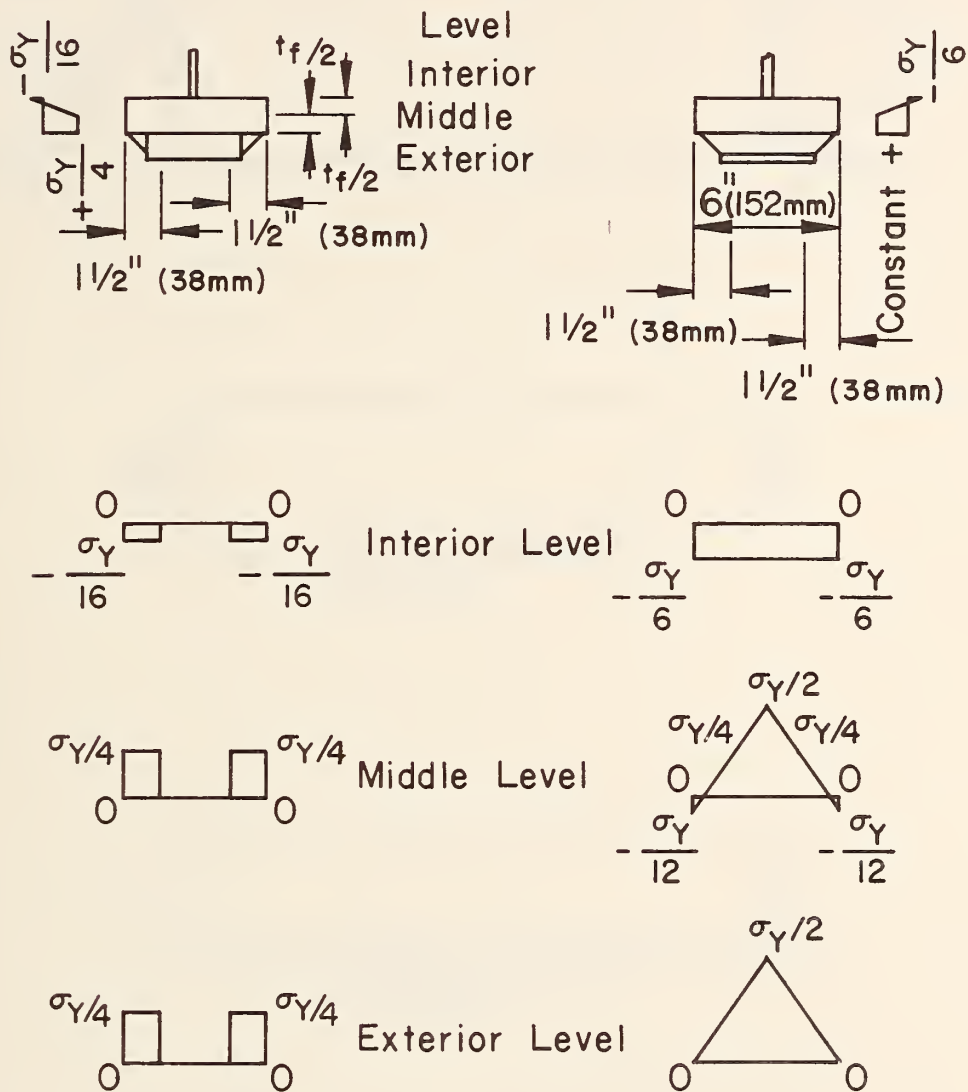


Fig. B.25 Local Weld Residual Stress Distribution for Welded Cover Plate Beams

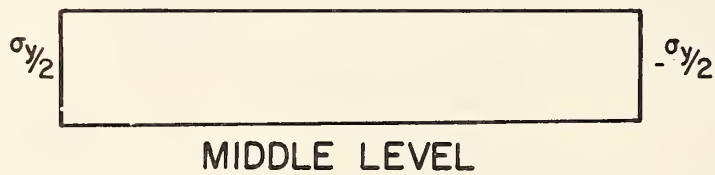
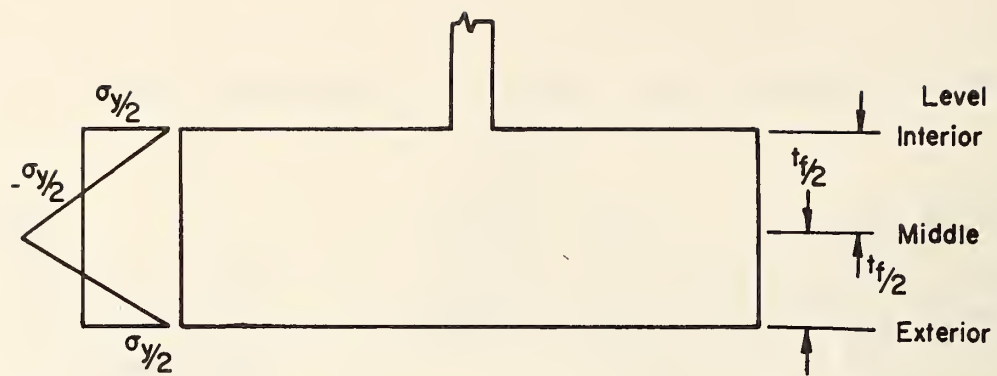


Fig. B.26 Local Weld Residual Stress Distribution
for Flange Transition

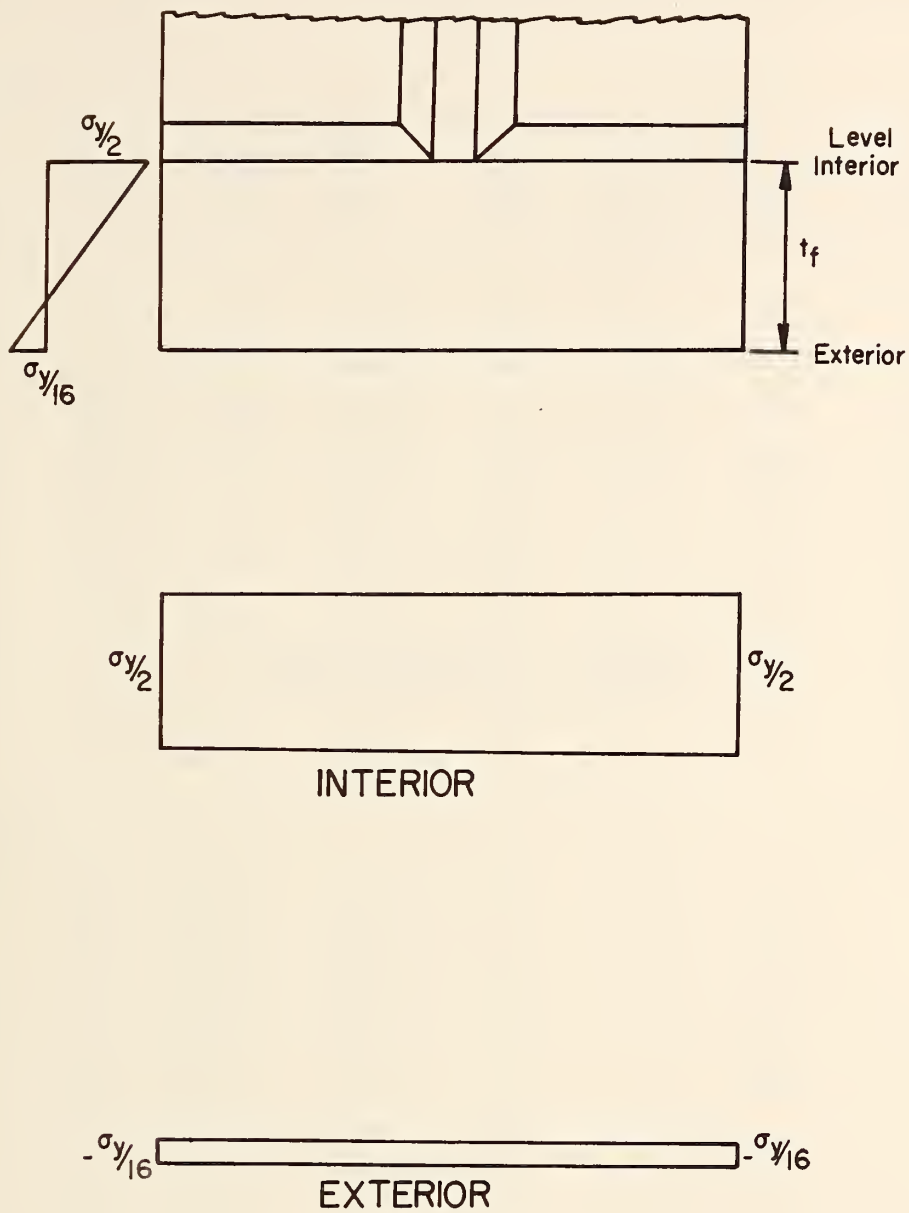


Fig. B.27 Local Weld Residual Stress Distribution for Transverse Stiffener Welded to the Flange

APPENDIX C - MATERIAL TESTS

Table C.1 Dynamic & Static Fracture Toughness (A36, 3/8 in PL)

Steel Type A36
 Thickness 3/8 in

Specimen No.	\bar{B} in	Temp. °F	A_o in	P_{max} kip	Time sec	K_{WIL} ksi√in	DTE in lb/in ²
<u>Dynamic</u>					$\times 10^{-4}$		
1.201	0.38	0.0	1.050	18.0	10.0	168.8	4644.1
1.202	0.38	-40.0	1.045	15.0	7.0	139.0	879.4
1.203	0.38	-40.0	1.015	7.5	6.0	64.4	983.4
1.204	0.38	-80.0	1.000	6.6	3.0	59.5	400.0
1.205	0.38	-80.0	1.145	6.2	3.5	62.9	586.5
1.206	0.38	-40.0	0.980	15.7	8.0	139.2	918.8
1.214	0.38	-10.0	1.030	14.4	8.0	132.9	16.2
1.215	0.38	-40.0	1.115	14.6	8.0	145.0	1969.2
1.216	0.38	-150.0	1.116	4.8	3.0	49.4	17.4
1.217	0.38	-145.0	0.990	5.2	4.0	46.5	15.9
<u>Static</u>					$\times 1$		
1.220	0.38	-230.0	1.000	4.0	0.50	36.0	---
1.210	0.38	-250.0	1.010	5.3	0.60	48.1	---
1.218	0.38	-210.0	1.080	8.7	0.95	83.6	---
1.213	0.38	-200.0	0.960	6.5	1.40	56.7	---
1.219	0.38	-200.0	0.980	9.8	1.20	86.9	---
1.209	0.38	-150.0	1.000	15.0	0.90	135.1	---
1.212	0.38	-150.0	1.010	14.4	3.20	130.7	---
1.207	0.38	-110.0	1.050	13.7	3.00	128.5	---
1.208	0.38	-100.0	1.040	12.5	1.40	116.3	---

1 in. = 25.4 mm

1 kip = 6.89 MPa

1 ksi√in = 1.1 MPa√m

1 in-lb/in² = 0.175 mN/m² × 10³

°F = $\frac{9}{5}$ °C + 32

Table C.2 Dynamic & Static Fracture Toughness (A36, 2 in PL)

Steel Type A36
 Thickness 2 in

Specimen No.	\bar{B} in	Temp. °F	A_o in	P_{max} kip	Time sec	K_{WIL} ksi√in	DTE in lb/in ²
<u>Dynamic</u>					$\times 10^{-4}$		
2.202	1.50	- 80.0	1.100	21.5	4.2	52.5	155.8
2.203	1.50	- 40.0	1.050	23.0	4.0	53.9	270.8
2.204	1.50	- 80.0	1.050	20.0	4.0	46.9	274.9
2.206	1.50	0.0	0.990	26.3	6.0	58.7	324.4
2.209	1.50	25.0	1.020	27.5	5.0	62.9	961.6
2.210	1.50	70.0	0.980	48.0	10.0	106.4	0.0
2.214	1.50	0.0	1.140	21.3	5.0	53.7	483.9
2.216	1.50	25.0	1.060	29.0	5.5	68.6	1682.5
2.217	1.50	50.0	1.050	35.0	6.5	82.1	2453.3
2.219	1.50	- 40.0	1.035	17.5	6.0	40.5	378.6
<u>Static</u>					$\times 1$		
2.208	1.50	-200.0	1.030	16.8	0.80	38.8	---
2.218	1.50	-190.0	0.950	22.5	1.10	48.7	---
2.211	1.50	-150.0	1.030	19.0	0.90	43.8	---
2.213	1.50	-150.0	1.035	19.7	1.10	45.8	---
2.215	1.50	-110.0	1.000	37.5	1.80	84.7	---
2.220	1.50	-110.0	0.985	35.7	1.60	79.5	---
2.205	1.50	-100.0	1.000	33.0	1.50	74.9	---
2.207	1.50	-100.0	1.190	34.2	1.60	90.4	---
2.212	1.50	- 75.0	1.070	42.0	2.20	100.2	---
2.201	1.50	- 50.0	1.000	41.7	2.10	94.0	---

See footnote on Table C.1 for Metric Conversion.

Table C.3 Dynamic & Static Fracture Toughness (A36, 3 in PL)

Steel Type A36
Thickness 3 in

Specimen No.	\bar{B} in	Temp. °F	A_o in	P_{max} kip	Time sec	K_{WIL} ksi \sqrt{in}	DTE in lb/in ²
<u>Dynamic</u>					$\times 10^{-4}$		
3.201	1.50	0.0	1.035	22.7	5.5	52.6	431.6
3.202	1.50	0.0	1.065	22.0	5.5	52.2	396.9
3.202	1.50	- 40.0	1.115	21.5	5.0	53.2	288.6
3.209	1.50	- 10.0	1.250	20.0	4.5	55.6	484.6
3.212	1.50	- 10.0	1.035	23.0	5.5	53.3	598.5
3.214	1.50	- 80.0	1.050	21.0	6.0	49.2	242.1
3.216	1.50	- 80.0	1.055	17.0	5.5	40.0	283.8
3.217	1.50	- 80.0	1.035	19.6	6.0	45.4	232.1
3.218	1.50	- 40.0	1.115	20.5	5.5	50.7	254.6
3.220	1.50	- 10.0	1.075	26.0	6.0	62.2	519.5
<u>Static</u>					$\times 1$		
3.219	1.50	-250.0	1.045	15.5	0.80	36.2	---
3.214	1.50	-245.0	1.030	21.5	1.10	49.6	---
3.211	1.50	-200.0	1.000	15.2	1.10	34.2	---
3.208	1.50	-200.0	1.085	30.6	1.00	49.7	---
3.210	1.50	-175.0	1.070	33.3	1.60	79.4	---
3.215	1.50	-170.0	1.040	38.0	2.10	88.4	---
3.206	1.50	-150.0	1.050	24.5	1.30	57.5	---
3.207	1.50	-150.0	1.055	36.5	1.00	85.9	---
3.213	1.50	-148.0	1.035	39.0	1.90	91.7	---
3.205	1.50	-100.0	1.025	43.0	2.20	98.8	---

See footnote on Table C.1 for Metric Conversion.

Table C.4 Dynamic & Static Fracture Toughness (A588, 3/8 in PL)

Steel Type A588
 Thickness 3/8 in

Specimen No.	\bar{B} in	Temp. °F	A_o in	P_{max} kip	Time sec	K_{WIL} ksi√in	DTE in lb/in ²
<u>Dynamic</u>							
4.201	0.38	0.0	1.000	15.5	7.0	139.7	8000.0
4.202	0.38	- 40.0	0.995	12.0	6.0	107.7	1691.8
4.204	0.38	-145.0	0.975	5.6	3.0	49.5	695.3
4.207	0.38	- 80.0	0.980	6.4	4.5	56.8	617.8
4.210	0.38	- 80.0	1.085	4.8	3.0	46.3	484.6
4.211	0.38	- 40.0	1.000	8.2	5.5	73.9	2144.0
4.213	0.38	- 40.0	1.035	9.0	6.0	83.4	1921.6
4.214	0.38	-160.0	0.925	5.2	3.0	44.2	771.1
<u>Static</u>							
4.212	0.38	-250.0	1.820	3.0	0.60	61.5	---
4.216	0.38	-250.0	1.000	6.7	0.80	60.4	---
4.217	0.38	-240.0	1.050	5.7	0.90	53.5	---
4.219	0.38	-205.0	1.020	5.9	0.65	54.0	---
4.206	0.38	-200.0	1.025	11.0	1.00	101.1	---
4.209	0.38	-200.0	1.130	4.0	0.50	40.1	---
4.218	0.38	-190.0	1.000	12.7	1.20	114.4	---
4.208	0.38	-175.0	1.010	7.8	1.00	70.4	---
4.203	0.38	-150.0	1.025	12.5	1.50	114.9	---
4.205	0.38	-150.0	1.020	16.6	2.31	152.0	---
4.220	0.38	-100.0	1.000	17.5	2.40	157.7	---

See footnote on Table C.1 for Metric Conversion.

Table C.5 Dynamic & Static Fracture Toughness (A588, 2 in PL)

Steel Type A588

Thickness 2 in

Specimen No.	\bar{B} in	Temp. °F	A_o in	P_{max} kip	Time sec	K_{WII} ksi \sqrt{in}	DTE in lb/in ²
<u>Dynamic</u>					$\times 10^{-4}$		
5.201	1.49	0.0	1.070	20.1	6.0	48.2	344.4
5.203	1.49	-40.0	1.000	22.5	4.5	51.0	310.1
5.206	1.49	25.0	0.980	26.0	4.0	58.2	618.0
5.208	1.49	-40.0	1.080	22.5	4.0	54.4	318.8
5.209	1.49	50.0	1.100	23.3	5.0	57.3	839.3
5.215	1.49	-80.0	1.050	20.0	4.5	47.2	499.7
5.218	1.49	0.0	1.230	18.7	5.0	51.6	394.0
5.220	1.49	-80.0	1.150	19.5	4.0	50.0	343.9
<u>Static</u>					$\times 1$		
5.207	1.49	-200.0	1.000	16.2	0.65	36.7	---
5.222	1.49	-150.0	1.105	28.5	1.60	69.9	---
5.214	1.49	-150.0	0.995	21.5	1.10	48.7	---
5.202	1.49	-125.0	1.220	18.5	0.92	50.3	---
5.217	1.49	-125.0	1.180	23.0	0.70	60.6	---
5.219	1.49	-125.0	1.060	16.5	0.65	39.3	---
5.205	1.49	-100.0	1.035	20.5	1.00	47.8	---
5.221	1.49	-100.0	1.310	19.8	0.80	58.2	---
5.212	1.49	-100.0	0.925	33.5	1.80	71.6	---
5.213	1.49	-100.0	1.300	27.2	1.50	79.7	---
5.223	1.49	- 75.0	1.200	22.3	1.20	59.7	---
5.204	1.49	- 75.0	1.625	14.0	0.80	57.0	---
5.211	1.49	- 50.0	1.135	22.4	1.30	56.7	---
5.210	1.49	- 50.0	1.040	34.4	1.60	80.6	---
5.216	1.49	- 20.0	1.800	12.8	0.80	64.3	---

See footnote on Table C.1 for Metric Conversion.

Table C.6 Dynamic & Static Fracture Toughness (A588, 3 in PL)

Steel Type A588

Thickness 3 in

Specimen No.	\bar{B} in	Temp. °F	A_o in	P_{max} kip	Time sec	K_{WIL} ksi \sqrt{in}	DTE in lb/in ²
<u>Dynamic</u>					$\times 10^{-4}$		
6.201	1.5	0.0	1.100	22.7	4.5	55.6	370.5
6.202	1.5	0.0	1.135	23.0	4.5	57.9	266.0
6.203	1.5	-185.0	1.335	12.6	4.0	37.9	269.1
6.206	1.5	- 40.0	1.105	22.5	4.5	55.2	126.6
6.208	1.5	- 45.0	1.115	26.0	6.5	64.3	0.0
6.213	1.5	-150.0	1.070	17.2	5.0	41.0	169.9
6.215	1.5	-105.0	1.030	17.5	4.0	40.4	247.7
<u>Static</u>					$\times 1$		
6.214	1.5	-200.0	1.120	22.4	1.10	55.7	---
6.212	1.5	-200.0	1.070	17.3	0.95	41.2	---
6.220	1.5	-190.0	1.035	18.8	0.85	43.6	---
6.211	1.5	-150.0	1.080	46.4	3.00	111.5	---
6.204	1.5	-150.0	1.070	32.5	1.70	77.5	---
6.210	1.5	-150.0	1.155	35.3	1.70	90.4	---
6.205	1.5	-150.0	1.085	20.1	1.00	48.5	---
6.217	1.5	-148.0	1.100	19.9	1.10	48.6	---
6.207	1.5	-125.0	1.115	50.5	3.00	125.0	---
6.208	1.5	-100.0	1.050	51.0	3.20	119.6	---
6.219	1.5	-100.0	1.110	25.0	1.30	61.6	---
6.216	1.5	- 60.0	1.130	25.6	1.50	64.1	---

See footnote on Table C.1 for Metric Conversion.

Table C.7 Dynamic & Static Fracture Toughness (A514, 3/8 in PL)

Steel Type A514

Thickness 3/8 in

Specimen No.	\bar{B} in	Temp. °F	A_o in	P_{max} kip	Time sec	K_{WIL} ksi \sqrt{in}	DTE in lb/in ²
<u>Dynamic</u>					$\times 10^{-4}$		
7.201	0.38	- 40.0	1.000	17.0	8.0	153.2	4512.0
7.202	0.38	- 40.0	0.985	18.0	8.0	160.3	4272.0
7.203	0.38	-195.0	0.975	5.6	4.0	49.0	410.9
7.206	0.38	- 80.0	0.975	10.5	8.0	92.7	1485.4
7.207	0.38	-150.0	1.005	7.1	5.0	63.8	481.2
7.208	0.38	-195.0	1.040	5.6	4.0	51.6	506.1
7.212	0.38	- 80.0	0.980	9.6	7.0	85.1	1204.0
7.213	0.38	- 10.0	0.975	24.0	13.0	212.0	9070.6
7.215	0.38	- 10.0	1.000	20.0	15.0	180.2	16.0
<u>Static</u>					$\times 1$		
7.218	0.38	-250.0	1.170	3.6	0.60	39.4	---
7.217	0.38	-205.0	1.080	5.0	0.70	48.1	---
7.210	0.38	-200.0	1.100	4.5	0.60	44.0	---
7.211	0.38	-200.0	1.060	5.0	0.55	47.2	---
7.219	0.38	-150.0	1.060	5.8	0.75	54.9	---
7.220	0.38	-150.0	1.060	7.0	0.75	66.2	---
7.205	0.38	-150.0	1.000	7.6	0.80	68.5	---
7.216	0.38	-150.0	1.990	8.0	0.85	71.5	---
7.204	0.38	-100.0	1.000	9.5	0.90	85.6	---
7.214	0.38	-100.0	1.050	8.5	0.80	79.7	---

See footnote on Table C.1 for Metric Conversion.

Table C.8 Dynamic & Static Fracture Toughness (A514, 1½ in PL)Steel Type
Thickness

Specimen No.	\bar{B} in	Temp. °F	A_o in	P_{max} kip	Time sec	K_{WIL} ksi√in	DTE in lb/in ²
<u>Dynamic</u>					$\times 10^{-4}$		
8.202	1.57	- 40.0	1.075	52.0	8.0	118.9	1183.2
8.203	1.57	- 40.0	1.060	63.0	14.0	142.3	1024.4
8.204	1.57	0.0	1.450	37.0	6.0	118.9	2569.1
8.206	1.57	0.0	1.020	65.0	9.0	142.1	2092.3
8.208	1.57	- 80.0	1.075	45.0	7.5	102.9	567.8
8.209	1.57	- 80.0	1.080	44.0	8.0	101.0	605.1
<u>Static</u>					$\times 1$		
8.218	1.57	-200.0	1.050	27.1	1.50	60.7	---
8.211	1.57	-170.0	1.580	19.5	1.10	77.2	---
8.215	1.57	-170.0	1.420	21.4	1.50	66.7	---
8.219	1.57	125.0	1.030	46.9	1.90	103.3	---
8.207	1.57	-120.0	1.700	18.8	0.90	79.3	---
8.210	1.57	-109.0	1.125	47.0	1.50	112.0	---
8.205	1.57	-109.0	1.115	32.5	0.60	76.8	---
8.216	1.57	- 90.0	1.000	58.8	2.90	126.5	---
8.214	1.57	- 90.0	1.025	50.1	2.60	110.0	---
8.217	1.57	- 70.0	1.020	64.3	3.00	140.6	---
8.201	1.57	- 70.0	1.050	70.5	2.80	158.0	---
8.220	1.57	- 40.0	1.390	59.0	3.00	178.7	---

See footnote on Table C.1 for Metric Conversion.

Table C.9 Dynamic & Static Fracture Toughness (A514, 2 in PL)

Steel Type A514

Thickness 2 in

Specimen No.	\bar{B} in	Temp. °F	A_o in	P_{max} kip	Time sec	K_{WIL} ksi \sqrt{in}	DTE in lb/in ²
<u>Dynamic</u>					$\times 10^{-4}$		
9.207	1.50	-195.0	1.115	20.5	10.0	50.7	432.9
9.208	1.50	-145.0	1.145	23.0	10.0	58.4	513.2
9.209	1.50	-160.0	1.040	25.5	10.0	59.3	542.9
9.210	1.50	-240.0	1.520	14.5	8.0	52.4	394.6
9.217	1.50	-195.0	1.015	21.5	10.0	49.0	346.6
9.218	1.50	-240.0	1.015	17.0	9.0	38.8	318.4
<u>Static</u>					$\times 1$		
9.217	1.50	-250.0	1.300	18.5	1.3	53.9	---
9.215	1.50	-250.0	1.044	21.5	1.0	50.0	---
9.220	1.50	-215.0	1.035	24.0	1.2	55.6	---
9.206	1.50	-200.0	1.030	29.0	1.6	67.0	---
9.205	1.50	-200.0	1.020	32.7	1.4	75.0	---
9.204	1.50	-150.0	1.000	36.0	1.8	81.1	---
9.203	1.50	-150.0	1.020	38.0	1.8	87.0	---
9.202	1.50	-150.0	1.000	47.5	2.2	107.0	---
9.201	1.50	-100.0	1.000	62.5	3.0	140.8	---
9.212	1.50	-100.0	1.100	47.0	2.7	114.9	---
9.214	1.50	-100.0	1.020	41.5	2.1	95.0	---
9.216	1.50	-100.0	1.320	38.0	2.3	112.7	---

See footnote on Table C.1 for Metric Conversion.

Table C.10 Dynamic & Static Fracture Toughness (A36, W36x260 Web)

Steel Type A36

Thickness W36x260 Web

Specimen No.	\bar{B} in	Temp. °F	A_o in	P_{max} kip	Time sec	K_{WIL} kis \sqrt{in}	DTE in lb/in ²
<u>Dynamic</u>					$\times 10^{-4}$		
13.210	0.80	-150.0	1.020	9.7	5.0	41.5	265.2
13.211	0.80	-150.0	1.030	8.8	5.0	38.0	472.1
13.212	0.80	- 95.0	1.060	12.8	6.0	56.7	224.2
13.213	0.80	-100.0	1.045	10.5	5.0	46.0	345.3
13.214	0.80	- 40.0	1.200	9.6	4.5	47.9	408.3
13.217	0.80	- 80.0	1.145	11.6	5.0	55.2	363.9
13.218	0.80	- 40.0	1.230	10.5	5.0	53.8	8.5
13.220	0.80	- 40.0	1.115	10.4	5.0	48.3	517.2
<u>Static</u>					$\times 1$		
13.209	0.80	-250.0	0.980	9.5	0.75	39.5	---
13.201	0.80	-245.0	0.900	9.8	1.00	38.3	---
13.216	0.80	-210.0	1.000	8.0	0.70	33.8	---
13.202	0.80	-200.0	0.930	11.5	1.10	46.0	---
13.205	0.80	-200.0	1.020	9.8	0.90	42.1	---
13.204	0.80	-160.0	1.040	12.8	1.10	55.8	---
13.203	0.80	-150.0	1.040	13.0	1.10	56.7	---
13.206	0.80	-150.0	1.030	12.3	1.00	53.2	---
13.207	0.80	-150.0	1.050	12.1	1.00	53.2	---
13.218	0.80	-115.0	1.030	24.2	1.80	104.7	---
13.208	0.80	-115.0	1.030	24.0	1.80	103.8	---

See footnote on Table C.1 for Metric Conversion.

Table C.11 Dynamic & Static Fracture Toughness (A36, W36x260 Flange)

Steel Type A36

Thickness W36x260 Flange

Specimen No.	\bar{B} in	Temp. °F	A_o in	P_{max} kip	Time sec	K_{WIL} ksi \sqrt{in}	DTE in lb/in ²
<u>Dynamic</u>					$\times 10^{-4}$		
13.301	1.40	0.0	1.035	27.0	5.0	67.0	274.8
13.303	1.40	- 40.0	1.050	19.5	4.0	49.0	131.9
13.305	1.40	- 80.0	1.270	14.2	4.5	43.1	223.0
13.306	1.40	- 80.0	1.230	15.2	4.5	44.5	130.8
13.308	1.40	-100.0	0.990	15.8	5.0	37.8	106.6
13.311	1.40	-105.0	1.080	14.8	5.0	38.1	196.6
13.313	1.40	- 40.0	1.080	17.0	5.0	43.8	129.5
<u>Static</u>					$\times 1$		
13.316	1.40	-255.0	1.000	13.8	0.75	33.3	---
13.313	1.40	-250.0	1.000	12.3	0.70	29.7	---
13.320	1.40	-200.0	1.030	15.5	0.75	38.9	---
13.307	1.40	-200.0	1.020	17.5	1.50	42.9	---
13.312	1.40	-190.0	1.030	20.6	1.00	50.9	---
13.314	1.40	-150.0	1.100	23.8	1.30	62.3	---
13.309	1.40	-150.0	0.965	24.8	1.20	58.2	---
13.304	1.40	-150.0	1.540	22.5	1.20	89.0	---
13.310	1.40	-120.0	1.010	43.1	2.20	104.5	---
13.302	1.40	-100.0	1.030	34.8	1.50	86.0	---
13.315	1.40	- 90.0	1.095	48.5	2.90	127.8	---

See footnote on Table C.1 for Metric Conversion

Table C.12 Dynamic & Static Fracture Toughness (A588, W36x230 Web)

Steel Type A588
 Thickness W36x230 Web

Specimen No.	\bar{B} in	Temp. °F	A_o in	P_{max} kip	Time sec	K_{WIL} ksi \sqrt{in}	DTE in lb/in ²
<u>Dynamic</u>					$\times 10^{-4}$		
14.210	0.75	-100.0	1.015	8.5	5.0	38.8	354.7
14.211	0.75	-100.0	1.000	11.8	5.5	53.2	520.0
14.214	0.75	- 40.0	1.335	18.2	9.0	109.5	1335.7
14.215	0.75	-150.0	1.535	7.0	5.0	51.4	163.8
14.216	0.75	- 40.0	1.590	8.9	6.0	69.3	3971.6
14.218	0.75	-160.0	1.640	6.5	5.0	53.5	294.1
14.219	0.75	-100.0	1.000	11.0	6.0	49.6	280.0
14.220	0.75	- 80.0	0.995	11.6	6.0	50.3	263.3
<u>Static</u>					$\times 1$		
14.207	0.75	-250.0	1.040	11.6	1.00	54.0	---
14.206	0.75	-245.0	1.090	10.2	1.00	49.4	---
14.201	0.75	-200.0	1.175	11.0	0.85	57.3	---
14.209	0.75	-200.0	1.120	13.1	1.10	65.1	---
14.211	0.75	-180.0	0.980	12.5	1.10	55.4	---
14.204	0.75	-150.0	1.035	26.8	1.10	124.2	---
14.208	0.75	-150.0	1.000	24.0	2.30	108.1	---
14.203	0.75	-125.0	1.025	24.1	2.00	113.5	---
14.205	0.75	-125.0	1.025	24.7	4.40	113.5	---
14.202	0.75	-100.0	1.035	32.5	4.60	150.0	---

See footnote on Table C.1 for Metric Conversion

Table C.13 Dynamic & Static Fracture Toughness (A588, W36x230 Flange)

Steel Type A588

Thickness W36x230 Flange

Specimen No.	\bar{B} in	Temp. °F	A_o in	P_{max} kip	Time sec	K_{WIL} ksiv \sqrt{in}	DTE in lb/in ²
<u>Dynamic</u>					$\times 10^{-4}$		
14.320	1.20	- 80.0	1.015	15.2	6.5	43.3	403.0
14.319	1.20	- 80.0	1.085	15.2	6.5	45.9	297.9
14.313	1.20	-100.0	1.035	17.6	6.0	51.0	279.9
14.317	1.20	-100.0	1.035	14.4	6.0	40.5	162.8
14.315	1.20	-140.0	0.990	14.8	6.5	41.3	288.6
14.317	1.20	-150.0	1.025	11.5	5.0	33.0	308.9
14.311	1.20	-180.0	1.000	14.0	6.0	39.4	90.0
14.312	1.20	-185.0	1.025	13.7	6.0	39.4	344.3
<u>Static</u>					$\times 1$		
14.310	1.20	-245.0	1.010	14.0	0.65	39.7	---
14.308	1.20	-245.0	1.040	13.0	0.70	37.8	---
14.307	1.20	-200.0	1.030	25.0	1.20	72.1	---
14.305	1.20	-200.0	1.045	24.5	1.50	71.5	---
14.303	1.20	-200.0	1.045	20.0	1.20	59.0	---
14.306	1.20	-150.0	1.000	28.2	1.50	79.4	---
14.309	1.20	-150.0	1.040	33.8	1.80	98.3	---
14.301	1.20	-150.0	1.020	41.3	2.10	117.2	---
14.302	1.20	-150.0	1.050	18.7	1.10	55.8	---
14.304	1.20	-143.0	1.400	17.8	1.10	71.2	---

See footnote on Table C.1 for Metric Conversion.

Table C.14 Standard & Precracked CVN Data (A36, 3/8 in PL)

Steel Type A36
 Thickness 3/8 in

SL No.	Test ¹ Temp. (°F)	CVN ² Energy (ft-lbs)	Lateral ³ Expansion (Mils)	Percent Shear (%)	A _o ⁴ (in)	CVN ⁵ (ft-lbs)
<u>Standard</u>						
1	-100	9.5	6.0	0	----	----
2	- 50	15.0	22.0	20	----	----
3	- 50	13.0	14.0	10	----	----
4	- 25	8.0	9.0	10	----	----
5	- 25	7.0	11.0	20	----	----
6	0	41.0	46.0	50	----	----
7	0	40.0	44.0	40	----	----
8	+ 25	65.0	81.0	100	----	----
9	+ 25	56.0	62.0	80	----	----
10	+ 50	88.0	81.0	100	----	----
11	+ 50	93.5	63.0	100	----	----
12	+ 70	81.0	78.0	100	----	----
13	+ 70	80.0	74.0	100	----	----
14	+212	81.0	83.0	100	----	----
15	+212	91.0	80.0	100	----	----
<u>Precracked</u>						
1	-100	6.0	3.0	10	.12	6.90
2	- 50	5.0	7.0	20	.12	5.75
3	- 50	4.0	6.0	10	.12	4.60
4	- 25	7.5	13.0	30	.12	8.63
5	- 25	12.0	7.0	40	.13	14.32
6	0	10.5	18.0	40	.12	12.08
7	0	11.5	19.0	60	.17	16.17
8	+ 25	19.0	30.0	80	.15	24.53
9	+ 25	14.5	22.0	50	.13	17.30
10	+ 50	51.0	60.0	98	.14	63.24
11	+ 50	48.0	52.0	90	.12	55.20
12	+ 70	52.5	60.0	100	.12	60.38
13	+ 70	47.0	58.0	100	.14	58.28
14	+212	46.0	58.0	100	.13	54.88
15	+212	47.0	58.0	100	.13	56.07

¹ °F = 9/5°C + 32

² 1 ft-lb = 1.356J

³ 1 mil = 0.0254 mm

⁴ 1 in = 25.4 mm

⁵ Normalized with respect to standard notch depth

Table C.15 Standard & Precracked CVN Data (A36, 2 in PL)

Steel Type A36
 Thickness 2 in

SL No.	Test ¹ Temp. (°F)	CVN ² Energy (ft-lbs)	Lateral ³ Expansion (Mils)	Percent Shear (%)	A _o ⁴ (in)	CVN ⁵ (ft-lbs)
<u>Standard</u>						
1	-100	11.0	8.0	0	----	----
2	- 50	5.0	5.0	0	----	----
3	- 50	4.0	3.0	0	----	----
4	- 25	4.0	7.0	0	----	----
5	- 25	6.0	8.0	0	----	----
6	0	26.0	32.0	50	----	----
7	0	33.0	27.0	40	----	----
8	+ 25	34.0	45.0	40	----	----
9	+ 25	30.0	38.0	40	----	----
10	+ 50	60.0	56.0	80	----	----
11	+ 50	53.0	53.0	70	----	----
12	+ 70	76.0	76.0	95	----	----
13	+ 70	62.0	54.0	90	----	----
14	+212	72.0	63.0	100	----	----
15	+212	66.0	63.0	100	----	----
<u>Precracked</u>						
1	-100	5.5	----	----	.12	6.33
2	- 50	2.5	3.0	0	.12	2.88
3	- 50	4.0	8.0	5	.12	4.60
4	- 25	4.5	7.0	10	.13	5.37
5	- 25	5.0	14.0	20	.14	6.20
6	0	9.0	13.0	30	.12	10.35
7	0	9.5	14.0	40	.12	10.93
8	+ 25	16.0	8.0	0	.12	18.40
9	+ 25	12.0	22.0	40	.13	14.32
10	+ 50	22.5	34.0	60	.13	26.84
11	+ 50	24.5	37.0	60	----	----
12	+ 70	32.0	44.0	80	.13	38.18
13	+ 70	54.0	58.0	90	.11	58.90
14	+212	40.5	54.0	100	.14	50.22
15	+212	42.5	55.0	100	.13	50.70

See footnote on Table C.14 for Metric Conversions.

Table C.16 Standard & Precracked CVN Data (A36, 3 in PL)

Steel Type A36
Thickness 3 in

SL No.	Test ¹ Temp. (°F)	CVN ² Energy (ft-lbs)	Lateral ³ Expansion (Mils)	Percent Shear (%)	A _o ⁴ (in)	CVN ⁵ (ft-lbs)
<u>Standard</u>						
1	-100	8.0	5.0	0	----	----
2	- 50	5.5	5.0	0	----	----
3	- 50	9.0	13.0	0	----	----
4	- 25	13.0	15.0	0	----	----
5	- 25	7.5	13.0	0	----	----
6	0	14.5	25.0	0	----	----
7	0	38.0	41.0	10	----	----
8	+ 25	26.0	35.0	10	----	----
9	+ 25	28.5	40.0	20	----	----
10	+ 50	49.0	58.0	20	----	----
11	+ 50	62.5	68.0	40	----	----
12	+ 70	74.0	67.0	40	----	----
13	+ 70	49.0	52.0	40	----	----
14	+212	102.0	84.0	100	----	----
15	+212	105.0	80.0	100	----	----
<u>Precracked</u>						
1	-100	5.0	7.0	0	.12	5.75
2	- 50	2.0	8.0	0	.12	2.30
3	- 50	3.5	9.0	0	.12	4.025
4	- 25	3.0	7.0	0	.12	3.45
5	- 25	4.0	9.0	0	.12	4.60
6	0	6.0	12.0	0	.13	7.16
7	0	6.5	18.0	10	.13	7.75
8	+ 25	11.0	22.0	20	.12	12.65
9	+ 25	10.5	23.0	20	.12	12.08
10	+ 50	21.0	35.0	20	.08	21.07
11	+ 50	20.0	28.0	30	.12	23.00
12	+ 70	25.0	39.0	40	.14	31.00
13	+ 70	24.0	37.0	50	.13	28.63
14	+212	57.0	52.0	100	.14	70.68
15	+212	61.0	60.0	100	.13	72.77

See footnote on Table C.14 for Metric Conversions

Table C.17 Standard & Precracked CVN Data (A588, 3/8 in PL)

Steel Type A588
 Thickness 3/8 in

SL No.	Test ¹ Temp. (°F)	CVN ² Energy (ft-lbs)	Lateral ³ Expansion (Mils)	Percent Shear (%)	A _o ⁴ (in)	CVN ⁵ (ft-lbs)
<u>Standard</u>						
1	-100	10.0	8.0	0	----	----
2	- 50	8.0	9.0	10	----	----
3	- 50	12.5	19.0	10	----	----
4	- 25	11.0	12.0	10	----	----
5	- 25	12.5	15.0	10	----	----
6	0	49.5	55.0	60	----	----
7	0	45.0	48.0	50	----	----
8	+ 25	62.0	62.0	90	----	----
9	+ 25	64.0	62.0	100	----	----
10	+ 50	65.5	62.0	100	----	----
11	+ 50	66.0	57.0	90	----	----
12	+ 70	70.0	70.0	100	----	----
13	+ 70	74.5	66.0	100	----	----
14	+212	65.0	65.0	100	----	----
15	+212	63.5	56.0	100	----	----
<u>Precracked</u>						
1	-100	6.0	3.0	0	.12	6.90
2	- 50	9.0	12.0	20	.12	10.35
3	- 50	7.5	14.0	20	.13	8.95
4	- 25	5.0	9.0	20	.13	5.97
5	- 25	8.5	12.0	30	.13	10.14
6	0	17.5	20.0	40	.13	20.88
7	0	15.0	24.0	40	.14	18.60
8	+ 25	32.0	40.0	70	.12	36.80
9	+ 25	20.5	28.0	95	.22	37.11
10	+ 50	39.5	46.0	100	.14	48.98
11	+ 50	50.0	51.0	100	.14	62.00
12	+ 70	48.5	46.0	100	.17	68.24
13	+ 70	27.0	44.0	100	.21	46.22
14	+212	46.0	52.0	100	.12	52.90
15	+212	47.0	53.0	100	.12	54.05

See footnote on Table C.14 for Metric Conversions.

Table C.18 Standard & Precracked CVN Data (A588, 2 in PL)

Steel Type A588
 Thickness 2 in

SL No.	Test ¹ Temp. (°F)	CVN ² Energy (ft-lbs)	Lateral ³ Expansion (Mils)	Percent Shear (%)	A _o ⁴ (in)	CVN ⁵ (ft-lbs)
<u>Standard</u>						
1	-100	17.0	15.0	0	----	----
2	- 50	7.0	12.0	0	----	----
3	- 50	15.0	18.0	0	----	----
4	- 25	16.5	13.0	0	----	----
5	- 25	10.0	2.0	0	----	----
6	0	30.0	31.0	0	----	----
7	0	29.0	32.0	0	----	----
8	+ 25	23.0	23.0	10	----	----
9	+ 25	15.0	22.0	10	----	----
10	+ 50	73.0	82.0	20	----	----
11	+ 50	62.0	54.0	20	----	----
12	+ 70	77.0	65.0	30	----	----
13	+ 70	46.5	44.0	20	----	----
14	+212	104.0	88.0	100	----	----
15	+212	106.0	83.0	100	----	----
<u>Precracked</u>						
1	-100	5.0	2.0	0	.12	5.75
2	- 50	2.5	5.0	0	.11	2.73
3	- 50	3.0	9.0	0	.12	3.45
4	- 25	3.5	3.0	0	.12	4.03
5	- 25	4.0	3.0	0	.12	4.60
6	0	5.0	6.0	0	.12	5.75
7	0	5.0	---	-	.12	5.75
8	+ 25	8.0	14.0	10	.12	9.20
9	+ 25	7.0	17.0	10	.12	8.05
10	+ 50	20.5	23.0	40	.12	23.58
11	+ 50	15.0	23.0	30	.12	17.25
12	+ 70	20.0	25.0	40	.12	23.00
13	+ 70	25.0	25.0	20	.12	28.75
14	+212	80.0	61.0	100	.12	92.00
15	+212	77.0	66.0	100	.12	88.55

See footnote on Table C.14 for Metric Conversions.

Table C.19 Standard & Precracked CVN Data (A588, 3 in PL)

Steel Type A588
Thickness 3 in

SL No.	Test ¹ Temp. (°F)	CVN ² Energy (ft-lbs)	Lateral ³ Expansion (Mils)	Percent Shear (%)	A _o ⁴ (in)	CVN ⁵ (ft-lbs)
<u>Standard</u>						
1	-100	7.5	5.0	0	----	----
2	- 50	4.0	5.0	0	----	----
3	- 50	7.0	6.0	0	----	----
4	- 25	5.0	8.0	0	----	----
5	- 25	6.0	7.0	0	----	----
6	0	31.5	32.0	0	----	----
7	0	29.0	35.0	0	----	----
8	+ 25	35.0	40.0	10	----	----
9	+ 25	18.5	18.0	0	----	----
10	+ 50	68.0	45.0	10	----	----
11	+ 50	69.0	64.0	20	----	----
12	+ 70	82.0	79.0	40	----	----
13	+ 70	85.0	71.0	50	----	----
14	+212	105.0	79.0	100	----	----
15	+212	104.0	91.0	100	----	----
<u>Precracked</u>						
1	-100	4.0	6.0	0	.12	4.60
2	- 50	2.0	3.0	0	.12	2.30
3	- 50	3.0	4.0	0	.18	4.42
4	- 25	4.5	9.0	0	.12	5.18
5	- 25	5.0	14.0	5	.12	5.75
6	0	5.5	8.0	0	.13	6.56
7	0	5.0	10.0	0	.13	5.97
8	+ 25	35.0	----	-	----	----
9	+ 25	18.5	----	-	----	----
10	+ 50	20.0	22.0	40	.13	23.86
11	+ 50	21.5	26.0	40	.12	24.73
12	+ 70	25.0	31.0	50	.12	28.75
13	+ 70	19.0	26.0	50	.12	21.85
14	+212	58.5	59.0	100	.15	75.52
15	+212	76.0	71.0	100	.12	87.40

See footnote on Table C.14 for Metric Conversions

Table C.20 Standard & Precracked CVN Data (A514, 3/8 in PL)

Steel Type A514
 Thickness 3/8 in

SL No.	Test ¹ Temp. (°F)	CVN ² Energy (ft-lbs)	Lateral ³ Expansion (Mils)	Percent Shear (%)	A _o ⁴ (in)	CVN ⁵ (ft-lbs)
<u>Standard</u>						
1	-100	10.0	7.0	10	----	----
2	- 50	15.5	10.0	20	----	----
3	- 50	11.5	11.0	20	----	----
4	- 25	12.5	11.0	20	----	----
5	- 25	12.0	11.0	20	----	----
6	0	21.0	21.0	60	----	----
7	0	17.5	24.0	90	----	----
8	+ 25	23.0	21.0	80	----	----
9	+ 25	22.5	21.0	70	----	----
10	+ 50	28.0	25.0	90	----	----
11	+ 50	27.0	24.0	90	----	----
12	+ 70	28.0	23.0	100	----	----
13	+ 70	25.5	27.0	100	----	----
14	+212	22.0	----	-	----	----
15	+212	20.0	----	100	----	----
<u>Precracked</u>						
1	-100	6.0	----	-	----	----
2	- 50	6.5	----	-	----	----
3	- 50	6.0	----	-	----	----
4	- 25	5.5	8.0	20	.13	6.56
5	- 25	6.0	8.0	20	.12	6.90
6	0	9.0	12.0	40	.14	11.16
7	0	10.0	11.0	50	.13	11.93
8	+ 25	14.0	15.0	60	.12	16.10
9	+ 25	25.5	15.0	90	----	----
10	+ 50	21.0	19.0	90	.11	22.91
11	+ 50	16.0	16.0	90	.15	20.66
12	+ 70	20.5	21.0	100	.11	22.37
13	+ 70	22.0	27.0	100	.11	24.00
14	+212	20.0	26.0	-	----	----
15	+212	22.0	21.0	100	.12	25.30

See footnote on Table C.14 for Metric Conversions.

Table C.21 Standard & Precracked CVN Data (A514, 1-1/2 in PL)

Steel Type A514
 Thickness 1-1/2 in

SL No.	Test ¹ Temp. (°F)	CVN ² Energy (ft-lbs)	Lateral ³ Expansion (Mils)	Percent Shear (%)	A _o ⁴ (in)	CVN ⁵ (ft-lbs)
<u>Standard</u>						
1	-100	31.0	26.0	30	----	----
2	- 50	32.0	32.0	40	----	----
3	- 50	30.0	20.0	40	----	----
4	- 25	44.0	33.0	80	----	----
5	- 25	36.5	27.0	50	----	----
6	0	62.0	39.0	100	----	----
7	0	62.0	42.0	100	----	----
8	+ 25	59.0	39.0	100	----	----
9	+ 25	64.0	46.0	100	----	----
10	+ 50	63.0	48.0	100	----	----
11	+ 50	60.0	43.0	-	----	----
12	+ 70	60.0	39.0	100	----	----
13	+ 70	64.0	48.0	100	----	----
14	+212	67.0	50.0	100	----	----
15	+212	70.0	51.0	100	----	----
<u>Precracked</u>						
1	-100	15.0	11.0	20	.12	17.25
2	- 50	20.0	19.0	30	.12	23.00
3	- 50	16.0	15.0	40	.12	18.40
4	- 25	18.0	12.0	30	.11	19.64
5	- 25	17.0	20.0	40	.12	19.55
6	0	31.0	26.0	70	.11	33.82
7	0	35.0	26.0	90	.13	41.76
8	+ 25	35.0	28.0	80	.12	40.25
9	+ 25	40.0	33.0	90	.11	43.64
10	+ 50	47.0	39.0	100	.13	56.07
11	+ 50	48.5	40.0	100	.12	55.78
12	+ 70	43.5	34.0	100	.12	50.03
13	+ 70	46.5	37.0	100	.12	53.48
14	+212	50.0	42.0	100	.11	54.55
15	+212	43.0	39.0	100	.13	51.30

See footnote on Table C.14 for Metric Conversions.

Table C.22 Standard & Precracked CVN Data (A514, 3 in PL)

Steel Type A514
 Thickness 3 in

SL No.	Test ¹ Temp. (°F)	CVN ² Energy (ft-lbs)	Lateral ³ Expansion (Mils)	Percent Shear (%)	A _o ⁴ (in)	CVN ⁵ (ft-lbs)
<u>Standard</u>						
1	-100	37.0	28.0	40	----	----
2	- 50	53.0	41.0	90	----	----
3	- 50	42.0	37.0	60	----	----
4	- 25	52.5	43.0	100	----	----
5	- 25	40.0	38.0	70	----	----
6	0	64.5	56.0	100	----	----
7	0	56.0	45.0	100	----	----
8	+ 25	64.0	56.0	100	----	----
9	+ 25	62.0	50.0	100	----	----
10	+ 50	64.5	50.0	100	----	----
11	+ 50	62.0	47.0	100	----	----
12	+ 70	59.0	49.0	100	----	----
13	+ 70	66.0	52.0	100	----	----
14	+212	63.0	61.0	100	----	----
15	+212	61.0	56.0	100	----	----
<u>Precracked</u>						
1	-100	16.5	12.0	20	.11	18.00
2	- 50	22.0	29.0	50	.11	24.00
3	- 50	24.5	30.0	40	.12	28.18
4	- 25	26.0	29.0	80	.12	29.90
5	- 25	34.5	33.0	80	.11	37.64
6	0	38.0	34.0	95	.14	47.12
7	0	45.0	44.0	95	.12	51.75
8	+ 25	41.5	39.0	100	.12	47.73
9	+ 25	40.0	40.0	100	.13	47.72
10	+ 50	44.0	38.0	100	.14	54.56
11	+ 50	45.5	40.0	100	.13	54.28
12	+ 70	46.0	40.0	100	.12	52.90
13	+ 70	43.0	43.0	100	.12	49.45
14	+212	44.0	29.0	100	.22	79.64
15	+212	45.0	36.0	100	.12	51.75

See footnote on Table C.14 for Metric Conversions.

Table C.23 Standard & Precracked CVN Data (A36, in PL)

Steel Type A36
Thickness

SL No.	Test ¹ Temp. (°F)	CVN ² Energy (ft-lbs)	Lateral ³ Expansion (Mils)	Percent Shear (%)	A _o ⁴ (in)	CVN ⁵ (ft-lbs)
<u>Standard</u>						
1	-100	5.0	5.0	0	----	----
2	- 50	4.0	8.0	0	----	----
3	- 50	4.0	9.0	0	----	----
4	- 25	5.5	6.0	0	----	----
5	- 25	5.0	----	-	----	----
6	0	33.5	39.0	20	----	----
7	0	33.0	42.0	30	----	----
8	+ 25	70.0	63.0	50	----	----
9	+ 25	33.0	47.0	30	----	----
10	+ 50	94.0	66.0	70	----	----
11	+ 50	107.0	71.0	80	----	----
12	+ 70	115.0	70.0	100	----	----
13	+ 70	129.0	92.0	100	----	----
14	+212	120.0	85.0	100	----	----
15	+212	123.0	95.0	100	----	----
<u>Precracked</u>						
1	-100	5.5	1.0	0	.11	6.00
2	- 50	3.0	----	-	----	----
3	- 50	2.0	8.0	0	.11	2.18
4	- 25	10.0	15.0	10	.13	11.93
5	- 25	5.5	10.0	10	.12	6.33
6	0	12.0	21.0	10	.15	15.49
7	0	9.0	15.0	20	.11	9.819
8	+ 25	17.5	27.0	20	.12	20.13
9	+ 25	19.5	30.0	30	.12	22.43
10	+ 50	39.0	47.0	60	.13	46.53
11	+ 50	67.0	54.0	90	.11	73.10
12	+ 70	80.0	79.0	100	.12	92.00
13	+ 70	79.0	60.0	100	.12	90.85
14	+212	97.0	85.0	100	.12	111.55
15	+212	86.0	75.0	100	.12	98.90

See footnote on Table C.14 for Metric Conversions

Table C.24 Standard & Precracked CVN Data (A36, 1-7/16 in PL)

Steel Type A36

Thickness 1-7/16 in

SL No.	Test ¹ Temp. (°F)	CVN ² Energy (ft-lbs)	Lateral ³ Expansion (Mils)	Percent Shear (%)	A _o ⁴ (in)	CVN ⁵ (ft-lbs)
<u>Standard</u>						
1	-100	7.0	4.0	0	----	----
2	- 50	15.0	18.0	20	----	----
3	- 50	11.5	11.0	10	----	----
4	- 25	14.0	17.0	20	----	----
5	- 25	7.5	7.0	20	----	----
6	0	25.0	29.0	40	----	----
7	0	61.0	58.0	100	----	----
8	+ 25	63.0	57.0	100	----	----
9	+ 25	59.5	59.0	100	----	----
10	+ 50	61.0	61.0	100	----	----
11	+ 50	60.0	38.0	100	----	----
12	+ 70	60.0	60.0	100	----	----
13	+ 70	63.0	52.0	100	----	----
14	+212	60.0	58.0	100	----	----
15	+212	64.0	65.0	100	----	----
<u>Precracked</u>						
1	-100	5.5	1.0	0	.12	6.33
2	- 50	10.0	15.0	40	.12	11.50
3	- 50	7.0	----	40	.13	8.35
4	- 25	15.0	21.0	50	.12	17.25
5	- 25	11.5	18.0	40	.12	13.23
6	0	47.0	50.0	100	.12	54.05
7	0	18.0	24.0	50	.11	19.64
8	+ 25	40.0	44.0	100	.13	47.72
9	+ 25	44.0	51.0	100	.12	50.60
10	+ 50	46.0	48.0	100	.12	52.90
11	+ 50	51.5	54.0	100	.11	56.19
12	+ 70	49.0	58.0	100	.11	53.46
13	+ 70	44.0	51.0	100	.12	50.60
14	+212	43.0	50.0	100	.12	49.45
15	+212	37.0	49.0	100	.13	44.14

See footnote on Table C.14 for Metric Conversion

Table C.25 Standard & Precracked CVN Data (A588, 3/4 in PL)

Steel Type A588
 Thickness 3/4 in

SL No.	Test ¹ Temp. (°F)	CVN ² Energy (ft-lbs)	Lateral ³ Expansion (Mils)	Percent Shear (%)	A _o ⁴ (in)	CVN ⁵ (ft-lbs)
<u>Standard</u>						
1	-100	6.0	1.0	-	----	----
2	- 50	44.0	39.0	10	----	----
3	- 50	16.0	21.0	10	----	----
4	- 25	35.0	42.0	10	----	----
5	- 25	10.0	10.0	0	----	----
6	0	239.0	91.0	100	----	----
7	0	229.0	99.0	100	----	----
8	+ 25	239.0	90.0	100	----	----
9	+ 25	213.0	87.0	100	----	----
10	+ 50	218.0	100.0	100	----	----
11	+ 50	235.5	98.0	100	----	----
12	+ 70	239.0	91.0	100	----	----
13	+ 70	----	----	-	----	----
14	+212	218.0	97.0	100	----	----
15	+212	228.0	99.0	100	----	----
<u>Precracked</u>						
1	-100	6.0	----	0	----	----
2	- 50	2.0	3.0	0	.12	2.30
3	- 50	3.0	3.0	0	.12	3.45
4	- 25	5.5	4.0	10	.12	6.33
5	- 25	3.0	11.0	0	.12	3.45
6	0	6.5	11.0	10	.12	7.48
7	0	6.0	8.0	10	.12	6.90
8	+ 25	12.5	16.0	40	.13	14.91
9	+ 25	11.0	17.0	40	.17	15.47
10	+ 50	32.0	34.0	20	.11	34.91
11	+ 50	24.5	----	20	----	----
12	+ 70	22.5	29.0	60	.14	27.90
13	+ 70	25.0	26.0	40	.12	28.75
14	+212	122.0	87.0	100	.12	140.30
15	+212	103.0	75.0	100	.13	122.88

See footnote on Table C.14 for Metric Conversion.

Table C.26 Standard & Precracked CVN Data (A588, 1-7/16 in PL)

Steel Type A588
 Thickness 1-7/16 in

SL No.	Test ¹ Temp. (°F)	CVN ² Energy (ft-lbs)	Lateral ³ Expansion (Mils)	Percent Shear (%)	A _o ⁴ (in)	CVN ⁵ (ft-lbs)
<u>Standard</u>						
1	-100	12.0	10.0	0	----	----
2	- 50	20.0	25.0	30	----	----
3	- 50	35.5	36.0	20	----	----
4	- 25	13.5	15.0	10	----	----
5	- 25	35.0	36.0	20	----	----
6	0	82.0	70.0	60	----	----
7	0	85.0	104.0	100	----	----
8	+ 25	36.0	40.0	40	----	----
9	+ 25	107.5	80.0	95	----	----
10	+ 50	127.0	94.0	100	----	----
11	+ 50	132.0	95.0	100	----	----
12	+ 70	106.0	90.0	100	----	----
13	+ 70	84.5	63.0	90	----	----
14	+212	92.0	77.0	100	----	----
15	+212	94.0	81.0	100	----	----
<u>Precracked</u>						
1	-100	5.5	6.0	0	.12	6.33
2	- 50	3.0	2.0	0	.12	3.45
3	- 50	4.5	9.0	0	.12	5.18
4	- 25	6.5	16.0	10	.11	7.09
5	- 25	10.0	18.0	30	.12	11.50
6	0	9.0	13.0	20	.11	9.82
7	0	14.5	18.0	30	.12	16.68
8	+ 25	17.5	24.0	50	.13	20.88
9	+ 25	16.0	26.0	40	.13	19.09
10	+ 50	30.0	40.0	60	.11	32.73
11	+ 50	34.0	36.0	70	.11	37.09
12	+ 70	41.0	54.0	90	.12	47.15
13	+ 70	32.5	43.0	80	.13	38.77
14	+212	48.0	42.0	100	.14	59.52
15	+212	59.0	59.0	100	.13	70.39

See footnote on Table C.14 for Metric Conversion.

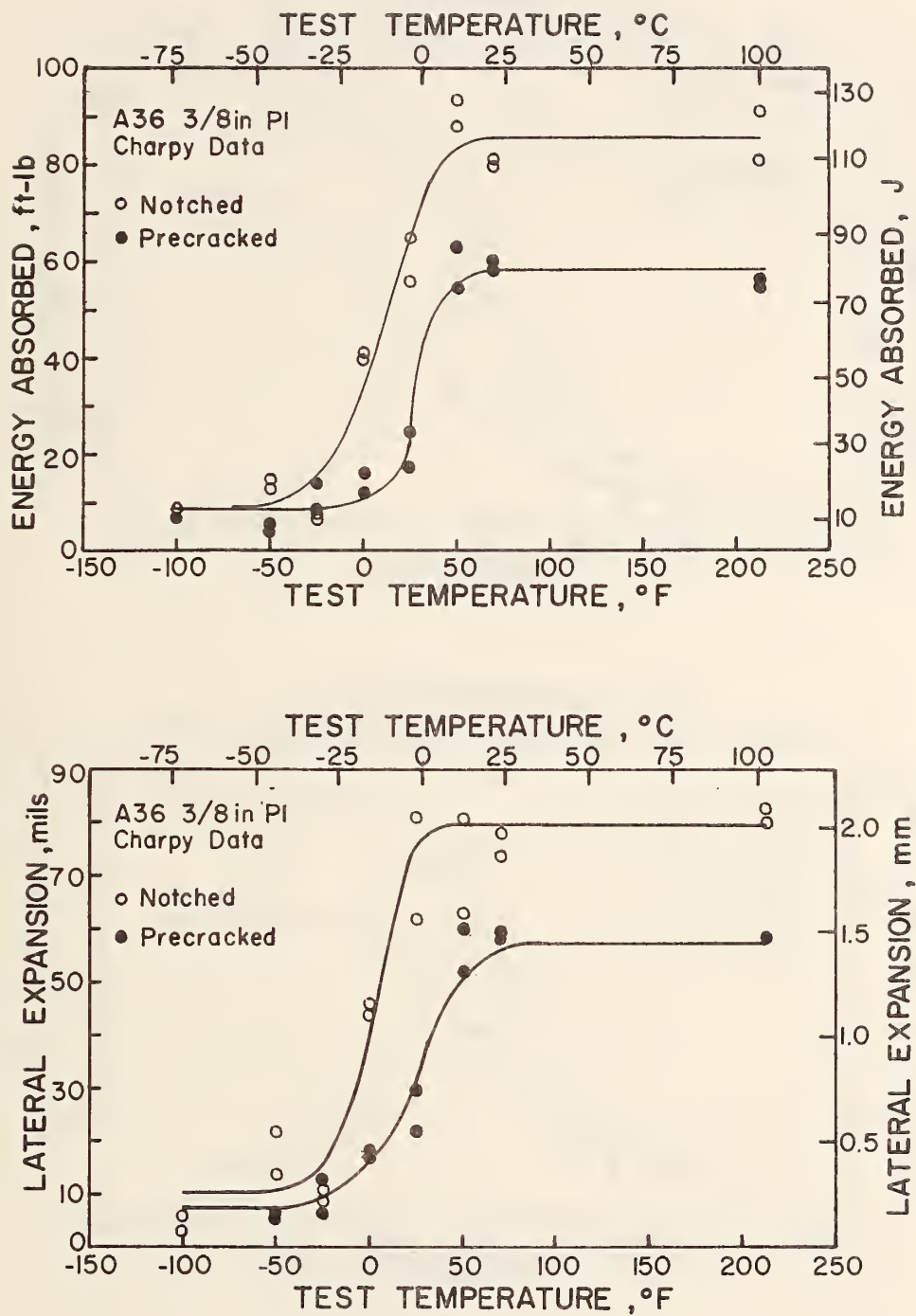


Fig. C.1 A36, 3/8 in. Plate CVN

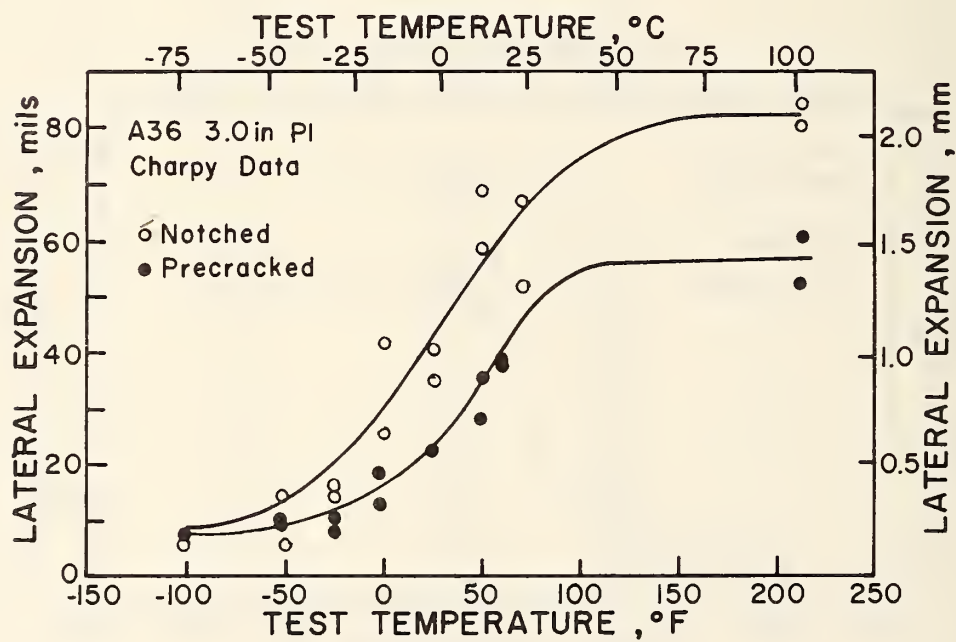
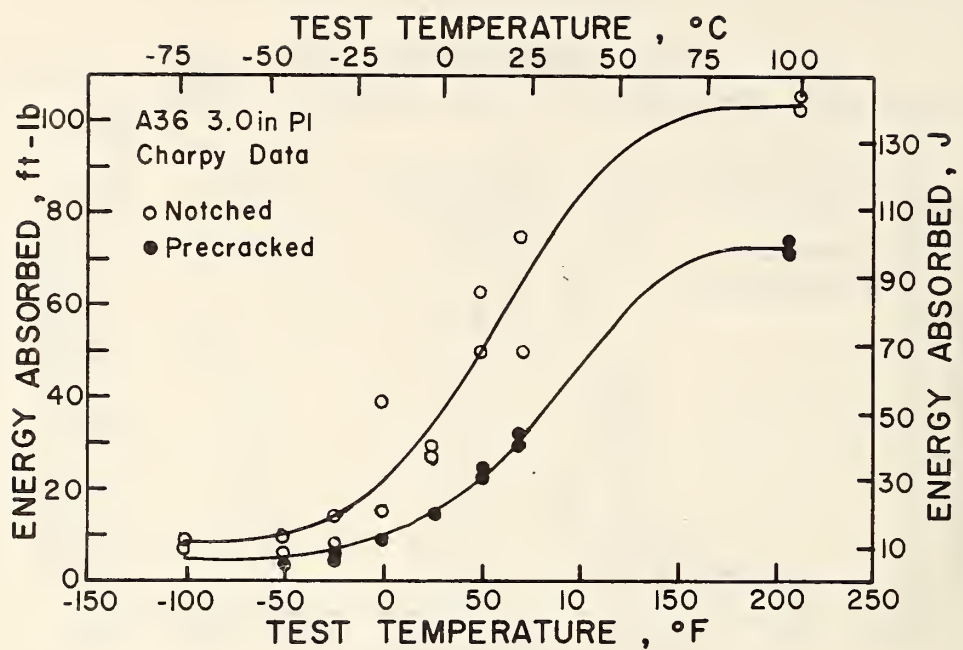


Fig. C.2 A36, 3 in. Plate CVN

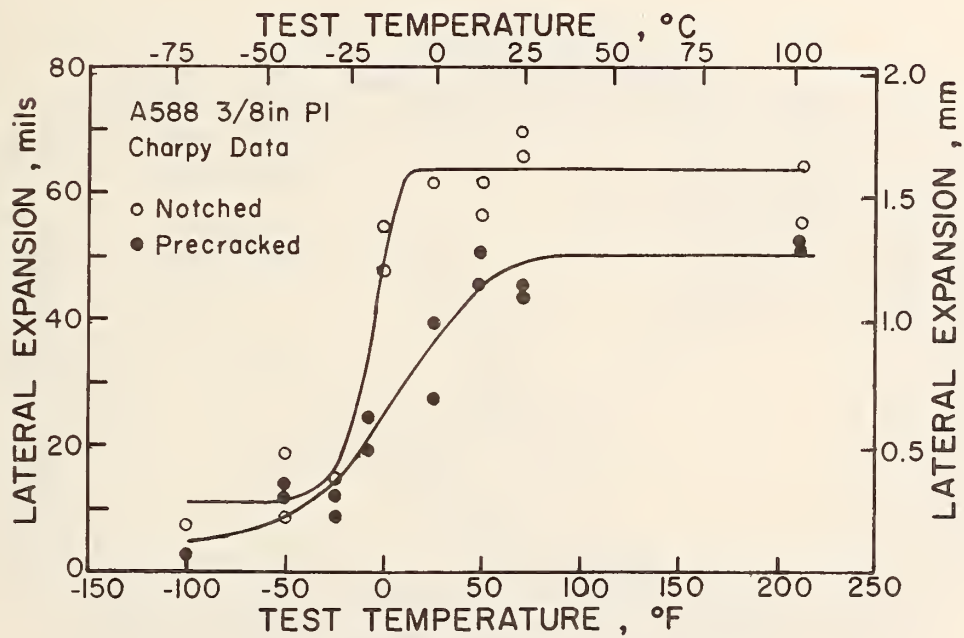
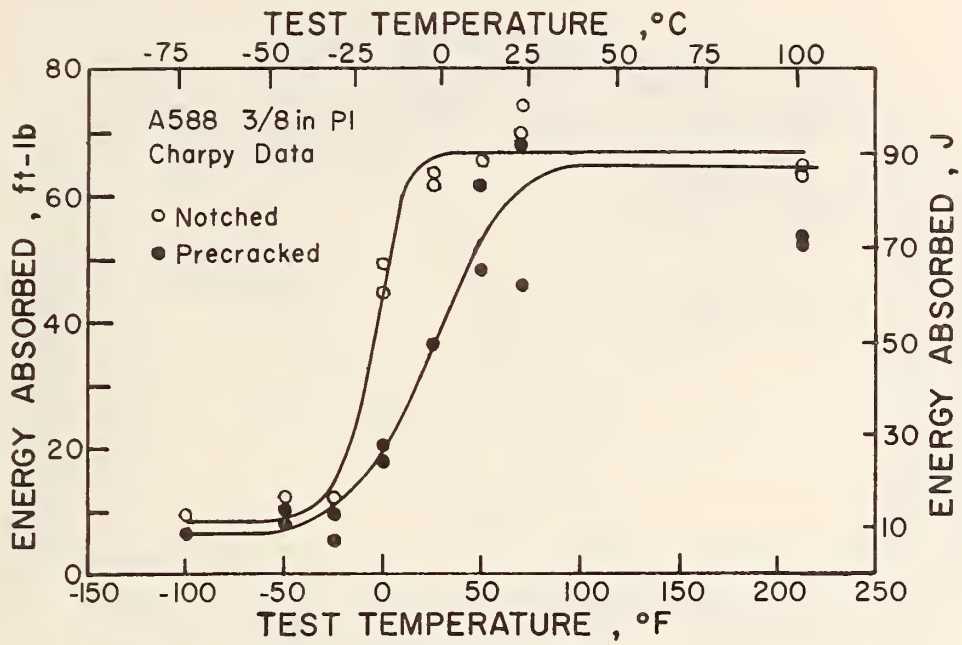


Fig. C.3 A588, 3/8 in. Plate CVN

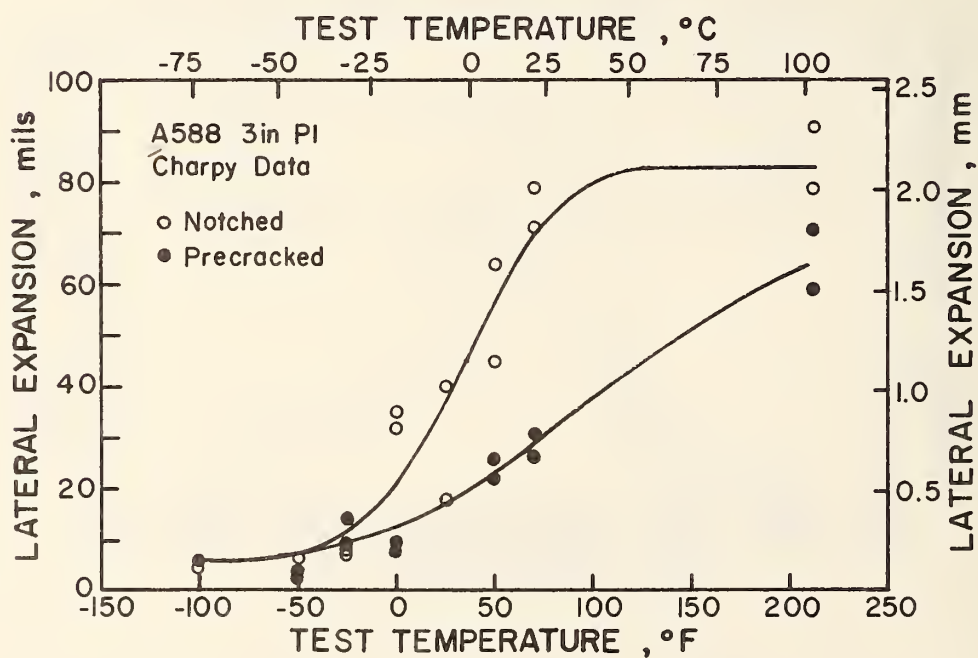
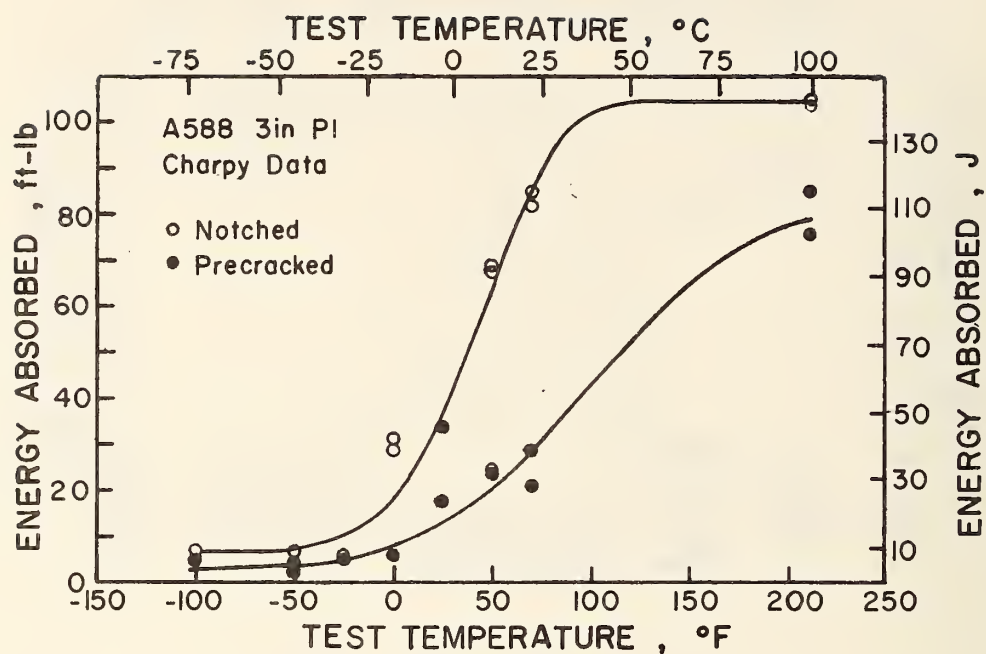


Fig. C.4 A588, 3 in. Plate CVN

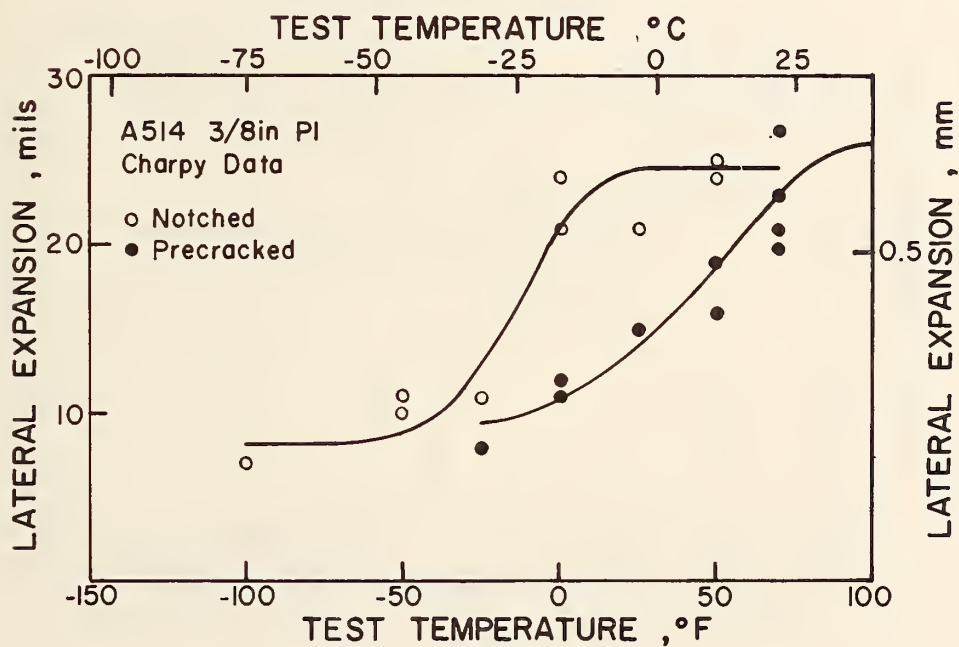
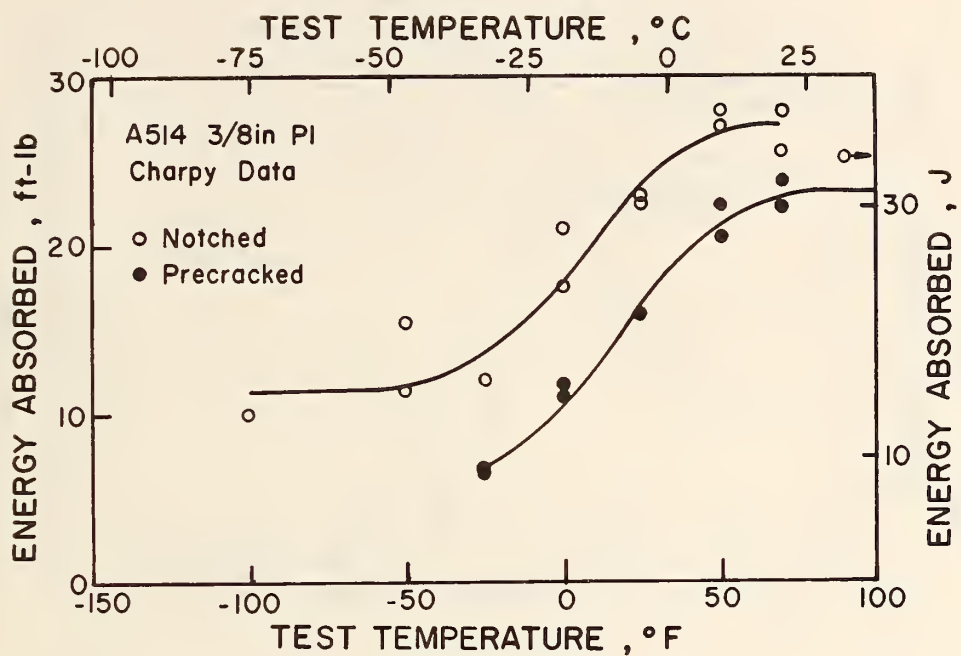


Fig. C.5 A514, 3/8 in. Plate CVN

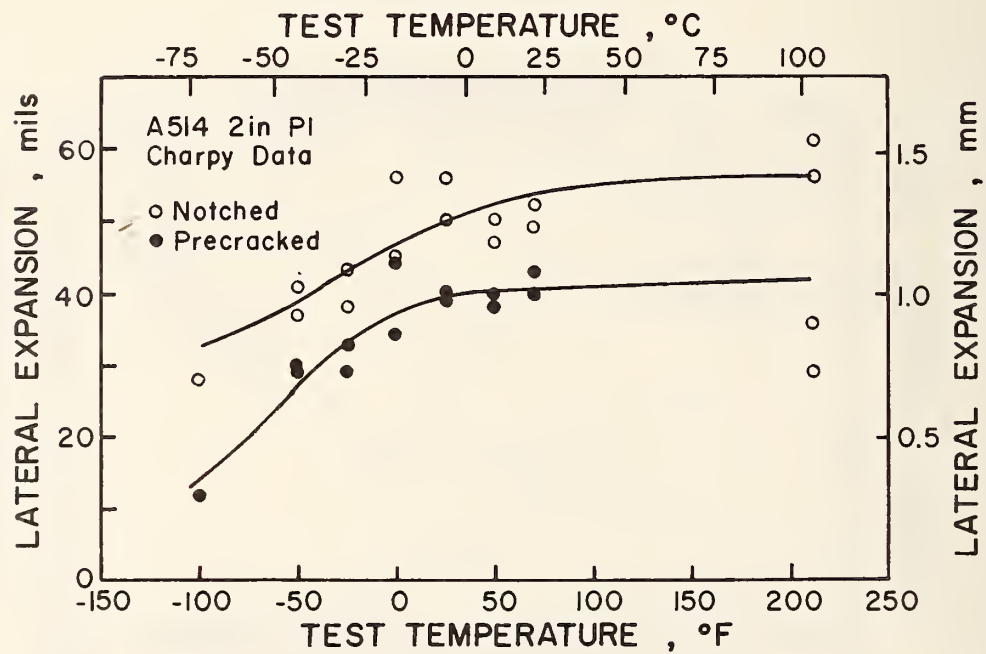
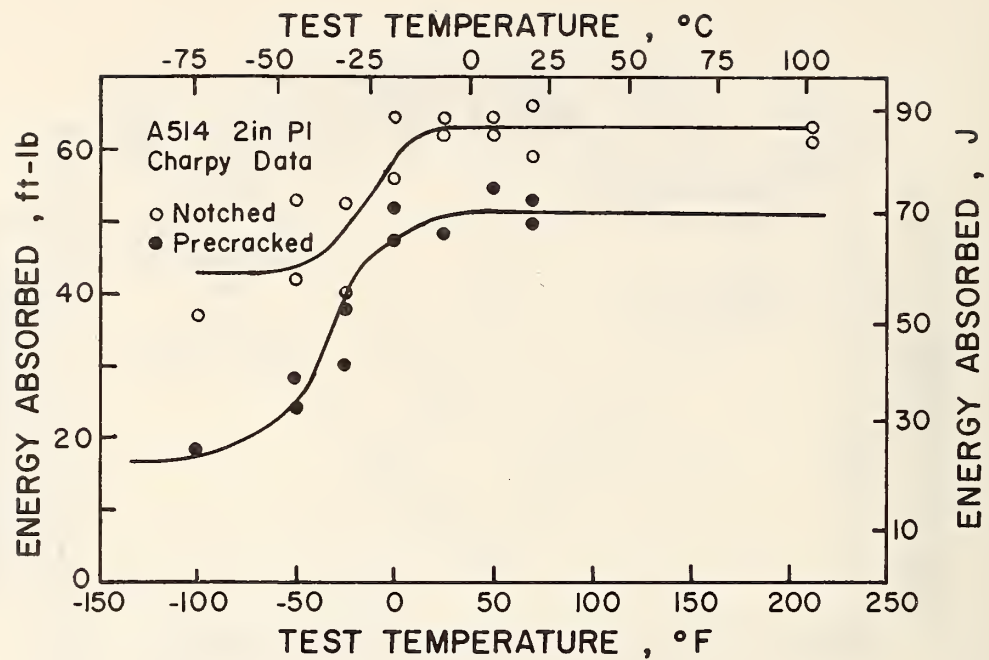


Fig. C.6 A514, 2 in. Plate CVN

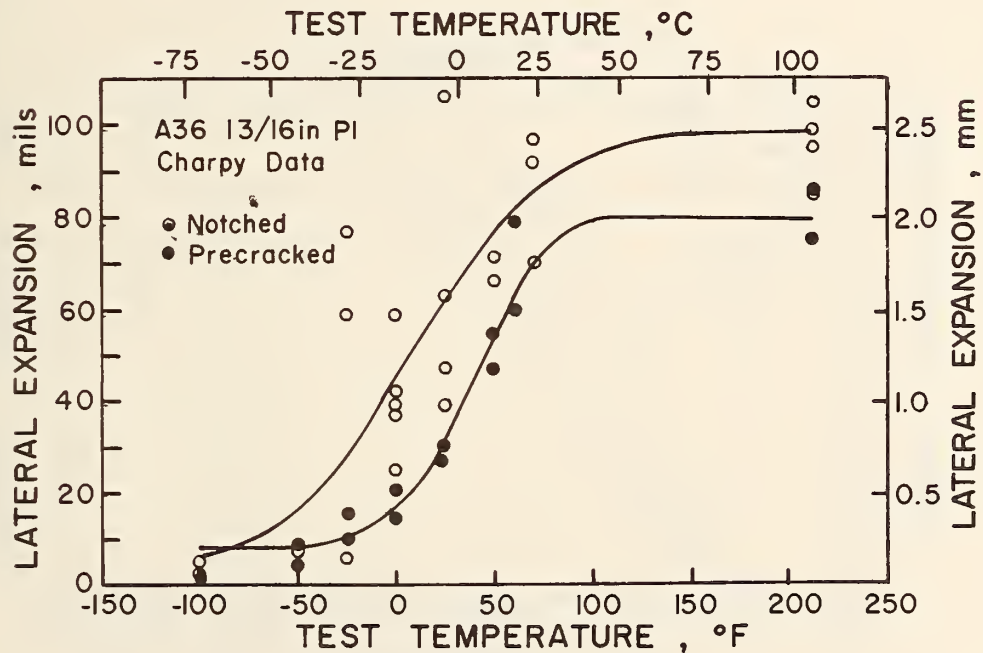
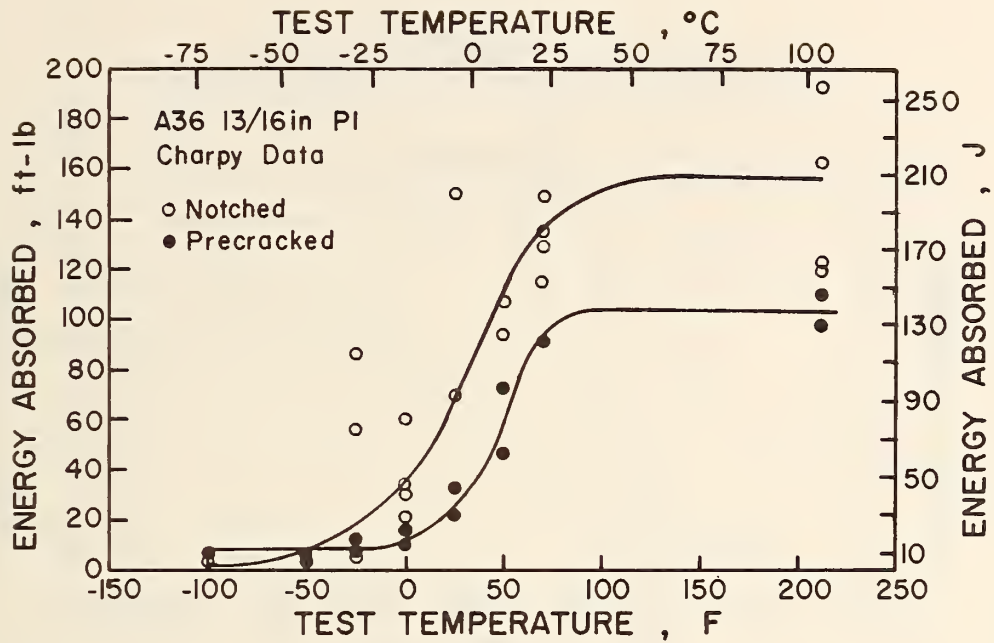


Fig. C.7 A36, W36X260, Web CVN

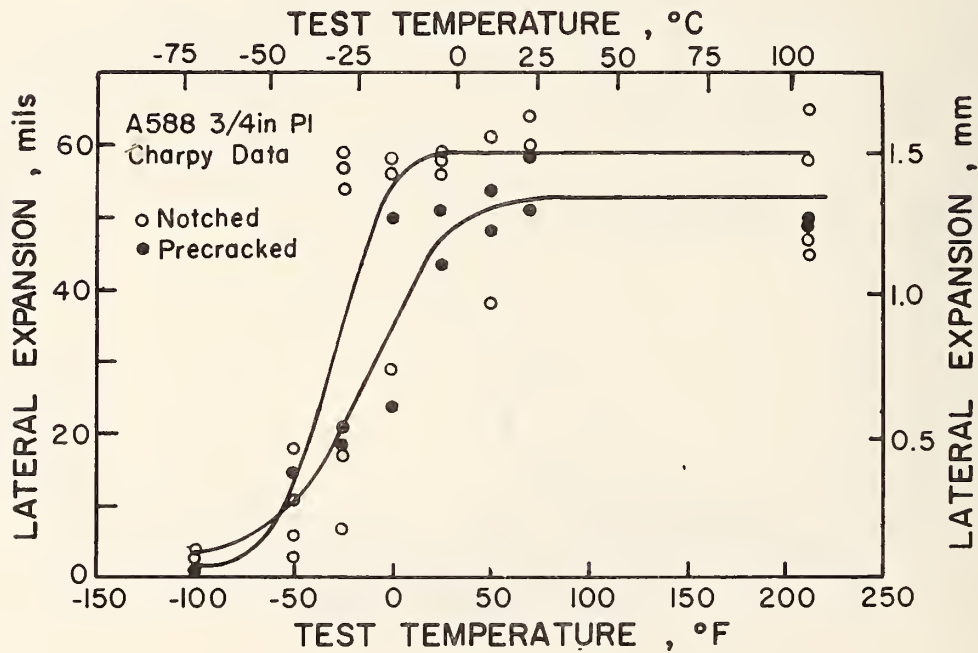
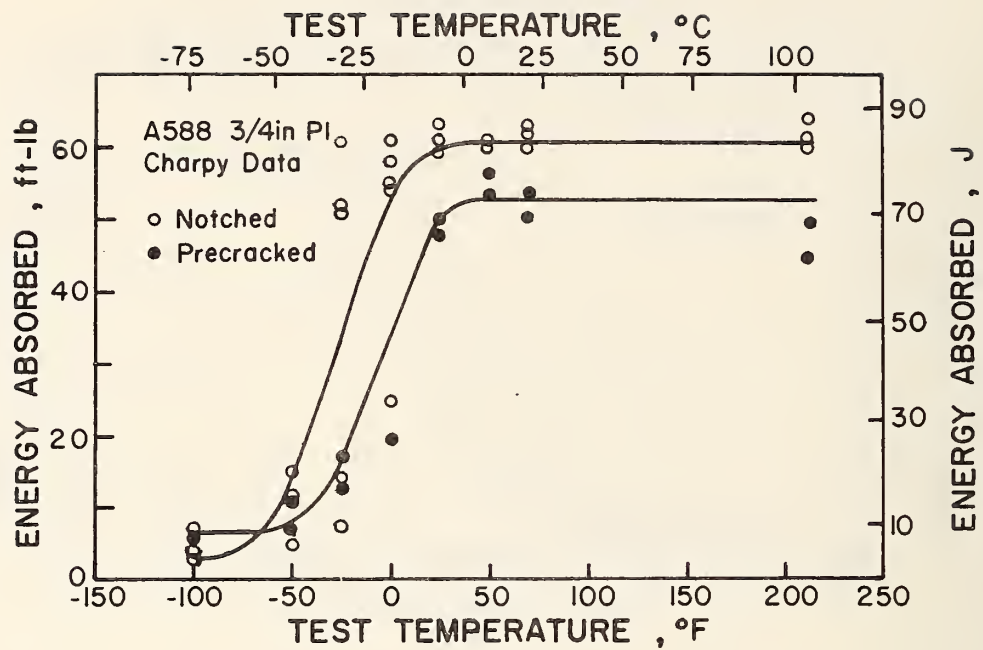


Fig. C.8 A588, W36X230, Web CVN

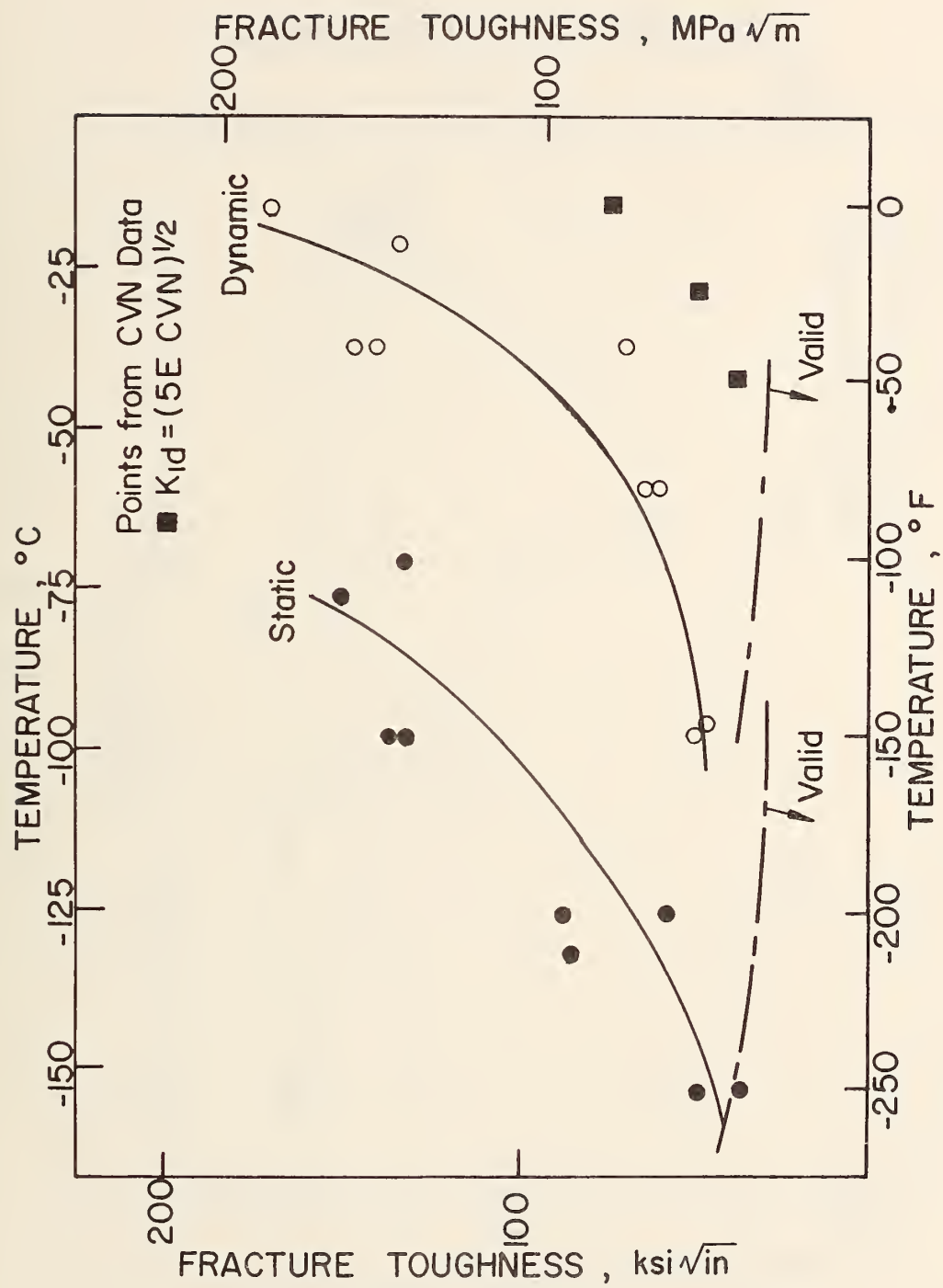


Fig. C.9 Fracture Toughness vs. Temperature (A36, 3/8 in. PL)

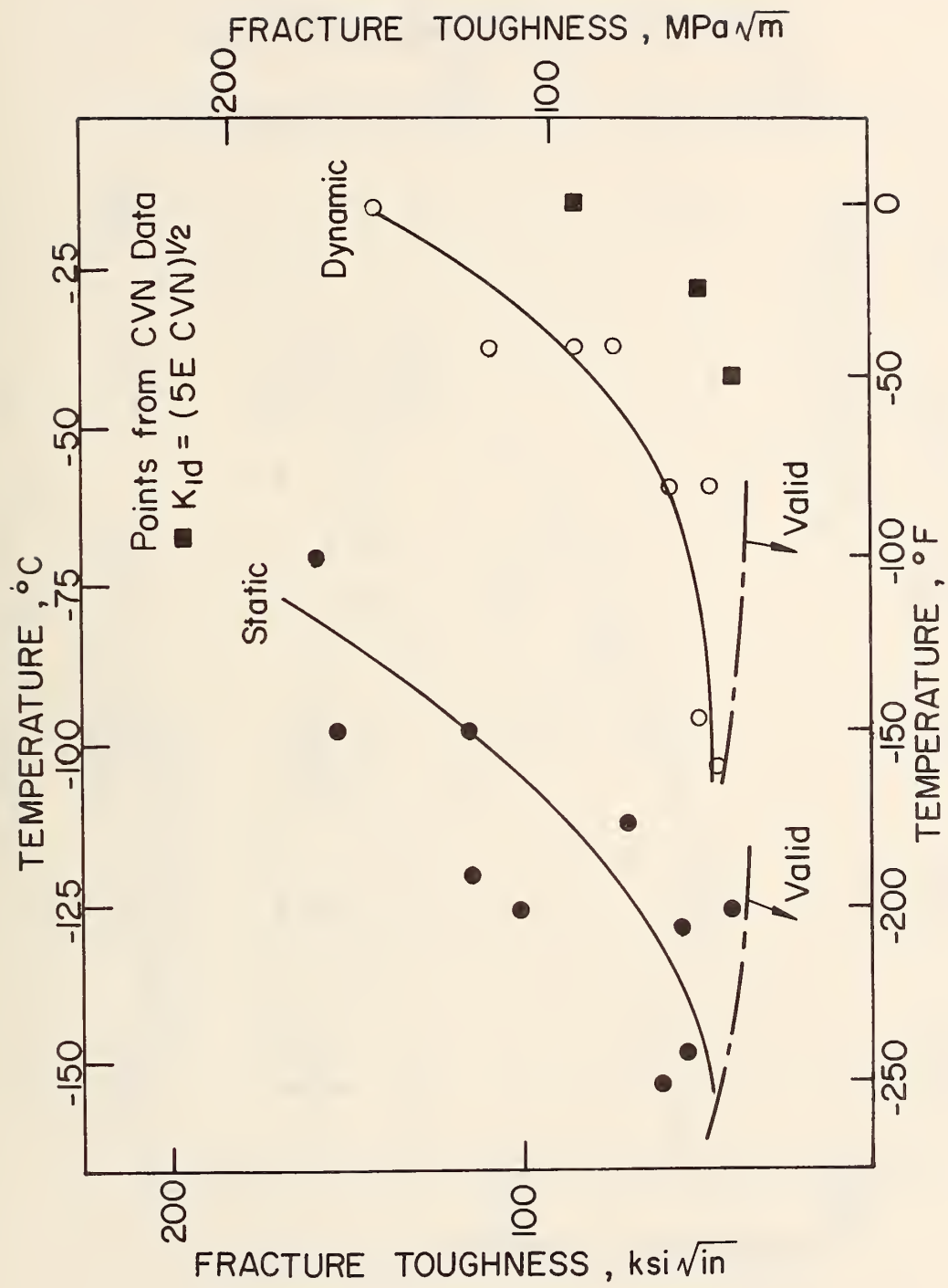


Fig. C.11 Fracture Toughness vs. Temperature (A588, 3/8 in. PL)

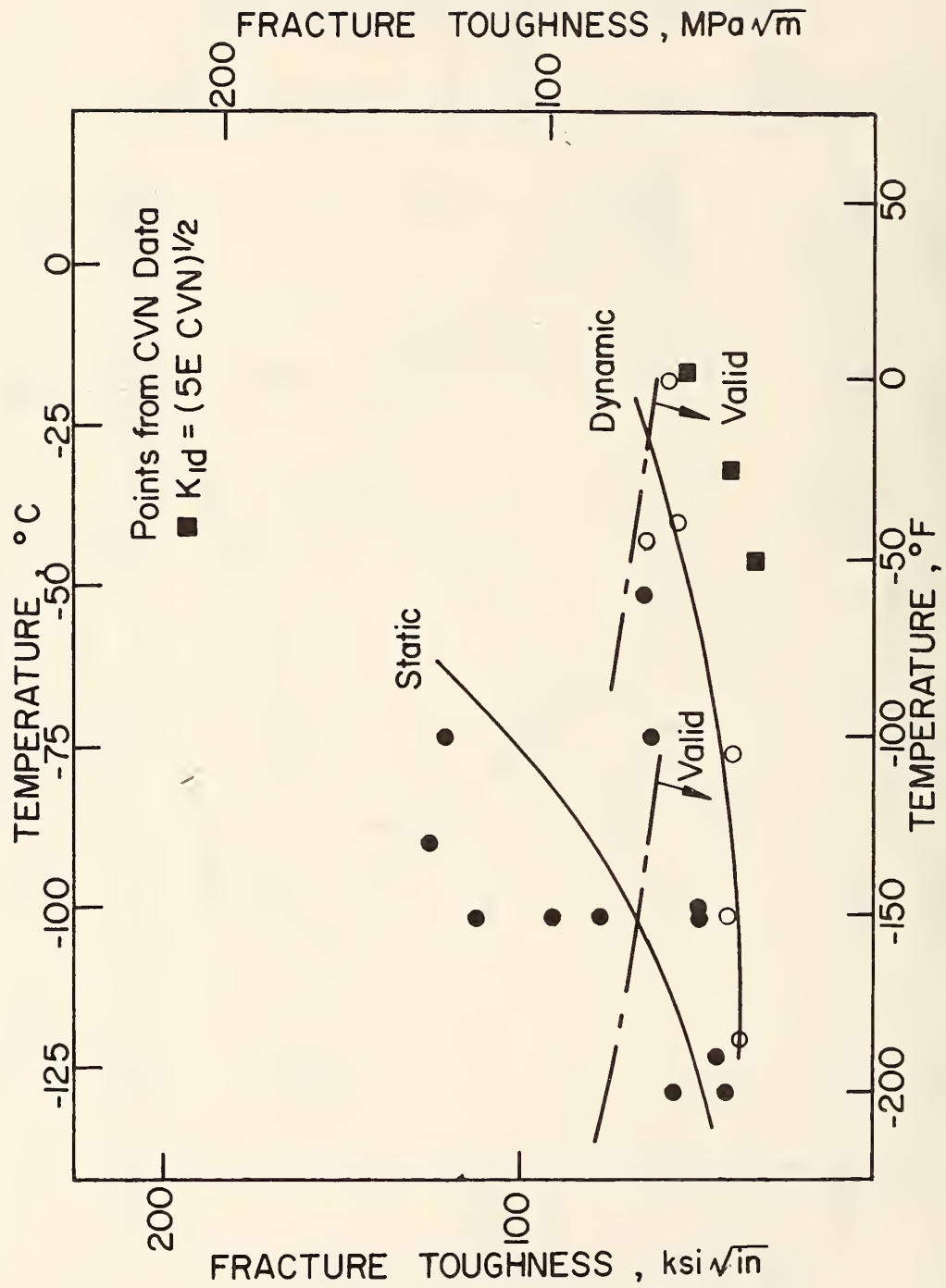


Fig. C.12 Fracture Toughness vs. Temperature (A588, 3 in. PL)

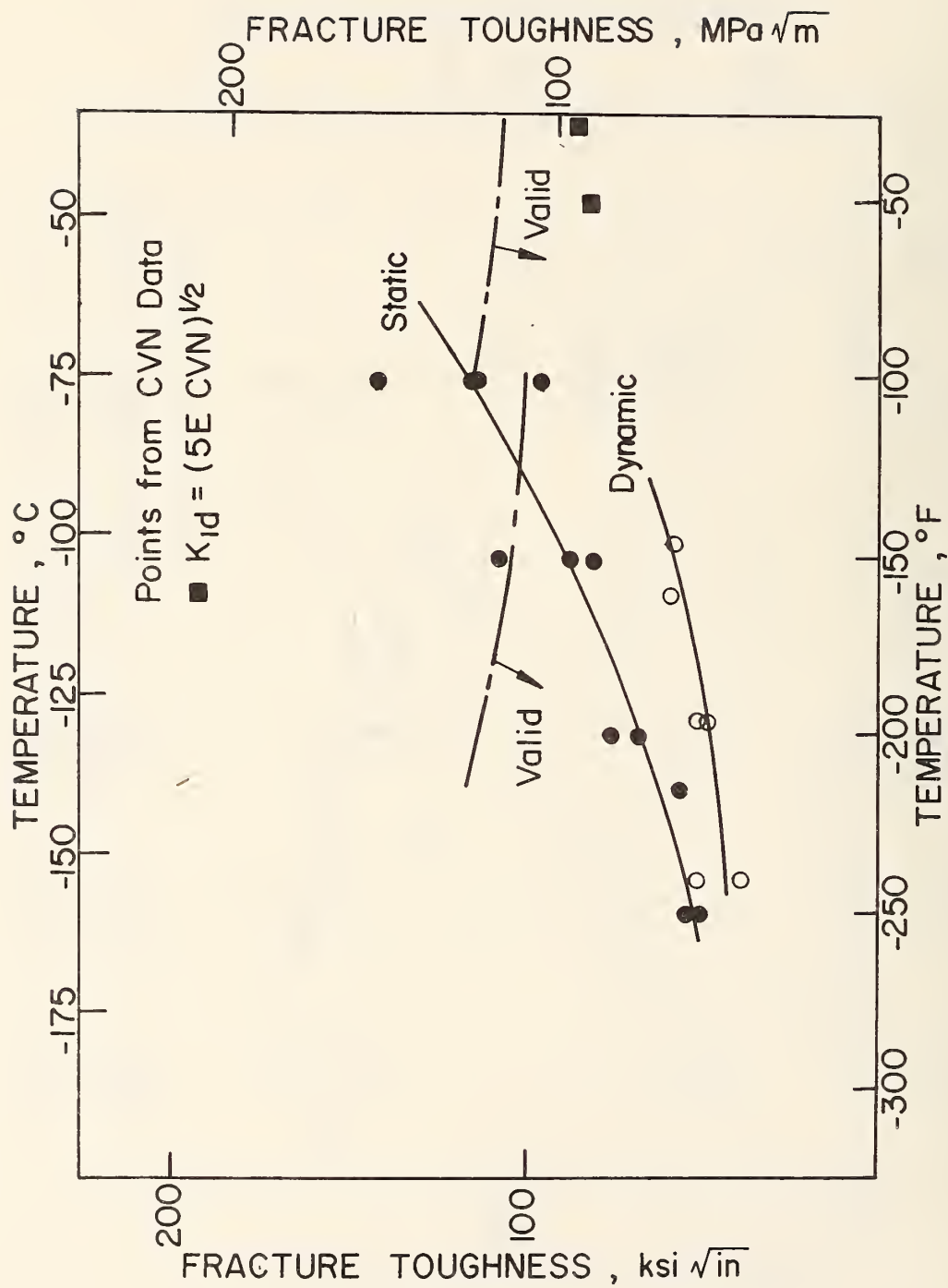


Fig. C.14 Fracture Toughness vs. Temperature (A514, 2 in. PL)

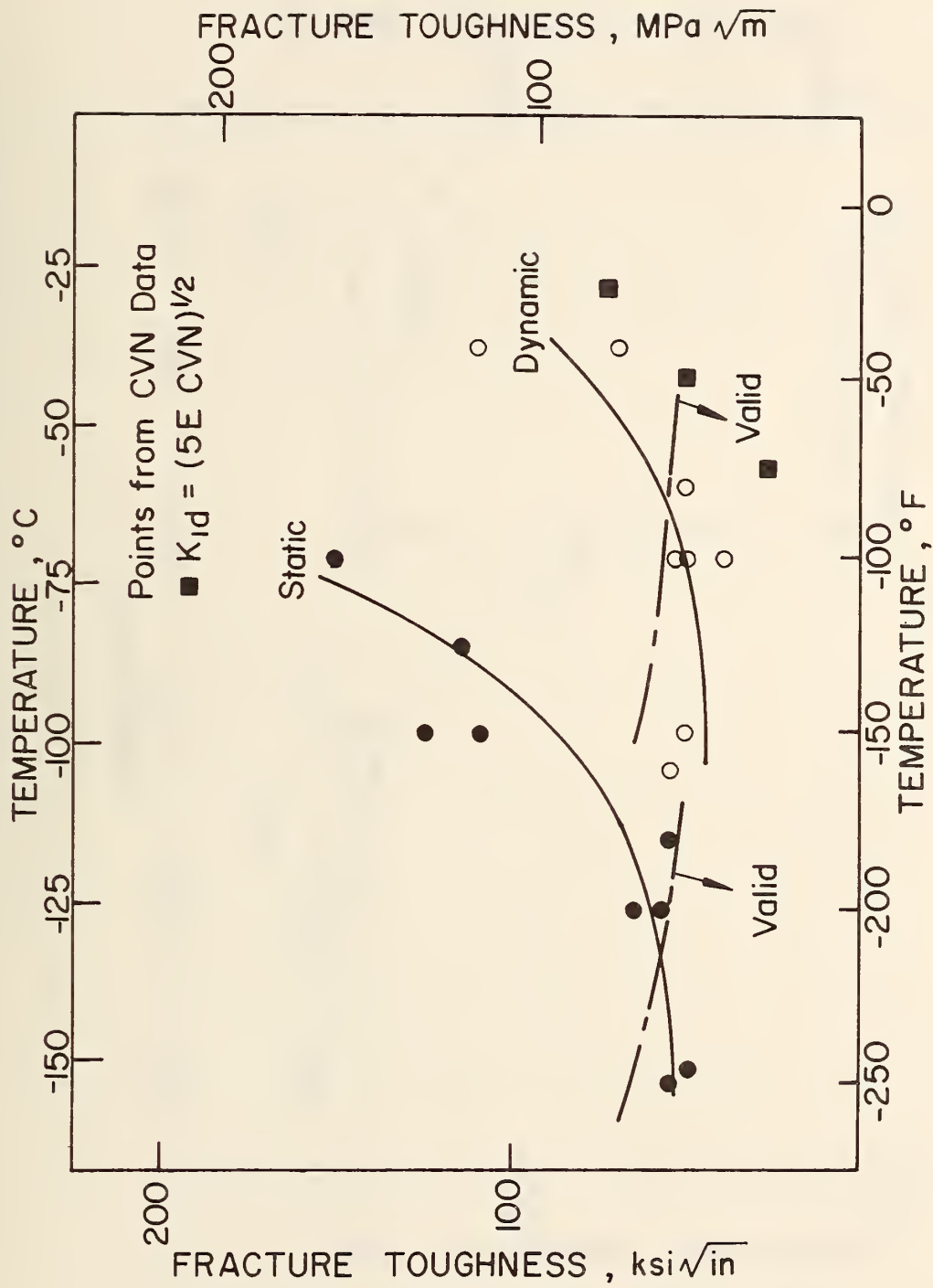


Fig. C.15 Fracture Toughness vs. Temperature (A36, W36X260, Web)

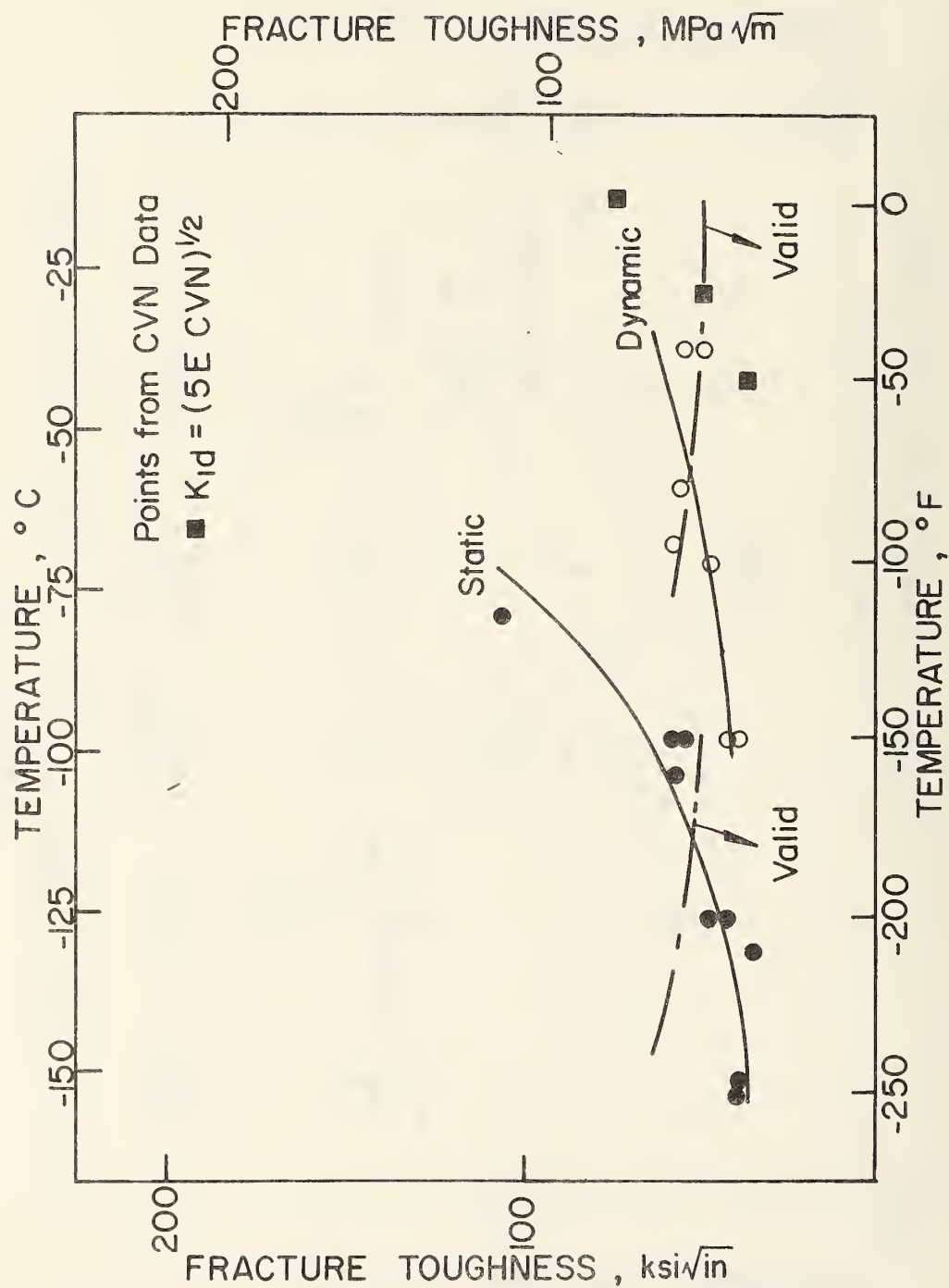


Fig. C.16 Fracture Toughness vs. Temperature (A588, W36X230, Web)

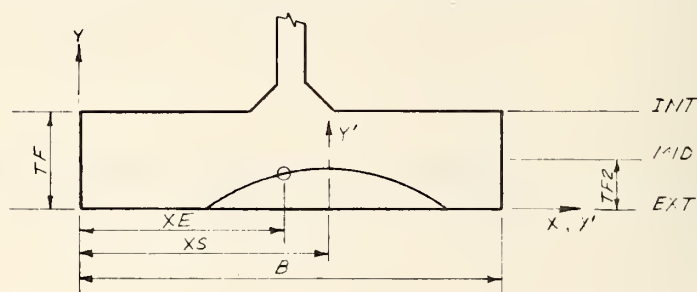
APPENDIX D - STRESS INTENSITY ESTIMATE

PROGRAM STRINT(INPUT,TAPE1=INPUT,OUTPUT,TAPE2=OUTPUT)

BEAM 31A*****

PURPOSE

PROGRAM TO ESTIMATE THE STRESS INTENSITY FOR AN ELLIPTICAL CRACK
GROWING THROUGH THE FLANGE THICKNESS. APPLIED STRESS CONTRIBUTIONS,
NOMINAL SECTION RESIDUAL STRESS CONTRIBUTIONS, AND LOCAL WELD RESIDUAL
STRESS CONTRIBUTIONS ARE ESTIMATED SEPARATELY.



RESIDUAL STRESS INPUT DATA

4 CARDS PER FLANGE LEVEL / 5 LEVELS / 20 CARDS TOTAL

2 LEVELS FOR NOMINAL SECTION RESIDUAL STRESSES

INTERIOR

EXTERIOR

3 LEVELS FOR LOCAL WELD RESIDUAL STRESSES

INTERIOR

MIDDLE

EXTERIOR

ALL RESIDUAL STRESS DATA IS READ IN BF10.0 FORMAT. FOR EACH LEVEL,

READ 12 X DISTANCES ACROSS THE FLANGE WIDTH IN INCREASING ORDER

(2 CARDS). ALSO READ THE 12 RESPECTIVE RESIDUAL STRESSES FOR

EACH POINT (NEXT 2 CARDS). THE FIRST POINT ON THE FLANGE WIDTH

SHOULD BE AT X=0. AND THE LAST POINT SHOULD BE AT X= B. A LINEAR

VARIATION BETWEEN EACH POINT IS ASSUMED.


```

C
C THIRD LAST DATA CARD
C
C SCF      STRESS CONCENTRATION FACTOR
C GOPT     OPTIMUM SEMIMAJOR AXIS DIMENSION FOR THE STRESS CONCENTRATION
C          DECAY WITH CRACK SIZE (SEE REF 19)
C CSD      CRACK SIZE INCREMENT
C AF       LARGEST VALUE OF THE MINOR AXIS CRACK SIZE DESIRED
C AI       (FROM STRESS CONCENTRATION DECAY ROUTINE)
C          =0.0 FOR SHARP REENTRANT CORNER, COVER PLATE DETAILS
C          = THE SMALLEST MESH SIZE IN THE FINITE ELEMENT STRESS
C          CONCENTRATION STUDY FOR A SMOOTH RADIUS REENTRANT CORNER,
C          LATERAL ATTACHMENT DETAILS
C SAS      UNIFORM APPLIED STRESS
C *****
C
C SECOND LAST DATA CARD
C
C XS       AXIS SHIFT BETWEEN THE LOCAL ELLIPSE
C          COORDINATES AND THE REFERENCE AXIS COORDINATES
C XE       DISTANCE IN FLANGE COORDINATE SYSTEM TO THE POINT ON THE CRACK
C          FRONT AT WHICH THE K VALUE IS TO BE FOUND
C B        FLANGE WIDTH
C TF       FLANGE THICKNESS
C TF2      DISTANCE BETWEEN THE EXTERNAL AND MIDDLE LEVELS
C INC      MESH SIZE FOR THE NUMERICAL INTEGRATION
C *****
C
C LAST DATA CARD
C
C FF       =1.0 FOR ELLIPTICAL SURFACE CRACKS
C          =2.0 FOR ELLIPTICAL CORNER CRACKS
C C        SEMIMAJOR AXIS OF THE ELLIPTICAL CRACK
C          C REMAINS CONSTANT THROUGHOUT THE PROGRAM WHILE THE SEMIMINOR
C          CRACK SIZE, A, IS INCREMENTED
C AR       INITIAL SEMIMINOR AXIS CRACK SIZE, A
C *****
C *****
C
C NOMENCLATURE
C
C FS       CORRECTION FACTOR FOR FREE SURFACE
C FW       CORRECTION FACTOR FOR FINITE WIDTH
C FE       CORRECTION FACTOR FOR ELLIPTICAL CRACK SHAPE
C FG       CORRECTION FACTOR FOR STRESS CONCENTRATION
C
C KAS      STRESS INTENSITY CONTRIBUTION FROM THE APPLIED STRESS
C KCHECK   NUMERICAL INTEGRATION CHECK, SHOULD BE EQUAL TO KAS
C KRESID   STRESS INTENSITY CONTRIBUTION FROM THE
C          NOMINAL SECTION RESIDUAL STRESSES
C KLW      STRESS INTENSITY CONTRIBUTION FROM THE
C          LOCAL WELD RESIDUAL STRESSES
C KTOT     KAS + KRESID + KLW
C
C ANFI     SEE FIGURE 5.12
C *****
C *****
C *****

```

```

REAL INC,KRESID,KAS,KLW,KTOT,KCHECK
DIMENSION XI(12),RSI(12)
DIMENSION EX(12),RSE(12)
DIMENSION XLWI(12),SRLWI(12)
DIMENSION XLWM(12),SRLWM(12)
DIMENSION XLWE(12),SRLWE(12)

C
C
      READ(1,1000) (XI(I),I=1,12)
      READ(1,1000) (RSI(I),I=1,12)
      WRITE(2,1005)
1005 FORMAT(///,10X,*INTERIOR FLANGE SURFACE RESIDUAL STRESS DISTRIBUTION*,/)
      WRITE(2,1006) (XI(I),I=1,12)
      WRITE(2,1006) (PSI(I),I=1,12)
      READ(1,1000) (EX(I),I=1,12)
      READ(1,1000) (RSE(I),I=1,12)
      WRITE(2,1007)
1007 FORMAT(///,10X,*EXTERIOR FLANGE SURFACE RESIDUAL STRESS DISTRIBUTION*,/)
      WRITE(2,1006) (EX(I),I=1,12)
      WRITE(2,1006) (RSE(I),I=1,12)
      READ(1,1000) (XLWI(I),I=1,12)
      READ(1,1000) (SRLWI(I),I=1,12)
      WRITE(2,1008)
1008 FORMAT(///,10X,*LOCAL RESIDUAL STRESS DISTRIBUTION-----INTERIOR FLANGE SURFACE*,/)
      WRITE(2,1006) (XLWI(I),I=1,12)
      WRITE(2,1006) (SPLWI(I),I=1,12)
      READ(1,1000) (XLWM(I),I=1,12)
      READ(1,1000) (SRLWM(I),I=1,12)
      WRITE(2,1008)
1008 FORMAT(///,10X,*LOCAL RESIDUAL STRESS DISTRIBUTION-----MID FLANGE THICKNESS*,/)
      WRITE(2,1006) (XLWM(I),I=1,12)
      WRITE(2,1006) (SRLWM(I),I=1,12)
      READ(1,1000) (XLWE(I),I=1,12)
      READ(1,1000) (SRLWE(I),I=1,12)
      WRITE(2,1009)
1009 FORMAT(///,10X,*LOCAL RESIDUAL STRESS DISTRIBUTION-----EXTERIOR FLANGE SURFACE*,/)
      WRITE(2,1006) (XLWE(I),I=1,12)
      WRITE(2,1006) (SRLWE(I),I=1,12)
1006 FORMAT(12F10.3)
1007 FORMAT(8F10.4)
1002 FORMAT(12F10.4)
      WRITE(2,2001)
2001 FORMAT(///,* SCF GOPT CSD AF AI S
1AS*)
      READ(1,1000) SCF,GOPT,CSD,AF,AI,SAS
      WRITE(2,1002) SCF,GOPT,CSD,AF,AI,SAS
      WRITE(2,2002)
2002 FORMAT(///,* XS XE B TF TF2 I
1NC*)
      READ(1,1000) XS,XE,B,TF,TF2,INC
      WRITE(2,1002) XS,XE,B,TF,TF2,INC
      WRITE(2,1009)
1009 FORMAT(///,* FF C AB*)
      READ(1,1000) FF,C,AB
      WRITE(2,1002) FF,C,AB

```

```

      NN=(AF-AB)/CSD
      PI=4.0*ATAN(1.0)
      XXX=0.
      YYY=0.0
100  FORMAT(8F10.0)
      WRITE(2,2000)
2000 FORMAT(///,*,
1      FS          A      C      FG      FW      FE
2, )          KCHECK      KAS      KRESID      KLW      KTOT*
C
C
      DO 101 I=1,NN
      RI=I
      A=RI*CSD+AB
      PIA02B= PI*A/(2.0*TF)
      SKS=1.0-(A/C)**2
C
C      ROUTINE TO FIND FG
C
      IF(SCF.GT.3.0) GO TO 201
      IF(A.LE.AI) GO TO 102
      HOPT=GOPT*(SCF-1.0)/2.0
      GO TO 200
201 HOPT=GOPT*2.0/(SCF-1.0)
200 CONTINUE
      AMOD=A-AI
      HBYG=HOPT/GOPT
      IF(SCF.GT.3.0) GO TO 202
      ZBYG=AMOD/GOPT+HBYG
      CALL ELMINOR(ZBYG,HBYG,FG)
      GO TO 203
202 XBYG=AMOD/GOPT+1.0
      CALL ELMAJOR(XBYG,HBYG,FG)
203 CONTINUE
      GO TO 109
102 FG=SCF
109 CONTINUE
C
C      ROUTINE TO FIND FS
C
      FS=1.0
C
C      ROUTINE TO FIND FW
C
      FWS=(1.0/PIA02B)*TAN(PIA02B)
      FW=SQRT(FWS)
C
C      ROUTINE TO FIND FE
C
      IF(A.GT.TF) GO TO 19
      IF(A.GT.TF) GO TO 19
      CALL ELIPINT(A,C,PI,ELITL)
      FE=1.0/ELITL
20 GO TO 18
19 FE=1.0
18 CONTINUE

```

```

C
C
C
ROUTINE TO CALCULATE THE STRESS INTENSITY
FA1=FF*FW*FS
XSAS=-1.0
CALL ELIPS(XSAS,SAS,A,XS,XE,B,TF,INC,XI,RSI,XXX,YYY,EX,RSE,KRESID
1,FI,TF2,C)
KRESID=FA1*KRESID
XSAS=0.0
CALL ELIPS(XSAS,SAS,A,XS,XE,B,TF,INC,XLWI,SRLWI,XLWM,SRLWM,XLWE,S
1RLWE,KLW,FI,TF2,C)
KLW=FA1*KLW*0.5
XSAS=1.0
CALL ELIPS(XSAS,SAS,A,XS,XE,B,TF,INC,XLWI,SRLWI,XXX,YYY,XLWE,SRLW
1E,KCHECK,FI,TF2,C)
KCHECK=KCHECK*FA1*FG
FA=FW*FS*FG
FEE=(1.0-SKS*COS(FI)**2)**0.25
FEP=FEE*FE
KAS=FA*FEP*SAS*SQRT(PI*A)
KTOT=KRESID+KAS*KLW
WRITE(2,110) A,C,FG,FW,FE,FS,KCHECK,KAS,KRESID,KLW,KTOT
110 FORMAT(11F11.3)
101 CONTINUE
ANFI=(180.0/PI)*FI
WRITE(2,103) ANFI,FI
103 FORMAT(12F10.4)
WRITE(2,5000)
5000 FORMAT(/////////)
STOP
END

```

```

SUBROUTINE ELIPS(XSAS,SAS,A,XS,XE,B,TF,INC,ZI,RSI,ZM,RSM,EX,RSE,K
1RESID,FI,TF2,C)
REAL KRESID,INC
DIMENSION ZI(12),RSI(12),EX(12),RSE(12)
DIMENSION ZM(12),RSM(12)

C
C
C SUBROUTINE TO NUMERICALLY INTEGRATE THE STRESS FROM THE CRACK SURFACE

XA=XE-XS
FUBAR=ABS(1.0-(XA/C)**2)
YA=A*SQRT(FUBAR)
XO=XS
XEND1=B
XEND2=XS+C

C
C
C CENTER MESH ON MINOR AXIS

RN=C/INC
IRN=RN
RIRN=IRN
RIRN=RIRN+0.5
XIC=XS-C
XI=XS-RIRN*INC
IF(XI.LE.XIC) XI=XI+INC

C
M=B/INC
YO=0.0
PI=4.0*ATAN(1.0)
SKS=1.0-(A/C)**2
Z=XA/C
FI=ACOS(Z)
ANFI=(180./PI)*FI
N=TF/INC
KRESID=0.0
DO 100 I=1,M
  RK=I-1
  XB=RR*INC+XI
  IF(XB.GT.XEND2) GO TO 99
  IF(XB.GT.XEND1) GO TO 99
  YB=0.0
  XM=XB-XS
  YE=A*SQRT(1.0-(XM/C)**2)
  IF(XSAS) 1050,1060,1020
1050 CALL RESID(ZI,RSI,EX,RSE,XB,SRSA,SRSB)
  GO TO 1030
1060 IF(YE.GT.TF2) GO TO 1061
  CALL RESID(ZM,RSM,EX,RSE,XB,SRSA,SRSB)
  GO TO 1030
1061 CALL RESID(ZM,RSM,EX,RSE,XB,SRSA,SRSB)
  CALL RESID(ZI,RSI,ZM,RSM,XB,SRSC,SRSD)
  GO TO 1030
1020 SRS=SAS
1030 CONTINUE
  DO 101 II=1,N
    EF=1.0
    RI=II
    IF(RI.EQ.1.0) EF=0.5
    YB=YB+EF*INC

```

```

      YM=YB
      IF(YB.GT.YE) GO TO 100
      YCOXA=YM*C/(XM*A)
      FI1=ATAN(YCOXA)
      ALPHA=YM/(A*SIN(FI1))
      AB=SQRT((XE-XB)**2+(YA-YB)**2)
      OB=SQRT((XO-XB)**2+(YO-YB)**2)
      OA=SQRT((XO-XE)**2+(YO-YA)**2)
      IF(XSAS) 1038,1039,1040
1038 GRAD=(SRSA-SRSB)/TF
      SRS=GRAD*YM+SRSB
      GO TO 1040
1039 IF(YM.GT.TF2) GO TO 4000
      GRAD=(SRSA-SRSB)/TF2
      SRS=GRAD*YM+SRSB
      GO TO 1040
4000 TF3=TF-TF2
      GRAD=(SRSC-SRSD)/TF3
      SRS=GRAD*(YM-TF2)+SRSD
      GO TO 1040
1040 CONTINUE
      P=SRS*INC*INC
      T1=P*SQRT(A)/((PI**1.5)*AB*AB)
      T2=SQRT(OB/OA)
      T3=SQRT(1.0/(ALPHA*ALPHA)-1.0)
      T4=(1.0-SKS*(COS(FI1))**2)**0.25
      KRESID=T1*T2*T3/T4+KRESID
101 CONTINUE
100 CONTINUE
99 CONTINUE
      RETURN
      END

```

```

SUBROUTINE RESID(XI,RSI,XE,RSE,XB,SRSI,SRSE)
DIMENSION XI(12),RSI(12),XE(12),RSE(12)
IF(XI(1).LE.XB.AND.XB.LT.XI(2)) I=1
IF(XI(2).LE.XB.AND.XB.LT.XI(3)) I=2
IF(XI(3).LE.XB.AND.XB.LT.XI(4)) I=3
IF(XI(4).LE.XB.AND.XB.LT.XI(5)) I=4
IF(XI(5).LE.XB.AND.XB.LT.XI(6)) I=5
IF(XI(6).LE.XB.AND.XB.LT.XI(7)) I=6
IF(XI(7).LE.XB.AND.XB.LT.XI(8)) I=7
IF(XI(8).LE.XB.AND.XB.LT.XI(9)) I=8
IF(XI(9).LE.XB.AND.XB.LT.XI(10)) I=9
IF(XI(10).LE.XB.AND.XB.LT.XI(11)) I=10
IF(XB.GE.XI(11)) I=11
J=I+1
SLOPE=(RSI(J)-RSI(I))/(XI(J)-XI(I))
SRSI=SLOPE*(XB-XI(I))+RSI(I)
IF(XE(1).LE.XB.AND.XB.LT.XE(2)) I=1
IF(XE(2).LE.XB.AND.XB.LT.XE(3)) I=2
IF(XE(3).LE.XB.AND.XB.LT.XE(4)) I=3
IF(XE(4).LE.XB.AND.XB.LT.XE(5)) I=4
IF(XE(5).LE.XB.AND.XB.LT.XE(6)) I=5
IF(XE(6).LE.XB.AND.XB.LT.XE(7)) I=6
IF(XE(7).LE.XB.AND.XB.LT.XE(8)) I=7
IF(XE(8).LE.XB.AND.XB.LT.XE(9)) I=8
IF(XE(9).LE.XB.AND.XB.LT.XE(10)) I=9
IF(XE(10).LE.XB.AND.XB.LT.XE(11)) I=10
IF(XB.GE.XE(11)) I=11
J=I+1
SLOPE2=(RSE(J)-RSE(I))/(XE(J)-XE(I))
SRSE=SLOPE2*(XB-XE(I))+RSE(I)
RETURN
END

```



```

SUBROUTINE ELMAJOR(YBYG,HBYG,FG)
R = SQRT(1.0/(1.0-(HBYG*HBYG)))
COSHIN = ALOG(R+SQRT(R*R-1.0))
A2 = COSHIN
S = R*YBYG
COSHIN = ALOG(S+SQRT(S*S-1.0))
AL2 = COSHIN

```

C

```

X1 = (EXP(A2)+EXP(-1.0*A2))/2.0
X2 = ((EXP(AL2)-EXP(-1.0*AL2))/2.0)**2
X3 = (EXP(AL2)+EXP(-1.0*AL2))/(EXP(AL2)-EXP(-1.0*AL2))
X4 = EXP(A2)*(EXP(2.0*A2)-3.0)*(1.0+0.5*X3)*EXP(-2.0*AL2)+X1*X3

```

C

```

FG = 1.0+0.5*X1/X2*X4
RETURN
END

```

```

SUBROUTINE ELMINOR(ZBYG,HBYG,FG)
R = SQRT(1.0/(1.0-(HBYG*HBYG)))
COSHIN = ALOG(R+SQRT(R*R-1.0))
A2 = COSHIN
S = R*ZBYG
SINHIN = ALOG(S+SQRT(S*S+1.0))
AL2 = SINHIN

```

C

```

X1 = 1.0 + 2.0*EXP(2.0*A2) + EXP(4.0*A2)
X2 = 3.0 + 4.0*EXP(-2.0*AL2) + EXP(-4.0*AL2)
X3 = (EXP(2.0*AL2)-EXP(-2.0*AL2))/2.0
X4 = (EXP(2.0*AL2)+EXP(-2.0*AL2))/2.0
X5 = (EXP(2.0*A2)+EXP(-2.0*A2))/2.0
X6 = X4 + X5/2.0 + 1.50
X7 = (X4+1.0)**2.0

```

C

```

FG = (X1*X2/8.0 + X3*X6)/X7
RETURN
END

```

```

SUBROUTINE ELIPINT(A,C,PI,ELITL)
SK=SQRT(1.0-(A/C)**2)
ENEG=1.0
ENEGPS=0.0
ELIPO=0.0
DO 21 IJ=1,100,2
RIJ=IJ
RIJ1=IJ+1
ENEG=ENEG*RIJ*RIJ*SK*SK/(RIJ1*RIJ1)
FNEGP=ENEG/RIJ
ENEGPS=ENEGPS+FNEGP
ELIPN=(PI/2.0)*(1.0-ENEGPS)
DIF=ABS(ELIPN-ELIPO)
IF(DIF.LE.0.005) GO TO 22
ELIPO=ELIPN
21 CONTINUE
22 CONTINUE
ELITL=ELIPN
RETURN
END

```

APPENDIX E - NOMENCLATURE

a	= effective crack length, a_e
a_e	= $a_p + r_y$
a_p	= visual indication of physical crack size at fracture
a'	= equivalent crack size
\bar{B}	= 3 point bend specimen width
b	= flange width
C	= semi-major axis crack size for an elliptical crack
c	= dimension from the plate edge to the end or beginning of the approximated block of residual stress (see Fig. 4.17)
E	= Young's Modulus, 29000 ksi
E_k	= elliptical integral of the second kind
$F(a)$	= $F_E F_G F_S F_W$
F_E	= elliptical crack front correction, $\frac{1}{E_k}$ for $\phi = 90^\circ$
F_G	= stress concentration correction
F_S	= free surface correction
F_W	= finite width correction
K	= linear elastic fracture mechanics stress intensity factor, $\text{ksi}\sqrt{\text{in}} = K_{AS} + K_{RS} + K_{LW} + K_{WR}$
K_{AS}	= stress intensity contributions from the applied stress
K_{RS}	= stress intensity contribution from the nominal section residual stresses
K_{LW}	= stress intensity contribution from the local weld residual stresses
K_{WIL}	= K Wilson See Eq. 2

K_{WR}	= stress intensity contribution from the web restraint
K_c	= fracture toughness value
K_{Id}	= fracture toughness value from the dynamic material test
K_T	= stress concentration factor
k	$= \left[1 - \left(\frac{a}{C} \right)^2 \right]^{-1/2}$
L	= span length, three-point bend specimen (10.0 in)
\bar{L}	= gage length
L_g	= length of attachment
P	= applied load
R	= transition radius
r_y	= plastic zone size
t	= loading time to maximum load
t_o	= time of load application for a static tensile test
T	= testing temperature
T_{cp}	= cover plate thickness
T_f	= flange thickness
T_f'	= equivalent flange thickness
T_g	= thickness of gusset
v_f	= flange crack opening, $= v_{fAS} + v_{fRS}$
v_{fAS}	= flange crack opening from the applied stress
v_{fRS}	= flange crack opening from the residual stress
v_w	= web crack opening
v_{wAS}	= web crack opening from the applied stress

v_{wRS}	= web crack opening from the residual stress
W	= three-point bend specimen depth (3.0 in)
W_g	= gusset width
Y	= dimensionless ratio of (a/W) approximately 4
Z	= fillet weld leg size
β	= orientation angle for principle stresses
ϵ	= strain
σ_1, σ_2	= principle stresses
σ_{AS}	= applied stress
σ_y	= yield stress as a function of loading rate, temperature, and constraint
σ_{yd}	= yield stress as a function of loading rate and temperature
σ_{ys}	= static yield stress at room temperature
σ_r	= stress range
σ_{rs}	= residual stress
ϕ	= parametric angle, see Fig. 5.12

TE 662

•A3

no. FHWA-RD-

77-170

BORROWER

Form DOT F 172
FORMERLY FORM DC

DOT LIBRARY



00055829

